Dynamic NMR Studies of Molecular Motions and Order in Calamitic and Discotic Liquid Crystals

by

Jing Zhang

A dissertation
submitted to the Faculty of Graduate Studies
in partial fulfillment of the requirements for the degree of

Doctor of Philosophy

Department of Physics and Astronomy
University of Manitoba
Winnipeg, Manitoba, Canada

Contents

Abstract

This dissertation reports a study of three kinds of liquid crystals using modern solid state NMR techniques: chiral rod-like liquid crystals, bent-core mesogens and disc-like liquid crystals. The properties and structures of liquid crystals are first introduced in Chapter 1. To understand the principles of different NMR phenomena, quantum mechanical theory is adopted to study different nuclear spin interactions and NMR techniques in Chapter 2.

In the next part of this dissertation (Chapter 3-6), ^{2}H NMR methods are used to investigate the dynamics and structures of some liquid crystal phases. This is first done using the spin relaxation study. The parameters obtained from the model simulation can describe the molecular motion and internal dynamics in the fast motion region. Secondly, we investigate the dynamic process of discotic mesophases and unwound smectic C* phase using the line shape simulation study. 2D ^{2}H NMR exchange experiments are then performed to study the jump process in TGBA* phase and SmC* phase. The above investigation has demonstrated some powerful NMR methods for the dynamic study of liquid crystals.

The third part of the dissertation (Chapter 7-9) is concerned with ^{13}C NMR techniques. After we introduce the quantum theory of different pulse sequences, theoretical models are presented to fit observations such as chemical shifts and dipolar splittings. Moreover high resolution liquid ^{13}C NMR experiments are introduced to study some bent-core molecules. They are useful to assist the carbon peak assignments of these molecules. The structure and ordering information of liquid crystals can be determined in their mesophases.

Finally, a brief summary of the dissertation is given in the last chapter.

Acknowledgments

I would especially like to thank my supervisor, Prof. Ronald Y. Dong, for his continuous guidance, enthusiasm and support throughout my years as a graduate student. Dr. Dong was always there to meet and discuss ideas, to proofread my papers and chapters in my thesis, and to give me valuable comments. He showed me different ways to approach research problems and told me to be persistent to accomplish any goal. I have benefited tremendously from his restless ingeniousness. He also made the laboratory a wonderful workplace by providing good equipment and many reference books. Without his encouragement and constant guidance, I could not have finished this dissertation.

Special thanks also go to my advisory committee, Professors J. O'Neil, J. H. Page, J. van Lierop. A special thanks goes to Mr. Norm Finlay for his continuous technical support.

I am grateful to the Natural Sciences and Engineering Council of Canada, Canada Foundation for Innovation and Brandon University for research funding that made this project possible over the years.

I would also like to thank all my friends in Winnipeg and Brandon, who have helped and entertained me throughout my years in Canada. A special gratitude goes to my former fellow students Dr. Jiadi Xu and Mr. Yanbin Chen for their beneficial discussions and nice help.

A special thanks is extended to my parents, Yan-Min Zhang and Rong-Jie Zhang, my brother, Jian Zhang, for their unconditional support and encouragement over the years. Last but not least, I want to thank my husband, Hui Qiao, for his understanding, encouragement and constant support.

List of Tables

Chapter 1

Introduction to Liquid Crystals

1.1 Overview of Liquid Crystals

Liquid Crystalline (LC) materials provide mesomorphic phases of matter which are important both scientifically and technologically. They show a state of order intermediate between the familiar crystalline lattices and isotropic liquids. Molecules in all liquid crystal phases diffuse about much like the molecules of a liquid, but as they do so they maintain some degree of orientational order and sometimes some positional order also. The earlier discoveries of these kinds of materials were near the end of 19th century by Reinitzer and Lehmann [1, 2]. Then, the potential of liquid crystals as display devices was recognized around 1960. Today, there is a wide variety of applications for liquid crystals: wristwatches, calculators, laptop and TV screens, spatial light modulators, temperature sensors and many more. Liquid crystals can be divided into 'thermotropic'and 'lyotropic'types. Thermotropic LCs exhibit a phase transition into the LC phase as their temperature is changed, whereas lyotropic LCs exhibit phase transitions mainly as a function of solute concentration. Liquid crystals can be formed from molecules with different shapes: rod-like, banana-like and disc-like molecules. Rod-like molecules are the most common type of molecule that forms many different liquid crystal phases. Banana-shaped mesogens provide a new sub-field of thermotropic liquid crystals which have attracted not only great interest because of the fundamental liquid crystal physics, but also their possible practical applications. Disc-like liquid crystals are another interesting material and have different columnar liquid crystal phases.

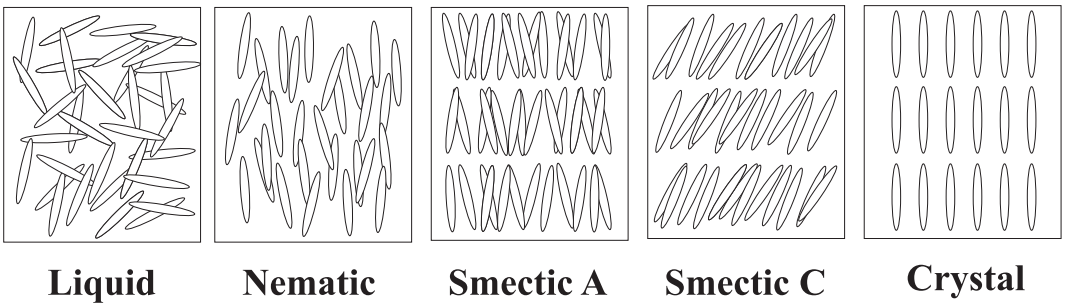

Figure 1.1: The mesophases of calamitic liquid crystals.

.

1.2 Calamitic Liquid Crystals

The most common molecules that form liquid crystal phases are rod-like, i.e., one molecular axis is much longer than the other two. Such compounds are called calamitic liquid crystals and many different mesophases are possible [3–6]. It is important that the molecule is fairly rigid in at least a portion of its length, since it must maintain an elongated shape in order to produce pairwise interactions that favor molecular alignment. Most calamitic liquid crystals are composed of two or more ring structures, which are linked together directly or via rigid linking groups, plus hydrocarbon chains at each end.

When a fully ordered molecular crystal is heated, thermal motions of the molecules increase within the lattice and eventually the vibrations become so intense that the regular arrangement of molecules is broken down with the loss of long-range orientational and positional order to give a disorganised isotropic liquid. A typical phase sequence by cooling from high temperature to low temperature for calamitic liquid crystals is isotropic liquid→ nematic→ smectic A→ smectic C→ smectic B→ solid. Some of the phases will be introduced below.

Nematic Phase

The nematic phase of calamitic liquid crystals is the simplest liquid crystal phase. In the nematic phase the centers of mass of constituent molecules are completely disordered with respect to each other while the long molecular axes statistically point in a preferred direction known as the director. There is no positional order in this phase, which is depicted in Fig. 1.1.

Smectic Phase

In smectic phases, molecules not only have the long range orientational order, but also possess

a certain degree of translational ordering resulting in a layered structure. The molecular centers of mass are, on the average, arranged in equidistant planes. There exist several different types of smectic phases, labelled SmA, SmB, SmC...,SmF [7]. The most common types are SmA and SmC, which are studied in this dissertation (Fig. 1.1). In the smectic A phase, the molecules within the layer are on average aligned parallel to the layer's normal and there is no long-range positional order within the layer. The constituent molecules of the smectic C are tilted within the layers. The smectic B (SmB) phase is more ordered than the SmA phase with the constituent molecules adopting a hexagonal ordering in the layer. The hexagonal nature of the SmB phase generates two tilted analogues called the smectic I (SmI) phase and the smectic F (SmF) phase where the molecules are tilted such that the hexagonal lattice tilts towards the apex and the side, respectively.

1.3 Chiral Liquid Crystals

Chirality means that an object or molecule cannot be superimposed on its mirror image by any translation or rotation. The subject of chirality in liquid crystals is complex and important. Chirality in liquid crystals, and in science generally, has been the subject of intense research in recent years, and is directly responsible for important technological applications. In most chiral liquid crystals, the chirality is generated by a carbon attached with four different structural moieties (chiral center). Two different ways of attachment can produce right hand or left hand chirality. Chiral liquid crystals can also be generated by adding a small amount of chiral dopant molecules into an achiral host phase [7].

The chiral liquid crystalline molecules organize into an asymmetric, chiral structure that takes the form of helices. Sometimes these phases with chiral structures are designated by an asterisk to differentiate them from their non-chiral analogues. For example, the chiral nematic and chiral smectic C phases are frequently designated as the N* and SmC* phases respectively. In some cases the asterisk is also used to indicate the molecules are chiral even if the phase possesses no chiral structure, e.g., SmA* phase.

Chiral Nematic phase

The structure of the chiral nematic phase consists of chiral molecules on one plane having a gentle rotation with respect to their neighbors on neighboring planes. The chirality of the molecules reveals itself as a helical twist of the director in the nematic phase as schematically shown in (Fig. 1.2). The gradual director change describes a helix which has a specific,

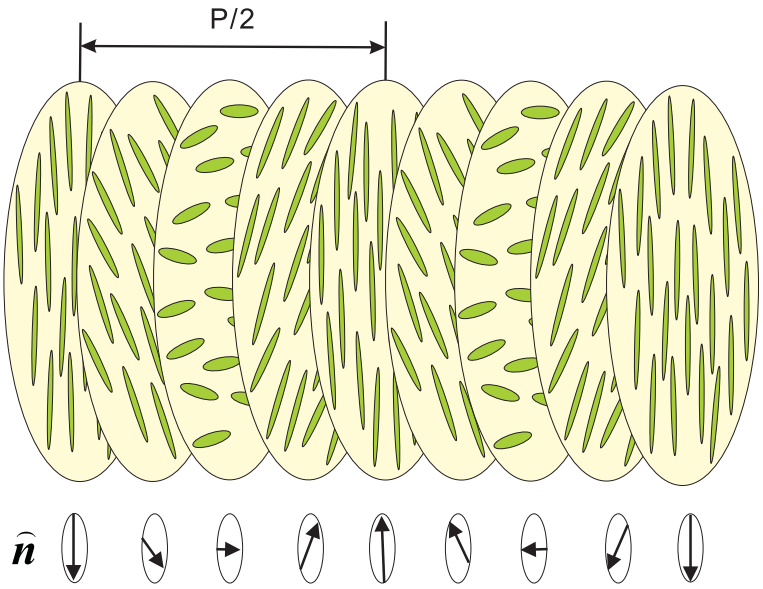

Figure 1.2: Schematic picture of a chiral nematic phase, where $\hat{n}$ is the direction of the directors.

temperature-dependent pitch P. The pitch of a chiral nematic phase is the distance along the helix over which the director has rotated by 360°. The chiral nematic phase is often called cholesteric phase, since many of the first compounds found to form this phase are derivatives of cholesterol.

Chiral Smectic phase

Besides the chiral nematic phase, there are many different types of tilted smectic liquid crystal phases (SmC*, SmI*, SmF*) which could exhibit chirality as a direct result of the molecular chirality of the constituent molecules. The chiral smectic C phase is by far the most important chiral phase. When the molecules of the SmC phase are chiral the phase structure is basically the same as SmC phase except that the molecular chirality causes a slight and gradual change in the direction of the molecular tilt, but there is no change in the tilt angle with respect to the layer normal. This change in tilt direction from layer to layer gradually describes a helix. Such a SmC* structure is shown in Fig. 1.3.

Frustrated Chiral Phase

Frustration occurs when the competition between different influences in a physical system favors incompatible ground states. It is fundamentally interesting to study the phenomenon of frustration in a wide range of systems. Under competing influences, a system can develop structures with complex spatial organizations, and can have a rich variety of transitions between different ordered subphases, or frustrated phases. Microscopic texture observations have demonstrated that some LC materials possess three stable frustrated phases: blue phase

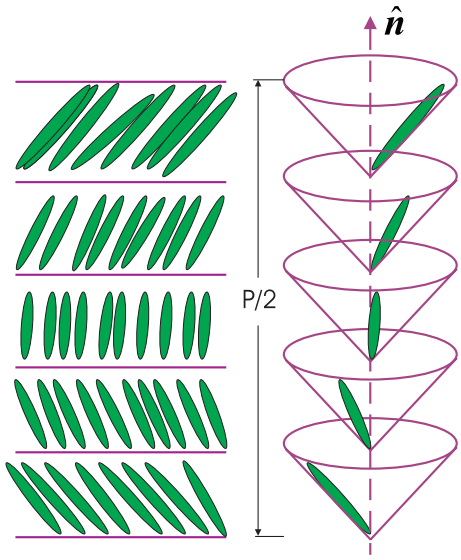

Figure 1.3: Schematic picture of a chiral smectic C phase, where $\hat{n}$ is the direction of the layer normal; P is the pitch length.

(BP), twist grain boundary SmA* (TGBA*) and twist grain boundary SmC* (TGBC*) phases. These are exhibited by highly chiral materials and occur above a chiral nematic phase for only a few degrees before the material clears to the isotropic liquid.

Blue phases exist in the first discovered LC material (cholesteryl benzoate) [1], whereas the recognition of them as distinct thermodynamically stable phases was not made until the 1970s [8, 9]. Theoretical and experimental work have demonstrated that cholesteric liquid crystals of short pitch can form up to three distinct blue phases [10, 11] between the transition of cholesteric phase (N*) and the isotropic phase (I). In order of increasing temperature they are named blue phase I (BPI), blue phase II (BPII) and blue phase III (BPIII). BPI and BPII are cubic phases and have body-centered cubic and simple cubic symmetry, respectively. BPIII is seemingly amorphous with a still unknown local structure. The currently accepted phase diagram for the blue phases as a function of temperature and chirality is shown in Figure 1.4 [12]. From this figure, it can be seen that liquid crystals with very low chirality do not exhibit any blue phases. As the chirality is slowly increased, BPI, BPII and finally BPIII come into existence, but BPII then disappears for very chiral substances. Recently, a critical point has been discovered between the BPIII and isotropic phases [13]. As beautiful in colour as they may be, the blue phases also have many other unique and extremely interesting properties. One of the most remarkable properties is that BPI and BPII phases exhibit a non-vanishing static shear modulus [14]. Shear causes an energetically unfavorable modification of the three-dimensional periodic orientational structure of the blue phase, which could be stabilized by a periodic network of singularities. Additionally, blue phases have been measured

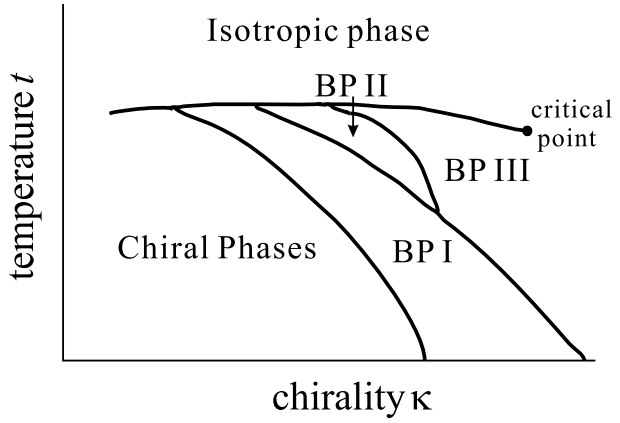

Figure 1.4: Diagrammatic phase diagram for the three blue phases as a function of chirality and temperature [12].

to display a strikingly large viscosity [15]. This phenomenon leads further to an insight that the possibility of a three-dimensional extended ordered structure can form in the blue phase.

Other frustrated smectic liquid crystal phases are twist grain boundary (TGB) phases. These TGB structures arise from the frustration between chirality and the smectic density wave. The first experimental observation of a TGBA* phase was made by Goodby et al [16], followed by numerous reports on other compounds. TGB phases can also be observed in mixtures of liquid crystal materials [17, 18], as well as in liquid crystals doped with chiral materials [19–21]. TGB phases exhibit three distinct structural features: a helical superstructure; smectic layers and a helical axis parallel to the smectic layer plane. The early TGBs exhibit a set of common characteristics, including narrow TGB phase temperature ranges, $T_R \approx 3°\mathrm{C}$, small angular jumps in layer orientation at the GBs [22], and Grandjean-like textures in a wedge cell which was observed by microscope [23]. However, beginning with the 1993 report of the nitrotolane system having homologs with ranges of TGB phases up to 100°C, a distinct class of TGB materials has emerged. In contrast to the usually rather narrow temperature region of TGB existence in single component systems, mixtures may exhibit broad ranges of TGB phases. Addition of a chiral dopant to a host material may also induce twist grain boundary phases with a broad temperature range of existence. Also, giant-block twist grain boundary(GTGB) smectic phases have appeared [24]. For a GTGB phase, the thickness of smectic blocks are usually $l_b > 200\ nm$ and the angular jumps between blocks are $60° < \phi_0 < 90°$. The new TGBs can be characterized by [17, 21, 25–27] : (i) large T_R values; (ii) modulated and/or undulated Grandjean textures; (iii) evidence for large angular jumps between blocks; (iv) electric field-induced unwinding of the TGB helix. The twist grain boundary smectic A* (TGBA*) phase is studied in this dissertation.

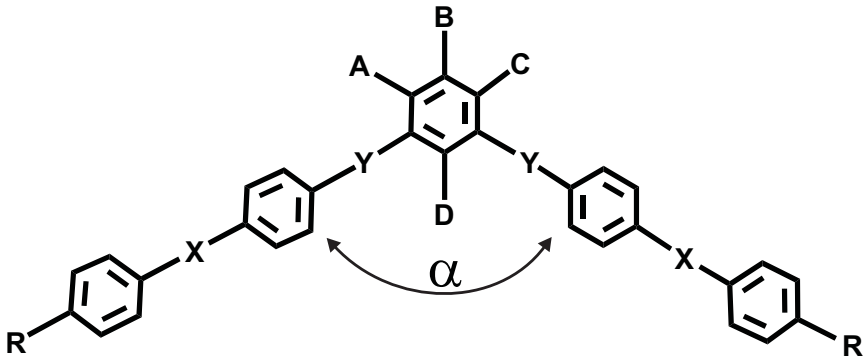

Figure 1.5: Molecular structure of a five rings banana molecule.

.

In addition to the discovery of new TGB and frustrated phases, many fascinating physical studies have been carried out on them in order to examine how various properties are influenced by the presence of a periodic array of defects. These include investigating the dielectric properties and anchoring at surfaces [28, 29], pressure and temperature on multicritical phenomena [30], pretransitional effects and optical studies in confined geometries [31, 32].

1.4 Banana Liquid Crystals

The first banana-shaped liquid crystals were prepared in the research group of Vorländer in 1929 [33]. Since then, many banana-like molecules have been synthesized, and almost all are characterized by a rigid core, formed by five aromatic rings, and two lateral flexible aliphatic chains [34, 35]. Fig. 1.5 represents the molecular structure of a five rings banana molecule, where X, Y and A, B, C, D are linking groups and substituted positions, respectively; R represents the lateral chain; α is the bending angle. Banana-shaped Liquid crystals have attracted considerable interest since they can form ferroelectric phases and their structures are chiral even though the molecule contains no chiral centers [36]. After the first few years of intense studies seven banana-liquid-crystal structures (phases) were distinguished and were tentatively labeled as B1-B7 [37]. The different banana phases are simply identified based on their typical textures and switching properties. The most common phase is B2, which is a fluid smectic phase, having the layer polarization being along the layers, and shows mainly antiferroelectric-type switching under electric fields $E > 6V/\mu m$. There are many theoretical models in the literature to address the question of chirality in the B phase [38, 39]. The short switching time ($\sim$10 ms) and high spontaneous polarization in banana-shaped liquid crystals are very important for many technological applications, such as well-known liquid crystal

displays. Additionally, the non-linear second order susceptibility for the second harmonic generation was found to be very large ($\sim$10 pm/V) for several banana-shaped liquid crystals in their B2 phase [40, 41]. Thus, banana-shaped molecules are very promising for the design of future nonlinear optical applications.

1.5 Discotic Liquid Crystals

Discotic liquid crystals (DLC) are usually composed of disklike molecules containing a rigid core surrounded by equatorial flexible chains. Theoretical calculations had shown, even before the discovery of discotics, that a transition from the isotropic to the nematic phase is possible, in principle, in an assembly of plate-like particles [42–44]. Also, the existence of discotic mesophases was anticipated from theoretical considerations and from analogy with similar phases observed in pyrolitically treated carbonaceous materials [45, 46]. However the first discotic liquid crystal was found in 1977 by the Indian researcher S. Chandrasekhar [47]. Here the molecule has one central benzene ring surrounded by six alkyl chains. A number of similar mesogens were found soon afterwards [48–50] and the basic columnar structure was verified by the x-ray work of Levelut [51, 52]. Since then, discotics have been widely investigated. Depending on the temperature and molecular geometry, discogenic molecules can form either nematic phases or discotic columnar phases with long-range ordering of the columns in a two-dimensional lattice and only short-range intracolumnar order [53–55]. In a columnar phase, the column is formed by stacking up disklike molecules with flexible side chains. These side chains enable the sliding of columns predominantly parallel to adjacent ones. The nematic phase is an orientationally ordered arrangement of discs without any long-range translational order. In recent years, a variety of compounds with quite different molecular architectures can also exhibit columnar mesophases [56–61]. The detailed structures of the various discotic phases and some of their important physical properties are described below.

1.5.1 Discotic Molecules

Generally speaking, discotic molecules have flat (or nearly flat) cores with six or eight long chain substituents, commonly with ester or ether linkage groups. Mostly, the cores of disotic compounds are benzene, triphenylene and truxene, which are shown in Fig. 1.6(a), (b), (c) [49]. For a long time discotic liquid crystals based on these cores were the most studied not only because they are comparatively easy to synthesize but also because they have most of the

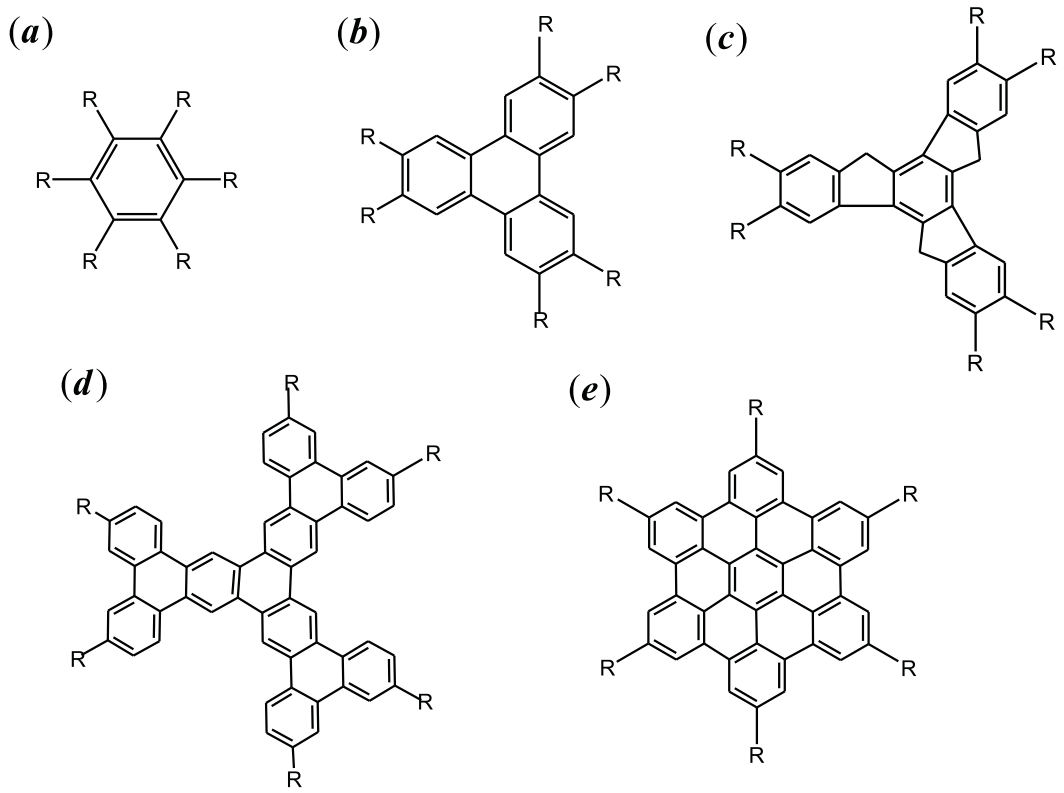

Figure 1.6: Molecular structural formulas of some discotic mesogens: (a) benzene derivatives; (b) triphenylene derivatives; (c) truxene derivatives; (d) hexaphenyltriphenylene derivatives; (e) hexabenzocoronene derivatives. R represents the side chains.

.

properties of the columnar phases. Recently, discotic molecules with very large aromatic cores attracted particular attention because they show high charge-carrier mobilities and hence improved conduction properties. Fig. 1.6(e) is an example of hexabenzocoronene derivatives, which produce highly ordered columnar mesophases [62]. Molecular discogens with larger cores such as hexaphenyltriphenylene derivatives have been synthesized (Fig. 1.6(d)) [63–65]. They are intercalated into a stack of triphenylenes to form a binary, stoichiometric mixture, which exhibits high charge-carrier mobilities and high conductivities.

Besides the monomeric discotic molecules, discotic dimers and polymers also exhibit similar mesophases as the corresponding monomers. The discotic dimers are composed of two monomeric units which are connected by a spacer. However, there are relatively few reports of discotic dimers. The reason is largely due to the difficulties in preparing monofunctionalised discotic precursors. In recent years there has been some interest in the synthesis of triphenylene based dimers [66]. Discotic polymer liquid crystals have also attracted considerable interest [67–72]. The polymer structures are illustrated in Fig. 1.7. The basic monomer units are disc-like mesogens which are attached to the polymer backbone in the main chain

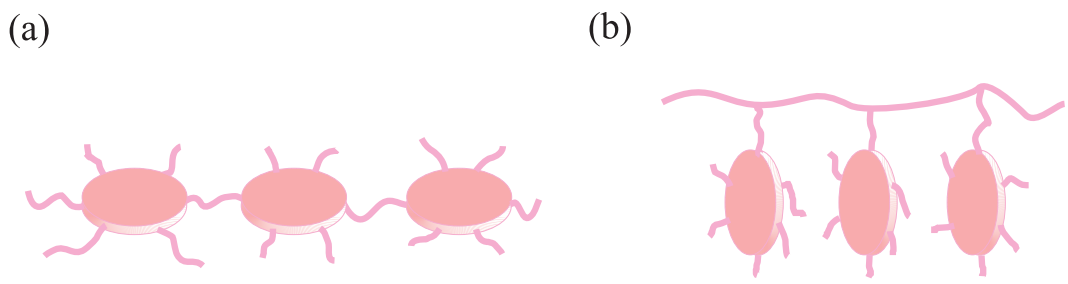

Figure 1.7: Discotic polymers: (a) the main-chain polymer and (b) the side-group polymer.

.

(Fig. 1.7(a)) or as side groups (Fig. 1.7(b)). The dimers or polymers show discotic liquid crystalline behavior and special properties [53, 73, 74]. They can be ordered macroscopically, either by magnetic fields [69, 75], or by mechanical forces [76, 77]. Cooling below the glass transition temperature results in highly ordered anisotropic glasses [69, 76, 77].

1.5.2 Discotic Phases

Optical and x-ray studies have revealed that the discotic molecules can form a series of new mesophases, which are quite different from the classical nematic or smectic types. In Fig. 1.8, the structures of several discotic mesophases are shown: discotic nematic phase (N_D), ordered or disordered hexagonal phase (D_{ho} or D_{hd}), ordered or disordered rectangular phase D_{ro} or D_{rd}), oblique phase (D_{ob}) and tilted discotic phase (D_t). The structure of known discotic columnar phases can be summarized according to the different symmetry classes of the two-dimensional lattice of columns and according to the way the molecules are stacked within the columns [58].

Discotic Nematic Phase

Discotic materials may generate a nematic phase, which is referred to as a discotic nematic phase (N_D). The N_D phase is the least ordered discotic liquid crystal phase and the least viscous.

Hexagonal Columnar Phase

Fig. 1.8 also shows the molecular arrangement in the hexagonal columnar phase (D_h), which is further classified depending upon whether the molecules within the columnar arrays are ordered (D_{ho}) or disordered (D_{hd}). The lattice distance from a molecule to its nearest neighbor in nearby columns is identical whatever the direction.

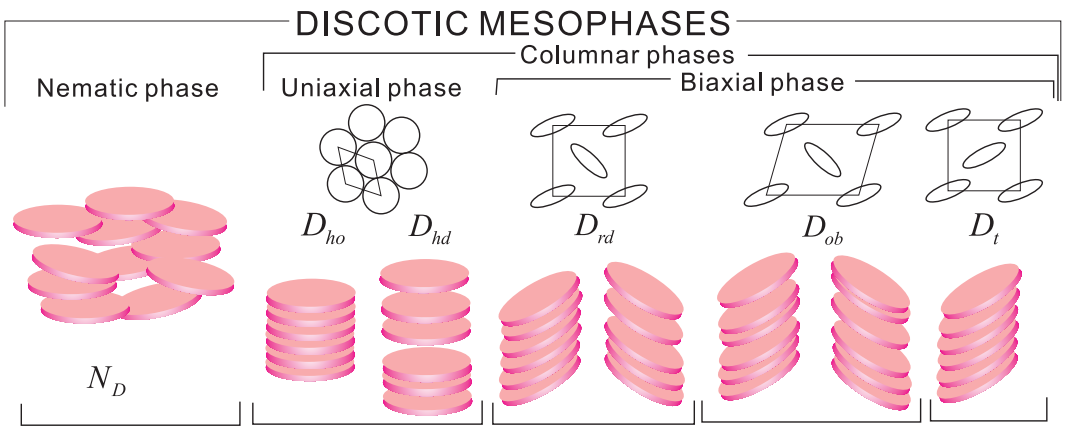

Figure 1.8: Different discotic mesophases of disc-like molecules. Plane views of the two dimensional lattices; ellipses denote discs that are tilted with respect to the column axis [78].

.

Rectangular Columnar Phase

Fig. 1.8 shows the molecular arrangement in the rectangular columnar phase, and as yet only rectangular phases in which the constituent molecules are disordered within the columns (D_{rd}) have been identified. This phase is optically biaxial. For biaxial phases, there are another two kinds of biaxial phases D_{ob} and D_t. D_{ob} refers to oblique arrangement of columns and in D_t phase, the molecular symmetry axis is on average tilted with respect to the columnar axis.

1.5.3 Properties and Applications

Discotic molecules have been studied, mainly for their photoconductive properties and novel charge transport properties. These properties make the discotic molecules good candidates for potential applications in conducting and photoconducting systems. As a matter of fact, the columnar structure of flat discotic conjugated molecules in the mesophase is well suited for electronic transport parallel to the columnar axis. Efforts have also been undertaken to increase the phase stability and the temperature range of the columnar mesophase. This can be achieved with large discotic molecules, since usually the larger the central part of the molecules, the more stable the columnar phase is [79]. Furthermore, in order to improve the physical properties of columnar structures, it was envisaged to build more ordered structures by processing the corresponding materials into thin Langmuir-Blodgett films [80]. Due to their ability to self-organize in highly anisotropic structures at the air-water interface, thin films of discotic molecules may present a considerable interest for applications such as pressure

sensors or anisotropic conductors [81, 82].

1.6 Order Parameters

A distinguishing characteristic of the liquid crystalline state is the tendency of the molecules to point along a preferred direction as the molecules undergo diffusion and rotation. This preferred direction is called the director and is denoted by the unit vector $\hat{n}$. The ordering of molecules in mesophases can be described by the average of the second Legendre polynomial for a rigid rod-like molecule,

$$S = \langle P_2(\cos\beta)\rangle = \left\langle \frac{3}{2}\cos^2\beta - \frac{1}{2} \right\rangle \tag{1.1}$$

where β is the angle between the long molecular axis and the director, and the brackets denote an average over many molecules at the same time or the average over time for a single molecule. The order parameter S can be measured based on diamagnetism, optical birefringence, nuclear magnetic resonance, or Raman scattering measurements. For perfect order, the order parameter has a value of one. Typical values for the order parameter of a liquid crystal range between 0.3 and 0.9 as a function of temperature, and depend on the nature of molecular motion. Now S changes value on going from one phase to the other and may therefore be used to monitor the phase transition.

More generally, the orientation of molecules in mesophases can be described by an orientational distribution function $f(\Omega)$, where Ω denotes Eulerian angles (α, β, γ) that transform between the molecular and the director frame as illustrated in Fig. 1.9. The average of any single-molecule property $X(\Omega)$ over the orientations of all the molecules is defined by [83]

$$\langle X\rangle = \int_0^{2\pi} d\alpha \int_0^{\pi} d\beta \sin\beta \int_0^{2\pi} d\gamma X(\Omega) f(\Omega) \tag{1.2}$$

In terms of the Wigner rotation matrices of rank L, the orientation distribution function can be expanded as

$$f(\Omega) = \sum_{L=0}^{\infty} \sum_{m,m'=-L}^{L} \frac{2L+1}{8\pi^2} \alpha_{Lm'm} D^L_{m'm}(\Omega) \tag{1.3}$$

Applying the normalization condition, the expanded coefficients $\alpha_{Lm'm}$ can be obtained, i.e. $\alpha_{Lm'm} = \left\langle D^{L*}_{m'm}(\Omega)\right\rangle$. For rodlike molecules, the pseudo-potential $V(\Omega)$ is independent

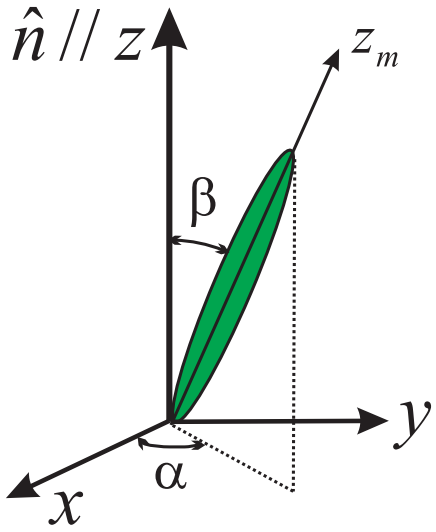

Figure 1.9: Illustration of molecule orientation (x_m, y_m, z_m) in the director frame (x, y, z). α, β are polar angles from the director frame to the molecular frame.

of α and γ due to the uniaxial phase symmetry and the cylindrical molecule symmetry, respectively. The orientation distribution function then becomes

$$\begin{aligned} f(\Omega) &= \frac{f(\beta)}{4\pi^2} \\ f(\beta) &= \sum_{L=0}^{\infty} \frac{2L+1}{2} \langle P_L(\cos\beta)\rangle \, P_L(\cos\beta) \end{aligned} \tag{1.4}$$

where $P_L(\cos\beta) = D^L_{00}(\beta)$. The expansion coefficients in $f(\beta)$ are the orientational order parameters $\langle P_L \rangle$ given by

$$\langle P_L \rangle = \int_0^1 P_L(\cos\beta) f(\cos\beta) d(\cos\beta) \tag{1.5}$$

Among all the orientation parameters of different ranks, only second rank order parameters can be determined from the line position in NMR spectra, although $< P_4 >$ can be inferred from NMR relaxation data.

1.7 Liquid Crystal Samples

The following liquid crystalline samples were studied:

10B1M7-d_{21}

1-methylheptyl 4'-(4-n-decyloxybenzoyloxy)biphenyl-4-carboxylate (10B1M7) is deuterated in its decyloxy chain. The chiral liquid crystal 10B1M7 shows various mesophases at different

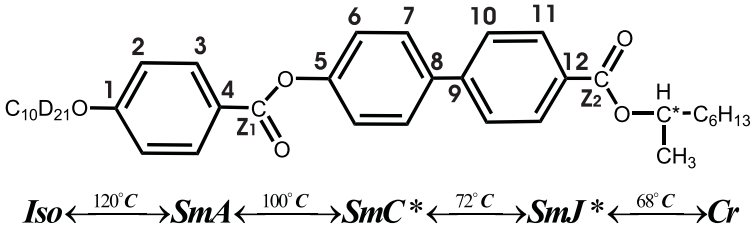

Figure 1.10: The molecular structure of 10B1M7-d_{21}. The transition temperatures are for the non-deuterated sample. The asterisk indicates the chiral carbon center. The labeled numbers are the carbon sites in the ring part.

.

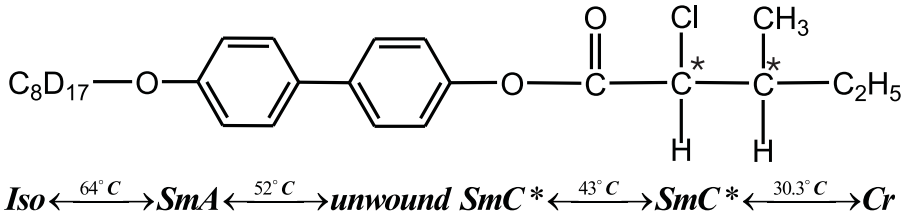

Figure 1.11: The molecular structure of BP8Cl with its transition temperatures. The asterisk indicates the chiral carbon center.

.

ranges of temperature. Its structure is sketched in Fig. 1.10 [84]. The deuterated sample was synthesised by the Pisa group [85]. The synthesis and its characterization were reported elsewhere by other research groups [85, 86]. Our partially deuterated 10B1M7-d_{21} are shown in Fig. 1.10 and the transition temperatures are about 5°C lower than the values shown in the figure. Both ^{2}H and ^{13}C NMR studies were performed on this sample in the smectic A phase and smecitc C* phase.

BP8Cl

4'-(octyloxy)-d_{17} biphenyl-4-yl2-chloro-3-methylpentanoate(BP8Cl) and its transition temperatures are shown in Fig. 1.11. This partially deuterated compound was chosen to study the smectic C* phase by ^{2}H NMR techniques.

11EB1M7-d_2 and 11EB1M7-d_8

4-[4'-(1-methyl heptyloxy)] biphenyl 4-(10-undecenyloxy) benzoate (11EB1M7) is deuterated in the ring part (Fig.1.12). There are many mesophases for this sample [87]. It is the frustrated chiral phases that are of interest here. ^{2}H NMR experiments were done on TGBA* phase. Also ^{13}C NMR studies were carried out on this sample. In particular, TGBA* phase shows no field alignment. This provides a good sample to check the application of 2D exchange

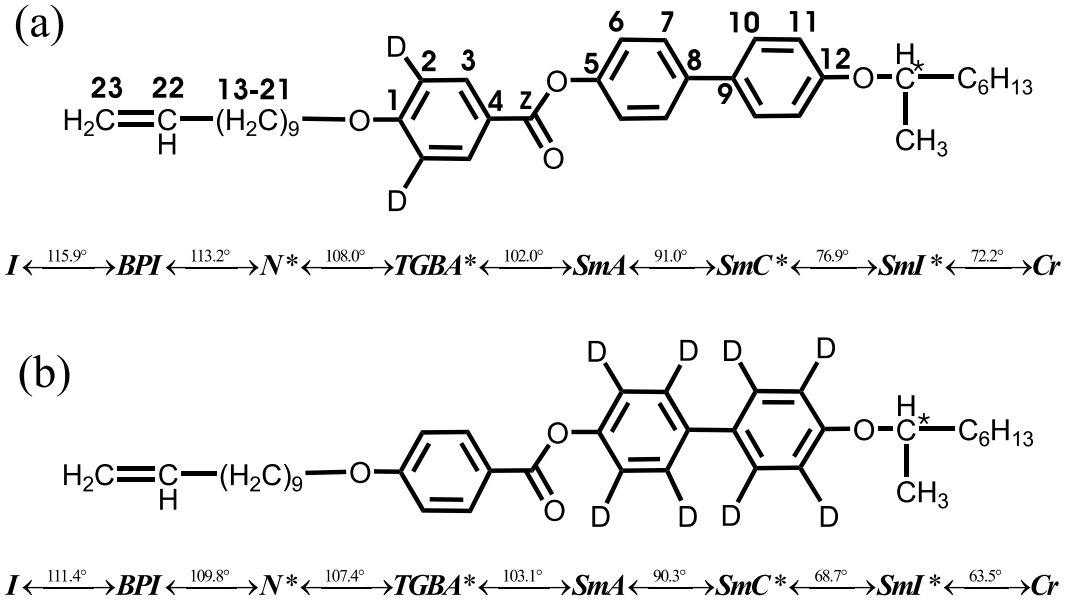

Figure 1.12: Molecular structure of (a) 11EB1M7-d_2 and (b) 11EB1M7-d_8 with their phase transition temperatures. The asterisk indicates the chiral carbon center. Some of the carbon sites are labeled for ^{13}C NMR study.

.

NMR techniques in an unoriented mesophase.

ZLL7/*

(S)-2-methylbutyl-[4'-(4"-heptyloxyphenyl)-benzoyl-4-oxy-(S)-2-((S)-2')-benzoyl) -propionyl)]-propionate(ZLL7/*)(Fig. 1.13). There are partially deuterated samples and a non-deuterated sample. ^{2}H NMR experiments were done on the SmC* phase. Also ^{13}C NMR studies were carried out on the non-deuterated sample. The transition temperatures of ZLL7/*-biphe-D2 were reported before as follows [88]:

$$Iso \overset{127°C}{\longleftrightarrow} SmA \overset{98°C}{\longleftrightarrow} SmC^* \overset{93°C}{\longleftrightarrow} SmC^*_A \overset{69°C}{\longleftrightarrow} SmC^*_{re} \overset{62°C}{\longleftrightarrow} hex \overset{50°C}{\longleftrightarrow} Crystal$$

The transition temperatures of ZLL7/* were reported before as follows [88]:

$$Iso \overset{129°C}{\longleftrightarrow} SmA \overset{104°C}{\longleftrightarrow} SmC^* \overset{98°C}{\longleftrightarrow} SmC^*_A \overset{71°C}{\longleftrightarrow} SmC^*_{re} \overset{65°C}{\longleftrightarrow} hex \overset{54°C}{\longleftrightarrow} Crystal$$

10BrPBBC and 10ClPBBC

The molecular structure and the transition temperatures of (a) 4-Bromo-1,3-phenylene bis[4-(9-decen-1-yloxy)-1,1-biphenyl- 4-carboxylate] (10BrPBBC) and (b) 4-Chloro-1,3-phenylene

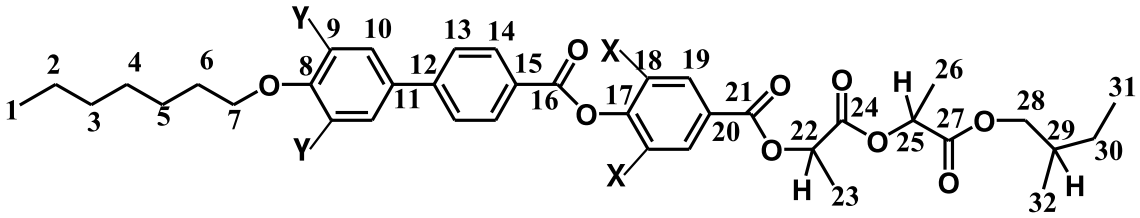

Figure 1.13: Molecular structure of ZLL7/*: ZLL7/* (X=H, Y=H) and ZLL7/*-biphe-D2 (X=H, Y=D). The carbon sites are labeled for ^{13}C NMR study.

.

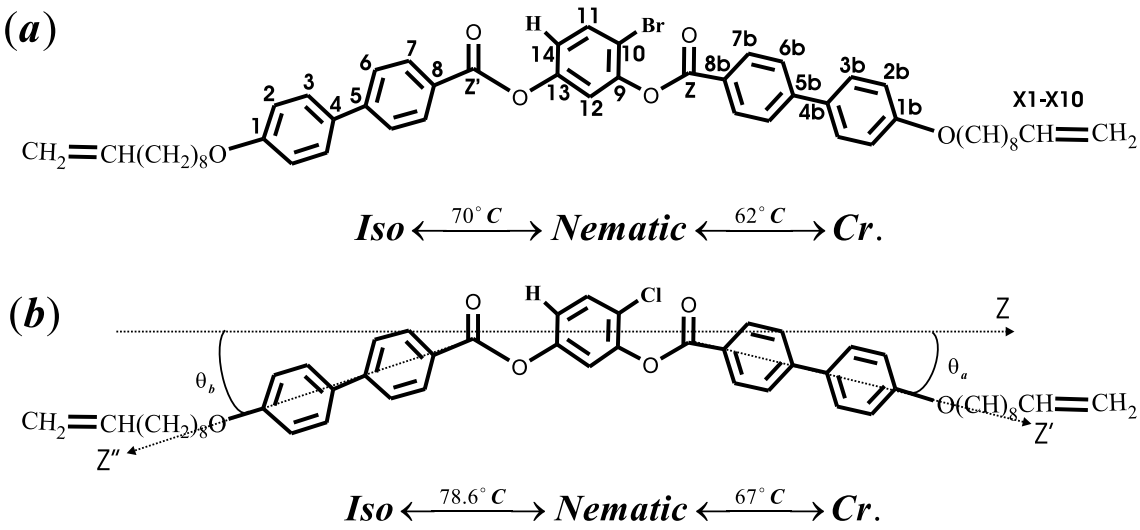

Figure 1.14: Molecular structure of (a) 10BrPBBC and (b) 10ClPBBC with their phase transition temperatures. The carbon sites are labeled for ^{13}C NMR study.

.

bis[4-(9-decen-1-yloxy)-1,1-biphenyl- 4-carboxylate] (10ClPBBC) are shown in Fig. 1.14 [89]. These two samples allow us to study banana-shaped mesogens by ^{13}C NMR studies.

A131

The molecular structure and the transition temperatures of 2-Methyl-3-{[4-(4-octyl-benzoyloxy)-benzylidene]-amino}-benzoic acid 4-(4-dodecyl-phenylazo)-phenyl ester are shown in Fig. 1.15. ^{13}C NMR studies were performed on this sample, since it is known to show a biaxial nematic phase.

HAT5a-d$_6$ and DHAT5-C$_{14}$

The molecular structure and the transition temperatures of (a) 2,7,10,11-tetrapentyloxy 3,6-diacetoxy triphenylene(HAT5a-d$_6$) and (b) Hexadecandioic acid bis-(3,6,7,10,11-pentakis-pentyloxy-triphenylen-2-yl) ester(DHAT5-C$_{14}$) are shown in Fig. 1.16 [67]. ^{2}H NMR studies were done on these two deuterated samples.

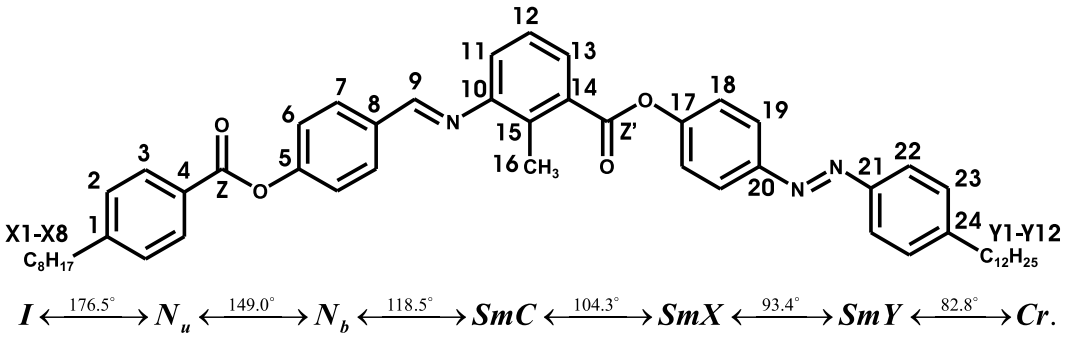

Figure 1.15: Molecular structure of A131 with its phase transition temperatures, where N_u and N_b refer to the uniaxial nematic phase and biaxial nematic phase respectively. The carbon sites are labeled for ^{13}C NMR study.

.

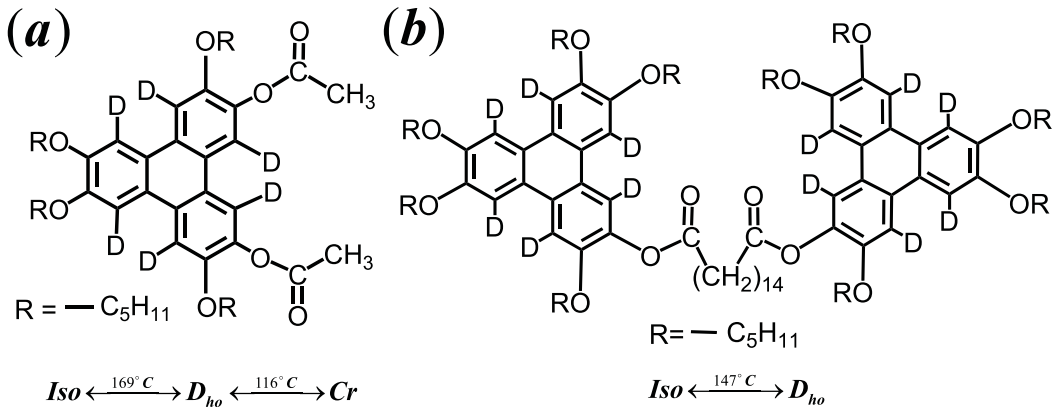

Figure 1.16: Molecular structure of (a) HAT5a-d_6 and (b) DHAT5-C_{14} with their phase transition temperatures.

.

All the above samples were selected for specific research goals. Firstly, relaxation study has been applied to uniaxial phase, i.e. SmA phase [84], but biaxial phase such as SmC* phase has rarely been studied quantitatively. In this dissertation, a chain deuterated 10B1M7-d_{21} was selected to assist this research. The sample shows both SmA and SmC* phases. Secondly, it is hard to detect the phase biaxiality of SmC* using the carbon-13 NMR method. To achieve this goal, angular dependent study has been introduced in the ^{2}H NMR investigation. BP8Cl was selected for this study, since it shows soliton-like distortions in the SmC* phase. The aim is to verify the applicability of Landau theory to explain the effect of magnetic field. Thirdly, discotic phases made from discotic triphenylenes molecules have very high charge and energy transformation. HAT5a-d_6 and DHAT5-C_{14} were selected to study the molecular dynamics and the dimeric discotic liberation under the effect of the spacer group by means of ^{2}H NMR techniques. TGBA* phase is another new and interesting phase whose molecular

dynamics has never been studied by NMR method before. In this dissertation, the sample 11EB1M7 was specially selected and a 2D ^{2}H exchange experiment was introduced to study the diffusion motion of the molecules along the helix in TGBA* phase. Banana-like molecules are another class of promising new liquid crystals for technological applications, and the structure and ordering of this kind of molecules are in need of intensive investigations. Since deuteration of these new LC materials is unavailable, ^{13}C NMR techniques are adopted in this dissertation. The information of chemical shift anisotropy (CSA) tensors is obtained by SUPER experiment. We have chosen 10BrPBBC, 10ClPBBC and A131 for this purpose. The reliability of the CSA results from SUPER experiments is double checked by the SUPER experiment on ZLL7, whose CSA tensors can be compared with the results from density functional theory (DFT). In addition, A131 shows a biaxial nematic phase which is new in thermotropic liquid crystals of bent-core molecules. High resolution liquid NMR techniques were used to facilitate the peak assignments for the isotropic spectrum of this sample. The work on the ordering of this kind of molecules in the biaxial nematic is another objective of this dissertation.

References

[1] Reinitzer, F. *Monatsh. Chem.* **1888**, *9*, 421.

[2] Lehmann, O. *Z. Phys. Chem.* **1889**, *4*, 462.

[3] Tschierske, C.; Lunow, A.; Zaschke, H. *Liq. Cryst.* **1990**, *8*, 885.

[4] Pudlo, P.; Thiem, J.; Vill, V. *Chemische Berichte* **1990**, *123*, 1129.

[5] Kroin, T.; Palangana, A. J.; Figueiredoneto, A. M. *Phys. Rev. A* **1989**, *39*, 5373.

[6] Kohne, B.; Praefcke, K.; Omar, R. S.; Frolow, F. *Zeitschrift Fur Naturforschung Section B-a J. Chem. Sci.* **1986**, *41*, 736.

[7] Collings, P. J.; Hird, M. *Introduction to Liquid Crystals*; Taylor & Francis, 1997.

[8] Armitage, D.; Price, F. P. *J. Appl. Phys.* **1976**, *47*, 2735.

[9] Coates, D.; Gray, G. W. *Phys. Lett. A* **1973**, *A 45*, 115.

[10] Crooker, P. P. *Liq. Cryst.* **1989**, *5*, 751.

[11] Stegemeyer, H.; Blumel, T.; Hiltrop, K.; Onusseit, H.; Porsch, F. *Liq. Cryst.* **1986**, *1*, 3.

[12] Yang, D. K.; Crooker, P. P. *Phys. Rev. A* **1987**, *35*, 4419.

[13] Kutnjak, Z.; Garland, C. W.; Passmore, J. L.; Collings, P. J. *Phys. Rev. Lett.* **1995**, *74*, 4859.

[14] Kleiman, R. N.; Bishop, D. J.; Pindak, R.; Taborek, P. *Phys. Rev. Lett.* **1984**, *55*, 2137.

[15] Stegemeyer, H.; Pollmann, P. *Mol. Cryst. Liq. Cryst.* **1982**, *82*, 123.

[16] Goodby, J. W.; Waugh, M. A.; Stein, S. M.; Chin, E.; Pindak, R.; Patel, J. S. *J. Am. Chem. Soc.* **1989**, *111*, 8119.

[17] Kuczynski, W.; Stegemeyer, H. *Mol. Cryst. Liq. Cryst.* **1995**, *260*, 377.

[18] Patel, J. S.; Lee, S. D.; Suh, S. W.; Goodby, J. W. *Liq. Cryst.* **1993**, *13*, 313.

[19] Archer, P.; Dierking, I. *Liq. Cryst.* **2006**, *33*, 257.

[20] Chen, W. R.; Hwang, J. C. *Mol. Cryst. Liq. Cryst.* **2004**, *423*, 85.

[21] Dierking, I. *Liq. Crys.* **2001**, *28*, 165.

[22] Navailles, L.; Barois, P.; Nguyen, H. T. *Phys. Rev. Lett.* **1993**, *71*, 545.

[23] Dierking, I.; Lagerwall, S. T. *Liq. Cryst.* **1999**, *26*, 83.

[24] Fernsler, J.; Hough, L.; Shao, R. F.; Maclennan, J. E.; Navailles, L.; Brunet, M.; Madhusudana, N. V.; Mondain-Monval, O.; Boyer, C.; Zasadzinski, J.; Rego, J. A.; Walba, D. M.; Clark, N. A. *Proceedings Nat. Acad. Sciences U.S.A.* **2005**, *102*, 14191.

[25] Pramod, P. A.; Pratibha, R.; Madhusudana, N. V. *Curr. Sci.* **1997**, *73*, 761.

[26] Ribeiro, A. C.; Barois, P.; Galerne, Y.; Oswald, L.; Guillon, D. *Eur. Phys. J. B* **1999**, *11*, 121.

[27] Brunet, M.; Navailles, L.; Clark, N. A. *Eur. Phys. J. E* **2002**, *7*, 5.

[28] Ismaili, M.; Bougrioua, F.; Isaert, N.; Legrand, C.; Nguyen, H. T. *Phys. Rev. E* **2002**, *65*, 011701.

[29] Kundu, S.; Majumder, T. P.; Roy, S. K.; Darius, M.; Haase, W. *Ferroelectrics* **2000**, *244*, 339.

[30] Anakkar, A.; Isaert, N.; Ismaili, M.; Buisine, J. M.; Nguyen, H. T. *Phys. Rev. E* **1999**, *60*, 620.

[31] Hubert, P. *Liq. Cryst.* **1999**, *26*, 1379.

[32] Chanishvili, A.; Chilaya, G.; Neundorf, M.; Pelzl, G.; Petriashvili, G. *Cryst. Resear. Tech.* **1996**, *31*, 679.

[33] Vorlander, D. *Ber. Dtsch. Chem. Ges.* **1929**, *62*, 2831.

[34] Eremin, A.; Wirth, I.; Diele, S.; Pelzl, G.; Schmalfuss, H.; Kresse, H.; Nadasi, H.; Fodor-Csorba, K.; Gacs-Baitz, E.; Weissflog, W. *Liq. Cryst.* **2002**, *29*, 775.

[35] Pelzl, G.; Diele, S.; Grande, S.; Jakli, A.; Lischka, C.; Kresse, H.; Schmalfuss, H.; Wirth, I.; Weissflog, W. *Liq. Cryst.* **1999**, *26*, 401.

[36] Niori, T.; Sekine, T.; Watanabe, J.; Furukawa, T.; Takezoe, H. *J. Mater. Chem.* **1996**, *7*, 1231.

[37] Pelzl, G.; Diele, S.; Weissflog, W. *Adv. Mater.* **1999**, *11*, 707.

[38] Tschierske, C.; Dantlgraber, G. *Pramana-J. Phys.* **2003**, *61*, 455.

[39] Kurosu, H.; Kawasaki, M.; Hirose, M.; Yamada, M.; Kang, S.; Thisayukta, J.; Sone, M.; Takezoe, H.; Watanabe, J. *J. Phys. Chem. A.* **2004**, *108*, 4674.

[40] Etxebarria, J.; Folcia, C. L.; Ortega, J.; Ros, M. B. *Phys. Rev. E* **2003**, *67*, 042702.

[41] Ortega, J.; Folcia, C. L.; Etxebarria, J.; Gimeno, N.; Ros, M. B. *Phys. Rev. E.* **2003**, *68*, 011707.

[42] Ishihara, A. *J. Chem. Phys.* **1951**, *19*, 1142.

[43] Straley, J. P. *Phys. Rev. A* **1974**, *10*, 1881.

[44] Alben, R. *Phys. Rev. Lett.* **1973**, *30*, 778.

[45] Gasparoux, H.; Destrade, C.; Fug, G. *Molecular Crystals and Liquid Crystals* **1980**, *59*, 109.

[46] Kats, E. I. *Zhurnal Eksperimentalnoi i Teoreticheskoi Fiziki* **1978**, *75*, 1819.

[47] Chandrasekhar, S.; Sadashiva, B. K.; Suresh, K. A. *Pramana* **1977**, *9*, 471.

[48] Dubois, J. C. *Ann. De Phys.* **1978**, *3*, 131.

[49] Destrade, C.; Tinh, N. H.; Gasparoux, H. *Mol. Cryst. Liq. Cryst.* **1981**, *71*, 111.

[50] Destrade, C.; Tinh, N. H.; Malthete, J.; Jacques, J. *Phys. Lett.* **1980**, *79A*, 189.

[51] Levelut, A. M. *J. Chim. Phys. Physico-Chimie Biologique* **1983**, *80*, 149.

[52] Levelut, A. M. *J. Physique Lett.* **1979**, *40*, L81.

[53] Kreuder, W.; Ringsdorf, H. *Makromol. Chem. Rapid Commun.* **1983**, *4*, 807.

[54] Levelut, A. M. *J. Chim. Phys., Physico-Chimie Biologique* **1983**, *80*, 149.

[55] Voigtmartin, I. G.; Durst, H.; Brzezinski, V.; Krug, H.; Kreuder, W.; Ringsdorf, H. *Angew. Chem. Int. Ed. Engl.* **1989**, *28*, 323.

[56] Goldfarb, D.; Belsky, I.; Luz, Z. *J. Chem. Phys.* **1983**, *79*, 6203.

[57] Goldfarb, D.; Luz, Z.; Zimmermann, H. *J. Chem. Phys.* **1983**, *78*, 7065.

[58] Goldfarb, D.; Poupko, R.; Luz, Z.; Zimmermann, H. *J. Chem. Phys.* **1983**, *79*, 4035.

[59] Kawada, H.; Matsunaga, Y.; Takamura, T.; Terada, M. *Can. J. Chem.* **1988**, *66*, 1867.

[60] Kuebler, S. C.; Boeffel, C.; Spiess, H. W. *Liq. Crys.* **1995**, *18*, 309.

[61] Leisen, J.; Werth, M.; Boeffel, C.; Spiess, H. W. *J. Chem. Phys.* **1992**, *97*, 3749; triphenylene.

[62] Fechtenkotter, A.; Tchebotareva, N.; Watson, M.; Mullen, K. *Tetrahedron* **2001**, *57*, 3769.

[63] Boden, N.; Bushby, R. J.; Cooke, G.; Lozman, O. R.; Lu, Z. *J. Am. Chem. Soc.* **2001**, *123*, 7915.

[64] Boden, N.; Bushby, R. J.; Liu, Q. Y.; Lozman, O. R. *J. Mater. Chem.* **2001**, *11*, 1612.

[65] Boden, N.; Bushby, R. J.; Lu, Z. B.; Lozman, O. R. *Liq. Crys.* **2001**, *28*, 657.

[66] Boden, N.; Bushby, R. J.; Cammidge, A. N.; Martin, P. S. *J. Mater. Chem.* **1995**, *5*, 1857.

[67] Kranig, W.; Huser, B.; Spiess, H. W.; Kreuder, W.; Ringsdorf, H.; Zimmermann, H. *Adv. Mater.* **1990**, *2*, 36.

[68] Kranig, W.; Boeffel, C.; Spiess, H. W. *Macromolecules* **1990**, *23*, 4061.

[69] Huser, B.; Spiess, H. W. *Makromol. Chem., Rapid Commun.* **1988**, *9*, 337.

[70] Imrie, C. T.; Henderson, P. A. *Curr. Opin. Colloid Interface Sci.* **2002**, *7*, 298.

[71] Bacher, A.; Bleyl, I.; Erdelen, H.; Haarer, D.; Paulus, W.; Schmidt, H. *Adv. Mater.* **1997**, *9*, 1031.

[72] Picken, S. J.; Kouwer, P. H. J.; Jager, W. F.; Wubbenhorst, M. R.; Mijs, W. J. *Mol. Cryst. Liq. Cryst.,* **2004**, *411*, 1545.

[73] Kreuder, W.; Ringsdorf, H.; Tschirner, P. *Makromol. Chem., Rapid Commun.* **1985**, *6*, 367.

[74] Wenz, G. *Makromol. Chem., Rapid Commun.* **1985**, *6*, 577.

[75] Goldfarb, D.; Luz, Z.; Zimmermann, H. *J. De Phys.* **1981**, *42*, 1303.

[76] Huser, B.; Pakula, T.; Spiess, H. W. *Macromolecules* **1989**, *22*, 1960.

[77] Herrmann-Schonherr, O.; Wendorff, J. H.; Kreuder, W.; Ringsdorf, H. *Makromol. Chem., Rapid Commun.* **1986**, *7*, 97.

[78] Goldfarb, D. Ph.D. Thesis, the Scientific Council of the Weizmann Institute of Science, Rehovot, Israel, 1984.

[79] Herwig, P.; Kayser, C. W.; Mullen, K.; Spiess, H. W. *Adv. Mater.* **1996**, *8*, 510.

[80] Vandevyver, M.; Albouy, P. A.; Mingotaud, C.; Perez, J.; Barraud, A. *Langmuir* **1993**, *9*, 1561.

[81] Karthaus, O.; Ringsdorf, H.; Tsukruk, V. V.; Wendorff, J. H. *Langmuir* **1992**, *8*, 2279.

[82] Jin, S.; Tiefel, T. H.; Wolfe, R.; Sherwood, R. C.; Mottine, J. J. *Science* **1992**, *255*, 446.

[83] Dong, R. Y. *Nuclear Magnetic Resonance of Liquid Crystals*; Springer-Verlag, 1997.

[84] Dong, R. Y.; Chiezzi, L.; Veracini, C. A. *Phys. Rev. E.* **2002**, *65*, 041716.

[85] Catalano, D.; Cavazza, M.; Chiezzi, L.; Geppi, M.; Veracini, C. *Liq. Cryst.* **2000**, *27*, 621.

[86] Goodby, J.; Patel, J.; Chin, E. *J. Mater. Chem.* **1992**, *2*, 197.

[87] Catalano, D.; Chiezzi, L.; Domenici, V.; Geppi, M.; Veracini, C. A. *J. Phys. Chem. B* **2003**, *107*, 10104.

[88] Catalano, D.; Domenici, V.; Marini, A.; Veracini, C. A.; Bubnov, A.; Glogarova, M. *J. Phys. Chem. B* **2006**, *110*, 16459.

[89] Fodor-Csorba, K.; Vajda, A.; Jákli, A.; Slugovc, C.; Trimmel, G.; Demus, D.; Gács-Baitz, E.; Holly, S.; Galli, G. *J. Mater. Chem.* **2004**, *14*, 2499.

Chapter 2

NMR Theory and Spectroscopy

2.1 Introduction

Nuclear magnetic resonance (NMR) was discovered independently by Felix Bloch and Edward Mills Purcell in 1946, both of whom shared the Nobel Prize in physics in 1952 for their discovery [1, 2]. Since then, NMR has been developed into a tool that is unequal in the study of an abundance of physical, chemical and biological systems. NMR is a phenomenon associated with the interactions between the magnetic moments of the spinning nuclei in matter and the applied static and rotating magnetic fields [3]. The atomic nucleus which has a non-zero spin angular momentum and a magnetic moment should possess either odd mass, odd atomic number, or both. The more common nuclei that possess a spin include ${}^{1}_{1}\mathrm{H}$, ${}^{2}_{1}\mathrm{H}$, ${}^{13}_{6}\mathrm{C}$, ${}^{14}_{7}\mathrm{N}$, ${}^{17}_{8}\mathrm{O}$, and ${}^{19}_{9}\mathrm{F}$.

Since anisotropic NMR interactions usually dominate over the isotropic ones in partially ordered systems, NMR has been developed into a unique tool for studying molecules that form liquid-crystal phases, as well as for monitoring small, well characterized solute molecules that serve to probe the anisotropic environment of these phases [4]. A NMR spectrum of a liquid crystal contains, in principle, both static and dynamic information. The position and the relative intensities of the peaks can give the partially averaged spin interactions [5], while the line widths of these peaks may provide dynamic information. The Hamiltonian [6] of the spin system is needed to describe quantum mechanically spin interactions in NMR. The three dominant spin interactions: chemical shielding, dipole coupling and quadrupole coupling [3], are briefly described below. They can all be used to give quantitative information on the molecular structure, conformation and dynamics of a molecular system. The hardware of a NMR spectrometer and some elementary NMR techniques are also briefly described in this

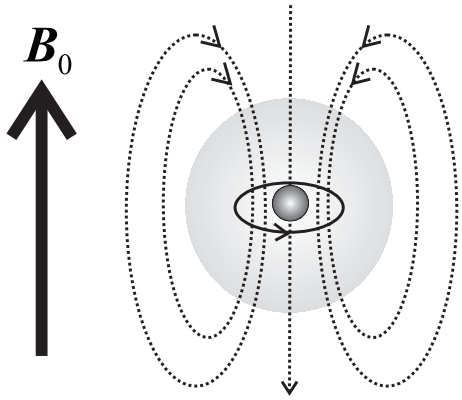

Figure 2.1: The diamagnetic shielding of a nucleus caused by the surrounding electrons.

.

chapter.

2.2 Zeeman Interaction and Chemical Shift Interaction

Zeeman Interaction

The Zeeman interaction $\hat{H}_Z$ between the magnetic moment of a nucleus and the static NMR magnetic field $\vec{B}_0$ is linear in the spin operator:

$$\hat{H}_Z = -\gamma\hbar\vec{I}\cdot\vec{B}_0 \tag{2.1}$$

where $\vec{I}$ is the nuclear spin, γ is the gyromagnetic ratio of the nucleus and $\hbar$ is the reduced Planck constant [3]. The magnetic field is taken to define the z axis of the laboratory frame, and the interaction energy is

$$H_Z = -\gamma\hbar B_0 m_z = \hbar\omega_0 m_z \tag{2.2}$$

where m_z is the z component of $\vec{I}$ $(-I_z \leq m_z \leq I_z)$ and ω_0 is the Larmor frequency.

Chemical Shift Interaction

The chemical shielding interaction arises because of the interaction of the nuclear spin with its surrounding electrons. When an external magnetic field is applied to an atom, not only are the nuclear spins perturbed, but their surrounding electrons are affected since they also have magnetic moments (Fig. 2.1). The external field induces circulating currents from the electrons that in turn produce small magnetic fields (typically $\sim 1 \times 10^6$ smaller than B_0), which either add to or subtract from the external field experienced by the nucleus. Therefore, the effective magnetic field experienced by the nucleus is altered, thereby altering

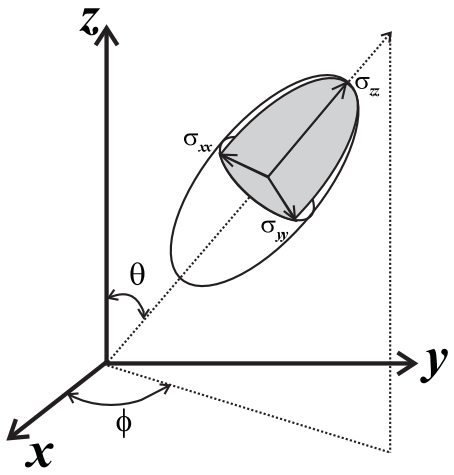

Figure 2.2: The principal axes of the shielding ellipsoid in the laboratory coordinate system, where θ and ϕ are the polar angles.

.

its resonance frequency. Accordingly, the chemical shift interaction can be incorporated into Eq. (2.1) to give

$$\hat{H}_Z = -\gamma\hbar\vec{I}\cdot(1-\hat{\sigma})\cdot\vec{B}_0 \tag{2.3}$$

where $\hat{\sigma}$ is a second-rank tensor that has nine components and describes the chemical shift anisotropy. In the case of the symmetric chemical shift tensor, $\hat{\sigma}$ consists of six independent components. This interaction is proportional to the applied magnetic field and therefore is more significant at higher field strengths.

The chemical shift anisotropy (CSA) results from the fact that the atoms in molecules rarely possess spherically symmetric electron distributions; instead, the electron density can be visualized as an ellipsoid, typically elongated along bonds or nonbonding p-orbitals (Fig. 2.2). The degree to which the electron density affects the resonance frequency of a nucleus depends on the orientation of the electron cloud (and hence the orientation of the molecule) with respect to B_0. The shape of these three-dimensional ellipsoids is defined by the principal tensor components σ_{xx}, σ_{yy}, σ_{zz}. These three principal values and the orientation of the ellipsoid provide all the information necessary to describe the CSA of a nuclear spin [7, 8]. Other important definitions [9, 10] stemming from these are the isotropic chemical shift, σ_{iso}, given by,

$$\sigma_{iso} = \frac{\sigma_{xx}+\sigma_{yy}+\sigma_{zz}}{3} \tag{2.4}$$

and the anisotropy parameter, η, given by,

$$\eta = \frac{\sigma_{yy}-\sigma_{xx}}{\sigma_{zz}-\sigma_{iso}} \tag{2.5}$$

The methods used to measure the chemical shift anisotropy of a particular nucleus depend primarily on the state of the sample. In powder samples, the molecules are randomly oriented and all possible molecular orientations exist. For single crystals, all the molecules are aligned in the same direction in a crystalline lattice. However, molecules in liquids randomly and rapidly sample the full range of orientations, so that even a strongly asymmetric electron distribution will appear spherical when viewed on the NMR timescale. This provides a clue to how the CSA can be eliminated.

Chemical Shift

The chemical shift of a nucleus is the difference between the resonance frequency of the nucleus and a reference standard (REF). This quantity is reported in parts per million (**ppm**) and given the symbol δ,

$$\delta = (\nu - \nu_{REF}) \times 10^6 / \nu_{REF} \tag{2.6}$$

For ^{1}H and ^{13}C in NMR spectroscopy, this standard is often tetramethylsilane, $Si(CH_3)_4$, abbreviated TMS. This compound was chosen initially because the protons of its methyl groups are more shielded than those of most other known compounds. The chemical shift is a very precise indication of the chemical environment around a nucleus [11].

As a result of the electron distribution, the nucleus will experience an effective magnetic field (B_{eff}) which is a combination of the externally applied magnetic field and the magnetic field generated by the electron density surrounding the nucleus. Within a molecule there are factors which can increase or decrease the electron density surrounding a nucleus. Factors which reduce the electron density are said to "deshield" the nucleus since B_{eff} at the nucleus increases. Similarly, factors which increase the electron density are said to "shield" the nucleus since B_{eff} at the nucleus decreases. Since the electron's magnetic field opposes the external magnetic field, the nucleus is "shielded" from the full strength of the external magnetic field, making B_{eff} normally less than B_0. If the magnetic field strength is reduced by shielding, the resonance frequency of a spin transition decreases. Figure 2.3 illustrates these relations. For example, for molecules AB when B has more electronegativity than A, then the ability of B to attract electrons is larger than A, and B will pull more electron density from A. In this case, A is more deshielded and the NMR signal of A will be farther away from the reference TMS signal which is set at 0 ppm. This association with the reference signal is called the Chemical Shift. If the NMR signal is farther away from this standard signal, then the signal occurs further downfield. Such a Chemical Shift will have a larger ppm value.

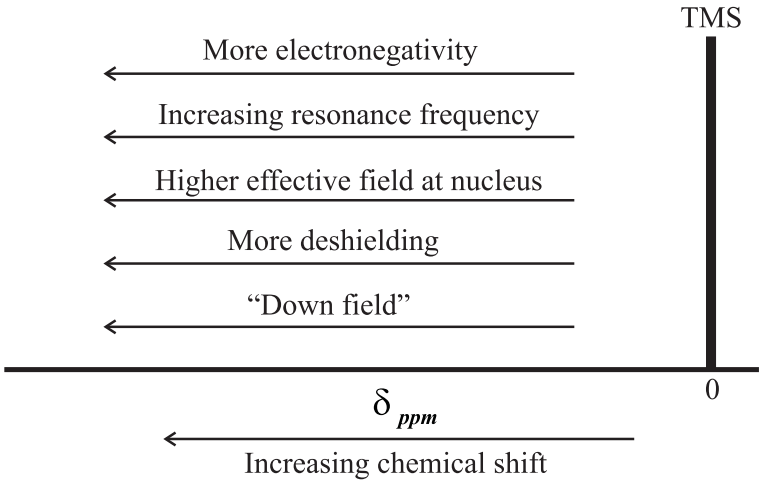

Figure 2.3: Schematic illustration of the relations between the chemical shift and other parameters.

.

2.3 Nuclear Electric Quadrupole Interaction

The quadrupolar interaction H_Q occurs when $I > 1/2$ and arises from the interaction of the nuclear electric quadrupole moment eQ with the nonspherically symmetric electric field gradient at the site of the nucleus due to the electronic charge distribution of the atom or molecule [3]:

$$\hat{H}_Q = \frac{eQ}{2I(2I-1)}\mathbf{I}\cdot\mathbf{V}\cdot\mathbf{I} \tag{2.7}$$

where Q is the electric quadrupole moment, $\mathbf{I}$ is the spin angular momentum, e is the charge of the electron, and $\mathbf{V}$ is the electric field gradient tensor. The quadrupolar Hamiltonian can be written in the principal axis (X, Y, Z) system [3] of the electric field gradient tensor V_{ij}:

$$\hat{H}_Q = \frac{e^2qQ}{4I(2I-1)}[3I_Z^2 - I(I+1) + \frac{1}{2}\eta(I_+^2 + I_-^2)] \tag{2.8}$$

where $|V_{ZZ}| \geq |V_{YY}| \geq |V_{XX}|$, $eq = V_{ZZ}$ and asymmetry parameter $\eta = \frac{V_{XX}-V_{YY}}{V_{ZZ}}$. In liquid crystalline phases, molecules undergo rapid anisotropic rotations and translational diffusion motions, and the quadrupolar Hamiltonian becomes time averaged to $\overline{H_Q}$. In the high field limit, $\overline{H_Q}$ of deuterons can be treated as a first order perturbation on the H_Z Hamiltonian. Since quadrupolar nuclei have very broad lines and their line shapes are very sensitive to changes in the motion of the molecules, they serve as a good probe for studying the dynamics of different molecular moieties.

2.4 Nuclear Dipole-Dipole Interaction

Nuclear spin possesses a magnetic moment, and in a collection of spins they interact through space. This gives dipole-dipole interactions. From the classical expression of the interaction between two point magnetic dipoles, the interaction Hamiltonian for dipolar coupling between two spins I_i and I_j is [3]

$$\hat{H}_{ij}^{D} = -\frac{\mu_0 \gamma_i \gamma_j \hbar^2}{4\pi} \left(\frac{\mathbf{I_i} \cdot \mathbf{I_j}}{r_{ij}^3} - 3\frac{(\mathbf{I_i} \cdot \mathbf{r})(\mathbf{I_j} \cdot \mathbf{r})}{r_{ij}^5} \right) \tag{2.9}$$

where r_{ij} is the internuclear distance, μ_0 is the permeability of free space ($= 4\pi \times 10^7 NA^{-2}$), γ_i and γ_j are the gyromagnetic ratios of the I_i and I_j spins, respectively. Expressing equation (2.9) in spherical polar coordinates and expanding the scalar products, we can obtain:

$$\hat{H}_{ij}^{D} = \frac{\mu_0 \gamma_i \gamma_j \hbar^2}{4\pi r_{ij}^3} (A + B + C + D + E + F) \tag{2.10}$$

where:

$$\begin{aligned} A &= I_{iz} I_{jz} (1 - 3\cos^2\theta_{ij}) \\ B &= -\frac{1}{4}(1 - 3\cos^2\theta_{ij})[I_i^+ I_j^- + I_i^- I_j^+] \\ C &= -\frac{3}{2}\sin\theta_{ij}\cos\theta_{ij} e^{-i\phi}[I_i^+ I_{jz} + I_{iz} I_j^+] \\ D &= C^* \\ E &= -\frac{3}{4}\sin^2\theta_{ij} e^{-i2\phi} I_i^+ I_j^+ \\ F &= E^* \end{aligned} \tag{2.11}$$

I_i^+, I_j^+ and I_i^-, I_j^- are the raising and lowering operators, respectively, of spins I_i and I_j, and the polar angles θ and ϕ describe the orientation of the internuclear vector with respect to the external magnetic field (Fig. 2.4). When NMR experiments are done in large magnetic fields, only terms A and B give first order contributions. In addition, in mesophases having cylindrical symmetry and the director aligned along the field, the ensemble average of terms C – F is zero. Under the hypothesis of uncorrelated motions we obtain

$$\begin{aligned} \hat{H}_{ij}^{D} &= \frac{\mu_0 \gamma_i \gamma_j \hbar^2}{4\pi r_{ij}^3} < 1 - 3\cos^2\theta_{ij} > \left[I_{iz} I_{jz} - \frac{1}{4}(I_i^+ I_j^- + I_i^- I_j^+) \right] \\ &= \frac{\mu_0 \gamma_i \gamma_j \hbar^2}{4\pi r_{ij}^3} \frac{< 1 - 3\cos^2\theta_{ij} >}{2} [3 I_{iz} I_{jz} - \mathbf{I_i} \cdot \mathbf{I_j}] \end{aligned} \tag{2.12}$$

Since $-\frac{1}{4}(I_i^+ I_j^- + I_i^- I_j^+)$ does not contribute to $\hat{H}_{ij}^{D}$ for two unlike spins I and S, Eq. (2.12) can be simplified to:

$$\hat{H}_{ij}^{D} = \frac{\mu_0 \gamma_i \gamma_j \hbar^2}{4\pi r_{ij}^3} \frac{< 1 - 3\cos^2\theta_{ij} >}{2} \cdot 2 I_z S_z \tag{2.13}$$

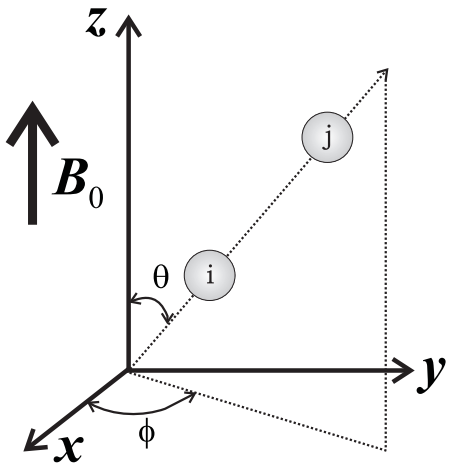

Figure 2.4: Schematic display of the interaction between two spins illustrating the Euler angles θ and ϕ of the interaction vector frame in the laboratory frame.

.

The constant term in front of equations (2.12) and (2.13) are the homonuclear and heteronuclear dipolar coupling constants, respectively. The brackets in $< 1-3\cos^2\theta_{ij} >$ term indicate the ensemble or time average. In liquid state NMR spectroscopy, the reorientation time of a molecule in solution is much faster than the time the dipolar coupling needs to evolve, thus averaging the $< 1-3\cos^2\theta_{ij} >$ term of dipolar coupling Hamiltonian to zero. In the solid state, although the sample comprises randomly oriented crystallites, the internuclear vector remains invariant over time. So the resonance frequency produced by each crystallite depends on its orientation with respect to the magnetic field. Since the crystallites are oriented in all possible directions, different dipolar couplings produce a powder pattern NMR spectrum.

2.5 Motionally Averaged Hamiltonian

In liquid crystals, molecules have fast rotations, and a study of the molecular dynamics requires the average nuclear spin Hamiltonians: chemical shielding, dipole-dipole and electric quadrupole. All of these spin interactions may be formally written in terms of irreducible spherical tensor operators, $T_{L,m}$ and $R_{L,m}$ [6]:

$$H_\lambda = C_\lambda \sum_L \sum_{m=-L}^{L} (-1)^m R^\lambda_{L,-m} T^\lambda_{L,m} \tag{2.14}$$

where C_λ is an appropriate interaction constant for a spin interaction labeled by λ. $R_{L,m}$ and $T_{L,m}$ are irreducible spherical tensor operators, which define the spatial part and spin part of

the Hamiltonian, respectively. For symmetric second-rank tensors, $R_{L,m}$ will be nonzero only when $L = 0$ and 2. If $R_{L,m}$ is considered in the principal axis system, only components with $m = 0, \pm L$ are nonzero. The components of $R^{\lambda}_{L,m}$ are denoted by $\rho^{\lambda}_{L,m}$ in their respective principal axis systems. The coordinate transformation gives:

$$R_{L,m} = \sum_{m'} D^{L}_{m',m}(\alpha, \beta, \gamma)\rho_{L,m'} \tag{2.15}$$

where $\Omega = (\alpha, \beta, \gamma)$ denotes the Euler angles that transform the principal axis system to the laboratory system. In the high-field approximation, the time-averaged Hamiltonian of Eq. (2.14) can be written as:

$$\bar{H_{\lambda}} = C_{\lambda} \langle R_{2,0} \rangle T_{2,0} \tag{2.16}$$

The values of C_{λ}, $\rho_{L,m}$, $T_{2,0}$ are given in Table 2.1 [6].

Table 2.1: List of constants C_{λ}, irreducible spherical operators $\rho_{L,m}$ and irreducible spin basis set $T_{2,0}$.

λ(interaction)	C_{λ}	$\rho_{0,0}$	$\rho_{2,0}$	$\rho_{2,\pm2}$	$T_{2,0}$
Dipole	$-\frac{\mu_0}{2\pi}\gamma_i\gamma_j\hbar^2$	0	$\sqrt{\frac{3}{2}}r_{ij}^{-3}$	0	$\frac{1}{\sqrt{6}}[3I_{iz}I_{jz} - \mathbf{I_i} \cdot \mathbf{I_j}]$
Quadrupole	$\frac{eQ}{2I(2I-1)}$	0	$\sqrt{\frac{3}{2}}eq$	$\frac{1}{2}eq\eta$	$\frac{1}{\sqrt{6}}[3I_z^2 - (\mathbf{I})^2]$
Shielding	$\gamma\hbar$	$-\frac{\sigma_{xx}+\sigma_{yy}+\sigma_{zz}}{\sqrt{3}}$	$\sqrt{\frac{3}{2}}(\sigma_{zz} - \sigma_{iso})$	$\frac{\sigma_{xx}-\sigma_{yy}}{2}$	$\sqrt{\frac{2}{3}}I_zB_0$

2.6 Quantum-mechanical calculations of NMR time evolutions

2.6.1 Density Matrix Operator

The description of a nuclear spin system in liquid crystals under the influence of radio frequency pulses requires a quantum mechanical formalism that specifies the state of a spin system by a state function. As we know, in quantum mechanics the state of a system is specified by a state vector $|\psi_1\psi_2... >$ [12]. But in nature there are more than 10^{20} particles in a system such as electrons, nuclei, atoms, molecules, etc. It is impossible to get the solution of Schrödinger's equation in such a large system. Hence the density matrix formalism is used. Suppose that an assembly of N identical spin systems is considered. If the spin system is in a state of wave function or ket $|\psi_k >$, the expectation value of a physical variable given by its operator Q is

$$< Q >_k =< \psi_k|Q|\psi_k > \tag{2.17}$$

In general, the ket $|\psi_k>$ is time-dependent and may be expanded using a complete orthonormal basis of m stationary kets $|\phi_i>$:

$$|\psi_k>=\sum_{i=1}^{m} C_i^k(t)|\phi_i> \tag{2.18}$$

So the ensemble average of this variable can be written as:

$$\begin{aligned} < Q > &= \sum_{k=1}^{N} < Q >_k /N \\ &= \sum_k \sum_{i,j} C_i^{k*}(t) C_j^k(t) < \phi_i|Q|\phi_j > /N \\ &= \sum_{i,j} < \phi_i|Q|\phi_j > \rho_{ji}(t) \end{aligned} \tag{2.19}$$

This allows one to define the density operator $\hat{\rho}$, whose matrix elements in the orthonormal basis $|\phi_i>$ are

$$\rho_{ji} =< \phi_j|\hat{\rho}|\phi_i >= \sum_k C_j^k C_i^{k*}/N = \overline{C_j C_i^*} \tag{2.20}$$

where the bar means an ensemble average. From Eq. (2.20), the density matrix is Hermitian, $\rho_{ij}^* = \rho_{ji}$. The number of independent matrix elements needed to specify the density matrix depends on the number of orthonormal basis states that are needed to specify the system.

The time evolution of the density matrix is obtained from the time dependent Schrödinger's equation:

$$\frac{d}{dt}|\psi >= -i\hat{H}|\psi > \tag{2.21}$$

For simplification, here we set $\hbar$ to 1. From Equation (2.18), the Liouville-von Neumann equation for the time dependence of the density operator $\hat{\rho}$ is obtained [3, 12]:

$$\frac{\partial \hat{\rho}}{\partial t} = i[\hat{\rho}(t), \hat{H}] \tag{2.22}$$

which has the formal solution [7]

$$\hat{\rho}(t) = \exp\left[-i\int_0^t dt' \hat{H}(t')\right] \hat{\rho}(0) \exp\left[i\int_0^t dt' \hat{H}(t')\right] \tag{2.23}$$

If the Hamiltonian $\hat{H}$ is time-independent, the solution of Eq. (2.22) is given by:

$$\hat{\rho}(t) = e^{-i\hat{H}t}\hat{\rho}(0)e^{i\hat{H}t} = \hat{U}(t)\hat{\rho}(0)\hat{U}^+(t) \tag{2.24}$$

where $\hat{U}(t)$ is called a 'propagator'. To evaluate the formal solution of Eq. (2.24), one makes use of the Baker-Campbell-Hausdorff relation [9, 12]

$$\begin{aligned}\hat{\rho}(t) &= e^{-i\hat{H}t}\hat{\rho}_0 e^{i\hat{H}t} \\ &= \hat{\rho}_0 + [-i\hat{H}t, \hat{\rho}_0] + \frac{1}{2}[-i\hat{H}t, [-i\hat{H}t, \hat{\rho}_0]] + \frac{1}{6}[-i\hat{H}t, [-i\hat{H}t, [-i\hat{H}t, \hat{\rho}_0]]] + \ldots \\ &= \hat{\rho}_0 - \frac{it}{1!}\underbrace{[\hat{H}, \hat{\rho}_0]}_{\hat{r}_1} + \frac{(it)^2}{2!}\underbrace{[\hat{H}, \hat{r}_1]}_{\hat{r}_2} - \frac{(it)^3}{3!}\underbrace{[\hat{H}, \hat{r}_2]}_{\hat{r}_3} + \ldots \end{aligned} \tag{2.25}$$

The last line of the above equation shows that the cumulation of the commutators in the middle line can be avoided by calculating the commutators sequentially, exploiting $\hat{r}_{n+1} = [\hat{H}, \hat{r}_n]$. For instance, with $\hat{\rho}(0) = \hat{\rho}_0 = \hat{I}_x$, one can calculate the action of the $\vec{B}_0$ field by the Zeeman Hamiltonian $\hat{H} = \omega_0 \hat{I}_z$. To evaluate the time evolution series of Eq. (2.25), we need the commutators:

$$\begin{aligned}\hat{r}_1 &= [\hat{H}, \hat{\rho}_0] = i\omega_0 \hat{I}_y \\ \hat{r}_2 &= [\hat{H}, \hat{r}_1] = \omega_0^2 \hat{I}_x = \omega_0^2 \hat{\rho}_0 \end{aligned} \tag{2.26}$$

So Eq. (2.25) can be rewritten as

$$\begin{aligned}\hat{\rho}(t) &= \hat{\rho}_0 \left(1 + \frac{(i\omega_0 t)^2}{2!} + \frac{(i\omega_0 t)^4}{4!} + \ldots\right) - \frac{\hat{r}_1}{\omega_0}\left(\frac{(i\omega_0 t)^1}{1!} + \frac{(i\omega_0 t)^3}{3!} + \ldots\right) \\ &= \hat{\rho}_0 \cos\omega_0 t - i\frac{\hat{r}_1}{\omega_0}\sin\omega_0 t \\ &= \hat{I}_x \cos\omega_0 t + \hat{I}_y \sin\omega_0 t \end{aligned} \tag{2.27}$$

This represents a quantum mechanical derivation of the precession of the magnetization around the $\vec{B}_0$ field. Further examples for the calculation of the time evolution operators will be given in the following subsections, which will serve as the basis for many other NMR signals and spectral features discussed in the dissertation of one dimensional and two dimensional experiments.

2.6.2 Interaction Representation

In the Schrödinger representation, the operators are time-independent (except for explicitly time-dependent potentials) and the kets representing the quantum states develop in time. In the Heisenberg representation, the kets stay the same, while the time dependence is in the operators. These differing representations describe the same physics, viz., matrix elements of operators between kets must be the same in both. Which is more natural to use

depends on the problem at hand [12]. In fact, for perturbation theory problems with a time-dependent potential, an intermediate representation, the `interaction representation`, is very convenient. In any system where the Hamiltonian can be split into two parts

$$\hat{H} = \hat{H}_0 + \hat{H}_1 \tag{2.28}$$

it is often convenient to separate the time-dependence due to the unperturbed Hamiltonian (which is assumed time-independent). The density operator in the interaction representation is [9]

$$\hat{\rho}_I(t) = e^{i\hat{H}_0 t}\hat{\rho}(t)e^{-i\hat{H}_0 t} \tag{2.29}$$

The Liouville-von Neumann equation in the $\hat{H}_0$-interaction representation now reads:

$$\frac{\partial\hat{\rho}_I(t)}{\partial t} = i[\hat{\rho}_I(t), \hat{H}_{1,I}] \tag{2.30}$$

$\hat{H}_0$ does not appear as such in the equation: its direct effect has been transformed away. Indirectly, however, $\hat{H}_0$ plays an important role in the transformation of the other Hamiltonian:

$$\hat{H}_{1,I} = e^{i\hat{H}_0 t}\hat{H}_1 e^{-i\hat{H}_0 t} \tag{2.31}$$

This transformation is same as was applied to $\hat{\rho}(t)$ in Eq. (2.29). The equivalence of the interaction representation (2.29)-(2.31) and the results of the original Liouville-von Neumann equation of motion (2.22) can be proved by inserting the expressions for $\hat{\rho}_I(t)$ and $\hat{H}_{1,I}$ into Eq. (2.30), which yields Eq. (2.22).

As an example, the Hamiltonian $\hat{H} = \omega_0\hat{I}_z + 2\omega_1\hat{I}_x\cos\omega_0 t + \hat{H}_{int}$ is considered, where $2\omega_1\hat{I}_x\cos\omega_0 t$ describes the effect of a radio frequency pulse and $\hat{H}_{int}$ is another interaction that is secular. The Liouville-von Neumann equation is written as

$$\frac{\partial\hat{\rho}}{\partial t} = i[\hat{\rho}(t), \omega_0\hat{I}_z + 2\omega_1\hat{I}_x\cos\omega_0 t + \hat{H}_{int}] \tag{2.32}$$

Multiplying by $\hat{R} = e^{i\omega_0 t\hat{I}_z}$ on the left and $\hat{R}^+$ on the right in the above equation and making use of

$$\hat{R}\frac{\partial\hat{\rho}(t)}{\partial t}\hat{R}^+ = \frac{\partial\hat{\rho}_I(t)}{\partial t} + i[\hat{\rho}_I(t), \omega_0\hat{I}_z] \tag{2.33}$$

where $\hat{\rho}_I(t) = \hat{R}\hat{\rho}(t)\hat{R}^+$ is the density matrix in the rotating frame, one can get

$$\begin{aligned}
\frac{\partial\hat{\rho}_I(t)}{\partial t} &= \hat{R}i[\hat{\rho}(t), \omega_0\hat{I}_z + 2\omega_1\hat{I}_x\cos\omega_0 t + \hat{H}_{int}]\hat{R}^+ - i[\hat{\rho}_I(t), \omega_0\hat{I}_z] \\
&= i[\hat{\rho}_I(t), 2\omega_1\hat{R}\hat{I}_x\hat{R}^+\cos\omega_0 t + \hat{H}_{int}] \\
&= i[\hat{\rho}_I(t), 2\omega_1(\hat{I}_x\cos\omega_0 t + \hat{I}_y\sin\omega_0 t)\cos\omega_0 t + \hat{H}_{int}] \\
&= i[\hat{\rho}_I(t), \omega_1\hat{I}_x + \hat{H}_{int}] + i[\hat{\rho}_I(t), \omega_1(\hat{I}_x\cos 2\omega_0 t + \hat{I}_y\sin 2\omega_0 t)] \\
&\cong i[\hat{\rho}_I(t), \omega_1\hat{I}_x + \hat{H}_{int}]
\end{aligned} \tag{2.34}$$

where the radio frequency field becomes time independent in the rotating frame and the term involving counter-rotating component at $2\omega_0$ can be safely ignored.

In a similar fashion, take any time independent interaction $\hat{H}_{int}$ plus another interaction $\hat{H}_{other}$

$$\frac{\partial\hat{\rho}}{\partial t} = i[\hat{\rho}(t), \hat{H}_{int} + \hat{H}_{other}] \tag{2.35}$$

To get rid of $\hat{H}_{int}$, transform into a new frame by applying the unitary transformation $\hat{R} = e^{i\hat{H}_{int}t}$ (i.e. in the interaction representation)

$$\frac{\partial\hat{R}}{\partial t} = i\hat{H}_{int}\hat{R} \tag{2.36}$$

then

$$\frac{\partial\hat{\rho}_T}{\partial t} = i[\hat{\rho}_T(t), \hat{H}_T] \tag{2.37}$$

This method is referred to as the toggling frame transformation where the subscript T is used to label the density operator and the effective Hamiltonian $\hat{H}_T$ is given in the interaction representation as:

$$\hat{H}_T = \hat{R}\hat{H}_{other}\hat{R}^+ \tag{2.38}$$

2.6.3 Correction Terms in Average Hamiltonian Theory - The Magnus Expansion

A time-dependent Hamiltonian can in general be written by dividing time into intervals τ_0, τ_1, ..., τ_n with time independent Hamiltonians in each interval $\hat{H}(\tau_0)$, $\hat{H}(\tau_1)$, ..., $\hat{H}(\tau_n)$. One can solve this problem at the end of the nth interval:

$$\hat{\rho}(t) = e^{i\hat{H}(\tau_n)\tau_n}\cdots e^{i\hat{H}(\tau_1)\tau_1}e^{i\hat{H}(\tau_0)\tau_0}\hat{\rho}(0)e^{-i\hat{H}(\tau_0)\tau_0}e^{-i\hat{H}(\tau_1)\tau_1}\cdots e^{-i\hat{H}(\tau_n)\tau_n} \tag{2.39}$$

It is useful to have a more compact way of writing this result using the Dyson time-ordering operator, $\mathbf{T_D}$, which ensures that the product is applied to $\hat{\rho}(0)$ in the proper order to maintain causality [13]. So the above equation can be rewritten as

$$\hat{\rho}(t) = \mathbf{T_D}(\prod_{k=0}^{N} e^{i\hat{H}(\tau_k)\tau_k})\hat{\rho}(0)\mathbf{T_D}(\prod_{k=0}^{N} e^{-i\hat{H}(\tau_k)\tau_k}) \tag{2.40}$$

By applying the Baker-Campbell-Hausdorff relation

$$e^{\hat{B}}e^{\hat{A}} = e^{\hat{B}+\hat{A}+\frac{1}{2}[\hat{A},\hat{B}]+\frac{1}{12}([\hat{B},[\hat{B},\hat{A}]]+[[\hat{B},\hat{A}],\hat{A}]+\ldots} \tag{2.41}$$

many times to the propagator product in Eq. (2.40) and taking the limit $\tau_k \to 0$, one can rewrite $\hat{\rho}(t)$ as

$$\hat{\rho}(t) = e^{i\hat{H}_{eff}t}\hat{\rho}(0)e^{-i\hat{H}_{eff}t} \tag{2.42}$$

with

$$\hat{H}_{eff} = \hat{H}^{(0)} + \hat{H}^{(1)} + \hat{H}^{(2)} + +\hat{H}^{(3)} + \ldots \tag{2.43}$$

This is the well known Magnus expansion of the Hamiltonian [14], the first few terms of which are:

$$\begin{aligned}
\hat{H}^{(0)} &= \frac{1}{t}\int_0^t \hat{H}(t_1)dt_1 \\
\hat{H}^{(1)} &= -\frac{i}{2t}\int_0^t dt_1 \int_0^{t_1} dt_2[\hat{H}(t_1), \hat{H}(t_2)] \\
\hat{H}^{(2)} &= \frac{-1}{6t}\int_0^t dt_1 \int_0^{t_1} dt_2 \int_0^{t_2} dt_3 \left\{[\hat{H}(t_1), [\hat{H}(t_2), \hat{H}(t_3)]] + [\hat{H}(t_3), [\hat{H}(t_2), \hat{H}(t_1)]]\right\}
\end{aligned} \tag{2.44}$$

Using the first term in the expansion, the density matrix evolves under a Hamiltonian that is averaged over the time during which it is applied. In the theory of spin flip line narrowing as well as in multiquantum excitation, the effect of applying sequences of pulses has been analyzed using the time averaged Hamiltonian. This formalism is used in section 2.6.4.

2.6.4 Heteronuclear Decoupling and Cross Polarization

In the preceding subsection, the average Hamiltonian theory was introduced for analyzing the coherent averaging of homonuclear dipolar couplings. This theory can also be applied to many other NMR problems such as heteronuclear decouplings and cross polarization, which are the interactions between I and S spins. Heteronuclear decoupling by continuous irradiation is a standard procedure in the majority of NMR experiments on organic solids. The Hamiltonians of the $\vec{B}_1$ field and the heteronuclear dipolar interactions appear in the propagator. This propagator can be analyzed by means of average Hamiltonian theory, which shows that the average heteronuclear dipolar Hamiltonian vanishes. Consider the total Hamiltonian in the rotating frame

$$\hat{H}_{rot} = \gamma B_1 \hat{I}_x + 2\omega_{IS}\hat{I}_z\hat{S}_z \tag{2.45}$$

where ω_{IS} is the I-S dipolar interaction frequency. The effective Hamiltonian in an interaction representation using $\hat{R} = e^{i\gamma B_1 \hat{I}_x t}$ is

$$\begin{aligned}(\hat{H}_{rot})_I &= 2\omega_{IS}\hat{R}\hat{I}_z\hat{S}_z\hat{R}^+ \\ &= 2\omega_{IS}(\hat{I}_z\cos\omega_1 t - \hat{I}_y\sin\omega_1 t)\hat{S}_z \end{aligned} \tag{2.46}$$

The zeroth order in average Hamiltonian theory is

$$\begin{aligned}(\hat{H}^{(0)}_{rot})_I &= \frac{2}{t}\omega_{IS}S_{zz}\int_0^t(\hat{I}_z\cos\omega_1 t_1 - \hat{I}_y\sin\omega_1 t_1)dt_1 \\ &= 0 \ \texttt{(when } \omega_1 \gg \omega_{IS}\texttt{)} \end{aligned} \tag{2.47}$$

This means the dipolar Hamiltonian can be averaged to zero as $t \to \infty$ by applying a strong radio frequency field (compared to ω_{IS}) at the Larmor frequency of one of the nuclear species.

Cross polarization from protons to rare spins takes an important place in ^{13}C and ^{15}N NMR spectroscopy. It is also an indispensable element of multidimensional heteronuclear experiments. Initially in thermal equilibrium

$$\hat{\rho}_{eq} = \omega_I\hat{I}_z + \omega_S\hat{S}_z \tag{2.48}$$

where $\omega_i = \gamma_i B_0$. The state of the system following a $\pi/2$ pulse along x applied on resonance to each spin, in an interaction representation obtained via the transformation

$$\hat{R} = e^{i(\omega_I\hat{I}_z + \omega_S\hat{S}_z)t} \tag{2.49}$$

is $\rho_0 = \omega_I\hat{I}_y + \omega_S\hat{S}_y$ in the so called double rotating frame. Under spin locking conditions, the above does not result in any further nutation, and the Hamiltonian including the $I-S$ coupling is

$$\hat{H}_{rot} = \omega_I\hat{I}_y + \omega_S\hat{S}_y + 2\omega_{IS}\hat{I}_z\hat{S}_z \tag{2.50}$$

By considering a second transformation to another interaction representation via

$$\hat{R}_1 = e^{i(\omega_I\hat{I}_y + \omega_S\hat{S}_y)t} \tag{2.51}$$

the effective Hamiltonian becomes

$$\begin{aligned}(\hat{H}_{rot})_I &= 2\omega_{IS}\hat{R}_1\hat{I}_z\hat{S}_z\hat{R}_1^+ \\ &= 2\omega_{IS}(\hat{I}_z\cos\omega_I t + \hat{I}_x\sin\omega_I t)(\hat{S}_z\cos\omega_S t + \hat{S}_x\sin\omega_S t) \end{aligned} \tag{2.52}$$

The zeroth order term in the Magnus expansion of $\hat{H}_{rot}$ is

$$(\hat{H}^{(0)}_{rot})_I = \omega_{IS}(\hat{I}_z\hat{S}_z + \hat{I}_x\hat{S}_x) \tag{2.53}$$

and is non-zero only if $\omega_I = \omega_S$, which is (by orthogonality of trigonometric function with respect to integration) the Hartmann-Hahn condition. The result represents a form of heteronuclear Hamiltonian that leads to polarization transfer between I and S spins due to cross terms between its components $\hat{I}_z\hat{S}_z$ and $\hat{I}_x\hat{S}_x$.

2.6.5 Product Operators

Quantum mechanics, specifically in the form of density matrix theory, is the best way to describe the NMR process. However, product operator formalism can give a complete and rigorous quantum mechanical description of NMR experiments and is well suited to calculating the outcome of modern multiple-pulse experiments [11, 15]. To understand the theory of some pulse sequences in the dissertation, the product operators are introduced here, which have very clear physical meaning and the effects of pulses and delays can be thought of as geometrical rotations.

For a single spin 1/2, the density operator $\hat{\rho}(t)$ can be represented as a sum of different amounts of the spin angular momentum operators $\hat{I}_x$, $\hat{I}_y$ and $\hat{I}_z$

$$\hat{\rho}(t) = a(t)\hat{I}_x + b(t)\hat{I}_y + c(t)\hat{I}_z \tag{2.54}$$

where $a(t)$, $b(t)$ and $c(t)$ vary with time during radio frequency pulses and delays. Since at equilibrium only z magnetization exists, it is usually defined as $\hat{\rho}_{eq} = \hat{I}_z$. The density operator at time t, $\hat{\rho}(t)$, is computed from Eq. (2.24). As an example, Eq. (2.27) was derived. Based on these derivations, standard rotation rules are introduced and the results after the motion all have the same form [11, 15]

$$e^{-i\theta\hat{I}_a}\,\{\texttt{old operator}\}\,e^{i\theta\hat{I}_a} = \cos\theta\,\{\texttt{old operator}\} + \sin\theta\,\{\texttt{new operator}\} \tag{2.55}$$

where $\{\texttt{old operator}\}$, $\{\texttt{new operator}\}$ and $\hat{I}_a$ are determined from the three possible angular momentum operators according to the Figure 2.5(a-c). The label in the center indicates which axis the rotation is about. For convenience, the arrow notation is often used and the Hamiltonian is written over the arrow which connects the old and new density operators. For example, Eq. (2.27) can be expressed as

$$\hat{I}_x \xrightarrow{\omega_0 t\hat{I}_z} \hat{I}_x\cos\omega_0 t + \hat{I}_y\sin\omega_0 t \tag{2.56}$$

For two spins, each spin will need three operators with $\hat{I}_{1x}$, $\hat{I}_{1y}$, $\hat{I}_{1z}$ for spin 1 and $\hat{I}_{2x}$, $\hat{I}_{2y}$, $\hat{I}_{2z}$ for spin 2. $\hat{I}_{1z}$ (or $\hat{I}_{2z}$) represents z-magnetization with equal polarization across all transitions of spin 1 (or 2). The transverse operators $\hat{I}_{1x}$ (or $\hat{I}_{2x}$) and $\hat{I}_{1y}$ (or $\hat{I}_{2y}$) are representative of the spin 1 (or 2) doublet with all doublet components in-phase along the x- or y-axis of the rotating frame. As the two spins are coupled, there will be another nine combined operators to describe the magnetization. $2\hat{I}_{1x}\hat{I}_{2z}$, $2\hat{I}_{1y}\hat{I}_{2z}$, $2\hat{I}_{1z}\hat{I}_{2x}$ and $2\hat{I}_{1z}\hat{I}_{2y}$ represent anti-phase magnetizations. Specifically, $2\hat{I}_{1x}\hat{I}_{2z}$ represents the x-magnetization of spin 1 anti-phase with respect to spin 2, and so on. Another four product operators $2\hat{I}_{1x}\hat{I}_{2y}$,

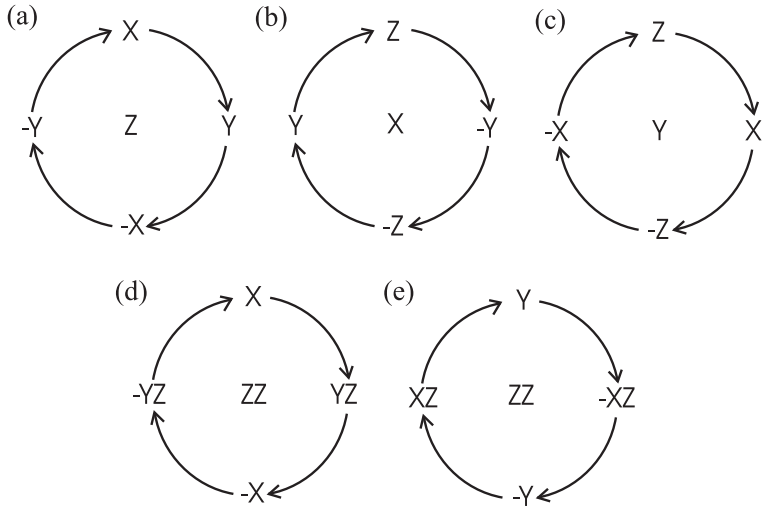

Figure 2.5: Rotational diagrams of the product operators [11].

.

$2\hat{I}_{1y}\hat{I}_{2x}$, $2\hat{I}_{1x}\hat{I}_{2x}$ and $2\hat{I}_{1y}\hat{I}_{2y}$ contains x and/or y operators. They correspond to two spin coherences and can not be observed. The term $2\hat{I}_{1z}\hat{I}_{2z}$ is also not observable and describes a non-equilibrium population distribution. The evolutions of the two spin operators are same as those of a single spin, since the rotations applied to each spin do not affect the other. For example, the term $2\hat{I}_{1x}\hat{I}_{2z}$ evolves under a 90° pulse about the y axis applied to both spins, $\frac{\pi}{2}\hat{I}_{1y} + \frac{\pi}{2}\hat{I}_{2y}$ and this process can be separated into two successive rotations

$$2\hat{I}_{1x}\hat{I}_{2z} \xrightarrow{\frac{\pi}{2}\hat{I}_{1y}} -2\hat{I}_{1z}\hat{I}_{2z} \xrightarrow{\frac{\pi}{2}\hat{I}_{2y}} -2\hat{I}_{1z}\hat{I}_{2x} \tag{2.57}$$

When considering the effect of coupling between two spins, the Hamiltonian will be a product of two operators such as $\hat{H}_J = \pi J_{12} 2\hat{I}_{1z}\hat{I}_{2z}$ with the scalar coupling J_{12} in Hz. Evolution under $\hat{H}_J$ will cause the interconversion of in-phase and anti-phase magnetization according to Figure 2.5(d-e). The rotation angle here is $\pi J_{12} t$. For example,

$$2\hat{I}_{1x}\hat{I}_{2z} \xrightarrow{\pi J_{12} t 2\hat{I}_{1z}\hat{I}_{2z}} \cos(\pi J_{12} t) 2\hat{I}_{1x}\hat{I}_{2z} + \sin(\pi J_{12} t)\hat{I}_{1y} \tag{2.58}$$

If spin 1 and spin 2 are different nuclear species, such as ^{13}C and ^{1}H, it is possible to choose a 180° pulse to either or both spins, as shown in Figure 2.6, to refocus the effect of coupling. Thus the different spin echo sequences are usually used in heteronuclear spin systems. For sequence (a) in Fig. 2.6 the evolution of the signal during the first delay is

$$\hat{I}_{1x} \xrightarrow{\pi J_{12}\tau 2\hat{I}_{1z}\hat{I}_{2z}} \cos(\pi J_{12}\tau)\hat{I}_{1x} + \sin(\pi J_{12}\tau) 2\hat{I}_{1y}\hat{I}_{2z} \tag{2.59}$$

After the 180° x-pulse,

$$\cos(\pi J_{12}\tau)\hat{I}_{1x} + \sin(\pi J_{12}\tau) 2\hat{I}_{1y}\hat{I}_{2z} \xrightarrow{\pi\hat{I}_{1x}} \cos(\pi J_{12}\tau)\hat{I}_{1x} - \sin(\pi J_{12}\tau) 2\hat{I}_{1y}\hat{I}_{2z} \tag{2.60}$$

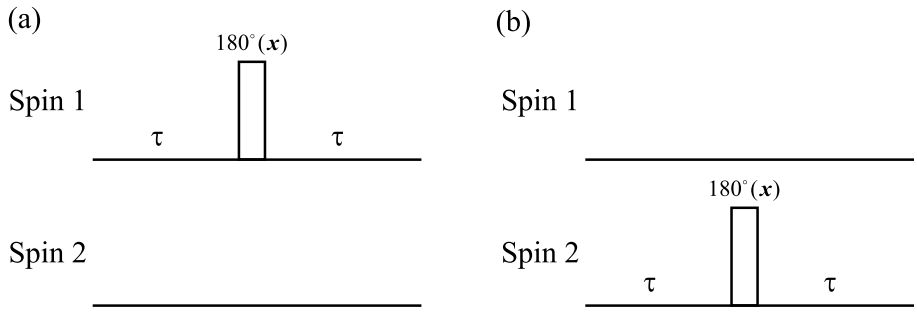

Figure 2.6: Two sets of different spin echo sequences that can be applied to heteronuclear spin systems [11], where τ is the delay time.

.

Under the scalar coupling during the second delay τ, the two terms on the right evolve to give

$$\cos(\pi J_{12}\tau)\hat{I}_{1x} - \sin(\pi J_{12}\tau)2\hat{I}_{1y}\hat{I}_{2z} \overset{\pi J_{12}\tau 2\hat{I}_{1z}\hat{I}_{2z}}{- - - \rightarrow} \hat{I}_{1x} \tag{2.61}$$

Similarly, for sequence (b) in Fig. 2.6 the final evolution is exactly the same as in sequence (a). So the effect of scalar coupling has been refocused. These sequences will be adopted to understand some ^{1}H and ^{13}C NMR pulse sequences such as HETCOR in Chapter 9.2 of the dissertation.

2.7 Relaxation Processes

The evolution of a macroscopic system towards thermal equilibrium is given the name 'relaxation'. Two different relaxation time constants are typically observed.

Materials containing an ensemble of weakly interacting nuclei will reach thermal equilibrium with the populations in energy levels described by the Boltzmann distribution [3]. This will require an exchange of spin energy between the nuclei and their surroundings, conventionally called the 'lattice', and will occur in a characteristic time T_1, the spin-lattice relaxation time. This time constant is sometimes called the longitudinal time constant. Consider the behavior of the macroscopic magnetization M_z which is the vector sum ($\sum \mu_{\mathbf{z}}$) of nuclear dipole components along the polarizing field B_z. Achievement of the equilibrium longitudinal magnetization M_0 is often described by a simple exponential recovery, which depends on the initial state. If it is assumed that $M_z = 0$ at $t = 0$ then

$$M_z(t) = M_0(1 - e^{-t/T_1}) \tag{2.62}$$

From the equation, T_1 can be determined by measuring $M_z(t)$ at different times t. The magnitude of the relaxation time T_1 depends highly on the type of nuclei (nuclei with spin 1/2 and low gyromagnetic ratio usually have a long relaxation time, whereas nuclei with spin$>$ 1/2 have a very short relaxation times) and other factors like the physical state (solid or liquid), the viscosity of the sample and the temperature. For deuterons ($I = 1$), there are two different spin lattice relaxation times: T_{1Z} (Zeeman spin lattice relaxation time) refers to recovery of Zeeman polarization after an initial perturbation, and T_{1Q} (Quadrupolar spin lattice relaxation time) describes the decay of quadrupole order. The relaxing polarization is generally measured with the Jeener-Broekaert pulse sequence, which yields a series of partially relaxed spectra as a function of relaxation delay t. This pulse sequence will be introduced in the next chapter.

The other time constant is usually called the spin-spin relaxation time T_2. It is associated with low-frequency, axial (parallel to $\vec{B_0}$) components of the fluctuating magnetic fields, and occurs simultaneously with the longitudinal relaxation. Fluctuating differences in $\vec{B_0}$ from place to place in the sample give rise to a range of changing Larmor frequencies for the nuclei, and hence a progressively random and irreversible dephasing of some of the transverse magnetization. As energy is exchanged only between nuclei in this process, the process is therefore termed as spin-spin relaxation, or more commonly transverse relaxation as it causes the x, y components of $\vec{M}$, $M_{x,y}$, to decrease to zero. The transverse magnetization will decay to zero according to:

$$\frac{dM_{x(y)}}{dt} = \gamma(\vec{M} \times \vec{B})_{x(y)} - \frac{M_{x(y)}}{T_2} \tag{2.63}$$

$$M_{x(y)} = M_{x(y)0} e^{-t/T_2} \tag{2.64}$$

Relaxation times are usually temperature sensitive. In other words the relaxation times depend on the motion of the molecule. Although the T_1 and T_2 processes happen simultaneously, in the solid state the T_2 process is usually much faster than the T_1 process. However, T_1 is equal to T_2 in isotropic liquids, due to the rapid motional processes.

2.8 NMR Instrumentation

NMR spectrometers have now become very complex instruments capable of performing lots of sophisticated experiments. So it is important to understand how the spectrometer works. Basically, the spectrometer is composed of three parts which all work in concert to produce a spectrum: magnet, probe, transmitter and receiver system (Fig. 2.7).

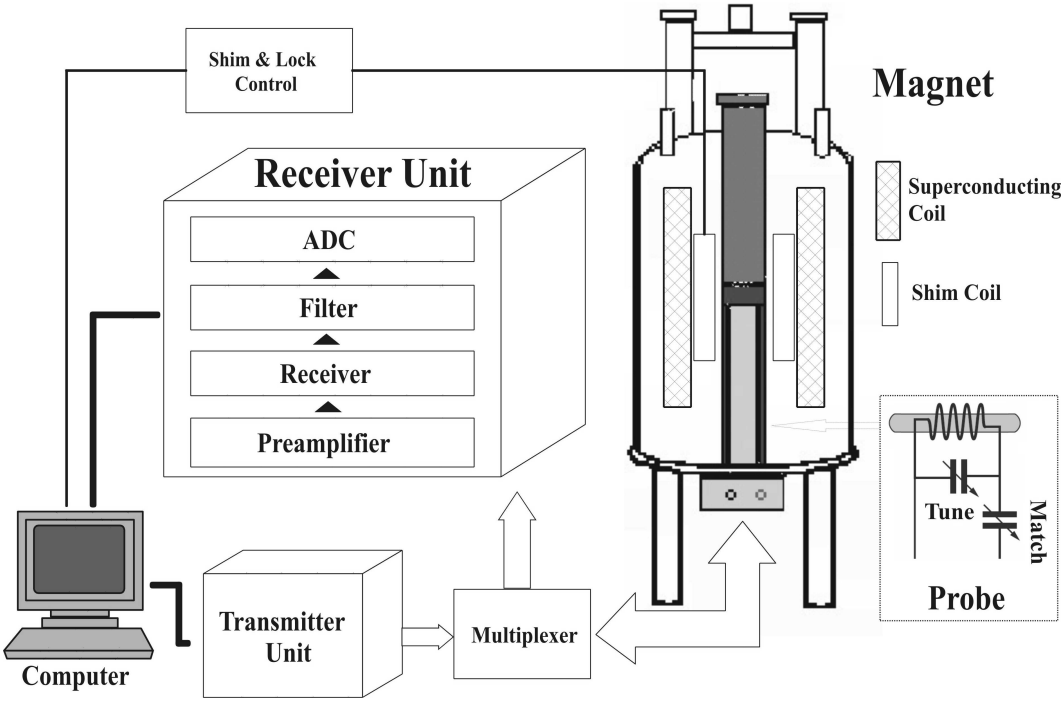

Figure 2.7: Schematic of the key components of a NMR spectrometer. [16]

.

Magnet

The first requirement for NMR is a magnet, usually a superconducting magnet, which generates a strong magnetic field called $\vec{B_0}$ in the center of the magnet. Important characteristics of any magnet are strength of the field, stability of the field and homogeneity of the field. The purpose of the magnet is to align all the NMR active nuclei and the spin states will satisfy the Boltzmann distribution. Stronger magnets are preferred since strength determines how far the nuclei energy levels are separated. Most magnets are in the range of 6-18 Teslas, which correspond to a ^1H operating frequency of 250-750 MHz. In our laboratory the magnet of our spectrometer is 9.4 Teslas, which corresponds to a ^1H operating frequency of 400 MHz. The field inhomogeneities could be caused by the magnet design, materials in the probe, variations in the thickness of the sample tube, etc. To correct minor spatial inhomogeneities in the $\vec{B_0}$ magnetic field, a set of 'room temperature' shim coils is used. A shim coil is designed to create a small magnetic field which will oppose and cancel out an inhomogeneous component in the $\vec{B_0}$ magnetic field. Because these variations may exist in a variety of functional forms (linear, parabolic, etc.), shim coils are needed to create a variety of opposing fields. By passing the appropriate amount of current through each coil in the set of shim coils, a homogeneous $\vec{B_0}$ magnetic field can be achieved.

Probe

The probe is housed in a cylindrical metal tube which can be inserted into the bore of the magnet. It contains the radio frequency (RF) coil, sample spinner, temperature heating element, and sometimes gradient coils. In our solid probes the RF coil is placed perpendicular to $\vec{B_0}$ and generates a magnetic field $\vec{B_1}$ which oscillates normal to $\vec{B_0}$. The sample is positioned within the RF coil in the probe. Another requirement of a RF coil is that the $\vec{B_1}$ field needs to be homogeneous over the volume of the sample. This $\vec{B_1}$ field causes the nuclei in the sample to change their spin states. The RF coil also picks up the induced electric signal as the nuclei relax back to their original states. In our laboratory there are four different probes for special purposes: a two-channel probe for proton-decoupled X channel signal detection of a solid-state NMR signal, a Magic Angle Spinning (MAS) probe in which the sample can be rotated at the magic angle (54.74°), a goniometer probe for precisely rotating the sample along an axis perpendicular to the external magnetic field for single-crystal studies, and a high-resolution probe for liquid-state NMR study.

Transmitter and Receiver System

The signal picked up by the NMR coil is only of the order of μV. Before the small signal is sent to the receiver, a preamplifier close to the probe is first used for amplifying the signal to a sufficient level. Then the free induction decay (FID) signal is further amplified by the receiver and digitized by an analogue to digital converter (ADC) before storing in the computer [11]. The ADC only samples the signal at regular intervals. The time interval between two data points is the dwell time (DW). According to the Fourier transform theory, DW controls the spectral width (SW) of NMR spectra (SW=1/DW). Another problem we need to consider is that the detected signal is only the M_x or M_y component, while the total magnetization is $M_+ = M_x + iM_y = M_0 e^{i\omega t}$ (where M_0 is the longitudinal magnetization at $t = 0$). Therefore, the phase information of the NMR signal is missing. The quadrature detection method has been used to overcome this problem. The NMR signal from the probe will be split into two parts and recorded by two receivers in quadrature (i.e. a 90° phase shift). Then the real and imaginary part of the complex time domain NMR signal can be recorded at the same time. In our spectrometer, there is only one receiver, then the quadrature detection is achieved by switching the receiver phase by 90° when recording the NMR signal, i.e., one real data point followed by an imaginary data point. The spectral width becomes 1/2DW now. In practice there exist instrumental and other phase shifts, and the two detected FIDs are not the idealised M_x and M_y. For example, one obtains the detected $M_x = M_0 cos(\omega t + \phi)$ and $M_y = M_0 sin(\omega t + \phi)$, where ϕ is the phase error. Fourier transformation of this set of FIDs will not give a pure absorption spectrum. However, it is possible to recover the pure absorption spectrum by phase correction using the processing software.

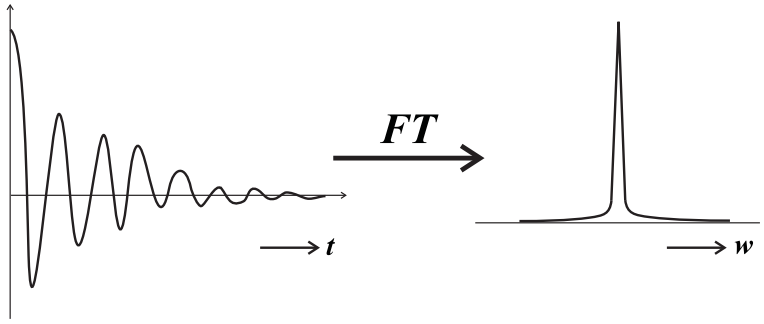

Figure 2.8: Representation of Fourier transformation between the 1D time signals and corresponding absorptive spectrum of a single spin species.

.

2.9 NMR Techniques

Nuclear magnetic resonance has progressed rapidly over the last two decades as a result of the improved instrumental technology and development of novel approaches. In this section, several important techniques are addressed.

Fourier Transformation

Fourier transformation(FT) plays a key role in pulsed NMR. It serves to obtain the NMR frequency spectrum from the measured nuclear FID signal in the time domain. In this approach, all the NMR signals of the studied system, with various frequencies, are measured simultaneously in the time domain. The Fourier transformation then sorts the signals out according to their frequencies, with the spectral intensity reflecting the weight of each frequency component in the total signal [17]. The definition of the Fourier transformation is:

$$f(t) \overset{FT}{\leftrightarrow} F(\omega) = \int_{-\infty}^{\infty} f(t) e^{-i\omega t} dt \tag{2.65}$$

From the last section, it is known that the signal obtained by the receiver is $M_+ = M_x + iM_y = M_0 e^{i\omega t+\phi}$. For example, we know that the transverse magnetization decays over time and can be represented by an exponential decay with a time constant T_2. The signal then becomes

$$M_+(t) = M_0 e^{i\omega t+\phi} e^{(-t/T_2)} \tag{2.66}$$

Fourier transformation of the FID signal such as that given in Eq. (2.66) gives the frequency domain signal known as the spectrum (Fig. 2.8). The real part of the frequency spectrum shows the absorption mode line, and the imaginary part of the spectrum gives a lineshape known as the dispersion mode line.

Multidimentional Spectroscopy

In addition to the one-dimensional (1D) NMR spectroscopy, two and three-dimensional spec-

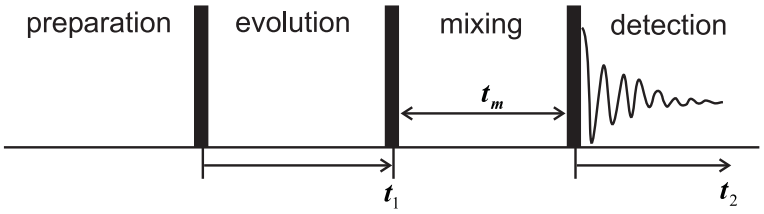

Figure 2.9: Principle of 2D experiments with preparation, evolution time t_1, mixing time t_m and the detection period t_2. In the experiment, the duration of t_1 is incremented. Usually, for each t_1 value several scans are taken.

.

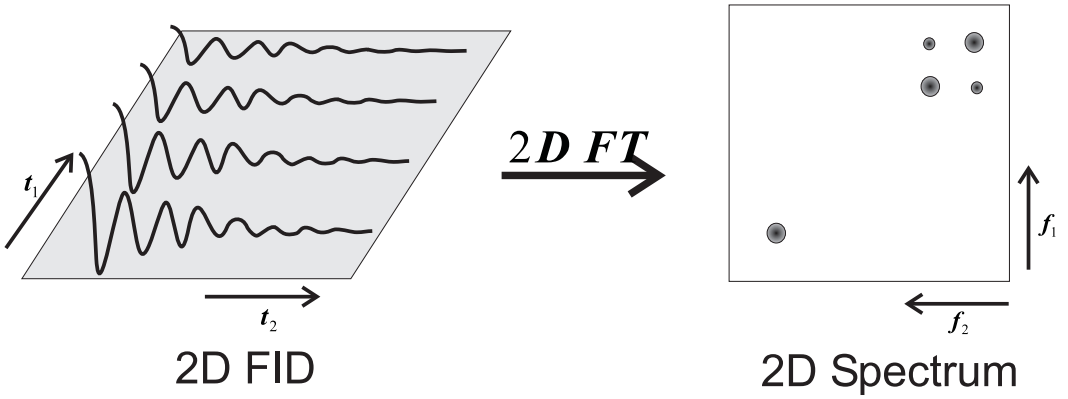

Figure 2.10: Representation of Fourier transformation between the 2D time signals and corresponding contour spectrum.

.

troscopy (2D and 3D) are very useful to increase the spectral resolution and provide routes to new information not accessible from 1D spectra [9]. The principle of 2D spectroscopy is outlined here. In 2D spectroscopy, Fourier transformations are performed on two dimensions:

$$f(t_1, t_2) \overset{FT}{\leftrightarrow} S(\omega_1, \omega_2) = \int_{-\infty}^{\infty} \int_{-\infty}^{\infty} f(t_1, t_2) e^{-i\omega_1 t_1} e^{-i\omega_2 t_2} dt_1 dt_2 \tag{2.67}$$

The basic 2D NMR experiment consists of exciting the nuclei with groups of pulses before receiving the FID. The time evolution of the experiment can be partitioned into several periods: preparation, evolution (t_1), mixing (t_m) and detection (t_2) (Fig. 2.9) [9]. The changes of the magnetization during the evolution period t_1, which is incremented in successive subexperiments, are detected indirectly as modulations of the nuclear induction signal observed during the detection period t_2. The signal in the time domain is then Fourier transformed in both dimensions to yield the 2D spectrum. The spectrum is conventionally displayed as a contour diagram (Fig. 2.10). In this dissertation, several 2D NMR experiments are discussed.

In practice, one finds that the approach of two simple successive Fourier Transformations will produce a 2D spectrum:

$$\begin{aligned} S(\omega_1,\omega_2) &= \int_{-\infty}^{\infty}\int_{-\infty}^{\infty} f(t_1,t_2)\left[\cos\omega_1 t_1 - i\sin\omega_1 t_1\right]\left[\cos\omega_2 t_2 - i\sin\omega_2 t_2\right] dt_1 dt_2 \\ &= \int_{-\infty}^{\infty}\int_{-\infty}^{\infty} f(t_1,t_2)\left[\cos\omega_1 t_1\cos\omega_2 t_2 - \sin\omega_1 t_1\sin\omega_2 t_2\right] dt_1 dt_2 \\ &\quad -i\int_{-\infty}^{\infty}\int_{-\infty}^{\infty} f(t_1,t_2)\left[\cos\omega_1 t_1\sin\omega_2 t_2 + \sin\omega_1 t_1\cos\omega_2 t_2\right] dt_1 dt_2 \end{aligned} \tag{2.68}$$

which contains a mixture of absorptive and dispersive contributions in both the real and imaginary parts. This causes the "phase twist"of spectral lines. Now the real part

$$\int_{-\infty}^{\infty}\int_{-\infty}^{\infty} f(t_1,t_2)\left[\cos\omega_1 t_1\cos\omega_2 t_2\right] dt_1 dt_2$$

of the 2D spectrum is purely absorptive and has optimum resolution and no spectral distortions. To solve this phase problem, the data processing must be modified. If we set:

$$\begin{aligned} f_c(t_1,t_2) &= f(t_1,t_2)\cos\omega_1 t_1 e^{-i\omega_2 t_2} \\ f_s(t_1,t_2) &= i f(t_1,t_2)\sin\omega_1 t_1 e^{-i\omega_2 t_2} \end{aligned} \tag{2.69}$$

The idea is to set the imaginary part to zero before the second Fourier Transformation:

$$\begin{aligned} S_c(\omega_1,\omega_2) &= Re\int_{-\infty}^{\infty}\cos\omega_1 t_1\left[Re\int_{-\infty}^{\infty} f(t_1,t_2)e^{-i\omega_2 t_2}dt_2\right] dt_1 \\ &= Re\int_{-\infty}^{\infty} cos\omega_1 t_1\left[\int_{-\infty}^{\infty} f(t_1,t_2)\cos\omega_2 t_2 dt_2\right] dt_1 \\ &= \frac{1}{2}Re\int_{-\infty}^{\infty}\left(e^{i\omega_1 t_1}+e^{-i\omega_1 t_1}\right)\left[\int_{-\infty}^{\infty} f(t_1,t_2)\cos\omega_2 t_2 dt_2\right] dt_1 \end{aligned} \tag{2.70}$$

$$\begin{aligned} S_s(\omega_1,\omega_2) &= Re\int_{-\infty}^{\infty} i\sin\omega_1 t_1\left[Re\int_{-\infty}^{\infty} f(t_1,t_2)e^{-i\omega_2 t_2}dt_2\right] dt_1 \\ &= Re\int_{-\infty}^{\infty} i\sin\omega_1 t_1\left[\int_{-\infty}^{\infty} f(t_1,t_2)\cos\omega_2 t_2 dt_2\right] dt_1 \\ &= \frac{1}{2}Re\int_{-\infty}^{\infty}\left(e^{i\omega_1 t_1}-e^{-i\omega_1 t_1}\right)\left[\int_{-\infty}^{\infty} f(t_1,t_2)\cos\omega_2 t_2 dt_2\right] dt_1 \end{aligned} \tag{2.71}$$

And therefore the absorptive spectrum is:

$$S_c(\omega_1,\omega_2) + S_s(\omega_1,\omega_2) = \int_{-\infty}^{\infty}\int_{-\infty}^{\infty} f(t_1,t_2)\left[\cos\omega_1 t_1\cos\omega_2 t_2\right] dt_1 dt_2 \tag{2.72}$$

which provides sign discrimination of frequencies in both dimensions. Sometimes it is sufficient to work off-resonance with a single pulse sequence. One can measure the data points

of $f_c(t_1, t_2)$ and $f_s(t_1, t_2)$, then store them as one data set. Another way is by producing the signal at various t_1 only by changing the phase of the second pulse in the pulse program by 90° [9].

Magic Angle Spinning

Magic angle spinning (MAS) is a technique often used to perform experiments in solid-state NMR spectroscopy [18, 19]. In any condensed phase, a nuclear spin experiences a great number of interactions. The main three interactions (dipolar, chemical shift anisotropy, quadrupolar) often lead to very broad and featureless lines. However, these three interactions in solids may be made time-dependent and be averaged by MAS. By spinning the sample (1-70 kHz) at the magic angle θ_m (ca. 54.74°, where $\cos^2\theta_m$=1/3) with respect to the direction of the magnetic field, the normally wide lines narrow, therefore increasing the resolution for better identification and analysis of the spectrum. The nuclear dipole-dipole interaction between magnetic moments of nuclei averages to zero while the chemical shift anisotropy, a nucleus-electron interaction, averages to a non-zero isotropic value. The quadrupolar interaction is only partially averaged by MAS leaving a residual second order quadrupolar interaction.

The physical spinning of a NMR sample is achieved via an air turbine mechanism [20]. These turbines (or rotors) come in a variety of diameters (outside diameter), from 2.0–15.0 mm, and are usually spun on air or nitrogen gas. The rotors are made from a number of different materials such as ceramics. The cylindrical rotors are axially symmetric about the axis of rotation. Samples are packed into the rotors and these are then sealed with a end cap. These caps are made from a number of different materials depending on the application required. In our lab, we have both plastic Kel-F caps used at near the ambient temperature and Boron Nitride caps used for variable temperature experiments. MAS experiments were used in our ^{13}C NMR study.

Pulse Techniques

Modern spectrometers are controlled entirely by computers. The pulsed NMR technique for doing complex experiments that have arisen over the past two decades involves the use of a sequence of RF pulses issued at certain time delays. And now the pulse technique was become an important method for physicists and chemists to investigate atoms and molecules in matter. Based on the quantum theory, different pulse sequences can be designed to realize a particular purpose: relaxation study, chemical shifts, decoupling, etc. In the following chapters, several pulse sequences will be introduced for specific experiments.

References

[1] Bloch, F.; Hansen, W. W.; Packard, M. *Phys. Rev.* **1946**, *70*, 474.

[2] Purcell, E. M.; Torrey, H. C.; Pound, R. V. *Phys. Rev.* **1946**, *69*, 37.

[3] Abragam, A. *Principles of Nuclear Magnetism*; Oxford University Press: Oxford, 1986.

[4] Burnell, E. E.; de Lange, C. A. *NMR of Ordered Liquids*; Kluwer Academic Publishers: Netherlands, 2003.

[5] Veracini, C. A. NMR spectra in liquid crystals the partially averaged spin hamiltonian; In *Nuclear Magnetic Resonance of Liquid Crystals*; Emsley, J. W., Ed.; D. Reidel Publishing Company: Netherlands, 1985; Chapter 5, p 99.

[6] Dong, R. Y. *Nuclear Magnetic Resonance of Liquid Crystals*; Springer-Verlag, 1997.

[7] Mehring, M. *High Resolution NMR Spectroscopy in Solids*; Springer-Verlag Berlin, 1976.

[8] Slichter, C. P. *Principles of Magnetic Resonance, 2nd Edition*; Springer-Verlag: Berlin, Heidelberg, New York, 1978.

[9] Schmidt-Rohr, K.; Spiess, H. W. *Multidimensional Solid-State NMR and Polymers*; Academic Press, 1994.

[10] Duer, M. J. *Introduction to Solid-State NMR spectroscopy*; Blackwell Publishing Ltd, 2004.

[11] Keeler, J. *Understanding NMR Spectroscopy*; Wiley, 2005.

[12] Sakurai, J. J. *Modern Quantum Mechanics*; Addison-Wesley: Redwood City, 1985.

[13] Dyson, F. J. *Phys. Rev.* **1949**, *75*, 486.

[14] Magnus, W. *Comm. Pure Appl. Math.* **1954**, *7*, 649.

[15] Sorensen, O. W.; Eich, G. W.; Levitt, M. H.; Bodenhausen, G.; Ernst, R. R. *Progress in NMR Spectroscopy* **1983**, *16*, 163.

[16] Xu, J. Ph.D. Thesis, University of Manitoba, 2006.

[17] Ernst, R. R.; Anderson, W. A. *Rev. Sci. Instrum.* **1966**, *37*, 93.

[18] Andrew, E. R.; Bradbury, A.; Eades, R. G. *Nature* **1959**, *183*, 1802.

[19] Lowe, I. J. *Phys. Rev. Lett.* **1959**, *2*, 285.

[20] Taylor, R. E. *Concepts in Magnetic Resonance Part A* **2004**, *22A*, 37.

Chapter 3

^{2}H NMR Spin Relaxation Study of Calamitic and Discotic Liquid Crystals

3.1 Introduction

^{2}H NMR

A nucleus in an external magnetic field has two or several spin energy levels which are produced by the interactions between the nuclear magnetic moments and the applied field. When ^{2}H nuclei stay in a large external magnetic field, there are two main contributions to their energy: Zeeman energy and quadrupolar energy. The spin Hamiltonian may be written as:

$$H = H_Z + H_Q \tag{3.1}$$

From Eq. (2.16), the time-averaged quadrupolar Hamiltonian in the high field approximation is [1]:

$$\bar{H}_Q = \frac{eQ}{2I(2I-1)} \langle R_{2,0} \rangle \frac{1}{\sqrt{6}} \left[3I_z^2 - I(I+1) \right] \tag{3.2}$$

where the bar over the Hamiltonian denotes the time average due to internal bond rotations and anisotropic motions of the molecule . $\langle R_{2,0} \rangle$ is the corresponding time-averaged second rank irreducible spherical tensor. The various energy levels of (3.2) are denoted as E_m. There are now several transition frequencies $\nu_{\Delta m} = \frac{E_{m-1} - E_m}{h}$ $(\Delta m = \pm 1)$ responsible for the observed resonance lines. The frequencies of the lines correspond to transitions $m \leftrightarrow m-1$. For the deuteron $I = 1$, we have $E_{\pm 1} = \frac{eQ}{2} \langle R_{2,0} \rangle \frac{1}{\sqrt{6}}$ and $E_0 = \frac{eQ}{2} \langle R_{2,0} \rangle \frac{-2}{\sqrt{6}}$. So the resonance frequencies will be $\nu_1 = \frac{E_0 - E_1}{h}$ and $\nu_{-1} = \frac{E_{-1} - E_0}{h}$. The transition frequencies are written as

$$\nu_Q = \frac{\omega_Q}{2\pi} = \nu_{\pm 1} = \pm \sqrt{\frac{3}{8}} \frac{eQ}{h} \langle R_{2,0} \rangle \tag{3.3}$$

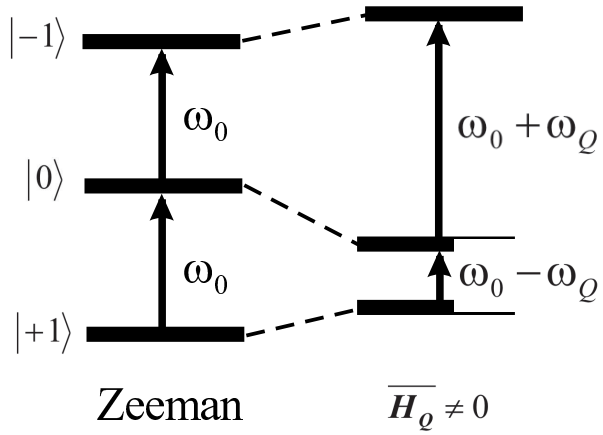

Figure 3.1: Energy level diagram of deuteron (η=0 assumed) in a large external magnetic field. $\omega_0/2\pi$ is the Larmor frequency.

.

Considering both Zeeman and quadrupole interactions, the explanatory diagram of energy levels for a deuteron spin in anisotropic media is displayed in Fig. 3.1.

Relaxation

When a collection of nuclei is irradiated at the characteristic resonant frequency of the nuclei, the population of each spin state is changed due to the excitation by the alternating magnetic field. After the rf-pulse, the spin system relaxes back to its equilibrium state, and the magnitude of the magnetization along the z-axis can be detected. Various theories and experiments have been developed to study the relaxation process since it can give information about the 'lattice' and the dynamics of the nuclei. The study of liquid crystal dynamics using nuclear spin relaxation measurements goes back to 1969 by Doane, Blinc and their coworkers [2, 3]. Practically all of the early work relied upon proton relaxation measurements [4]. However, since several different types of interactions are responsible for the overall relaxation of many chemically distinct protons it was quite difficult to assess the relative importance of the different motional processes, and selective deuteration was soon recognized [5]. Deuterium relaxation measurements are potentially the most useful for investigating molecular motions at different sites in liquid crystal molecules [6–10]. For this reason the techniques of deuteron relaxation have been employed to study the dynamics of the rod-like and disc-like liquid crystals.

The molecules in liquid crystals have different motions such as molecular rotations, translational self-diffusion, order director fluctuations, and internal motions if molecules are non-rigid. To study these motions, the spin relaxation processes need to be detected and their rates measured. These relaxation rates for experimental observables can be expressed in

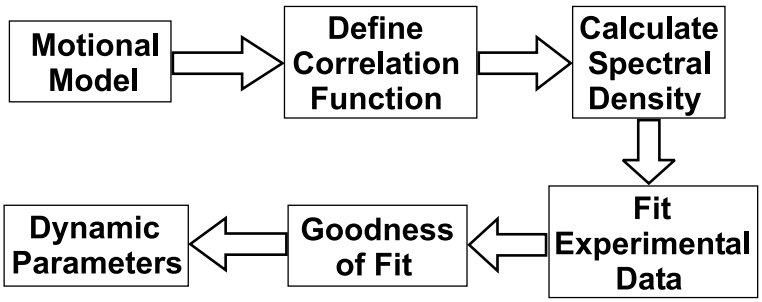

Figure 3.2: Schematic diagram of theoretical relaxation study process.

.

terms of the spectral density functions which characterize the spectrum of molecular fluctuations. Accordingly different theoretical models are introduced to describe the specific motion [11]. Generally, the relaxation study is divided into several steps: set up a motional model; define the correlation functions based on the model; calculate the spectral densities; fit the experimental data; decide the dynamic parameters from the fit of the results(Fig. 3.2). In this chapter, the experimental method to measure the relaxation times will be first introduced. And then we use two theoretical models, a rotational diffusion model [12–16] and an anisotropic viscosity model [17, 18], to study the dynamics of 10B1M7-d_{21} and HAT5a-d_6, respectively. The results are discussed in the following sections.

3.2 Pulse Sequences

Solid Echo Sequence

The solid echo pulse sequence [19] has become a routine way to acquire quadrupole splittings in liquid crystals. The ^{2}H solid state NMR spectra usually show a range up to 250kHz because of the interaction of the deuteron quadrupole moment with the electric field gradient. Since the instrument (e.g. dead time in NMR probe) cannot respond fast enough to capture the full FID over this short time scale, and to acquire a true FID signal by a simple 90° pulse is impossible. Therefore, the formation of a solid echo (Fig. 3.3) is a good technique for overcoming the effects of the dead time in determining the FID shape. By adjusting the echo delay τ, the true FID can be obtained. The formation of a solid echo can be demonstrated with density matrix theory [11, 20]. The spins initially in the I_z state, are first subjected to a 90°_x pulse (see Fig. 3.3). During the pulse, the Hamiltonian $\omega_1 I_x$ induces a 90° rotation in the $I_z - I_y$ plane bringing the spin state to $-I_y$. Following the pulse, the spins evolve under an inhomogeneous quadrupolar interaction

$$H_Q = \omega_Q(I_z^2 - \mathbf{I}^2/3) = \omega_Q Q_z \tag{3.4}$$

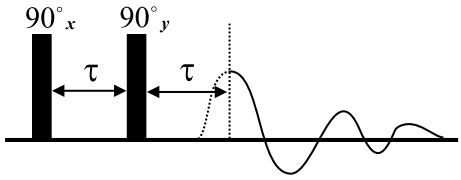

Figure 3.3: The solid echo sequence. τ is the variable interval between pulses. Acquisition of the echo signal starts at 2τ.

.

where ω_Q varies if the sample contains a distribution of the principal axis systems for the electric quadrupole interactions. This causes a fanning-out precession of I_y in the $I_y - J_y$ plane so that just before the second pulse the density matrix for each spin packet has two components

$$\rho(\tau^-) = -I_y \cos\omega_Q\tau + J_y \sin\omega_Q\tau \tag{3.5}$$

Since a 90°_y pulse does not affect I_y and causes J_y to precess in the $J_y - K_y$ plane at $-2\omega_1$, the density matrix just after the second 90°_y pulse is

$$\begin{aligned} \rho(\tau^+) &= -I_y \cos\omega_Q\tau + (J_y \cos\pi - K_y \sin\pi)\sin\omega_Q\tau \\ &= -I_y \cos\omega_Q\tau - J_y \sin\omega_Q\tau \end{aligned} \tag{3.6}$$

where J_y and K_y are components of quadrupolar polarization [11]. Further evolution of the density matrix under the quadrupole Hamiltonian leaves $\rho(t)$ in the $I_y - J_y$ plane and results in refocusing of all spin packets along y at time 2τ (see Fig. 3.3):

$$\begin{aligned} \rho(2\tau) &= -\cos\omega_Q\tau(I_y \cos\omega_Q\tau - J_y \sin\omega_Q\tau) - \sin\omega_Q\tau(J_y \cos\omega_Q\tau + I_y \sin\omega_Q\tau) \\ &= -I_y \end{aligned} \tag{3.7}$$

At a time before 2τ, there is a building up of the free induction decay reaching a maximum at 2τ from the first pulse and then decaying to zero to give a solid echo signal.

Jeener-Broekaert Pulse Sequence

The Jeener-Broekaert (JB) Pulse Sequence (a three pulse sequence) [21] is used to measure spin-lattice relaxation times by first maximizing the quadrupolar order, or 'spin alignment' according to Spiess [22]. An additional 45° pulse added to the JB sequence can produce the net effect of subtracting the equilibrium M_∞ signal (the equilibrium magnetization at infinite time) from the JB signal. This would minimize any long-term instability in the NMR signal immediately after the second 45° pulse. Besides, if a dead time problem exists making observation of signal soon after the second 45°_y pulse difficult, a refocusing 90°_y pulse may be added as in the solid echo sequence. When several doublets are of interest to be measured

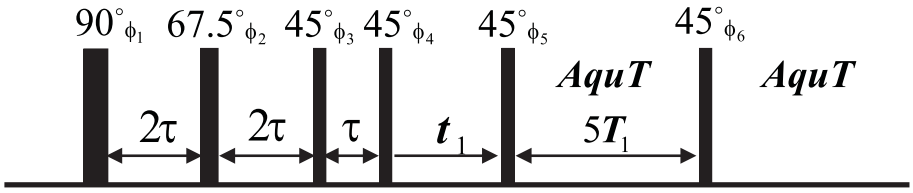

Figure 3.4: The Broadband Jeener-Broekaert pulse sequence.

.

in the same spectrum, a separate experiment with a specific τ is required to maximize the quadrupolar order of each doublet. Alternatively, broadband excitation may be used to irradiate several doublets identically using a broadband JB (BBJB) sequence, also called the Wimperis sequence [21, 23–26] (see Fig. 3.4). This is particularly useful if the NMR spectrum represents a powder sample. Also, the BBJB has the advantage of saving time on a relaxation experiment of an aligned sample with several doublets. The BBJB sequence with M_∞ subtraction and proper phase cycling is routinely used to measure spin-lattice relaxation times in the present work.

To calculate both T_{1Z} and T_{1Q} from the decay curve composed of measurements with 15 different t_1 values, the sum $S(t)$ and difference $D(t)$ of the spectrum and its reverse with respect to Larmor frequency, are given by [11]

$$\begin{aligned} S(t) &\propto exp(-t/T_{1Z}) \\ D(t) &\propto exp(-t/T_{1Q}) \end{aligned} \tag{3.8}$$

3.3 Correlation Function and Spectral Density

In NMR relaxometry, correlation functions of the orientation of atom-atom vectors are of prime importance. The time correlation function [27] is of great value for the analysis of dynamical processes in condensed phases. Correlation times that describe the rate of molecular reorientation are derived from these. Generally speaking, a correlation function is the correlation between random variables at two different points in space or time. If one considers the correlation function between random variables at the same point but at two different times then the correlation function is defined as

$$G(t) =< A(\tau)A(t+\tau) > \tag{3.9}$$

where the angle brackets represent an ensemble average and A is the dynamic variable of interest. If we compare the value of $< A(t+\tau) >$ with $< A(\tau) >$, the two values will be

correlated at sufficiently short times. This property allows one to apply the time correlator formalism to a trajectory in a molecular dynamics simulation. The spectral density is obtained from the Fourier transform of the correlation function

$$J(\omega) = Re \int_0^\infty G(\tau) exp(-i\omega\tau) d\tau \tag{3.10}$$

In the study of spin-lattice relaxation [11], the definition of the correlation function and spectral density are derived from Eq. (2.22) using the Bloch-Wangsness-Redfield theory [28–30] as

$$J_{m_L}(\omega) = Re \int_0^\infty G_{m_L}(\tau) exp(-i\omega\tau) d\tau \tag{3.11}$$

where the correlation functions of the fluctuating Hamiltonian are

$$G_{m_L}(\tau) = \left\langle \left\{ D^2_{m_L,0}[\Omega_{L,Q}(t)] - \overline{D^2_{m_L,0}} \right\} \left\{ D^{2*}_{m_L,0}[\Omega_{L,Q}(t+\tau)] - \overline{D^{2*}_{m_L,0}} \right\} \right\rangle \tag{3.12}$$

with the angular brackets being used to indicate the ensemble average over the molecules in the sample. The Euler angles $\Omega_{L,Q}(t)$ denote the orientation of the principal axis of a spin interaction tensor in the laboratory frame. In general, in liquid crystals there are three types of terms that contribute to $G_{m_L}(\tau)$: director fluctuations, molecular reorientation, and a cross-term arising from both of these motions. The above formalism is only valid in the motionally narrowing regime.

On the other hand, spectral densities can be simply related to the measured relaxation rates (T_1^{-1} or T_2^{-1}). For spin-1 systems, by using Jeener-Broekaert sequence, Zeeman spin-lattice relaxation time T_{1Z} and quadrupolar spin-lattice relaxation time T_{1Q} can be measured simultaneously. ^{2}H T_{1Z} and T_{1Q} are related to the spectral densities $J_m(m\omega_0, \Theta)$ for the director oriented at an angle Θ with respect to the external magnetic field as follows [31]:

$$\frac{1}{T_{1Q}} = 3J_1(\omega_0, \Theta) \tag{3.13}$$

$$\frac{1}{T_{1Z}} = J_1(\omega_0, \Theta) + 4J_2(2\omega_0, \Theta) \tag{3.14}$$

where ω_0 is the Larmor frequency. For the director aligned along the external magnetic field, Eqs. (3.13) and (3.14) enable the determination of spectral densities $J_1(\omega_0, 0°)$ and $J_2(2\omega_0, 0°)$. When the director is perpendicular to the external magnetic field, the spectral densities $J_1(\omega_0, 90°)$ and $J_2(2\omega_0, 90°)$ will be determined.

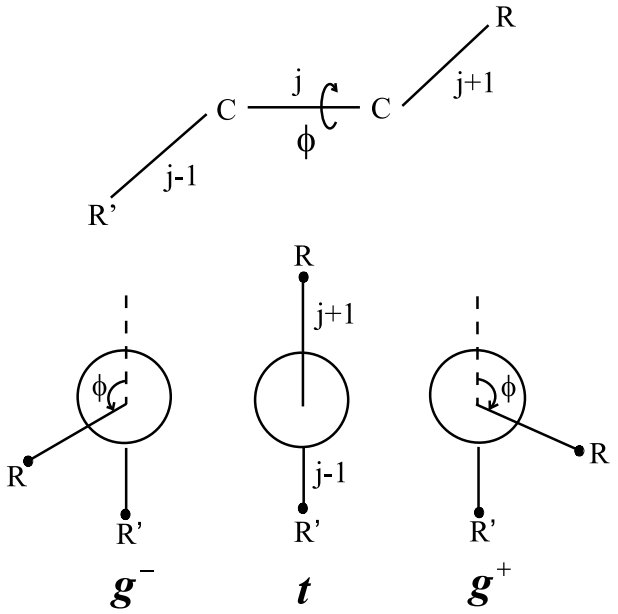

Figure 3.5: The *trans* and two symmetric *gauche* states viewed along the jth C-C bond in an alkyl chain.

.

3.4 The Additive Potential Method

The constituent molecules of liquid crystals usually contain an aromatic core and one or more flexible side chains. Since the flexible chains not only occupy space but also contribute to the anisotropic potential and interactions, they are partially responsible for molecular ordering in liquid crystals. In attempting to interpret the deuterium quadrupolar splitting $\Delta\nu_Q$, which is both temperature dependent and site dependent, it is necessary to assume that molecular conformations are independent of molecular orientation, thereby separating the internal and overall motions. The additive potential (AP) method was first used by Marcelja [32] to explicitly take the conformations of an alkyl chain into account when calculating physical properties of liquid crystals, and extended subsequently by Emsley, Luckhurst and Stockley [33]. Due to the internal degrees of freedom, the chain does not always exist in an all-trans conformation. It is necessary to determine all of the allowed conformations and their relative weights $P_{eq}(n)$, the equilibrium probability for finding the molecule in the nth conformation. To do so, the rotational isomeric state (RIS) model of Flory [34] is used. In this model, the bond lengths are taken to be fixed and the only angle allowed to vary is the bond rotation angle ϕ (See Fig. 3.5). Rotation about each carbon-carbon (C-C) bond in the chain may take one of the three dihedral angles ($\phi = 0, \pm 112°$). These correspond to the *trans* (t) and two symmetric *gauche* ($g^{\pm}$) states of the group R and R' with respect to one another (Fig. 3.5). In the RIS model, only states in the potential minima are assumed to be appreciably

populated. This is due to the very steep potential barriers between these minima. The *gauche* states have higher internal energy in comparison to that of the *trans* state by an amount E_{tg}. When the chain contains a g^+g^- or a g^-g^+ linkage, an additional internal energy $E_{g^\pm g^\mp}$ may have to be added because these linkages bring parts of the chain near to one another, the so-called 'pentane effect'. The internal energy is assumed to depend on the number of gauche linkages (N_g) and the number of $g^\pm g^\mp$ linkages ($N_{g^\pm g^\mp}$) in the chain of the nth conformer:

$$U_{int}(n) = N_g E_{tg} + N_{g^\pm g^\mp} E_{g^\pm g^\mp} \tag{3.15}$$

To evaluate $P_{eq}(n)$, one needs both the internal energy $U_{int}(n)$ and the external potential energy $U_{ext}(n,\omega)$ of the nth conformer, where ω denotes the polar angles of the director in a frame that is attached to a particular rigid fragment. The potential of mean torque $U_{ext}(n,\omega)$ is responsible for the alignment of a conformer and results from the molecular field of its neighbors. To minimize the number of parameters in $U_{ext}(n,\omega)$, it is assumed that the molecule can be divided into a small number of rigid segments. Each segment is associated with an interaction tensor that is independent of the conformation. The interaction tensor of the molecule is calculated by transforming the interaction tensors from their segmental axis systems into a common system and then adding them together. This is the basis of the AP method. The potential of mean torque for a particular conformation can be approximated by a second rank term [35]:

$$U_{ext}(n,\omega) = -\sum_m (-1)^m \epsilon^n_{2,m} C_{2,-m}(\omega) \tag{3.16}$$

where $C_{2,-m}(\omega)$ is a modified spherical harmonic and $\epsilon^n_{2,m}$, the interaction tensor for conformation n, is given by

$$\epsilon^n_{2,m} = \sum_j \epsilon^j_{2,m}(n) \tag{3.17}$$

and the sum over j is to add together interaction tensors of all the rigid subunits. In the jth segmental axis frame, $\epsilon^j_{2,r}$ represents the local interaction of the jth rigid subunit. Suppose that the aromatic core of the molecule has an interaction tensor $\epsilon^a_{2,r}$ and each C-C segment has an interaction tensor $\epsilon^c_{2,r}$. If both of them are assumed to have cylindrical symmetry, the unique components of $\epsilon^a_{2,r}$ and $\epsilon^c_{2,r}$ are X_a and X_{cc}, respectively. X_a and X_{cc} are, therefore, the model parameters, which may be varied to reproduce the observed quadrupolar splittings.

As introduced in Dong's book [11], the normalized probability of finding a molecule in conformation n making an orientation ω with the director is

$$f(n,\omega) = \frac{1}{Z} exp[-U_{int}(n)/k_BT] exp[-U_{ext}(n,\omega)/k_BT] \tag{3.18}$$

where Z, the conformation-orientational partition function, is

$$Z = \sum_n exp[-U_{int}(n)/k_BT]Q_n \tag{3.19}$$

and Q_n, the orientational partition function of conformation n, is

$$Q_n = \int exp[-U_{ext}(n,\omega)/k_BT]d\omega \tag{3.20}$$

So the probability of finding the molecule with conformation n in a mesophase is given by

$$P_{eq}(n) = \int f(n,\omega)d\omega = \frac{1}{Z}exp[-U_{int}(n)/k_BT]Q_n \tag{3.21}$$

In the deuterium NMR experiment, the quadrupolar splittings of individual conformers at the ith site can be written as [11]

$$(\Delta\nu_Q)_i = \frac{3}{2}\left(\frac{e^2qQ}{h}\right)_i \sum_n P_{eq}(n)\left[S_{bb}^{n,i} + \frac{1}{3}\eta^i(S_{aa}^{n,i} - S_{cc}^{n,i})\right] \tag{3.22}$$

where η^i is the asymmetry parameter of the quadrupole interaction and may be taken to be zero for methylene deuterons in an alkyl chain. $S_{aa}^{n,i}$, $S_{bb}^{n,i}$ and $S_{cc}^{n,i}$ are segmental order parameters in the principal axis frame (a,b,c) for the quadrupole interaction of the ith C-D bond in the molecule with conformation n. And the direction of the b axis is selected along the C-D bond. By fitting the experimental ^{2}H quadrupolar splittings, two temperature independent variables (E_{tg} and $E_{g^\pm g^\mp}$) and two temperature dependent interaction parameters (X_a and X_c) are obtained. In this dissertation, the AP method has been applied to study the orientational order profiles in a flexible mesogen 10B1M7-d_{21}.

3.5 Rotational Diffusion Model

We assume that molecular reorientation takes place through a sequence of small angular steps. The equilibrium probability $P(\Omega)$ is given by the Boltzmann distribution:

$$P(\Omega) = \frac{\exp[-U(\Omega)/kT]}{\int d\Omega \exp[-U(\Omega)/kT]} \tag{3.23}$$

where k is the Boltzmann constant, T is the temperature, and $U(\Omega)$ is the potential of mean torque acting on the molecule [36]. The symmetry of $U(\Omega)$ is determined by the symmetry of the molecule and that of the mesophase.

Given that the molecule is at orientation Ω_0 at time $t = 0$, the conditional probability $P(\Omega_0|\Omega,t)$ of finding it at orientation Ω at time t can be described [12] by a differential

equation for the rotational diffusion process

$$\frac{\partial P(\Omega_0|\Omega,t)}{\partial t} = -\sum_{\alpha\beta} L_\alpha D_{\alpha\beta}\left[L_\beta + L_\beta\left(\frac{U(\Omega)}{kT}\right)\right] P(\Omega_0|\Omega,t) \tag{3.24}$$

where $L_\beta + L_\beta\left(\frac{U(\Omega)}{kT}\right)$ is an approximate expansion of $L_\beta \exp\left[\frac{U(\Omega)}{kT}\right]$. $L_\beta (= L_x, L_y \text{ or } L_z)$ is a component of a dimensionless angular momentum operator $\vec{L}$, and $\hat{D}$ is a rotational diffusion tensor. Here we choose a molecule-fixed frame in which $\hat{D}$ is diagonal

$$\hat{D} = \begin{pmatrix} D_{xx} & 0 & 0 \\ 0 & D_{yy} & 0 \\ 0 & 0 & D_{zz} \end{pmatrix} = \rho \begin{pmatrix} 1+\epsilon & 0 & 0 \\ 0 & 1-\epsilon & 0 \\ 0 & 0 & \eta \end{pmatrix} \tag{3.25}$$

where

$$\rho \equiv \frac{D_{xx}+D_{yy}}{2}, \;\; \epsilon \equiv \frac{D_{xx}-D_{yy}}{D_{xx}+D_{yy}}, \;\; \eta \equiv \frac{2D_{zz}}{D_{xx}+D_{yy}} \tag{3.26}$$

ρ refers to tumbling rate of the molecule, η is the ratio between spinning and tumbling rates of the molecule, and ϵ is an asymmetry parameter of the diffusion tensor. In the case of a symmetric top molecule [13, 14], $\epsilon = 0$, ρ becomes $D_\perp$, the diffusion constant about an axis perpendicular to the long molecular axis, and η is the ratio between the diffusion constant about the long molecular axis $D_\parallel$ and $D_\perp (D_\parallel / D_\perp)$. The above diffusion equation becomes [15]

$$\begin{aligned} \frac{1}{D_\perp}\frac{\partial P(\Omega_0|\Omega,t)}{\partial t} &= -\left\{L_x^2 + L_x\left[L_x\frac{U(\Omega)}{kT}\right]\right\} P(\Omega_0|\Omega,t) \\ &\quad -\left\{L_y^2 + L_y\left[L_y\frac{U(\Omega)}{kT}\right]\right\} P(\Omega_0|\Omega,t) \\ &\quad -\eta\left\{L_z^2 + L_z\left[L_z\frac{U(\Omega)}{kT}\right]\right\} P(\Omega_0|\Omega,t) \\ &= \mathbf{\Gamma} P(\Omega_0|\Omega,t) \end{aligned} \tag{3.27}$$

where $\mathbf{\Gamma}$ is the diffusion operator. The symmetrized form of Eq. (3.27) can be written as

$$\frac{1}{D_\perp}\frac{\partial \hat{P}(\Omega_0|\Omega,t)}{\partial t} = \hat{\Gamma}\hat{P}(\Omega_0|\Omega,t) \tag{3.28}$$

where the symmetrized diffusion operator

$$\begin{aligned} \hat{\Gamma} &= P^{-1/2}(\Omega)\mathbf{\Gamma}P^{1/2}(\Omega) \\ &= -\left\{\nabla^2 + \frac{1}{2}\left[\nabla^2\frac{U(\Omega)}{kT}\right] - \frac{1}{4}\left[L_+\frac{U(\Omega)}{kT}\right]\left[L_-\frac{U(\Omega)}{kT}\right] - \frac{1}{4}\eta\left[L_z\frac{U(\Omega)}{kT}\right]^2\right\} \end{aligned} \tag{3.29}$$

$$\hat{P}(\Omega_0|\Omega,t) = P^{-1/2}(\Omega)P(\Omega_0|\Omega,t)P^{1/2}(\Omega_0) \tag{3.30}$$

with the nabla operator $\nabla^2 = L_x^2 + L_y^2 + \eta L_z^2$, $L_\pm = L_x \pm iL_y$ being the angular momentum step operator and $\hat{P}(\Omega_0|\Omega,t)$ is the symmetrized conditional probability. Eq. (3.28) can be solved using a matrix representation in a basis of normalized Wigner matrices

$$\mathcal{D}^L_{m,n}(\Omega) = \sqrt{(2L+1)/8\pi^2} D^L_{m,n}(\Omega) \tag{3.31}$$

In particular,

$$\hat{P}(\Omega_0|\Omega,t) = \sum_{Lmn} C^{mn}_L(\Omega_0,t)\mathcal{D}^L_{m,n}(\Omega) \tag{3.32}$$

where the expansion coefficients, C^{mn}_L, are evaluated by using the initial condition $\hat{P}(\Omega_0|\Omega,0)$ $= \delta(\Omega - \Omega_0)$ to give

$$C^{mn}_L(\Omega_0,0) = \mathcal{D}^{L*}_{m,n}(\Omega_0) \tag{3.33}$$

By substituting Eq. (3.32) in Eq. (3.28), multiplying both sides on the left by $\mathcal{D}^{L*}_{m,n}(\Omega)$ and integrating over Ω, a system of linear differential equations is obtained:

$$\frac{1}{D_\perp}\dot{C}(t) = \hat{R}C(t) \tag{3.34}$$

where

$$\hat{R}_{L'm'n',Lmn} = \int d\Omega \mathcal{D}^{L'*}_{m',n'}(\Omega)\hat{\Gamma}\mathcal{D}^L_{m,n}(\Omega) \tag{3.35}$$

By solving Eq. (3.34) as an eigenvalue problem using a basis set of $m = 40$ and $n = 20$, the symmetrized conditional probability $\hat{P}(\Omega_0|\Omega,t)$ can be obtained [11]. This is required to evaluate the reorientational correlation functions because

$$\begin{aligned} g^L_{mn}(t) &= \left\langle D^L_{m,n}(\Omega_0) D^{L*}_{m,n}(\Omega)\right\rangle \\ &= \int d\Omega_0 P^{1/2}(\Omega_0) D^L_{m,n}(\Omega_0) \times \int d\Omega P^{1/2}(\Omega)\hat{P}(\Omega_0|\Omega,t) D^{L*}_{m,n}(\Omega) \end{aligned} \tag{3.36}$$

For $L = 2$, the above equation can be rewritten in a form more immediately useful for computer programming, i.e., as an infinite sum of decaying exponentials [15]:

$$g^2_{mn}(t) = \sum_K (A^2_{mn})_K exp[(B^2_{mn})_K t] \tag{3.37}$$

where $(B^2_{mn})_K/D_\perp$, the decay constants, are the eigenvalues of the diffusion matrix and $(A^2_{mn})_K$, the relative weights of the exponentials, are the corresponding eigenvectors. As a simplified example, for cylindrical molecules in uniaxial mesophases the numerical solutions have been provided by Vold and Vold [16]:

$$g^2_{m_L m_M}(t) = c_{m_L m_M} \sum_{j=1}^{3} a^{(j)}_{m_L m_M} exp\left[-t/\tau^{(j)}_{m_L m_M}\right] \tag{3.38}$$

where $c_{m_L m_M}$ are the mean square of the Wigner rotation matrices, and $a^{(j)}_{m_L m_M}$ represent normalized weights of each exponential whose time constant

$$\left[\tau^{(j)}_{m_L m_M}\right]^{-1} = \frac{6D_\perp}{b^{(j)}_{m_L m_M}} + m_M^2(D_\parallel - D_\perp) \tag{3.39}$$

The $a^{(j)}_{m_L m_M}$, $b^{(j)}_{m_L m_M}$ and $c_{m_L m_M}$ coefficients for all the correlation functions are given numerically as a polynomial in $< P_2 >$.

3.6 Decoupled Model for Correlated Internal Motions

To describe the correlated internal bond rotations and the overall reorientation of a molecule, a decoupled model based on a master rate equation has been developed [11, 37, 38]. Firstly, to evaluate the correlation function in Eq. (3.12), it is necessary to find the conditional probability $p_{il_0}[\Omega_{LM}, t|\Omega_{LM}(0), 0]$ that at time t, the molecule has configuration i and orientation Ω_{LM} given that at $t = 0$, the molecule has configuration l and $\Omega_{LM}(0)$. Using the assumption of decoupling internal and external motions, it can be expressed as the product of configuration and orientation conditional probabilities:

$$p_{il_0}[\Omega_{LM}, t|\Omega_{LM}(0), 0] = p(i, t|l, 0)p[\Omega_{LM}, t|\Omega_{LM}(0), 0] \tag{3.40}$$

Now using the above conditional probability to express the ensemble average of $\left\langle D^2_{m_L,0}[\Omega_{LQ}(t)] \times D^{2*}_{m_L,0}[\Omega_{LQ}(t+\tau)]\right\rangle$,

$$\begin{aligned} G_{m_L}(t) &= \sum_{i,l} \int\int d\Omega_{LM} d\Omega_{LM}(0) \left(D^2_{m_L,0}[\Omega_{LQ}(0)] D^{2*}_{m_L,0}[\Omega_{LQ}(t)] - \overline{D^2_{m_L,0} D^{2*}_{m_L,0}} \right) \\ &\quad \times P_{eq}(l) p_{il_0}[\Omega_{LM}, t|\Omega_{LM}(0), 0] \end{aligned} \tag{3.41}$$

where $P_{eq}(l)$ is the equilibrium probability of occurrence of configuration l, which can be obtained by using Eq. (3.21), and $p[\Omega_{LM}, t|\Omega_{LM}(0), 0]$ is the orientation conditional probability described by Eq. (3.24). The configuration conditional probability $p(i, t|l, 0)$ is required to evaluate internal correlation functions $\left\langle D^2_{m_N,0}[\Omega_{NQ}(0)] D^{2*}_{m'_N,0}[\Omega_{NQ}(t)] \right\rangle$. Here we use the subscripts L, M, N and Q to denotes the lab frame, molecular frame, segmental frame and principal axis frame, respectively. Thus, for $m_L = 1$ or 2:

$$\begin{aligned} G_{m_L}(t) &= \sum_{m_M} \sum_{m_N} \sum_{m'_N} D^2_{m_M, m_N}(\Omega_{MN}) D^{2*}_{m_M, m'_N}(\Omega_{MN}) g^2_{m_L m_M}(t) \\ &\quad \times \left\langle D^2_{m_N,0}[\Omega_{NQ}(0)] D^{2*}_{m'_N,0}[\Omega_{NQ}(t)] \right\rangle \end{aligned} \tag{3.42}$$

where $\overline{D^2_{m_N,0}} = 0$ has been assumed. For $m_L = 0$ there is an additional term in Eq. (3.42), which involves the square of $\overline{P_2}$ [39]. The internal correlation functions describe internal

motion of the chain with respect to the N frame. For the conformer with configuration i, $\beta^i_{N,Q}$ and $\alpha^i_{N,Q}$ are used to denote the polar angles of the C-D bond in the N frame, and the internal correlation functions can be evaluated according to

$$\left\langle D^2_{m_N,0}[\Omega_{NQ}(0)]D^{2*}_{m'_N,0}[\Omega_{NQ}(t)]\right\rangle = \sum_{i,l} p_{eq}(l)exp(-im_N\alpha^l_{N,Q})d^2_{m_N0}(\beta^l_{N,Q}) \times p(i,t|l,0)exp(im'_N\alpha^i_{N,Q})d^2_{m'_N0}(\beta^i_{N,Q}) \quad (3.43)$$

It is necessary to find the configuration conditional probability $p(i,t|l,0)$ in Eq. (3.43) to obtain the internal correlation functions. This is achieved by following the master equation method of Wittebort and Szabo [40]. Conformational transitions between N distinct configurations occur via one-bond, two-bond, or three-bond motion [41, 42] in the chain. These bond motions are characterized by phenomenological jump rate constants k_1, k_2, k_3, respectively. In general, there is more than one elementary jump rate constant for each type of bond motion due to the difference in the number of *gauche* linkages in the two affected conformations. But this is ignored for simplicity. Transitions among configurations are described by a master equation:

$$\frac{\partial}{\partial t}p_{il_0}(t) = \sum_{j=1}^{N} R_{ij}p_{jl_0}(t) \quad (3.44)$$

where R_{ij} is the rate constant for transition from configuration j to configuration i. R_{ij} is related to the elementary jump rate constant r_{ij} which depends on the type of bond motion in the transition. r_{ij} is zero if a transition cannot occur via one of the three types of bond motion. The diagonal matrix elements of R are the negative of the sum of all jump rates that deplete the configuration i,

$$R_{ii} = -\sum_{j\neq i} R_{ji} \quad (3.45)$$

R_{ij} must also satisfy the detailed-balance principle,

$$R_{ij}P_{eq}(j) = R_{ji}P_{eq}(i) \quad (3.46)$$

Because of this requirement and $r_{ij} = r_{ji}$, $R_{ij} = P_{eq}(i)r_{ij}$. The master equation can again be solved as an eigenvalue problem to give the conditional probability

$$p_{il_0}(t) = x^{(1)}_i[x^{(1)}_l]^{-1}\sum_{k=1}^{N} x^{(k)}_i x^{(k)}_l exp(-|\lambda_k|t) \quad (3.47)$$

where λ_k and $\vec{x}^{(k)}$ are eigenvalues and eigenvectors obtained from diagonalizing a symmetrized R matrix. There are N real and negative eigenvalues. One of these ($k = 1$) is zero, and the corresponding eigenvector $\vec{x}^{(1)}$ is given by the equilibrium distribution of configurations:

$$x^{(1)}_l = [P_{eq}(l)]^{1/2} \quad (3.48)$$

Using Eq. (3.47) in Eq. (3.41), the correlation function $G_{m_L}(t)$ can be obtained, and the spectral density $J_{m_L}(m_L\omega)$ also can be derived based on the definition Eq. (3.11). In this dissertation the chain dynamics of 10B1M7-d_{21} will be studied based on this method (See sec.3.8.2).

3.7 Anisotropic Viscosity Model

The Anisotropic Viscosity Model (AVM) [17, 18] differs from the small step rotational diffusion model in the manner of solving the rotation diffusion equation. When the viscosity anisotropy of the mesophase is taken into account, the rotational diffusion tensor is assumed to have a diagonal form in the laboratory frame with its z axis along the director. Using a rotational diffusion tensor that is time-independent and diagonal in the laboratory frame, Eq. (3.27) was solved whose rotational diffusion operator $\mathbf{\Gamma}$ now involves derivatives with respect to α and β only. According to this model, the principal components of the diffusion tensor refer to rotational motions about the space-fixed axes. For symmetric tops in uniaxial phase ($D_{xx} = D_{yy}$), the eigenfunctions of $\mathbf{\Gamma}$ in terms of Wigner functions are independent of the choice of frame. Here we use α-motion to denote the precession motion of the molecule about the director and β-motion to denote the tumbling motion of the molecule about an axis perpendicular to the director. Modifying the Eq. (3.39) with different symbols $D_\alpha = D_\parallel$ and $D_\beta = D_\perp$, the time constant for each exponential is now given by

$$\left[\tau^{(j)}_{m_L m_M}\right]^{-1} = \frac{6D_\beta}{b^{(j)}_{m_L m_M}} + m_L^2(D_\alpha - D_\beta) \tag{3.49}$$

while the correlation functions $g^2_{m_L m_M}(t)$ are still given by Eq. (3.38) for cylindrical molecules reorienting in uniaxial mesophases. The AVM is applicable in mesophases in which the order parameter is close to 1.

3.8 Chain Dynamics study of 10B1M7-d_{21}

3.8.1 Introduction

^{2}H NMR spin-lattice relaxation times are particularly important to obtain detailed dynamic information of biaxial molecules in uniaxial phases, since the theories have been developed to link the spectral densities to dynamic parameters (such as diffusional coefficients and activation energies) describing the individual overall molecular, internal and collective motions

over a broad timescale. Even though relaxation times can also be measured in tilted smectic phases (e.g. SmC*), there are several difficulties in linking them to the dynamic parameters. These difficulties are both theoretical and experimental and are either due to the phase biaxiality or to the dependence of the relaxation times on the polar angles defining the position of the local phase director with respect to the external magnetic field. In fact, theoretical models taking into account phase biaxiality [43, 44] are quite complex and such a model would require an unavailably large set of experimental data.

Recently, a new approach for SmC* was proposed based on the assumption of phase uniaxiality and has allowed the quantitative analysis of relaxation times in tilted smectic phases by means of existing theoretical models [45, 46]. The present work aims to test the application of this approach on the relaxation data obtained from an achiral chain: deuterated 10B1M7-d_{21}. This compound has been studied previously at 15.1 and 46MHz [47], and the decoupled model was used successfully to gain motional parameters such as spinning ($D_{\parallel}$) and tumbling ($D_{\perp}$) diffusion constants of the molecule, as well as internal jump rates in the SmA phase. The present investigation extends the study to a new frequency (61.4MHz) by measuring the deuterium spin-lattice relaxation in the SmA and SmC* phases of 10B1M7-d_{21}. In this dissertation, the data in SmA and SmC* phases are analyzed to provide more reliable motional information. Moreover, the biaxial phase of SmC* phase is studied by treating it as an uniaxial phase while considering the tilt angle.

3.8.2 Theoretical Spectral Densities

The complete description of the molecular chain dynamics is based on the AP method, the small step rotational diffusion model and the decoupled model. The decoupled model has successfully been used to understand the internal dynamics of flexible chain(s) in many different liquid crystals studied by the proton and deuteron spin relaxation [48–58]. These studies have shown that the three-bond motion tends to give rather high k_3 (about 10^{17}-$10^{18}s^{-1}$) values in some of the studied materials. To overcome the apparent high k_3 rate, a modified decoupled model has later been proposed [38, 59] in which the three-bond motion is replaced by the type-II motion of Helfand [60]. Helfand has classified conformational transitions in the chain into three different types (type-I, -II and -III motions). The one-bond (k_1) motion is given by $ijklm \rightarrow ijklm'$, while the two-bond motion is for $ijklm \rightarrow ijkl'm$ and $ijkl'm'$. These two are called type-III motions by Helfand [60], while type-II motion consists of kink formation ($tttt \rightarrow g^{\pm}tg^{\mp}t$) described by a jump rate k'_g and *gauche* migration $tttg \rightarrow tgtt$ described by k_g. The type-I motion (e.g. k_3 motion) should call for high activation

energies [61, 62] because several bonds must be activated almost simultaneously. Thus the type-I motion was totally discarded in the modified decoupled model.

For an alkyloxy chain, the O-C_α bond is taken to be fixed on the phenyl ring plane with a C_{ar}-O-C_α angle of 126.4° where the subscript ar denotes aromatic, and the ∠C-C-C, ∠C-C-H and ∠H-C-H are assumed to be 113.5°, 107.5° and 113.6°, respectively [63]. The O-C bond is treated the same as a C-C bond, and the ∠O-C-C is set the same as ∠C-C-C. To construct the external mean potential $U_{ext}(n,\omega)$ using the AP method, we limit the conformations to those with relatively high probabilities. A decyloxy chain, which contains six or more *gauche* C-C bonds, can be safely ignored. Even the conformations with two consecutive *gauche* C-C bonds (i.e., $g^\pm g^\pm$ and $g^\pm g^\mp$) can be ignored. With these assumptions, the number of conformations (N) in 10B1M7-d_{21} is reduced to 683. This represents a great reduction from the possible maximum number of 19683. Based on the AP method introduced before, the $P_{eq}(n)$ is obtained from fitting the chain splittings.

In setting up the transition rate matrix R among the N conformations, the following conditions are imposed: (1) No direct transition between g^+ and g^- states as this costs too much energy; (2) transitions between *gtgtt* and *tgtgt* cannot proceed directly as these also cost too much energy (however, $gtgtt \rightleftharpoons ttttt \rightleftharpoons tgtgt$ are possible); (3) no three-bond (k_3) motion is allowed. There are 2776 transitional elements in R when considering both forward and reverse transitions. Among the 1338 forward transitions, there are 342 type-III motions about the C_8-C_9 bond (k_1 motions), 170 type-III motions about the C_7-C_8 bond (k_2 motions), and 876 type-II motions. For the latter type, 438 transitions are for the gauche migration (e.g., $ttttg^\pm tt \rightleftharpoons ttg^\pm tttt$) and 438 transitions are for the kink formation (e.g., $ttttttt \rightleftharpoons ttg^- tg^+ tt$). The spectral densities of the C_i deuterons on the chain of 10B1M7-d_{21} when the director $\hat{n}$ is along the $\vec{B}$ field can be written as [11]:

$$
\begin{aligned}
J_m^{(i)}(m\omega, 0^\circ) \;=\; & \frac{3\pi^2}{2}(q_{CD}^{(i)})^2 \sum_n \sum_{n'} \sum_{k=1}^{N} \\
& \left(\sum_{l=1}^{N} \sum_p d_{n0}^2 \left(\theta_{N,Q}^{(i)l}\right) d_{np}^2(\theta) \times exp\left[-i\left(n\varphi_{N,Q}^{(i)l}\right)\right] x_l^{(1)} x_l^{(k)} \right) \\
& \times \left(\sum_{l'=1}^{N} \sum_{p'} d_{n'0}^2 \left(\theta_{N,Q}^{(i)l'}\right) d_{n'p'}^2(\theta) \times exp\left[-i\left(n'\varphi_{N,Q}^{(i)l'}\right)\right] x_{l'}^{(1)} x_{l'}^{(k)} \right) \\
& \times \sum_j \frac{(\beta_{mnn'}^2)_j \left[(\alpha_{mnn'}^2)_j + |\lambda_k|\right]}{m^2\omega^2 + \left[(\alpha_{mnn'}^2)_j + |\lambda_k|\right]^2}
\end{aligned}
\tag{3.50}
$$

where $q_{CD}^{(i)} = 165kHz$ is the quadrupolar coupling constant. $\theta_{N,Q}^{(i)l}$ and $\varphi_{N,Q}^{(i)l}$ are the polar angles for the C_i-D bond of the conformer l in the molecular N frame fixed on the phenyl

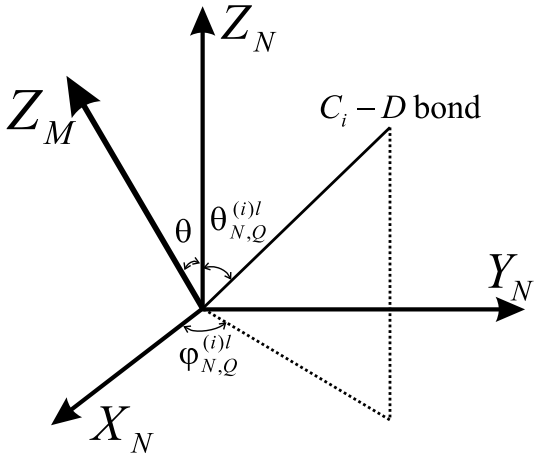

Figure 3.6: Illustration of the Euler angle transformation: $\theta^{(i)l}_{N,Q}$ and $\varphi^{(i)l}_{N,Q}$ are the polar angles for the C_i-D bond of the conformer l in the molecular N frame fixed on the phenyl ring core, θ is the angle between the Z_N-axis (or para axis) and the long molecular axis (Z_M) of 10B1M7-d_{21}.

.

ring core, θ is the angle between the Z_N-axis (or para axis) and the long molecular axis (Z_M) of 10B1M7-d_{21} (See Figure 3.6). When constructing the R matrix elements, the computer program can search and decide which kind of conformational transformation motion for each element. λ_k and $\vec{x}^{(k)}$ are the eigenvalues and eigenvectors from diagonalizing the R matrix. $(\alpha^2_{mnn'})_j/D_\perp$, the decay constants, and $(\beta^2_{mnn'})_j$, the relative weights of the exponentials in the correlation functions, are the eigenvalues and eigenvectors from diagonalizing the matrix of rotational diffusion operator Γ.

In the SmC* phase, molecules tilt uniformly in all layers, but the tilt rotates azimuthally when going from one layer to the next one to form a helicoidal structure. The observed quadrupolar doublet is found to be independent of the azimuthal angle on the NMR time scale. The new approach suggests that the observed spectral densities in the SmC* phase can be understood by taking into account the tilt angle β of the molecular 'director' with respect to the external $\vec{B}$ field. One can express the spectral densities $J_m(m\omega, \beta)$ as follows [8]:

$$\begin{aligned} J_1(\omega,\beta) &= \frac{3}{2}\left(\cos^2\beta\sin^2\beta\right) J_0(\omega, 0^\circ) \\ &\quad + \frac{1}{2}\left(1 - 3\cos^2\beta + 4\cos^4\beta\right) J_1(\omega, 0^\circ) \\ &\quad + \frac{1}{2}\left(1 - \cos^4\beta\right) J_2(\omega, 0^\circ) \qquad (3.51) \\ J_2(2\omega,\beta) &= \frac{3}{8}\left(1 - \cos^2\beta\right)^2 J_2(2\omega, 0^\circ) \\ &\quad + \frac{1}{2}\left(1 - 4\cos^4\beta\right) J_1(2\omega, 0^\circ) \\ &\quad + \frac{1}{8}\left(1 + 6\cos^2\beta + \cos^4\beta\right) J_2(2\omega, 0^\circ) \qquad (3.52) \end{aligned}$$

in which the azimuthal angle ϕ, describing the rotation of tilt in the helical structure, has been set to zero, and all biaxial spectral densities [64] have been ignored. It is proposed that the lack of ϕ dependence in quadrupolar doublets and spin relaxation rates is the basis of using Eqs.(3.50-3.52) in the SmC* phase of 10B1M7-d_{21}. A θ value of 8° was used in Eq. (3.50) [47], which is the Z_N-axis (or para axis) and the long molecular axis (Z_M) of 10B1M7-d_{21}. The fitting of deuterium splittings in the SmA and SmC* phase was carried out based on the AP method.

3.8.3 Experimental Methods

The chiral liquid crystal 10B1M7-d_{21} has various mesophases at different ranges of temperature. The molecular structure and phase transition temperatures already have been shown in Fig. 1.10. All deuterium experiments were carried out at 61.4 MHz. Temperature of the sample was controlled with a Bruker variable-temperature unit. Experiments were always performed after the sample was slowly cooled from the isotropic phase. Enough waiting time between each temperature change was taken to assure temperature stabilization and equilibration. Figure 3.7 shows the typical deuterium spectrum in the SmA and SmC* phases of 10B1M7-d_{21}. The NMR probe was always re-tuned for every temperature change to avoid slight de-tuning of the probe. The temperature gradient across the sample in the NMR probe was estimated to be less than 0.3°C.

The Zeeman(T_{1Z}) and quadrupolar(T_{1Q}) spin-lattice relaxation times were measured simultaneously using a broadband Jeener-Broekaert pulse sequence [23] modified to subtract the equilibrium magnetization. The ^{2}H 90° pulse length was 2.6 μs, and the relaxation delay was between 0.3 and 1.5 s depending on the T_1 values. In every experiment, 15 partially relaxed spectra were collected. T_{1Z} and T_{1Q} were derived from Eq. (3.8). It should be noted that the deuteron peaks for C_1 and C_2 , as well as those of C_5 and C_6 overlap to make them indistinguishable. The T_1 values for the overlapped sites were measured as a single value. During the analysis of the relaxation data, especially in the SmC* phase, we noticed that the peaks for $C_{1,2}$, C_3, and C_4 became progressively more unresolved with decreasing temperature. This could lead to unacceptable errors when calculating areas to extract the T_{1Z} and T_{1Q} values. To ascertain the relaxation measurements for these sites, a peak deconvolution method based on the Bruker software has been employed to isolate $C_{1,2}$, C_3, and C_4 peaks where possible in order to obtain their proper areas.

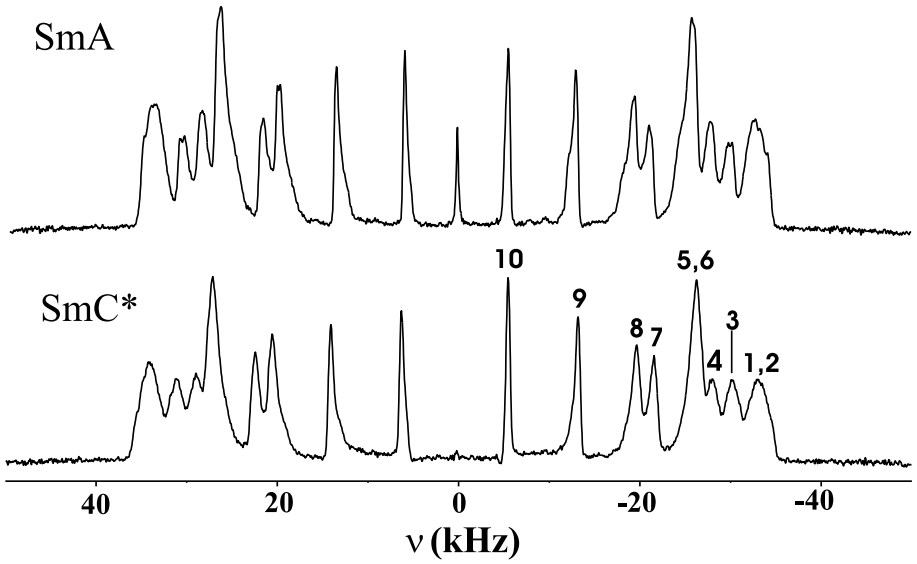

Figure 3.7: Typical deuterium NMR spectra of 10B1M7-d_{21} in its SmA and SmC* phases. The peak assignments are based on the assumption that the splittings decrease monotonically down the chain.

.

3.8.4 Results and Discussion

The observed deuterium splittings are shown as a function of the temperature in Fig. 3.8. To fit the spectral densities, we first fit the quadrupolar splittings in the smectic phases using the AP method in terms of two adjustable parameters X_a and X_c, the interaction parameters of the 'core' and C-C bond, respectively. We define $\lambda = X_c/X_a$. Both X_a and λ are varied at each temperature to give the theoretical splitting curves shown in Fig. 3.8. The derived order parameters S_{zz} and $S_{xx} - S_{yy}$ for the 'average' conformer are shown in Fig. 3.9, while X_a and λ are plotted versus the temperature in Fig. 3.10. S_{zz} and X_a are seen to decrease with decreasing temperature in the SmC* phase due to the onset of tilt angle. The average tilt angle (shown also in Fig. 3.9) used in Eqs. (3.51-3.52) is derived from several quadrupolar splittings from the chain in the SmC* phase by comparing them with their extrapolated values from the SmA phase [65]. Now S_{zz} and $S_{xx} - S_{yy}$ are used to give the potential $U(\Omega)$ of mean torque in solving the rotational diffusion equation. In the SmC* phase, S_{zz} values are those extrapolated from the SmA phase [45]. X_a and λ are needed to evaluate the $P_{eq}(n)$ (Eq. (3.21)), the equilibrium probability of the nth conformer. The X_a values used in the SmC* phase are also extrapolated from the SmA phase, while λ as well as $S_{xx} - S_{yy}$ are those given in Figs.3.9-3.10.

The relaxation times T_{1Z} and T_{1Q}, measured by JB sequence, are plotted in Figure 3.11.

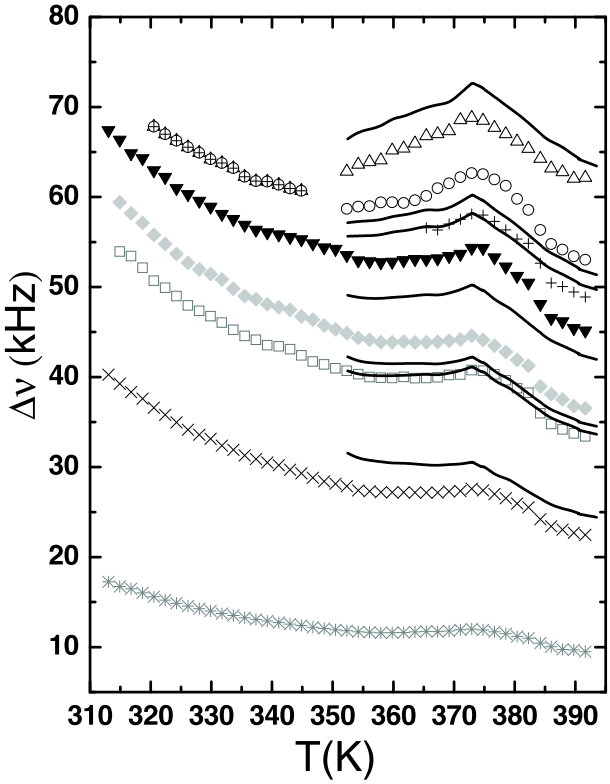

Figure 3.8: Plot of quadrupolar splittings of 10B1M7-d_{21} versus the temperature. Solid down triangles, diamonds denotes $C_{5,6}$ and C_7 sites. Open up triangles, circles, pulses, squares and crosses, stars denote $C_{1,2}$, C_3, C_4, C_8, C_9 and C_{10}, respectively. Solid curves are calculated splittings, starting from the top, $C_{1,2}$, C_3, C_4, $C_{5,6}$, C_7, C_8 and C_9 sites.

.

Figures 3.12 and 3.13 show the deuterium spectral densities $J_1(\omega)$ and $J_2(2\omega)$ versus the temperature at 61.4 MHz for deuterons of carbon sites 1 to 9 in 10B1M7-d_{21} in both SmA and SmC* phases, together with those reproduced from the literature [66] at 15.1 and 46 MHz. We first carried out individual analysis using Eq. (3.50) to fit the spectral densities at each temperature. To do the global analysis of SmA phase, nine temperatures are used together with the following Arrhenius type relations:

$$\begin{aligned} D_\perp &= D_\perp^0 exp[-E_a^{D_\perp}/RT] \\ D_\parallel &= D_\parallel^0 exp[-E_a^{D_\parallel}/RT] \\ k_i &= k_i^0 exp[-E_a^{k_i}/RT] \\ k_g &= k_g^0 exp[-E_a^{k_g}/RT] \\ k_g' &= k_g'^0 exp[-E_a^{k_g'}/RT] \end{aligned} \tag{3.53}$$

where $k_i = k_1$ or k_2, $D_\perp^0$, $D_\parallel^0$, k_i^0, k_g^0 and $k_g'^0$ are preexponential constants and E_a with an appropriate superscript is the corresponding activation energy. The fitting has produced

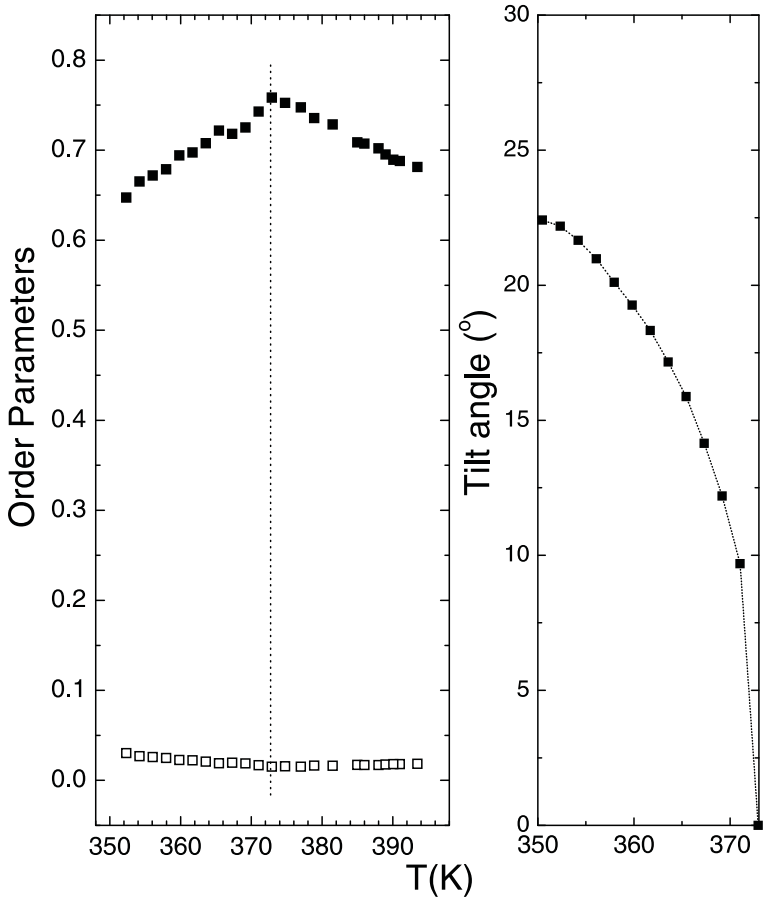

Figure 3.9: a) Plots of S_{zz} (solid square) and $S_{xx} - S_{yy}$ (open square) versus the temperature in the SmA and SmC* phase of 10B1M7-d_{21}. b) Plot of the tilt angle versus the temperature in the SmC* phase of 10B1M7-d_{21}.

global target parameters, which are summarized in Table 3.1 together with their error limits. In fitting the smoothed experimental spectral densities, we minimized the mean-squared percent deviation F with AMOEBA. The fitting quality factor Q is defined by

$$Q = \frac{\sum_k \sum_\omega \sum_i \sum_m \left[J_m^{(i)calc}(m\omega) - J_m^{(i)expt}(m\omega) \right]_k^2}{\sum_k \sum_\omega \sum_i \sum_m \left[J_m^{(i)expt}(m\omega) \right]_k^2} \tag{3.54}$$

where the sum over k is for nine temperatures. We obtained a Q value of 3.7%. The calculated spectral densities are shown in Figs. 3.12-3.13 by solid (J_1) and dashed (J_2) curves. Note that the calculated spectral densities for overlapped sites are averaged before fitting to their experimental values. As seen in these figures, the fittings of the two lower frequencies have not changed in a noticeable way in comparison with ref. [47] after including an additional frequency in the fitting. Some systematic deviations between calculated and experimental spectral densities do exist for some sites (e.g. $C_{1,2}$), and we believe that these discrepancies likely stem from the simplifying assumptions used in our decoupled model for a relatively

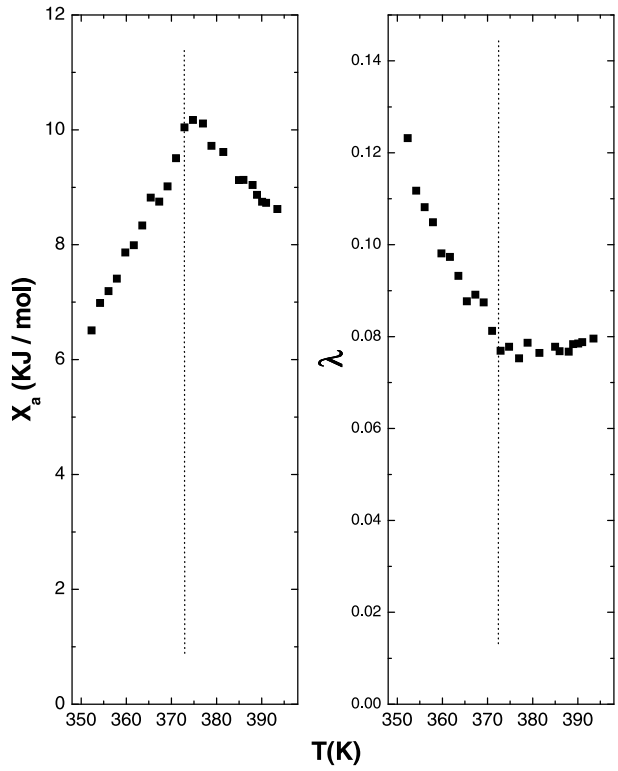

Figure 3.10: Plots of interaction parameters X_a and $\lambda(= X_c/X_a)$ versus the temperature of 10B1M7-d_{21} at 61.4 MHz.

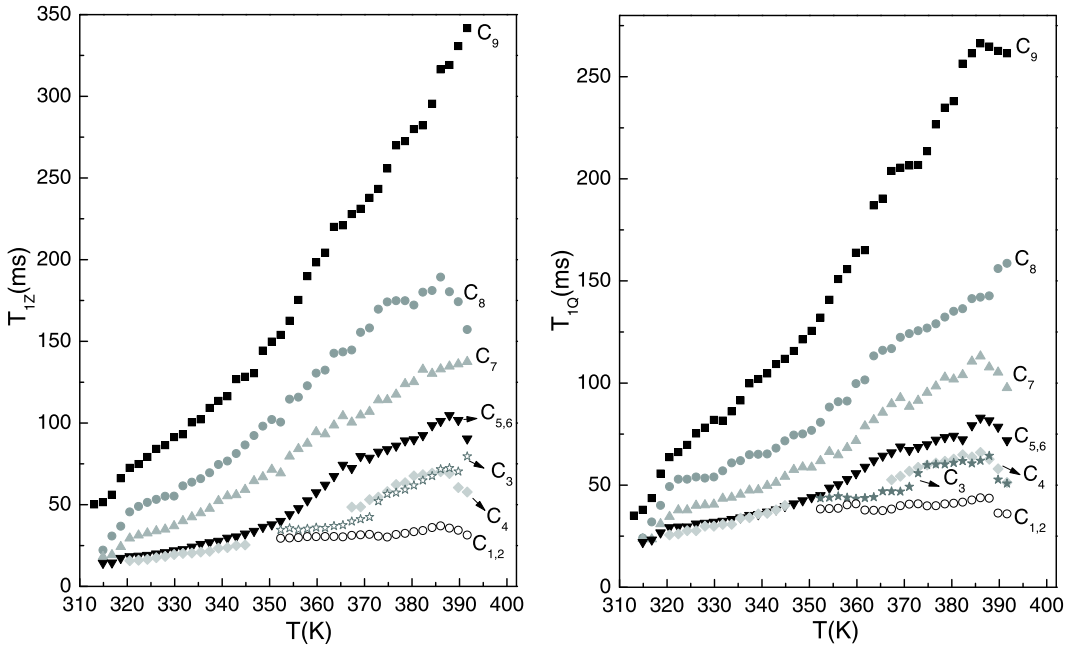

Figure 3.11: Plots of T_{1Z} and T_{1Q} versus the temperature of 10B1M7-d_{21} at 61.4 MHz.

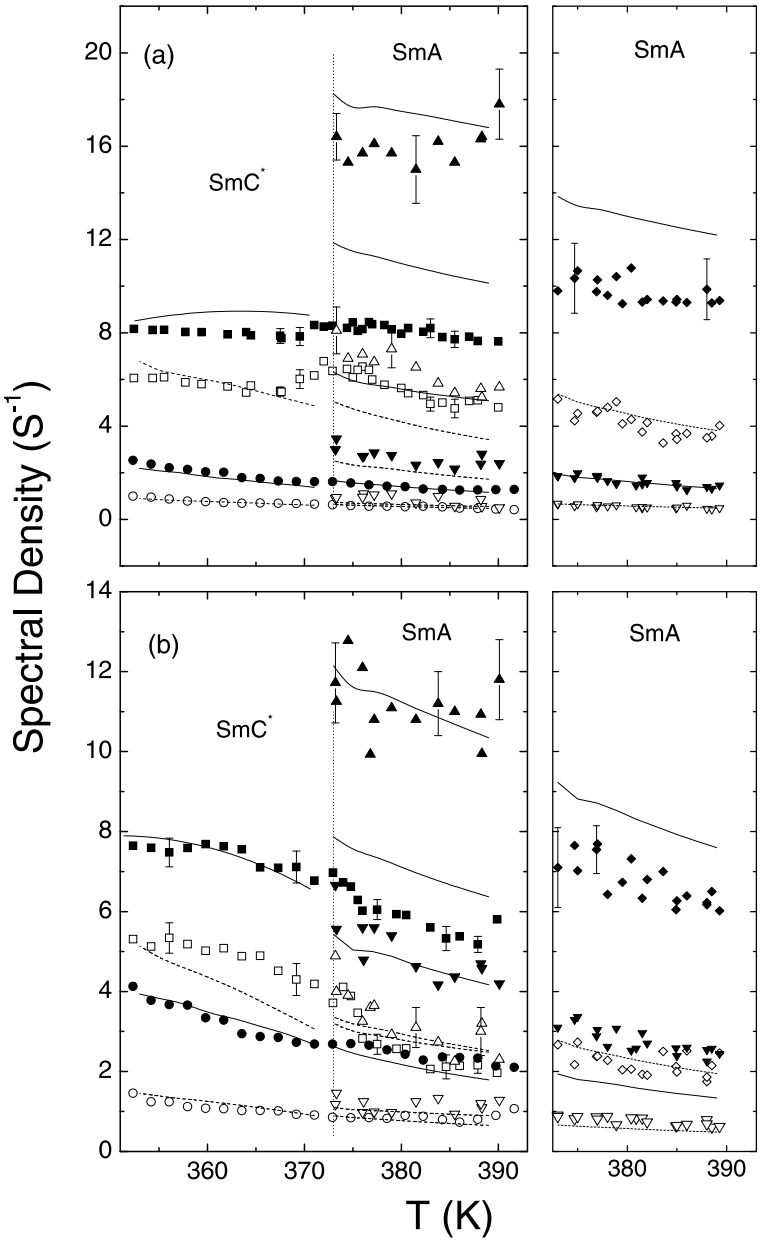

Figure 3.12: Plots of spectral densities versus the temperature in the SmA and SmC* phase of 10B1M7-d_{21} at 15.1 and 61.4 MHz (left panel) and 46 MHz (right panel). Closed and open symbols denote $J_1(\omega)$ and $J_2(2\omega)$, respectively. (a) uptriangles (15.1), diamonds (46) and squares (61.4) are for $C_{1,2}$, while downtriangles (15.1), triangles (46), and circles (61.4) are for C_9 deuterons, respectively, (b) uptriangles (15.1), diamonds (46) and squares (61.4) are for C_3, while downtriangles (15.1), triangles (46), and circles (61.4) are for C_8 deuterons, respectively. Solid and dashed lines denote calculated spectral densities for $J_1(\omega)$ and $J_2(2\omega)$, respectively.

.

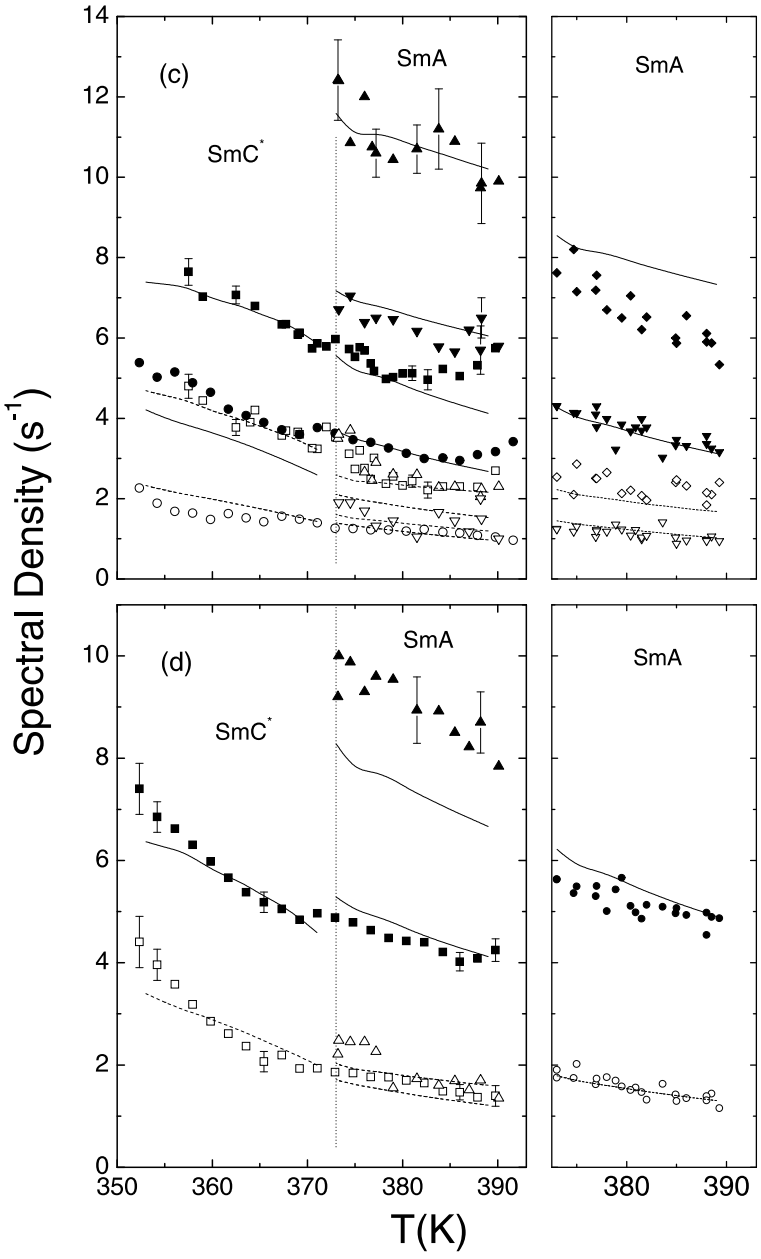

Figure 3.13: Same as figure 3.12 with (c) uptriangles (15.1), diamonds (46) and squares (61.4) are for C_4, while downtriangles (15.1), triangles (46), and circles (61.4) are for C_7 deuterons, respectively, (d) uptriangles (15.1), circles (46) and squares (61.4) are for $C_{5,6}$.

.

Table 3.1: Global parameters and their error limits in s^{-1} for the SmA phase.

	k_1^0	$E_a^{k_1}$	k_2^0	$E_a^{k_2}$	k_g^0	$E_a^{k_g}$
Value	6.89×10^{14}	12.1	4.28×10^{24}	75.9	2.17×10^{18}	35.5
Upper limit	$(9.54 \times 10^{15})^*$	16.8	NA	84.9	7.11×10^{18}	37.9
Lower limit	1.62×10^{14}	$(3.85)^*$	2.47×10^{23}	51.0	1.01×10^{18}	31.7
	$k_g'^0$	$E_a^{k_g'}$	$D_\perp^0$	$E_a^{D_\perp}$	$D_\parallel^0$	E_a^D
Value	5.12×10^{19}	53.2	2.63×10^9	13.6	3.77×10^{15}	41.9
Upper limit	2.38×10^{21}	$(63.4)^*$	5.45×10^9	15.7	7.83×10^{15}	43.5
Lower limit	$(2.06 \times 10^{18})^*$	41.0	1.36×10^9	11.3	2.26×10^{15}	39.6

* The stars in parentheses are for an increase of 50% in F.

long chain molecule. The error limit for a particular global parameter was estimated by varying the one under consideration while keeping all other global parameters identical to those for the optimized F value, to give a doubling in F. Some parameters are found to be not too sensitive in the fitting. Hence numbers in parentheses are for an increase of 50% in F. The jump constants and rotational diffusion coefficients in the SmA phase are plotted versus the reciprocal temperature in Figure 3.14. A global target analysis to minimize F was carried out with ten temperatures in SmC* phase at 61.4 MHz, yielding a Q value of 0.9% in this phase. The smaller Q is a result of fitting data at a single frequency. The calculated spectral densities based on Eqs. (3.50)-(3.52) are shown as solid and dashed curves in Figs. 3.12 and 3.13. From the fittings in this phase, the global target parameters are obtained and summarized in Table 3.2 together with their error limits.

Table 3.2: Global parameters and their error limits in s^{-1} for the SmC* phase.

	k_1	k_2	$E_a^{k_g}$	$k_g'^0$
Value	9.94×10^{12}	1.02×10^{17}	175.5	7.27×10^{17}
Upper limit	5.85×10^{13}	NA	$(181.8)^*$	1.51×10^{18}
Lower limit	3.37×10^{12}	4.02×10^{13}	172.0	3.70×10^{17}
	$E_a^{k_g'}$	$D_\perp^0$	$E_a^{D_\perp}$	$D_\parallel$
Value	30.6	2.46×10^{14}	45.6	5.70×10^9
Upper limit	32.6	3.58×10^{14}	46.9	7.70×10^9
Lower limit	28.4	1.62×10^{14}	44.5	4.43×10^9

* The star in parentheses is for an increase of 50% in F.

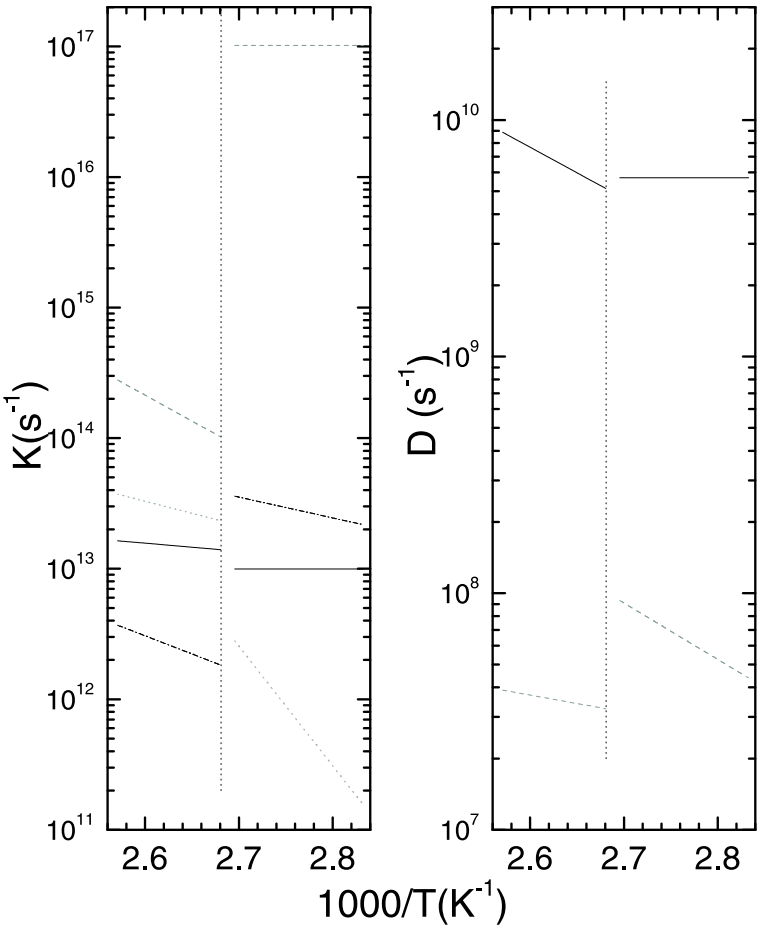

Figure 3.14: (a) Plots of jump rate constants k_1 (solid lines), k_2 (dashed lines), k_g (dotted lines) and k'_g (dash-dotted lines) versus the reciprocal temperature, (b) plots of rotational diffusion constants $D_{\|}$ (solid lines) and $D_{\perp}$ (dashed lines) versus the reciprocal temperature.

We note that several global parameters had very weak temperature behaviors, and their activation energies (i.e. $E_a^{k_1}$, $E_a^{k_2}$ and E_a^D) were, therefore, set at zero. The number of variables for fittings in the SmC* phase was reduced to 8, as k_g^0 was also fixed at 1.44×10^{37}. The uncertainty in this value was estimated by increasing it by a factor of 3, resulting in a doubling of F. The internal jump rates, $D_{\|}$ and $D_{\perp}$ in the SmC* phase are also plotted in Fig. 3.14. At the SmA-SmC* transition, all motional parameters appear to jump discontinuously. Some parameters, such as $D_{\perp}$ and k_g, have much higher activation energies. The higher activation energy for tumbling motion in the SmC* phase of 10B1M7-d_{21} is found to agree with the finding in the same phase of 8BEF5 [45]. Also the gauche migration appears to be more hindered in this phase. The present study, therefore, suggests that the simple approach in extracting dynamical information in the chiral C phase is appropriate for the core and the chain deuterons, at least in two chiral mesogens.

In summary, we believe that the usage of Eqs. (3.51) and (3.52) to account for the spectral

densities in the chiral C phase is reasonable and biaxial spectral densities may not be an important factor in this phase as far as chain deuterons are concerned. In other words, we have demonstrated that molecules in the helical structure of a tilted phase appear to sense a macroscopically uniaxial symmetry to a first approximation. However, more NMR studies of this kind are needed to further confirm its validity.

3.9 Ring Dynamics study of HAT5a-d_6

3.9.1 Introduction

Self-organizing liquid crystalline compounds with disc-shaped molecules are of interest because the columnar phases formed by them give special anisotropic physical properties such as one-dimensional photoconductivity and electron conductivity [67–71]. It is for this reason that molecular engineering, structural and physical property studies of discotic compounds, including their low molar mass and polymeric columnar liquid crystals, currently provide very active research areas [72–78]. Among all columnar liquid crystals, those of triphenylene derivatives have been the most studied, not only because the flexibility of the molecular engineering due to their simple molecular structure and symmetry, but also for their stability conferred by the aromatic core. Since the first report on columnar triphenylene liquid crystals in 1978 [79], various liquid crystals based on this simple aromatic discogen with different substituents have been obtained. Very high charge carrier mobility has been observed in highly ordered columnar phases of triphenylene discotic liquid crystals [67, 68].

In the discotic columnar phase, stacks of molecular disks (separated by ca. 0.35 nm) form columns, which in turn aggregate into a two-dimensional lattice (e.g. hexagonal, or rectangular). The π^* shells of adjacent molecules in the stack tend to overlap. Because of the π overlap between the electronically active transport units, the columns provide one-dimensional pathways for charge and energy migration. One of the main factors affecting the charge transport properties of discotic materials is expected to be positional disorder, i.e., the nonparallel arrangement of disks and longitudinal and lateral displacements of molecular cores within the stacks [80]. Deviations from an ideal stacking will lead to energy transport along the one dimensional pathway becoming incoherent, and the transport proceeds by successive transitions from one localized site to another. In fact, the temperature-dependent disorder is related to the temperature-dependent broadening of density of states in the "hopping" model [81]. For this reason, the relation between the dynamical behavior of the discotic LC and the

understanding of the charge transport is an important issue.

It is known that discotic molecules possess a negative anisotropic magnetic susceptibility $\Delta\chi(= \chi_{\parallel} - \chi_{\perp})$. For a perfectly aligned sample, the directors in the columnar phase lie in a plane perpendicular to the external magnetic field, and the disc-shaped molecules can randomly reorient about their columnar axes. Aligned columnar phases can be achieved by cooling from the isotropic phase when in a sufficiently strong magnetic field [82]. The spectrum of an aligned sample at 0° orientation (i.e. Z axis of the sample frame is along the NMR field) shows a quadrupolar doublet for each distinct deuteron. Spin relaxation studies have been used to study the dynamics of discotic liquid crystals by many research groups [54, 83–88] and this method can successfully determine motional parameters. In this section, the spin relaxation method is adopted to measure the deuteron spin-lattice relaxation rates of a ring-deuterated HAT5a-d_6 in the high temperature region, from which rotational diffusion constants can be derived based on the anisotropic viscosity model [17].

3.9.2 Theory

It is well established [83] that for discotic mesogens, spin relaxation by molecular reorientations can be satisfactorily described by the anisotropic viscosity model (AVM) [17]. In the anisotropic viscosity model, one needs to solve the rotational diffusion equation

$$\frac{\partial}{\partial t}P(\Omega,t) = \Gamma_{\Omega}P(\Omega,t) \tag{3.55}$$

where the diffusion operator Γ_{Ω} contains the potential of mean torque $U(\Omega)$, the rotational diffusion tensor $\mathbf{D}$, and $P(\Omega,t)$ is the probability of finding a molecule with orientation Ω at time t. At each temperature, the mean potential is specified by the order parameter S value. In particular, the $\mathbf{D}$ tensor is diagonalized in the director frame. If the molecular Z_M axis is taken to be close to the mesophase director (due to $S \approx 1$), Γ_{Ω} involves derivatives with respect to α and β, and the diffusion tensor $\mathbf{D}$ has two principal elements D_{α} and D_{β} in the director frame, which are for diffusive rotations of the molecule about the director, and perpendicular to the director axis, respectively [17]. The spectral densities $J_m(w)$ for the ring deuterons of HAT5a-d_6 can be obtained by Fourier transform of the correlation functions using the notation given in reference [15]:

$$J_n(n\omega) = \frac{3\pi^2}{2}(q_{CD})^2 \sum_m \left[d^2_{m0}(\beta_{M,Q})\right]^2 \sum_K \frac{(\beta^2_{mn})_K(\alpha^2_{mn})_K}{(\alpha^2_{mn})^2_K + \omega^2} \tag{3.56}$$

where $q_{CD} = 185$KHz, $\beta_{M,Q} = 90°$ which is the angle between the C-D bond and the molecular Z_M axis, $(\alpha^2_{mn})_K/D_{\beta}$, and $(\beta^2_{mn})_K$ are the eigenvalues and eigenvectors from diagonalizing

the diffusion operator matrix. Note that D_α and D_β appear in $(\alpha^2_{mn})_K$. In Eqs.(3.51) and (3.52) by setting $\beta = 90°$, one can get:

$$\begin{aligned} J_1(w, 90°) &= \frac{1}{2}[J_1(w) + J_2(w)] \\ J_2(2w, 90°) &= \frac{3}{8}J_0(2w) + \frac{1}{2}J_1(2w) + \frac{1}{8}J_2(2w) \end{aligned} \tag{3.57}$$

Using Eqs.(3.56) and (3.57), the fitting of spectral densities was carried out for HAT5a-d_6.

3.9.3 Experiment

All experimental details are the same as described in Section 3.8.3. The molecular structure of HAT5a-d_6 has been shown in Fig. 1.16. Since it is a ring deuterated sample, the deuterium spectrum of the aligned sample shows a doublet. We used 1024 scans at lower temperature to get a good FID signal. The recycle time between scans was 0.3s. No attempt was made to measure (T_1)'s at temperatures higher than 393K, partly due to the fear of further sample degradation and partly due to temperature instability in our probe. The accuracy of spin relaxation measurements was estimated to be better than 5%.

3.9.4 Results and Discussion

In the high temperature region, the molecular motion will be fast and one can not get molecular dynamic information by fitting the FID intensity and spectral lineshape (See Chapter 4). That is why the spin-lattice relaxation technique is adopted to study dynamics at high temperatures. Firstly to get the reorientation potential for spectral densities, the order parameter (see Table 4.1) is calculated from the quadrupolar splittings shown in Fig. 3.15. The derived spectral densities $J_1(w_0, 90°)$ and $J_2(2w_0, 90°)$ from the deuteron spin-lattice relaxation rates in Eq. (3.13) and (3.14) are plotted as a function of temperature in Figure 3.16. By using the AVM, the spectral densities can be calculated from Eqs. (3.56) and (3.57). A minimization ('AMOEBA') routine was used to minimize the sum-squared error F:

$$F = \sum_k \sum_m [J^{calc}_m(mw_0, 90°) - J^{expt}_m(mw_0, 90°)]^2_k \tag{3.58}$$

where the sum over k is for nine temperatures, $m = 1$ or 2. In this global target method, the following Arrhenius-type relations are assumed:

$$\begin{aligned} D_\alpha &= D^0_\alpha exp[-E^\alpha_a/RT] \\ D_\beta &= D^0_\beta exp[-E^\beta_a/RT] \end{aligned} \tag{3.59}$$

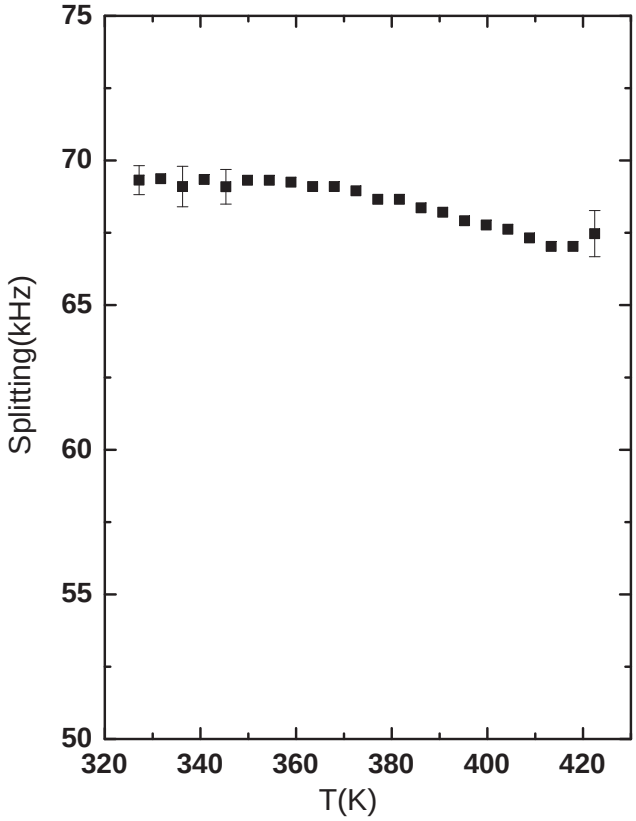

Figure 3.15: Plot of quadrupolar splitting versus the temperature for HAT5a-d_6.

The fittings are good as demonstrated by the solid curves in Fig. 3.16 and the derived diffusion constants D_α and D_β are plotted in Figure 3.17. The activation energy for α motion $E_a^\alpha \approx$ 6.0kJ/mol and for β motion $E_a^\beta \approx 31.8$kJ/mol. These activation energies appear to be low in comparison with those found in similar compounds [83], most likely due to the unavailability of relaxation measurements at another Larmor frequency. The activation energy results will be compared with the other results derived from spectral analyses in the next chapter.

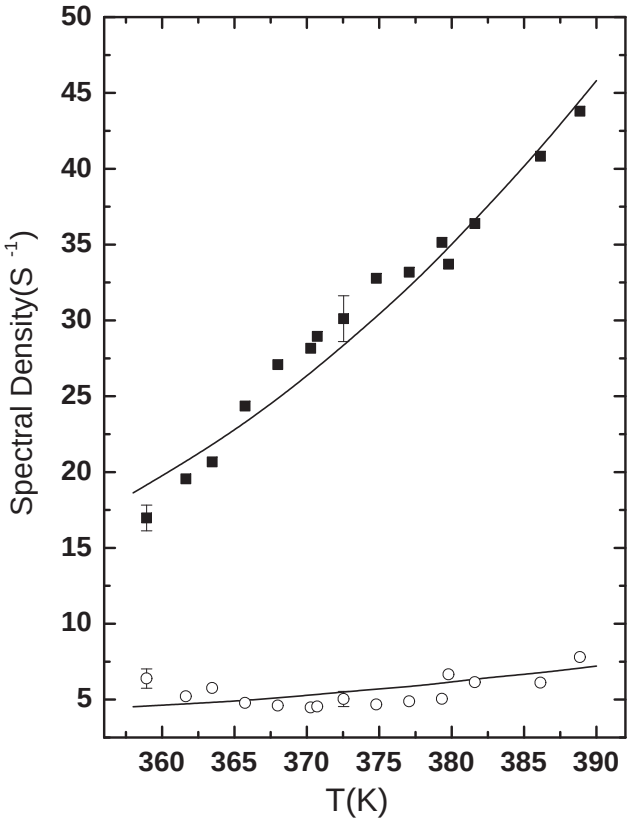

Figure 3.16: Plot of spectral densities $J_1(w_0, 90°)$ (■) and $J_2(2w_0, 90°)$ (○) versus the temperature for HAT5a-d_6. Solid curves represent calculated spectral densities based on anisotropic viscosity model.

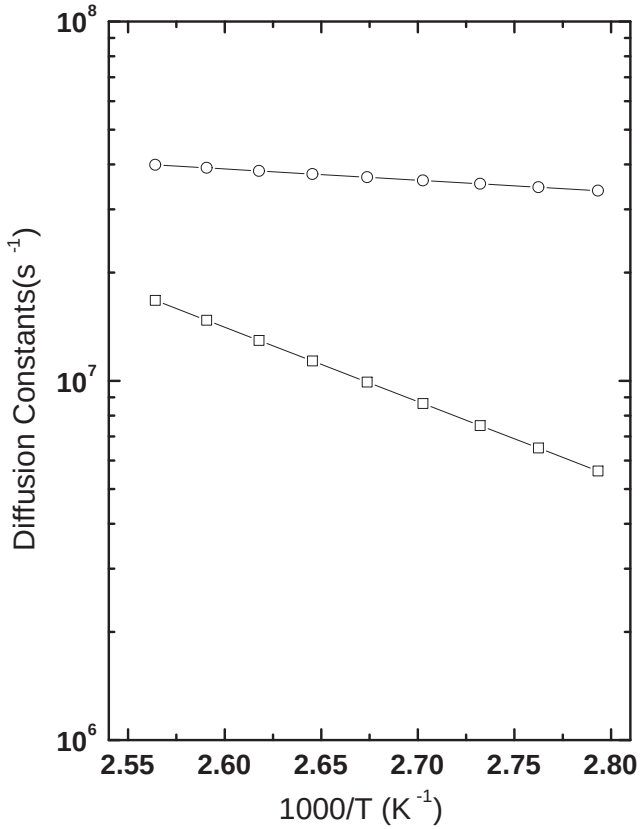

Figure 3.17: Plot of rotational diffusion constants D_α $(-\circ-)$ and D_β $(-\square-)$ versus the reciprocal temperature for HAT5a-d_6.

References

[1] Abragam, A. *Principles of Nuclear Magnetism*; Oxford University Press: Oxford, 1986.

[2] Doane, J. W.; Visintainer, J. J. *Phys. Rev. Lett.* **1969**, *23*, 1421.

[3] Blinc, R.; Hogenboom, D. L.; O'Reilly, D. E.; Peterson, E. M. *Phys. Rev. Lett.* **1969**, *23*, 969.

[4] Wade, C. G. *Ann. Rev. Phys. Chem.* **1977**, *28*, 47.

[5] Visintainer, J. J.; Dong, R. Y.; Bock, E.; Tomchuk, E.; Dewey, D. B.; Kuo, A.; Wade, C. G. *J. Chem. Phys.* **1977**, *66*, 3343.

[6] Orwoll, R. D.; Wade, C. G.; Fung, B. M. *J. Chem. Phys.* **1975**, *63*, 986.

[7] Dong, R. Y.; Lewis, J.; Tomchuk, E.; Bock, E. *J. Chem. Phys.* **1978**, *69*, 5314.

[8] Barbara, T. M.; Vold, R. R.; Vold, R. L. *J. Chem. Phys.* **1983**, *79*, 6338.

[9] Emsley, J. W.; Lindon, J. C.; Luckhurst, G. R. *Mol. Phys.* **1976**, *32*, 1187.

[10] Beckmann, P. A.; Emsley, J. W.; Luckhurst, G. R.; Turner, D. *Mol. Phys.* **1983**, *50*, 699.

[11] Dong, R. Y. *Nuclear Magnetic Resonance of Liquid Crystals*; Springer-Verlag, 1997.

[12] Nordio, P. L.; Segre, U. Magnetic Resonance Spectroscopy - Static Behaviour; In *The molecular Physics of Liquid Crystals*; Luckhurst, G. R.; Gray, G. W., Eds.; Academic Press: London, 1979.

[13] Nordio, P. L.; Rigattig, G.; Segre, U. *J. Chem. Phys.* **1972**, *56*, 2117.

[14] Nordio, P. L.; Rigattig, G.; Segre, U. *Mol. Phys.* **1973**, *25*, 129.

[15] Tarroni, R.; Zannoni, C. *J. Chem. Phys.* **1991**, *95*, 4550.

[16] Vold, R. R.; Vold, R. L. *J. Chem. Phys.* **1988**, *88*, 1443.

[17] Polnaszek, C. F.; Bruno, G. V.; Freed, J. H. *J. Chem. Phys.* **1973**, *58*, 3185.

[18] Polnaszek, C. F.; Freed, J. H. *J. Phys. Chem.* **1975**, *79*, 2283.

[19] Powles, J. G.; Strange, J. H. *Proc. Phys. Soc.* **1963**, *82*, 6.

[20] Vega, A. J.; Luz, Z. *J. Chem. Phys.* **1987**, *86*, 1803.

[21] Jeener, J.; Broekaert, P. *Phys. Rev.* **1967**, *157*, 232.

[22] Spiess, H. W. *J. Chem. Phys.* **1980**, *72*, 6755.

[23] Wimperis, S. *J. Magn. Reson.* **1990**, *86*, 46.

[24] Wimperis, S. *J. Magn. Reson.* **1989**, *83*, 509.

[25] Wimperis, S.; Bodenhausen, G. *Chem. Phys. Lett.* **1986**, *132*, 194.

[26] Hoatson, G. L. *J. Magn. Reson.* **1991**, *94*, 152.

[27] Ditzian, R. V. *Phys. Lett. A* **1971**, *34*, 409.

[28] Redfield, A. G. *IBM J. Res. Dev.* **1957**, *1*, 19.

[29] Wangsness, R. K.; Bloch, F. *Phys. Rev.* **1953**, *89*, 728.

[30] Bloch, F. *Phys. Rev.* **1956**, *102*, 104.

[31] Vold, R. R. NMR spin relaxation; In *Nuclear Magnetic Resonance of Liquid Crystals*; Emsley, J. W., Ed.; D. Reidel Publishing Company: Netherlands, 1985.

[32] Marcelja, S. *J. Chem. Phys.* **1974**, *60*, 3599.

[33] Emsley, J. W.; Luckhurst, G. R.; Stockley, C. P. *Proc. R. Soc. London A* **1982**, *381*, 117.

[34] Flory, P. J. *Statistical Mechanics of Chain Molecules*; Interscience: New York, 1969.

[35] Cotter, M. A. The Van Der Waals Approach to Nematic Liquids; In *The molecular Physics of Liquid Crystals*; Luckhurst, G. R.; Gray, G. W., Eds.; Academic Press: London, 1979.

[36] Luckhurst, G. R. Molecular Field Theories of Nematics; In *The molecular Physics of Liquid Crystals*; Luckhurst, G. R.; Gray, G. W., Eds.; Academic Press: London, 1979.

[37] Dong, R. Y. *Phys. Rev. A* **1991**, *43*, 4310.

[38] Dong, R. Y. *Chem. Phys. Lett.* **2000**, *329*, 92.

[39] DONG, R. Y. *Phys. Rev. A* **1991**, *43*, 4310.

[40] Wittebort, R. J.; Szabo, A. *J. Chem. Phys.* **1978**, *69*, 1722.

[41] Valeur, B.; Jarry, J. P.; Geny, F. *J. Polym. Sci. B* **1975**, *13*, 667.

[42] Valeur, B.; Monnerie, L.; Jarry, J. P. *J. Polym. Sci. B* **1975**, *13*, 675.

[43] Berggren, E.; Zannoni, C. *Mol. Phys.* **1995**, *85*, 299.

[44] Berggren, E.; Tarroni, R.; Zannoni, C. *J. Chem. Phys.* **1993**, *99*, 6180.

[45] Domenici, V.; Geppi, M.; Veracini, C. A. *Chem. Phys. Lett.* **2003**, *382*, 518.

[46] Dong, R. Y.; Chen, Y. B.; Veracini, C. A. *Chem. Phys. Lett.* **2005**, *405*, 177.

[47] Dong, R. Y.; Chiezzi, L.; Veracini, C. A. *Phys. Rev. E.* **2002**, *65*, 041716.

[48] Struppe, J.; Noack, F. *Liq. Cryst.* **1996**, *20*, 595.

[49] Dong, R. Y.; Richards, G. M. *J. Chem. Soc.-Faraday Trans.* **1992**, *88*, 1885.

[50] Dong, R. Y.; Friesen, L.; Richards, G. M. *Mol. Phys.* **1994**, *81*, 1017.

[51] Dong, R. Y. *Mol. Phys.* **1996**, *88*, 979.

[52] Calucci, L.; Geppi, M.; Veracini, C. A.; Dong, R. Y. *Chem. Phys. Lett.* **1998**, *296*, 357.

[53] Shen, X. D.; Dong, R. Y. *J. Chem. Phys.* **1998**, *108*, 9177.

[54] Shen, X.; Dong, R. Y.; Boden, N.; Bushby, R. J.; Martin, P. S.; Wood, A. *J. Chem. Phys.* **1998**, *108*, 4324.

[55] Dong, R. Y. *Phys. Rev. E* **1999**, *60*, 5631.

[56] Dong, R. Y.; Carvalho, A.; Sebastiao, P. J.; Nguyen, H. T. *Phys. Rev. E* **2000**, *62*, 3679.

[57] Dong, R. Y.; Cheng, M. *J. Chem. Phys.* **2000**, *113*, 3466.

[58] Dong, R. Y.; Morcombe, C. R.; Calucci, L.; Geppi, M.; Veracini, C. A. *Phys. Rev. E* **2000**, *61*, 1559.

[59] Dong, R. Y. *J. Chem. Phys.* **2001**, *114*, 5897.

[60] Helfand, E. *J. Chem. Phys.* **1971**, *54*, 4651.

[61] Helfand, E.; Wasserman, Z. R.; Weber, T. A. *Macromolecules* **1980**, *13*, 526.

[62] Skolnick, J.; Helfand, E. *J. Chem. Phys.* **1980**, *72*, 5489.

[63] Counsell, C. J. R.; Emsley, J. W.; Luckhurst, G. R.; Sachdev, H. S. *Mol. Phys.* **1988**, *63*, 33.

[64] Berggren, E.; Zannoni, C. *Mol. Phys.* **1995**, *85*, 299.

[65] Catalano, D.; Chiezzi, L.; Domenici, V.; Geppi, M.; Veracini, C. A.; Dong, R. Y.; Csorba, K. F. *Macromol. Chem. Phys.* **2002**, *203*, 1594.

[66] Dong, R. Y.; Chiezzi, L.; Veracini, C. A. *Phys. Rev. E* **2002**, *65*, 041716.

[67] D. Craats, A. M. v.; Siebbeles, L. D. A.; Bleyl, I.; Haarer, D.; Berlin, Y. A.; Zharikov, A. A.; Warman, J. M. *J. Phys. Chem. B* **1998**, *102*, 9625.

[68] Simmerer, J.; G., B.; Paulus, W.; Kettner, A.; Schuhmacher, P.; Adam, D.; Etzbach, K.; Siemensmeyer, K.; Wendorff, J. H.; Ringsdorf, H.; Haarer, D. *Adv. Mater.* **1996**, *8*, 815.

[69] Haase, W.; Kilian, D.; Athanassopoulou, M. A.; Knawby, D.; Swager, T. M.; Wrobel, S. *Liq. Cryst.* **2002**, *29*, 133.

[70] Haarer, D.; Adam, D.; Simmerer, J.; Closs, F.; Funhoff, D.; Haussling, L.; Siemensmeyer, K.; Ringsdorf, H.; Schuhmacher, P. *Mol.Cryst. Liq. Cryst.* **1994**, *252*, 155.

[71] Vaughan, G. B. M.; Heiney, P. A.; McCauley, J. P.; Smith, A. B. *Phys. Rev. B* **1992**, *46*, 2787.

[72] Adam, D.; Closs, F.; Frey, T.; Funhoff, D.; Haarer, D.; Schuhmacher, P.; Siemensmeyer, K. *Phys. Rev. Lett.* **1993**, *70*, 457.

[73] Boden, N.; Bushby, R. J.; Clements, J. *J. Chem. Phys.* **1993**, *98*, 5920.

[74] Boden, N.; Bushby, R. J.; Clements, J.; Movaghar, B.; Donovan, K. J.; Kreouzis, T. *Phys. Rev. B* **1995**, *52*, 13274.

[75] Bushby, R. J.; Lozman, O. R. *Curr. Opin. Colloid Interface Sci.* **2002**, *7*, 343.

[76] Chandrasekhar, S. *Phil. Tran. R. Soc. Lond. A* **1983**, *309*, 93.

[77] Chandrasekhar, S.; Ranganath, G. S. *Rep. Prog. Phys.* **1990**, *53*, 57.

[78] Davidson, P.; Clerc, M.; Ghosh, S. S.; Maliszewskyj, N. C.; Heiney, P. A.; Hynes, J.; Smith, A. B. *J. Phys. II France* **1995**, *5*, 249.

[79] Billard, J.; Dubois, J. C.; Huuttnh, N.; Zann, A. *Nouveau J. De Chimie-New J. Chem.* **1978**, *2*, 535.

[80] de Craats, A. M.; Siebbeles, L. D. A.; Bleyl, I.; Haarer, D.; Berlin, Y. A.; Zharikov, A. A.; Warman, J. M. *J. Phys. Chem. B* **1998**, *102*, 9625.

[81] Bassler, H. *Adv. Mater.* **1993**, *5*, 662.

[82] Goldfarb, D.; Luz, Z.; Zimmermann, H. *J. Phys.* **1981**, *42*, 1303.

[83] Dong, R. Y.; Boden, N.; Bushby, R. J.; Martin, P. *Mol. Phys.* **1999**, *97*, 1165.

[84] Dong, R. Y.; Morcombe, C. R. *Liq. Cryst.* **2000**, *27*, 897.

[85] Joghems, E. A.; Biesheuvel, C. A.; Bulthuis, J. E. A. *Liq. Crys.* **1993**, *13*, 427.

[86] Martins, A. F.; Ribeiro, A. C. *Portgal. Phys.* **1980**, *11*, 169.

[87] Ribeiro, A. C.; Martins, A. F. *Portgal. Phys.* **1985**, *16*, 117.

[88] Sandstrom, D.; Zimmermann, H.; Maliniak, A. *J. Phys. Chem.* **1994**, *98*, 8154.

Chapter 4

^{2}H NMR Angular Dependent Study of Core Dynamics in Discotic Columnar Phase

4.1 Discotic Liquid Crystals (DLC)

4.1.1 Introduction

The interest in mesophases formed by disklike molecules has been steadily growing since their discovery in 1977 [1]. In the majority of the mesophases formed by disklike molecules, the discs are stacked one on top of the other in columns which constitute a commonly observed hexagonal phase. The centers of the columns are occupied by the molecular cores, which are essentially parallel to one another. The intercolumnar space is occupied by the highly disordered tails. Generally, the intercolumnar distance is 20-40Å, depending on the lateral chain length, while the stacking distance is less than 4.5Å [2–9]. Therefore, interactions between neighboring molecules within the same column should be much stronger than interactions between molecules in neighboring columns. The columns provide one-dimensional pathways for rapid charge and energy migration. The charge transport has been shown to be highly anisotropic with up to three orders of magnitude higher conductivity in the directions of the columnar stacks [10]. The possibility of a rapid, channeled transport in combination with the ability of discotic materials to form liquid crystalline phases makes them interesting candidates for applications in photocopying, electrophotography, nonlinear optics, and molecular electronics [11–14].

To date, optical texture observations, x-ray diffraction, differential scanning calorimatory, time of flight and NMR techniques have been adopted to study discotic liquid crystals [15,

16]. But little is known about the molecular dynamics in the columnar phase. NMR is a powerful method to investigate the dynamics of molecules in the columar phase due to its high sensitivity to molecular motion. Several NMR investigations of discotic compounds have been reported in the literature [16–18]. In all the NMR studies, ^{2}H NMR has often been used because of the relatively simple 'planar powder' spectra observed in aligned samples of discotics. These spectra can be easily interpreted and contain atomic resolution due to specific deuteration [19]. Therefore, in the current work ^{2}H NMR method, which is mainly sensitive to molecular motion on a time scale of 10^{-6}-10^{-9}s, is used to investigate the dynamics in the columnar phase.

Currently among discotic liquid crystals, those of triphenylene derivatives have been the most studied, but until now few papers report the motional dynamics of discotic triphenylene derivatives. Here partially deuterated monomeric and dimeric triphenylene discotic liquid crystals are studied by the ^{2}H NMR method. The molecular structures and their corresponding phase transition temperatures are shown in Figure 1.16. In this chapter, the lineshape simulation based on different theories will be introduced first. Based on the theories, the simulation results and discussion will be addressed in the following sections.

4.1.2 Monomeric triphenylene discotic liquid crystals

Liquid crystalline triphenylenes have been the subject of many previous charge transport studies, mainly because of their ease of processability and low melting points. All monomeric triphenylene discotic molecules consist of an aromatic triphenylene core of four connected six-membered rings which are peripherally substituted with six aliphatic side chains. The side chains are coupled to the aromatic macrocycle via oxygen atoms or sulfur. In columnar phases of monomeric discotic liquid crystals, there is in general no lateral correlation between the molecules in the neighboring columns; the columns can freely slide relative to each other and the molecules randomly reorient about the columnar axes. This makes it possible to achieve highly anisotropic charge transport in the direction of the columnar stacks. Because of these properties, their potential applications in conducting, photoconducting systems, optical data storage, light emitting diodes, photovoltaic solar cells, gas sensors, and other devices have been envisaged [14].

To this end, the dynamics of monomeric triphenylene discotic liquid crystals are important to study. Up to now, some properties of triphenylene monomeric discotic liquid crystals exploited before are summarized in Figure 4.1 [10, 20, 21]. Both order and dynamics in LC promote

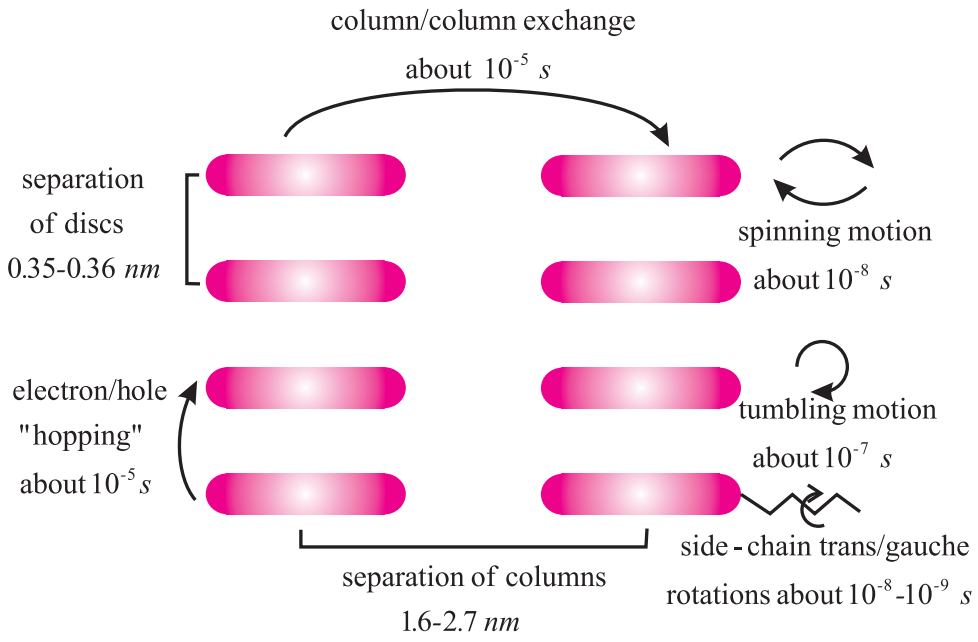

Figure 4.1: Dimension and dynamics of triphenylene discotic liquid crystals.

.

dynamical transport processes. In this dissertation, the anisotropic viscosity model has been used to study monomeric discotic liquid crystals (HAT5a-d_6) to extract relevant motional parameters (Chapter 3) from deuteron spin-lattice relaxation times. Here the lineshape and signal intensity simulation methods are introduced to study this sample at low temperatures.

4.1.3 Dimeric triphenylene discotic liquid crystals

Discotic dimers of triphenylene are another class of promising liquid crystalline material, because of their enhanced photoconductivity and electron conductivity. The triphenylene dimers are formed by linking two monomeric units via a spacer of roughly twice the length of the free side chain, as shown in Figure 4.2. Thus, correlation is imposed by the spacers that link the monomeric units. If the two subunits of a dimer reside in the same column they may undergo, as a pair, limited diffusive reorientation, while if they occupy neighboring columns their freedom to reorient is even more restricted by the intercolumnar interactions [22]. The thermal stability of the mesophase governs the width of its temperature range. In the case of monomeric triphenylene derivatives the width of the temperature range does not exceed 50°C, while dimeric triphenylene derivatives exhibit a liquid crystalline phase over much wider temperature intervals from just below their clearing points at close to 400K down to at least 130K [22]. Experiments have indicated that they show high carrier mobilities

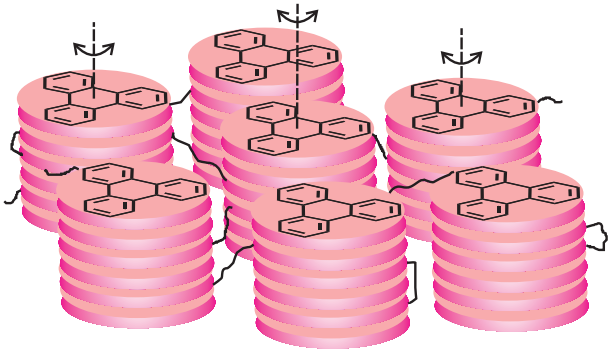

Figure 4.2: Schematic representation of dimeric discotic molecules in a columnar phase.

.

($1 \times 10^{-3} cm^2/Vs$) exceeding those for commonly used photoconductive polymers by two or three orders of magnitude [14]. The novel charge transport properties are potentially exploitable in applications ranging from sensing devices to high resolution xerography.

In the past, several papers have been published on dimeric discotic liquid crystals (DLC) [22–24]. It is known that the length of the spacer and of the side groups will affect the clearing temperature. The spectra of the dimer are significantly different from that of monomer. Neither the single quadrupole splitting for the planar distribution of directors nor the broad spectrum with four singularities for a powder of planar distributions is observed. They usually exhibit the singularities of a rigid solid Pake spectrum with a quadrpolar splitting of $150 kHz$ and show a broad central feature, indicating restricted mobility. Up to now few dynamic studies of dimeric DLC by the NMR method have appeared [22, 25] in the literature, partly due to the difficulty of aligning their discotic phases in the NMR magnetic field. Here we have chosen to study a core deuterated triphenylene dimer DHAT5-C_{14} whose structure is given in Figure 1.16.

4.1.4 Aligned and Powder Samples in Magnetic Field

In contrast to liquid crystal phases of rod-shaped molecules which may be readily aligned in moderate magnetic fields, discotics are not easily aligned in magnetic fields so that quantitative study of their phase transition behavior has till now not been possible. Aligned columnar phases can be achieved by cooling from the isotropic phase while in a sufficiently strong magnetic field [26]. In an aligned sample, the column axis (director) is perpendicular to the magnetic field direction (See Fig. 4.3). The spectrum of an aligned sample at 0° orientation (i.e. Z axis of the sample frame is along the NMR field) shows a quadrupolar doublet for each

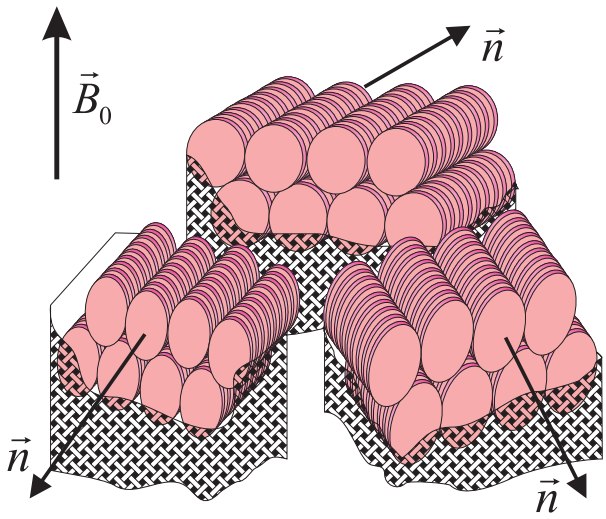

Figure 4.3: Domain distribution of aligned discotic liquid crystals.

.

distinct deuteron. The quadrupole splitting of the aromatic deuterons gives the orientational order parameter S at different temperatures, usually ranging between 0.9-0.95. This reflects that the molecular cores are highly ordered in the columns.

When an aligned sample is rotated in the NMR field using a goniometer probe from 0° to 90°, one can also observe different spectral patterns. If the system under study has motions in the intermediate regime (rate of the order of the interaction responsible for the observed spectral pattern), these spectral patterns contain information on the dynamic processes [27]. It is well known that ultra-slow motional processes (rate less than 10^3 s^{-1}) cannot be studied by deuterium lineshape analysis, while the same is true if the motional processes are fast (rate of the order of the Larmor frquency, ca. 10^7 s^{-1}). Recently, dynamic information in chiral smectic phases of rod-like mesogens has been derived from the angular dependent solid echo intensities and spectral patterns collected at fixed τ values [28, 29]. The present study exploits the same approach to gain molecular dynamic information from a discotic (HAT5a-d_6) sample, in which two of the six pendant chains are much shorter in length [30]. This serves to show the general applicability of the approach to a very different phase structure. The system is chosen because it shows a rather wide discotic columnar D_{ho} phase. In particular, it is expected that at the low end of this phase, molecular reorientations about the columnar axis would be in the intermediate regime, while at the high temperature region this process should likely approach the fast motion regime. In the latter regime, the spin relaxation technique has already been used in Chapter 3.

Since DHAT5-C_{14} cannot be aligned in our NMR field of 9.4T even by cooling from the

isotropic melt, the deuterium study is carried out in a powder sample. From the echo intensities and spectral patterns the structure information of the dimer can be studied.

Aligned Sample

In aligned deuterated LC, the ^{2}H spin(s) gives rise to a spectrum of two lines with spectral frequencies given in Eq. (3.3). So far, all the descriptions were developed in the laboratory fixed frame. However, to study the dynamics of the core-deuterated discotic liquid crystals, the various molecular properties are more conveniently described in the principal axis system (PAS) of the quadrupolar interaction for the C-D bond system. The transformation from PAS frame to the LAB frame can be achieved using Wigner rotation matrices $D(\Omega)$, where Ω denotes the corresponding Euler angles. Since angular dependent experiments for aligned sample are done by rotating the sample, we need to adopt a sample frame which is the same as the lab frame when there is no rotation. Hence we use the transformation:

$$\text{Sample frame } (X_S,Y_S,Z_S) \overset{(0,\theta_0,0)}{\Longrightarrow} \text{Lab frame } B_0$$
$$\text{Sample frame } (X_S,Y_S,Z_S) \overset{(\alpha,\beta,0)}{\Longrightarrow} \text{Director frame } (X_D,Y_D,Z_D)$$

Now $< R_{2,0} >$ can be expressed as:

$$< R_{2,0} >= \sum_{mn} \left\langle D^2_{m,0}(0,\theta_0,0) D^{2*}_{m,n}(\alpha,\beta,0) \right\rangle \left\langle R^D_{2,n} \right\rangle \tag{4.1}$$

where the superscript D denotes the director frame. θ_0 is the angle between the magnetic field and the Z_S axis of the sample frame. If there is no sample rotation, θ_0 will be 0. (α,β,0) are the Euler angles that give the orientation of the director frame in the sample frame (X_S,Y_S,Z_S) (Fig. 4.4). Then the spectral frequencies in the director frame (X_D,Y_D,Z_D) can be written as [31]:

$$\begin{aligned} \nu^{\pm}(\phi) &= \pm\frac{3}{4}\bar{\nu}_Q\{P_2(\cos\theta_0)[P_2(\cos\beta)+\frac{\bar{\eta}}{2}\sin^2\beta] \\ &\quad +\frac{3}{4}\sin^2\theta_0[\sin^2\beta\cos 2\alpha+\frac{\bar{\eta}}{3}(1+\cos^2\beta)\cos 2\alpha] \\ &\quad +\frac{3}{4}\sin 2\theta_0[\sin 2\beta\cos\alpha-\frac{\bar{\eta}}{3}\sin 2\beta\cos\alpha]\} \end{aligned} \tag{4.2}$$

where $\bar{\eta} = (\bar{V}_{XX} - \bar{V}_{YY})/\bar{V}_{ZZ}$ is a time-averaged asymmetry parameter, $\bar{\nu_Q} = eQ\bar{V}_{ZZ}/h$ is a time-averaged nuclear quadrupolar coupling constant along the director. Since both $\bar{\nu_Q}$ and $\bar{\eta}$ depend on ϕ (see below), $\nu^{\pm}(\phi)$ is ϕ dependent. The $\bar{V}_{ii}$ are the principal elements of the electric field tensor in the director frame (X_D, Y_D, Z_D). To analyze the effect of rotational diffusion or jump on the observed deuteron spectra, one needs to introduce a molecular frame. The Euler angles for coordinate transformation from the director frame (X_D, Y_D, Z_D) to the

molecular frame (X_M,Y_M,Z_M) are (0,θ,0), while they are (ϕ,$\frac{\pi}{2}$,$\frac{\pi}{2}$) for transformation from the (X_M,Y_M,Z_M) to the C-D bond frame (q_X,q_Y,q_Z), viz.

$$\text{Director frame } X_D,Y_D,Z_D \overset{(0,\theta,0)}{\Longrightarrow} \text{Molecular frame } (X_M,Y_M,Z_M)$$
$$\text{Molecular frame } (X_M,Y_M,Z_M) \overset{(\phi,\frac{\pi}{2},\frac{\pi}{2})}{\Longrightarrow} \text{C-D bond frame } (q_X,q_Y,q_Z)$$

Figure 4.4 shows the relevant coordinate systems and the Euler angles describing transformations between them. Thus, we have:

$$\begin{aligned}
\langle R^D_{2,0}\rangle &= \sum_{st}\left\langle D^{2*}_{0,s}(0,\theta,0)D^{2*}_{s,t}(\phi,\frac{\pi}{2},\frac{\pi}{2})\right\rangle \rho_{2,t} \\
\langle R^D_{2,2}\rangle &= \sum_{st}\left\langle D^{2*}_{2,s}(0,\theta,0)D^{2*}_{s,t}(\phi,\frac{\pi}{2},\frac{\pi}{2})\right\rangle \rho_{2,t} \\
\langle R^D_{2,-2}\rangle &= \sum_{st}\left\langle D^{2*}_{-2,s}(0,\theta,0)D^{2*}_{s,t}(\phi,\frac{\pi}{2},\frac{\pi}{2})\right\rangle \rho_{2,t}
\end{aligned} \tag{4.3}$$

where

$$\rho_{2,0} = \sqrt{\frac{3}{2}}eq, \quad \rho_{2,\pm1} = 0, \quad \rho_{2,\pm2} = \frac{1}{2}eq\eta \tag{4.4}$$

Now

$$\begin{aligned}
\bar{V}_{ZZ} &= \sqrt{\frac{2}{3}} < R^D_{2,0} > \\
&= -\frac{1}{2}eq\left[< P_2(\cos\theta) > (1+\eta) - \frac{3-\eta}{2}\overline{\cos 2\phi} < \sin^2\theta >\right] \\
\bar{V}_{XX} - \bar{V}_{YY} &= < R^D_{2,2} > + < R^D_{2,-2} > \\
&= -\frac{3}{4} < \sin^2\theta > \cdot eq \cdot (1+\eta) + \frac{1}{4}(1+ < \cos^2\theta >) \cdot eq \cdot \overline{\cos 2\phi} \cdot (3-\eta)
\end{aligned} \tag{4.5}$$

and when θ is small, one obtains:

$$\bar{\nu}_Q = -\frac{q_{CD}}{2}(1+\eta)S, \quad \bar{\eta} = -\frac{(3-\eta)\overline{\cos 2\phi}}{(1+\eta)S} \tag{4.6}$$

where $S =< P_2(\cos\theta) >$ is the orientational order parameter of the molecule, $q_{CD} = \frac{e^2Qq}{h}$ and η is the asymmetry parameter of the nuclear quadrupole interaction. From the quadrupolar splitting, S can be calculated to a first approximation using

$$\Delta\nu = \frac{3}{8}q_{CD}(1+\eta)S \tag{4.7}$$

This equation is obtained from Eq. (4.2) with the approximation of $\bar{\eta} = 0$ ($\theta_0 = 0°$, $\beta = 90°$).

Powder Sample

For a powder discotic sample, the molecules have various orientations in the magnetic field. In this case, we only need to consider the following transformations:

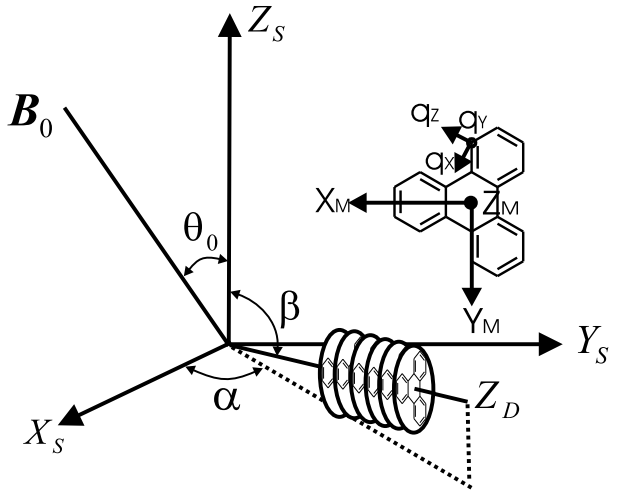

Figure 4.4: Illustration of the sample frame (X_S,Y_S,Z_S), the direction of the magnetic field, B_0, the direction of the director, Z_D, the molecular frame (X_M,Y_M,Z_M), and the principal axis frame of the electric field gradient (q_X,q_Y,q_Z). The Euler angles for the coordinate transformation from (X_M,Y_M,Z_M) to (q_X,q_Y,q_Z) are (ϕ,$\frac{\pi}{2}$,$\frac{\pi}{2}$).

$$\text{Molecular frame } (X_M,Y_M,Z_M) \overset{(\alpha,\beta,0)}{\Longrightarrow} \text{Lab frame } B_0$$
$$\text{Molecular frame } (X_M,Y_M,Z_M) \overset{(\phi,\frac{\pi}{2},\frac{\pi}{2})}{\Longrightarrow} \text{C-D bond frame } (q_X,q_Y,q_Z)$$

The polar angles α and β specify the long molecular axis in the laboratory frame defined by the external magnetic field. The ϕ angle specifies the azimuthal angle of a C-D bond in the molecular frame, and $< R_{2,0} >$ can be expressed as:

$$< R_{2,0} >= \sum_{mn} \left\langle D^2_{m,0}(\alpha,\beta,0) D^{2*}_{m,n}(\phi,\frac{\pi}{2},\frac{\pi}{2}) \right\rangle \rho_{2,n} \tag{4.8}$$

Using Eq. (3.3), the spectral frequencies of the absorption spectrum are given by [22]:

$$\nu^{\pm}(\phi) = \pm\frac{3}{4}\frac{e^2qQ}{h} \cdot \frac{1}{2}\left[3\sin^2\beta\cos^2(\alpha-\phi) - 1 - \eta(\cos^2\beta - \sin^2\beta\sin^2(\alpha-\phi))\right] \tag{4.9}$$

where η is the asymmetry parameter.

4.2 Simulation Routines of Discotic Liquid Crystals

4.2.1 Introduction

In dynamic NMR spectroscopy the kinetic parameters for a particular process are usually determined by comparing the experimental and simulated dynamic spectra. In this section

we outline the theory for calculating such spectra in solid echo experiments, and derive the necessary equations for writing the computing codes to generate the dynamic line shape for both monomeric and dimeric DLC.

To obtain the FID signal, one needs to solve the Bloch-McConnell equation of motion [32, 33]:

$$\frac{d}{dt}\mathbf{M}(t) = -\mathbf{R}\mathbf{M}(t) \tag{4.10}$$

where $\mathbf{M}(t)$ is a column vector of magnetizations from the molecules, and $\mathbf{R}$ is the 'exchange' matrix for describing the dynamic process. In a solid echo experiment, immediately after the first $(\pi/2)_x$ pulse all magnetizations lie along $-y$ with magnitudes proportional to their relative abundance

$$\mathbf{M}(0^+) = c\mathbf{P} \tag{4.11}$$

where $\mathbf{P}$ is a real vector whose components P_i are the fractional populations of the site i, and c is a constant which in the following is taken as 1. During the interval between the two pulses the complex magnetizations M_i evolve according to Eq. (4.10), so that just before the second pulse, at τ^-, we have

$$\mathbf{M}(\tau^-) = e^{-\mathbf{R}\tau}\mathbf{M}(0^+) = e^{-\mathbf{R}\tau}\mathbf{P} \tag{4.12}$$

Immediately after the $(\pi/2)_y$ pulse it evolves to its complex conjugate

$$\mathbf{M}(\tau^+) = \mathbf{M}(\tau^-)^* = (e^{-\mathbf{R}\tau})^*\mathbf{P} \tag{4.13}$$

The components $j_i = M_i(2\tau)$ of the echo signal $(\mathbf{J})$ are computed similarly in the interval τ to 2τ to give:

$$\begin{aligned} \mathbf{J} &= \mathbf{M}(2\tau) = e^{-\mathbf{R}\tau}\mathbf{M}(\tau^+) \\ &= e^{-\mathbf{R}\tau}(e^{-\mathbf{R}\tau})^*\mathbf{P} \end{aligned} \tag{4.14}$$

The echo intensity E is computed by summing over all components j_i,

$$E = \mathbf{1}\cdot\mathbf{J} = \mathbf{1}\cdot e^{-\mathbf{R}\tau}(e^{-\mathbf{R}\tau})^*\mathbf{P} \tag{4.15}$$

where $\mathbf{1}$ is a vector whose components are all equal to unity. Finally the free induction decay corresponding to the second half of the echo signal is

$$\begin{aligned} F &= Re\left\{\mathbf{1}\cdot\mathbf{M}(2\tau+t)\right\} = Re\left\{\mathbf{1}\cdot e^{-\mathbf{R}t}\mathbf{J}\right\} \\ &= Re\left\{\mathbf{1}\cdot e^{-\mathbf{R}(t+\tau)}(e^{-\mathbf{R}\tau})^*\mathbf{P}\right\} \end{aligned} \tag{4.16}$$

In practice [34], to save the computation time the exponential matrix is expressed in terms of the diagonal matrix $\mathbf{\Lambda}$, which contains the eigenvalues λ_i of $\mathbf{R}$, and the matrix $\mathbf{S}$ of its eigenvectors:

$$e^{\mathbf{R}\tau} = \mathbf{S}e^{\mathbf{\Lambda}\tau}\mathbf{S}^{-1}, \qquad e^{-\mathbf{R}t} = \mathbf{S}e^{-\mathbf{\Lambda}t}\mathbf{S}^{-1} \tag{4.17}$$

where $\mathbf{S}^{-1}\mathbf{R}\mathbf{S} = \mathbf{\Lambda}$. Substituting Eq. (4.17) in Eqs. (4.15) and (4.16), the echo amplitude and FID become:

$$\begin{aligned} E &= \mathbf{1}\cdot\left[\mathbf{S}e^{-\mathbf{\Lambda}\tau}\mathbf{S}^{-1}\right]\left[\mathbf{S}e^{-\mathbf{\Lambda}\tau}\mathbf{S}^{-1}\right]^{*}\mathbf{P} \\ F &= Re\left\{\mathbf{1}\cdot\left[\mathbf{S}e^{-\mathbf{\Lambda}(t+\tau)}\mathbf{S}^{-1}\right]\left[\mathbf{S}e^{-\mathbf{\Lambda}\tau}\mathbf{S}^{-1}\right]^{*}\mathbf{P}\right\} \end{aligned} \tag{4.18}$$

It should be noted that these equations still require specific models to describe the jump process. They do give exact line shapes in the regime where the specific dynamic rates are of the order of, or even larger than, the quadrupole interaction. They do not apply, however, when the rates are of the order of the Larmor frequency where the nonsecular terms, neglected in the above treatment, may become important. In this regime it is more appropriate to use relaxation equations derived from the full spin Hamiltonian [35].

To study the dynamics of monomeric DLC through simulation of the experimental lineshapes at different rotation angles, one may consider either a symmetric threefold jump process [33] or a planar diffusive process [36]. For threefold jumps in a plane, the molecules jump by $\pm\frac{2\pi}{3}$ about their symmetry axes (which are nearly parallel to the columnar axis), while planar diffusion can be described as a reorientation mechanism via infinitesimally small steps with a diffusion constant D_R. To describe the dynamics of dimeric DLC, the spectral simulation is considered by adopting a potential distribution due to the core confinement by the spacers. The details of the lineshape calculation based on these models are summarized below.

4.2.2 Threefold Jump Model

To simulate the motion of the core, we consider a three-site jump model. However, this does not mean that the motion actually is a simple threefold jump. In particular it is known that similar lineshapes can also be calculated using a rotational diffusion model around one axis [37]. Here the three-site jump method is adopted because of its shorter computation time in simulation. During the jump process, the magnetizations $M(\phi,t)$, $M(\phi+2\pi/3,t)$, $M(\phi-2\pi/3,t)$ are coupled by the jump process with a 'jump'matrix

$$\mathbf{R} = \begin{pmatrix} i2\pi\nu(\phi) + 2K_J + \frac{1}{T_2} & -K_J & -K_J \\ -K_J & i2\pi\nu(\phi+\frac{2}{3}\pi) + 2K_J + \frac{1}{T_2} & -K_J \\ -K_J & -K_J & i2\pi\nu(\phi-\frac{2}{3}\pi) + 2K_J + \frac{1}{T_2} \end{pmatrix} \tag{4.19}$$

where K_J is the jump rate, $1/T_2$ is an exchange independent relaxation term, and $\nu(\phi)$ is given in Eq. (4.2) and Eq. (4.9) for an aligned sample and a powder sample, respectively. The echo intensity for a particular ϕ is computed by summing over all components M_i using Eq. (4.15) with $P_i = 1/3(i = 1, 2, 3)$.

Aligned Sample

For an aligned sample, from Eq. (4.2) we know that the line shape is related to θ_0, α, β and ϕ. For a specific ϕ angle, the NMR signal according to Eq. (4.16) is

$$F(\theta_0, \alpha, \beta, \phi, t) = Re\{\mathbf{1} \cdot \mathbf{M}(2\tau + t)\} \tag{4.20}$$

and

$$F(\theta_0, \alpha, \beta, t) = \int_0^{2\pi} F(\theta_0, \alpha, \beta, \phi, t) d\phi \tag{4.21}$$

The overall time-domain signal is obtained by integrating over α and β:

$$F(\theta_0, t) = \int_{\frac{\pi}{2}-3\sigma}^{\frac{\pi}{2}+3\sigma} \int_0^{2\pi} F(\theta_0, \alpha, \beta, t)[\frac{1}{\sqrt{2\pi}\sigma} e^{-\frac{(\beta-\pi/2)^2}{2\sigma^2}}] e^{-\Sigma^2 t^2/2} \sin\beta d\alpha d\beta \tag{4.22}$$

where $e^{-\Sigma^2 t^2/2}$ is used to account for the observed line broadening, which is controlled by a fitting parameter Σ. Although the sample is aligned, the directors do not in practice all lie perfectly on a plane perpendicular to the magnetic field, but are distributed around it. In this equation a Gaussian distribution has been assumed with a characteristic width, σ. In practice, integration was performed by summing over ϕ and α at intervals of 2.8 degrees and summing over β at intervals of 3 degrees between $\frac{\pi}{2} - 3\sigma$ and $\frac{\pi}{2} + 3\sigma$. The absorption spectrum is proportional to the Fourier transform of the FID signal:

$$S(\theta_0, \omega) = \int_0^{\infty} F(\theta_0, t) e^{-iwt} dt \tag{4.23}$$

By lineshape simulation, the jump rate K_J can be obtained. An alternative method is to fit the quadrupole echo intensity $I^{calc}(\theta_0, 2\tau)$ as a function of sample rotation angle by using Eq. (4.22) at $t = 0$. Here a minimization routine can be used to minimize the sum-squared error f:

$$f = \sum_m [I^{expt}(\theta_0, 2\tau) - I^{calc}(\theta_0, 2\tau)]_m^2 \tag{4.24}$$

where m is the number of different θ_0 and the superscripts *expt* and *calc* denote experimental and calculated intensity, respectively. The best fit allows the determination of K_J. The fitting of echo intensities is necessary when the motional rates are close to $\geq 10^7 s^{-1}$.

Powder Sample

For a powder sample, the FID for a particular crystallite based on Eq. (4.9) is related to α, β and ϕ. Since the molecules have various orientations, the signal will not be affected by the value of ϕ. In the program, to save the computing time, ϕ was set as 0 and the FID is given by

$$F(\alpha, \beta, t) = Re\{\mathbf{1} \cdot \mathbf{M}(2\tau + t)\} \tag{4.25}$$

So the final FID intensity is obtained by summing over all α and β to give

$$F(t) = \int_0^{\pi} \int_0^{2\pi} F(\alpha, \beta, t) d\alpha sin\beta d\beta \tag{4.26}$$

The simulated spectrum is obtained by Fourier transform of $F(t)$, i.e.

$$S(w) = \int_0^{\infty} F(t) \cdot e^{-iwt} dt \tag{4.27}$$

4.2.3 Planar Diffusion Model

In the planar diffusion mechanism, molecules are assumed to undergo infinitesimal jumps. Dynamic spectra according to this model of motion can be computed by several approaches, for example, by dividing the ϕ plane into N segments and allowing jumps between adjacent segments. The simulated spectrum obtained in the limit, $N \rightarrow \infty$, leads to a diffusion constant D_R, which may be related to the jump rate K_J. A more efficient procedure for calculating the dynamic line shape due to planar diffusion is to make use of the expansion method [38–45]. For the random planar diffusive motion, the diffusion operator is:

$$\Gamma_{\phi} = D_R \frac{\partial^2}{\partial \phi^2} \tag{4.28}$$

Then Eq. (4.10) can be rewritten as:

$$\frac{d}{dt} M(\phi, t) = [-i\omega(\phi) - 1/T_2 + D_R \frac{\partial^2}{\partial \phi^2}] M(\phi, t) \tag{4.29}$$

Here we consider the aligned sample and using Eq. (4.2), ω can be expanded as a series of $e^{in\phi}$:

$$\omega(\phi) \quad = \quad 2\pi\nu(\phi) = A + B(e^{i\phi} + e^{-i\phi}) + C(e^{i2\phi} + e^{-i2\phi}) \tag{4.30}$$

with

$$\begin{aligned} A &= -\frac{3}{4}\pi q_{CD}(1+\eta)S\{P_2(\cos\theta_0)P_2(\cos\beta) \\ &\quad +\frac{3}{4}\sin^2\theta_0\sin^2\beta\cos 2\alpha + \frac{3}{4}\sin 2\theta_0\sin 2\beta\cos\alpha\} \\ B &= 0 \\ C &= \frac{3}{8}\pi q_{CD}(3-\eta)\{\frac{1}{2}P_2(\cos\theta_0)\sin^2\beta \\ &\quad +\frac{1}{4}\sin^2\theta_0(1+cos^2\beta)\cos 2\alpha - \frac{1}{4}\sin 2\theta_0\sin 2\beta\cos\alpha\} \end{aligned} \tag{4.31}$$

Here B is zero since the aromatic C-D bond is orthogonal to the planar normal of the disc-like molecule. We know that the FID signal is proportional to the real part of the integral over $M(\phi,t)$:

$$F(\theta_0,\alpha,\beta,t) \propto Re\int_0^{2\pi} d\phi M(\phi,t) \tag{4.32}$$

To find $M(\phi,t)$, it is first expanded into a complete set of exponential functions:

$$M(\phi,t) = \sum_{k'=-\infty}^{\infty} a_{k'}(t)e^{ik'\phi} \tag{4.33}$$

Substituting (4.33) and (4.30) into (4.29), and multiplying by $e^{-ik\phi}$, one gets after integrating over ϕ:

$$\frac{da_k(t)}{dt} = -[iA + \frac{1}{T_2} + k^2 D_R]a_k(t) - iC[a_{k+2}(t) + a_{k-2}(t)] \tag{4.34}$$

Adding up the equations for $a_k(t)$ and $a_{-k}(t)$ and defining

$$\begin{aligned} \bar{a}_0(t) &= \sqrt{2}a_0(t) \\ \bar{a}_k(t) &= a_k(t) + a_{-k}(t), k \neq 0 \end{aligned} \tag{4.35}$$

Eq. (4.34) can be written as

$$\frac{d\bar{\mathbf{a}}(t)}{dt} = -\mathbf{R}\bar{\mathbf{a}}(t) \tag{4.36}$$

or

$$\frac{d}{dt}\begin{pmatrix} \bar{a}_0(t) \\ \bar{a}_1(t) \\ \bar{a}_2(t) \\ \vdots \\ \bar{a}_k(t) \end{pmatrix} = -\begin{pmatrix} iA+\frac{1}{T_2} & 0 & i\sqrt{2}C & & & \\ 0 & iA+\frac{1}{T_2}+D_R+iC & 0 & iC & & \\ i\sqrt{2}C & 0 & iA+\frac{1}{T_2}+4D_R & 0 & iC & \\ & & & & \ddots & \\ & & & iC & 0 & iA+\frac{1}{T_2}+k^2D_R \end{pmatrix}\begin{pmatrix} \bar{a}_0(t) \\ \bar{a}_1(t) \\ \bar{a}_2(t) \\ \vdots \\ \bar{a}_k(t) \end{pmatrix}$$

To find $\bar{\mathbf{a}}(t)$, the matrix R can be truncated at some sufficiently high k value (in our study, k=6 suffices). For the quadrupole echo experiment,

$$\begin{aligned} \bar{\mathbf{a}}(t) &= e^{-\mathbf{R}(\tau+t)}[e^{-\mathbf{R}\tau}]^*\bar{\mathbf{a}}(0) \\ &= [Se^{-\Lambda(t+\tau)}S^{-1}][Se^{-\Lambda\tau}S^{-1}]^*\bar{\mathbf{a}}(0) \end{aligned} \tag{4.37}$$

where S is a unitary matrix which diagonalizes $\mathbf{R}$ to give Λ as before. When $t = 0$, $M(\phi, 0) = 1$ and is independent of ϕ. Initially, $\bar{a}_k(0) = 0, k \neq 0$ and $\bar{a}_0(0) = 1$. If we define $\mathbf{Z} = [Se^{-\Lambda(t+\tau)}S^{-1}][Se^{-\Lambda\tau}S^{-1}]^*$, then one has

$$\begin{aligned} F(\theta_0, \alpha, \beta, t) &= \mathbf{1} \cdot \bar{\mathbf{a}}(t) = \mathbf{1} \cdot \mathbf{Z}\bar{\mathbf{a}}(0) \\ &= \begin{pmatrix} 1 & 1 & \cdots & 1 \end{pmatrix} \begin{pmatrix} Z_{00} & Z_{01} & \cdots & Z_{0k} \\ Z_{10} & Z_{11} & \cdots & Z_{1k} \\ \vdots & \vdots & \ddots & \vdots \\ Z_{k0} & Z_{k1} & \cdots & Z_{kk} \end{pmatrix} \begin{pmatrix} \bar{a}_0(0) \\ \bar{a}_1(0) \\ \vdots \\ \bar{a}_k(0) \end{pmatrix} \\ &= \sum_{n=0}^{k} Z_{n0} \end{aligned} \tag{4.38}$$

This $F(\theta_0, \alpha, \beta, t)$ is substituted into Eqs.(4.22) and (4.23) to get the theoretical spectrum. Since the ϕ dependency was explicitly considered mathematically, and hence was not required in the simulation. The integration is still needed over α and β angles as before.

4.2.4 Theory for Dimeric Discotic Liquid Crystals

In monomeric discotic liquid crystals, there is in general no lateral correlation between molecules in different columns, since the columns can freely slide relative to each other. However, in dimeric discotics, the spacers that link the monomeric units impose correlation among columns. Therefore we need to adopt a model to simulate the dimer librations under the effect of a restricting potential due to the spacer. As a first attempt to interpret the results we tried to simulate the spectra using the diffusion method. Although in principle it is reasonable, it is hard to define a restoring potential that is solvable [37]. To simulate the spectra and mimic the effect of the spacer on the core's reorientations, we adopted the infinitesimal jump method proposed by Zamir et. al. [22]. The potential energy in which the core reorients is assumed as

$$V(\phi) = V_0\phi^2 \tag{4.39}$$

where V_0 is a positive parameter with dimensions J/rad^2, while ϕ is the angular deviation of the spacer from its equilibrium (minimum energy) direction (see Figure 4.5). The probability

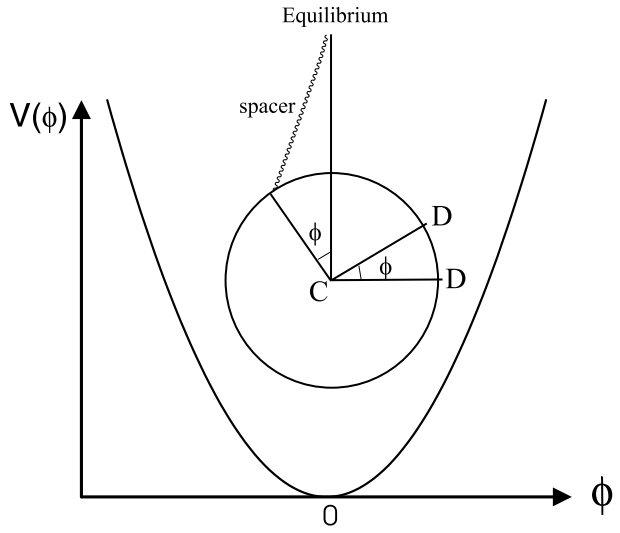

Figure 4.5: The schematic sketch of dimer potential in which a C-D bond reorients.

to find each C-D bond at ϕ_i obeys a normalized equilibrium distribution:

$$P^0(\phi_i) = \sqrt{\frac{V_0}{kT\pi}} e^{-V_o\phi_i^2/kT} \tag{4.40}$$

The librational motion of the core under the restricting potential of the spacer is assumed to obey a diffusion equation for the distribution, $P(\phi, t)$, of the C-D bonds of the form:

$$\begin{aligned} \frac{d}{dt}P(\phi,t) &= \left[D_R\frac{\partial^2}{\partial\phi^2} + \frac{D_R}{kT}\frac{\partial V(\phi)}{\partial\phi}\frac{\partial}{\partial\phi} + \frac{D_R}{kT}\frac{\partial^2 V(\phi)}{\partial\phi^2}\right] \times P(\phi,t) \\ &= \Gamma(\phi)P(\phi,t) \end{aligned} \tag{4.41}$$

where D_R is a reorientational diffusion constant. Using equation (4.39), $\Gamma(\phi)$ becomes

$$\Gamma(\phi) = D_R\frac{\partial^2}{\partial\phi^2} + \left[\frac{2V_0\phi D_R}{kT}\frac{\partial}{\partial\phi} + \frac{2V_0 D_R}{kT}\right] \tag{4.42}$$

in which the first term corresponds to free self-diffusion and the second to a potential driven diffusion. The corresponding Liouville equation for the magnetization (in the rotating coordinate system) then becomes

$$\frac{d}{dt}M(t) = -\left[i\omega + \frac{1}{T_2}\right] M(t) + \Gamma(\phi)M(t) \tag{4.43}$$

where $\omega = 2\pi\nu$ and ν is the quadrupolar frequency defined in Equation (4.9) in the case of a powder sample, and $1/T_2$ is the phenomenological relaxation term.

Now the Bloch-McConnell equations including the effect of chemical exchange [46] are:

$$\frac{d}{dt}M^i(t) = -\left[i\omega(\phi_i) + \sum_{j\neq i} k_{ji} + \frac{1}{T_2}\right] M^i(t) + \sum_{j\neq i} k_{ij}M^j(t) \tag{4.44}$$

where i labels different jump site and k_{ij} specifies jump rate between the i^{th} and j^{th} segments corresponding to different ϕ values. If we assume the jump is only occurring among neighboring segments, Equation (4.44) then becomes

$$\frac{d}{dt}M^i(t) = -\left[i\omega(\phi_i) + k_{i+1,i} + k_{i-1,i} + \frac{1}{T_2}\right] M^i(t) + k_{i,i+1}M^{i+1}(t) + k_{i,i-1}M^{i-1}(t) \quad (4.45)$$

or

$$\frac{d}{dt}\begin{pmatrix} M_1(t) \\ M_2(t) \\ M_3(t) \\ \vdots \\ M_n(t) \end{pmatrix} =$$

$$\begin{pmatrix} i\omega(\phi_1) + k_{2,1} + \frac{1}{T_2} & k_{1,2} & & & & \\ k_{2,1} & i\omega(\phi_2) + k_{3,2} + k_{1,2} + \frac{1}{T_2} & k_{2,3} & & & \\ & k_{3,2} & i\omega(\phi_3) + k_{4,3} + k_{2,3} + \frac{1}{T_2} & k_{3,4} & & \\ & & & \ddots & & \\ & & & & k_{n,n-1} & i\omega(\phi_n) + k_{n-1,n} + \frac{1}{T_2} \end{pmatrix}$$

$$\times \begin{pmatrix} M_1(t) \\ M_2(t) \\ M_3(t) \\ \vdots \\ M_n(t) \end{pmatrix}$$

Comparing Eq. (4.10) and (4.45), one can get the elements of the matrix **R**:

$$\begin{aligned} R_{n,n} &= i\omega(\phi_n) + k_{n+1,n} + k_{n-1,n} + \frac{1}{T_2} \\ R_{n,n\pm1} &= -k_{n,n\pm1} \\ &\texttt{others are zero}. \end{aligned} \quad (4.46)$$

Using Eq. (4.18) we can calculate the FID signal $F = F(\alpha, \beta, t)$.

To relate the jump rates to the diffusion constant D_R, one needs to compare equation (4.43) and equation (4.45). First, we expand the magnetization $M^{i+1}(t)$ into a Taylor series

$$M^{i+1}(t) = M^i(t) + \frac{\partial M^i(t)}{\partial \phi}\delta\phi + \frac{1}{2}\frac{\partial^2 M^i(t)}{\partial^2 \phi}(\delta\phi)^2 + \cdots$$

and substitute the series up to second order terms to the Equation (4.45) to give:

$$\begin{aligned} \frac{d}{dt}M^i(t) &= -\left[i\omega(\phi_i) + 1/T_2\right] M^i(t) + [\frac{1}{2}(k_{i,i+1} + k_{i,i-1})(\delta\phi)^2\frac{\partial^2}{\partial\phi^2} \\ &\quad +(k_{i,i+1} + k_{i,i-1})\frac{\partial}{\partial\phi} + (k_{i,i+1} + k_{i,i-1} - k_{i+1,i} - k_{i-1,i})]M^i(t) \end{aligned} \quad (4.47)$$

where $\delta\phi$ is the jump angle between two neighboring segments. By comparing this equation with Equation (4.43) the following relation can be obtained:

$$\begin{aligned} D_R &= \frac{1}{2}(k_{i,i+1} + k_{i,i-1})(\delta\phi)^2 \\ 2V_0\phi_i D_R/kT &= (k_{i,i+1} - k_{i,i-1})(\delta\phi) \\ 2V_0 D_R/kT &= k_{i,i+1} - k_{i,i-1} - k_{i+1,i} - k_{i-1,i} \end{aligned} \quad (4.48)$$

Combining with the microscopic reversibility [47] $k_{i,j}P(\phi_j) = k_{j,i}P(\phi_i)$ $(i \neq j)$, the jump rates can be expressed in terms of a reorientational diffusion constant D_R as follows [22]:

$$\begin{aligned} k_{0,\pm1} &= D_R/(\delta\phi)^2 \\ k_{\pm1,0} &= k_{0,\pm1}e^{V_o(\delta\phi)^2/kT} \\ k_{\pm1,\pm2} &= 2D_R/(\delta\phi)^2 - k_{\pm1,0} \\ k_{\pm2,\pm1} &= k_{\pm1,\pm2}e^{-2V_o(\delta\phi)(\phi_{\pm1}+\frac{\delta\phi}{2})/kT} \end{aligned} \tag{4.49}$$

By successive applications of these, all jump rates can be obtained in Eq. (4.46) to give the **R** matrix. The number of segments included in the calculation is limited to the range ϕ, outside of which the equilibrium population $P^0(\phi)$ is negligible ($< 1\%$), and the jump angle $\delta\phi$ is defined as range/(number of segments). In our simulation, the number of segments was 17; so the dimension of the R matrix was 17×17. Finally, Eqs.(4.26) and (4.27) are then used to find the simulated powder spectrum using V_o/kT and D_R as the main adjustable parameters.

4.3 Experiment

The core deuterated samples of HAT5a-d_6 and DHAT5-C_{14} are shown in Figure 1.16. The reported transition temperatures between the D_{ho} and isotropic phase of protonated samples HAT5a-d_6 and DHAT5-C_{14} are 442K and 420K [30], respectively. This transition temperature in our deuterated HAT5a-d_6 sample was estimated at 438±2K based on the NMR spectra. The uncertainty is mainly due to a significant biphasic region. ^{2}H spectra and the echo maximum intensities at different rotation angles were recorded. To get a good free induction decay (FID) in DHAT5-C_{14}, signal averaging required 2000 scans.

The aligned HAT5a-d_6 sample was obtained by cooling slowly in the magnet from the isotropic phase to the desired temperature in the D_{ho} phase. In the low temperature range, our angular dependent experiments did not show any observable field-induced sample reorientation and columnar destruction in the studied θ_0 region of $0° - 90°$. However, at high temperatures, the FID intensities at high sample rotation angles ($> 50^o$) did show considerable deviations from the predictions of the theoretical model. At high sample rotation angles, the director(s) tends to reorient by the magnetic torque due to the NMR field. The discrepancies are perhaps due partly to a small amount of impurity in the sample and partly to the magnetic torque on the molecules. The director reorientation is particularly easy at high temperatures where viscosities are lower.

4.4 Study of Monomer

4.4.1 Aligned Sample

The temperature dependence of the quadrupolar splitting of the aromatic deuterons in HAT5a-d_6 has been shown in Figure 3.15 (See section 3.9.4). From the quadrupolar splitting, S can be calculated using Eq. (4.7) (Table 4.1). To obtain the dynamic parameters for the molecular motion, the threefold jump model and planar diffusion model (PDM) are both used. The lineshapes calculated by these two models are quite similar and it is hard to tell which model (jump or diffusion) is better [36]. We therefore present the results based on the planar diffusion model, partly due to the treatment of relaxation data based on the anisotropic viscosity model (AVM). The comparison of these two methods will be addressed later.

Typical ^{2}H NMR spectra of HAT5a-d_6 collected with $\tau = 30\mu s$ at different θ_0 for six temperatures are shown in Figure 4.6. There is a dramatic spectral change when the sample is rotated from 0° to 90°. Most spectra exhibit a small doublet, likely caused by a small amount of impurity in the sample. When the sample temperature was lowered, the intensity of the impurity doublet tended to increase. But this signal did not affect our lineshape simulation. The simulated spectra for these temperatures are also shown in Figure 4.6 based on Eq. (4.23). The same set of simulation parameters (Eq. (4.22)) was used for all rotation angles. These are listed in Table 4.1. In the simulation, the best results were obtained using $\Sigma = 15$ kHz and $\eta = 0.064$. To get quantitative information, the diffusion constant D_R is varied to match the observed lineshapes with the simulated spectra at different rotation angles. The lineshape at $\theta_0 = 90°$ tends to control the D_R value, and this is particularly true at high temperatures (e.g. see 357 K spectrum in Figure 4.6).

As mentioned before, when the temperature increases, the molecular motion becomes faster ($D_R \geq 10^7 \text{rad}^2/\text{s}$). As a consequence, the lineshape simulation is unable to give a reliable D_R value (i.e. to achieve a good fit of the 90° spectral pattern, D_R tends to be driven to higher values). As seen in Figure 4.6, the powder spectral lineshape at $\theta_0 = 90°$ and 357K could not be reproduced faithfully with the D_R value of $9.7 \times 10^6 \text{rad}^2/\text{s}$. Instead a D_R value of $1.7 \times 10^7 \text{rad}^2/\text{s}$ would fit it better, while unaffecting those at low angles. Hence an angular dependent study of the echo intensity is adopted. To demonstrate this method and extract the diffusion constant from the echo intensities, Figure 4.7 shows the normalised intensity $I(\theta_0, 2\tau)/I(\theta_0, 2\tau)_{max}$ versus the rotation angle (0° to 50°) for two different τ values

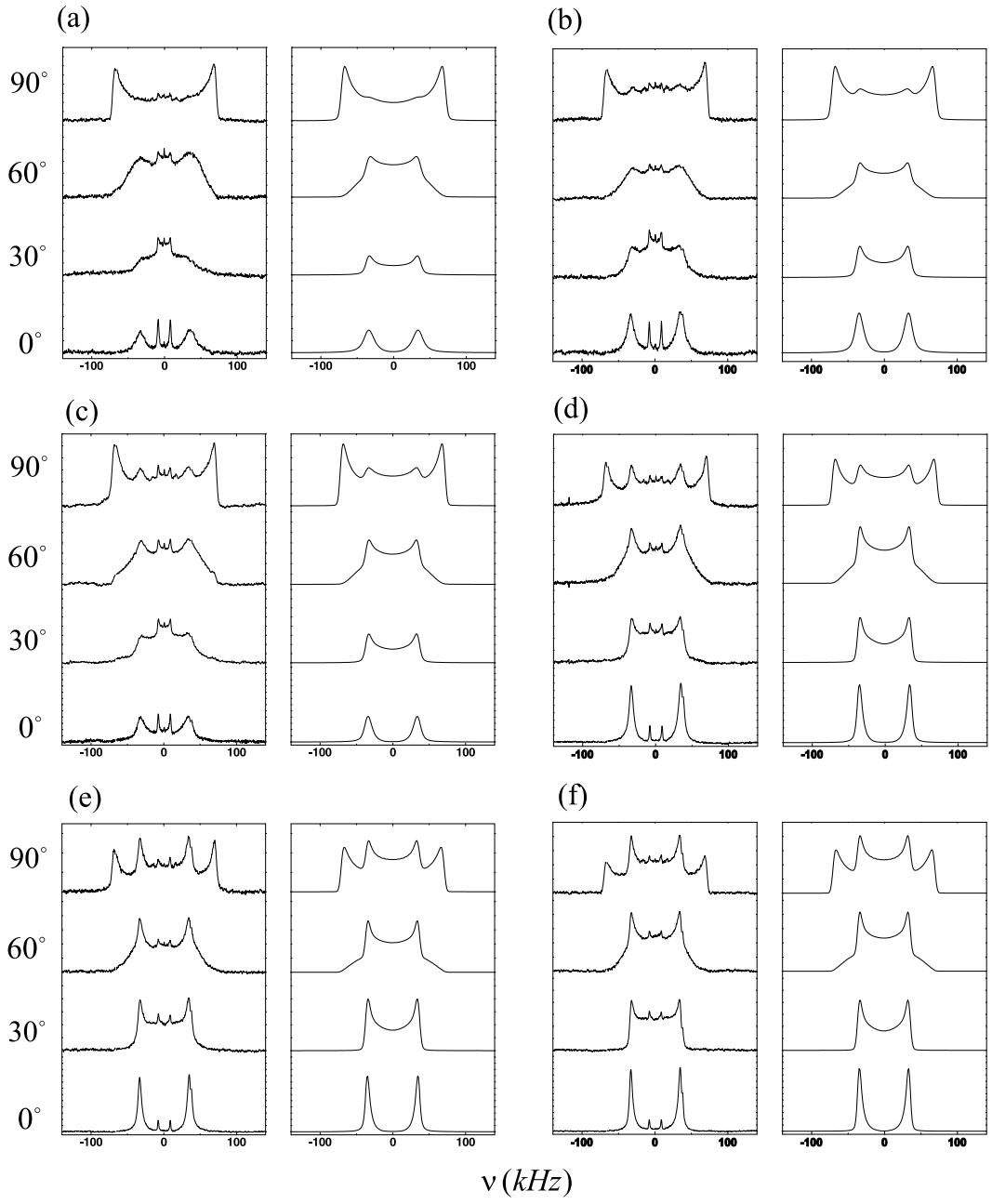

Figure 4.6: Experimental (left) and corresponding calculated (right) ^{2}H NMR spectra for HAT5a-d_6 using planar diffusion model for different θ_0 at 332K(a), 337K(b), 342K(c), 347K(d), 352K(e) and 357K(f).

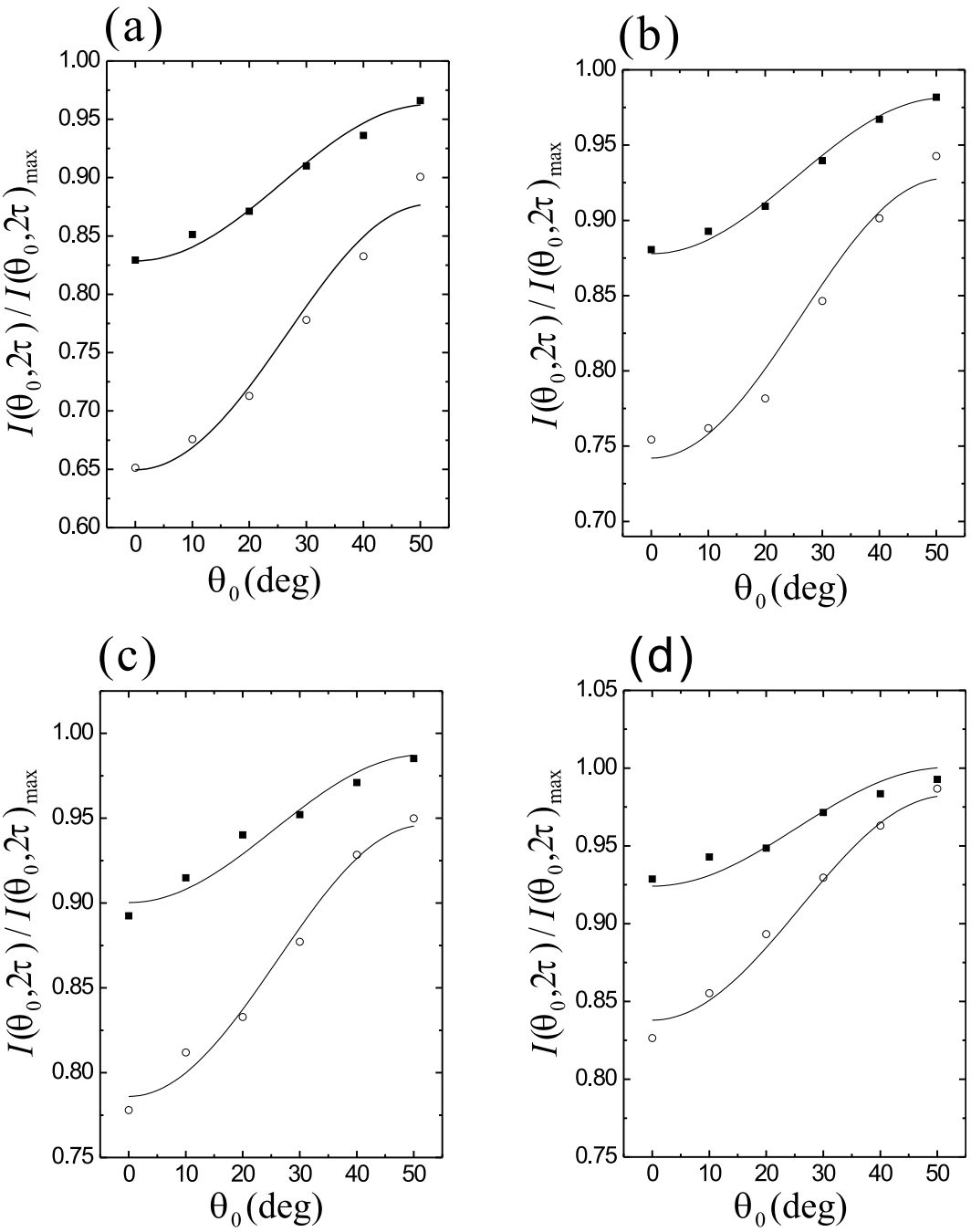

Figure 4.7: Experimental and calculated normalized echo intensity $I(\theta_0, 2\tau)/I(\theta_0, 2\tau)_{max}$ for HAT5a-d_6 at $T = 352K$ (a), $T = 357K$ (b), $T = 362K$ (c) and $T = 367K$ (d), with $\tau = 15\mu s$ (■) and $\tau = 30\mu s$ (○).

Table 4.1: Parameters used in the simulation of experimental NMR spectra of HAT5.

$Temp.(K)$	$D_R(\mathrm{rad}^2/\mathrm{s})$	S	$\sigma(deg)$	$1/T_2(\mathrm{kHz})$
332	$(1.5 \pm 0.1) \times 10^6$	0.956±0.005	9±1	4
337	$(2.3 \pm 0.1) \times 10^6$	0.954±0.005	9±1	4
342	$(2.8 \pm 0.1) \times 10^6$	0.952±0.005	9±1	1
347	$(5.0 \pm 0.1) \times 10^6$	0.948±0.005	9±1	1
352[1]	$(7.3 \pm 0.1) \times 10^6$	0.945±0.005	11±1	0.1
357[1]	$(9.7 \pm 0.1) \times 10^6$	0.941±0.005	11±1	0.1
362	$(1.3 \pm 0.1) \times 10^7$	0.939±0.005	9±1	/
367	$(1.5 \pm 0.1) \times 10^7$	0.937±0.005	9±1	/

1. Fitting parameters for both lineshape and FID intensity (T_2 is not used).

at four temperatures. The fitting parameters are also given in Table 4.1. The σ values seem to be independent of the temperature. The diffusion constant D_R is plotted versus the reciprocal temperature in Figure 4.8 to demonstrate that the reorientational process is thermally activated. From $D_R = D_R^0 exp[-E_a/RT]$, the activation energy $E_a = 69 \pm 3\mathrm{kJ/mol}$ is found. This value is consistent with the results of relaxation study of similar monomers [48, 49].

In our simulations, both a threefold jump model and a planar diffusion model were used to fit the lineshape. Since the spectrum at $\theta_0 = 90^\circ$ is sensitive to K_J or D_R, we calculate the spectra based on these two models at this angle as shown in Figure 4.9. It may be seen that pairwise matching of spectra is obtained for $K_J/D_R \approx 1.3$ to 1.5, so that if one prefers to interpret the spectra in the above by the threefold jump model, the K_J may be found by scaling accordingly. It is also demonstrated that in the fast motion limit ($K_J \geq 1.5 \times 10^7/\mathrm{s}$ or $D_R \geq 1.0 \times 10^7 \mathrm{rad}^2/\mathrm{s}$) the lineshape will not change regardless of the model.

4.4.2 Comparison of Results by Different Methods

Comparing the results of diffusion constants at the same temperature derived here and spin relaxation data (PDM and AVM), we find that $D_\beta < D_R < D_\alpha$. This seems reasonable because in the AVM (Chapter 3) two parameters D_α and D_β are used to describe the molecular motion: diffusive precession motion and libration motion of the molecular plane, while in the PDM only D_R is used to describe the 'planar' rotational diffusive motion, which should mimic the combined effect of α and β motion. However, it is noticed that the activation energies

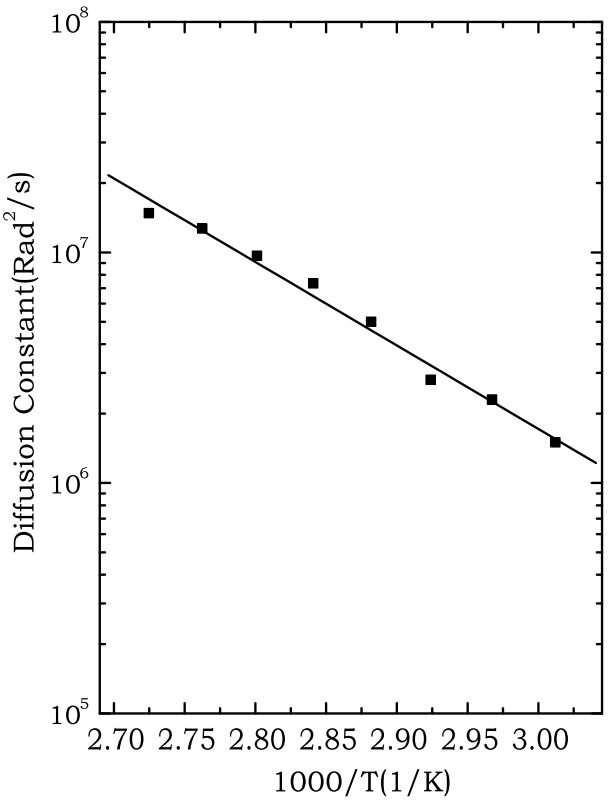

Figure 4.8: Plot of the planar diffusion constant,D_R versus the reciprocal temperature for HAT5a-d_6.

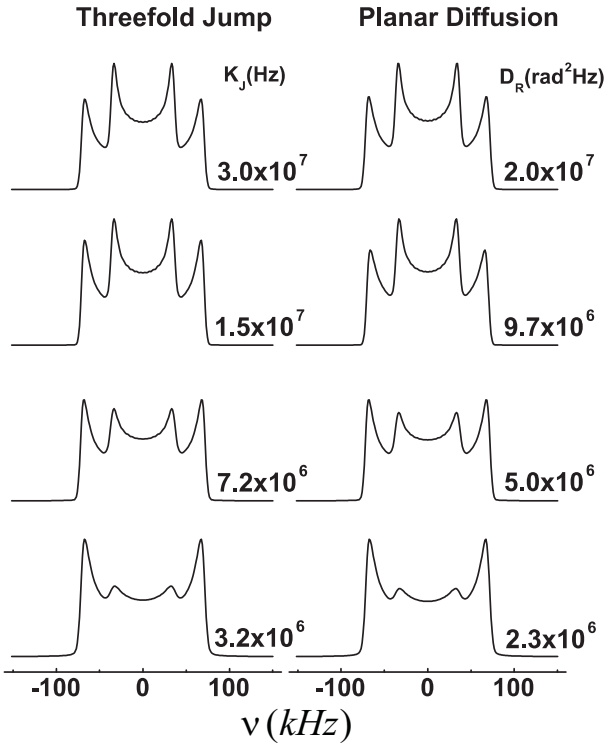

Figure 4.9: Comparison of simulated spectra for HAT5a-d_6 at $\theta_0 = 90°$ calculated for the threefold jump model (left) and the planar diffusion model.

obtained from PDM are larger than those from AVM. We believe that the activation energy of D_R from PDM is likely more correct, since the activation energies found from the AVM are based on the relaxation data collected at a single Larmor frequency.

In summary, the present study has combined the nuclear spin relaxation and dynamic NMR spectroscopy to study axial motions of an aligned discotic monomer with dissimilar side chains as a function of temperature in the columnar D_{ho} phase. The derived motional parameters from the two approaches are compared. In particular, the present study has demonstrated that angular dependent echo intensities at fixed τ in a quadrupolar echo experiment can be particularly sensitive in pinning down the rate process when its rate approaches the fast motion regime. The spinning motion of the molecular core is found at a rate of ca. 10^7 s^{-1} in HAT5a-d_6. This number is significantly lower than the typical "hopping"rate of electrons/holes (10^{10} s^{-1}) in discotic LC. Thus, the dynamic disorder in the columnar phases appears to be static as far as charge transport process is concerned.

4.4.3 Powder Sample

The deuterium powder spectra of HAT5a-d_6 are shown as a function of temperature in Figure 4.10. Based on the three-site jump model outlined in the theory section, these spectra were simulated based on Eq. (4.27) to give the jump rates. The simulated spectra are shown in the right column of Figure 4.10. The linewidth and asymmetry parameter were taken as $1/T_2$=$2\times10^3 s^{-1}$ and η=0.064 for the aromatic deuteron(s). The jump rate K_J obtained in the simulations ranges from ∼15 kHz to ∼5 MHz, and is shown as a function of the reciprocal temperature in Figure 4.12. Also shown in this figure are the typical K_J values obtained from the aligned sample for comparison. At lower temperatures the spectra of the powder samples are weak, so there are some uncertainties in the simulation. Within experimental uncertainties, both aligned and powder samples give the same K_J values. The activation energy is found to be ca. 70 kJ/mol. When the temperature was higher than 350K, sharp lines appeared around $\pm 35kHz$ (Figure 4.11) in spectra which cannot be reproduced by simulation. This suggests that partial alignment of the sample occurred in the range of higher temperatures, so that we can not simulate the spectra using the model for a powder.

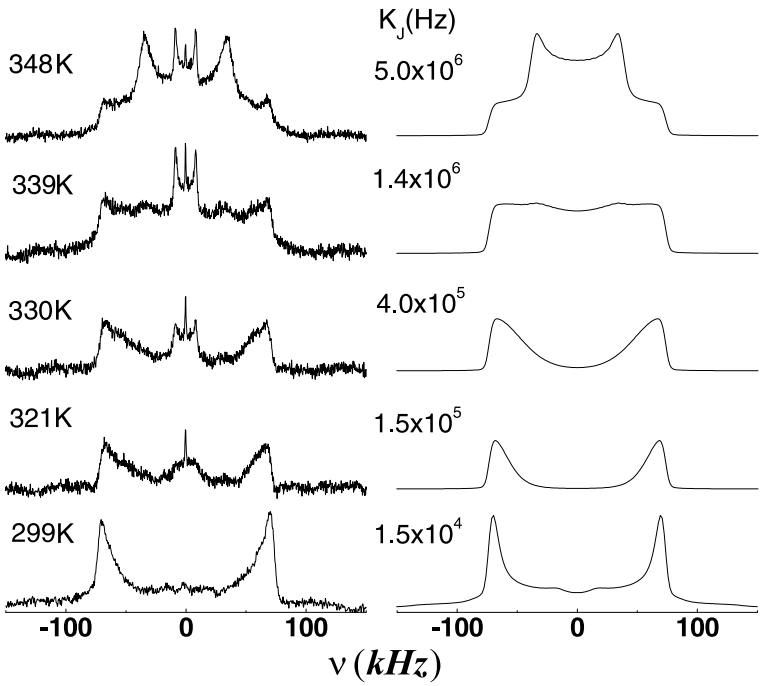

Figure 4.10: Experimental and simulated DNMR spectra using $\tau = 30\mu$s of HAT5a-d_6.

.

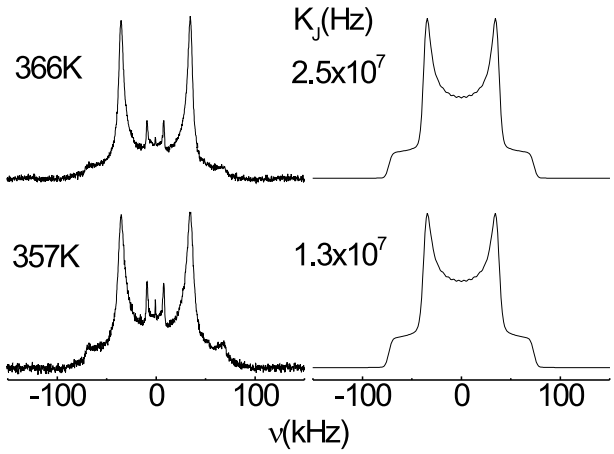

Figure 4.11: Experimental and simulated DNMR spectra using $\tau = 30\mu$s of HAT5a-d_6 at higher temperatures. The sharp partially aligned peaks can not be well simulated.

.

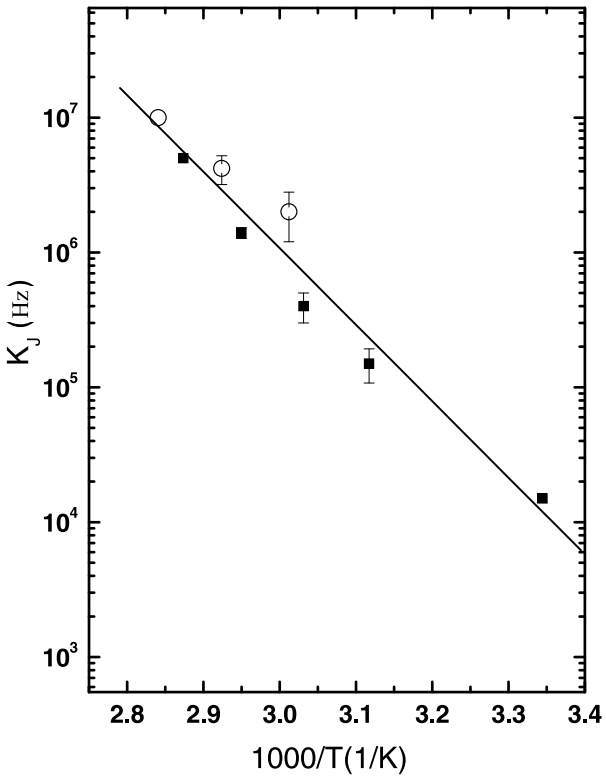

Figure 4.12: Plot of jump rate versus the reciprocal temperature for HAT5a-d_6. Solid and open symbols denote data from powder and aligned sample, respectively.

.

4.5 Study of Dimer

Figure 4.13 shows several powder spectra recorded in DHAT5-C_{14} by heating from its crystal phase. Note that the temperature was kept well below the clearing temperature to avoid any possible partial alignment of the sample. As shown in this figure, no significant line shape change was observed as a function of temperature, except at 390K a relatively sharp line starts to emerge. Upon heating the sample from room temperature, one can observe a gradually increasing broad central feature between the two edge singularities before the appearance of a tiny sharp line at 390K. This observation indicates that most dimer molecules undergo restricted motion in a powder sample, while some molecules have 'fast' overall molecular motion at high temperatures to give an isotropic peak in the middle of the spectrum. Hence only the spectral patterns and echo intensities at one temperature (297K) were studied. Line shape analysis was adopted to study the time-domain behavior of the spectral patterns or signal intensities as a function of the time interval τ between the 90° pulses in the quadrupole echo experiment [50]. The experiments were done using different τ values ranging from 20 to 250 μs and the spectra are shown in Figure 4.14. It may be seen that increasing τ not only

reduces the overall signal intensity due to the transverse relaxation, but also causes some notable changes in the line shape. In simulating these spectra, the number of segments was chosen as 17 giving a corresponding jump angle $\delta\phi$ of 13.5°. The linewidth and asymmetry parameter were taken as $1/T_2$=5×10^{3}s^{-1} and η=0.064 for the aromatic deuteron(s). The quadrupole coupling constant q_{CD} was set at 193 kHz to simulate the separation between the 90° singularities. The simulated spectra calculated using Eqs. (4.18), (4.26) and (4.27) with D_R and V_0/kT as adjustable parameters are also shown in Fig. 4.14. This procedure produces a D_R value of 300 rad^{2}s^{-1} and V_0/kT=1 rad^{-2}, and the experimental and simulated spectra are consistent, especially near the 90° singularities. Since both the D_R and V_0/kT values simultaneously affect the simulation, one way to ascertain these values is to fit the (normalized) echo intensity as a function of τ at 296K by minimizing the sum-square error f shown in Figure 4.15.

$$f = \sum_m \left[\left(\frac{I(2\tau)}{I(2\tau_0)} \right)^{expt} - \left(\frac{I(2\tau)}{I(2\tau_0)} \right)^{calc} \right]_m^2 \tag{4.50}$$

where m is the number of different τ. And $I(2\tau)$ is obtained from Eq. (4.27), $I(2\tau_0)$ is the signal intensity when $\tau_0 = 20\mu s$. Two scenarios are considered to give the simulated (solid) curves shown in the same figure. In Figure 4.15 (a), we fix V_0/kT=1 rad^{-2} and vary D_R to give a value of 250 rad^{2}s^{-1}, while in Figure 4.15 (b), D_R is fixed at 300 rad^{2}s^{-1} and the minimization procedure produces a V_0/kT=0.7 rad^{-2}. It is clear that no visible difference exists between these two minimizations and the above minimization results place some error limits on the results derived from the line shape simulation. It is noted that the lineshapes observed as a function of temperature in the dimer DTHE5 by Zamir et al. [22] appear quite different. The two triphenylene residues are the same in DTHE5 dimer and DHAT5-C_{14} dimer, but the former is connected by an -O$(CH_2)_{10}$O- rather than an -OCO$(CH_2)_{14}$OCO- spacer. At the same temperature, our V_0/kT is about a factor of 10 lower and D_R is 2 orders of magnitude smaller. It is not clear at present why an addition of two C=O bonds in the spacer has such a profound effect on the librational dynamics. Thus, more studies are required to further our understanding.

4.6 Comparison of the Dynamics between Monomer and Dimer

To compare the planar motions of monomer and dimer, we can use the simple experimental relation $D_R = K_J/1.5$ for HAT5a-d_6, which can give the magnitude of D_R for the powder sample HAT5a-d_6 (e.g. $D_R = 10^3$ rad^2/s at 299K). By comparing the diffusive rates for the two DLC samples, it is concluded that the planar motion in the dimer is at least 30 times

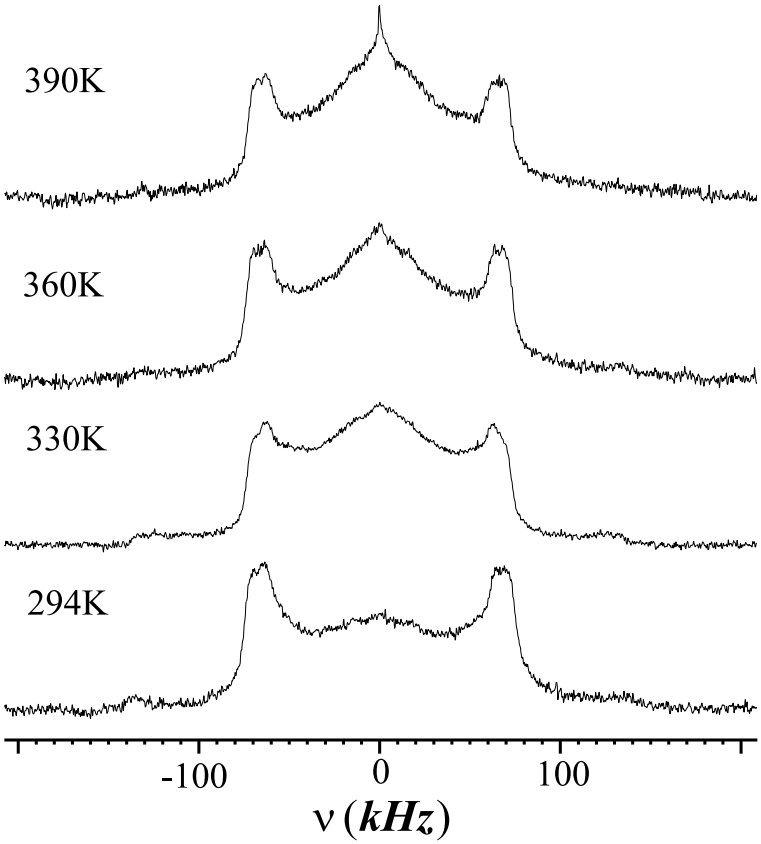

Figure 4.13: Typical DNMR spectra of a core deuterated dimer DHAT5-C_{14} using $\tau = 30$ μs at several temperatures.

.

smaller than that of the monomer. This could lead to an enhancement of charge and energy transport in discotic dimer systems. Comparing the DNMR spectra, the line shape of the monomer is more temperature dependent than that of the dimer. From the analysis above, it is obvious that the planar diffusion of the subunits in the dimer at room temperature is much slower (a factor of ca. 30) than that of the monomer. Thus, the presence of the spacer has stabilized the columnar structure and lengthened the stability range of the mesophase, which may well be the reason for the observed enhancement in charge and energy transport in dimeric DLC [14].

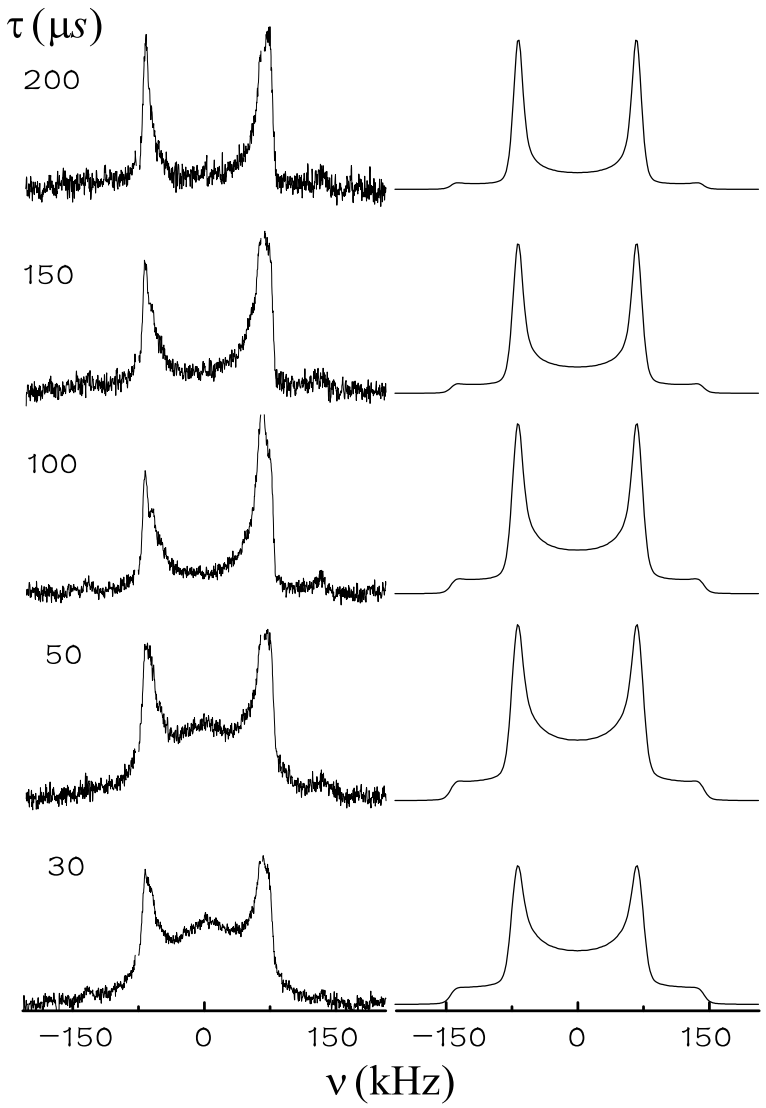

Figure 4.14: Experimental and simulated DNMR spectra of DHAT5-C_{14} at 296K.

.

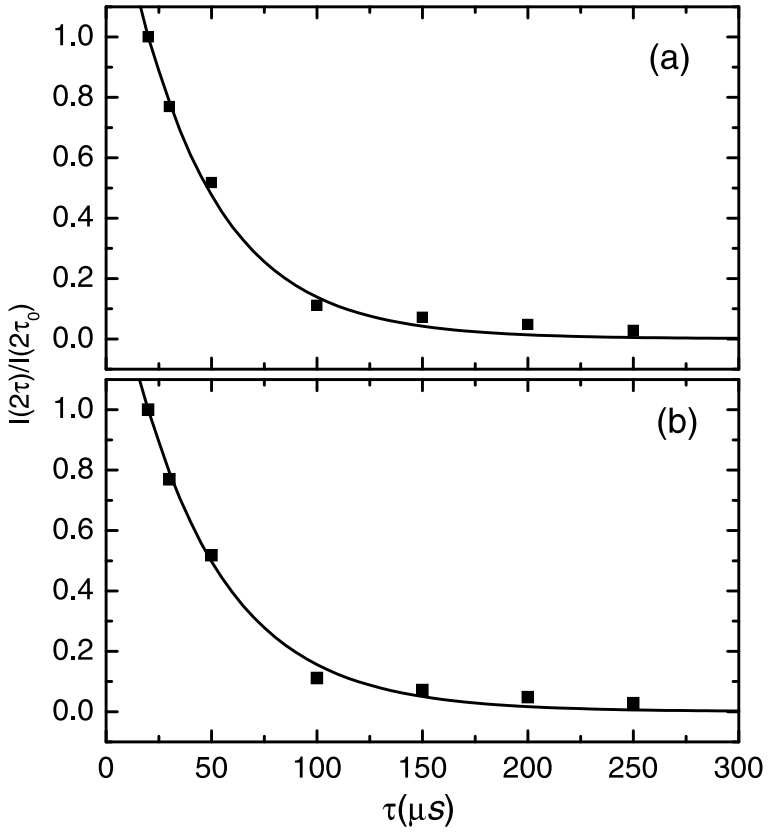

Figure 4.15: Experimental and simulated normalized echo intensities of DHAT5-C_{14} at 296K (see text for details).

.

References

[1] Chandrasekhar, S.; Sadashiva, B. K.; Suresh, K. A. *Pramana* **1977**, *9*, 471.

[2] Bengs, H.; Closs, F.; Frey, T.; Funhoff, D.; Ringsdorf, H.; Siemensmeyer, K. *Liq. Cryst.* **1993**, *15*, 565.

[3] Blanzat, B.; Barthou, C.; Tercier, N.; Andre, J. J.; Simon, J. *J. Am. Chem. Soc.* **1987**, *109*, 6193.

[4] Blasse, G.; Dirksen, G. J.; Meijerink, A.; Vanderpol, J. F.; Neeleman, E.; Drenth, W. *Chem. Phys. Lett.* **1989**, *154*, 420.

[5] Gregg, B. A.; Fox, M. A.; Bard, A. J. *J. Phys. Chem.* **1989**, *93*, 4227.

[6] Markovitsi, D.; Lecuyer, I.; Clergeot, B.; Jallabert, C.; Strzelecka, H.; Veber, M. *Liq. Cryst.* **1989**, *6*, 83.

[7] Markovitsi, D.; Lecuyer, I.; Lianos, P.; Malthete, J. *J. Chem. Soc., Faraday Trans.* **1991**, *87*, 1785.

[8] Markovitsi, D.; Lecuyer, I.; Simon, J. *J. Phys. Chem.* **1991**, *95*, 3620.

[9] Schouten, P. G.; Warman, J. M.; Dehaas, M. P.; Fox, M. A.; Pan, H. L. *Nature* **1991**, *353*, 736.

[10] Boden, N.; Bushby, R. J.; Clements, J.; Movaghar, B.; Donovan, K. J.; Kreouzis, T. *Phys. Rev. B* **1995**, *52*, 13274.

[11] Bacher, A.; Bleyl, I.; Erdelen, H.; Haarer, D.; Paulus, W.; Schmidt, H. *Adv. Mater.* **1997**, *9*, 1031.

[12] Christ, T.; Glusen, B.; Greiner, A.; Kettner, A.; Sander, R.; Stumpflen, V.; Tsukruk, V.; Wendorff, J. H. *Adv. Mater.* **1997**, *9*, 48.

[13] Markovitsi, D.; Germain, A.; Millie, P.; Lecuyer, P.; Gallo, L. K.; Argyrakis, P.; Bengs, H.; Ringsdorf, H. *J. Phys. Chem.* **1995**, *99*, 1005.

[14] Adam, D.; Closs, F.; Frey, T.; Funhoff, D.; Haarer, D.; Schuhmacher, P.; Siemensmeyer, K. *Phys. Rev. Lett.* **1993**, *70*, 457.

[15] Destrade, C.; Tinh, N. H.; Malthete, J.; Levelut, A. M. *J. Physique* **1983**, *44*, 597.

[16] Boden, N.; Bushby, R. J.; Hardy, C.; Sixl, F. *Chem. Phys. Lett.* **1986**, *123*, 359.

[17] Dvinskikh, S. V.; Furo, I.; Zimmermann, H.; Maliniak, A. *Phys. Rev. E.* **2002**, *65*, 050702.

[18] Rutar, V.; Blinc, R.; Vilfan, M. *J. Physique* **1982**, *43*, 761.

[19] Dong, R. Y. *Nuclear Magnetic Resonance of Liquid Crystals*; Springer-Verlag, 1997.

[20] Boden, N.; Bushby, R. J.; Clements, J. *J. Chem. Phys.* **1993**, *98*, 5920.

[21] Shen, X.; Dong, R. Y.; Boden, N.; Bushby, R. J.; Martin, P. S.; Wood, A. *J. Chem. Phys.* **1998**, *108*, 4324.

[22] Zamir, S.; Poupko, R.; Luz, Z.; Huser, B.; Boeffel, C.; Zimmermann, H. *J. Am. Chem. Soc.* **1994**, *116*, 1973.

[23] Imrie, C. T.; Henderson, P. A. *Curr. Opin. Colloid Interface Sci.* **2002**, *7*, 298.

[24] D. Craats, A. M. v.; Siebbeles, L. D. A.; Bleyl, I.; Haarer, D.; Berlin, Y. A.; Zharikov, A. A.; Warman, J. M. *J. Phys. Chem. B* **1998**, *102*, 9625.

[25] Kranig, W.; Boeffel, C.; Spiess, H. W. *Macromolecules* **1990**, *23*, 4061.

[26] Goldfarb, D.; Luz, Z.; Zimmermann, H. *J. Phys.* **1981**, *42*, 1303.

[27] Luz, Z. Dynamic NMR in liquid crystals and liquid crystalline solutions; In *NMR of Ordered Liquids*; Burnell, E. E.; de Lange, C. A., Eds.; Kluwer Academic Publishers: Netherlands, 2003.

[28] Xu, J.; Veracini, C. A.; Dong, R. Y. *Phys. Rev. E* **2005**, *72*, 051703.

[29] Xu, J.; Veracini, C. A.; Dong, R. Y. *Phys. Rev. E* **2006**, *73*, 011705.

[30] Kranig, W.; Huser, B.; Spiess, H. W.; Kreuder, W.; Ringsdorf, H.; Zimmermann, H. *Adv. Mater.* **1990**, *2*, 36.

[31] Vaz, M. J.; Yaniv, Z.; Dong, R. Y.; Doane, J. W. *J. Magn. Reson.* **1985**, *62*, 461.

[32] McConnell, H. M. *J. Chem. Phys.* **1958**, *28*, 430.

[33] Zamir, S.; Poupko, R.; Luz, Z.; Alexander, S. *J. Chem. Phys.* **1991**, *94*, 5939.

[34] Gordon, R. G.; Messenger, T. Chapter XIII; In *Electron Spin Relaxation in Liquids*; Muus, L. T.; Atkins, P. W., Eds.; Plenum Press: New York, 1972.

[35] Vega, A. J.; Fiat, D. *J. Magn. Reson.* **1975**, *19*, 21.

[36] Poupko, R.; Luz, Z.; Spielberg, N.; Zimmermann, H. *J. Am. Chem. Soc.* **1989**, *111*, 6094.

[37] Zamir, S.; Luz, Z.; Poupko, R.; Alexander, S.; Zimmermann, H. *J. Chem. Phys.* **1991**, *94*, 5927.

[38] Schwartz, L. J.; Meirovitch, E.; Ripmeester, J. A.; Freed, J. H. *J. Phys. Chem.* **1983**, *87*, 4453.

[39] Shiotani, M.; Freed, J. H. *J. Phys. Chem.* **1981**, *85*, 3873.

[40] Luz, Z.; Poupko, R.; Samulski, E. T. *J. Chem. Phys.* **1981**, *74*, 5825.

[41] Vega, A. J.; English, A. D. *Macromolecules* **1980**, *13*, 1635.

[42] Campbell, R. F.; Meirovitch, E.; Freed, J. H. *J. Phys. Chem.* **1979**, *83*, 525.

[43] Baram, A.; Luz, Z.; Alexander, S. *J. Chem. Phys.* **1976**, *64*, 4321.

[44] Vega, A. J.; Fiat, D. *J. Magn. Reson.* **1974**, *13*, 260.

[45] Freed, J. H.; Bruno, G. V.; POLNASZE, C. F. *J. Phys. Chem.* **1971**, *75*, 3385.

[46] Vega, A. J.; Luz, Z. *J. Chem. Phys.* **1987**, *86*, 1803.

[47] Wittebort, R. J.; Olejniczak, E. T.; Griffin, R. G. *J. Chem. Phys.* **1987**, *86*, 5411.

[48] Shen, X.; Dong, R. Y.; Boden, N.; Bushby, R. J.; Martin, P. S.; Wood, A. *J. Chem. Phys.* **1998**, *108*, 4324.

[49] Dong, R. Y.; Boden, N.; Bushby, R. J.; Martin, P. S. *Mol. Phys.* **1999**, *97*, 1165.

[50] Muller, K.; Poupko, R.; Luz, Z. *J. Magn. Reson.* **1969**, *90*, 19.

Chapter 5

Structure and Magnetic Field Response of a Chiral Smectic C* phase: ^{2}H NMR Study

5.1 Introduction

Smectic C liquid crystals can be considered as stacks of molecular layers. Each layer corresponds to a two-dimensional liquid where the director $\hat{n}$ is inclined by a tilt angle θ_0 with respect to the layer normal. If the constituent molecules are chiral, a spontaneous electric polarization is present in each layer. This results in a chiral smectic C* phase, and the consequence of the molecular chirality is the appearance of a helical superstructure: the azimuthal direction of the tilt changes by a small amount when going from layer to layer. The corresponding helical pitch is usually of the order of a few μm or several hundreds smectic layers. Chiral liquid crystalline materials have received much attention in recent years because of their scientific and technical potentials, for example, in nonlinear optics, information storage, and display devices.

Significant research has been directed at characterizing the structure of the recently discovered smectic C* and chiral subphases. A typical phase sequence for a bulk sample of chiral molecules is $isotropic \rightarrow SmA \rightarrow SmC^*$ upon decreasing temperature in zero field. One property of the SmC* phase is the occurrence of a reentrant phenomenon in the presence of a magnetic field. Musevic et al. [1] have observed that there exists a range of magnetic field strength for which the following sequence of phase transitions occurs with decreasing temperature: $SmA \rightarrow SmC^* \rightarrow SmC \rightarrow SmC^*$. Another is that these compounds display a Lifshitz point which is the meeting point of the three phase boundaries $SmA \rightarrow SmC^*$, $SmA \rightarrow SmC$ and $SmC \rightarrow SmC^*$. The reentrance of SmC* phase can be explained by

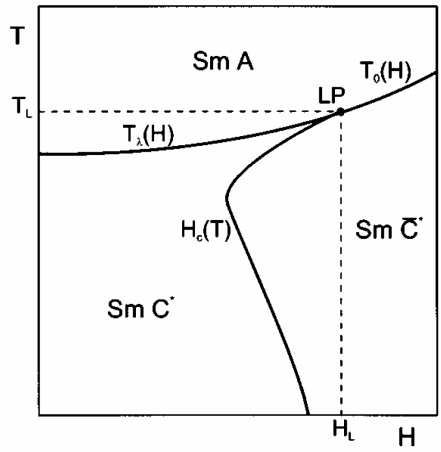

Figure 5.1: Theoretically predicted (H, T) phase diagram of a ferroelectric liquid crystal. The external field is applied perpendicular to the helix. LP is the Lifshitz point(H_L,T_L) [1].

Landau theory [2]. The (H, T) phase diagram and the temperature dependent $H_c(T)$ of a ferroelectric liquid crystal predicted by theory are shown in Fig. 5.1. At a certain critical field H_c, the helical structure at a fixed temperature will be completely unwound, and the sample becomes a spatially homogenous Sm$\bar{C}$* (or SmC) phase. [1]. In this diagram, SmA, SmC^* and unwound Sm$\bar{C}$* phase merge together at the so-called Lifshitz point. This diagram also shows the probability of the appearance of a reentrant SmC* phase below the Sm$\bar{C}$* phase. In this chapter, a sample ZLL7/*-biphe-D2 which has a reentrant SmC* phase was selected to do an angular dependent study by rotating the sample in the magnetic field.

On the other hand, soliton-like distortions of the helical structure have been observed by various experimental techniques when the magnetic field is applied normal to the helical axis. If the magnetic field strength is high enough (either parallel or perpendicular to the pitch axis), the distorted helical structure will be unwound into a homogeneously ordered Sm$\bar{C}$* phase. The effect of magnetic field on the SmC* phase has been extensively studied [1, 3]. A deuterium angular-dependent study has recently been reported on the investigation of soliton-like deformations in a SmC* phase of another chiral LC (S)-[4-(2-methylbutyl)phenyl]-4'-octylbiphenyl carboxylate (8BEF5) [4]. The critical field for unwinding the helical structure has also been determined far away from the triple (Lifshitz) point [5] in the (H, T) phase diagram. In 8BEF5, the angular variation in the sample rotation experiments at each temperature is, however, limited to small angles ($< 25°$). The general Landau theory [1, 6] can only be tested within this small range of angles. In the present study, BP8Cl has been chosen even though its SmC* phase at 9.4T has a rather narrow temperature range, because one can do an angular dependent study over a wide range of sample rotation angles in the NMR magnetic field. This enables us to critically test the Landau theory.

5.2 Theory

5.2.1 Chiral Smectic C* Phase

Here, we consider a case where the liquid crystal ($\Delta\chi > 0$) sample is magneto-aligned by the NMR magnetic field H initially, and is then rotated by θ with respect to H (see Fig. 5.2). In the aligned SmC^* phase, the pitch axis is aligned along the external magnetic field. Using the following coordinate transformation

$$\text{Director frame } (\hat{n}) \overset{(\alpha,\beta,0)}{\Longrightarrow} \text{Lab frame } (X_L, Y_L, Z_L)$$

where α, β are the polar angles of the applied H field in the director frame, $< R_{2,0} >$ in the laboratory frame can be expressed as:

$$< R_{2,0} >= \sum_m \left\langle D^2_{m,0}(\alpha,\beta,0)\right\rangle \left\langle R^D_{2,n}\right\rangle \tag{5.1}$$

where the superscript D denotes the director frame. From Eq. (3.3) the ^{2}H spin(s) can produce a spectrum of two lines with spectral frequencies given in the director frame [7] by

$$\nu^{\pm} = \pm\frac{3}{4}\bar{\nu}_Q(\frac{3}{2}\cos^2\beta - \frac{1}{2} + \frac{\bar{\eta}}{2}\sin^2\beta\cos 2\alpha) \tag{5.2}$$

where $\bar{\nu}_Q = eQ\bar{V}_{zz}/h$ is a time-averaged nuclear quadrupolar coupling constant along the long molecule (Z_M) axis, and $\bar{\eta} = (\bar{V}_{xx} - \bar{V}_{yy})/\bar{V}_{zz}$ is a time-averaged asymmetry parameter, with $\bar{V}_{zz} = \sqrt{\frac{2}{3}} < R^D_{2,0} >$ and $(\bar{V}_{xx} - \bar{V}_{yy}) =< R^D_{2,2} > + < R^D_{2,-2} >$. As the NMR field is fixed, the aligned sample is rotated in a goniometer probe in order to do the angular dependent study. When the pitch axis is set at a non-zero θ angle, the following relations can be obtained from the geometry in Fig. 5.2

$$\cos\beta = \quad \cos\theta\cos\theta_0 + \sin\theta\sin\theta_0\cos\phi \tag{5.3}$$

$$\cos\theta = \quad \cos\beta\cos\theta_0 + \sin\beta\sin\theta_0\cos\alpha \tag{5.4}$$

where θ is the sample rotation angle, θ_0 is the molecular tilt angle and ϕ is the molecular azimuthal angle measured with respect to the plane formed by the layer normal and the H field (i.e. w.r.t. x axis in Fig. 5.2). From Eqs.(5.3) and (5.4), one can get

$$\sin\beta\cos\alpha = \sin\theta_0\cos\theta - \cos\theta_0\sin\theta\cos\phi \tag{5.5}$$

Using Eqs. (5.3)-(5.5), Eq. (5.2) can be rewritten as:

$$\begin{aligned}\nu^{\pm} \quad = \quad & \pm\frac{3}{4}\bar{\nu}_Q[\frac{3+\bar{\eta}}{2}(\sin\theta\sin\theta_0\cos\phi + \cos\theta\cos\theta_0)^2 \\ & +\bar{\eta}(\cos\theta_0\sin\theta\cos\phi - \sin\theta_0\cos\theta)^2 - \frac{1+\bar{\eta}}{2}]\end{aligned} \tag{5.6}$$

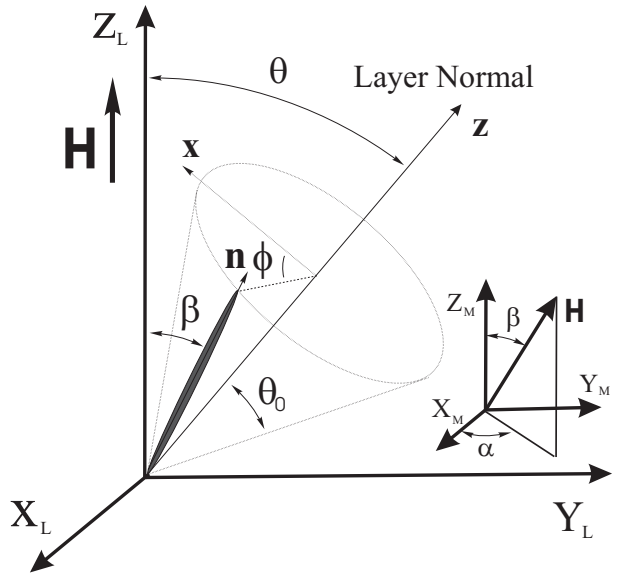

Figure 5.2: The geometry of a sample rotation experiment. **n** is the molecular director. (X_L, Y_L, Z_L) is the laboratory frame, (X_M, Y_M, Z_M) is the molecular frame, whereas the (x, y, z) frame is fixed to the LC smectic layers. $(\alpha,\ \beta,\ 0)$ are the polar angles of the applied H field in the director frame. θ is the rotation angle. ϕ and θ_0 are Euler angles from the (x, y, z) frame to the laboratory frame [4].

.

Furthermore the observed spectrum of the rotated sample is the sum of frequencies from the molecules in the helical structure which are uniformly distributed on the surface of the cone shown in Fig. 5.2 [7]. The spectral distribution is given by

$$I(\nu) = \frac{dN}{d\nu} = \left(\frac{dN}{d\phi}\right)\left(\frac{d\phi}{d\nu}\right) \tag{5.7}$$

where N is the number of molecules, $dN/d\phi$ is the distribution of molecules along the smectic layer normal, and is a constant for a uniform distribution along the pitch axis. Now we consider $d\phi/d\nu$. When $d\nu/d\phi = 0$, the NMR spectrum $I(\nu)$ shows singularities. Since

$$\frac{d\nu}{d\phi} = \frac{3}{4}\bar{\nu}_Q\left[(3+\bar{\eta})\cos\beta\frac{d\cos\beta}{d\phi} + 2\bar{\eta}\sin\beta\cos\alpha\frac{d(\sin\beta\cos\alpha)}{d\phi}\right] \tag{5.8}$$

and

$$\begin{aligned}\frac{d\cos\beta}{d\phi} &= -\sin\theta\sin\theta_0\sin\phi \\ \frac{d(\sin\beta\cos\alpha)}{d\phi} &= \sin\theta\cos\theta_0\sin\phi\end{aligned} \tag{5.9}$$

from Eqs. (5.3)-(5.5), then

$$\frac{d\nu}{d\phi} = \frac{3}{4}\bar{\nu}_Q\sin\theta\sin\phi\cdot\Theta \tag{5.10}$$

where

$$\Theta = (\bar{\eta} - 3)(\sin\theta_0 \cos\theta_0 \cos\theta) + (\bar{\eta} - 3)\sin\theta \sin^2\theta_0 \cos\phi - 2\bar{\eta}\sin\theta\cos\phi \tag{5.11}$$

Hence $\frac{d\nu}{d\phi} = 0$ when $\phi = 0$ or π, and two singularities (s_1, s_2) are produced by setting $\cos\phi = \pm 1$ in Eq. (5.6):

$$s_1^{\pm} = \pm\frac{3}{4}\bar{\nu}_Q[1 - \frac{1}{2}(3 - \bar{\eta})\sin^2(\theta - \theta_0)] \tag{5.12}$$

$$s_2^{\pm} = \pm\frac{3}{4}\bar{\nu}_Q[1 - \frac{1}{2}(3 - \bar{\eta})\sin^2(\theta + \theta_0)] \tag{5.13}$$

and there is another singularity when $\Theta = 0$, that is

$$\cos\phi = \frac{(\bar{\eta} - 3)\sin\theta_0\cos\theta_0\cos\theta}{(3 - \bar{\eta})\sin\theta\sin^2\theta_0 + 2\bar{\eta}\sin\theta} = \frac{(3 - \bar{\eta})\sin 2\theta_0}{(3 - \bar{\eta})2\sin^2\theta_0 + 4\bar{\eta}} \cdot \frac{1}{\tan\theta} \tag{5.14}$$

By substituting the above $\cos\phi$ in Eq. (5.6), the third singularity can be obtained

$$s_3^{\pm} = \pm\frac{3}{4}\bar{\nu}_Q[\frac{(3 + \bar{\eta})\bar{\eta}\cos^2\theta}{(3 - \bar{\eta})\sin^2\theta_0 + 2\bar{\eta}} - \frac{1}{2}(1 + \bar{\eta})] \tag{5.15}$$

Since $|\cos\phi| \leq 1$ in Eq. (5.14), to get this singularity θ needs to satisfy $\frac{\pi}{2} \geq \theta \geq \tan^{-1}[(3 - \bar{\eta})\sin 2\theta_0/((3 - \bar{\eta})2\sin^2\theta_0 + 4\bar{\eta})]$. Now $\bar{\eta}$, $\bar{\nu}_Q$ and θ_0 can be determined by fitting the angular dependent positions of the singularities as a function of sample rotation angle [7, 8]. Here a minimization routine can be used to fit the experimentally observed singularities by minimizing the sum-squared error f:

$$f = \sum_i \sum_{n=1}^{3} [s_n^{expt}(\theta_0) - s_n^{calc}(\theta_0)]_i^2 \tag{5.16}$$

where i is the number of different θ and the superscripts *expt* and *calc* denote experimental and calculated, respectively. The best fit allows the determination of $\bar{\nu}_Q$ and tilt angle θ_0. The experimental spectra in the SmC^* phase and its reentrant variety can be simulated by Fourier transforming the FID calculated using the following integral and Eqs. (5.6) [5]:

$$F(\theta_0, t) \propto \int_0^{2\pi} \cos(2\pi\nu(\phi, \theta)t)e^{-\sigma^2 t^2/2}d\phi \tag{5.17}$$

where $e^{-\sigma^2 t^2/2}$ is to account for the spectral line broadening with a fitting parameter σ, i.e. the absorption spectrum is:

$$S(\theta_0, \omega) = \int_0^{\infty} F(\theta_0, t)e^{-i\omega t}dt \tag{5.18}$$

By lineshape simulation, one can also determine the $\bar{\nu}_Q$ and tilt angle θ_0 to complement the fitting of the singularities.

5.2.2 Soliton-like Deformation in Chiral SmC* Phase

At a sufficiently high magnetic field, the helix can show soliton-like distortions. The helix is usually more easily distorted by applying the magnetic field normal to the pitch axis. As the NMR field is fixed, the aligned sample is rotated by an angle θ in a goniometer probe in order to have a non-zero field component in the direction perpendicular to the pitch axis. At temperatures far away from the Lifshitz point, the distortion can be treated by a general Landau theory under the constant amplitude approximation [5]. In chiral smectic C* phases, the orientation of molecules is dependent on the tilt angle θ_0 and azimuthal angle ϕ (Fig. 5.2). If the layer normal is defined as the z axis, and the xy-plane is in the smectic layer plane, the orientation of the molecule can be described by $\vec{n} = (n_x, n_y, n_z) = (\sin\theta_0 \cos\phi, \sin\theta_0 \sin\phi, \cos\theta_0)$.

The basic features of the (H,T) phase diagram of a ferroelectric liquid crystal in an external magnetic field can be derived from a simple Landau free energy expansion [9–11]

$$\begin{aligned} g(z) &= g_A + \frac{1}{2}a(T)(n_x^2 + n_y^2) + \frac{1}{4}b(n_x^2 + n_y^2)^2 - \\ &\quad \Lambda(n_x\frac{\partial n_y}{\partial z} + n_y\frac{\partial n_x}{\partial z}) + \frac{K_{33}}{2}[(\frac{\partial n_y}{\partial z})^2 + (\frac{\partial n_x}{\partial z})^2] - \frac{1}{2}\mu_0\Delta\chi(\vec{H}\cdot\vec{n})^2 \end{aligned} \tag{5.19}$$

Here g_A is the equilibrium free energy of the SmA phase, μ_0 is the permeability of free space, and $\Delta\chi = \chi_\parallel - \chi_\perp$, the diamagnetic anisotropy of the molecules, is assumed to be positive. $a(T)$ is used to explain the temperature variation in the tilt angle and is linearly temperature-dependent, while b, Λ and K_{33} are temperature independent. Λ is the coefficient of the Lifshitz terms (or Lifshitz invariant), which give the helicoidal modulation. K_{33} is the bend elastic constant. In tilted smectic phases, the molecular tilt angle θ_0 is not changed significantly by the external field, while the azimuthal angle ϕ varies with the field following a profile $\phi(z)$. This is called the constant amplitude approximation (CAA). Under the CAA approximation, only the terms depending on the ϕ angle in the free energy density of SmC^* phase are of interest. At any angle θ with respect to magnetic field, Eq. (5.19) can be rewritten as [1, 5, 12]

$$\begin{aligned} g(z) &= -\sin^2\theta_0\Lambda\frac{d\phi}{dz} + \sin^2\theta_0\frac{1}{2}K_{33}(\frac{d\phi}{dz})^2 \\ &\quad -\frac{1}{2}\mu_0\Delta\chi H^2(\frac{1}{2}\sin^2\theta\sin^2\theta_0\cos 2\phi + \frac{1}{2}\sin 2\theta\sin 2\theta_0\cos\phi) \end{aligned} \tag{5.20}$$

Using the Euler-Lagrange minimization method to minimize $g(z)$ with respect to ϕ and $\partial\phi/\partial z$, that is

$$\frac{\partial g(z)}{\partial\phi} - \frac{d}{dz}\left[\frac{\partial g(z)}{\partial(d\phi/dz)}\right] = 0, \tag{5.21}$$

the following well-known Sine-Gordon equation for ϕ is derived,

$$2\xi'^2\frac{d^2\phi}{dz^2}+\frac{d}{d\phi}(\cos 2\phi+4A\cos\phi)=0 \tag{5.22}$$

where $A=\cot\theta\cot\theta_0$, $\xi'=\xi\frac{\sqrt{2}}{\sin\theta}$, and $\xi=\sqrt{\frac{K_{33}}{\mu_0|\Delta\chi|H^2}}$ is the magnetic coherence length. Then, integrating over $d\phi$ gives

$$\xi'^2(\frac{d\phi}{dz})^2+\cos 2\phi+4A\cos\phi=\frac{1+4A}{\kappa^2} \tag{5.23}$$

where $0\leq\kappa\leq 1$ is a constant of integration that defines the helical distortion. Now the ϕ distribution for the tilt direction can be obtained as

$$\frac{d\phi}{dz}=\frac{1}{\xi'\kappa}\sqrt{1+4A-\kappa^2(\cos 2\phi+4A\cos\phi)} \tag{5.24}$$

When $\kappa=1$, the helix is completely unwound, while there is no distortion when $\kappa=0$. By integrating Eq. (5.24), the pitch length of the soliton-like deformed helix can be obtained

$$P=\xi'\kappa\int_0^{2\pi}\frac{d\phi}{\sqrt{(1+4A)-\kappa^2(\cos 2\phi+4A\cos\phi)}}=\xi' kE_1(\kappa) \tag{5.25}$$

$E_1(\kappa)=\int_0^{2\pi}\frac{d\phi}{\sqrt{(1+4A)-\kappa^2(\cos 2\phi+4A\cos\phi)}}$ is defined to simplify the above equation. To relate the κ value to the external magnetic field H, we need to minimize the free energy of this system by substituting $\frac{d\phi}{dz}$ in Eq. (5.24) into Eq. (5.20) [13] and the average free energy per unit volume (G) is:

$$\begin{aligned}
G &= \frac{1}{P}\int_0^P g(z)dz \\
&= -\frac{\sin^2\theta_0 K_{33}}{2P}\int_0^P\left[\frac{4\pi}{P_0}\frac{d\phi}{dz}-(\frac{d\phi}{dz})^2+\frac{1}{\xi'^2}(\cos 2\phi+4A\cos\phi)\right]dz \\
&= -\frac{\sin^2\theta_0 K_{33}}{2P}\left[\int_0^{2\pi}(\frac{4\pi}{P_0}-\frac{d\phi}{dz})d\phi+\int_0^{2\pi}\frac{1}{\xi'^2}(\cos 2\phi+4A\cos\phi)\frac{dz}{d\phi}d\phi\right]
\end{aligned} \tag{5.26}$$

where $P_0=\frac{2\pi K_{33}}{\Lambda}$ is a constant and represents the ground state pitch length. After integrating the two terms in the square brackets, the above equation gives:

$$G=-\frac{\sin^2\theta_0 K_{33}}{2}\left\{\frac{8\pi^2}{P_0\xi'\kappa E_1(\kappa)}+\frac{1}{\xi'^2\kappa^2}\left[(1+4A)-2\frac{E_2(\kappa)}{E_1(\kappa)}\right]\right\} \tag{5.27}$$

where $E_2(\kappa)=\int_0^{2\pi}\sqrt{(1+4A)-\kappa^2(\cos 2\phi+4A\cos\phi)}d\phi$. Since we know the relation

$$\frac{d}{d\kappa}\left[\frac{E_2(\kappa)}{\kappa}\right]=-\frac{(1+4A)E_1(\kappa)}{\kappa^2}, \tag{5.28}$$

Eqs. (5.27) and (5.28) allow the derivative of $G(\kappa)$ with respect to κ to be expressed as

$$\frac{dG}{d\kappa}=-\frac{\sin^2\theta_0 K_{33}}{2P}\left[\frac{8\pi^2}{P_0\xi'}-\frac{2}{\xi'^2}\frac{E_2(\kappa)}{\kappa}\right]\frac{d}{d\kappa}\left(\frac{1}{\kappa E_1(\kappa)}\right) \tag{5.29}$$

The free energy is minimum when $dG/d\kappa = 0$, leading to

$$\frac{E_2(\kappa)}{\kappa} = \frac{4\pi^2\xi'}{P_0} = \frac{4\sqrt{2}H_c^0}{\sin\theta H} \tag{5.30}$$

where $H_c^0 = \frac{\pi\Lambda}{2K_{33}}\sqrt{\frac{K_{33}}{\mu_0|\Delta\chi|}}$ is the critical magnetic field to unwind the chiral smectic helix when the magnetic field is perpendicular to the helical axis. To be consistent with the literature [5], one can also define $e(\kappa) = \frac{E_2(\kappa)}{2\sqrt{A}}$ such that Eq. (5.30) can be written as

$$\frac{e(\kappa)}{\kappa} = \sqrt{\frac{\tan\theta_0}{\sin 2\theta}}\frac{4H_c^0}{H} \tag{5.31}$$

Since $e(1) = 2\sqrt{2}\sqrt{\tan\theta\tan\theta_0}[\sqrt{1+A} + Aln\frac{1+\sqrt{1+A}}{\sqrt{A}}]$, the critical field H_c can be obtained [5]

$$\frac{H_c^0}{H_c} = \sin\theta[\sqrt{1+A} + Aln\frac{1+\sqrt{1+A}}{\sqrt{A}}] \tag{5.32}$$

From the above equation, we know that the critical magnetic field H_c to unwind the SmC^* helix depends on the magnetic field direction with respect to the helix axis. According to this theory, the critical field (H_c^0) for unwinding the helical structure in the SmC^* phase can be obtained by fitting the observed (distorted) spectra to the ones calculated from the Fourier transform of the FID given by the following integral [4, 5, 8]:

$$F(\theta_0, t) = F(\theta_0, 0)\int_0^{2\pi}\frac{dz}{d\phi}\int\Gamma(\theta_0' - \theta_0)\cos(2\pi\nu(\phi,\theta,\theta_0')t)d\theta_0' e^{-\sigma^2t^2/2}d\phi \tag{5.33}$$

where $\nu(\phi,\theta,\theta_0)$ is obtained from Eq. (5.6), $e^{-\sigma^2t^2/2}$ is to account for the spectral line broadening by a fitting parameter σ and a Gaussian distribution is assumed [14] here for the distribution of the local director, i.e.

$$\Gamma(\theta_0' - \theta_0) = \frac{1}{\omega\sqrt{2\pi}}e^{-(\theta_0'-\theta_0)^2/2\omega^2} \tag{5.34}$$

with $2\sqrt{2\ln 2}\cdot\omega$ being the full width at half maximum (FWHM) of the distribution. If a uniform ϕ distribution in the helix is distorted by the NMR magnetic field, a new ϕ distribution ($dz/d\phi$) is required [4, 5]. Now κ in Eq. (5.24) is treated as a fitting parameter, and is related to the critical field H_c^0, the magnetic field H and the rotation angle by Eq. (5.31) [4]. In the SmC^* phase, the orientational order parameter is high, thereby leading to a small ω value. Under this condition, $F(\theta_0, t)$ can be rewritten as [4]

$$F(\theta_0, t) = F(\theta_0, 0)\int_0^{2\pi}\frac{dz}{d\phi}cos(2\pi\nu(\phi,\theta,\theta_0)t)e^{-\sigma^2t^2/2-(2\pi\omega\frac{\partial\nu}{\partial\theta_0})^2t^2}d\phi \tag{5.35}$$

The observed lineshape is simulated by Fourier transforming Eq. (5.35) numerically. By comparing the simulated 1D spectra with the corresponding experimental spectra, $\kappa(\theta)$ can be obtained. The critical field for unwinding the helix at a certain temperature can be obtained using Eq. (5.31).

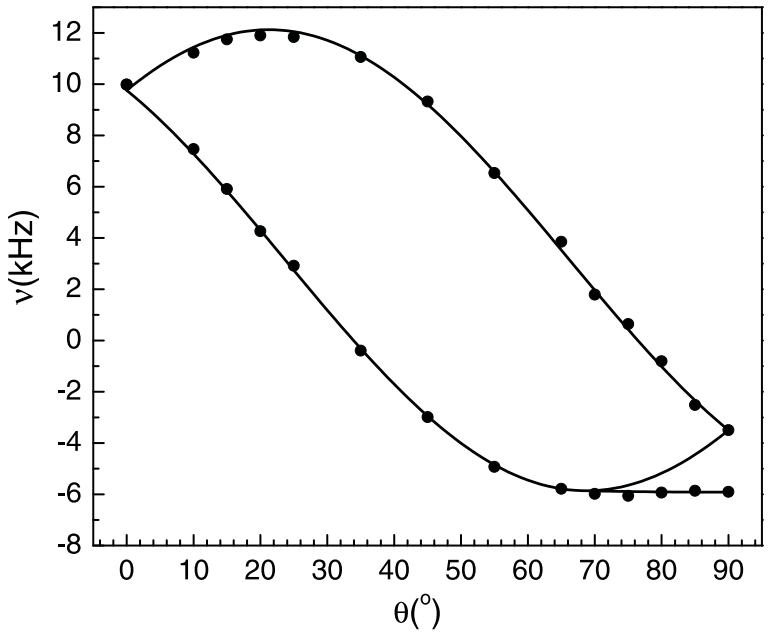

Figure 5.3: Plot of the angular-dependent positions of the characteristic singularities in ZLL7/*-biphe-D2 at 66°C(•). The solid lines are fitted curves.

.

5.3 Chiral SmC* phase of ZLL7/*

The molecular structure of ZLL7/*-biphe-D2 and its transition temperatures have been given in section 1.7. The quadrupolar splittings of ZLL7/*-biphe-D2 have already been reported by Catalano as a function of temperature [15] at two magnetic field strengths. Partially unwound smectic C* phase has been observed at 9.4T. For this sample, we have tried to study the structure and dynamics in different SmC phases by means of angular dependent studies. Unfortunately at high temperatures, the sample was found to reorient once it was rotated to a high rotation angle making such studies impossible. However, by cooling down the temperature to SmC^*_{re} phase at T=66°C, the sample was stable enough to carry out angular dependent experiments by successively increasing the rotation angle θ to 90 degrees. The angular-dependent characteristic singularities are plotted in Fig. 5.3 for this temperature. The solid lines are fitted curves using Eqs.(5.12),(5.13) and (5.15) to give $\bar{\nu}_Q = 16.1kHz$, $\theta_0 = 21.3°$, and $\bar{\eta} = 0$. The last quantity signifies that the present SmC^*_{re} phase is not biaxial as seen in most chiral SmC* phase [8]. Since the ZLL7/* was deuterated in the aromatic part, the observed $\bar{\nu}_Q$ of the C-D bond can be approximated by the following equation to give the local order parameter of the para axes in the biphenyl fragment as long as the biphenyl part defines the most ordered axis of the molecule. Analogous to Eqs.(4.3-4.6), one has

$$\bar{\nu}_Q = \left(\frac{e^2qQ}{h}\right)^{ar} P_2[\cos(60°)]S^{bi}_{zz} \tag{5.36}$$

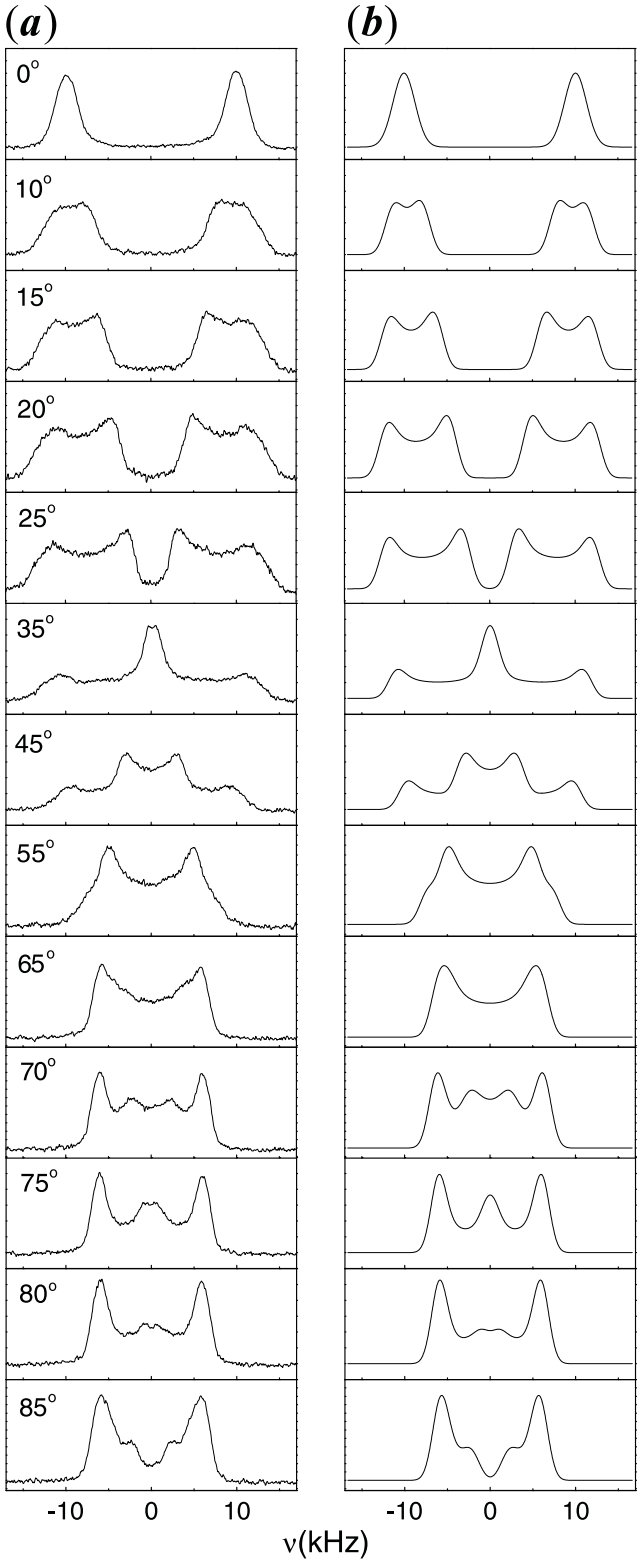

Figure 5.4: Experiment(a) and simulation(b) spectra for ZLL7/*-biphe-D2 at 66°C.

.

where 60° is the nominal angle between the C-D bond, the z axis is along the biphenyl para axes and the quadrupolar coupling constant $\left(\frac{e^2qQ}{h}\right)^{ar} = 185kHz$ is used. In this equation, the fast rotational motion of the molecule and the ring flips in the biphenyl have already been considered. Using Eq. (5.36), the local order parameter for the biphenyl part can be derived as $S_{zz}^{bi} = 0.69$, which is consistent with the result reported in the literature [15]. It would appear that the long molecular axis lies along the para axes of the biphenyl. The tilt angle determined here is, however, smaller than the value of ca. 25° obtained optically at 66°C [15].

When fitting the angular dependent ^{2}H NMR line shapes, we have adopted the tilt angle $\theta_0 = 21.3 \pm 0.2°$ and a motional-averaged coupling constant $\bar{\nu}_Q = 16.1 \pm 0.5kHz$ found above. The line broadening parameter σ is changed to reflect the line widths at various θ. A value of σ=$5 \pm 0.5kHz$ was found and the corresponding calculated deuteron spectra are shown in Fig. 5.4. As seen in this figure, the simulations can faithfully reproduce the experimental results in support of the derived parameters found by fitting the edge singularities. It is noted that there is no helical distortion detected at 66°C in ZLL7/*, i.e. $\kappa = 0$.

5.4 SmC* phase of BP8Cl

The molecular structure of BP8Cl with the deuteron sites labeled down the chain and its transition temperatures have been shown in Fig. 1.11. Here, we focus on the methyl deuterons at the last carbon site C_8 whose deuteron spin-lattice relaxation times are the largest. Typical deuterium 1D spectra of the aligned sample in different phases are plotted in Fig. 5.5. The observed deuterium splittings are plotted versus the temperature in Fig. 5.6. As seen in this diagram, only the quadrupolar splitting of C_7 and C_8 can be discerned in the SmC* phase due to the severe line broadening. Furthermore, the transition between the Sm$\bar{C}$* and SmC* phase in BP8Cl involves a biphasic region (about 4 degrees) clearly seen from the C_8 signals.

Fig. 5.7(a) shows a typical set of angle-dependent spectral patterns observed at 311.5K . Our experiments show that at this temperature there is no observable field-induced sample reorientation and layer destruction. This was checked experimentally by reproducing the measurement after waiting for half an hour. It should be noted that the present sample behaves quite differently from the smectogen 8BEF5 [4], viz. the C_α deuteron(s) of 8BEF5 shows edge singularities only at small rotation angles ($\theta < 25°$). The angular-dependent characteristic singularities at this temperature are shown in Fig. 5.8. The solid lines in this

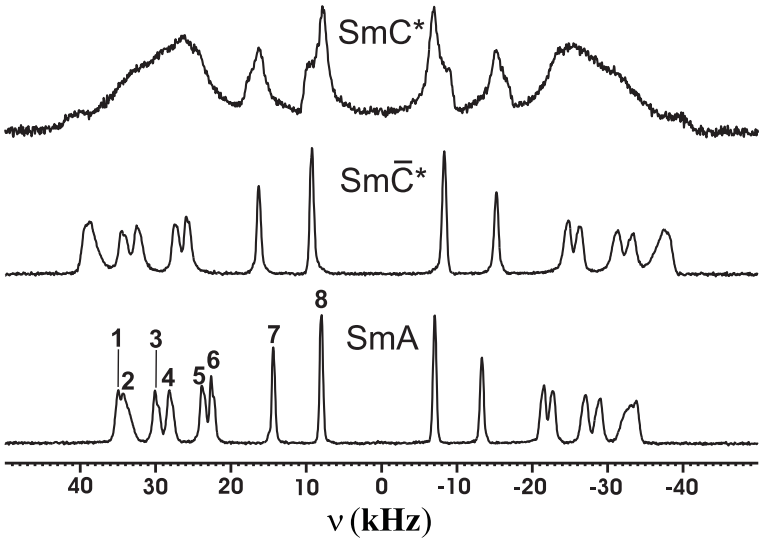

Figure 5.5: Typical ^2H NMR spectra collected in different LC phases of BP8Cl. Peak assignments are labeled in the lower spectrum.

.

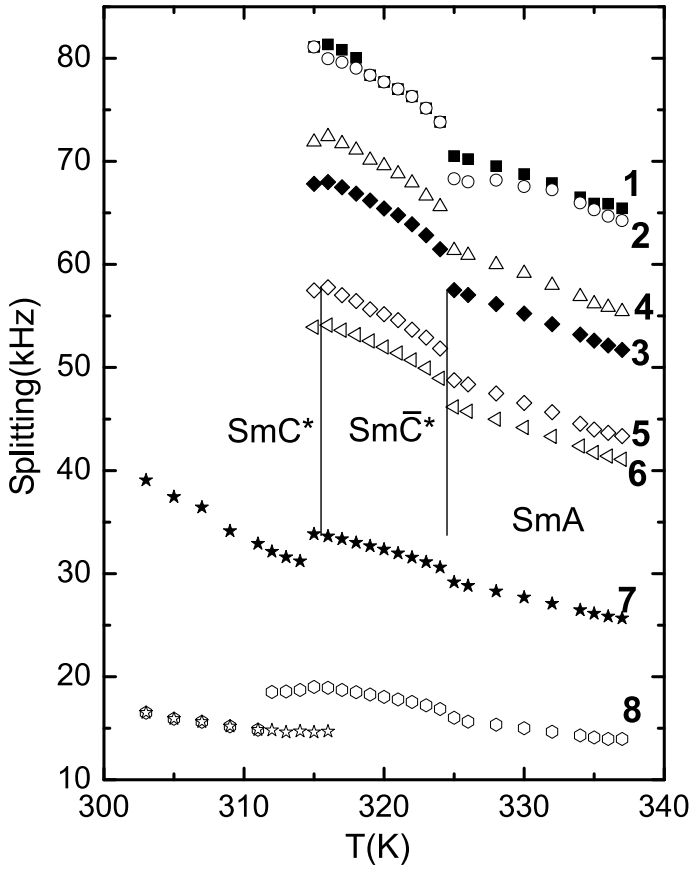

Figure 5.6: Plot of quadrupolar splittings of BP8Cl versus the temperature. Deuteron lines are labeled by their carbon numbers.

.

figure are fitted curves using Eqs.(5.12), (5.13) and (5.15) to give $\bar{\nu}_Q = 10.0$kHz, $\theta_0 = 23.3^0$, and $\bar{\eta} = 0$ at 311.5K. The last quantity again signifies that the present SmC* phase is not biaxial. Note that θ can now be extended to 90°. Hence, BP8Cl could provide a better test of Landau theory. When fitting the angular-dependent ^{2}H NMR line shapes, the tilt angle and time-averaged coupling constant were set at $\theta_0 = 23.3 \pm 0.2^0$ and $\bar{\nu}_Q = 10.0 \pm 0.5$kHz. For a known rotation angle θ, the integration constant κ was varied to give the 'best' simulated line shapes for C_8 deuterons shown in Fig. 5.7(b). The line broadening parameters σ and ω were also fitted to reflect the observed line widths. The fitting parameters for different angles are summarized in Table 5.1. We note that κ was non-zero when the sample was rotated by an angle away from the external magnetic field, which meant that the helical structure had some soliton-like behaviors. Since the spectral line width seemed to change with θ, the line broadening parameter σ was varied between $1.6 - 9$ at different rotation angles. This variation only changes the line width without affecting the spectral features. Thus, κ has been uniquely obtained and is independent of other parameters.

Table 5.1: Fitting parameters in the spectral simulation of BP8Cl for different θ at 311.5K.

θ(deg.)	$\kappa(\pm 0.02)$	σ(kHz)(± 0.3)	ω(deg.)(± 0.2)
0	0	4.5	0
5	0.35	3.5	0.45
10	0.45	5	0.45
15	0.63	5	0.52
20	0.70	4	0.55
25	0.75	5	0.55
30	0.80	5.5	0.35
35	0.82	7	0.7
40	0.85	9	0.75
45	0.86	6	0.75
50	0.84	6.5	0.3
55	0.84	3.5	0.1
60	0.85	2.5	0.2
65	0.84	2	0.65
70	0.80	1.8	1
75	0.70	1.7	1
80	0.70	1.7	0.8
85	0.98	1.6	1.3
90	0.98	1.6	1.3

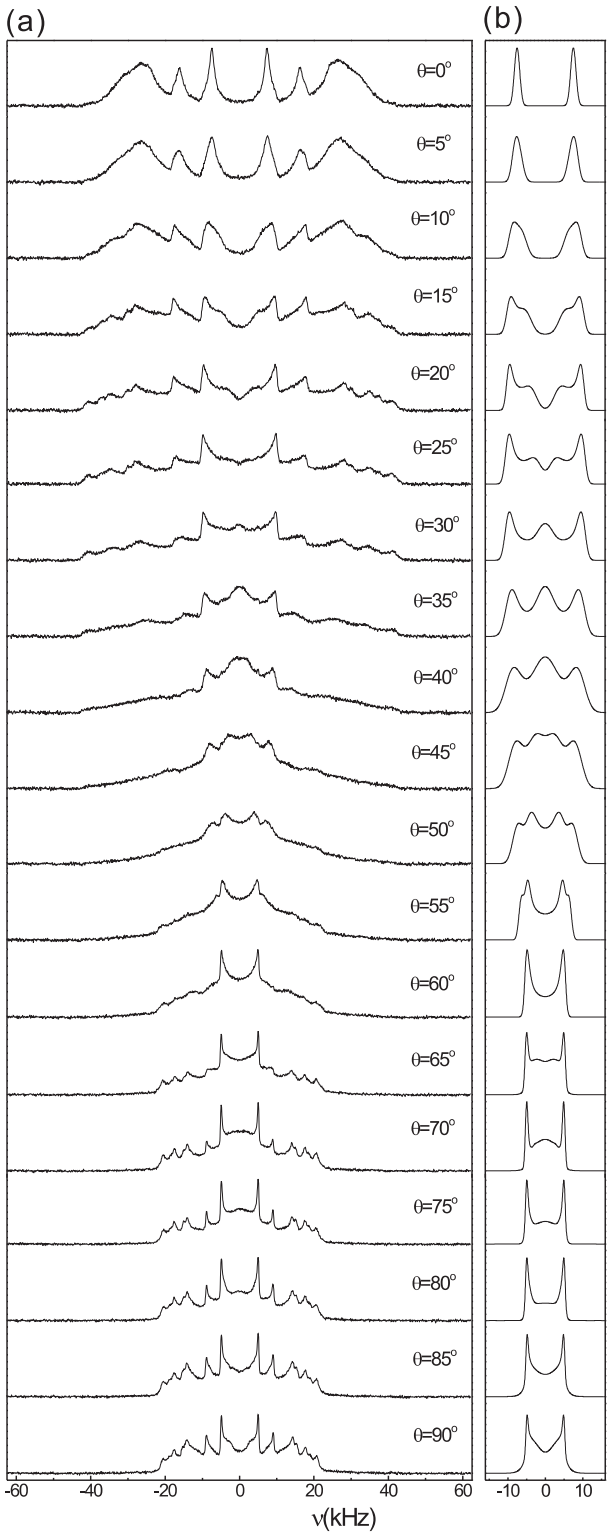

Figure 5.7: (a) Experimental and (b) Simulated angular dependent ^{2}H NMR line shapes in the SmC* phase of BP8Cl at 311.5K.

.

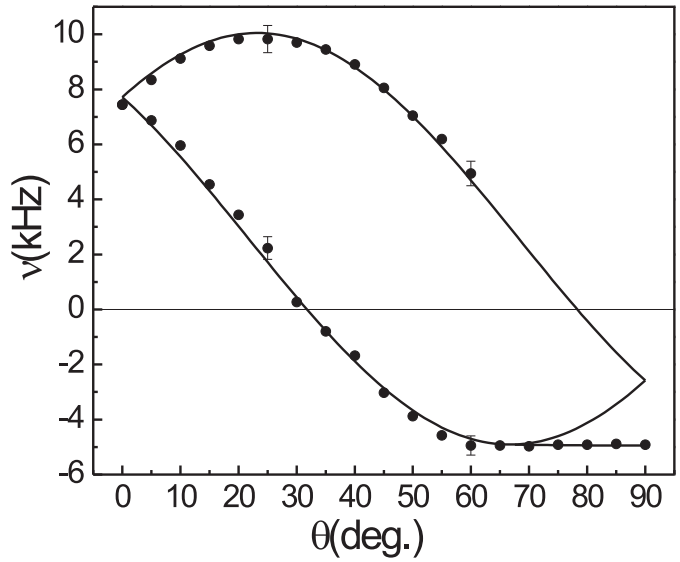

Figure 5.8: Plot of the angular-dependent singularities ($2|s_i|$) in BP8Cl at 311.5K(•). The solid lines are fitted curves.

.

We have also simulated the line shapes at 308.5K to give $\bar{\nu}_Q = 10.4 \pm 0.5$ kHz and $\theta_0 = 25.0 \pm 0.2^0$. The fitting of the angular-dependent singularities at this temperature is shown in Fig. 5.9. Fig. 5.10 shows plots of $\kappa/e(\kappa)$ versus $\sqrt{(\sin 2\theta)}$ for θ between 0° and 90° at these temperatures, and according to Eq. (5.31), their slopes determine the critical field at a particular temperature. From Fig. 5.10, H_c^0 is seen to decrease slightly with increasing temperature in qualitative agreement with the theoretical prediction [3]. The magnitude of H_c^0 for BP8Cl is on the order of 29.9T at low temperature which is about a factor of 3 higher than the NMR field used in this study. At higher temperatures, the critical fields must be lower (∼9T) in order to produce the Sm$\bar{C}$* phase. It would appear that the sample viscosity and flow behaviors must be rather sensitive to temperature. Unfortunately, at the present magnetic field, the SmC* phase only exists in a narrow temperature range, thereby excluding a detailed study of $H_c(T)$ in BP8Cl.

In this work, the angular-dependent spectral technique has been used to study helical distortions over a wide angle range (up to 90^o). In the SmC* phase, the tilt direction changes azimuthally from one layer to another layer to form a helix. By rotating the sample in a goniometer probe, the ^{2}H NMR spectra reflect the change in the orientational distribution with respect to the H field and/or partial 'unwinding'of the helix. Spectral line shape simulation has also been used to give the tilt angles at different temperatures. Moreover, the distorted

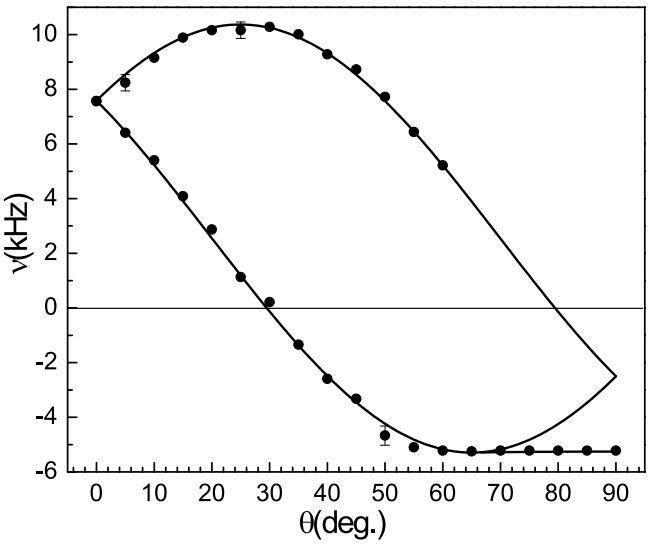

Figure 5.9: Plot of the angular-dependent singularities ($2|s_i|$) in BP8Cl at 308.5K(•). The solid lines are fitted curves.

.

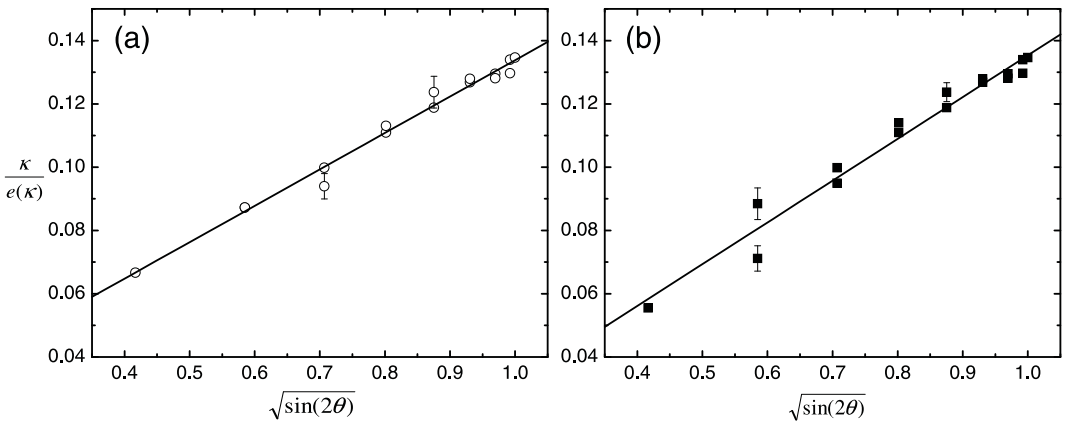

Figure 5.10: Plot of $\kappa/e(\kappa)$ versus $\sqrt{(\sin 2\theta)}$ for (a) 308.5K(circle) and (b) 311.5K(square). The solid lines are fitted lines according to Eq. (5.31). The H_c^0 is found to be 30±2T and 27±5T at 308.5K and 311.5K, respectively.

.

azimuthal distribution based on Landau theory is successfully used in the simulation to get the critical field for BP8Cl. The study of the dynamics on this sample using 2D ^{2}H NMR method will be addressed in the next chapter.

References

[1] Musevic, I.; Zeks, B.; Blinc, R.; Rasing, T.; Wyder, P. *Phys. Rev. Lett.* **1982**, *48*, 192.

[2] Benguigui, L.; Jacobs, A. E. *Ferroelectrics* **1988**, *84*, 379.

[3] Kutnjak-Urbanc, B.; Zeks, B. *Phys. Rev. E* **1993**, *48*, 455.

[4] Xu, J.; Veracini, C. A.; Dong, R. Y. *Chem. Phys. Lett.* **2005**, *416*, 47.

[5] Zalar, B.; Gregorovic, A.; Simsic, M.; Zidansek, A.; Blinc, R. *Phys. Rev. Lett.* **1998**, *80*, 4458.

[6] Landau, L. D.; Lifshitz, E. M. *Am. J. Phys.* **1959**, *27*, 371.

[7] Wu, B. G.; Doane, J. W. *J. Magn. Reson.* **1987**, *75*, 39.

[8] Xu, J.; Veracini, C. A.; Dong, R. Y. *Phys. Rev. E* **2005**, *72*, 051703.

[9] Michelson, A. *Phys. Rev. B* **1977**, *16*, 577.

[10] Goodby, J. W.; Blinc, R.; Clark, N. A.; Lagerwal, S. T.; Osipov, M. A.; Pikin, S. A.; Sakurai, T.; Yoshino, K.; B.Žekš *Ferroelectric Liquid Crystals: Principles, Properties and Applications*; Gordon and Breach Science Publishers, 1991.

[11] Blinc, R.; Žekš, B. *Phy. Rev. A* **1978**, *18*, 740.

[12] Skarabot, M.; Blinc, R.; Musevic, I.; Rastegar, A.; Rasing, T. *Phys. Rev. E* **2000**, *61*, 3961.

[13] Collings, P. J.; Hird, M. *Introduction to Liquid Crystals*; Taylor & Francis, 1997.

[14] Firouzi, A.; Schaefer, D. J.; Tolbert, S. H.; Stucky, G. D.; Chmelka, B. F. *J. Am. Chem. Soc.* **1997**, *119*, 9466.

[15] Catalano, D.; Domenici, V.; Marini, A.; Veracini, C. A.; Bubnov, A.; Glogarova, M. *J. Phys. Chem. B* **2006**, *110*, 16459.

Chapter 6

Molecular Dynamics Study by 2D ^{2}H Exchange NMR Experiment

6.1 Introduction

NMR is a technique which is well suited to study dynamic processes, such as the rates of chemical reactions. The time window investigated in NMR is in the range of nanoseconds to seconds. In particular, studies of molecular order and dynamics are of major interest for the characterization of LC phases. NMR techniques provide a powerful tool for such studies [1]. A very useful method to study the molecular dynamics is to use NMR exchange spectroscopy and lineshape analysis. In general chemical exchange involves a nucleus moving from one environment to another. It is a form of chemical kinetics, governed by forward and reverse rate constants, and the associated equilibrium constant. The original lineshape theory of the exchange was derived by coupling Bloch equations corresponding to two different chemical sites. This gave an equation for the NMR signal strength as a function of frequency, thereby tracing out the lineshape [2]. To demonstrate the exchange effect on the lineshape, a simple example is used to describe how one can use NMR to study the exchange processes between two sites A and B with an exchange rate k:

$$A \underset{k}{\overset{k}{\rightleftharpoons}} B \tag{6.1}$$

which usually happens in internal rotations about a bond, ring puckering, proton exchange, or bond rearrangements. To describe chemical exchange, one can use Bloch-McConnell equa-

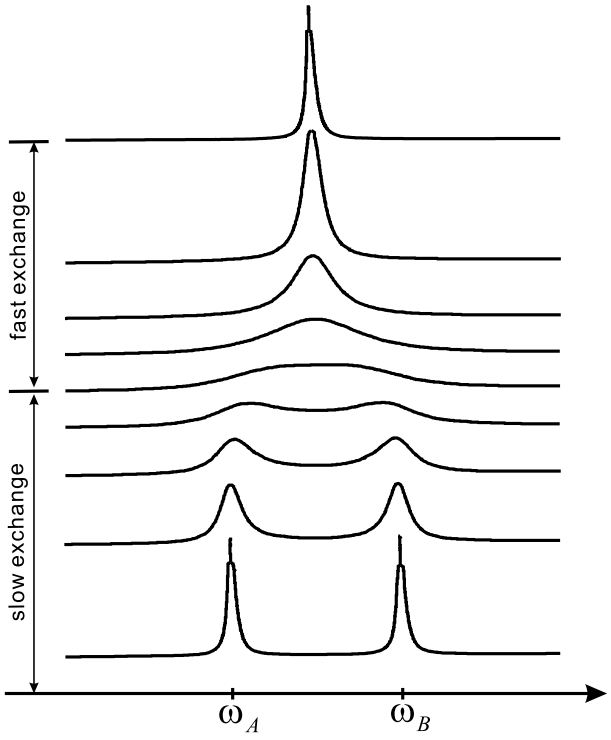

Figure 6.1: The illustrative lineshapes of two sites exchange by varying the rate constant k. The slow exchange corresponds to $k < k_c$ and fast exchange corresponds to $k > k_c$.

.

tions [3–5], and the above kinetics can be described by:

$$\begin{aligned}\frac{d}{dt}M_A(t) &= -(i\omega_A + k + \frac{1}{T_2})M_A(t) + kM_B(t)\\ \frac{d}{dt}M_B(t) &= -(i\omega_B + k + \frac{1}{T_2})M_B(t) + kM_A(t)\end{aligned} \tag{6.2}$$

where the spin-lattice relaxation process has been neglected. Now the NMR signal in the time domain can be obtained by solving Eq. (6.2). After Fourier transformation, the real part of the frequency domain signal can be expressed as [2]:

$$Re[S(\omega)] \propto \frac{k(\omega_A - \omega_B)^2}{2\left[(\omega-\omega_A)^2(\omega-\omega_B)^2 + 4k^2(\omega - \frac{\omega_A+\omega_B}{2})^2\right]} \tag{6.3}$$

Therefore with increasing rate constants, the lineshape varies: in the slow exchange limit, we have two lines; as the rate constant increases the lines broaden and merge into one broad line until we reach the coalescence rate $k_c = \frac{\pi|\omega_A-\omega_B|}{\sqrt{2}}$; past the k_c in the fast exchange limit, we have one line whose linewidth is inversely proportional to the rate of exchange (See figure 6.1).

The NMR exchange experiment was proposed to study the molecular dynamics [6] based on the lineshape observation. Its basic principle is to measure the NMR frequency of the

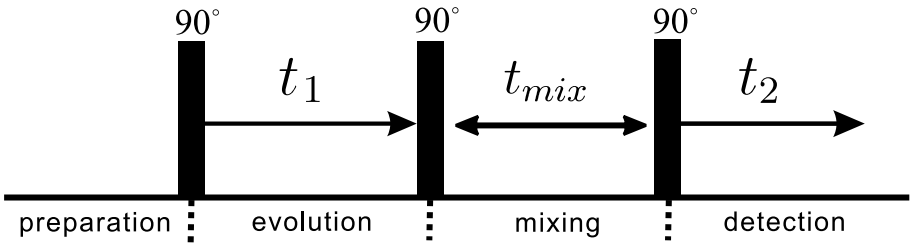

Figure 6.2: Basic scheme of 2D exchange spectroscopy. Initially, transverse magnetization is prepared by a 90° pulse. In the course of the evolution period, the magnetization vectors acquire precession frequency information and become 'frequency labeled'. The exchange process predominantly takes place during the mixing period while the magnetization is longitudinal. A third 90° pulse rotates the longitudinal magnetization after exchange into the xy plane for detection.

.

same nucleus in a molecular segment at two different times in order to detect slow dynamics through a change in its NMR frequency. In the two-dimensional exchange experiment (Figure 6.2), the various components of the initially created transverse spin magnetization are frequency-labeled by letting them precess at their characteristic resonance frequencies during the 'evolution period' of duration t_1. The exchange process to be investigated takes place predominantly during the following 'mixing time' of fixed length t_{mix}. This period is of central importance in acquiring knowledge about the exchange process in question. Finally, the exchanged magnetization components are measured by letting them precess at their new resonance frequencies and the induced FID is recorded as a function of the time variable t_2. As it is usual in 2D spectroscopy, the experiment has to be repeated for a number of equally spaced values of the evolution time t_1. The result is a data matrix $f(t_1, t_2)$, and double Fourier transformation of $f(t_1, t_2)$ gives the desired 2D spectrum $S(\omega_1, \omega_2)$. The appearance of an off-diagonal peak at frequencies ω_1, ω_2 in this 2D spectrum indicates that an exchange process during the mixing period has transferred magnetization components at the precession frequency ω_1 to the new frequency ω_2. Thus the 2D spectrum can be considered as a qualitative map of the kinetic matrix, which describes the exchange process, and is of particular value for elucidating complex exchange problems. Figure 6.3 displays 2D spectra for the case of two sites A and B, with equal populations initially. Cross peaks at (ω_A, ω_B) and (ω_B, ω_A) indicate that the exchange process has occurred. As they rise, the diagonal peaks lose intensity. The two-dimensional spectral density $S(\omega_1, \omega_2; t_m)$ represents the probability of finding a nucleus with a NMR frequency ω_1, and after a time interval t_m later, with a new NMR frequency ω_2 [8].

In this chapter, the dynamics and structure of both TGBA* phase and SmC* phase are studied by the 2D ^{2}H exchange experiment. This is based on the modulation of quadrupolar

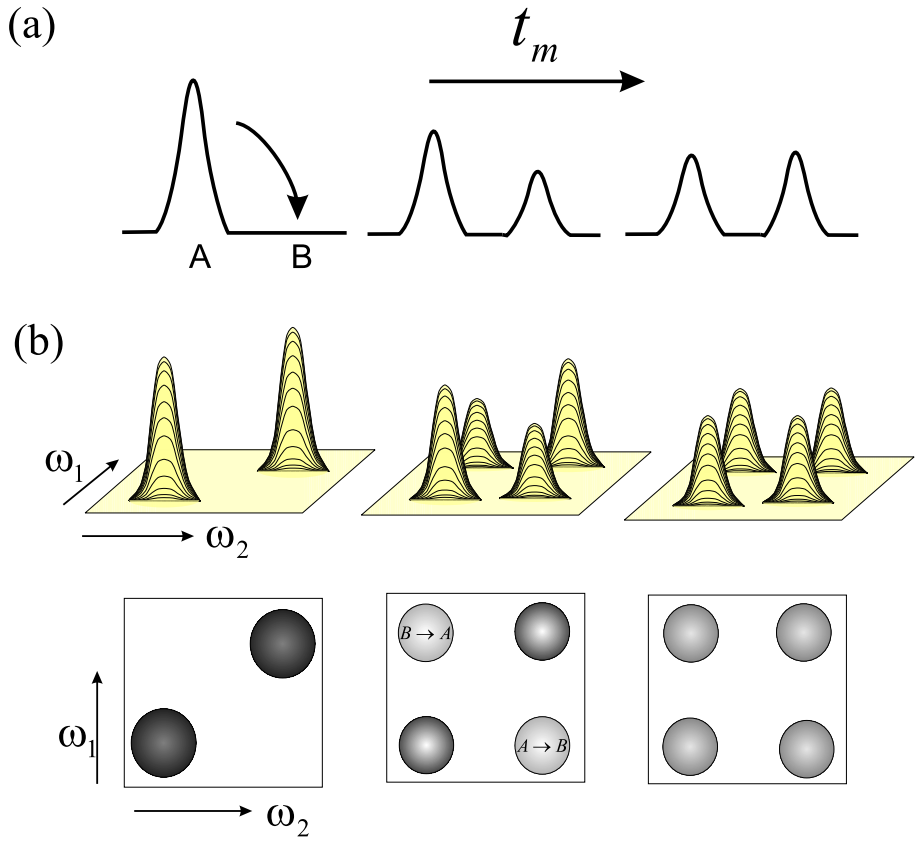

Figure 6.3: Schematic comparison of the detection of slow exchange between two peaks in 1D and 2D exchange experiment. (a) 1D exchange experiment with selective excitation of line A, followed by exchange to line B at longer mixing times t_m. (b) 2D exchange spectra with their corresponding contour plots. [7].

.

interaction(s) due to the self-diffusion of nuclei-bearing molecules in a magnetic field. The self-diffusion (or jump process) and the geometry of SmA blocks in the TGBA* phase of 11EB1M7, as well as the twist angle are investigated through simulating the 2D deuteron exchange spectra. The aligned BP8Cl sample is also studied here in its chiral smectic C phase at a rotation angle $\theta = 15°$ to obtain dynamic parameters through spectral simulation.

6.2 Two-dimensional ^{2}H Exchange Experiment

6.2.1 Pulse Sequence

In general deuteron NMR studies provide site specificity and are therefore very useful to clarify molecular or bond movements. In our study, the ^{2}H NMR exchange five-pulse sequence [9]

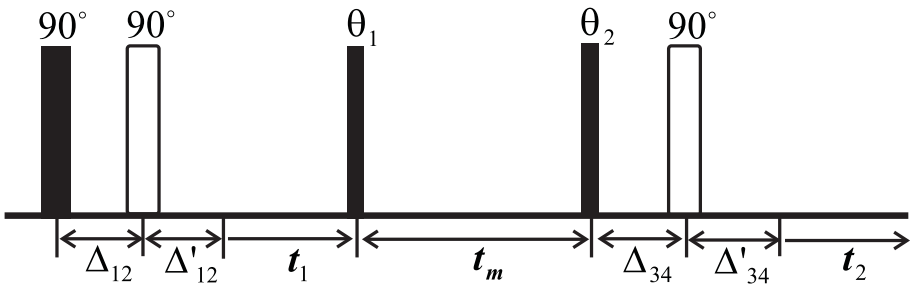

Figure 6.4: Two dimensional ^{2}H NMR exchange pulse sequence. Note that the lengths of the pulse symbols represent the lengths of the pulses used in the actual experiment: the broader symbol indicates 90° pulses, the narrower symbol indicates pulses with a length of 54.7°. Open symbols are used to distinguish the refocusing pulses.

.

shown in Figure 6.4 is used to get the 2D exchange spectrum. In this pulse sequence, there are two echo sequences used in order to alleviate deadtime problems. In the echo sequence $90° - \Delta_{12} - 90° - \Delta'_{12}$, an echo is created a time Δ'_{12} after the second 90° pulse, which allows the signal for $t_1 = 0$ to be measured exactly. Usually $\Delta_{12} = \Delta'_{12}$. The second echo sequence $\theta_2 - \Delta_{34} - 90° - \Delta'_{34}$ is to allow measurement of FID signal from $t_2 = 0$. Δ'_{34} is usually set to a few microseconds less than Δ_{34} to allow acquisition of the refocused signal before $t_2 = 0$. The flip angles $\theta_1 = \theta_2 = 54.7°$ were selected by considering the quadrupolar coupling and pulse effects [7]. For ^{2}H, the two time-domain (cosine and sine) signals are [9]

$$\begin{aligned} f_{cc}(t_1, t_2) &= \cos(\omega_e t_1)\cos(\omega_d t_2) \\ f_{ss}(t_1, t_2) &= \sin(\omega_e t_1)\sin(\omega_d t_2) \end{aligned} \tag{6.4}$$

where the subscripts e and d stand for evolution and detection, respectively. They are necessary to generate pure-absorption mode spectra with quadrature in both dimensions [10]. During the data processing, the 2D spectra are obtained from the cosine and sine time signals, which have to be added up to obtain a spectrum with sign discrimination in the F_1 dimension (see section 2.9).

6.2.2 Simulation

Since the NMR lineshape can reflect the molecular motion, many research groups have tried to get the molecular dynamic information in solid polymers by simulating the lineshapes. Generally, the NMR exchange lineshape is determined by the parameters of each site, and the exchange rate. If the populations of the sites are not equal, then these will be temperature dependent, due to the Boltzmann distribution. Each nuclear site is characterized by its

chemical shift, spin couplings, and a linewidth that is determined by relaxation times. Combining the magnetic field inhomogeneity with the natural linewidth gives an overall linewidth. These parameters will depend on temperature, in general, and may not be independent of each other. The exchange, the natural linewidth and the field inhomogeneity all contribute to the line broadening, and their effects are usually impossible to separate precisely. Spectra obtained well below the coalescence (i.e. slow motion limit) are useful, if they are accessible. Once the parameters for each site are defined, it is then a matter of guessing at a rate, and simulating the NMR spectrum. This calculated spectrum can then be compared to the experimental spectrum, and adjustments are made to the parameters to improve the simulation.

For 2D ^{2}H NMR exchange spectra, a lineshape simulation method involves calculating the free induction decay using the exchange-matrix formalism. The evolution of magnetization during the exchange experiment can still be described by the Bloch-McConnell equation given in (4.10), which is rewritten as [3–5]

$$\frac{d}{dt}\mathbf{M}(t) = -(\mathbf{\Gamma} + \mathbf{\Pi})\mathbf{M}(t) \tag{6.5}$$

where $\mathbf{\Gamma}$ is a diagonal matrix of the frequencies for various sites, and $\mathbf{\Pi}$ is the exchange matrix. Analogous to Eq. (4.15), the 2D exchange time domain signal in the intermediate motional regime is given by [11]

$$f(t_1, t_2) = \vec{\mathbf{1}} \cdot [e^{-(\mathbf{\Gamma}+\mathbf{\Pi})t_2} e^{-\mathbf{\Pi} t_m} e^{-(\mathbf{\Gamma}+\mathbf{\Pi})t_1} \mathbf{M}^0] \tag{6.6}$$

where $\mathbf{M}^0$ defines the initial magnetization, and the T_1 relaxation during t_m has been neglected. When the motional process is continuous, the NMR frequencies at various sites are changing continuously. In this case, Eq. (6.4) is usually used instead in order to simulate the spectrum, and this will be demonstrated in studying the dynamics of the chiral SmC* phase.

6.3 Structure and Dynamics of TGBA* Phase

6.3.1 TGB phases

Twist grain boundary phases occur in strongly chiral LC, in which there is a competition between the low energy layered structure and the formation of a helical macrostructure due to the packing requirement of the chiral LC molecules. These two structural elements are not compatible with each other, thereby causing defects to be introduced. In the case of

liquid crystalline TGBA*/TGBC* phases, these defects are regular arrays of parallel screw dislocation lines, giving grain boundaries between blocks with a local SmA/SmC* symmetry. Generally, TGB phases are observed in materials with short cholesteric pitch lengths in the range of a few hundred nanometers. The TGB phase of a chiral smectic liquid crystal exhibits a helical twist of molecular orientation among various smectic blocks. This is different from the case of achiral liquid crystals, in which twist modes are expelled. The coexistence of layering and twist is made possible by an array of screw dislocation walls or twist grain boundaries in the layering, which divide the layered structure into smectic blocks or grains. Twist grain boundary (TGB) phases, which occur between the cholesteric and respective smectic phases, are novel from a theoretical point of view. Indeed, the existence of a twist grain boundary smectic A (TGBA*) phase was predicted in 1988 by Renn and Lubensky [12] on the basis of an analogy between a smectic A (SmA) phase and a superconductor [13]. In this prediction, the twist grain boundary phase is the liquid crystal equivalent of Abrikosov flux lattice phase of a type II superconductor in an external magnetic field [12, 14]. Renn and Lubensky have proposed that the TGBA* phase structure involves slabs of SmA materials helically stacked along an axis which is parallel to the smectic layers. Thus, TGB phases exhibit a spiraling layer order. Various techniques, which include optical microscopy, x-ray diffraction, differential scanning calorimetry, dielectric spectroscopy etc. [15–19], have confirmed the above molecular arrangements in TGB phases.

The structure of the boundary regions between grains can influence mechanical, electrical, and transport properties of these chiral compounds to a great extent. Structure studies of the TGBA* phase by Srajer et al. [20] have shown that the ratio of the volume of the grain boundaries to that of the smectic blocks is less than 20%. Hence a relatively weak NMR signal can be expected from the molecules that are located in the region of the grain boundaries. Proton relaxation studies have been performed on a TGBA* phase [21], which pointed to the existence of translational molecular motions between the adjacent SmA blocks. However, there is still no report to directly study this translational motion.

TGBA* Phase

Despite the fact that TGBA* phases are smectic, their appearance under a polarizing microscopic observation shows strong similarities to the cholesteric phase, which generally occurs at a higher temperature. The first experimental observation of a TGBA* phase was reported by Goodby et al. [22], one year after the theoretical prediction. Numerous investigations of the TGBA* phase have been made since then. Grains with a local SmA* layer structure are separated by a regular array of screw dislocation lines (Fig. 6.5), whose directions are parallel to the Burgers vector. The parallel screw dislocations of a single grain boundary cause a grain

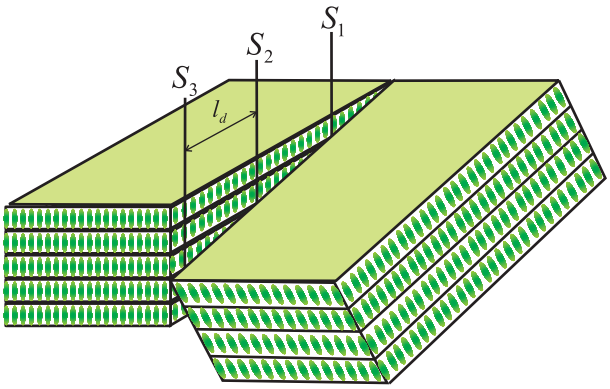

Figure 6.5: Schematic illustration of the smectic layer structure around set of screw dislocation lines S_i generating a discontinuous step in the layer structure, where l_d is the distance between dislocation lines. The direction of screw dislocations is parallel to Burgers vector as indicated by S_i [17].

.

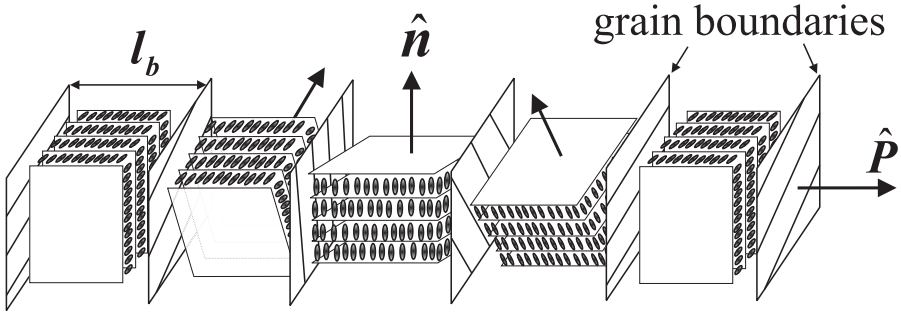

Figure 6.6: Schematic illustration of the TGBA* structure: A periodic stacking of successively twisted smectic blocks (length l_b) between grain boundaries giving a helix with a pitch length P. $\hat{n}$ is the local director.

.

to rotate by an angle with respect to its adjacent grain, thus forming a helical superstructure with twist axis perpendicular to the directors of each individual grain. The basic structural parameters of a TGBA* phase are the following quantities [17]: l is the smectic layer thickness, the helical pitch length P is the distance for a full 2π rotation of SmA blocks along the pitch axis, l_b is the distance between two neighboring grain boundaries, l_d is the distance between two neighboring dislocation lines within a grain boundary (See Figure 6.5), and ϕ_0 is the twist angle between two consecutive SmA blocks (Fig. 6.6). Typical l_b values reported in the literature are ca. 20-30 nm [19] and a twist angle of about 20 degrees is reported [23].

From geometric considerations, these parameters are related by the following relationships:

$$\phi_0 \approx l/l_d \tag{6.7}$$

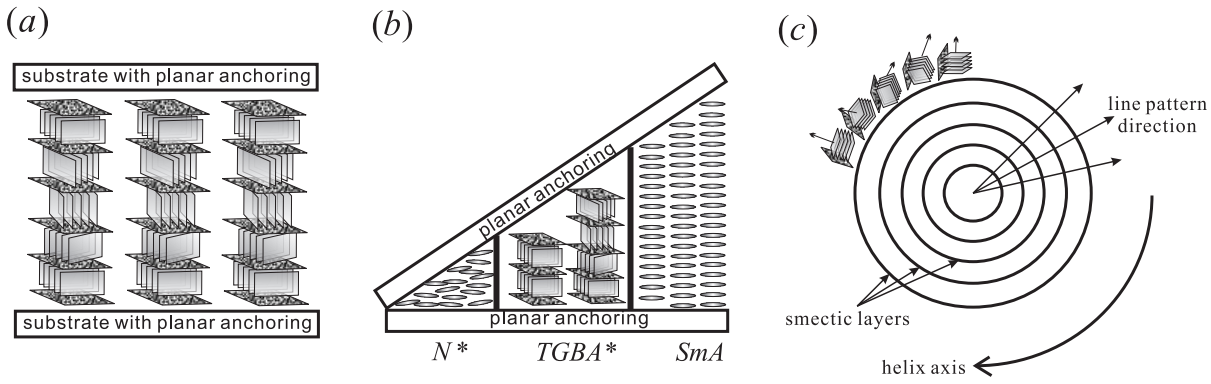

Figure 6.7: Schematic illustration of TGBA* phase (a) confined to a cell with planar boundary conditions; (b) in a wedge cell with planar boundary conditions under a temperature gradient; (c) in a droplet preparation with planar anchoring conditions [26].

.

and

$$\phi_0 = 2\pi l_b / P \tag{6.8}$$

Combination of Eqs. (6.7) and (6.8) gives

$$P = 2\pi l_b l_d / l \tag{6.9}$$

So the number of grain blocks along a 2π twist can be calculated by $360°/\phi_0$.

The optical Bragg diffraction, optical texture observations, contact method, pitch measurements, NMR spectroscopy and infrared spectroscopy have been used to explore the molecular structure of the TGBA* phase. Owing to the often narrow temperature range of the TGBA* phase, it is sometimes hard to detect its existence by differential scanning calorimetry, polarizing microscopy or texture observation. Even for a larger temperature range of TGBA* phase, its detection can sometimes be difficult based on textures. Different techniques have been developed to observe this phase. Subjecting the TGBA* phase to planar boundary conditions orients the molecular long axis parallel to the substrate, leading the smectic layer planes perpendicular to the glass plates. This implies that the TGBA* helix axis is oriented perpendicular to the substrate. Schematic illustration of a TGBA* phase with planar boundary conditions is shown in Figure 6.7(a). Preparation of a sample in a wedge cell geometry under a temperature gradient is quite illustrative of the structural similarities and differences of N*, TGBA*, and SmA* textures (See Figure 6.7(b)) [24]. The orientation of the helix axis in TGB phases can also be nicely demonstrated by the observation of a droplet (See Figure 6.7(c)) [25].

TGBC* Phases

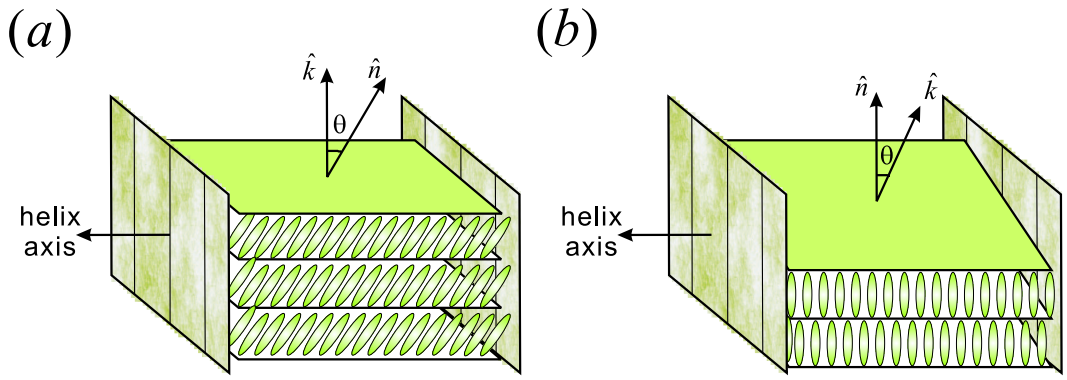

Figure 6.8: Schematic models of the TGBC* structure. (a) The smectic layer normal $\hat{k}$ is perpendicular to the twist axis and parallel to the direction of screw dislocations, and the director $\hat{n}$ tilted with respect to the direction of screw dislocations. (b) The smectic layer normal $\hat{k}$ is tilted with respect to the direction of screw dislocations, while the director is parallel to them [26].

.

Although the experimentally observed TGBA structure is as predicted, the situation with respect to the TGBC* phase is much more complex: it is not clear whether the observed TGBC* phases coincide with the few that have been predicted. TGBC* phases in which the molecules are tilted relative to the local layer normal were predicted in 1991 [27, 28] and subsequently observed experimentally by Nguyen and coworkers in 1992 [29]. In the TGBC* phase, the local layer normal $\hat{k}$ remains perpendicular to the pitch axis (Fig. 6.8).

Later on, various TGBC* structures were reported [29–31]. Owing to the local tilt of the molecules with respect to the smectic layer normal and the existence of a spontaneous polarization, several different structures were theoretically proposed for TGBC* phase [28]. One possible configuration is schematically depicted in Figure 6.8(a). As in the TGBA* phase the smectic layer normal $\hat{k}$ is perpendicular to the macroscopic twist axis, but the local director $\hat{n}$ is oriented by the molecular tilt angle θ with respect to the layer normal $\hat{k}$ [32]. Yet another possible TGBC* structure was proposed by Dozov et al. [33, 34] and is schematically depicted in Figure 6.8(b). The structure shows the director $\hat{n}$ is parallel to the screw dislocations and the layer normal $\hat{k}$ is inclined by the tilt angle θ with respect to the direction of screw dislocations. The x-ray investigation performed by Navailles et al. [30, 31] on oriented samples indicate that this kind of TGBC* phase is in fact the one generally observed. Ribeiro et al. had [35] published in 1999 results obtained with a single-component liquid crystalline material. By optical and structural x-ray studies, they showed that this TGBC phase exhibits a square grid pattern in planar geometry.

6.3.2 Experiment

The partially deuterated 11EB1M7 (Fig. 1.12(a)) sample is that used previously [36], and has the phenyl moiety deuterated at two carbon sites. Its phase sequence, shown also in Fig. 1.12(a), gives various phases as determined by optical microscopy and differential scanning calorimetry. The synthesis of 11EB1M7 and its characterization have been reported elsewhere [36–38]. To get a pure TGBA* phase, the sample was cooled down slowly inside the magnet from the isotropic phase. 1D ^{2}H spectra were obtained using two-pulse solid echo sequence [39]. The time interval between the two 90° pulses was 30 μs and the recycle time between scans was 0.1 s. The 2D ^{2}H NMR exchange five-pulse sequence (Fig. 6.4) was used to generate a 'cosine' and a 'sine' exchange spectrum [40], where $\Delta_{12} = \Delta_{34}$=30 μs is the delay for the two refocusing 90° pulses. The 90° pulse width was 2.6 μs. To get a good free induction decay (FID), signal averaging required 12000 scans in the TGBA* phase. After doing the 1D experiment, a 2D deuteron exchange experiment was performed at the same temperature. The exchange mixing time t_{mix} was chosen according to the molecular jump constant, and t_1 gave the time increment of the F1 dimension. The recycle time between scans was 0.12 s. With a typical number of 80 t_1 increments, about 14 hours were required to do a 2D exchange experiment.

6.3.3 TGBA* Phase Theory

To simulate the NMR spectrum of TGBA* phase, we need to know the spectral frequencies of specific sites. In TGBA* phase, the molecules have the same director $\hat{n}$ within a grain, and the grain directors $\hat{n}$ rotate and form a helix $\hat{P}$. In this case, the coordinate transformations that needed to be considered are:

$$\text{Pitch frame } (\hat{P}) \overset{(\alpha,\beta,0)}{\Longrightarrow} \text{External magnetic frame } (B_0)$$
$$\text{Pitch frame } (\hat{P}) \overset{(\phi,\frac{\pi}{2},\frac{\pi}{2})}{\Longrightarrow} \text{local director frame } (\hat{n})$$

Analogous to Eqs.(4.8) and (4.9), an absorption spectrum has two lines whose spectral frequencies are given by [41]:

$$\nu_Q(\phi) = \pm\frac{3}{4}\bar{\nu}_Q \cdot \frac{1}{2}\left[3\sin^2\beta\cos^2(\alpha-\phi) - 1 - \bar{\eta}(\cos^2\beta - \sin^2\beta\sin^2(\alpha-\phi))\right] \tag{6.10}$$

where $\bar{\nu}_Q = (eQ\bar{V}_{zz})/h$ is the time-averaged coupling constant in the local director frame, and $\bar{\eta}$ is the corresponding time-averaged asymmetry parameter. $(\alpha, \beta, 0)$ are the Euler angles that

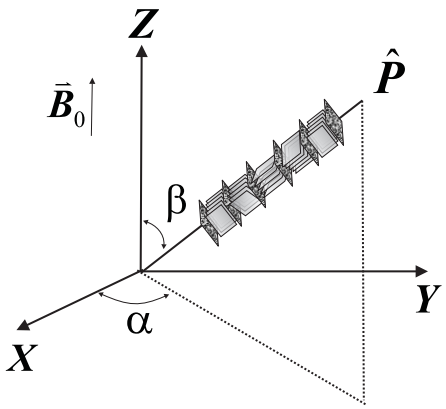

Figure 6.9: Coordinate transformation between the pitch frame and the Laboratory frame. α, β are the Euler angles that give the coordinate transformation from the TGBA* pitch frame $\hat{P}$ to the external magnetic field $\vec{B}_0$.

.

give the coordinate transformation from the TGBA* pitch frame to the external magnetic field (Figure 6.9), while the Euler angles $(\phi, \pi/2, \pi/2)$ transform from the pitch frame to the local director frame.

The helical axis is perpendicular to the local symmetry axes of the SmA blocks. For chiral molecules with positive anisotropic magnetic susceptibility $\Delta\chi(= \chi_{\parallel} - \chi_{\perp})$, the magnetic field exerts a torque on the structure, tending to align the local symmetry axis parallel to the field. The twist elastic energy due to the packing of chiral molecules tends to maintain the helical structure as long as the magnetic torque is insufficient to unwind the helix. Such a situation is common for chiral nematic phases. Considering the Frank free energy, one can show that the pitch axis of the helix is perpendicular to the field [42, 43]. Thus, $\beta = \pi/2$ for the helical axes, while the ϕ angle for the grain directors varies from 0 to 2π. Since the width of the twist grain boundary is small, its effect on the molecular movement has been considered as negligible in this study.

The observed DNMR lineshape can be described by a multisite jump problem (jump across twist boundaries from one block to the next) and the evolution of the magnetization for one pitch (N SmA blocks) can be calculated by Eq. (6.5), in which $\mathbf{M}(t) = \mathbf{M}(\phi, t)$ is a column vector with components $M_i(\phi')$ that denote magnetization from molecules within block i having a particular ϕ' $(\phi' = \phi + m\phi_0; m = 0, 1, ..., N-1)$ orientation; the kinetic matrix $\mathbf{\Pi}$ describes the reorientation process of the local director, and $\mathbf{\Gamma}$ is a diagonal matrix of the

NMR frequencies for N sites (blocks)

$$\mathbf{\Pi} = \begin{pmatrix} 2K_J & -K_J & 0 & \cdots & -K_J \\ -K_J & 2K_J & -K_J & \cdots & 0 \\ \vdots & \vdots & \ddots & \vdots & \vdots \\ -K_J & \cdots & \cdots & -K_J & 2K_J \end{pmatrix} \tag{6.11}$$

$$\mathbf{\Gamma} = \begin{pmatrix} i2\pi\nu_Q(\phi) + \frac{1}{T_2} & 0 & 0 & \cdots & 0 \\ 0 & i2\pi\nu_Q(\phi+\phi_0) + \frac{1}{T_2} & 0 & \cdots & 0 \\ \vdots & \vdots & \ddots & \vdots & \vdots \\ 0 & \cdots & \cdots & 0 & i2\pi\nu_Q(\phi+(N-1)\phi_0) + \frac{1}{T_2} \end{pmatrix} \tag{6.12}$$

with $\phi_0 = 360°/N$ and K_J is the jump rate from one block to the next, and $1/T_2$ is a jump independent relaxation term. In a quadrupole echo experiment, the magnetization $F^{\phi}(\alpha, \beta, t)$ is given by Eq. (4.16) with $\mathbf{R} = \mathbf{\Gamma} + \mathbf{\Pi}$. When $\beta = \pi/2$, the overall time-domain FID signal is obtained by integrating over α and ϕ:

$$F(t) = \int_0^{2\pi} \int_0^{2\pi} F^{\phi}(\alpha, \frac{\pi}{2}, t) d\phi d\alpha \tag{6.13}$$

The simulated spectrum is obtained by Fourier transformation of $F(t)$, i.e.

$$S(w) = \int_0^{\infty} F(t) \cdot e^{-\sigma^2 t^2} e^{-iwt} dt \tag{6.14}$$

where σ in $e^{-\sigma^2 t^2}$ is used to account for the Gaussian line broadening (needed in LC phases) in addition to the Lorentzian lineshape due to the T_2 effect.

The FID signal in a ^{2}H 2D exchange experiment for a pitch unit and at an azimuthal angle ϕ is also obtained from Eq. (6.6). The FID of the 'cosine' spectrum is

$$F_c^{\phi}(t_1, t_2; \alpha, t_{mix}) = \vec{\mathbf{1}} \cdot Re[e^{-(\mathbf{\Gamma}+\mathbf{\Pi})t_2}] e^{-\mathbf{\Pi} t_{mix}} Re[e^{-(\mathbf{\Gamma}+\mathbf{\Pi})t_1} \mathbf{M}^0] \tag{6.15}$$

and the FID of the 'sine' spectrum is

$$F_s^{\phi}(t_1, t_2; \alpha, t_{mix}) = \vec{\mathbf{1}} \cdot Im[e^{-(\mathbf{\Gamma}+\mathbf{\Pi})t_2}] e^{-\mathbf{\Pi} t_{mix}} Im[e^{-(\mathbf{\Gamma}+\mathbf{\Pi})t_1} \mathbf{M}^0] \tag{6.16}$$

where T_1 relaxation during t_{mix} has been neglected. In our study, only the simple case of $t_{mix} >> \tau_c$ ($\tau_c \approx 1/K_J$) is considered. The observed powder 'cosine' ('sine') exchange spectrum comes from all possible ϕ and α angles, and can be obtained by Fourier transforming over t_1 and t_2 the FID calculated from

$$\begin{aligned} F_c(t_1, t_2; t_{mix}) &= \int_0^{2\pi} \int_0^{2\pi} F_c^{\phi}(t_1, t_2; \alpha, t_{mix}) d\phi d\alpha \quad (\texttt{'cosine'FID}) \\ F_s(t_1, t_2; t_{mix}) &= \int_0^{2\pi} \int_0^{2\pi} F_s^{\phi}(t_1, t_2; \alpha, t_{mix}) d\phi d\alpha \quad (\texttt{'sine'FID}) \end{aligned} \tag{6.17}$$

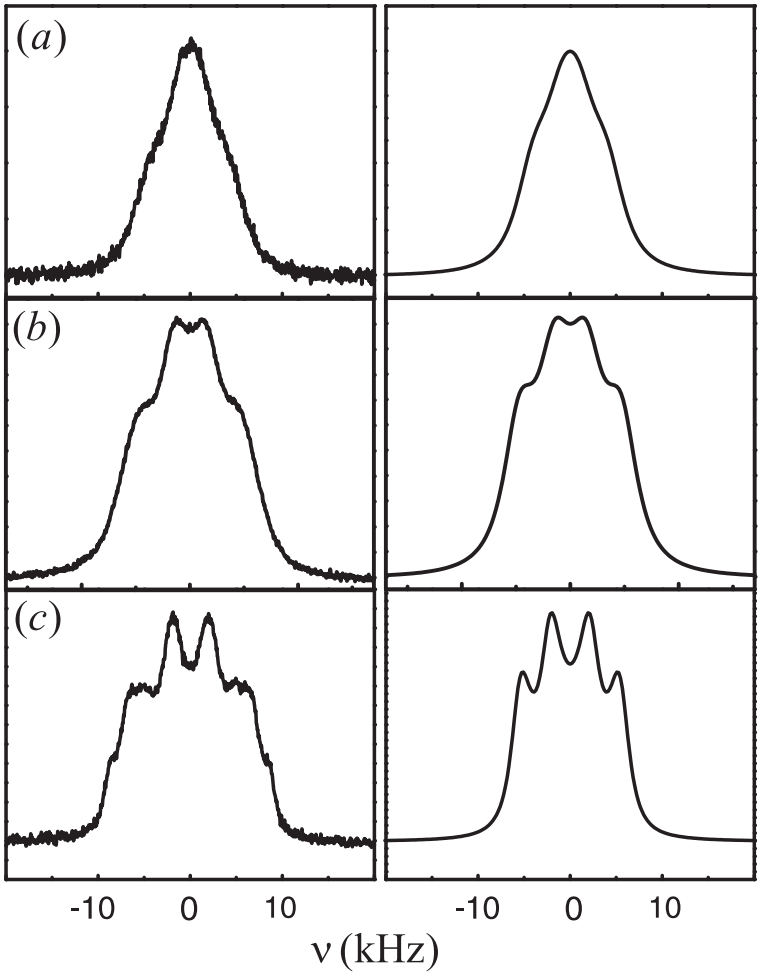

Figure 6.10: Experimental 1D spectrum in the TGBA* phase of 11EB1M7 at three temperatures with the corresponding simulated spectra in the right column where K_J is 3.2×10^4 s^{-1} at 380.5 K (a), 1.9×10^4 s^{-1} at 379.5 K (b), and 7.5×10^3 s^{-1} at 378 K (c). $\bar{\nu}_Q$ = 8.7 KHz, T_2= 0.5 ms, and $\sigma = 0.1$ Hz.

.

By comparing the simulated 2D exchange spectrum with the experimental spectrum, the arrangement of SmA blocks and the jump rate K_J can be obtained in the TGBA* phase.

6.3.4 Results and Discussion

The TGBA* phase of the 11EB1M7-d_2 sample has a rather narrow temperature range of 6 K, and deuterium 1D spectra have been reported in a previous study [36]. Although detailed information has been obtained in LC phases below the TGBA* phase, there was no attempt to quantify the 1D TGBA* spectrum except a powder-like pattern was noted. Though a helicoidal macrostructure of SmA blocks is known to exist in the TGBA* phase, the

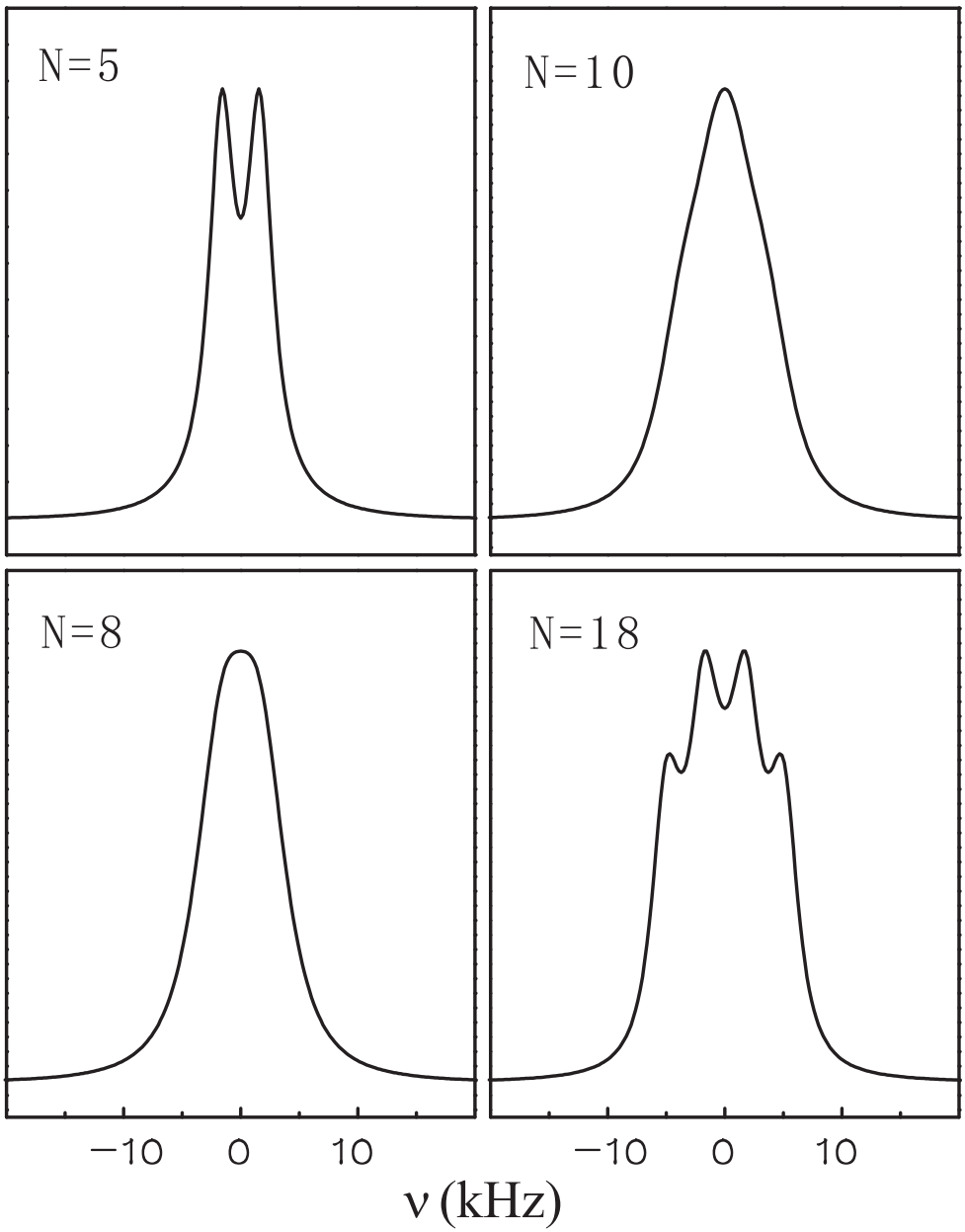

Figure 6.11: Simulated 1D spectra for different values of the number of jump sites N. $\bar{\nu}_Q = 8.7$ KHz, T_2= 0.5 ms, $\sigma = 0.1$ Hz and K_J=2×10^4 s^{-1}.

.

exact disposition of helical axes in a bulk phase inside a magnet has not yet been quantified experimentally. Based on the elastic and magnetic energy considerations, these helical axes tend to align perpendicular to the magnetic field. The present study has indeed confirmed such a supposition, because of the observed 'powder-like' pattern in the 1D and 2D DNMR spectra. Typical 1D spectra at different temperatures are shown in Fig. 6.10. These spectra are different from that seen for an isotropic powder or a 2D planar distribution of directors. When the temperature is lowered, the sample shows a small biphase region of TGBA* and SmA* phase (e.g. 378 K). In our simulation, the existence of twisted grain boundaries has been ignored. This is because of the fact that the twist grain boundary layer is small (ca. 1 nm) in comparison to the SmA block width l_b (ca. 20 nm). However, a fair justification is by comparing the simulated and experimental results. Also, we have set $\bar{\eta}$=0 in Eq. (6.10) as the fast spinning motion of molecules in the SmA block has averaged the deuterium quadrupolar interaction(s) along the local director. The 1D spectra have been simulated using the jump diffusion model (Eq. (6.13)) (i.e. the reorientational motion of local directors along a single pitch is treated as stochastic jumps among neighboring SmA blocks). In the present study, N=14 has been determined in the TGBA* phase of 11EB1M7. The simulated spectrum at 379.5 K (see Figure 6.10(b)) gives $\bar{\nu}_Q$ = 8.7 KHz, T_2= 0.5 ms, σ = 0.1 Hz, and K_J=(19±1)× 10^3 s^{-1} for the jump rate. As seen in Fig. 6.10 (b), the simulation reproduces the experimental spectrum rather well, supporting that the observed powder-like pattern is due to a 2D distribution of helical axes in a plane normal to the external magnetic field. It is conceivable that the β angle may deviate slightly from 90°, but such a possibility seems unimportant in our simulations. Thus, the twist angle ϕ_0 between neighboring SmA blocks at 379.5 K appears to be 26° ± 10°. The effect of different N values on the 1D spectra is demonstrated in the simulated spectra shown in Figure 6.11. As seen in this figure, the lineshape of 1D spectrum is rather sensitive to the N value when all other parameters are kept the same as indicated in the caption. However, a slight change from N=14 in combination with some variation of the K_J value can give similar simulated spectra. Hence, the above derived ϕ_0 value has a rather large uncertainty. However, it is consistent with those found by x-ray measurements (about 20°) in the TGBA* phase of similar LC [23].

In the deuterium 2D exchange spectra, exchange intensities are in the form of diffuse ellipses of varying magnitudes for different mixing times. Here we consider the simple case of a long mixing time. Figure 6.12 shows a 2D exchange spectrum in the TGBA* phase at 379.5 K with a mixing time of 3 ms. The experimental contour plot in the inset clearly demonstrates the exchange intensities from molecules jumping along the pitch axes. The simulated 2D exchange spectrum (shown also in Fig. 6.12) is obtained by adding the cosine and sine spectra calculated from Eq. (6.17). The agreement between the experimental and simulated

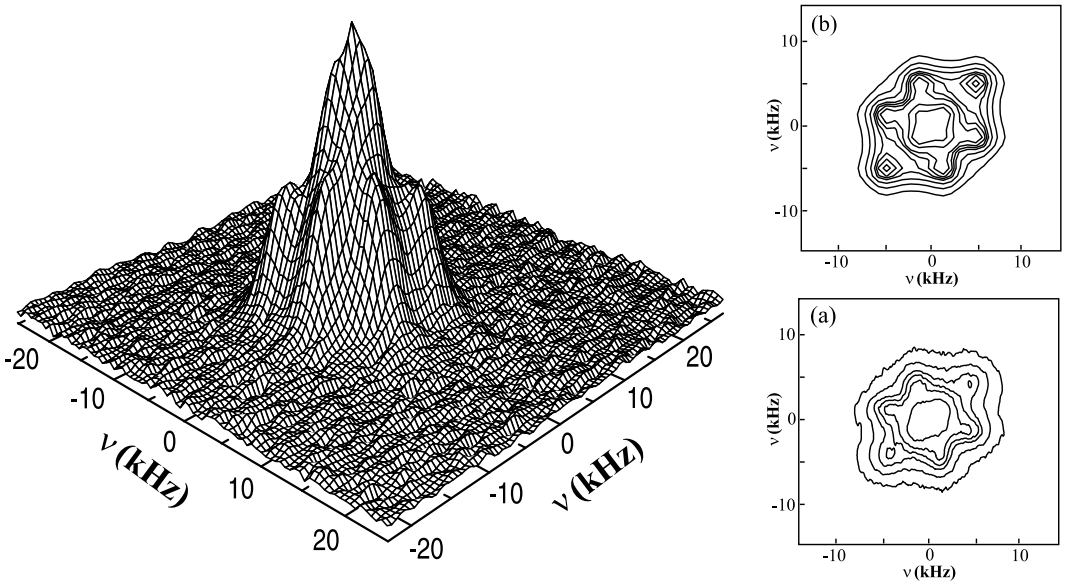

Figure 6.12: Experimental 2D exchange spectrum in the TGBA* phase of 11EB1M7 with $t_{mix} = 3$ ms at 380 K. Insets show the contour plot of an expanded region: (a) experimental and (b) simulated 2D exchange spectra. T_2= 0.5 ms, line broadening σ is 0.1 Hz and K_J=1.9×10^4 s^{-1}.

.

contour plots is quite reasonable. Figure 6.13 shows the theoretical predictions using all the simulation parameters obtained at 379.5 K except for the different K_J values. It is clear that the larger K_J value can better reproduce the experimental spectra at this temperature. The effect of t_{mix} values at 378 K is shown in Fig. 6.14 for 3 ms and 5 ms. This demonstrates that our mixing time of 3 ms satisfies the long mixing time limit. From the jump rate K_J for jumps between SmA blocks, one can estimate the self-diffusion constant $D_{\|}$ [44] along the pitch axis by

$$D_{\|} = 4K_J(l_b/\pi)^2 \tag{6.18}$$

under the assumption of free molecular diffusion between different SmA blocks. Unfortunately, the l_b has not been measured directly for 11EB1M7, but the self-diffusion measured in the SmA phase of similar chiral compounds [45] may serve as a guide. Using a typical block length l_b of 20 nm [46], we have estimated $D_{\|}$ using the above equation to give 3.2 $\times 10^{-12} m^2/s$ at 379.5 K. It would appear that the pitch length P in 11EB1M7 at 379.5 K is 0.3 μm, a value which has been determined in another chiral LC [19]. One should note the 1D lineshapes are strongly temperature dependent in Fig. 6.10. This must reflect the temperature behavior of the K_J value. Using the same fitting parameters except K_J for simulating 1D and 2D spectra at 379.5 K, 1D spectra at two other temperatures were simulated to give the simulated lineshapes shown in the same figure. The K_J values appear to vary from 7.5×10^3 s^{-1} to 3.2×10^4 s^{-1} over just a few degrees. Given the small temperature range

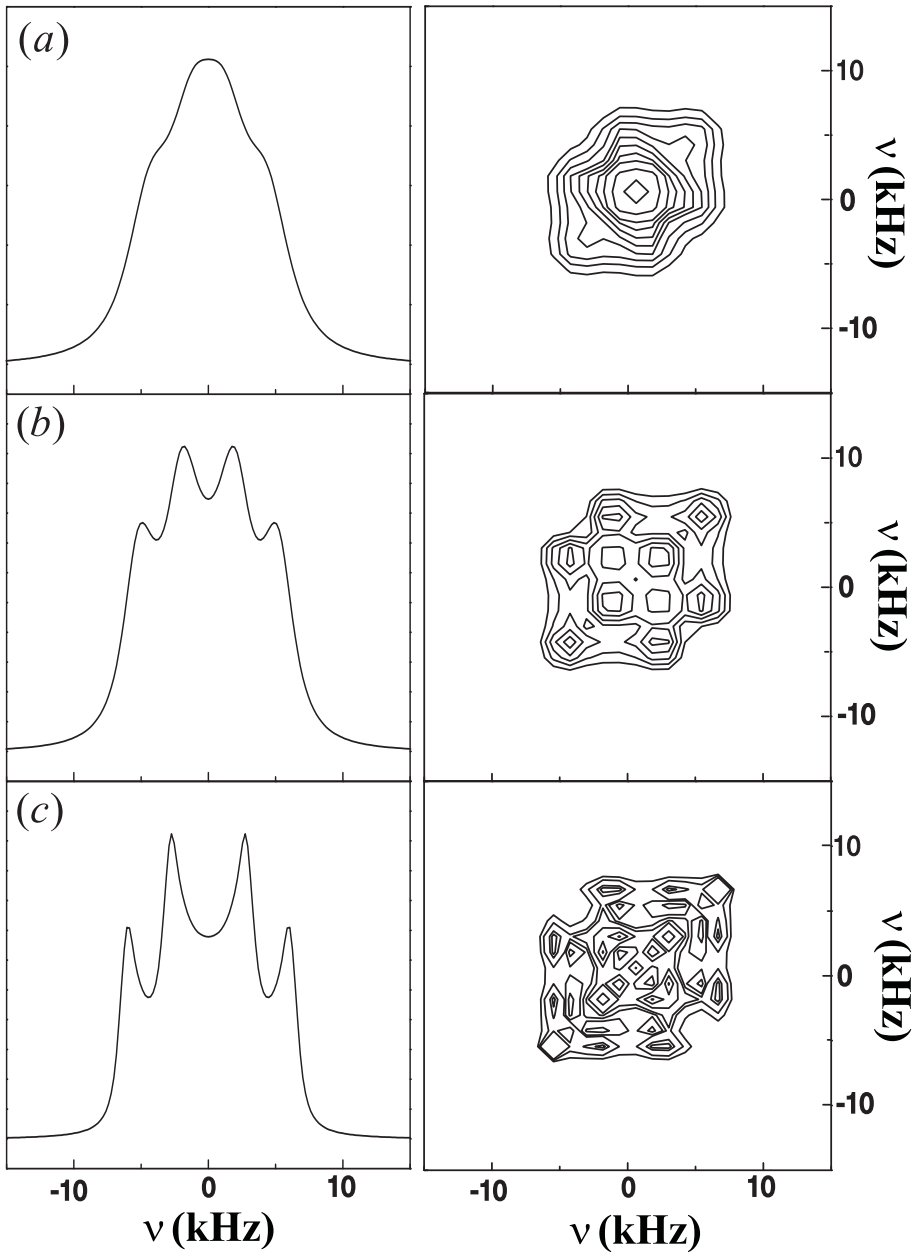

Figure 6.13: Simulated spectra using different K_J values: (a) 2.5×10^4 s^{-1}, (b) 1×10^4 s^{-1} and (c) 1×10^3 s^{-1}. The 1D spectra are shown in the left column and the corresponding 2D spectra in the right column. All other parameters are kept the same as those in Fig. 6.12.

.

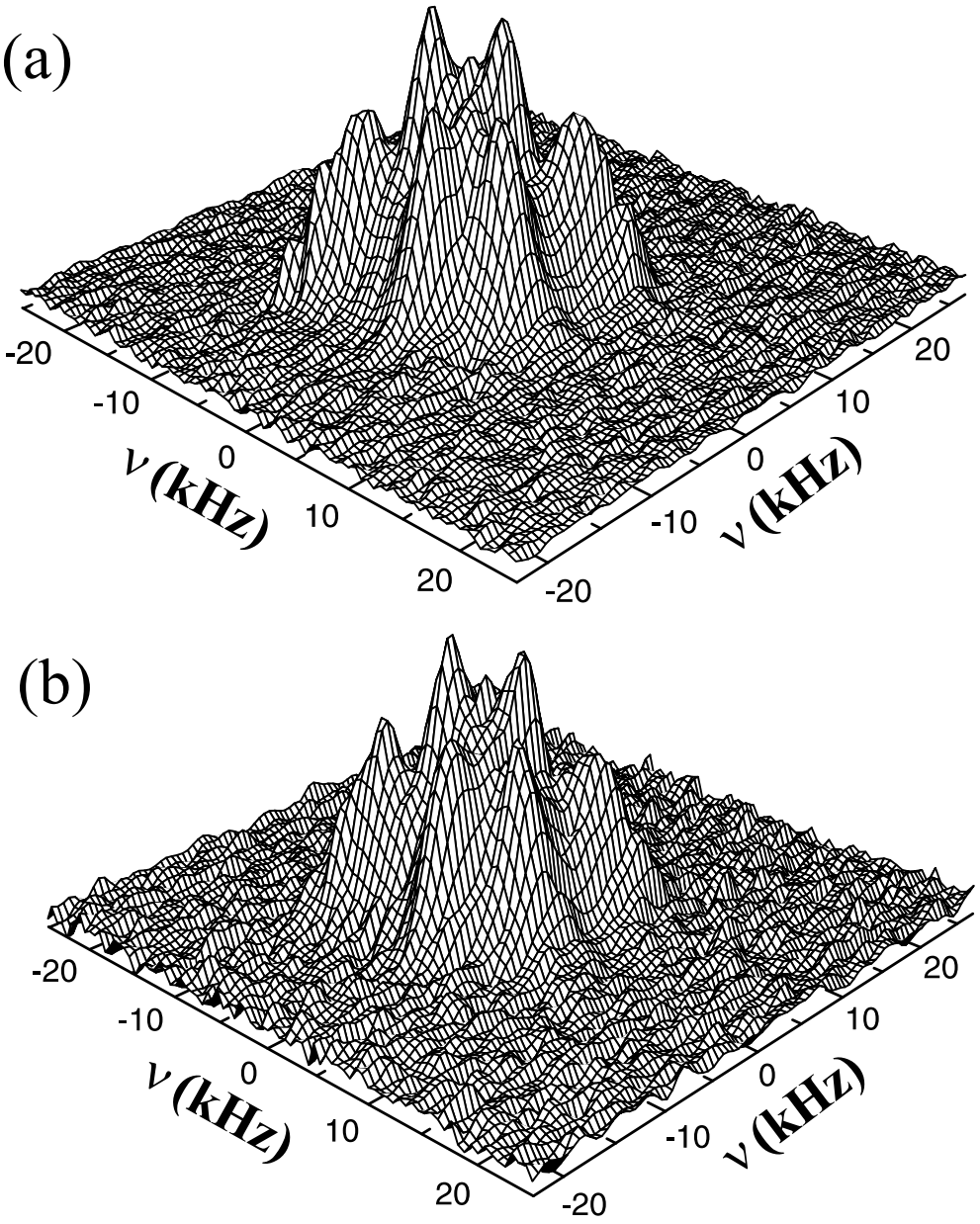

Figure 6.14: Experimental 2D exchange spectra for two different t_{mix} times: (a) 3 ms and (b) 5 ms, in the TGBA* phase of 11EB1M7 at 378 K.

.

of TGBA*, it is hard to check the K_J temperature dependence.

The present study has demonstrated the utility of the 2D exchange experiment as an important tool in ascertaining the jump diffusion rate of molecules between different SmA blocks in the TGBA* phase. This information can not be easily obtained by other experimental techniques. Furthermore, the twist angle ϕ_0 can be directly obtained by simulating both the ^{2}H 1D and 2D exchange spectra as demonstrated at one temperature (379.5 K). This ϕ_0 represents a first determination in 11EB1M7. When the SmA block length can be measured independently by other techniques such as x-ray, the 2D exchange spectrum can in fact shed light on the diffusion constant in a powder TGBA sample. It is believed that the present methodology can be applied to study other TGB phases such as TGBC* phases and giant-block TGB phases [47].

6.4 Molecular Diffusion Motion of BP8Cl

6.4.1 Introduction

In the tilted SmC layer, if the tilt direction of the molecules is essentially the same from layer to layer, the order is synclinic. If the tilt is in the opposite direction from one layer to the next, it is anticlinic order. Since the discovery of synclinic ordering in ferroelectric chiral smectic C (SmC*) phase of chiral LC over three decades ago [48], significant experimental and theoretical efforts have been directed to study the structure and dynamics of chiral synclinic and anticlinic phases [49–54]. While rotational diffusion of molecules has been studied in chiral phases by measuring deuteron spin relaxation times [49, 55], translational diffusion of molecules in these phases is harder to observe because of the very low self-diffusion constant, especially in anticlinic phases [45, 54]. Spatial modulations of the local electric field gradient (EFG) of a deuteron(s) by molecular self-diffusions along the helical axis are not effective in the SmC* phase to affect the one-dimensional deuterium line shapes in angular-dependent NMR studies. A two-dimensional (2D) deuterium exchange experiment [7] has been applied to study jump diffusive motions in the SmC* phase of an aligned chiral LC (10B1M7), and to directly detect the molecular self-diffusion in this phase [56]. Unfortunately, the self-diffusion constant cannot be uniquely obtained without a prior knowledge of the helical pitch length. Hence, the mentioned work has to assume a particular value for the pitch length. In the present study, we have applied the same technique to study self-diffusions in the SmC* phase of 4'-(octyloxy)-d17 biphenyl-4-yl2-chloro-3-methylpentanoate (BP8Cl). To alleviate

the above difficulty, the proton spin relaxation [57] over a wide range of Larmor frequencies in the same compound to shed light on the modulation of inter-molecular interactions due to molecular self-diffusions was performed. In this way, a consistent picture on the interlayer diffusion of molecules along the pitch axis is sought.

6.4.2 Experiment

The angular dependent study of chiral liquid crystal BP8Cl has been introduced in the last chapter. To study the molecular diffusion motion of this sample in the SmC* phase, 2D deuterium 'cosine'and 'sine'exchange spectra were collected using a 2D ^{2}H NMR exchange five-pulse sequence with $\Delta_{12} = \Delta_{12} = 30\mu s$. To get a good FID signal in the SmC* phase, we needed to average 64 FIDs after the last 90° pulse for each t_1 value. Before obtaining a 2D exchange spectrum, the aligned sample was first rotated in the goniometer probe by 15 degrees. This is necessary so that jumps across the soliton-like boundaries will result in observable changes in the angle between the local director and the field. The recycle time between scans was 1 s. With a typical number of 80 t_1 increments, about 1.5 hours were required to obtain a 2D exchange spectrum. The field-induced sample realignment during the 2D exchange experiment was found to be negligible by reproducing the 1D deuterium spectrum immediately after collecting each 2D exchange spectrum. In the present study, we still focus on the methyl deuterons at the last carbon site C_8.

6.4.3 Theory

When molecules diffuse along the pitch axis in the chiral SmC* phase, the molecule tilt direction (θ_0, ϕ) will change by following the tilt direction in each smectic layer. In the SmC^* phase, the tilt direction changes the azimuthal angle by a tiny amount between the neighboring layers. As a result, modulation of the NMR frequency by molecular self-diffusions is small over a short distant scale, and is hard to detect in a 1D spectrum [54]. A 2D exchange experiment can give a measure of model-independent reorientational data for molecules in slow dynamic situations [7]. Considering that a pitch length usually includes hundreds of smectic layers, we assume that the azimuthal angle (ϕ) of the molecular tilt is a linear function of diffusion length l along the pitch axis z, viz. the tilt direction will change by $\delta\phi = 2\pi l/P_t$, where P_t is the pitch length. The assumption is considered a good approximation even in the case of small soliton-like distortions. This is rationalized by the fact that the soliton-like region is vanishingly small in comparison to the pitch length. The interlayer self-diffusion is

a one dimensional diffusion problem, and the probability $P(\phi_0, \phi, t)$ of finding a molecule at position ϕ and at time t given a position ϕ_0 at $t = 0$ is [58]

$$P(\phi_0, \phi, t) = \frac{P_t}{\sqrt{16\pi Dt}} e^{-(\phi-\phi_0)^2/16\pi^2\varsigma t} \tag{6.19}$$

where D is a translational self-diffusion constant, and $\varsigma = D/P_t^2$ is treated as a fitting parameter. The 2D exchange spectrum $S(f_1, f_2; \phi_0)$ can be calculated from summing the 'cosine'(cc) and 'sine'(ss) spectra, which are the Fourier transform of the FIDs given by the following integrals [56]

$$\begin{aligned} F_{cc}(t_1, t_2; \phi_0, t_{mix}) &= \int\int \frac{P(\phi_0, \phi, t_{mix})}{\Omega(\phi)\Omega(\phi_0)} \cos[2\pi\nu(\phi)t_2] \cos[2\pi\nu(\phi_0)t_1] R'(\phi, \phi_0, t_1, t_2) d\phi d\phi_0 \\ F_{ss}(t_1, t_2; \phi_0, t_{mix}) &= \int\int \frac{P(\phi_0, \phi, t_{mix})}{\Omega(\phi)\Omega(\phi_0)} \sin[2\pi\nu(\phi)t_2] \sin[2\pi\nu(\phi_0)t_1] R'(\phi, \phi_0, t_1, t_2) d\phi d\phi_0 \end{aligned} \tag{6.20}$$

where $R'(\phi, \phi_0, t_1, t_2) = exp[-\sigma^2(t_1^2 + t_2^2)/2 - (2\pi\omega\frac{\partial\nu}{\partial\theta_0})^2_{\phi_0} t_1^2 - (2\pi\omega\frac{\partial\nu}{\partial\theta_0})^2_{\phi} t_2^2]$ is to account for the spectral line broadening, and $\nu(\phi)$ is again given by Eq. (5.6). And $\Omega(\phi) \propto dz/d\phi$ was defined in Eq. (5.24) to describe the ϕ distribution. It is important to realize that the slice of this 2D spectrum with $f_1 = \nu(\phi_0)$ is given by Fourier transforming the following FID with respect to t_2

$$F(t_2) = \int \frac{P(\phi_0, \phi, t_{mix})}{\Omega(\phi)} \{\cos[2\pi\nu(\phi)t_2] + \sin[2\pi\nu(\phi)t_2]\} e^{-\sigma^2 t_2^2/2 - (2\pi\omega\frac{\partial\nu}{\partial\theta_0})^2_{\phi} t_2^2} d\phi \tag{6.21}$$

Fixing ω values to those obtained in the 1D simulation, one can in principle get D by simulating the 2D spectrum using Eq. (6.20).

6.4.4 Results and Discussion

The BP8Cl sample has been studied in last chapter and the typical 1D ^{2}H NMR spectra in different LC phases have been shown in Figure 5.5. Several 2D exchange spectra were collected at 311.5K in the SmC* phase with different mixing times. It is important to have the aligned sample rotated away from the magnetic field (here $\theta = 15°$) in order to detect interlayer molecular self-diffusions. Our experiments had showed that it was hard to observe the cross-peaks for $t_{mix} < 100ms$, and there was no significant change in the 2D exchange spectra when $t_{mix} > 700ms$. Because of the serious overlaps among the ^{2}H peaks, only the C_8 signal is emphasized in the 2D spectrum shown here. Fig. 6.15 shows the 2D spectrum collected with $t_{mix} = 300ms$, while Fig. 6.16 shows the contour plots of $t_{mix} = 150ms$ and $500ms$. Note that all other experimental parameters are identical for these 2D exchange spectra. The 2D exchange spectrum was hard to simulate, especially because of the spectral overlap from the neighboring deuterons; instead a 1D spectrum obtained from the slice $f_1 = s_1$

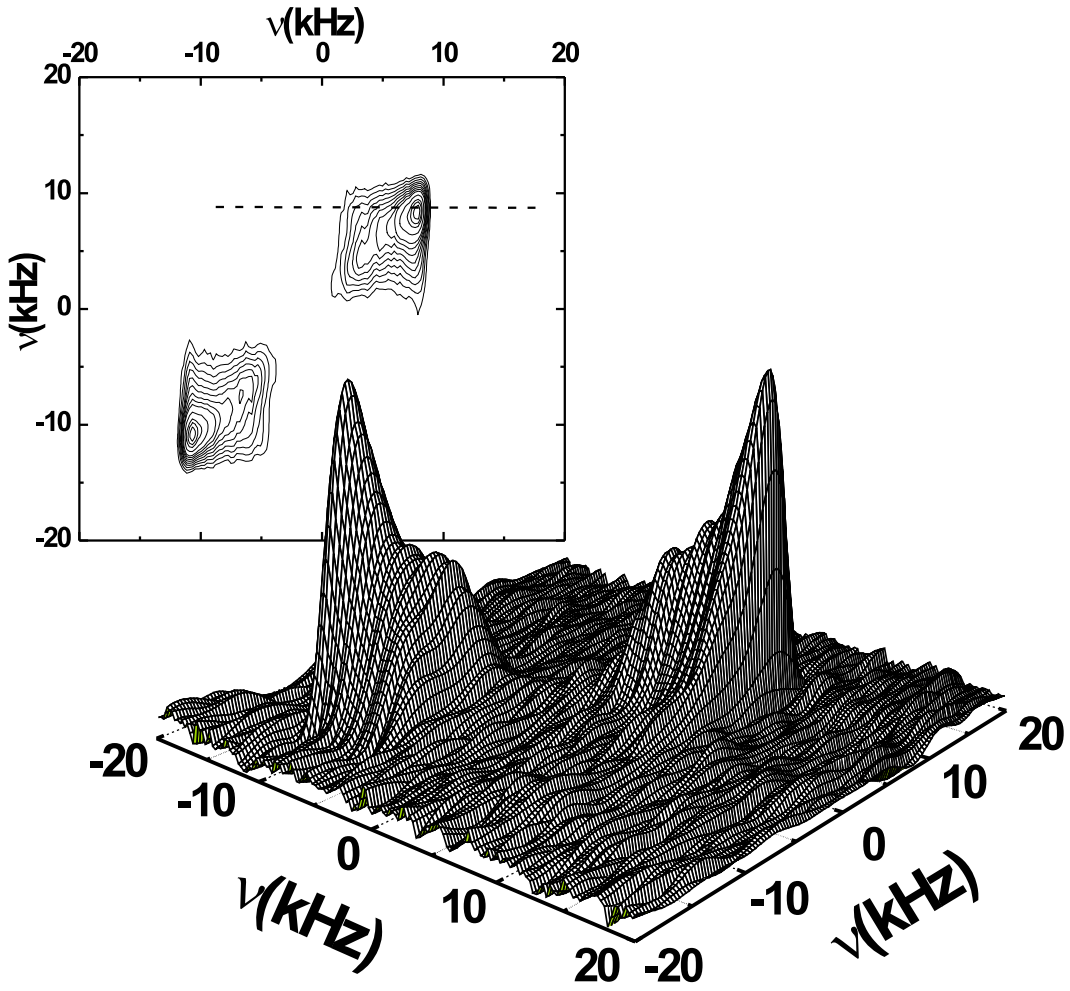

Figure 6.15: Plots of 2D ^{2}H exchange spectrum of BP8Cl in the SmC* phase at 311.5K, $\theta = 15^o$ and $t_{mix} = 300ms$. The spectrum was symmetrized with respect to the diagonal axis. Only the signal of the methyl deuterons (C_8) is emphasized in the surface plot for clarity. Dashed line in the contour plot is the slice that is shown in Fig. 6.17.

.

(or $f_1 = \nu(0)$) in a 2D spectrum (see dashed line in Fig. 6.15-6.16) could be more easily fitted. These 1D slices for several mixing times at 311.5K are shown in Fig. 6.17. Four parameters θ_0, κ, σ, ω were fixed to values obtained in the 1D spectrum simulation (Fig. 5.7), and the ς value was varied to get the best dashed spectra shown in Fig. 6.17. A ς value of $0.13 \pm 0.1s^{-1}$ was obtained from the fitting of all slices at different mixing times. The simulated 2D exchange spectra were then reconstructed (Fig. 6.18-6.20) using the above derived fitting parameters and their agreement with Fig. 6.15 and Fig. 6.16 is good. The self-diffusion constant can now be derived from ς and the pitch length, based on $D = \varsigma P_t^2$. However, the pitch length P_t is unknown for BP8Cl. Fortunately proton NMR T_1 dispersion study has been performed at $\theta = 0^\circ$ in BP8Cl (Fig. 6.21) [57]. Suffice to say that the proton T_1 dispersion over a wide range of Larmor frequency (4 kHz to 300 MHz) can be attributed to

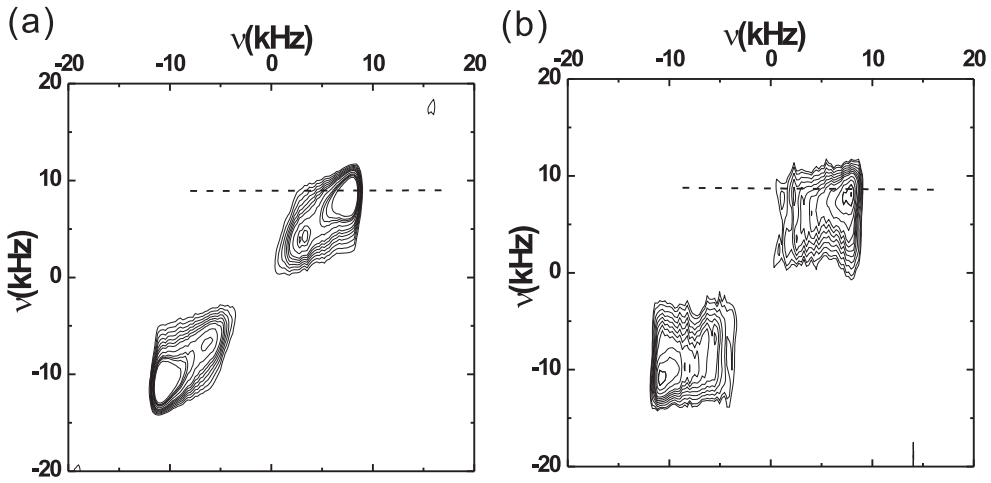

Figure 6.16: Contour plots of 2D ^{2}H exchange spectra of BP8Cl in the SmC* phase at 311.5K and $\theta = 15^o$. (a) $t_{mix} = 150ms$, (b) $t_{mix} = 500ms$. Dashed line in the contour plot gives the 1D spectrum at a particular mixing time shown in Fig. 6.17.

.

three different relaxation contributions: collective motions (C), individual molecular rotations (R) and molecular translational self-diffusions (SD) [59]. Correlation times associated with the local reorientations and with the translational SD were estimated from a model fit of the proton T_1 dispersion curve at each temperature. As seen in Fig. 6.21, it is observed that rotations/reorientations are clearly decoupled from the SD contribution in the T_1 dispersion graph. The diffusion constant D has, therefore, been obtained at several temperatures in the SmA and SmC* phase (Fig. 6.22). Assuming the usual Arrhenius temperature dependence for the translational self-diffusion, a value of $D = (1.1 \pm 0.1) \times 10^{-12} m^2/s$ has been estimated for T=311.5K. This D value and $\varsigma = 0.13 s^{-1}$ lead to a pitch length of 2.9±0.7 μm, which seems quite reasonable in comparison with typical pitch lengths (few microns) in SmC* phases. It has also been reported [60] in the literature that in one instance of SmC* phase the pitch length can range up to about $9.5\mu m$. Apart from the uncertainty in the estimated D value, the observed P_t value could be larger due to the fact that partial unwinding (or distortion) could exist even at $\theta = 15^\circ$ ($\kappa \neq 0$). It should be noted that the present 2D exchange technique can detect the self-diffusion only if $\theta \neq 0^\circ$. The reconstructed 2D exchange spectra for $t_{mix} = 150ms$ (Fig. 6.18), $300ms$ (Fig. 6.19), and $500ms$ (Fig. 6.20) are found to be in good agreement with the observed 2D spectra. The 2D exchange experiments are useful to reveal the self-diffusion of molecules in the SmC* phase. By fitting 1D slices and 2D experimental spectra, the diffusion constant can be estimated provided that the pitch length is known by another means. In particular, proton T_1 dispersion measurements have been

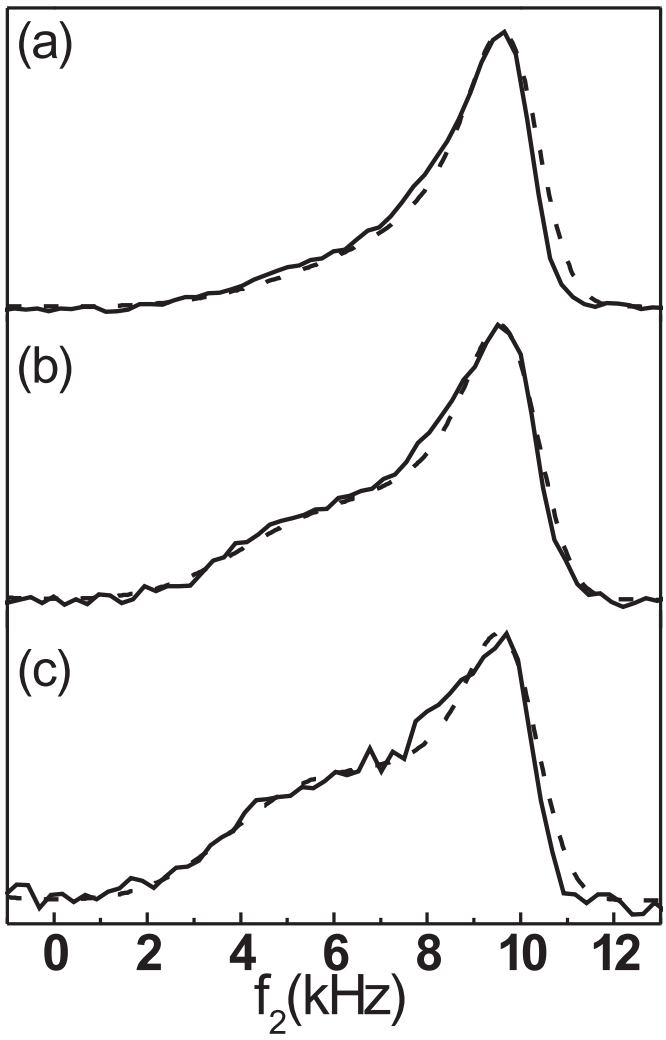

Figure 6.17: One-dimensional slices (solid lines) taken from the 2D exchange spectra of BP8Cl shown in Fig. 6.15 and 6.16 for (a) $t_{mix} = 150ms$, (b) $t_{mix} = 300ms$, (c) $t_{mix} = 500ms$. The simulated spectra (dashed lines) are obtained with $\varsigma = 0.13s^{-1}$, and κ was fixed at 0.63.

.

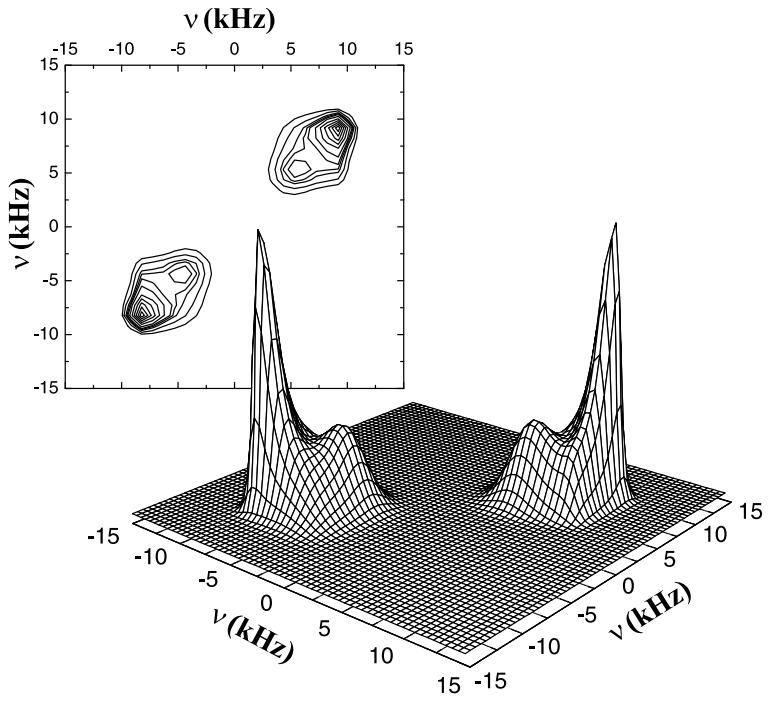

Figure 6.18: Simulated 2D ^{2}H exchange spectrum of BP8Cl at t_{mix}=150ms.

.

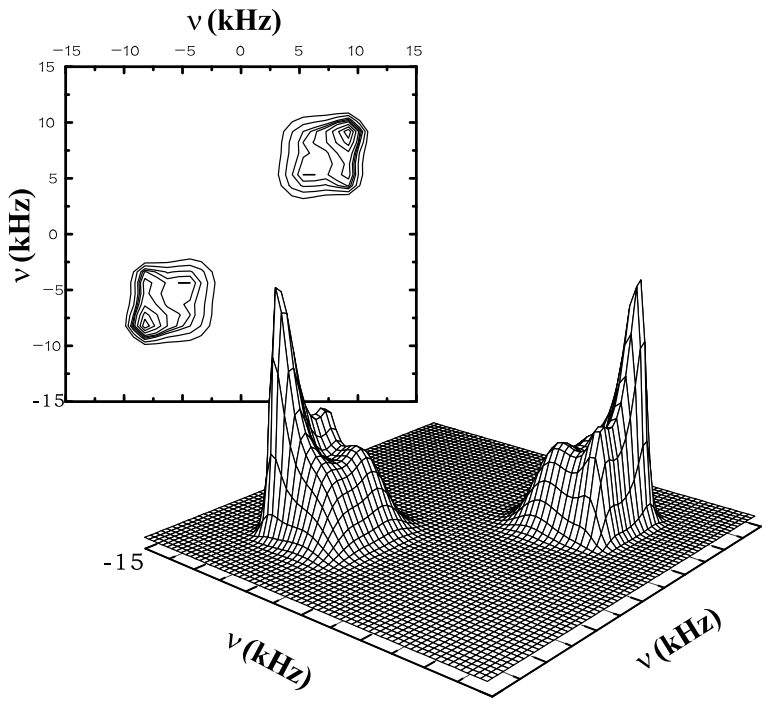

Figure 6.19: Simulated 2D ^{2}H exchange spectrum of BP8Cl at t_{mix}=300ms.

.

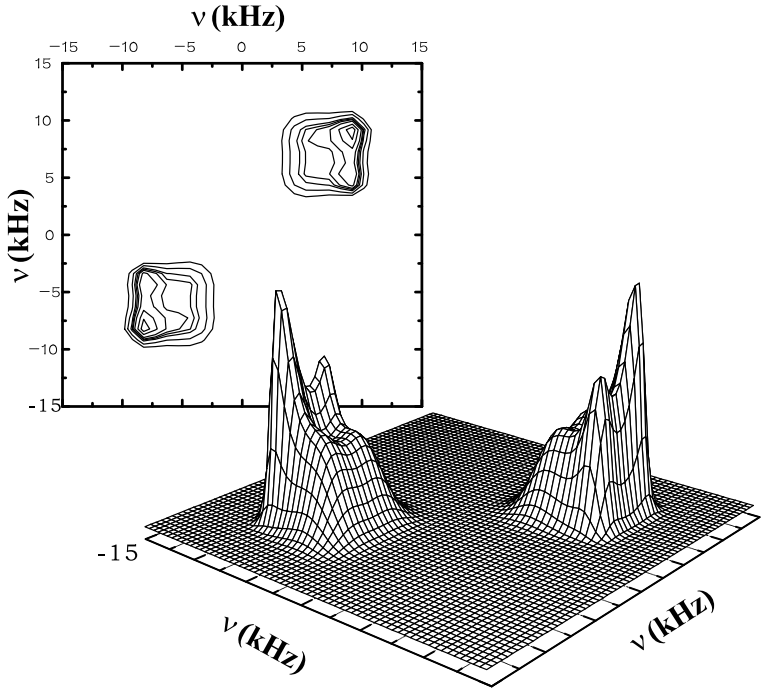

Figure 6.20: Simulated 2D ^{2}H exchange spectrum of BP8Cl at t_{mix}=500ms.

.

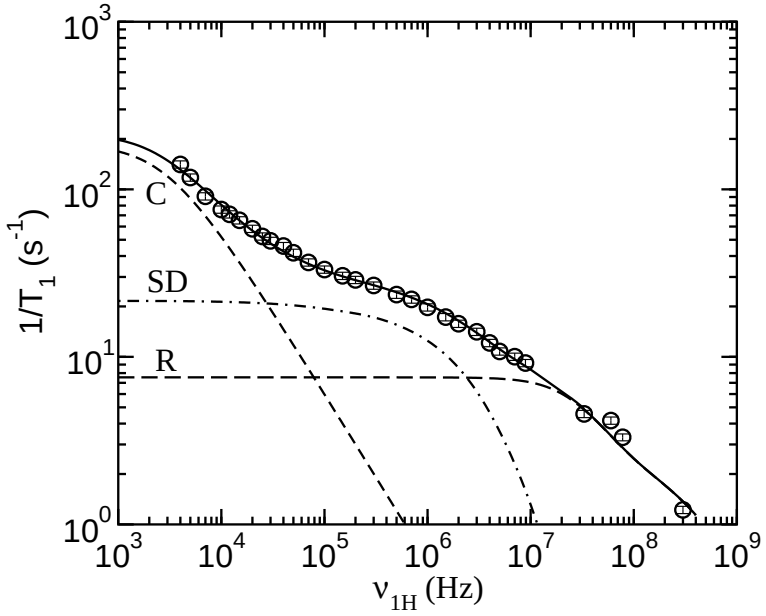

Figure 6.21: Proton $1/T_1$ dispersion in the SmC* phase at 322K and best fits to the molecular mechanisms: collective motion (C), translational self-diffusion (SD), and local rotations/reorientations (R). (Data obtained from reference [57]).

.

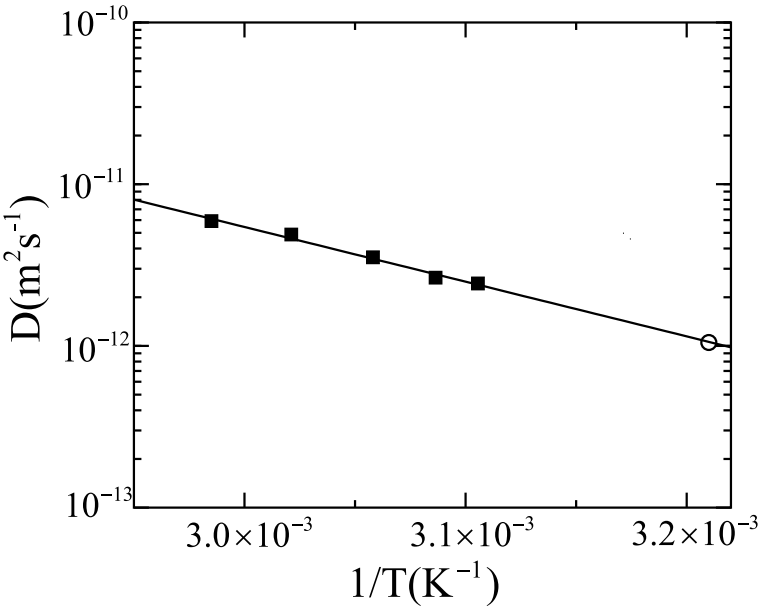

Figure 6.22: Translational self-diffusion constants obtained from the fits of T_1 (squares) dispersion. Arrhenius fit to the self-diffusion values (solid line) allows to estimate the D value at 311.5K (circle). (Data obtained from reference [57]).

.

used to get an estimated D value at 311.5K. This work has, therefore, put an upper limit on the pitch length of 2.9 μm at one temperature.

References

[1] Dong, R. Y. *NMR of Liquid Crystals*; Springer-Verlag: New York, 1997.

[2] Abragam, A. *Principles of Nuclear Magnetism*; Oxford University Press: Oxford, 1986.

[3] McConnell, H. M. *J. Chem. Phys.* **1958**, *28*, 430.

[4] Jeener, J.; Meier, B. H.; Bachmann, P.; Ernst, R. R. *J. Chem. Phys.* **1979**, *71*, 4547.

[5] Vega, A. J.; Luz, Z. *J. Chem. Phys.* **1987**, *86*, 1803.

[6] Jeener, J.; Meier, B. H.; Bachmann, P.; Ernst, R. R. *J. Chem. Phys.* **1979**, *71*, 4546.

[7] Schmidt-Rohr, K.; Spiess, H. W. *Multidimensional Solid-state NMR and Polymers*; Academic Press Inc., 1994.

[8] Wefing, S.; Kaufmann, S.; Spiess, H. W. *J. Chem. Phys.* **1988**, *89*, 1234.

[9] Schaefer, D.; Leisen, J.; Spiess, H. W. *J. Magn. Reson. A* **1995**, *115*, 60.

[10] Schmidt, C.; Blumich, B.; Spiess, H. W. *J. Magn. Reson.* **1988**, *79*, 269.

[11] Kaufmann, S.; Wefing, S.; Schaefer, D.; Spiess, H. W. *J. Chem. Phys.* **1990**, *93*, 197.

[12] Renn, S. R.; Lubensky, T. C. *Phys. Rev. A* **1988**, *38*, 2132.

[13] Gennes, P. G. D. *Solid State Comm.* **1972**, *10*, 753.

[14] Renn, S. R.; Lubensky, T. C. *Mol. Cryst. Liq. Cryst.* **1991**, *209*, 349.

[15] H, X.; Panarin, Y. P.; Vij, J. K.; Seed, A. J.; Hird, M.; Goodby, J. W. *J. Phys. : Condens. Matter.* **1995**, *7*, 7443.

[16] Li, M.-H.; Laux, V.; Nguyen, H.-T.; Sigaud, G.; Barois, P.; Isaert, N. *Liq. Cryst.* **1997**, *23*, 389.

[17] Dierking, I.; Lagerwall, S. T. *Liq. Cryst.* **1999**, *26*, 83.

[18] Ribeiro, A. C.; Dreyer, A.; ad J. F. Nicoud, L. O.; Soldera, A.; Guillon, D.; Galerne, Y. *J. Phys. II France* **1994**, *4*, 407.

[19] Ribeiro, A. C.; ad J. F. Nicoud, L. O.; Guillon, D.; Galerne, Y. *Eur. Phys. J. B* **1998**, *1*, 503.

[20] Srajer, G.; Pindak, R.; Waugh, M. A.; Goodby, J. W.; Patel, J. S. *Phys. Rev. Lett.* **1990**, *64*, 1545.

[21] Ribeiro, A. C.; Sebastiao, P. J.; Cruz, C. *Mol. Cryst. Liq. Cryst.* **2001**, *362*, 289.

[22] Goodby, J. W.; Waugh, M. A.; Stein, S. M.; Chin, E.; Pindak, R.; Patel, J. S. *J. Am. Chem. Soc.* **1989**, *111*, 8119.

[23] Navailles, L.; Barois, P.; Nguyen, H. T. *Phys. Rev. Let.* **1993**, *71*, 545.

[24] Dierking, I.; Lagerwall, S. T. *Liq. Cryst.* **1999**, *26*, 83.

[25] Dierking, I.; Giesselmann, F.; Zugenmaier, P. *Liq. Cryst.* **1994**, *17*, 17.

[26] Dierking, I. *Textures of Liquid Crystals*; Wiley-VCH, 2003.

[27] Renn, S. R.; Lubensky, T. C. *Mol. Cryst. Liq. Cryst.* **1991**, *209*, 349.

[28] Renn, S. R. *Phys. Rev. A* **1992**, *45*, 953.

[29] Nguyen, H. T.; Bouchta, A.; Navailles, L.; Barois, P.; Isaert, N.; Twieg, R. J.; Maaroufi, A.; Destrade, C. *J. De Phys. II* **1992**, *2*, 1889.

[30] Navailles, L.; Barois, P.; Nguyen, H. T. *Phys. Rev. Lett.* **1993**, *71*, 545.

[31] Navailles, L.; Pindak, R.; Barois, P.; Nguyen, H. T. *Phys. Rev. Lett.* **1995**, *74*, 5224.

[32] Luk'yanchuk, I. *Phys. Rev. E* **1998**, *57*, 574.

[33] Dozov, I. *Phys. Rev. Lett.* **1995**, *74*, 4245.

[34] Dozov, I.; Durand, G. *Europhys. Lett.* **1994**, *28*, 25.

[35] Ribeiro, A. C.; Barois, P.; Galerne, Y.; Oswald, L.; Guillon, D. *Eur. Phys. J. B* **1999**, *11*, 121.

[36] Catalano, D.; Chiezzi, L.; Domenici, V.; Geppi, M.; Veracini, C. A. *J. Phys. Chem. B* **2003**, *107*, 10104.

[37] Domenici, V.; Geppi, M.; Veracini, C. A. *ChemPhysChem* **2003**, *5*, 559.

[38] Domenici, V.; Geppi, M.; Veracini, C. A.; Zakharov, A. V. *J. Phys. Chem. B* **2005**, *109*, 18369.

[39] Powles, J. G.; Strange, J. H. *Proc. Phys. Soc.* **1963**, *82*, 6.

[40] Schaefer, D.; Leisen, J.; Spiess, H. W. *J. Magn. Reson., Ser. A* **1995**, *115*, 60.

[41] Zamir, S.; Poupko, R.; Luz, Z.; Huser, B.; Boeffel, C.; Zimmermann, H. *J. Am. Chem. Soc.* **1994**, *116*, 1973.

[42] Meyer, R. B. *Appl. Phys. Lett.* **1968**, *12*, 281.

[43] Meyer, R. B. *Appl. Phys. Lett.* **1969**, *14*, 208.

[44] Xu, J.; Veracini, C. A.; Dong, R. Y. *Phys. Rev. E* **2005**, *72*, 051703.

[45] Cifelli, M.; Domenici, V.; Veracini, C. A. *Mol. Cryst. Liq. Cryst.* **2005**, *429*, 167.

[46] Srajer, G.; Pindak, R.; Waugh, M.; Goodby, J. W.; Patel, J. S. *Phys. Rev. Lett.* **1990**, *64*, 1545.

[47] Fernsler, J.; Hough, L.; Shao, R. F.; Maclennan, J. E.; Navailles, L.; Brunet, M.; Madhusudana, N. V.; Mondain-Monval, O.; Boyer, C.; Zasadzinski, J.; Rego, J. A.; Walba, D. M.; Clark, N. A. *Proceedings Nat. Acad. Sciences U.S.A.* **2005**, *102*, 14191.

[48] Meyer, R. B.; Liebert, L.; Strzelecki, L.; Keller, P. *J. Phys. (paris)* **1975**, *36*, L69.

[49] Dong, R. Y.; Chiezzi, L.; Veracini, C. A. *Phys. Rev. E* **2002**, *65*, 041716.

[50] Galerne, Y.; Liebert, L. *Phys. Rev. Lett.* **1991**, *66*, 2891.

[51] Zalar, B.; Gregorovic, A.; Simsic, M.; Zidansek, A.; Blinc, R.; Keast, S.; Neubert, M. *Phys. Rev. Lett.* **1998**, *80*, 4458.

[52] Dolganov, P. V.; Bolotin, B. M.; Fukuda, A. *Phys. Rev. E* **2004**, *70*, 041708.

[53] Mach, P.; Pindak, R.; Levelut, A.-M.; Barois, P.; Nguyen, H. T.; Huang, C. C.; Furenlid, L. *Phys. Rev. Lett.* **1998**, *81*, 1015.

[54] Zalar, B.; Gregorovic, A.; Blinc, R. *Phys. Rev. E* **2000**, *62*, R37.

[55] Catalano, D.; Chiezzi, L.; Domenici, V.; Geppi, M.; Veracini, C.; Dong, R.; Csorba, K. *Macromol. Chem. Phys.* **2002**, *203*, 1594.

[56] Xu, J.; Dong, R. Y. *J. Phys. Chem. B* **2006**, *110*, 1221.

[57] Ferraz, A. *et al.*; private communication.

[58] Crank, J. *Mathematics of Diffusion*; Oxford university press, 1975.

[59] Carvalho, A.; Sebastião, P. J.; Ribeiro, A.; Nguyen, H. T.; Vilfan, M. *J. Chem. Phys.* **2001**, *115*, 10484.

[60] Ostrovskii, B. I.; Rabinovich, A. Z.; Sonin, A. S.; Strukov, B. A. *Sov. Phys. JETP* **1978**, *47*, 912.

Chapter 7

Ordering of Chiral Liquid Crystals: ^{13}C NMR Study

7.1 ^{13}C NMR

7.1.1 Introduction

Carbon-13 NMR spectroscopy is analogous to proton NMR and allows the identification of carbon atoms in an organic molecule just as proton NMR identifies hydrogen atoms in molecules. Since carbon is the element central to organic chemistry, carbon NMR plays an important role in determining the structure of unknown organic molecules and in the study of organic reactions and chemical processes. However, carbon NMR has a number of limitations that are not encountered in proton NMR. Since the major isotope of carbon, the ^{12}C isotope, has a spin quantum number of zero, it is therefore not magnetically active. The ^{13}C isotope is magnetically active with a spin quantum number of 1/2 much like a proton, but has a low abundance of 1.1%. Therefore, carbon NMR is much less sensitive than proton NMR. Also the carbon-13 gyromagnetic ratio (6.728284×10^7 radT^{-1}s^{-1}) is only 1/4 of that of proton, yielding a further drop in the sensitivity [1]. Another consequence of the low ^{13}C abundance is that the coupling between adjacent carbon-13 atoms is unlikely since 99% of the neighboring carbons are ^{12}C. However, protons attached to a carbon atom will split the carbon signal due to C-H dipolar couplings. The splitting will lower the signal to noise ratio. Hence high resolution carbon NMR spectra are usually obtained under the condition of proton decoupling, such that each nonequivalent carbon atom in a molecule will give a single ^{13}C peak. To compensate for the low natural abundance of ^{13}C nuclei, a greater number of scans is used to give a good ^{13}C spectrum.

7.1.2 Chemical Shifts of ^{13}C NMR

Chemically different carbons in an organic molecule do not experience the same magnetic field. Electrons shield the nucleus, thereby reducing the effective magnetic field at the nucleus which causes a spin transition to occur at a lower frequency. Thus, carbon chemical shift provides information about the electronic environment of a carbon nucleus. ^{13}C chemical shifts are reported relative to the standard, tetramethylsilane (TMS), in which the chemical shift of the four equivalent carbons is taken to be 0 ppm. Carbon chemical shifts are influenced by electronegative substituents and bonds, but more so by the shielding from the electronic distribution of non-spherical p-orbitals. The range of chemical shifts in which most carbon resonances appear is 0 to 220 ppm. This is about 10-20 times the range of proton chemical shifts. As a consequence, a peak can usually be observed for each carbon or each set of equivalent carbons. Since carbon atoms resonate over such a wide range, a systematic NMR study of the carbon chemical shifts can provide a tremendous advantage in solving structural problems. Figure 7.1 shows the typical ranges of absorption for various types of carbons [1]. The correlation chart can be divided into four sections. In the highest field, the saturated carbon atoms appear nearest to TMS (8 to 60 ppm). The next section of the correlation chart contains the carbons connected to electronegative atoms (40 to 80 ppm). The third section contains the alkyne and aromatic ring carbon atoms (100 to 175 ppm). And in the lowest field the carbonyl carbons appear (155 to 220 ppm). Thus, the chemical shift value of a carbon atom(s) can be used to identify the type of functional group present in the molecule.

7.2 One Dimensional ^{13}C Experiment With Proton Decoupling

As mentioned in Chapter 2, the heteronulear dipolar coupling (or dipole-dipole interaction) arises between the nuclear magnetic moments of two different spins. Thus the ^{13}C spectrum appears broadened due to the strong ^{1}H-^{13}C dipolar couplings. The typical coupling constant ($k = \mu_0\gamma_H\gamma_C\hbar/8\pi^2$) for a bonded ^{1}H-^{13}C pair is approximately 30kHzÅ^3. From Eq. (2.13), it is noted that there are two possible means of eliminating the dipolar interaction to give narrower ^{13}C lines. One approach gives to take advantage of the fact that the dipolar coupling is zero when the internuclear vector is oriented at the magic angle with respect to the magnetic field. This approach is the technique known as magic angle spinning which will be studied in Chapter 8. The second method to eliminate the effect of the ^{1}H nuclei on the ^{13}C spectrum is to manipulate the proton spins in such a way that their effects on the ^{13}C nuclei, when

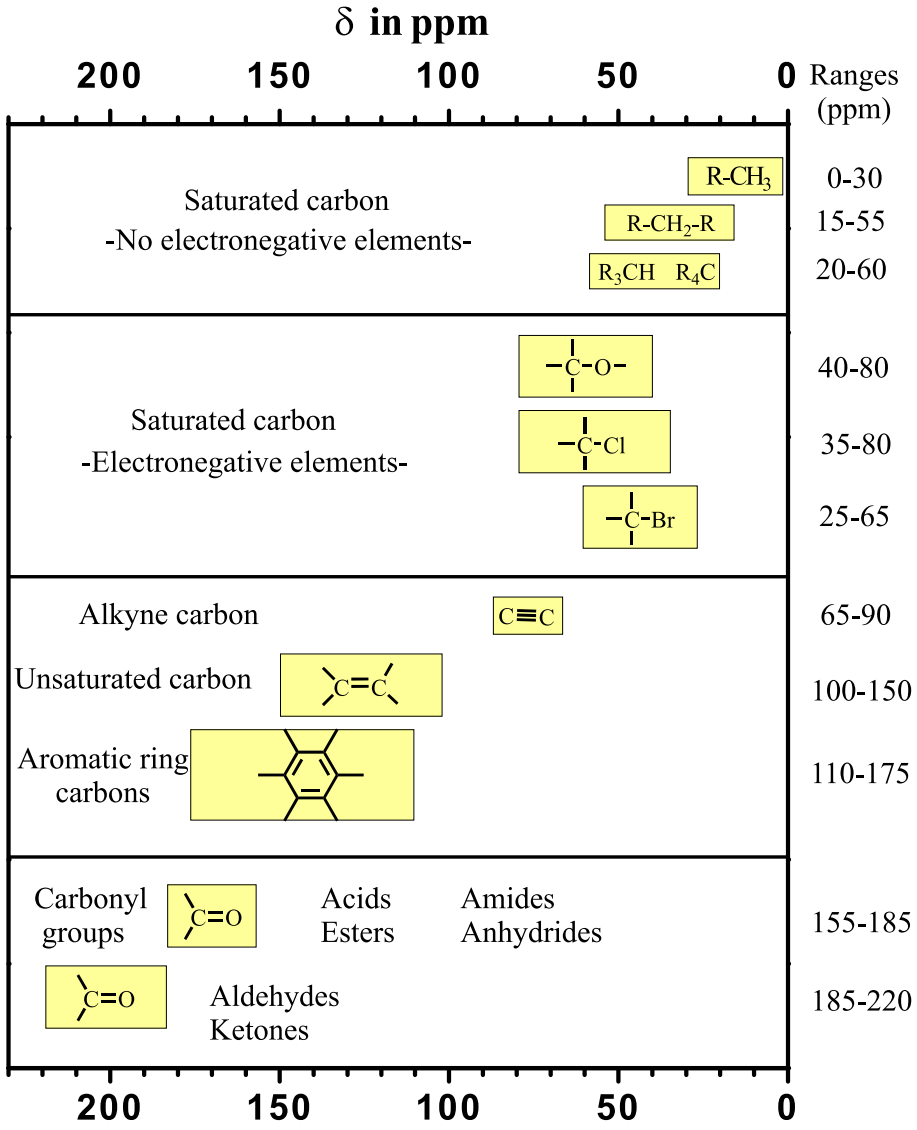

Figure 7.1: A correlation chart for ^{13}C chemical shifts (chemical shifts are listed in ppm from TMS). [1].

.

averaged over time, become zero. This is the solid-state version of proton spin decoupling: by applying radio frequency pulses that rotate the proton nuclear spins between their 'spin up' and 'spin down' states such that the average orientation of the ^{1}H magnetic moments tends to zero. The C-H dipolar coupling is therefore essentially averaged away.

Heteronuclear decoupling is one of the most important techniques in NMR spectroscopy, because it allows the acquisition of highly resolved and simplified spectra. Indeed, the invention of Composite Pulse Decoupling (CPD) sequence(s) has allowed more efficient decoupling [2]. A CPD sequence consists of a sequence of pulses, each with a specific flip angle and radio frequency phase. The CPD sequence for proton decoupling normally used for acquiring ^{13}C

spectra in liquids is named WALTZ-16 [3]. This works for most liquid state applications of ^{13}C spectroscopy. The widely used WALTZ-16 supercycle is

$$\textbf{WALTZ-16} = K\bar{K}\bar{K}K$$

with

$$K = 270(-90^\circ)360(90^\circ)180(-90^\circ)270(90^\circ)90(-90^\circ)180(90^\circ)360(-90^\circ)180(90^\circ)270(-90^\circ)$$

and

$$\bar{K} = 270(90^\circ)360(-90^\circ)180(90^\circ)270(-90^\circ)90(90^\circ)180(-90^\circ)360(90^\circ)180(-90^\circ)270(90^\circ)$$

The numbers outside the brackets are the actual pulse flip angles and the numbers within the brackets are the corresponding phase shifts.

A more efficient heteronuclear decoupling method for solids or liquid crystals is TPPM (two pulse phase modulation) [4]. In the TPPM decoupling sequence, a radio frequency irradiation is applied continuously, which can be expressed as two pulses P and $\bar{P}$ with opposite phases:

$$\textbf{TPPM} = P\bar{P}$$

where $P = 165(10^\circ)$ and $\bar{P} = 165(-10^\circ)$. The actual pulse width can be slightly different from 165° and the actual phase shift can be slightly different from ±10° without appreciably degrading the performance. If a system has ^{1}H chemical shift anisotropy, as well as other fields which resemble the Zeeman term in the spin Hamiltonian, they may generate perturbations for the proton resonance. In this case the continuous wave decoupling will fail due to the perturbations, but the TPPM approach can work well in this kind of system [5].

Later it is found that a stepwise change in the phase angle of the TPPM sequence, combined with overall phase cycling, offers even better results for broadband decoupling in liquid crystals and solids [6]. The method is called SPINAL-64, an acronym for Small Phase INcremental ALternation with 64 steps [7]. The basic elements are

$$Q = 165(10^\circ)165(-10^\circ)165(15^\circ)165(-15^\circ)165(20^\circ)165(-20^\circ)165(15^\circ)165(-15^\circ)$$

and

$$\bar{Q} = 165(-10^\circ)165(10^\circ)165(-15^\circ)165(15^\circ)165(-20^\circ)165(20^\circ)165(-15^\circ)165(15^\circ)$$

These elements are then combined into a supercycle SPINAL-64:

$$\textbf{SPINAL-64} = Q\bar{Q}\bar{Q}Q\ \bar{Q}QQ\bar{Q}$$

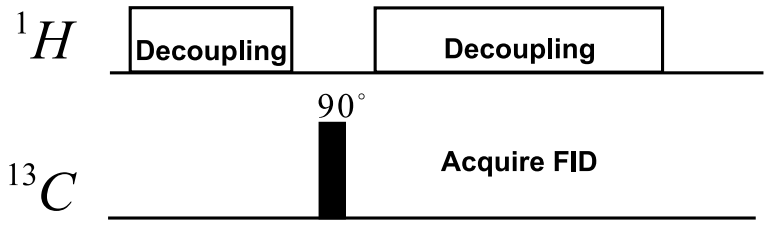

Figure 7.2: High-power proton decoupling pulse sequence.

.

Note that the performance of a CPD critically depends on the pulse width used in the CPD sequence as well as the decoupler power.

In NMR, spectra of rare spins such as ^{13}C are usually acquired with simultaneous decoupling of the abundant spins, which are most often protons, ^{1}H. This is achieved by removing spin-spin interactions (J couplings in liquid-state, heteronuclear dipolar interactions in solid-state), which otherwise might have deteriorating effects on the spectral resolution of ^{13}C spectra. The classic ^{13}C sequence is a 90° ^{13}C pulse followed by high-power ^{1}H decoupling (HPDEC) during acquisition [5], which has been adopted to study the isotropic phase of liquid crystals in this dissertation (See Figure 7.2). To set up this experiment, one needs to first determine the 90° pulse width for protons and carbons.

7.3 Cross Polarization

7.3.1 Introduction

In solid-state NMR spectroscopy, cross-polarization [8, 9] is a standard technique commonly used to enhance the sensitivity of rare spins and/or spins with low gyromagnetic ratio γ_S (S spins) by transferring polarization from the abundant, high γ_I spins (I spins). Since the low abundance of ^{13}C leads to a poor absorption of the radio frequency energy in a NMR experiment, one can overcome this limitation by exciting the protons in a sample followed by a sequence of two long-time pulses which make the ^{13}C and ^{1}H nuclei resonate at the same frequency, i.e., the so-called 'Hartman-Hahn' condition [8]. The process is called 'cross-polarization' and the duration of cross polarization is called the 'contact time' or 'spin-lock time'. Cross polarization usually involves a strong irradiation of the ^{13}C nuclei. Such experiments can also be used to determine the nature of spatial neighborhood of spin systems or to increase the repetition rate of experiments by exploiting differences in proton and carbon

relaxation times.

The cross polarization process is often explained and described by a thermodynamic analogy [9–11]. Suppose we have a system of abundant I and rare S spins, both of spin-1/2 nuclei. The observed NMR signal is proportional to the difference in populations of the two energy levels arising from the Zeeman interaction of the spins with the strong magnetic field B_0. Consider first the I spins, the relative populations of these two energy levels are governed by the Boltzmann distribution

$$\frac{N_{-1/2}}{N_{1/2}} = e^{-\hbar\gamma B_0/kT_L} \tag{7.1}$$

where N is the number of the spins, k is the Boltzmann constant, and T_L is the temperature of the lattice. The first step in the cross polarization experiment is to prepare the abundant I spin system into a low 'spin temperature' state. This is done by applying the spin-lock field B_{1I} along the y axis of the rotating frame immediately following the initial 90° pulse applied along the x axis. In the rotating frame, the relative populations of the two energy levels in the spin-locked state are

$$\frac{N_{-1/2}}{N_{1/2}} = e^{-\hbar\gamma B_{1I}/kT_I} \tag{7.2}$$

where T_I is the 'spin temperature' of the spin-locked abundant spins. By comparing Eqs. (7.1) and (7.2), one can get

$$T_I/T_L = B_{1I}/B_0 \tag{7.3}$$

Since $B_{1I} \ll B_0$, so $T_I \ll T_L$. Note that the quantity 'spin temperature' is inversely related to magnetization, so there exists a large polarization of the abundant I spin system spin locked along the y axis of the rotating frame. The second step of the cross polarization experiment is putting the S spin system into contact with the I spins by applying a radio frequency at the same time as the spin-locking field being applied to the I spins. At the 'Hartmann-Hahn' condition, the two spin systems are in efficient thermal contact so that they can exchange polarization. After a time $\tau \gg T_{IS}$, where T_{IS} denotes the cross-polarization time constant, the total spin system (I and S spins) reaches thermodynamic equilibrium characterized by a common spin temperature for the two spin subsystems. Cross-polarization relies on matching the amplitudes of the two radio frequency fields B_{1I} and B_{1S} at the Hartmann-Hahn condition, that is given by

$$\omega_{1I} = \omega_{1S} \tag{7.4}$$

or

$$\gamma_I B_{1I} = \gamma_S B_{1S} \tag{7.5}$$

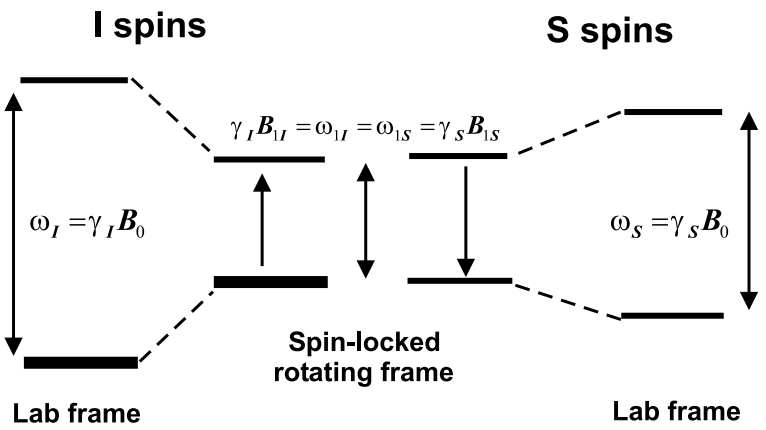

Figure 7.3: Energy level diagram of the I and the S spins. At the Hartmann-Hann condition the differences of the energy levels in the spin-locked rotating frame are equal and mutual spin flips allow for transfer of polarization from the I to the S spins.

.

At the Hartmann-Hahn condition, the energy-level splittings of the I and S spins match up in the rotating frame, and the energy-conserving flip-flop transitions in the dipole-dipole interaction are possible (See Figure 7.3). Cross-polarization in the rotating frame is widely used in NMR spectroscopy to enhance the spin polarization of rare nuclei with low gyromagnetic ratios in solids.

The cross polarization pulse sequence for polarization transfer from I spins to S spins is illustrated in Figure 7.4. The I spins are first excited by a 90° pulse which brings the I magnetization into the X-Y plane. Then the magnetization is 'spin-locked'by applying a radio frequency field, which is phase shifted from the excitation pulse by 90° at the resonance frequency of the I spins with a nutation frequency ω_{1I}. Polarization transfer from the spin-locked I spins to the S spins is achieved by simultaneously applying radio frequency of the S spins with a nutation frequency ω_{1S} which is matched to ω_{1I}. Here I and S spins are ^{1}H and ^{13}C, respectively. When the Hartmann-Hahn pulse is turned off, the ^{1}H radio frequency is left on during the acquisition of the ^{13}C free induction decay in order to provide ^{1}H decoupling. Before the cross polarization experiment, the 90° pulse widths for protons and carbons are first determined to insure that one is at least very close to the necessary Hartmann-Hahn matching condition for the ^{1}H-^{13}C cross polarization. Also the Hartmann-Hahn condition can be optimized by varying the ^{13}C radio-frequency power to obtain the largest ^{13}C signal intensity for quaternary carbons.

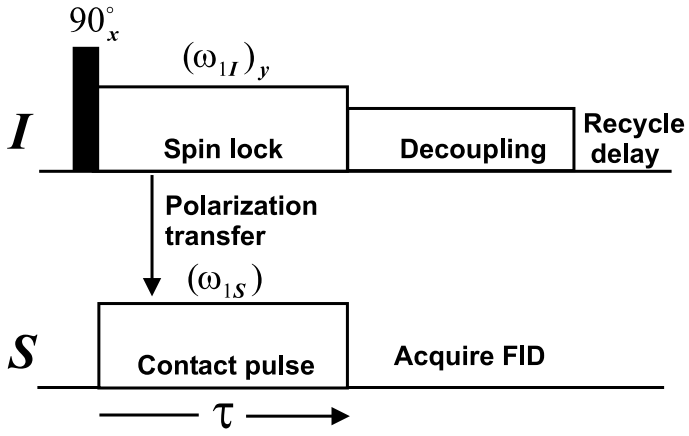

Figure 7.4: Cross polarization pulse sequence for polarization transfer from I spins to S spins.

.

7.3.2 Quantum Mechanics of Cross Polarization

It is worth pointing out that cross-polarization spectra obtained in double resonance experiments are of general theoretical interest because of the richness of different experimental regimes which can be realized. Here some details about the Hamiltonians for double resonance are addressed, including representative quantum-mechanical interaction representations for reference in the later chapters. The most common spin system encountered in double-resonance experiments contains two spin species I and S with different gyromagnetic ratios γ_I and γ_S. The sample, which contains N_I and N_S spins ($N_I \gg N_S$), is placed in a large static magnetic field $\vec{B}_0$. The field $\vec{B}_0$ is supposed to be along the $\vec{z}$ axis. In the laboratory frame, the high-field double-resonance Hamiltonian is [8]

$$H = H_I + H_S + H_{IS} + H_{rf}(t) \tag{7.6}$$

The Hamiltonians H_I and H_S are defined as

$$\begin{aligned} H_I &= H_{ZI} + H_{CI} + H_{II} \quad \texttt{with} \quad H_{ZI} = -\omega_I I_z \\ H_S &= H_{ZS} + H_{CS} + H_{SS} \quad \texttt{with} \quad H_{ZS} = -\omega_S S_z \end{aligned} \tag{7.7}$$

where H_{ZI} (or H_{ZS}) represents the Zeeman Hamiltonian, H_{CI} (or H_{CS}) is the chemical shift Hamiltonian, and H_{II} (or H_{SS}) describes the magnetic interactions between I (or S) spins. Also $\omega_I = \gamma_I B_0$ and $\omega_S = \gamma_S B_0$. $\hbar = 1$ is used for simplification. The Hamiltonian H_{IS} describes the interactions between I and S spin systems. $H_{rf}(t)$ describes the interaction of the spin system with the radio frequency magnetic fields of amplitudes B_{1I} and B_{1S} and frequencies ω_{1I} and ω_{1S}, respectively:

$$H_{rf}(t) = -2\omega_{1I} I_x \cos\omega_I t - 2\omega_{1S} S_x \cos\omega_S t \tag{7.8}$$

where $\omega_{1I} = \gamma_I B_{1I}$ and $\omega_{1S} = \gamma_S B_{1S}$. The time evolution of a statistical ensemble can be described by Schrödinger's equation $\partial\rho/\partial t = i[\rho(t), H]$ using the density operator $\rho(t)$. When the radio frequency fields used are large enough to produce good homonuclear and/or heteronuclear decoupling, it is convenient to transform the Hamiltonian to a doubly tilted frame since the spin-locked magnetizations of interest will lie along the effective fields in this frame. Hence, the statistical ensemble is described in a new quantum mechanical representation defined by the canonical transformation

$$\rho_{TR}(t) = (TR)\rho(t)(TR)^{+} \tag{7.9}$$

where

$$\begin{aligned} R = R_I R_S, \quad R_I = e^{(i\omega_I I_z t)}, \quad R_S = e^{(i\omega_S S_z t)} \\ T = T_I T_S, \quad T_I = e^{(i\theta_I I_y)}, \quad T_S = e^{(i\theta_S S_y)} \end{aligned} \tag{7.10}$$

The canonical transformation tilts the $\vec{Z}$ axis through the angles $\theta_I = \tan^{-1}[\omega_{1I}/\Delta\omega_I]$ and $\theta_S = \tan^{-1}[\omega_{1S}/\Delta\omega_S]$ with $\Delta\omega_I = \omega_I - \omega_{1I}$ and $\Delta\omega_S = \omega_S - \omega_{1S}$. The total Hamiltonian in the 'tilted rotating frame' may now be expressed as [11–13]:

$$\begin{aligned} H_{TR} \;=\; & -\omega_{eI} I_z - \omega_{eS} S_z + 2bI_x S_x \sin\theta_I \sin\theta_S + 2bI_z S_z \cos\theta_I \cos\theta_S \\ & -2bI_z S_x \cos\theta_I \sin\theta_S - 2bI_x S_z \sin\theta_I \cos\theta_S + P_2(\cos\theta_I) H_{II} + H_{II}^{ns} \end{aligned} \tag{7.11}$$

where

$$b = \frac{\mu_0 \gamma_I \gamma_S \hbar}{16\pi^2 r^3}(1 - 3\cos^2\theta) \tag{7.12}$$

r is the $I-S$ internuclear distance, θ is the angle between the internuclear vector and the static magnetic field, the effective fields are $\omega_{eI} = [\omega_{1I}^2 + (\Delta\omega_I)^2]^{1/2}$ and $\omega_{eS} = [\omega_{1S}^2 + (\Delta\omega_S)^2]^{1/2}$. $P_2(\cos\theta_I)H_{II}$ is the homonuclear dipolar interaction transformed to this frame. H_{II}^{ns} is the nonsecular part of the same dipolar Hamiltonian, which can be discarded by truncation [14]. This term is responsible for coupling between Zeeman and secular-dipolar I-spin reservoirs and the establishment of a common I and S spin temperatures. Here we will restrict our study to an isolated IS pair and drop these two terms. Close to the resonance or in a system with a weak IS coupling, then

$$|\omega_{1I}|, |\omega_{1S}| \gg |b|, |\Delta\omega_I|, |\Delta\omega_S| \tag{7.13}$$

which makes $\theta_I \approx 90^\circ$ and $\theta_S \approx 90^\circ$. For simplicity, the on resonance Hamiltonian can be expressed as

$$H_{TR} = -\omega_{eI} I_z - \omega_{eS} S_z + 2bI_x S_x \tag{7.14}$$

For the IS spin pair under consideration, it is convenient to further recast the Hamiltonian as

$$H_{TR} = (-\omega_\Sigma I_z^{14} + bI_x^{14}) + (-\omega_\Delta I_z^{23} + bI_x^{23}) \tag{7.15}$$

where $\omega_\Delta = \omega_{1I} - \omega_{1S}$, $\omega_\Sigma = \omega_{1I} + \omega_{1S}$ and the single-transition operators are defined by [13]

$$\begin{aligned} I_z^{23} &= \frac{I_z - S_z}{2}, \qquad I_z^{14} = \frac{I_z + S_z}{2} \\ I_x^{23} &= \frac{I_+S_- + I_-S_+}{2}, \qquad I_x^{14} = \frac{I_+S_+ + I_-S_-}{2} \end{aligned} \tag{7.16}$$

The initial I-spin 90_x° pulse changes the thermal equilibrium I_z polarization to an initial condition I_y which may be expressed in the tilted rotating frame as $\rho_{TR}(0) = I_z = I_z^{14} + I_z^{23}$. Eq. (7.15) shows that these two components experience different rotations in either the $\{|1>, |4>\}$ or the $\{|2>, |3>\}$ space about the instantaneous axes $\mathbf{n}^{14} = \{b, 0, \omega_\Sigma\}$ or $\mathbf{n}^{23} = \{b, 0, \omega_\Delta\}$ [15], where the states $|1>$, $|4>$, $|2>$, $|3>$ are accompanied by corresponding superscripts in equations (7.15) and (7.16). Therefore, the problem reduces to the independent evolution of two pseudo-spin $-1/2$ systems. After the cross-polarization interval τ, the tilted rotating frame S-spin polarization S_z (corresponding to S_y in the laboratory frame) is given by [15, 16]

$$\begin{aligned} \langle S_z \rangle (\tau) &\cong \frac{b^2}{b^2 + (\omega_\Delta)^2} \times \sin^2 \left[\frac{\tau}{2} \sqrt{b^2 + (\omega_\Delta)^2} \right] \\ &\cong \frac{b^2}{b^2 + (\omega_\Delta)^2} \times \frac{1}{2} \left\{ 1 - \cos \left[\tau \sqrt{b^2 + (\omega_\Delta)^2} \right] \right\} \end{aligned} \tag{7.17}$$

For a static sample b is time independent. The greatest enhancement of the S-spin magnetization is obtained when the usual Hartman-Hahn condition $\omega_\Delta = 0$, that is $\omega_{1I} = \omega_{1S}$, is met. For small resonance offsets, the condition becomes an equality in the amplitudes of the effective radio frequency fields. From Eq. (7.17), it is noticed that the size of the heteronuclear coupling b plays an important role. As long as b is large compared to the ω_Δ mismatch, cross polarization still takes place. The sensitivity to a given mismatch in limiting the amount of coherent magnetization transfer at the beginning of cross polarization is determined by the ratio of b to ω_Δ [17].

When the Hartmann-Hahn condition is exactly fulfilled, $\omega_\Delta = 0$, Eq. (7.17) will be simplified as

$$\langle S_z \rangle (\tau) \cong \frac{1}{2}[1 - \cos(b\tau)] \tag{7.18}$$

By introducing the spin-diffusion process, the observed magnetization (corresponding to $M_{S_z}(\tau)$ in the tilted rotating frame) after the spin lock will be expressed as [18, 19]

$$M_{S_z}(\tau) = M_{S_z}(0) \left[1 - \frac{1}{2} \exp\left(-\frac{\tau}{T_{II}} \right) - \frac{1}{2} \exp\left(-\frac{3\tau}{2T_{II}} \right) \cos(b\tau) \right] \tag{7.19}$$

where $M_{S_z}(0)$ is the initial magnetization at $\tau = 0$ and T_{II} represents the time constant for the spin-diffusion process among the abundant I spins. From Eq. (7.19) we know that the cross polarization rate depends not only on the spin-diffusion time T_{II} but also the dipolar coupling b. Figure 7.5 gives the theoretical calculation according to Eq. (7.19) for different values of T_{II} and b.

7.4 Theory of Chemical Shifts Analysis

From the time-averaged chemical shift Hamiltonian in Eq. (2.16), one can write in the high-field limit:

$$\overline{H_{CS}} = \gamma\hbar B_0 I_z \sigma_{iso} + \sqrt{\frac{2}{3}}\gamma\hbar B_0 I_z \langle R_{2,0}\rangle \tag{7.20}$$

where the bar over the Hamiltonian denotes the time average due to internal bond rotations and overall motions of the molecule, $\langle R_{2,0}\rangle$ is the corresponding time-averaged second rank irreducible spherical tensor which has been defined in Eq. (2.15). To describe the internal motions of the fragment and overall motions of the molecules, the following Euler transformations need to be considered:

$$\begin{gathered}
\text{Director frame } (\hat{\mathbf{n}}) \overset{(\phi_0,\theta_0,\psi_0)}{\Longrightarrow} \text{Lab frame } (\vec{B_0}) \\
\text{Director frame } (\hat{\mathbf{n}}) \overset{(\phi,\theta,\psi)}{\Longrightarrow} \text{Molecular frame } (X_m,Y_m,Z_m) \\
\text{Molecular frame } (X_m,Y_m,Z_m) \overset{(\alpha_F,\beta_F,\gamma_F)}{\Longrightarrow} \text{Fragment frame } (X_F,Y_F,Z_F) \\
\text{Fragment frame } (X_F,Y_F,Z_F) \overset{(0,\beta,\frac{\pi}{2})}{\Longrightarrow} \text{PAS frame } (\sigma_{xx},\sigma_{yy},\sigma_{zz})
\end{gathered}$$

These transformations are illustrated in Fig. 7.6. Accordingly, the general expression of $\langle R_{2,0}\rangle$ can be obtained:

$$\langle R_{2,0}\rangle = \sum_{qpnm} D_{q0}(\phi_0,\theta_0,\psi_0)\left\langle D^*_{qp}(\phi,\theta,\psi)D^*_{pn}(\alpha_F,\beta_F,\gamma_F)D^*_{nm}(0,\beta,\frac{\pi}{2})\right\rangle \rho_{2m} \tag{7.21}$$

where ρ_{2m} has already been defined in Table 2.1. The brackets denote the effect of time averaging and ensemble averaging. Now we first consider the transformation from the fragment frame (X_F,Y_F,Z_F) to the principal axis system (PAS) frame:

$$\begin{aligned}
R'_{2,0} &= \sum_m \left\langle D^*_{0m}(0,\beta,\frac{\pi}{2})\right\rangle \rho_{2m} = \sqrt{\frac{2}{3}}[P_2(\cos\beta)(\sigma_{zz}-\sigma_{yy}) + \frac{1}{2}(\sigma_{yy}-\sigma_{xx})] \\
R'_{2,\pm1} &= \sum_m \left\langle D^*_{\pm1m}(0,\beta,\frac{\pi}{2})\right\rangle \rho_{2m} = \mp\frac{1}{2}\sin 2\beta(\sigma_{zz}-\sigma_{yy}) \\
R'_{2,\pm2} &= \sum_m \left\langle D^*_{\pm2m}(0,\beta,\frac{\pi}{2})\right\rangle \rho_{2m} = \frac{1}{2}[(\sin^2\beta)\sigma_{zz} + (\cos^2\beta)\sigma_{yy} - \sigma_{xx}]
\end{aligned} \tag{7.22}$$

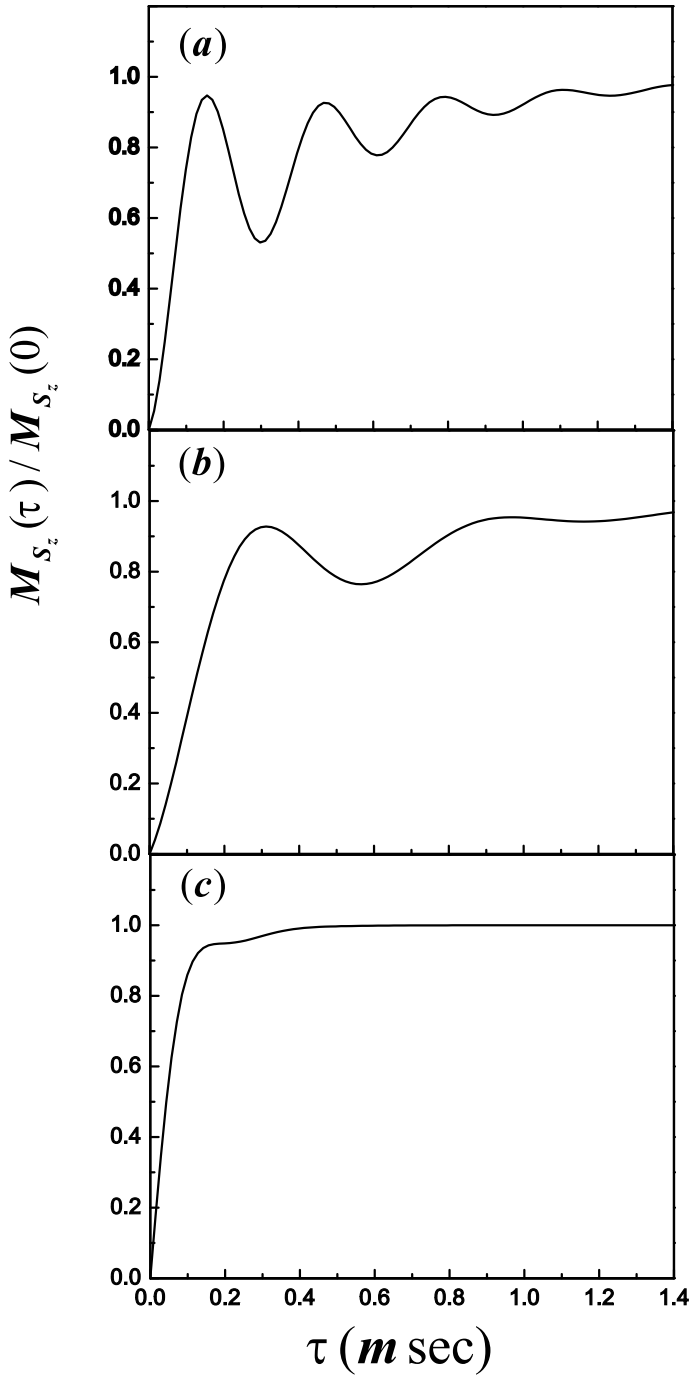

Figure 7.5: Evolution of normalized S spin magnetization $M_{S_z}(\tau)/M_{S_z}(0)$ as a function of the spin-diffusion time T_{II} and the dipolar coupling b calculated from Eq. (7.19). (a) The computed curve uses $T_{II} = 500\mu s$ and $b = 20kHz$. (b) The computed curve uses $T_{II} = 500\mu s$ and $b = 10kHz$. (c) The computed curve uses $T_{II} = 100\mu s$ and $b = 20kHz$.

.

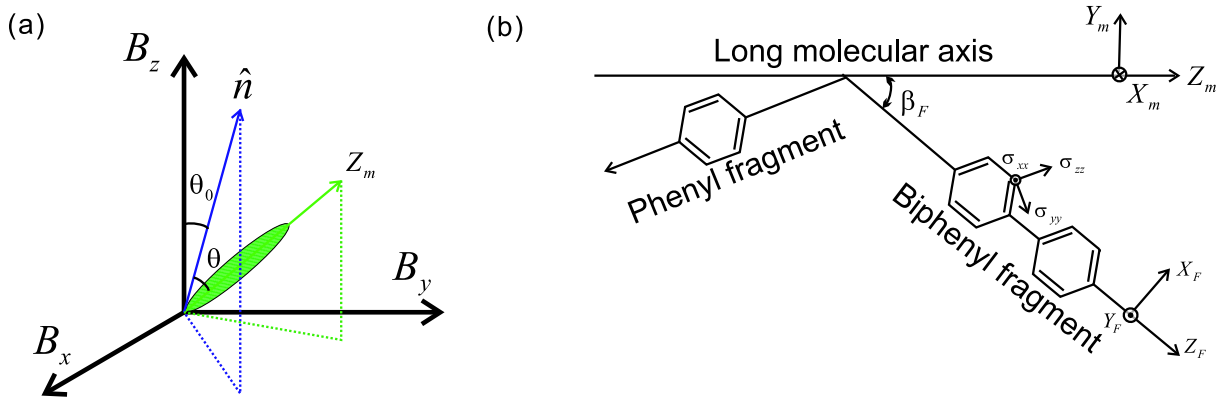

Figure 7.6: (a) The schematic of the orientation of a molecule with respect to the director $\hat{\mathbf{n}}$ in the magnetic field ($\vec{B}_0$). (b) The schematic of the principal axis system of a carbon chemical shift tensor (σ_{xx},σ_{yy},σ_{zz}), a fragment coordinate system (X_F,Y_F,Z_F), and the molecular coordinate system (X_m,Y_m,Z_m).

.

where the primed tensors $R'_{2,n}$ correspond to the fragment frame. In this study, from figure 7.6(a) the transformation from the fragment frame (X_F,Y_F,Z_F) to PAS frame (σ_{xx}, σ_{yy}, σ_{zz}) involves $\beta = 60°, 120°$ for protonated carbons, and $\beta = 0°$ for unprotonated (or quaternary) carbons. In practice, these angles might be slightly distorted from the above normal values ($< 2°$) due to the neighboring atoms, but the above β angles can still provide a good approximation for the calculation. It is also noted that in the phenyl or biphenyl groups, the ring usually carries out fast 180° flips, and $R'_{2,\pm1}$ is therefore averaged to zero ($\beta \leftrightarrow -\beta$). So when $q = 0$ in Eq. (7.21), one has

$$\begin{aligned}\langle R_{2,0}\rangle_0 = P_2(\cos\theta_0)\Bigg[&\sum_p \left\langle D^*_{0p}(\phi,\theta,\psi)D^*_{p0}(\alpha_F,\beta_F,\gamma_F)\right\rangle R'_{2,0} \\ &+\sum_p \left\langle D^*_{0p}(\phi,\theta,\psi)D^*_{p-2}(\alpha_F,\beta_F,\gamma_F)\right\rangle R'_{2,-2} \\ &+\sum_p \left\langle D^*_{0p}(\phi,\theta,\psi)D^*_{p2}(\alpha_F,\beta_F,\gamma_F)\right\rangle R'_{2,2}\Bigg]\end{aligned} \tag{7.23}$$

By summing over p, one can obtain:

$$\begin{aligned}&\sum_p D^*_{0p}(\phi,\theta,\psi)D^*_{p0}(\alpha_F,\beta_F,\gamma_F) \qquad (7.24)\\ = \quad & P_2(\cos\theta)P_2(\cos\beta_F) - \frac{3}{4}\sin 2\beta_F \sin 2\theta\cos(\alpha_F+\psi) + \frac{3}{4}\sin^2\beta_F\sin^2\theta\cos(2\alpha_F+2\psi)\end{aligned}$$

and

$$\begin{aligned}
&\sum_p D^*_{0p}(\phi,\theta,\psi)D^*_{p-2}(\alpha_F,\beta_F,\gamma_F) + \sum_p D^*_{0p}(\phi,\theta,\psi)D^*_{p2}(\alpha_F,\beta_F,\gamma_F) \qquad (7.25)\\
= \quad & \sqrt{\frac{3}{2}}P_2(\cos\theta)\sin^2\beta_F\cos 2\gamma_F\\
&+\sqrt{\frac{3}{8}}\sin 2\theta\sin\beta_F\left[(1+\cos\beta_F)\cos(\alpha_F+2\gamma_F+\psi)-(1-\cos\beta_F)\cos(\alpha_F-2\gamma_F+\psi)\right]\\
&+\sqrt{\frac{3}{2}}\sin^2\theta[(\frac{1+\cos\beta_F}{2})^2\cos(2\alpha_F+2\gamma_F+2\psi)+(\frac{1-\cos\beta_F}{2})^2\cos(2\alpha_F-2\gamma_F+2\psi)]
\end{aligned}$$

To simplify the derivation, the fragment and molecular frames are chosen such that $\alpha_F = 90°$ and $\gamma_F = 0°$ (See figure 7.6(b)). By defining three molecular order parameters:

$$\begin{aligned}
S_{00} &= \left\langle \tfrac{3}{2}\cos^2\theta - \tfrac{1}{2}\right\rangle = S_{zz}\\
S_{01} &= \langle \sin 2\theta \sin\psi\rangle\\
S_{02} &= \left\langle \sin^2\theta\cos 2\psi\right\rangle = \tfrac{2}{3}(S_{xx}-S_{yy}) \qquad (7.26)
\end{aligned}$$

Eq. (7.23) is rewritten as:

$$\begin{aligned}
\langle R_{2,0}\rangle_0 = P_2(\cos\theta_0)\Bigg\{&\left[P_2(\cos\beta_F)S_{00}+\frac{3}{4}\sin(2\beta_F)S_{01}-\frac{3}{4}\sin^2\beta_F S_{02}\right]R'_{2,0}\\
&+\left[\sqrt{\frac{3}{2}}\sin^2\beta_F S_{00}-\sqrt{\frac{3}{8}}\sin(2\beta_F)S_{01}-\sqrt{\frac{3}{8}}(1+\cos^2\beta_F)S_{02}\right]R'_{2,2}\Bigg\} \qquad (7.27)
\end{aligned}$$

Similarly, by defining three biaxial order parameters [20]:

$$\begin{aligned}
S_{10} &= \langle \sin 2\theta\sin\phi\rangle\\
S_{11} &= \langle \cos\theta\cos\phi\cos\psi - \cos 2\theta\sin\phi\sin\psi\rangle\\
S_{12} &= \left\langle \sin\theta\cos\phi\sin 2\psi + \tfrac{1}{2}\sin 2\theta\sin\phi\cos 2\psi\right\rangle \qquad (7.28)
\end{aligned}$$

one can get for $q = \pm 1$ $\langle R_{2,0}\rangle_{\pm 1}$:

$$\begin{aligned}
&\langle R_{2,0}\rangle_{-1} + \langle R_{2,0}\rangle_{+1}\\
= \quad & \sin 2\theta_0\sin\phi_0\Bigg\{\left[\frac{3}{4}P_2(\cos\beta_F)S_{10}+\frac{3}{2}\sin(2\beta_F)S_{11}+\frac{9}{8}\sin^2\beta_F S_{12}\right]R'_{2,0}\\
&+\left[\frac{3}{4}\sqrt{\frac{3}{2}}\sin^2\beta_F S_{10}-\sqrt{\frac{3}{2}}\sin(2\beta_F)S_{11}-\frac{3}{4}\sqrt{\frac{3}{2}}(1+\cos^2\beta_F)S_{12}\right]R'_{2,2}\Bigg\} \qquad (7.29)
\end{aligned}$$

And with another three biaxial order parameters [20]

$$\begin{aligned}
S_{20} &= \left\langle \sin^2\theta\cos(2\phi)\right\rangle\\
S_{21} &= \left\langle \sin\theta\sin 2\phi\cos\psi + \tfrac{1}{2}\sin 2\theta\cos 2\phi\sin\psi\right\rangle\\
S_{22} &= \left\langle \tfrac{1}{2}(1+\cos^2\theta)\cos 2\phi\cos 2\psi - \cos\theta\sin 2\phi\sin 2\psi\right\rangle \qquad (7.30)
\end{aligned}$$

$\langle R_{2,0}\rangle_{\pm 2}$ for $q = \pm 2$ becomes:

$$\begin{aligned} & \langle R_{2,0}\rangle_{-2} + \langle R_{2,0}\rangle_{+2} \\ = \quad & \sin^2\theta_0 \cos 2\phi_0 \left\{ \left[\frac{3}{4} P_2(\cos\beta_F) S_{20} - \frac{9}{8}\sin(2\beta_F) S_{21} - \frac{3}{2}\sin^2\beta_F S_{22} \right] R'_{2,0} \right. \\ & \left. + \left[\frac{3}{4}\sqrt{\frac{3}{2}}\sin^2\beta_F S_{20} + \frac{3}{4}\sqrt{\frac{3}{2}}\sin(2\beta_F) S_{21} - \sqrt{\frac{3}{2}}(1+\cos^2\beta_F) S_{22} \right] R'_{2,2} \right\} \end{aligned} \tag{7.31}$$

Finally, using the expression of $\langle R_{2,0}\rangle = \langle R_{2,0}\rangle_0 + \langle R_{2,0}\rangle_{-1} + \langle R_{2,0}\rangle_{+1} + \langle R_{2,0}\rangle_{-2} + \langle R_{2,0}\rangle_{+2}$, the observed chemical shift of a particular carbon site in a mesophase can be generally expressed as:

$$\begin{aligned} \langle\sigma\rangle &= \sigma_{iso} + \sqrt{\frac{2}{3}}\langle R_{2,0}\rangle \\ &= \sigma_{iso} + a\left(\sqrt{\frac{2}{3}} P_2(\cos\beta_F) R'_{2,0} + (\sin^2\beta_F) R'_{2,2} \right) \\ &\quad + b\left(\sqrt{\frac{3}{8}}(\sin 2\beta_F) R'_{2,0} - \frac{1}{2}(\sin 2\beta_F) R'_{2,2} \right) \\ &\quad + c\left(\sqrt{\frac{3}{8}}(\sin^2\beta_F) R'_{2,0} + \frac{1}{2}(1+\cos^2\beta_F) R'_{2,2} \right) \end{aligned} \tag{7.32}$$

with

$$\begin{aligned} a &= P_2(\cos\theta_0) S_{00} + \frac{3}{4}\sin 2\theta_0 \sin\phi_0 S_{10} + \frac{3}{4}\sin^2\theta_0 \cos 2\phi_0 S_{20} \\ b &= P_2(\cos\theta_0) S_{01} + \sin 2\theta_0 \sin\phi_0 S_{11} - \sin^2\theta_0 \cos 2\phi_0 S_{21} \\ c &= -P_2(\cos\theta_0) S_{02} + \sin 2\theta_0 \sin\phi_0 S_{12} - \sin^2\theta_0 \cos 2\phi_0 S_{22} \end{aligned} \tag{7.33}$$

This equation can be used to obtain the local order parameters from the ^{13}C NMR chemical shifts. Now, the phase biaxiality is normally difficult to observe in an aligned sample. In addition, it is hard to detect the phase biaxiality when θ_0 is small, according to Eq. (7.32). Therefore, the phase biaxiality is usually neglected in interpreting NMR chemical shifts. In this case, Eq. (7.32) can be reduced as:

$$\begin{aligned} \langle\sigma\rangle &= \sigma_{iso} + \sqrt{\frac{2}{3}}\langle R_{2,0}\rangle_0 \\ &= \sigma_{iso} + \sqrt{\frac{2}{3}} P_2(\cos\theta_0) \left\{ \left[P_2(\cos\beta_F) S_{00} + \frac{3}{4}\sin(2\beta_F) S_{01} - \frac{3}{4}\sin^2\beta_F S_{02} \right] R'_{2,0} \right. \\ &\quad \left. + \left[\sqrt{\frac{3}{2}}\sin^2\beta_F S_{00} - \sqrt{\frac{3}{8}}\sin(2\beta_F) S_{01} - \sqrt{\frac{3}{8}}(1+\cos^2\beta_F) S_{02} \right] R'_{2,2} \right\} \end{aligned} \tag{7.34}$$

which means that only θ_0 is needed in the transformation from the director frame to the lab frame. Indeed, it is found that the above equation is suitable for the SmC* phase of the

studied samples. Since the rotation about the long molecular axis becomes hindered in the SmC^* phase, then S_{01} will play an important role in interpreting the NMR chemical shifts. Thus, different segments of the molecule do not in general share a common principal axis system, which has been proved by optical [21] and x-ray measurements [22]. This rotation hindrance is important for creating polarization order in smectic layers.

If molecules carry on fast rotation along their long axes, such as in nematic and SmA phases, S_{01} is averaged to zero. When the director is aligned along the magnetic field ($\theta_0 = 0$), Eq. (7.34) can be rewritten as

$$\begin{aligned}\langle\sigma\rangle &= \sigma_{iso} + \left(\sqrt{\frac{2}{3}}P_2(\cos\beta_F)R'_{2,0} + (\sin^2\beta_F)R'_{2,2}\right)S_{00} \\ &\quad - \left(\sqrt{\frac{3}{8}}(\sin^2\beta_F)R'_{2,0} + \frac{1}{2}(1+\cos^2\beta_F)R'_{2,2}\right)S_{02} \end{aligned} \tag{7.35}$$

In our simulation, β_F was set as 0 to get the segmental order parameters S'_{zz} and $S'_{xx} - S'_{yy}$. Then one finds

$$\begin{aligned}\langle\sigma\rangle &= \sigma_{iso} + \sqrt{\frac{2}{3}}R'_{2,0}S'_{00} - R'_{2,2}S'_{02} \\ &= \sigma_{iso} + \frac{2}{3}S'_{zz}[P_2(\cos\beta)(\sigma_{zz} - \sigma_{yy}) + \frac{1}{2}(\sigma_{yy} - \sigma_{xx})] \\ &\quad + \frac{1}{3}(S'_{xx} - S'_{yy})[\sigma_{xx} - \cos^2\beta\sigma_{yy} - \sin^2\beta\sigma_{zz}] \end{aligned} \tag{7.36}$$

Thus we can get S'_{zz} and $S'_{xx} - S'_{yy}$ for the biphenyl fragment and the phenyl ring by fitting to the observed chemical shifts of carbons from each fragment, which have different chemical shift tensors. By comparing Eqs. (7.35) and (7.36), the relation [23]:

$$S'_{00} \approx S_{00}P_2(\cos\beta_F) \tag{7.37}$$

is found, which is useful to get the angle β_F (See Fig. 7.6).

7.5 Experiment

We have carried out 1D ^{13}C NMR measurements on aligned samples of partially deuterated 10B1M7, and partially deuterated 11EB1M7. The achiral chain of 10B1M7 was deuterated, but this did not influence the observation of aromatic carbon peaks. It is noted that the carbons on the phenyl of 11EB1M7-d_2 or on the biphenyl of 11EB1M7-d_8 could not be easily detected through cross polarization due to the ring deuteration. These two deuterated

samples were put together for the ^{13}C study. Since changes in the chain carbon chemical shifts are considerably less upon entering the ordered phases, the present study focuses on the chemical shifts observed from the aromatic parts of these two chiral smectogens. The NMR experiments were performed with a two-channel HX solid probe at 100.6 MHz for ^{13}C and 400 MHz for ^{1}H. The 1D isotropic ^{13}C spectrum was obtained by collecting FIDs with a WALTZ-16 proton decoupling sequence (See Figure 7.2). The ^{13}C spectra in SmA and SmC* phases were collected using the cross polarization pulse sequence (See Figure 7.4). The ^{1}H 90° pulse width was 3.1μs. Proton decoupling during the ^{13}C signal acquisition was accomplished with the SPINAL-64 pulse sequence having a decoupling field of 40.4 kHz. To avoid sample heating, the recycle delay between each FID acquisition was 7s. Each spectrum was obtained by signal averaging 128 or 256 scans. The temperature calibration of carbon data was carried out at a given air flow using the known temperature-dependent quadrupolar splittings of the studied liquid crystals [23].

7.6 ^{13}C NMR Study of 10B1M7

Figure 7.7 shows some typical ^{13}C spectra, with peak assignments, recorded at several different temperatures in 10B1M7. It is seen that the ^{13}C lines are broadened in the SmC* phase. Figure 7.8 shows a plot of the aromatic ^{13}C shifts versus temperature in the SmA and SmC* phase of 10B1M7. The carbon labels are those indicated in Fig. 1.10. Let us first look at the local order parameter matrices (i.e. Eq. (7.36)) of the phenyl and biphenyl fragments derived from the carbon chemical shift data, and compare them with the corresponding values obtained from the deuteron data [24]. Here the 'molecular' frame is identical to the local fragment frame attached to the studied fragment. Figure 7.9 shows the local order parameter S'_{zz} for 10B1M7 versus temperature, which is calculated using chemical shift tensors listed in Table 7.1. The choice of chemical shift tensors is based on those carbon sites found in similar LC and model compounds in the literature. This is necessary as such information is unavailable for 10B1M7. To alleviate this difficulty, CSA tensors in several new and not enriched LC compounds will be measured for the first time (See Chapter 8). As seen in this figure, the transition from SmA to SmC* phase is clearly delineated and the value of the phenyl ring is higher than that of the biphenyl fragment. The values of the phenyl and biphenyl fragments compare well with those derived from the deuteron splitting data [23], thereby supporting our ^{13}C peak assignments in the aromatic region. It is important to point out that Eq. (7.36) is strictly correct only for the SmA phase, since the gradual decreasing S'_{zz} for the phenyl and biphenyl fragments in the tilted SmC* phase, however, show slightly

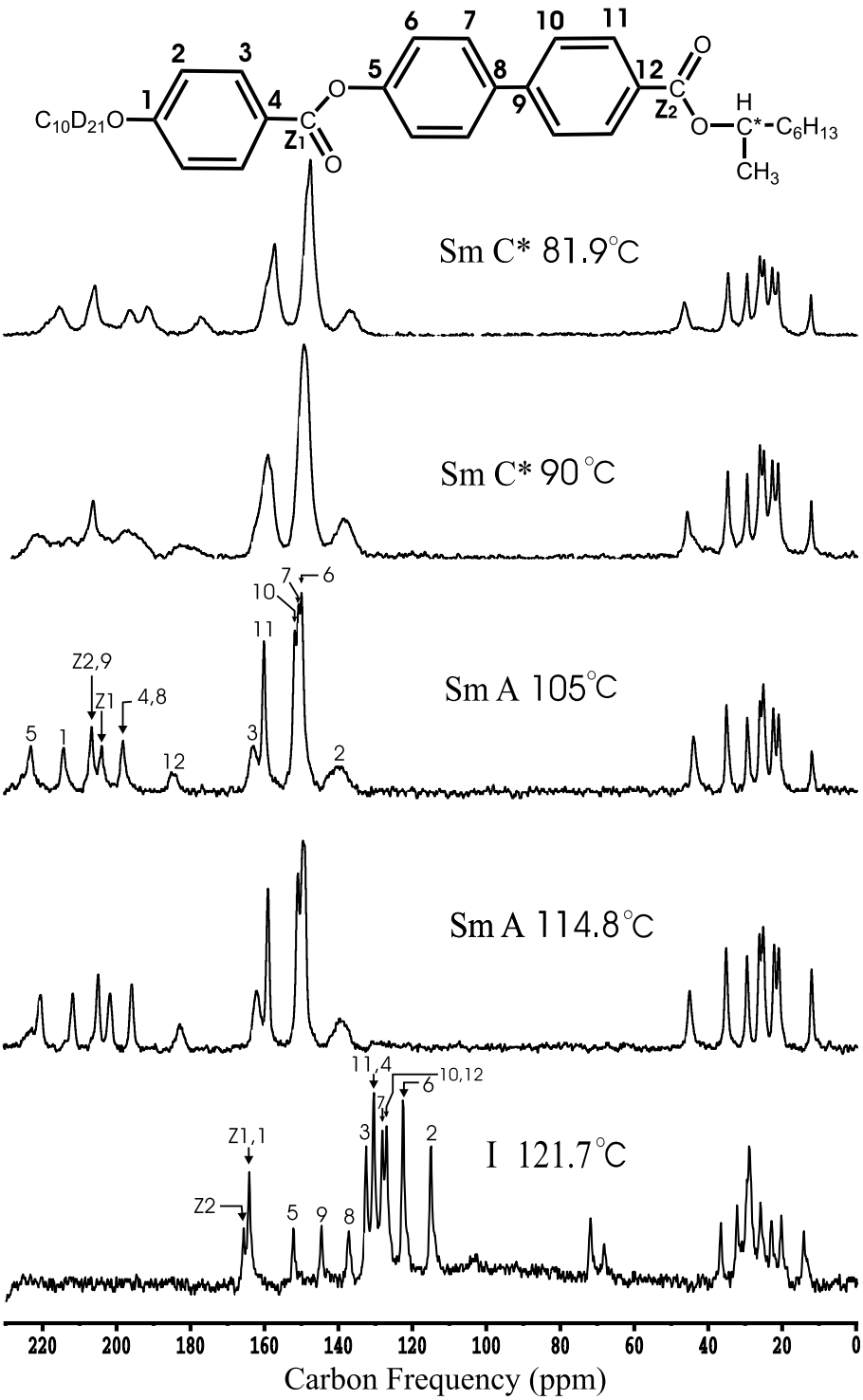

Figure 7.7: Typical ^{13}C spectra observed in the aligned sample of 10B1M7 at several temperatures by cooling from the isotropic phase. The carbon peak assignments in isotropic and smectic phases are indicated.

.

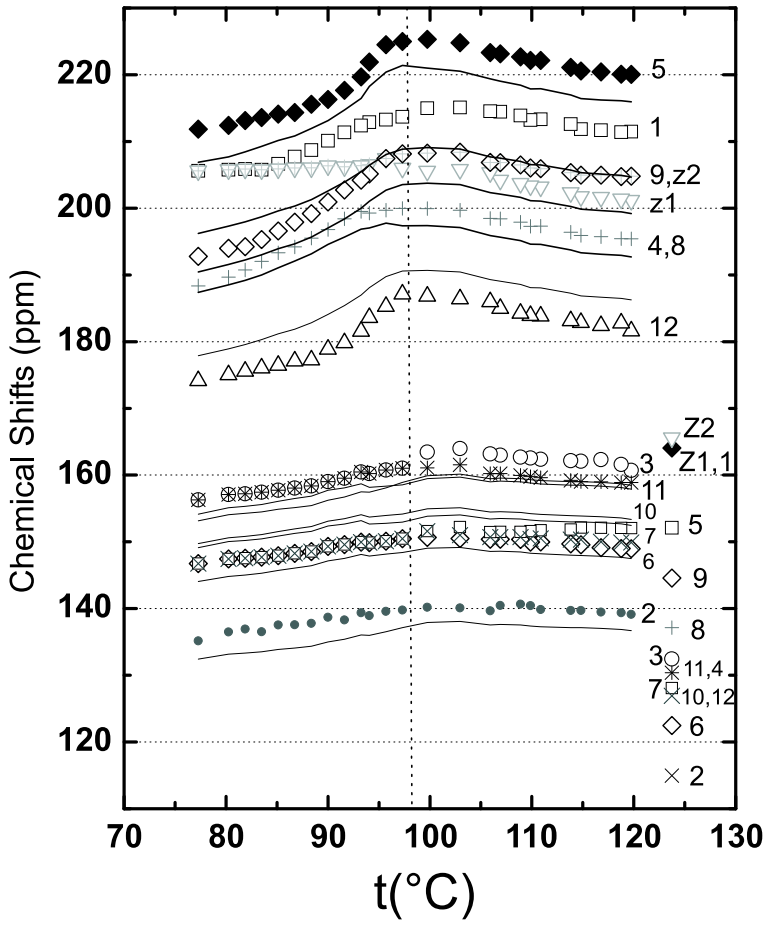

Figure 7.8: Plot of chemical shifts of aromatic carbons in the isotropic and smectic phases of 10B1M7. Solid lines denote, starting from the top, theoretical fitting curves for C5, C9, C4, C8, C12, C3, C11, C10, C7, C6 and C2.

.

different temperature behaviors. Thus, the observed S'_{zz} behaviors in the SmC* phase with decreasing temperature may well be due to the temperature dependent tilt angle. A proper treatment of molecular order parameters in the SmC* phase is required and will be considered below.

From the two local S'_{zz} values of the phenyl and biphenyl fragments at each temperature, one can calculate the angle between their para axes in the SmA phase. An average angle of 14.4° was estimated. This agrees well with 14.5° which was given before by deuteron NMR work [23]. Based on this information, one can then determine the location of the long Z_m axis for the molecular core in terms of β_F^{biph} and β_F^{ph}. From Eq. (7.37), the following relation can be obtained:

$$\frac{P_2(\cos\beta_F^{ph})}{P_2(\cos\beta_F^{biph})} = \frac{S'^{ph}_{zz}}{S'^{biph}_{zz}} \tag{7.38}$$

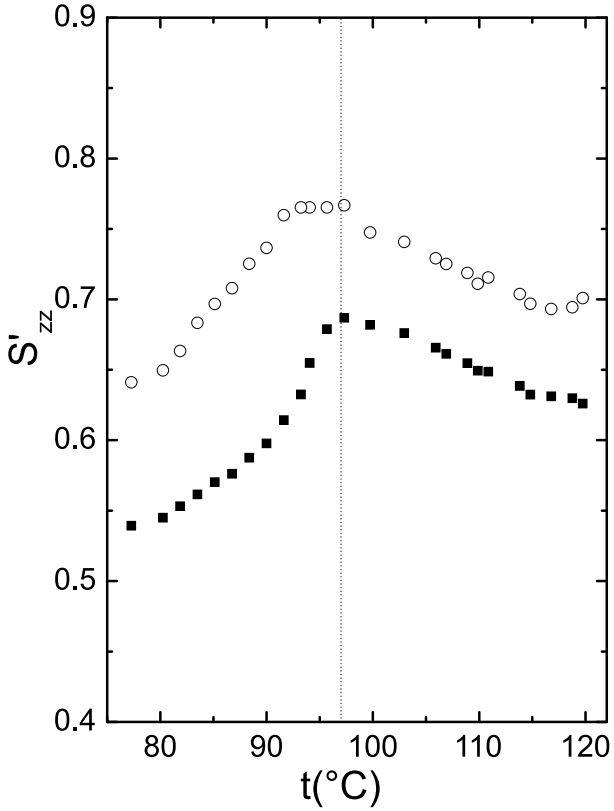

Figure 7.9: Plot of local order parameter S'_{zz} in the SmA and SmC* phase of 10B1M7. Open and closed symbols denote phenyl and biphenyl fragments, respectively.

.

Table 7.1: Chemical shift tensors in ppm of 10B1M7 (experimental values in parentheses have an accuracy of about 3 ppm).

Carbon	σ_{xx}	σ_{yy}	σ_{zz}	σ_{iso}	Reference
C2	18.7	131.7	184.7	111.7(114.9)	[25]
C3	15	153	226	131.3(132.4)	[25]
C4	14.6	147.4	219.3	127.1(130.4)	[26]
C5	71.7	137.4	255.9	155(152.1)	[27]
C6	30	149.3	183.0	120.8(122.5)	[28]
C7	21.8	145.5	217.9	128.4(128.1)	[27]
C8	14.4	169.1	235.9	139.8(137.1)	[26]
C9	20	173	236	143(144.6)	[27]
C10	21.3	150.2	200.8	124.1(126.9)	[27]
C11	15	153	226	131.3(130.4)	[29]
C12	14.6	147.4	219.3	127.1(126.9)	[26]

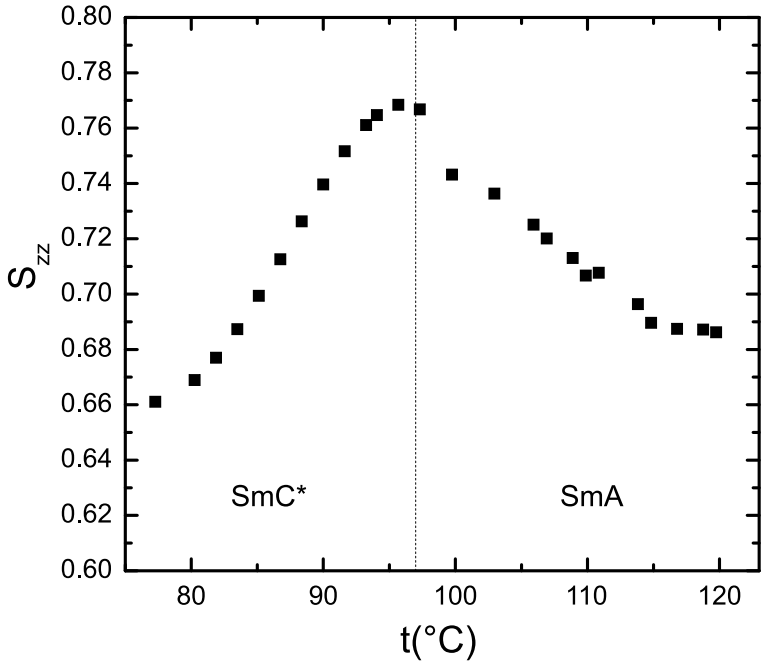

Figure 7.10: Plot of core (long molecular) order parameter S_{zz} in the SmA and SmC* phase of 10B1M7.

.

Using the above relation, the average β_F^{ph} is found to be around 0.1°, indicating that the phenyl para axis is close to the most ordered axis of the molecular core, a conclusion already made in a previous deuteron study [23]. In the following calculations, we assume a constant average β_F^{ph} for this sample over the range of studied temperatures. Since the core Z_m axis is known, it is more useful to discuss the orientational ordering of the molecular core in terms of S_{00}, S_{02} and S_{01}, using a molecular axis system (X_m, Y_m, Z_m). Even though Z_m is known, the choice of Y_m w.r.t. the X_F, Z_F plane on the biphenyl fragment can only be justified by additional experimental evidence (see below). In SmA phase, S_{01} is zero and the temperature behaviors of S'_{zz}'s of the phenyl and biphenyl fragments are found to be identical, while in the SmC* phase, a non-zero S_{01} is probably responsible for the observed different temperature behaviours of the S'_{zz}'s.

Using $\beta_F^{biph} = 14.2°$ and $\beta_F^{ph} = 0.1°$ in Eq. (7.35) to fit C2-C12 chemical shifts (C1 is not used due to the unavailability of its shift tensor) in the SmA phase, the core order parameters S_{00} (S_{zz}) and S_{02} (or $S_{xx} - S_{yy}$) can be obtained. S_{00} is identical to that of the phenyl fragment (See Figure 7.10), and S_{02} (or $S_{xx} - S_{yy}$) is shown in Fig. 7.11(a). Typical error limits (see below) of S_{00} are within 0.02, and of S_{02} are shown in Fig. 7.11(a). As seen in Fig. 7.6(b), the molecular frame is chosen with the Y_m axis attached on the biphenyl fragment plane, since the formalism is made particularly simple when the α_F angle is 90°. To allow a possible

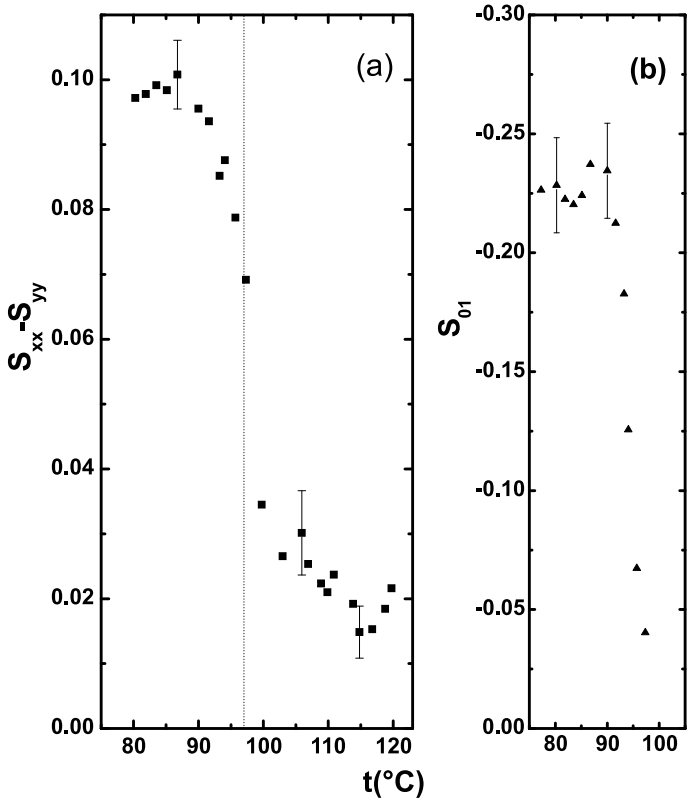

Figure 7.11: (a) Plot of the core order parameter $S_{xx} - S_{yy}$ as a function of temperature in the SmA and SmC* phase of 10B1M7. (b) plot of the core order parameter S_{01} in SmC* phase of 10B1M7.

.

twist between the biphenyl and phenyl fragments, the corresponding α_F angle for the phenyl carbon sites would be different from the assumed 90°. Strictly speaking Eq. (7.35) cannot be used for sites 2-4, but since β_F^{ph} is almost zero, a slight twist between the two fragments would not make Eq. (7.35) inappropriate for the phenyl carbons. In the SmC* phase, the same procedure is used but with Eq. (7.34) where the phase biaxiality has been ignored. The S_{zz} values in SmC* phase were fixed to those extrapolated from the S_{zz} values of the phenyl group in SmA phase, and the tilt angles were also determined from these extrapolated values (see Fig. 7.12), which are comparable to the tilt angle values found in a previous deuteron study [23]. Given the S_{zz} and the tilt angle, the fitting in the SmC* phase therefore involves only two unknown order parameters $S_{xx} - S_{yy}$ and S_{01}. These derived order parameters are shown in Fig. 7.11. We note that at the transition into the SmC* phase, S_{01} becomes non-zero and rises to a small plateau value of ca. -0.2. This indicates that the orientation of the PAS of the order matrix has deviated from the chosen molecular frame in the SmA phase. Furthermore, there appears a discontinuous jump in the molecular biaxial ordering at the SmA-SmC* transition. The negative S_{01} is simply a result of the choice of X_m and Y_m axes. The calculated chemical shifts based on the derived order parameters are shown as

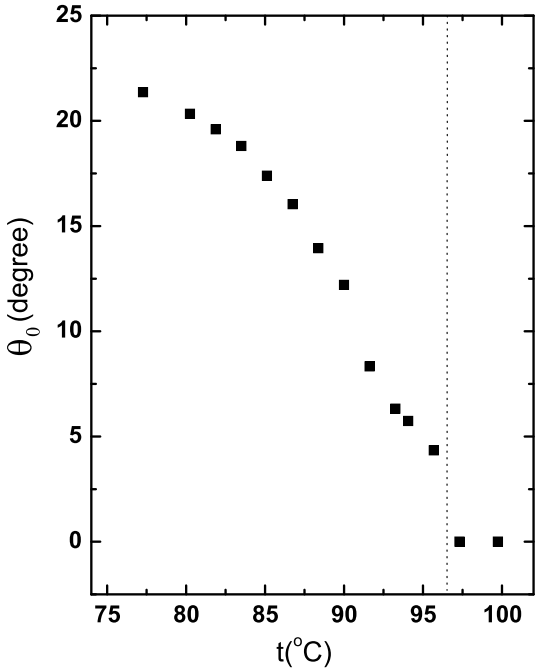

Figure 7.12: Plot of tilt angle versus temperature in the SmC* phase of 10B1M7. Dashed vertical line represents the transition temperature from the SmA phase to the SmC* phase.

.

solid curves in Fig. 7.8. The agreement between the experimental and calculated ^{13}C shifts for C2-C12 is acceptable in view of some uncertainties in the chemical shift tensors obtained from the literature.

7.7 ^{13}C NMR Study of 11EB1M7

The deuterated samples 11EB1M7-d_2 and 11EB1M7-d_8 were previously studied with a 7.05T Varian spectrometer by ^{2}H NMR experiments [30]. From Chapter 5, we know that the SmC* phase can be unwound when the applied magnetic field (B_0) is larger than the critical field. So before we did ^{13}C NMR experiments on these samples, ^{2}H NMR experiments were performed in the 9.4T magnet using the solid-echo pulse sequence to check the phase sequence. Figures 7.13 and 7.14 show plots of ^{2}H splittings as a function of temperature of 11EB1M7-d_2 and 11EB1M7-d_8, respectively. From these figures, it is noted that the quadrupolar splittings are different from the results in the literature [30], and the quadrupolar splittings do not decrease due to the tilt angle upon entering the SmC* phase [31]. This means that the SmC* phase was already unwound or partially unwound by the 9.4T magnetic field to give an unwound Sm$\bar{C}$* phase. In this Sm$\bar{C}$* phase, the smectic layers are tilted while the molecules are lined up along the B_0 field. Hence the quadrupolar splittings do not decrease upon decreasing the

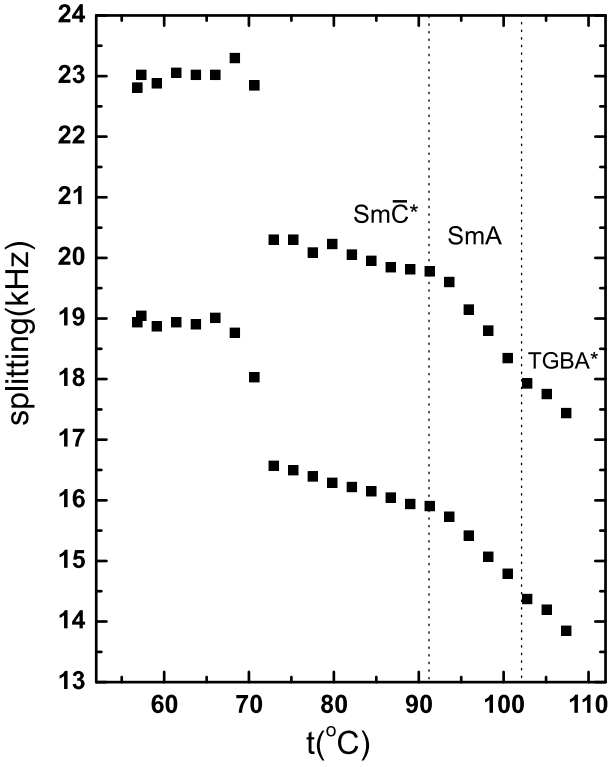

Figure 7.13: Quadrupolar splittings as a function of temperature measured for 11EB1M7-d_2 in the various phases. The two splittings are caused by the ^{1}H-^{2}H dipolar interactions.

.

temperature. The ^{13}C NMR study was performed in the SmA phase of 11EB1M7 using the above theory.

Figure 7.15 shows some typical ^{13}C spectra with the peak assignments at several different temperatures in 11EB1M7. The carbon labels are those indicated in Fig. 1.12. Figure 7.16 shows a plot of the aromatic ^{13}C shifts as a function of temperature in the SmA phase of 11EB1M7. Here we still consider the local order parameters first based on Eq. (7.36). According to the ^{2}H NMR study [30] in the SmA phase, the best fitting parameter of $S'_{xx}-S'_{yy}$ for the phenyl fragment is 0.047. Thus in our simulation, we have fixed $S'_{xx}-S'_{yy}$ for carbon sites 1,2,3,4 to this value. Figure 7.17 shows the local order parameters S'_{zz} and $S'_{xx}-S'_{yy}$ of the biphenyl fragment for 11EB1M7 versus temperature. The order parameters S'_{zz} (carbon sites 5-12) are quite consistent with the ^{2}H NMR results. As seen from the figure, the S'_{zz} value of the phenyl ring is higher than that of the biphenyl fragment. This finding compares well with 10B1M7 due to their similar structures. It is also noted that the $S'_{xx}-S'_{yy}$ values for the biphenyl fragments are negative, a consequence of the selection of the coordinate frame. The chemical shift tensors used here are listed in Table 7.2. It is important to notice that the chemical shift tensors of some carbon sites are same as those in 10B1M7 due to

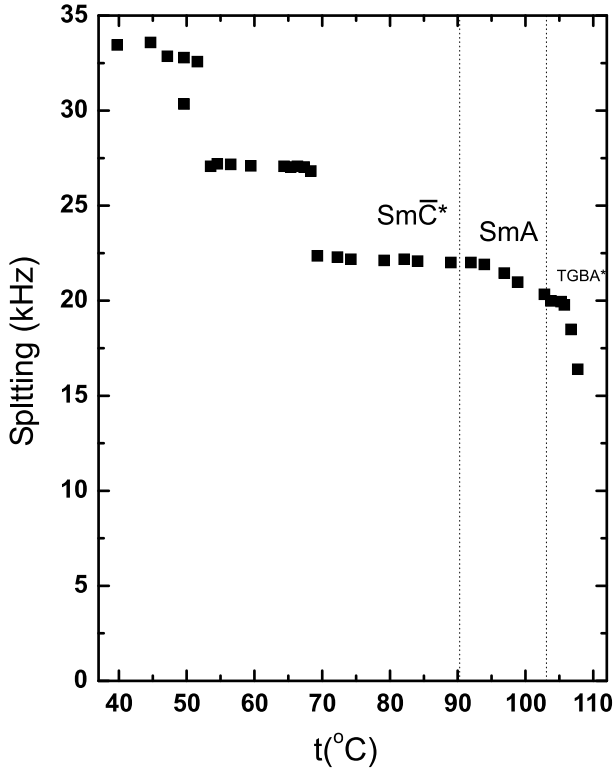

Figure 7.14: Quadrupolar splittings as a function of temperature measured for 11EB1M7-d_8 in the various phases.

.

the similar structure between 10B1M7 and 11EB1M7 in the phenyl fragment and part of the biphenyl fragment. The carbon peak assignments of these two molecules can reinforce each other. From the local S'_{zz} values of the phenyl and biphenyl fragments at each temperature, the average angle between their para axes in SmA phase is calculated as $11.7° \pm 0.5°$, which is consistent to the value of $11.6° \pm 1.5°$ found by ^{2}H NMR [30]. Using Eq. (7.38), the average β_F^{ph} angle between the phenyl fragment axis Z_F and the long molecular axis Z_m can be determined as 0.06°, which means the phenyl fragment axis Z_F is almost identical to the long molecular axis Z_m. Based on the above information, the molecular orientation ordering can now be considered. Using the angle of $\beta_F^{ph} = 0.06°$ for phenyl fragment and $\beta_F^{biph} = 11.64°$ for biphenyl fragment, Eq. (7.35) was used to fit σ for sites C1-C12 in the SmA phase. This study has confirmed an assumption on the location of long molecular axis in reference [30]. We have derived the molecular order parameters S_{00} (or S_{zz}) and S_{02} together with typical error limits shown in Fig. 7.18. The error bar in order parameters was estimated by fitting the chemical shift data using only sites from one ring in the biphenyl fragment. The calculated ^{13}C chemical shifts based on the derived order parameters are shown as solid curves in Figure 7.16.

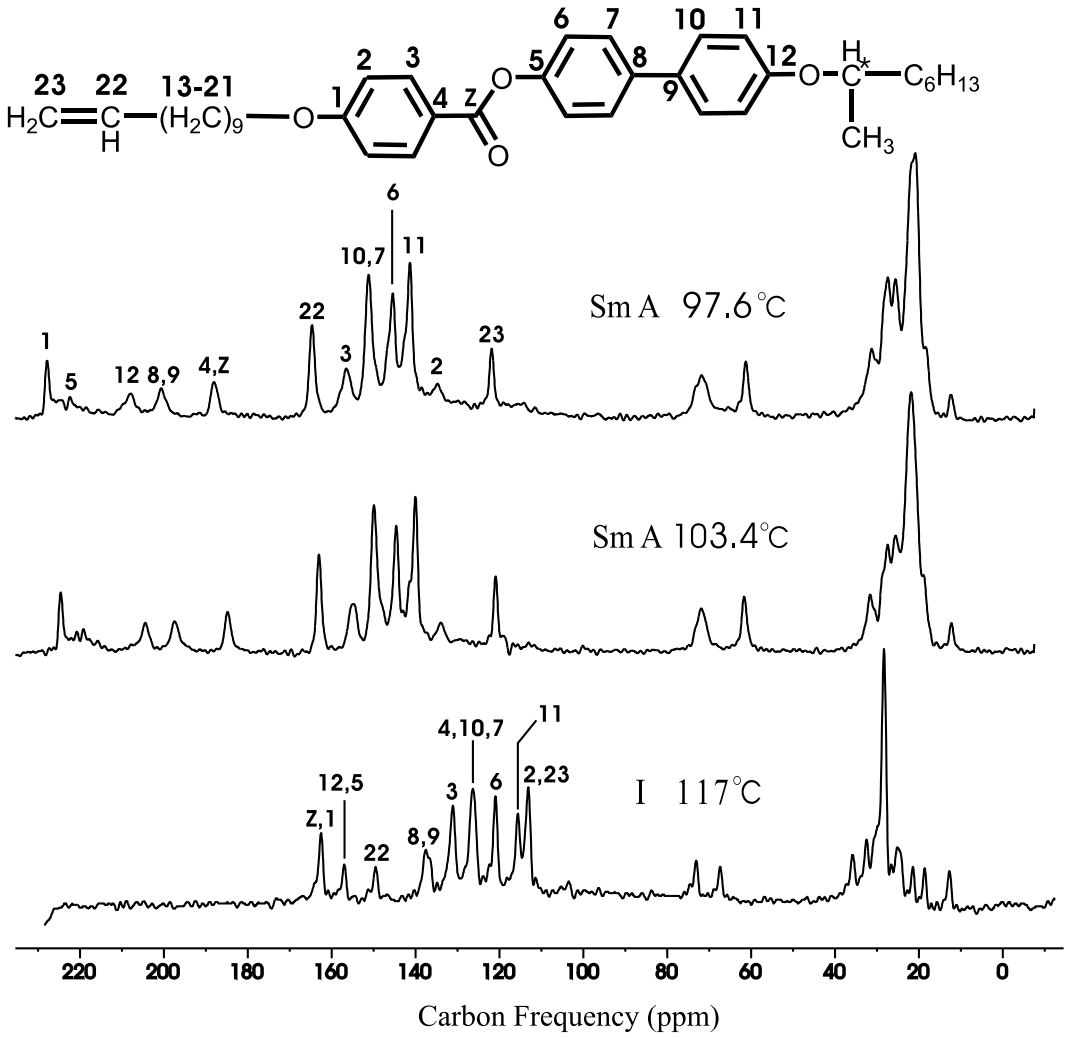

Figure 7.15: Typical ^{13}C spectra observed in the aligned sample of 11EB1M7 at several temperatures by cooling from the isotropic phase. The carbon peak assignments in isotropic and SmA phases are indicated.

.

7.8 Conclusion

The analyses of carbon chemical shift data in the ordered mesophases can in principle be useful for obtaining the structure and ordering of LC molecules. Because of possible incorrect peak assignments and difficulty often encountered in picking the proper chemical shift tensors for various carbon sites, the derived molecular information must be taken with care and/or collaborated by complementary information such as those found in the corresponding partially deuterated mesogen when possible. Indeed the present study has demonstrated that reliable ordering information can be obtained by combining carbon and deuteron results. In the SmA phase for both 10B1M7 and 11EB1M7, S_{zz} increases upon decreasing the temperature. The

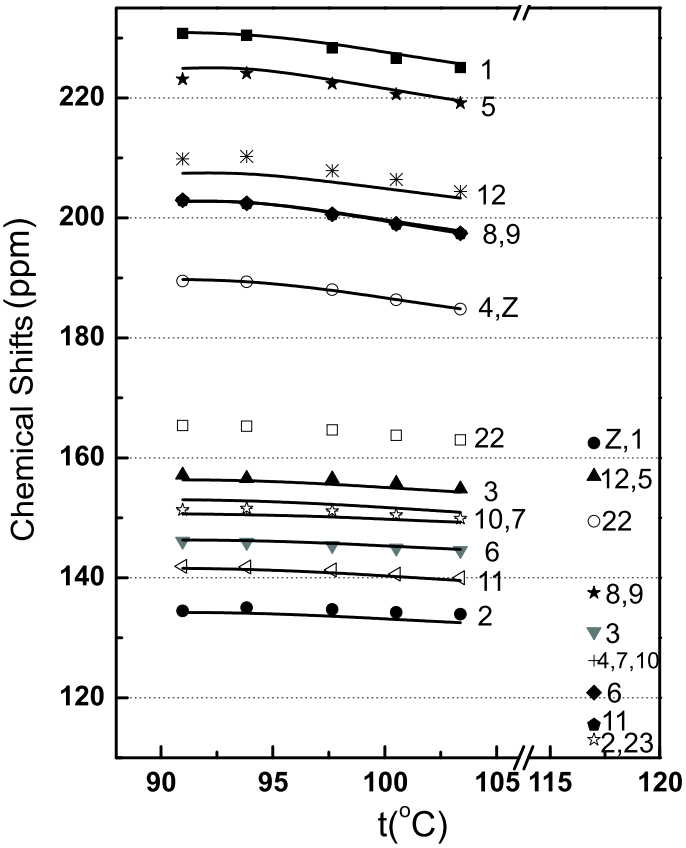

Figure 7.16: Plot of chemical shifts of aromatic carbons in the isotropic and SmA phases of 11EB1M7. Solid lines denote, starting from the top, theoretical fitting curves for C1, C5, C12, C8, C9, C4, C3, C10, C7, C6, C11 and C2.

.

S_{zz} value of 10B1M7 is slightly higher than that of 11EB1M7, which means that in the SmA phase, 10B1M7 seems to be more ordered than 11EB1M7, while the order parameters S_{02} of both molecules show comparable values. Due to their similar structures, the two samples also have similar angles between Z_F^{ph} and Z_F^{biph}, i.e. 14.4° for 10B1M7 and 11.7° for 11EB1M7. The angles β_F^{ph} between the phenyl fragment axis Z_F and long molecular axis Z_m are both small, 0.1° and 0.06° for 10B1M7 and 11EB1M7, respectively. The highlight of this work is that some chemical shift tensors are identical for analyzing the two similar structures of our samples and the results obtained are in good agreement with their deuteron works. This demonstrates that our theory and our peak assignments are correct. Furthermore, in the previous deuteron work on the 10B1M7 molecule, a possible change of the orientation of PAS of the order matrices in the tilted SmC* phase has not been addressed. It would appear that three molecular order parameters are a natural way to describe the orientational ordering of chiral molecules in the tilted smectic phase. It is pointed out that special techniques, such as orienting the pitch axis at a non-zero angle with respect to the magnetic field, are required

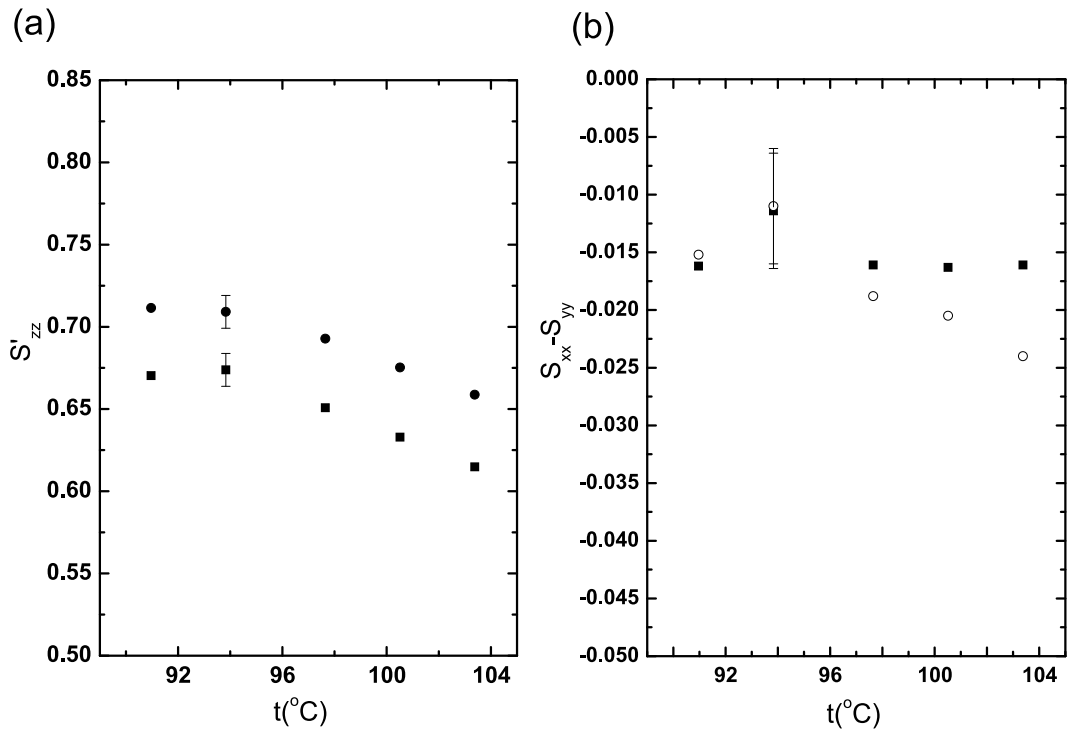

Figure 7.17: (a) Order parameters S'_{zz} of the phenyl(•) and biphenyl(■) fragments as a function of temperature. (b) Order parameters $S'_{xx} - S'_{yy}$ of phenyl ring 1234(■) and phenyl ring 5678(○) in the biphenyl fragments as a function of temperature.

.

Table 7.2: Chemical shift tensors in ppm of 11EB1M7 (experimental values in parentheses have an accuracy of about 3 ppm).

Carbon	σ_{xx}	σ_{yy}	σ_{zz}	σ_{iso}	Reference
C1	64	165.2	262.2	163.8(162.5)	[26]
C2*	18.7	131.7	184.7	111.7(113.0)	[25]
C3*	15	153	226	131.3(131.0)	[25]
C4*	14.6	147.4	219.3	127.1(126.2)	[26]
C5*	71.7	137.4	255.9	155(156.9)	[27]
C6*	30	149.3	183.0	120.8(120.9)	[28]
C7*	21.8	145.5	217.9	128.4(126.2)	[27]
C8*	14.4	169.1	235.9	139.8(137.5)	[26]
C9	14.4	169.1	235.9	139.8(137.5)	[26]
C10*	21.3	150.2	200.8	124.1(126.2)	[27]
C11	8.7	135.5	192.6	112.3(115.5)	[26]
C12	74	162	230	155.3(156.9)	[29]

* The chemical shift tensors are same as those for 10B1M7.

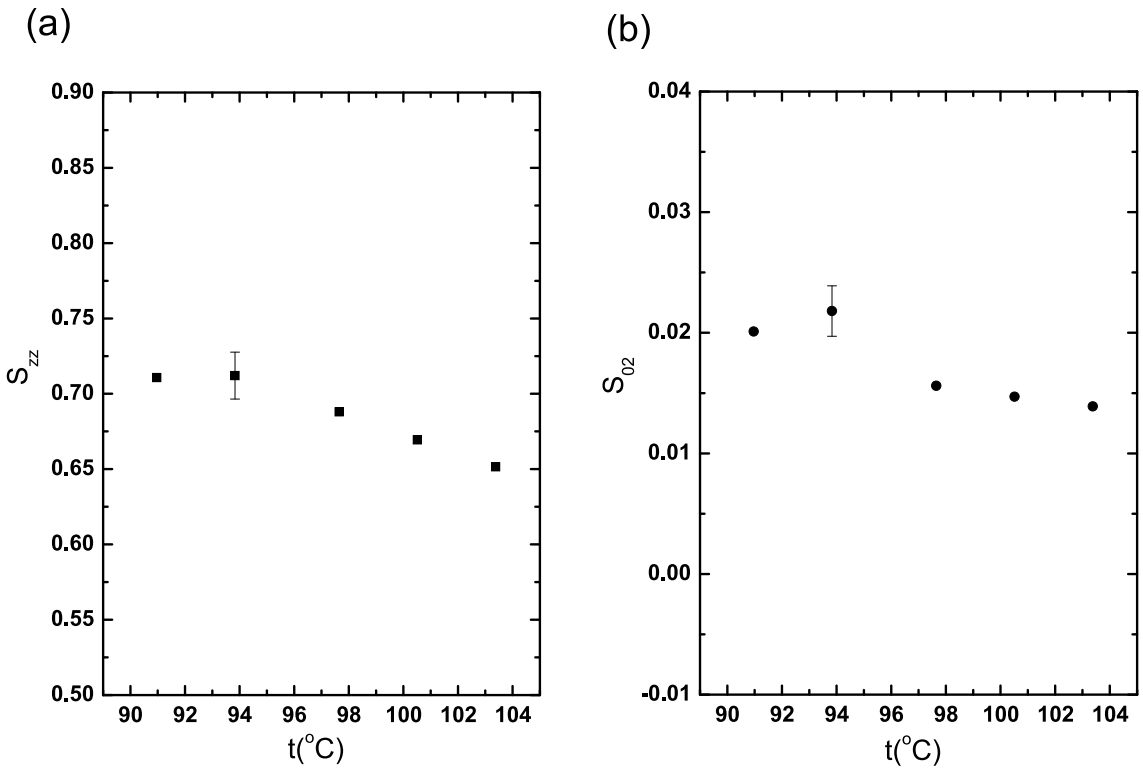

Figure 7.18: (a) Plot of the molecular order parameter S_{zz} as a function of temperature in the SmA phase of 11EB1M7. (b) Plot of the molecular order parameter S_{02} as a function of temperature in the SmA phase of 11EB1M7.

.

to detect any phase biaxiality in the SmC* phase. As shown in previous chapters the phase biaxiality is indeed negligible in the SmC* phase of chiral smectogens such as 10B1M7.

References

[1] Pavia, D. L.; Lampman, G. M.; Kriz, G. S. *Introduction to Spectroscopy*; Harcourt College Publishers, 2001.

[2] Freeman, R. *A Handbook of Nuclear Magnetic Resonance*; Longman Scientific and Technical, 1988.

[3] Waugh, J. S. *J. Magn. Reson.* **1982**, *49*, 517.

[4] Bennett, A. E.; Rienstra, C. M.; Auger, M.; Lakshmi, K. V.; Griffin, R. G. *J. Chem. Phys.* **1995**, *103*, 6951.

[5] Vanderhart, D. L.; Earl, W. L.; Garroway, A. N. *J. Magn. Reson.* **1981**, *44*, 361.

[6] Brauniger, T.; Wormald, P.; Hodgkinson, P. *Monatsh. Chem.* **2002**, *133*, 1549.

[7] Fung, B. M.; Khrtrin, A. K.; Ermolaev, K. *J. Magn. Reson.* **2000**, *142*, 97.

[8] Hartmann, S. R.; Hahn, E. L. *Phys. Rev.* **1962**, *128*, 2042.

[9] Pines, A.; Gibby, M. G.; Waugh, J. S. *J. Chem. Phys.* **1973**, *59*, 569.

[10] Slichter, C. P. *Principles of Magnetic Resonance*; Springer-Verlag Berlin, 1978.

[11] Mehring, M. *High Resolution NMR Spectroscopy in Solids*; Springer-Verlag Berlin, 1976.

[12] Demco, D. E.; Tegenfeldt, J.; Waugh, J. S. *Phys. Rev. B* **1975**, *11*, 4133.

[13] Wu, X. L.; Zilm, K. W. *J. Magn. Reson. A* **1993**, *104*, 154.

[14] Haeberlen, U.; Ellett, J. D.; Waugh, J. S. *J. Chem. Phys.* **1971**, *55*, 53.

[15] Levitt, M. H. *J. Chem. Phys.* **1991**, *94*, 30.

[16] Levitt, M. H.; Suter, D.; Ernst, R. R. *J. Chem. Phys.* **1986**, *84*, 4243.

[17] Wu, X. L.; Zilm, K. W. *J. Magn. Reson.* **1991**, *93*, 265.

[18] Müller, L.; Kumar, A.; Baumann, T.; Ernst, R. R. *Phys. Rev. Lett.* **1974**, *32*, 1402.

[19] Sinha, N.; Ramanathan, K. V. *Chem. Phys. Lett.* **2000**, *332*, 125.

[20] Allender, D. W.; Doane, J. W. *Phys. Rev. A* **1978**, *17*, 1177.

[21] Hodder, B.; Sambles, J. R.; Jenkins, S.; Richardson, R. M. *Phys. Rev. Lett.* **1999**, *85*, 3181.

[22] Keller, E. N.; Nachaliel, E.; Davidov, D. *Phys. Rev. A* **1986**, *34*, 4363.

[23] Catalano, D.; Cavazza, M.; Chiezzi, L.; Geppi, M.; Veracini, C. *Liq. Cryst.* **2000**, *27*, 621.

[24] Dong, R. Y.; Chiezzi, L.; Veracini, C. A. *Phys. Rev. E* **2002**, *65*, 041716.

[25] Wemmer, D. E.; Pines, A.; Whitehurst, D. D. *Phil. Trans. R. Soc. Lond. A.* **1981**, *300*, 15.

[26] Zheng, G.; Hu, J.; Zhang, X.; Shen, L.; Ye, C.; Webb, G. A. *J. Mol. Struct.* **1998**, *428*, 283.

[27] Nakai, T.; Fujimori, H.; Kuwahara, D.; Miyajima, S. *J. Phys. Chem. B* **1999**, *103*, 417.

[28] Xu, J.; Fodor-Csorba, K.; Dong, R. Y. *J. Phys. Chem. A* **2005**, *109*, 1998.

[29] Oulyadi, H.; Laupretre, F.; Monnerie, L. *Macromolecules* **1990**, *23*, 1965.

[30] Catalano, D.; Chiezzi, L.; Domenici, V.; Geppi, M.; Veracini, C. A. *J. Phys. Chem. B* **2003**, *107*, 10104.

[31] Dong, R. Y.; Xu, J.; Zhang, J.; Veracini, C. A. *Phys. Rev. E* **2005**, *72*, 061701.

Chapter 8

2D ^{13}C NMR Spectroscopy

8.1 Introduction

As one can see, 1D ^{13}C spectra of liquid crystals are far too complex to interpret as there are numerous peaks. By the introduction of additional spectral dimensions, these spectra may be better understood and can also give some extra information. The invention of multidimensional spectra was a major leap in NMR spectroscopy apart from the introduction of fast Fourier transformation to NMR. Two dimensional (2D) ^{13}C NMR spectroscopy has many different applications; the basic form of all these experiments is essentially the same. First, the magnetization is prepared in a state appropriate to whatever properties are to be detected in the indirect dimension. For instance, to detect a standard spectrum of the chemical shifts in the indirect dimension, the preparation period could involve a $\pi/2$ pulse or possibly a CP sequence. Next, the magnetization is allowed to evolve for a time t_1 under a specific NMR Hamiltonian. For instance, if one wishes the I spins in an $I-S$ spin system to evolve only under H_{II} and H_{CS}, the S spins should therefore be decoupled to remove H_{IS}. Following the evolution period t_1, an optional mixing pulse (or a sequence of pulses) is used to prepare the magnetization for the final detection period t_2. As in the initial preparation period, the mixing pulse(s) depends largely on the spectrum desired. In heteronuclear experiments, it is often necessary to transfer the magnetization from one set of spins to another. For instance, in an experiment to correlate ^{1}H and ^{13}C chemical shifts, the mixing period might involve CP from the ^{1}H spins to the ^{13}C spins. Once the mixing period is complete, the resulting magnetization is detected as usual in the direct dimension t_2. By performing a Fourier transformation in both t_1 and t_2 dimensions, a 2D spectrum is produced which correlates the interactions detected in the indirect dimension t_1 with the interactions detected in the direct dimension t_2. In this chapter, several 2D ^{13}C experiments such as SUPER and SLF

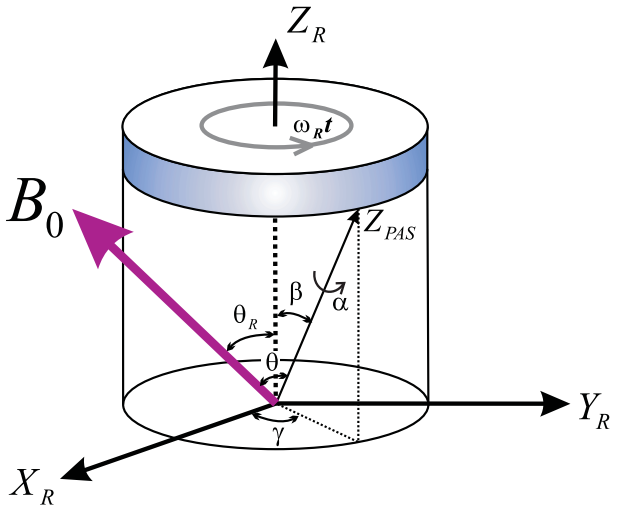

Figure 8.1: The magic angle spinning experiment. The sample is spun rapidly in a cylindrical rotor about a spinning axis oriented at the magic angle ($\theta_R = 54.74°$) with respect to the applied magnetic field. The angle θ is between B_0 with the principal Z_{PAS} axis of the interaction vector. (α,β,γ) are Euler angles to describe the transformation from the PAS frame to the rotor frame (X_R,Y_R,Z_R).

.

experiments are introduced.

8.2 Magic Angle Spinning Experiment

8.2.1 Theory of Magic Angle Spinning

Magic angle spinning (MAS) is used routinely in a vast majority of solid-state NMR experiments, where its primary task is to remove the effects of chemical shift anisotropy and to assist in the removal of heteronuclear dipolar-coupling effects. It has also been used to narrow spectral lines from quadrupolar nuclei and is increasingly the method of choice for removing the effects of homonuclear dipolar coupling on NMR spectra [1–4]. Consider a solid containing a single magnetically active nuclear spin species placed in a uniform magnetic field B_0 and the experimental setup is shown in Figure 8.1. The angle θ describes the orientation of the interaction vector in the magnetic field. The sample is spun rapidly in a cylindrical rotor about a spinning axis oriented at the magic angle ($\theta_R = 54.74°$) with respect to the applied magnetic field. (α,β,γ) are Euler angles to describe the transformation from the PAS frame of the spin interaction to the rotor frame (X_R,Y_R,Z_R). From Eq. (2.16) we know that the time averaged Hamiltonian $\bar{H}_\lambda$ is related to $\langle R_{2,0} \rangle$. By considering the following transformation

$$\text{PAS frame } (X_{PAS},Y_{PAS},Z_{PAS}) \overset{(\alpha,\beta,\gamma)}{\Longrightarrow} \text{Rotor frame } (X_R,Y_R,Z_R)$$
$$\text{Rotor frame } (X_R,Y_R,Z_R) \overset{(\omega_R t,\theta_R,0)}{\Longrightarrow} \text{Lab frame } B_0$$

where ω_R denotes the rotation frequency of the rotor, one can get

$$\begin{aligned}\langle R_{2,0}\rangle &= \sum_{mn}\left\langle D^2_{m,0}(\omega_R t,\theta_R,0)D^2_{nm}(\alpha,\beta,\gamma)\right\rangle \rho_{2,n}\\ &= a\rho_{2,0}+b\rho_{2,2}+c\rho_{2,-2}\\ &= a\rho_{2,0}+(b+c)\rho_{2,2}\end{aligned} \tag{8.1}$$

with

$$\begin{aligned}a &= P_2(\cos\theta_R)P_2(\cos\beta)+\frac{3}{4}\sin^2\theta_R\sin^2\beta\cos 2(\gamma+\omega_R t)\\ &\quad -\frac{3}{4}\sin 2\theta_R\sin 2\beta\cos(\gamma+\omega_R t)\\ b+c &= \sqrt{\frac{3}{2}}P_2(\cos\theta_R)\sin^2\beta\cos 2\alpha\\ &\quad +\sqrt{\frac{3}{2}}\sin^2\theta_R\left[(\frac{1+\cos\beta}{2})^2\cos 2(\gamma+\alpha+\omega_R t)+(\frac{1-\cos\beta}{2})^2\cos 2(\gamma-\alpha+\omega_R t)\right]\\ &\quad +\sqrt{\frac{3}{8}}\sin 2\theta_R\sin\beta\left[(1+\cos\beta)\cos(\gamma+2\alpha+\omega_R t)-(1-\cos\beta)\cos(\gamma-2\alpha+\omega_R t)\right]\end{aligned} \tag{8.2}$$

It is noticed that $\langle R_{2,0}\rangle$ contains two time independent terms, a term which oscillates at ω_R and a term which oscillates at $2\omega_R$. From Eq. (8.1) we know for $\theta_R = 0$,

$$\langle R_{2,0}\rangle = P_2(\cos\beta)\rho_{2,0}+\sqrt{\frac{3}{2}}\sin^2\beta\cos 2\alpha\rho_{2,2} \tag{8.3}$$

which is not dependent on the spinning speed of the sample. When $\theta_R = \arccos(1/\sqrt{3}) = 54.74°$, $\langle R_{2,0}\rangle$ is a periodic function with a fundamental frequency $f_R = \omega_R/2\pi$. The observed NMR line shape now contains sidebands at f_R or multiples of f_R. One might facetiously call the extra signals 'spinning echoes'. To demonstrate this effect, the chemical shift of a certain spin is considered as an example. From Eq. (7.20) we know the magnetization precesses with a frequency

$$\omega_{cs} = \gamma_s B_0\left[\sigma_{iso}+\sqrt{\frac{2}{3}}\langle R_{2,0}\rangle\right] \tag{8.4}$$

where γ_s is the gyromagnetic ratio. When the sample is spun at the magic angle $\theta_R = 54.74°$, and by separating α and $\gamma+\omega_R t$ in Eq. (8.2) according to the trigonometric addition theorem, Eq. (8.4) can be written as [3]

$$\begin{aligned}\omega_{cs} &= \gamma_s B_0[\sigma_{iso}+D_1\cos(\gamma+\omega_R t)+D_2\cos 2(\gamma+\omega_R t)\\ &\quad +D_3\sin(\gamma+\omega_R t)+D_4\sin 2(\gamma+\omega_R t)]\end{aligned} \tag{8.5}$$

where D_1, D_2, D_3, D_4 are coefficients which are explicitly given in ref. [3] as functions of α and β. For a nuclear site in a single crystal, the free induction decay is given by [5, 6]

$$g(t) = \exp\left[i\int_0^t \omega_{cs}(t')dt'\right] = \exp\left\{i\left[\Phi(t) - \Phi(0)\right]\right\} \tag{8.6}$$

where

$$\begin{aligned}\Phi(t) &= \int^t \omega_{cs}(t')dt' \\ &= \gamma_s B_0\left[\sigma_{iso}t + \frac{D_1}{\omega_R}\sin(\gamma+\omega_R t) + \frac{D_2}{2\omega_R}\sin 2(\gamma+\omega_R t)\right. \\ &\quad \left. -\frac{D_3}{\omega_R}\cos(\gamma+\omega_R t) - \frac{D_4}{2\omega_R}\cos 2(\gamma+\omega_R t)\right]\end{aligned} \tag{8.7}$$

From the property of the Bessel functions of the first kind, one gets

$$\exp(iz\sin\psi) = \sum_{k=-\infty}^{\infty}\exp(ik\psi)J_k(z) \tag{8.8}$$

So

$$\begin{aligned}\exp[i\Phi(t)] &= \exp\left\{i\gamma_s B_0\left[\sigma_{iso}t + \frac{D_1}{\omega_R}\sin(\gamma+\omega_R t) + \frac{D_2}{2\omega_R}\sin 2(\gamma+\omega_R t)\right.\right. \\ &\quad \left.\left. +\frac{D_3}{\omega_R}\sin(\gamma+\omega_R t-\frac{\pi}{2}) + \frac{D_4}{2\omega_R}\sin(2\gamma+2\omega_R t-\frac{\pi}{2})\right]\right\}\end{aligned} \tag{8.9}$$

can be expressed as [5]

$$\begin{aligned}&\exp[i\Phi(t)] \\ &= \sum_{k_1=-\infty}^{\infty} J_{k_1}\left(\frac{\gamma_s B_0 D_1}{\omega_R}\right)\sum_{k_2=-\infty}^{\infty} J_{k_2}\left(\frac{\gamma_s B_0 D_2}{2\omega_R}\right)\sum_{k_3=-\infty}^{\infty} J_{k_3}\left(\frac{\gamma_s B_0 D_3}{\omega_R}\right)\sum_{k_4=-\infty}^{\infty} J_{k_4}\left(\frac{\gamma_s B_0 D_4}{2\omega_R}\right) \\ &\quad \times\exp\left\{i\left[\gamma_s B_0\sigma_{iso}t + (\gamma+\omega_R t)(k_1+2k_2+k_3+2k_4) - \frac{\pi}{2}(k_3+k_4)\right]\right\}\end{aligned} \tag{8.10}$$

and

$$\begin{aligned}&g(t) = \\ &\sum_{k_1=-\infty}^{\infty} J_{k_1}\left(\frac{\gamma_s B_0 D_1}{\omega_R}\right)\sum_{k_2=-\infty}^{\infty} J_{k_2}\left(\frac{\gamma_s B_0 D_2}{2\omega_R}\right)\sum_{k_3=-\infty}^{\infty} J_{k_3}\left(\frac{\gamma_s B_0 D_3}{\omega_R}\right)\sum_{k_4=-\infty}^{\infty} J_{k_4}\left(\frac{\gamma_s B_0 D_4}{2\omega_R}\right) \\ &\times\exp\left\{i\left[\gamma_s B_0\sigma_{iso}t + (\gamma+\omega_R t)(k_1+2k_2+k_3+2k_4) - \frac{\pi}{2}(k_3+k_4)\right]\right\}\times \\ &\sum_{k_1'=-\infty}^{\infty} J_{k_1'}\left(\frac{\gamma_s B_0 D_1}{\omega_R}\right)\sum_{k_2'=-\infty}^{\infty} J_{k_2'}\left(\frac{\gamma_s B_0 D_2}{2\omega_R}\right)\sum_{k_3'=-\infty}^{\infty} J_{k_3'}\left(\frac{\gamma_s B_0 D_3}{\omega_R}\right)\sum_{k_4'=-\infty}^{\infty} J_{k_4'}\left(\frac{\gamma_s B_0 D_4}{2\omega_R}\right) \\ &\times\exp\left\{-i\left[\gamma(k_1'+2k_2'+k_3'+2k_4') - \frac{\pi}{2}(k_3'+k_4')\right]\right\}\end{aligned} \tag{8.11}$$

In order to concentrate on the important time dependence in the above expression for $g(t)$, it is convenient to define:

$$g(t) = \sum_{N=-\infty}^{\infty} F_N(\alpha, \beta, \gamma) \exp\left[i\left(\omega_{iso} + N\omega_R\right) t\right] \tag{8.12}$$

where $F_N(\alpha, \beta, \gamma)$, the sideband intensity coefficients, include all the time independent terms in Eq. (8.11) and $N = k_1 + 2k_2 + k_3 + 2k_4$. The spectrum is obtained by Fourier transformation of $g(t)$ to give:

$$I(\alpha, \beta, \gamma) = \sum_{N=-\infty}^{\infty} F_N(\alpha, \beta, \gamma)\delta\left(\omega - \omega_{iso} - N\omega_R\right) \tag{8.13}$$

Thus the Fourier transform of $g(t)$ consists of a central resonance at the isotropic chemical shift and a series of sidebands spaced ω_R apart. This property is also preserved under possible α, β and γ integration, for instance, in a powder sample. Since the sideband terms in $\Phi(t)$ are proportional to $1/\omega_R$, at slow spinning speeds the spinning sidebands will appear due to the incomplete averaging of the revolving CSA ellipsoid. These anisotropic effects will be reduced with increasing spinning speed ω_R.

Figure 8.2 show a series of ^{13}C MAS spectra of glycine at different spinning speeds [7]. As the spinning speed decreases, numerous peaks begin to appear at frequency distances of integer multiples of the spinning speed. In order to reduce a powder pattern to a single line at the isotropic chemical shift by magic-angle spinning, the rate of the sample spinning must be fast in comparison to the anisotropy of the CSA interaction being spun out. In fact, the sideband intensities contain information on the anisotropic chemical shift. Herzfeld and Berger [5] have developed graphical and numerical methods for extracting the principal values of a chemical shift tensor from the intensities of just a few sidebands.

8.2.2 Total Suppression of Spinning Sidebands

Although the spinning sidebands contain useful information such as the chemical shift anisotropies, the isotropic peaks and spinning sidebands are in general indistinguishable. Thus chemical shifts cannot be easily assigned and a qualitative chemical analysis is also impossible. To get around these problems, one can obtain spectra at more than one spinning speed, which show moving sidebands but static isotropic peaks and perhaps avoid overlaps of the isotropic peaks with sidebands. But in complex samples overlaps between isotropic and sideband peaks are impossible to avoid and the use of fast spinning to eliminate sidebands suffers a

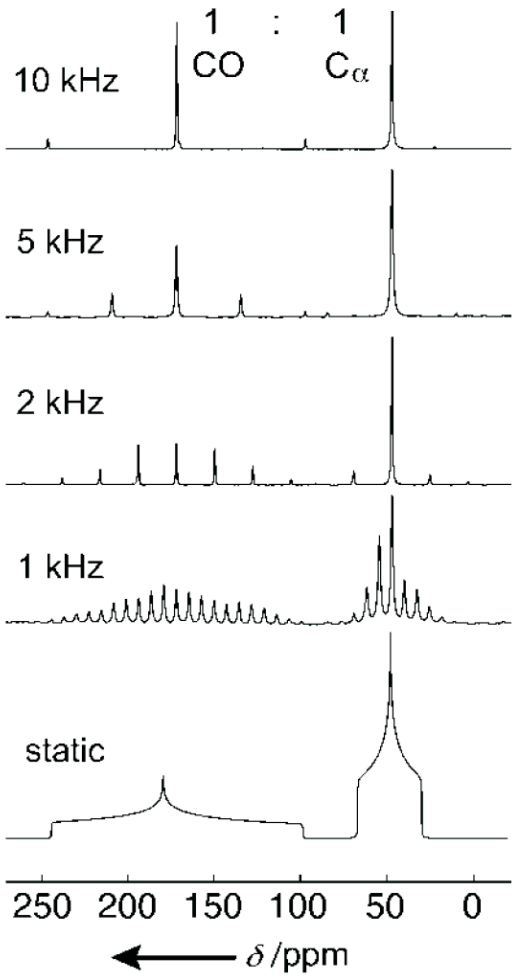

Figure 8.2: The effect of slow magic angle spinning rates on solid state ^{13}C NMR spectra of a ^{13}C labeled glycine powder sample. A set of spinning sidebands appears, with a center band at the isotropic chemical shift and further lines spaced by the spinning frequency [7].

.

serious problem, viz. permanent loss of information contained in the sidebands. If one defines $f(\gamma + \omega_R t) = \exp[i\Phi(t)]$, and when the time signal is

$$g(t) = f(\gamma + \omega_R t) \tag{8.14}$$

the spinning sidebands can be eliminated. The reason is that $g(t)$ is periodic with $t_R = 2\pi/\omega_R$ according to the harmonic time dependences in Eq. (8.7), the intensity of the sidebands at

$N\omega_R$ is obtained as

$$\begin{aligned} I'(\alpha,\beta,\gamma) &= \frac{1}{t_R}\int_0^{t_R} f(\gamma+\omega_R t)e^{-i\omega_R N t}dt \\ &= e^{iN\gamma}\int_0^{t_R} f(\gamma+\omega_R t)e^{-i(\gamma+\omega_R t)N}\frac{dt}{t_R} \\ &= e^{iN\gamma}\int_0^{2\pi} f(\gamma')e^{-i\gamma' N}\frac{d\gamma'}{2\pi} \quad \texttt{(with } \gamma'=\gamma+\omega_R t\texttt{)} \\ &= \frac{1}{2\pi}e^{iN\gamma}G_N(\alpha,\beta) \end{aligned} \tag{8.15}$$

with

$$G_N(\alpha,\beta)=\int_0^{2\pi} f(\gamma')e^{-i\gamma' N}d\gamma' \tag{8.16}$$

So for the powder samples, all γ values are equally probable so that we can simply integrate Eq. (8.15) over γ:

$$\int_0^{2\pi} I'(\alpha,\beta,\gamma)d\gamma = G_N(\alpha,\beta)\frac{1}{2\pi}\int_0^{2\pi} e^{iN\gamma}d\gamma = G_N(\alpha,\beta)\delta_{N,0} \tag{8.17}$$

In this case all sidebands will be eliminated when $N \neq 0$. Much interest was therefore generated after Dixon has demonstrated a method called total suppression of spinning sidebands (TOSS) [8, 9]. This uses a sequence of four properly spaced 180° pulses that essentially suppress the factor $\exp[-i\Phi(0)]$ and prepare the magnetization components of a powder sample such that only the center bands are left without any sidebands [10, 11]. Applying every 180° pulse at a time t_n (where $n = 1, 2, 3, 4, 5$), the sign of the precession frequency of each isochromat is inverted, and the effective phase is:

$$\begin{aligned} &\int_0^{t_1}\omega_{cs}(t')dt' - \int_{t_1}^{t_2}\omega_{cs}(t')dt' + \int_{t_2}^{t_3}\omega_{cs}(t')dt' - \int_{t_3}^{t_4}\omega_{cs}(t')dt' + \int_{t_4}^{t_5+t}\omega_{cs}(t')dt' \\ =\ & \Phi(t_1)-\Phi(0)-\Phi(t_2)+\Phi(t_1)+\Phi(t_3)-\Phi(t_2)-\Phi(t_4)+\Phi(t_3)+\Phi(t_5+t)-\Phi(t_4) \\ =\ & \Phi(t_5+t)+2\Phi(t_1)-2\Phi(t_2)+2\Phi(t_3)-2\Phi(t_4)-\Phi(0) \end{aligned} \tag{8.18}$$

From Eq. (8.14) it is known that to get signal without sidebands we need

$$\Phi(t_5+t)+2\Phi(t_1)-2\Phi(t_2)+2\Phi(t_3)-2\Phi(t_4)-\Phi(0)=\Phi_{eff}(t) \tag{8.19}$$

By substituting $\Phi(t)$ in Eq. (8.19) with Eq. (8.7) one can get the two conditions [3]

$$\begin{aligned} &-\frac{D_1}{\omega_R}2\sum_n(-1)^n\sin(\gamma+\omega_R t_n)+\frac{D_3}{\omega_R}\left[\cos\gamma+2\sum_n(-1)^n\cos(\gamma+\omega_R t_n)\right] \\ &-\frac{D_2}{2\omega_R}2\sum_n(-1)^n\sin 2(\gamma+\omega_R t_n)+\frac{D_4}{2\omega_R}\left[\cos 2\gamma+2\sum_n(-1)^n\cos 2(\gamma+\omega_R t_n)\right]=0 \end{aligned} \tag{8.20}$$

and

$$t_5 = 2t_4 - 2t_3 + 2t_2 - 2t_1 \tag{8.21}$$

According to Eqs. (8.21), the original TOSS pulse sequence has been introduced [8]. In order to compensate for pulse imperfections, pulse phase cycling and proper timings of the pulse centers are relevant. The widely used TOSS sequences are listed in Table 8.1 [3] and the corresponding time t_j and Δt_j are indicated in Figure 8.3. It is noticed that Dixon's original sequences are quite long, occupying over two full rotation periods, with two of the 180° pulses very closely spaced in time. The long duration of the sequences causes loss of signal for samples with a short spin-spin relaxation time T_2, and the proximity of the pulses causes timing difficulties at high spinning speeds. In extreme cases, the pulses collide and the sequence can not be implemented at all. To avoid these problems, some new sequences have been found which are shorter or employ more evenly spaced pulses [12–15].

Table 8.1: Timing of widely used TOSS sequences.

	$\Delta t_1/t_R$	$\Delta t_2/t_R$	$\Delta t_3/t_R$	$\Delta t_4/t_R$	$\Delta t_5/t_R$	$\sum_j \Delta t_j/t_R$
I	0.1226	0.0773	0.2236	1.0433	0.7744	2.2412
II	0.1885	0.0412	0.5818	0.9588	0.2297	2

* All the times are labeled in Figure 8.3 and the times here are given in units of the rotation periods [3].

8.2.3 CP-MAS Experiment

Magic-angle spinning (MAS), usually in combination with cross-polarization, has become the standard technique for the study of powder samples and obtaining high-resolution NMR spectra in solid state NMR [1, 2]. The efficiency of cross polarization depends on the Hartmann-Hahn matching condition and is influenced by the strength of the homo- and heteronuclear dipolar coupling. When the sample is spun at the magic angle, Eq. (7.12) can be written according to Eq. (8.1) as

$$\begin{aligned} b(t) &= \frac{\mu_0 \gamma_I \gamma_S \hbar}{16\pi^2 r^3}(1 - 3\cos^2\theta) \\ &= \frac{\mu_0 \gamma_I \gamma_S \hbar}{16\pi^2 r^3} 2 \sum_m D^2_{m,0}(\omega_R t, \theta_R, 0) D^2_{0,m}(\alpha, \beta, \gamma) \\ &= \frac{\mu_0 \gamma_I \gamma_S \hbar}{16\pi^2 r^3} \left[\sin^2\beta \cos 2(\gamma + \omega_R t) - \sqrt{2}\sin 2\beta \cos(\gamma + \omega_R t)\right] \end{aligned} \tag{8.22}$$

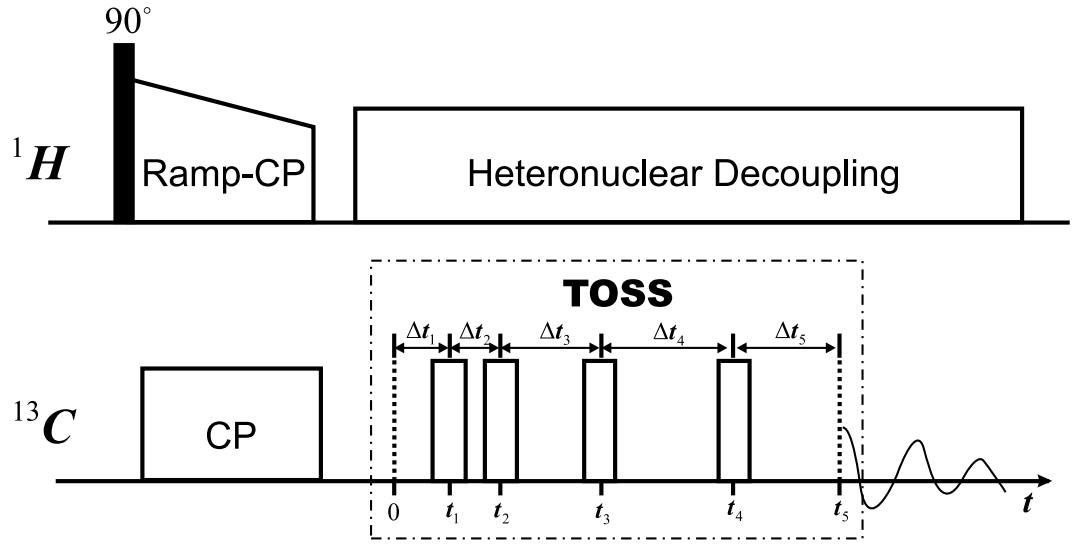

Figure 8.3: Ramp-CP with TOSS pulse sequence. The delay Δt_1 is the timing of the first pulse after the start of free precession, Δt_j, $j = 2, 3, 4$ are the spacings between the centers of the π pulses, and Δt_5 is the delay between the fourth pulse and the start of data acquisition.

.

which is time dependent. So it is convenient to express $b(t)$ in terms of Fourier components [16]:

$$b(t) = \sum_{k=-2}^{2} b_k \exp(ik\omega_R t) \tag{8.23}$$

where

$$\begin{aligned} b_0 &= 0 \\ b_{\pm 1} &= -\frac{\mu_0 \gamma_I \gamma_S \hbar}{32\pi^2 r^3} \sqrt{2} \sin 2\beta \exp(\pm i\gamma) \\ b_{\pm 2} &= -\frac{\mu_0 \gamma_I \gamma_S \hbar}{32\pi^2 r^3} \sin^2 \beta \exp(\pm i2\gamma) \end{aligned} \tag{8.24}$$

The situation in each subspace now becomes analogous to applying simultaneously two linearly polarized radio frequency fields. The coupling $b(t)$ is related to the sample rotation, and two general cases can be considered. If the couplings are much greater than the MAS speed, i.e. $|b_k| > \omega_R$, cross polarization can still take place at the unmodified Hartmann-Hahn condition $\omega_\Delta = 0$. A broad matching profile is observed over a wide range of Hartmann-Hahn mismatch conditions. However, when the $I - S$ coupling is weak and the spinning rate ω_R is high, i.e. $|b_k| \ll \omega_R$, the components b_k of $b(t)$ become important. Dipolar fluctuations can no longer compensate the slight rotating-frame energy mismatch of the two spin-lock fields and the cross-polarization matching curve is transformed into a series of sharp peaks separated by the rotor frequency [17, 18]. In this case, H_{TR} in Eq. (7.15) is transformed to

a new rotating frame using

$$U = \exp(-ik\omega_R I_z t) \tag{8.25}$$

In this frame, terms of $b(t)$ oscillating at $\pm k\omega_R$ become time independent. Similar to Eq. (7.17), the time-dependence of the polarization transfer to the S spin can be calculated:

$$\begin{aligned} \langle S_z \rangle (\tau) &\cong \frac{b_k^2}{b_k^2 + (\omega_\Delta - k\omega_R)^2} \times \sin^2 \left[\frac{\tau}{2} \sqrt{b_k^2 + (\omega_\Delta - k\omega_R)^2} \right] \\ &\cong \frac{b_k^2}{b_k^2 + (\omega_\Delta - k\omega_R)^2} \times \frac{1}{2} \left\{ 1 - \cos \left[\tau \sqrt{b_k^2 + (\omega_\Delta - k\omega_R)^2} \right] \right\} \end{aligned} \tag{8.26}$$

This expression indicates that efficient cross polarization between the I and S spins occurs only when $\omega_\Delta = \pm\omega_R$ or $\omega_\Delta = \pm 2\omega_R$, and describes how the Hartman-Hahn CP matching profile for isolated spin pairs is 'broken' into four spinning sidebands. When the term $|\omega_\Delta - k\omega_R|$ is larger than b_k, the polarization transfer diminishes, and as the heteronuclear coupling becomes smaller, the matching width of each sideband becomes narrower.

Under these conditions, the CP matching profile shows a rotor speed dependence even for strongly coupled systems. This imposes experimental difficulties for adjusting and maintaining the optimum Hartmann-Hahn match for magnetization transfer. Several techniques have been suggested for circumventing this problem either by a mechanical means or by introducing new pulse sequences which modulate the phase and/or amplitude of the CP pulses [16, 19–22]. The Variable Amplitude Cross Polarization (VACP) is one of the useful methods and restores a broad matching profile by simply modulating the proton field strength during the contact time [23]. The broad profile is crucial for NMR experiments, where stable cross polarization intensities are required over long time periods such as in rotational resonance NMR. It also compensates for field inhomogeneities in the NMR coil leading to larger signals [24]. In our experiment, a ramped-amplitude CP sequence (RAMP-CP) was used [25] (See Figure 8.3). This is achieved by varying the cross polarization field strength in a set of proton pulses of monotonically increasing amplitudes. With RAMP-CP, the parameters controlling the performance of the sequence are much easier to choose than the conventional VACP.

8.2.4 Measurements of CSA Principal Values

As seen in Chapter 7, the chemical shift anisotropy (CSA) is a useful observable in solid-state NMR, which can provide information not only on segmental orientations and reorientations but also on the local structure of molecules [26–28]. The CSA is also useful for distinguishing different groups with overlapping isotropic chemical shift ranges. Without sample rotation,

the chemical-shift anisotropy produces a characteristic powder pattern, with a central peak at its principal element σ_{yy}, and sharp steps at the two other principal values (See Figure 8.2). Such powder patterns have the advantage of giving the magnitudes of the principal CSA components directly either with or without spectral simulations. However, they do not give the CSA principal axes in relation to a particular molecule axis. When the sample is spun at the magic angle with spinning frequency ω_R, spinning sideband patterns are observed. The intensity distribution of the spinning sidebands is characteristic of the CSA tensor, and the distribution is widely used to experimentally determine CSA principal values [5]. However, typical organic compounds present a multitude of chemically inequivalent sites, and spectral overlap often prevents the extraction of CSA parameters using spectra from either static or slow spinning samples. To overcome this drawback a series of two-dimensional experiments has been proposed, and the common principle of these experiments is to use a second dimension to separate overlapping resonances according to their isotropic chemical shifts.

To obtain undistorted quasi-static CSA powder patterns under standard MAS conditions, a few techniques have been described [29–31]. These experiments involve different approaches to reintroduce CSAs under fast MAS and to yield isotropic spectra in the directly detected dimension (ω_2). SUPER (Separation of Undistorted Powder Patterns by Effortless Recoupling) [31, 32] is an example of such experiments using suitably rotation-synchronized radio frequency pulses, to recover static-like powder patterns, each contains the scaled principal values of the CSA tensor, in the indirect dimension (ω_1). The basic theory for the SUPER experiment is summarized as follows. From Eq. (8.5) the time dependence of the CSA frequency under MAS can be rewritten as

$$\omega_{cs}(t) \;=\; \omega_{iso} + \omega_{ani} \tag{8.27}$$

with

$$\begin{aligned} \omega_{iso} &= \gamma_s B_0 \sigma_{iso} \\ \omega_{ani} &= D'_1 \cos(\omega_R t) + D'_2 \cos 2(\omega_R t) + D'_3 \sin(\omega_R t) + D'_4 \sin 2(\omega_R t) \end{aligned} \tag{8.28}$$

where

$$\begin{aligned} D'_1 &= \gamma_s B_0 (D_1 \cos\gamma + D_3 \sin\gamma) \qquad D'_2 = \gamma_s B_0 (D_2 \cos 2\gamma + D_4 \sin 2\gamma) \\ D'_3 &= \gamma_s B_0 (-D_1 \sin\gamma + D_3 \cos\gamma) \qquad D'_4 = \gamma_s B_0 (-D_2 \sin 2\gamma + D_4 \cos 2\gamma) \end{aligned} \tag{8.29}$$

and the static frequency is obtained by setting $t = 0$

$$\omega_{cs}(0) = \omega_{iso} + \omega_{ani,stat} = \omega_{iso} + D'_1 + D'_2 \tag{8.30}$$

It is convenient to introduce a function $p(t)$, which takes the values 1 and 0, characterizing the actual precession frequency due to chemical shift as $p(t)\omega_{cs}(t)$. To achieve an effective quasi-static anisotropic frequency, the anisotropic part after a full rotor period should be given by [32]

$$\bar{\omega}_{ani} = \frac{1}{t_R}\int_0^{t_R} p(t)\omega_{ani}(t)dt = \chi\omega_{ani,stat} = \chi(D_1' + D_2') \tag{8.31}$$

where

$$p(t) = \begin{cases} 0 & \texttt{if } t_a < t < t_b \texttt{ or } t_R - t_b < t < t_R - t_a \\ 1 & \texttt{otherwise} \end{cases} \tag{8.32}$$

When $p(t) = 0$, the chemical shift anisotropy is zero and when $p(t) = 1$, the CSA is 'recoupled'. t_a and t_b are labeled in the SUPER pulse sequence shown in Figure 8.4. Note that

$$\frac{1}{t_R}\int_0^{t_R} p(t)\sin(\omega_R t)dt = \frac{1}{t_R}\int_0^{t_R} p(t)\sin(2\omega_R t)dt = 0 \tag{8.33}$$

since the integrand is an odd function. To satisfy Eq. (8.31), one needs

$$\begin{aligned} \chi &= \frac{1}{t_R}\int_0^{t_R} p(t)\cos(\omega_R t)dt = \frac{1}{t_R}\int_0^{t_R} p(t)\cos(2\omega_R t)dt \\ &= \frac{1}{t_R}\int_0^{t_R} p(t)\cos(n\omega_R t)dt \quad \texttt{(n=1,2)} \\ &= \frac{1}{t_R}\int_0^{t_R} \cos(n\omega_R t)dt - 2\frac{1}{t_R}\int_{t_a}^{t_b} \cos(n\omega_R t)dt \\ &= -2\frac{1}{t_R}\int_{t_a}^{t_b} \cos(n\omega_R t)dt \\ &= \frac{1}{n\pi}\left[\sin(n\omega_R t_a) - \sin(n\omega_R t_b)\right] \end{aligned} \tag{8.34}$$

By selecting the appropriate t_a and t_b values, the quasi-static anisotropic frequency can be obtained. In our experiment, $t_a/t_R = 0.25$ and $t_b/t_R = 0.415$ were used and the corresponding scaling factor χ was 0.15. Since the 360° pulse width is given by $\frac{t_b - t_a}{2}$, from the given values of t_a and t_b one can get the radio frequency of the 360° pulse as $\omega_{rf} = 12.12\omega_R$. As is well known, TOSS alone does not usually provide sideband suppression in 2D MAS experiments [3], and the 'γ integral'must be used together with TOSS to achieve sideband-free detection [33]. To compensate for the pulse length errors, a 64-step phase sequence was used to obtain the experimental spectra [32]. It is also noticed that if the isotropic chemical shift is also taken

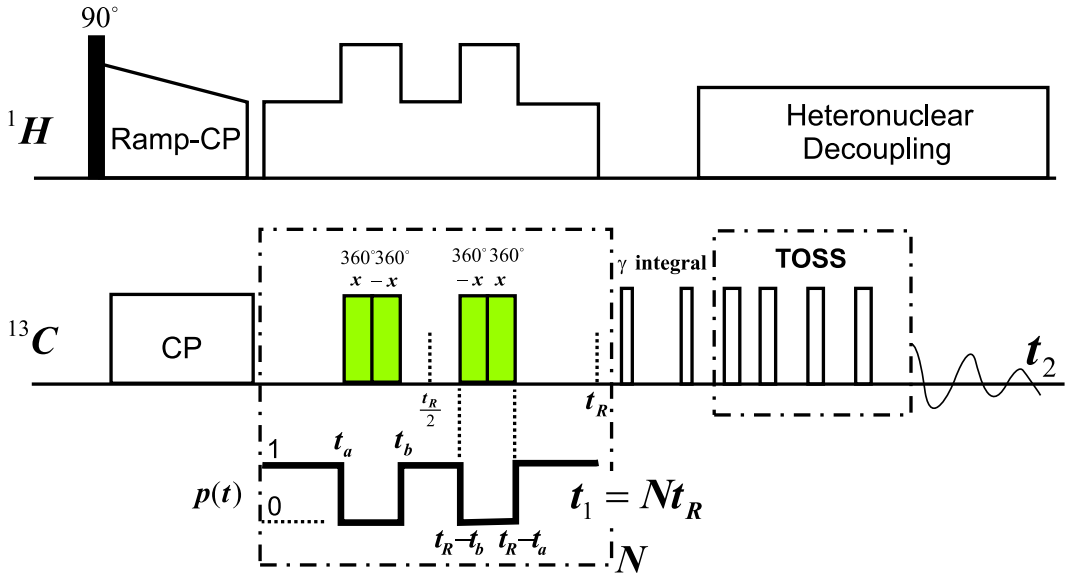

Figure 8.4: Pulse sequence of the SUPER NMR experiment. The increment of the evolution time t_1 is one rotation period t_R. At the bottom of the figure, the function $p(t)$ is shown.

.

into account, one can get [32]:

$$\begin{aligned}
\bar{\omega}_{cs} &= \frac{1}{t_R}\int_0^{t_R} p(t)\omega_{cs}(t)dt \\
&= \frac{1}{t_R}\int_0^{t_R} p(t)\omega_{iso}dt + \frac{1}{t_R}\int_0^{t_R} p(t)\omega_{ani}dt \\
&= \left[1 - 2\frac{t_b - t_a}{t_r}\right]\omega_{iso} + \chi(D_1' + D_2') \\
&= \xi\omega_{iso} + \chi\omega_{ani,stat}
\end{aligned} \tag{8.35}$$

According to this equation, the frequency in $\bar{\omega}_{cs}$ not only contains the scaled anisotropic chemical shift, but also includes a slightly scaled isotropic chemical shift. After Fourier transformation over t_2 and phasing in ω_2, the real parts of the sine and cosine signals of a specific site are

$$\langle\cos(\bar{\omega}_{cs}t_1)\rangle\,\delta(\omega_2 - \omega_{iso}) \quad \texttt{and} \quad \langle\sin(\bar{\omega}_{cs}t_1)\rangle\,\delta(\omega_2 - \omega_{iso}) \tag{8.36}$$

where $\bar{\omega}_{cs}$ is given by Eq. (8.35). The angle brackets indicate the powder average over all orientations. The two signal components can be combined to give a complex exponential in t_1

$$\begin{aligned}
s(t_1, \omega_2) &= \langle\cos(\bar{\omega}_{cs}t_1) + i\sin(\bar{\omega}_{cs}t_1)\rangle\,\delta(\omega_2 - \omega_{iso}) \\
&= \langle\exp(i\bar{\omega}_{cs}t_1)\rangle\,\delta(\omega_2 - \omega_{iso}) \\
&= \exp(i\xi\omega_{iso}t_1)\,\langle\exp(i\bar{\omega}_{ani}t_1)\rangle\,\delta(\omega_2 - \omega_{iso})
\end{aligned} \tag{8.37}$$

By using the properties of the δ function, the above equation can be rewritten as

$$s(t_1, \omega_2) = \exp(i\xi\omega_2 t_1) \left\langle \exp(i\bar{\omega}_{ani} t_1) \right\rangle \delta(\omega_2 - \omega_{iso}) \tag{8.38}$$

By multiplying the signal of Eq. (8.38) with a phase factor proportional to ω_2 and t_1,

$$s'(t_1, \omega_2) = \exp(-i\xi'\omega_2 t_1) s(t_1, \omega_2) \tag{8.39}$$

and if $\xi' = \xi - \chi$, then we can remove the isotropic-shift effect from the first dimension:

$$\begin{aligned} s'(t_1, \omega_2) &= \exp(-i\xi\omega_2 t_1) \exp(i\chi\omega_2 t_1) \exp(i\xi\omega_2 t_1) \left\langle \exp(i\bar{\omega}_{ani} t_1) \right\rangle \delta(\omega_2 - \omega_{iso}) \\ &= \exp(i\chi\omega_2 t_1) \left\langle \exp(i\bar{\omega}_{ani} t_1) \right\rangle \delta(\omega_2 - \omega_{iso}) \\ &= \exp(i\chi\omega_{iso} t_1) \left\langle \exp(i\chi\omega_{ani,stat} t_1) \right\rangle \delta(\omega_2 - \omega_{iso}) \\ &= \left\langle \exp(i\chi\omega_{cs}(0) t_1) \right\rangle \delta(\omega_2 - \omega_{iso}) \end{aligned} \tag{8.40}$$

After FT over the t_1 dimension, this gives a 2D spectrum with a specific powder pattern in the ω_1 dimension:

$$Re\left[S'(\omega_1, \omega_2)\right] = \left\langle \delta\left[\omega_1 - \chi\omega_{cs}(0)\right] \right\rangle \delta(\omega_2 - \omega_{iso}) \tag{8.41}$$

If the radio frequency irradiation of a peak is near ω_{iso}, the scaled CSA spectrum will sit in the middle of the ω_1 spectral range. However, the 2D spectrum usually covers a wide frequency range. To see the full powder spectrum one needs to foldback the 2D spectrum several times in ω_1 while shearing it parallel to the frequency domain ω_1 based on the above principle [3]. These undistorted quasi-static powder patterns are better than MAS sideband patterns, because the data analysis to obtain the principal CSA values is significantly simplified. The principal values can be read off with a cursor or ruler from the position of the peak and the two shoulders. This makes time-consuming simulations unnecessary. If simulations are desired, they are much simpler than those needed for MAS sideband patterns. In our CSA data simulations, WSOLIDS [34] software was used. SUPER [32] has already been demonstrated to produce a number of ^{13}C powder spectra in organic solids and polymers for different chemical (aromatic, unprotonated sp^2-hybridized, and aliphatic) sites. It has also been applied successfully on bent-core molecules in the solid state [35]. Here the SUPER method is employed to study both chiral and bent-core mesogens. When compared with typical principal values of CSA tensors from model compounds, this method may be used to aid the spectral assignment of a ^{13}C spectrum in the isotropic phase of these kinds of mesogens.

8.3 Separated Local Field Study

8.3.1 Homonuclear Dipolar Decoupling

Because molecular motions in solids and liquid crystals are strongly restricted, their NMR spectra are usually severely broadened by interactions such as quadrupole coupling, dipolar coupling, or chemical shift anisotropy. Various techniques have been used to reduce or eliminate these effects in order to decrease the linewidths of the NMR peaks. For $I = 1/2$ spin systems, the most prevalent line broadening is due to dipolar couplings. Methods to reduce the linewidth include magic angle spinning, homonuclear dipolar decoupling, and broadband heteronuclear decoupling. In the last chapter, we have discussed heteronuclear dipolar decoupling, in which the dipolar coupling between two sets of spins I and S is removed by a strong radio frequency field applied to the I spins while the S spins evolve. Here the homonuclear dipolar decoupling will be discussed. The main purpose is to remove H-H dipolar couplings as much as possible, so that the heteronuclear splittings in the 2D ^{13}C spectra can give accurate C-H dipolar couplings. The earliest method of homonuclear dipolar decoupling was off-resonance 'magic angle continuous wave' irradiation, proposed by Lee and Goldburg (LG) [36]. To understand the spin dynamics of the LG pulse sequence, a system of abundant spins needs to be considered. From Eq. (7.11), we know that the homonuclear dipolar interaction can be expressed in the tilted rotating frame as:

$$H_{II}^{TR} = P_2(\cos\theta_I) H_{II} \tag{8.42}$$

where $\theta_I = \tan^{-1}[\omega_{1I}/\Delta\omega_I]$ with $\Delta\omega_I = \omega_{0I} - \omega_{1I}$. So when θ_I is the magic angle, that is $\omega_{1I} = \sqrt{2}\Delta\omega_I$, H_{II}^{TR} is averaged to zero. The frequency of the effective field is $\omega_{eI} = \sqrt{3}\Delta\omega_I$ (See Fig. 8.5(a)). The Lee-Goldburg decoupling can be thought of as magic-angle spinning in a 'spin space'. In the experiment, the radio frequency source used to excite the spin system is set to differ from the Larmor frequency ω_{0I} by an offset $\Delta\omega_I$, so that the spin system would precess about the effective field along an axis forming the magic angle (54.74°) with respect to the magnetic field B_0, and the dipolar coupling term in the effective spin Hamiltonian would vanish. However, the Lee-Goldburg method is not very effective as this only eliminates the dipolar interaction to the zeroth order. Later on, multiple-pulse dipolar decoupling methods were proposed for further improvement [37–46]. These homonuclear dipolar decoupling sequences include WAHUHA [38, 39], MREV-8 [40, 41], BR-24 [42], BR-52 [42], BLEW-48 [43], and TREV-8 [44]. In 1989, Levitt and co-workers [37] demonstrated that the 'magic angle continuous wave'method of Lee and Goldburg [36] can be dramatically improved by frequency switching. In this sequence, the symmetrization is

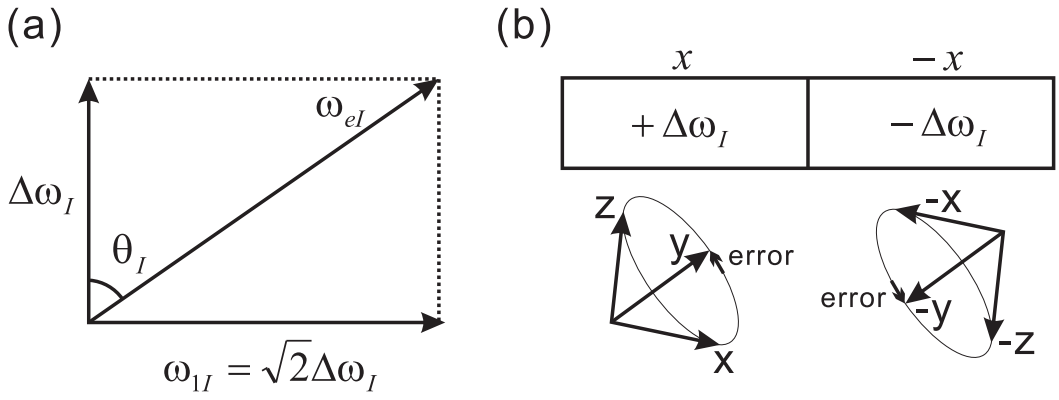

Figure 8.5: (a)The frequency relationships in the LG experiment. (b)Compensation for errors in the magnetization trajectories with the FS-LG sequence.

.

implemented by switching the offset between $+\Delta\omega_I$ and $-\Delta\omega_I$ and simultaneously changing the phase of the radio frequency irradiation by 180° (See Fig. 8.5(b)). The nonsecular part of dipolar Hamiltonian H_{II}^{ns} can also be removed by this procedure. This method is called the frequency-switched Lee-Goldburg (FS-LG) sequence and has become extremely useful in many applications. It has been shown that FS-LG is comparable to or better than those of many multiple-pulse dipolar decoupling methods [37].

8.3.2 LG-CP Theory

In the LG-CP scheme, the radio frequency irradiation of the I spin is applied off-resonance at the LG condition $\omega_{1I} = \sqrt{2}\Delta\omega_I$ in order to make the effective field at the magic angle, $\theta_I = \theta_m = 54.74°$, with respect to the static magnetic field. In this case the normal CP condition is changed and by setting $\theta_S = 90°$, the Hamiltonian in the 'tilted rotating frame' (Eq. (7.11)) can be rewritten as

$$H_{TR} = -\omega_{eI} I_z - \omega_{1S} S_z + 2bI_x S_x \sin\theta_m - 2bI_z S_x \cos\theta_m \tag{8.43}$$

In the CP experiment, the $I_z S_x$ can not be detected and is neglected in the discussion [47]. Similar to the derivation from Eq. (7.15)-(7.17), one can get the S-spin polarization after the cross-polarization interval τ:

$$\begin{aligned}\langle S_z \rangle(\tau) &\cong \frac{b^2 \sin^2\theta_m}{b^2 \sin^2\theta_m + (\omega_{eI} - \omega_{1S})^2} \times \sin^2\left[\frac{\tau}{2}\sqrt{b^2 \sin^2\theta_m + (\omega_{eI} - \omega_{1S})^2}\right] \\ &\cong \frac{b^2 \sin^2\theta_m}{b^2 \sin^2\theta_m + (\omega_{eI} - \omega_{1S})^2} \times \frac{1}{2}\left\{1 - \cos\left[\tau\sqrt{b^2 \sin^2\theta_m + (\omega_{eI} - \omega_{1S})^2}\right]\right\}\end{aligned} \tag{8.44}$$

When $\omega_{eI} = \omega_{1S}$, full polarization transfer is achieved. This condition is different from the normal Hartmann-Hahn condition, and leads to the power level for the S spin during CP being larger than that for the normal CP, and the difference is about $20\log(\omega_{eI}/\omega_{1I}) = 20\log\sqrt{3/2} = 1.76$dB. Under this condition, Eq. (8.44) can be simplified as

$$\langle S_z \rangle (\tau) \;\cong\; \frac{1}{2}[1 - \cos(b\tau \sin\theta_m)] \tag{8.45}$$

The observed magnetization $M_{S_z}(\tau)$ after LG-CP again takes the form analogous to that for normal CP:

$$M_{S_z}(\tau) = M_{S_z}(0)\left[1 - \frac{1}{2}\exp\left(-\frac{\tau}{T_{II}}\right) - \frac{1}{2}\exp\left(-\frac{3\tau}{2T_{II}}\right)\cos(b\tau\sin\theta_m)\right] \tag{8.46}$$

We notice that the introduction of the LG condition results in the scaling of the heteronuclear coupling, with a theoretical scaling factor of $\sin\theta_m = 0.816$ in the oscillatory cosine term. This term gives a doublet after Fourier transformation. There is also a non-oscillatory part responsible for the zero frequency peak, which may overlap with the C-H doublet located close to the center, causing difficulties in measuring small dipolar couplings. For attenuating the zero frequency peaks, polarization inversion (or phase-reversed normal CP) has been utilized before LG-CP [48, 49]. During the polarization inversion process, a doubling in the amplitude of the oscillatory component occurs together with reducing the initial intensity of the non-oscillatory component to zero.

From Eq. (8.46), the observed C-H dipolar splittings $\Delta\nu_{ij}$ can be understood using

$$\Delta\nu_{ij} = 2b\sin\theta_m \tag{8.47}$$

where b, the C-H dipolar coupling constant, similar to Eq. (8.22) is given by

$$\begin{aligned} b &= \frac{\mu_0\gamma_I\gamma_S\hbar}{16\pi^2 r^3}(1 - 3\cos^2\theta) \\ &= \frac{\mu_0\gamma_I\gamma_S\hbar}{16\pi^2 r^3} 2\sum_m D^2_{m,0}(\Omega_{LM}) D^2_{0,m}(\Omega_{MP}) \end{aligned} \tag{8.48}$$

where $\Omega_{MP} = (\phi_{ij}, \theta_{ij}, 0)$ denotes the Euler angles that carry the principal axis frame for dipole-dipole interaction to the local molecular frame and Ω_{LM} denotes the Euler angles that transform the local molecular frame into the laboratory frame. If we set

$$S_{z'z'} = \left\langle D^2_{0,0}(\Omega_{LM}) \right\rangle \quad \texttt{and} \quad S_{x'x'} - S_{y'y'} = \sqrt{\frac{3}{2}}\left\langle D^2_{2,0}(\Omega_{LM}) + D^2_{-2,0}(\Omega_{LM}) \right\rangle \tag{8.49}$$

Then Eq. (8.48) can be rewritten as

$$b = -(k/r^3_{ij})\left[P_2(\cos\theta_{ij})S_{z'z'} + \frac{1}{2}\sin^2\theta_{ij}(S_{x'x'} - S_{y'y'})\right] \tag{8.50}$$

with $k = \mu_0\gamma_H\gamma_C\hbar/8\pi^2$=30.21 kHzÅ^3 for a bonded C-H spin pair. In our study the values $r_{CH} = 1.09$Å and $r_{CC} = 1.4$Å were chosen. For the *ortho* and *meta* carbons on the phenyl ring, one has to consider both $\Delta\nu_1$ due to the attached proton and $\Delta\nu_2$ due to the nearby nonbonded proton. The observed dipolar splitting is then given by $\sqrt{(\Delta\nu_1)^2 + (\Delta\nu_2)^2}$. For the quaternary carbons, the two nonbonded protons are located at the same r_{ij} making the observed splitting being given by $\sqrt{2}\Delta\nu_{ij}$ [50].

8.3.3 Separated Local Field experiment

The coherent transfer of energy observed between strongly dipolar coupled heteronuclear spin systems in solids during cross-polarization has provided a means of resolving and characterizing dipole-dipole couplings. One particularly useful experiment is to record a two-dimensional spectrum in which the coordinate of a peak in one dimension is the dipolar splitting of the nuclei (e.g. ^{13}C-^{1}H) and the coordinate in the other dimension is the chemical shift of the nucleus (e.g. ^{13}C). This method is known as 2D separated local field (SLF) spectroscopy [50–56] and has been used to measure and assign C-H dipolar couplings. In the SLF method, a ^{13}C spin evolves under the influence of dipolar local fields produced by the surrounding protons. Homonuclear decoupling of the abundant spins such as protons by means of the Lee-Goldburg sequence and polarization inversion has also been incorporated (See Fig. 8.7). Dipolar oscillations during cross-polarization have also been observed in the case of partially ordered systems such as liquid crystals [50, 55]. The 2D version of the experiment has provided the determination of dipolar couplings and order parameter information in several studied systems.

SLF experiments are based on the cross-polarization process which gives rise to a S spin signal M_{S_z} that depends on the I-S contact time τ and is given by Eq. 8.46. In a 2D experiment, where the contact time τ corresponds to the evolution t_1 period, the Fourier transform along t_1 gives the oscillatory part in Eq. 8.46. In addition the S spins show chemical shifts in the detection period which might be resolvable in the absence of $I - S$ dipolar broadening. Now imagine giving the S spins an initial transverse polarization $\langle S_+(0)\rangle = \langle S_x\rangle + i\langle S_y\rangle$ at time zero which is then allowed to decay in two stages. In the first time interval, t_1, a line-narrowing FSLG irradiation is applied to the I spins resulting in suppressing H_{II} and scaling H_{IS} by a factor $\sin\theta_m$. Then H_{IS} is suppressed in the second time interval, t_2, by a strong on resonance irradiation of the I spin while free induction decay of the remainder of

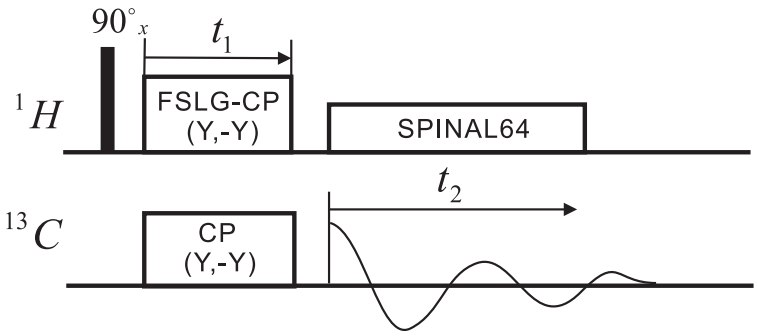

Figure 8.6: Pulse sequence of the SLF NMR experiment.

.

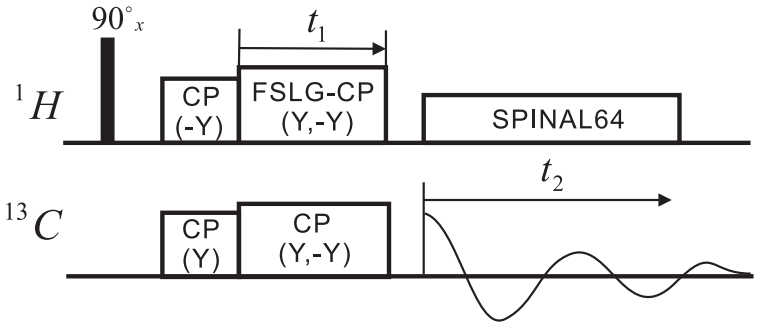

Figure 8.7: Pulse sequence of the PISLF NMR experiment.

.

the S is recorded (See Fig. 8.6). The signal observed at t_1, t_2 has the form [51]:

$$\begin{aligned}\langle S_+(t_1,t_2)\rangle &= \langle \exp[i(H_{cs}+\sin\theta_m H_{IS})t_1]\exp(iH_{cs}t_2)S_+ \\ &\quad \exp(-iH_{cs}t_2)\exp[-i(H_{cs}+\sin\theta_m H_{IS})t_1]\rangle \end{aligned} \tag{8.51}$$

A Fourier analysis of $\langle S_+(0,t_2)\rangle$ with respect to t_2 gives the pure chemical shift spectrum $f(\omega_2)$ of the S spectrum; a similar analysis of $\langle S_+(t_1,0)\rangle$ with respect to t_1 yields 'dipolar' slices, each containing a wide-line spectrum, $f(\omega_1)$, in which the effects of the $I-I$ interactions have been removed. Two-dimensional Fourier analysis yields an array, $f(\omega_1,\omega_2)$, in which dipolar spectra of all distinct S spins can be separated. In the present study, the SLF spectrum is reported here to aid the ^{13}C spectral assignment, and to obtain C-H dipolar couplings. These C-H couplings enable the determination of local order parameter tensors for the phenyl or biphenyl rings.

8.4 Measurements of CSA tensors

8.4.1 Study of ZLL7/*

The 2D ^{13}C SUPER experiment was performed in a solid sample at room temperature using a 4 mm double resonance CP/MAS probe. Sample temperature was regulated to within 0.1° by means of an air flow. The sample was rotating at a spinning speed (f_{rot}) of 4.8 kHz . Using the pulse sequence in Fig. 8.4, after a 90° (4.2 μs) proton irradiation and a ramp CP of 2 ms, four ^{13}C 2π pulses were used to recouple CSA during MAS. To avoid the signal being dephased by strong heteronuclear couplings during the recoupling 2π pulses, a cw proton decoupling field of 69 kHz was applied. During acquisition, a TPPM15 decoupling sequence was applied at a decoupling level of 30 kHz. The number of t_1 increments was 32, and the STATES-TPPI [57] quadrature detection method was used.

Figure 8.8 shows the 2D SUPER spectrum in the solid phase of ZLL7/*, together with the 1D isotropic spectrum (ω_2 projection) and ^{13}C peak assignments at the top. The CSA powder patterns of different carbon sites can be retrieved from the ω_1 slices of Figure 8.8. The assignment of the aromatic carbon signals in these compounds is based on the isotropic chemical-shift prediction using a commercial software (ChemOffice) and the observed CSA powder patterns. In Figure 8.9, the CSA powder patterns obtained for ZLL7/* from Figure 8.8 are shown. Each powder line shape (dotted lines) was simulated using the WSOLIDS simulation package [34] to determine the principal components of the CSA tensor, and they are shown as solid curves in this figure for direct comparison. The CSA tensors for ZLL7/* derived from the SUPER are summarized in Table 8.2. The numbers in parentheses are results from density functional theory (DFT) [58], which are consistent with the results obtained from SUPER.

8.4.2 Study of 10BrPBBC and 10ClPBBC

Several papers concerning ^{13}C NMR on bent-core mesogens have appeared in the literature [59–64]. All these studies point to the necessity of the knowledge of chemical shift anisotropy (CSA) tensors of different carbon sites, both the orientation and principal components for each CSA tensor, for the analyses of ^{13}C spectra in an aligned mesophase [62]. Since one of the obstacles in ^{13}C NMR study of bent-core LC is a lack of CSA tensors (in particular the ^{13}C sites of the central phenyl ring), the present study aims to use SUPER to give accurate

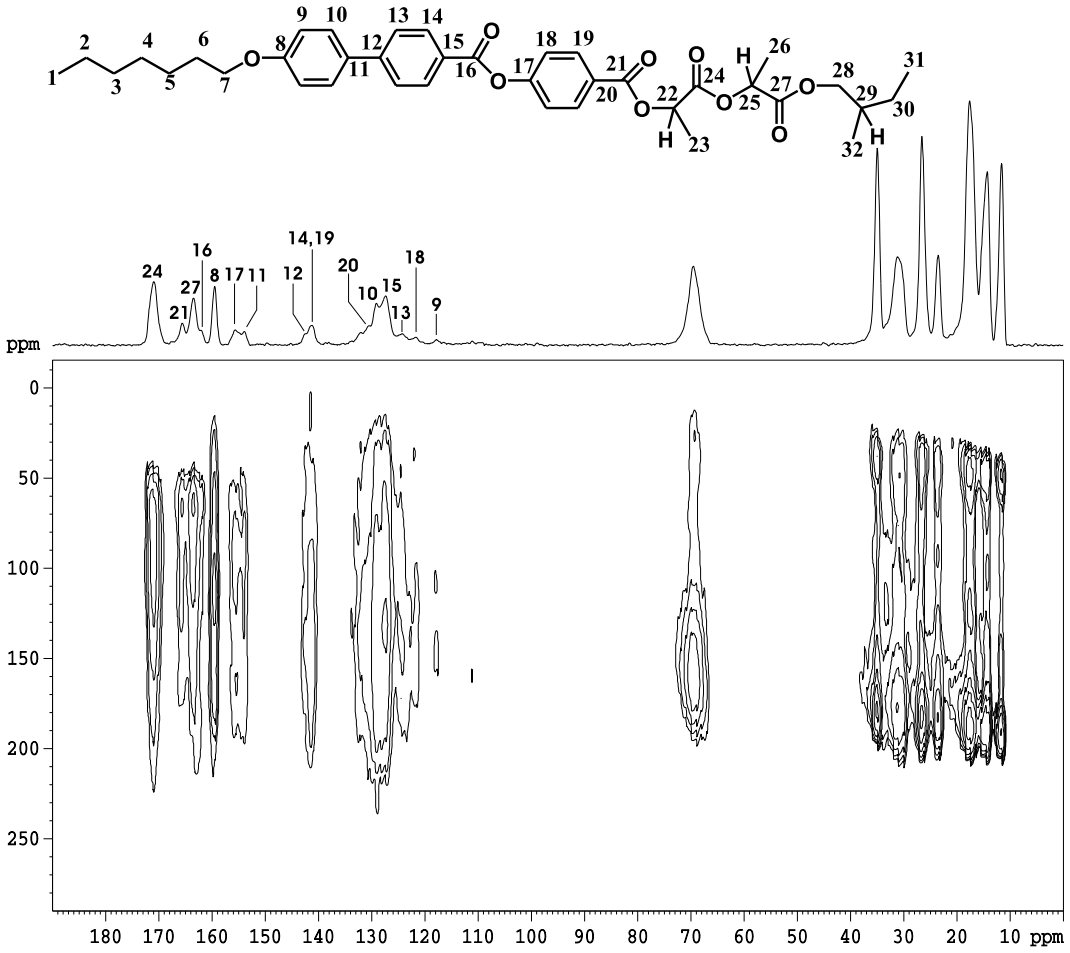

Figure 8.8: 2D SUPER spectrum in solid phase of ZLL7/*. Some carbon sites are labeled.

.

principal values in CSA tensors for two banana-shaped molecules. In particular, different substituents are used in the central phenyl ring to give 10BrPBBC and 10ClPBBC (see Fig. 1.14). The synthesis and characterization of 10ClPBBC and 10BrPBBC have appeared elsewhere [65]. Both show a nematic phase by cooling from the clearing temperature. In the 2D ^{13}C SUPER experiment, the 90° proton irradiation is $3.4\mu s$ and the sample was rotating at a spinning speed of 4.9 kHz. To avoid the signal being dephased by strong heteronuclear couplings during the recoupling 2π pulses, a proton decoupling field of 181 kHz is applied. During acquisition, the decoupling level of the TPPM15 decoupling sequence is at 124 kHz. The higher decoupling power was used to achieve better resolution. The number of t_1 increments was 32 with 512 scans per t_1 increment.

Figure 8.10 shows the 2D SUPER spectra in the solid phase of 10ClPBBC and 10BrPBBC, together with the 1D isotropic spectrum (ω_2 projection) and ^{13}C peak assignments at the top. The CSA powder patterns of different carbon sites can be retrieved from the ω_1 slices

Table 8.2: Comparison of CSA tensors for various carbon sites of ZLL7/* obtained by SUPER and density functional theory.

Sites	C8	C9	C10	C11	C12
σ_{xx}	99.19(100.0)	23(22.9)	27.55(25.7)	38.8(36.9)	39.65(40.4)
σ_{yy}	156.7(158.2)	134(130.1)	135.55(139.9)	166.8(171.0)	147.65(151.2)
σ_{zz}	222.7(220.3)	195(199.2)	223.55(221.9)	255.8(253.4)	239.65(235.3)
Sites	C13	C14	C15	C16	C17
σ_{xx}	45(37.1)	45.16(42.5)	18(18.8)	122.69(122.0)	77.01(72.0)
σ_{yy}	132(134.3)	157.16(160.5)	127(129.2)	128.69(125.3)	154.01(152.8)
σ_{zz}	195(200.6)	221.16(220.0)	236(233.1)	234.69(237.2)	237.01(238.2)
Sites	C18	C19	C20	C21	
σ_{xx}	24.25(17.3)	45.16(45.8)	20.45(25.4)	128.0(127.6)	
σ_{yy}	147.25(140.1)	157.16(157.9)	142.45(140.1)	135.0(136.5)	
σ_{zz}	213.25(206.0)	221.16(218.1)	228.45(225.8)	234.5(232.4)	

The numbers in parentheses are results from DFT.

of Figure 8.10. The assignment of the aromatic carbon signals in these compounds is also based on the isotropic chemical-shift prediction using a commercial software, those of similar compound studied in our laboratory and the observed CSA powder patterns. In Figure 8.11, the CSA powder patterns obtained from Fig. 8.10a for 10ClPBBC are shown together with the simulated line (solid lines). The CSA tensors derived from the simulations are summarized in Table 8.3. The observed powder patterns for the aromatic ether sites 1, 9 and 13 show nice powder patterns with σ_{yy} around 159ppm, which is consistent with the literature value [32]. The quaternary carbons 4, 5 and 8 also show good powder patterns. Other aromatic sites exhibit recognizable powder patterns, all with the σ_{yy} peak downfield from the isotropic shift (center of gravity), which is typical for aromatic protonated carbons.

The CSA tensors for 10BrPBBC derived from the powder spectra shown in Fig. 8.12 are summarized in Table 8.4. This information is used in the study of order described in section 9.4. The C_2 peak is overlapped with a carbon peak (X10) of the chain (See Fig. 8.10). Hence it is hard to get its CSA tensor. By comparing the CSA tensors of the carbon site 10 for 10ClPBBC and 10BrPBBC, we note that the isotropic shift for 10BrPBBC is smaller, which is due to the lower electronegativity of the bromine nucleus. We believe that the CSA tensors obtained here could be useful for ^{13}C NMR studies of other banana-shaped molecules. The present SUPER experiments have shown better spectral resolution than those reported previously for banana molecules [35], since almost all aromatic carbon sites can give good

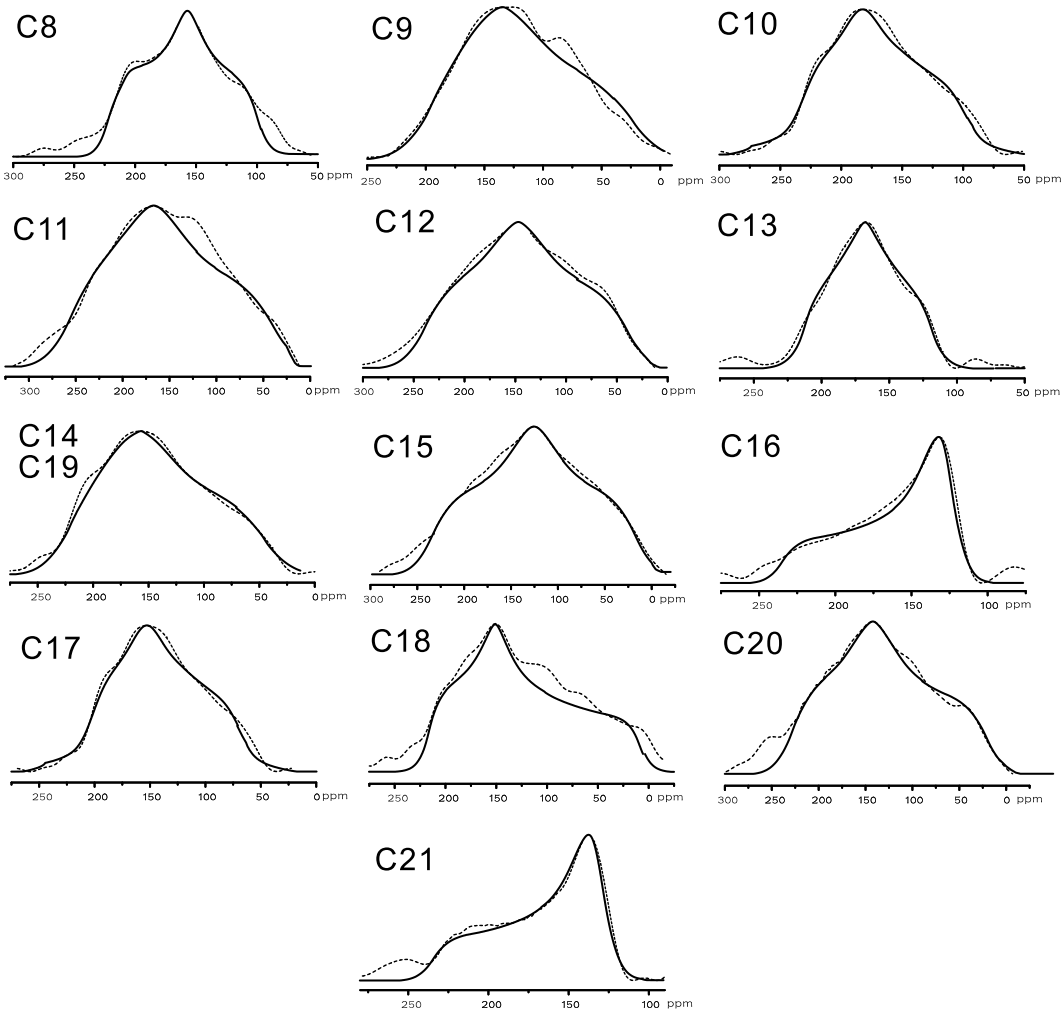

Figure 8.9: Cross sections from the 2D SUPER spectrum of ZLL7/*. Solid curves denote theoretical simulations of CSA powder patterns.

.

Table 8.3: CSA Tensors for various carbon sites of 10ClPBBC determined by SUPER.

sites	1	2	3,6	4	5	7
σ_{xx}	85.66	46.10	47.81	60.23	87.94	50.31
σ_{yy}	159.65	121.26	139.27	126.95	135.29	145.77
σ_{zz}	223.57	158.10	185.81	191.23	214.85	189.31
σ_{iso}	156.3	108.5	124.3	126.1	146.0	128.5
sites	8	9,13	10	11	12	14
σ_{xx}	48.20	81.49	47.74	59.71	66.88	58.73
σ_{yy}	139.05	158.55	124.74	127.29	115.92	121.12
σ_{zz}	195.20	226.40	184.74	174.71	158.88	164.73
σ_{iso}	127.5	155.5	119.1	120.6	113.9	114.9

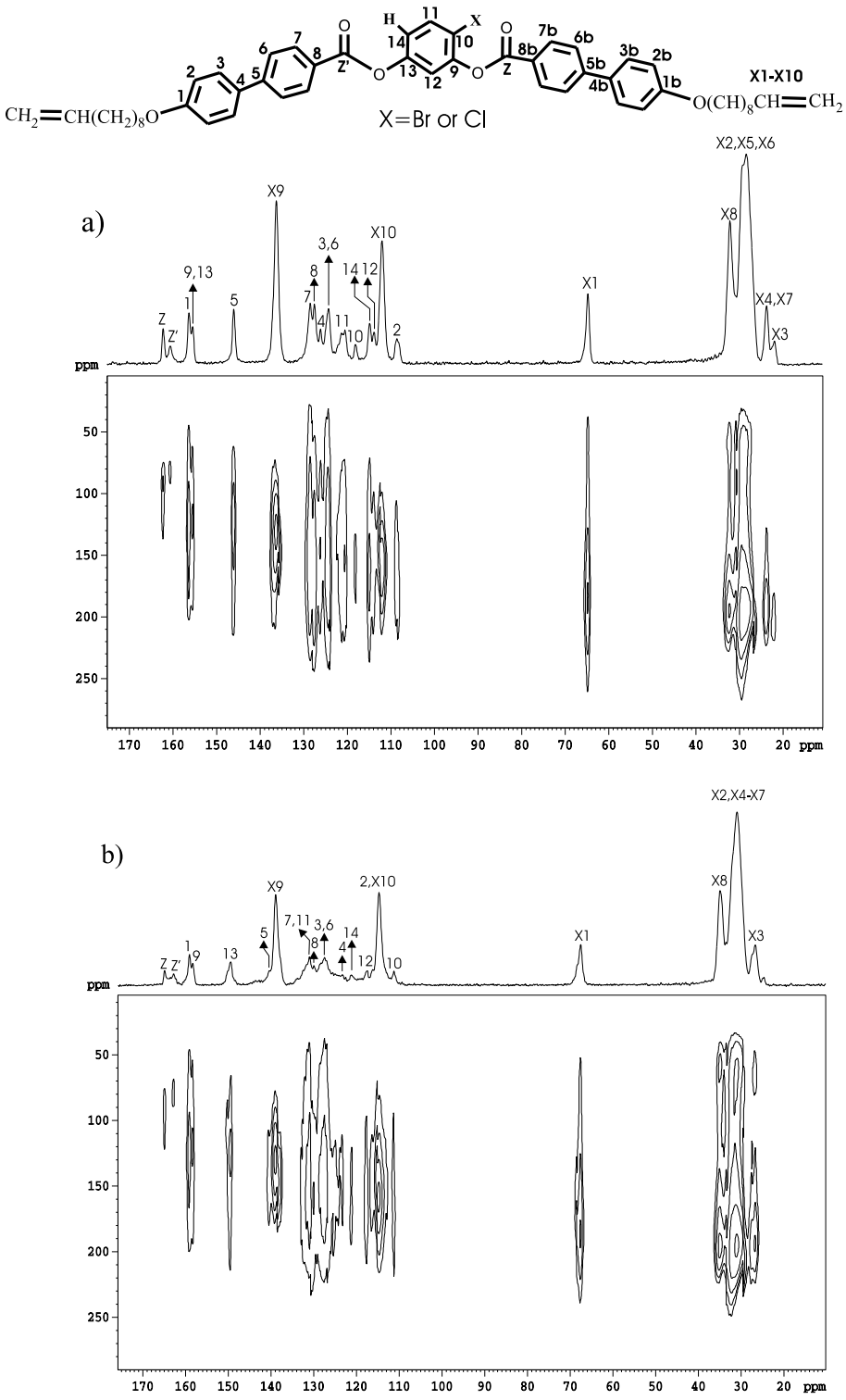

Figure 8.10: 2D SUPER spectrum in the solid phase of a) 10ClPBBC and b) 10BrPBBC. The labels X1 to X10 are for carbon chain sites starting from the core.

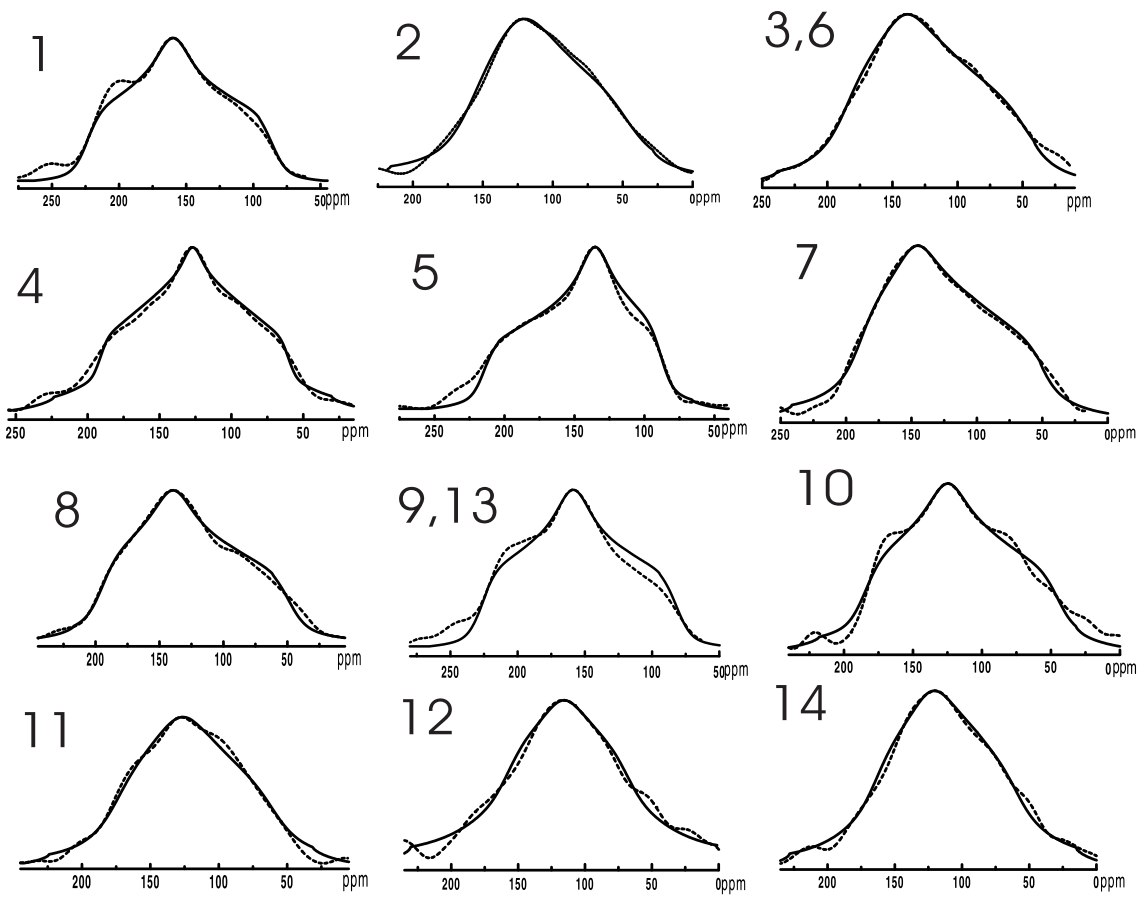

Figure 8.11: Cross sections from the 2D SUPER spectrum of 10ClPBBC. Solid curves denote theoretical simulations of CSA powder patterns.

Table 8.4: CSA Tensors for various carbon sites of 10BrPBBC determined by SUPER.

sites	1	3,6	4	5	7,8,11	9	10	12	13	14
σ_{xx}	93.4	56.6	46.7	83.9	44.1	90.3	47.3	33.9	88.6	43.8
σ_{yy}	159.1	133.3	128.3	140.6	144.8	157.3	121.1	135.6	136.6	132.2
σ_{zz}	224.4	192.6	192.7	196.9	204.1	227.3	165.3	182.9	223.1	187.8
σ_{iso}	159.0	127.5	122.6	140.5	131.0	158.3	111.2	117.5	149.4	121.3

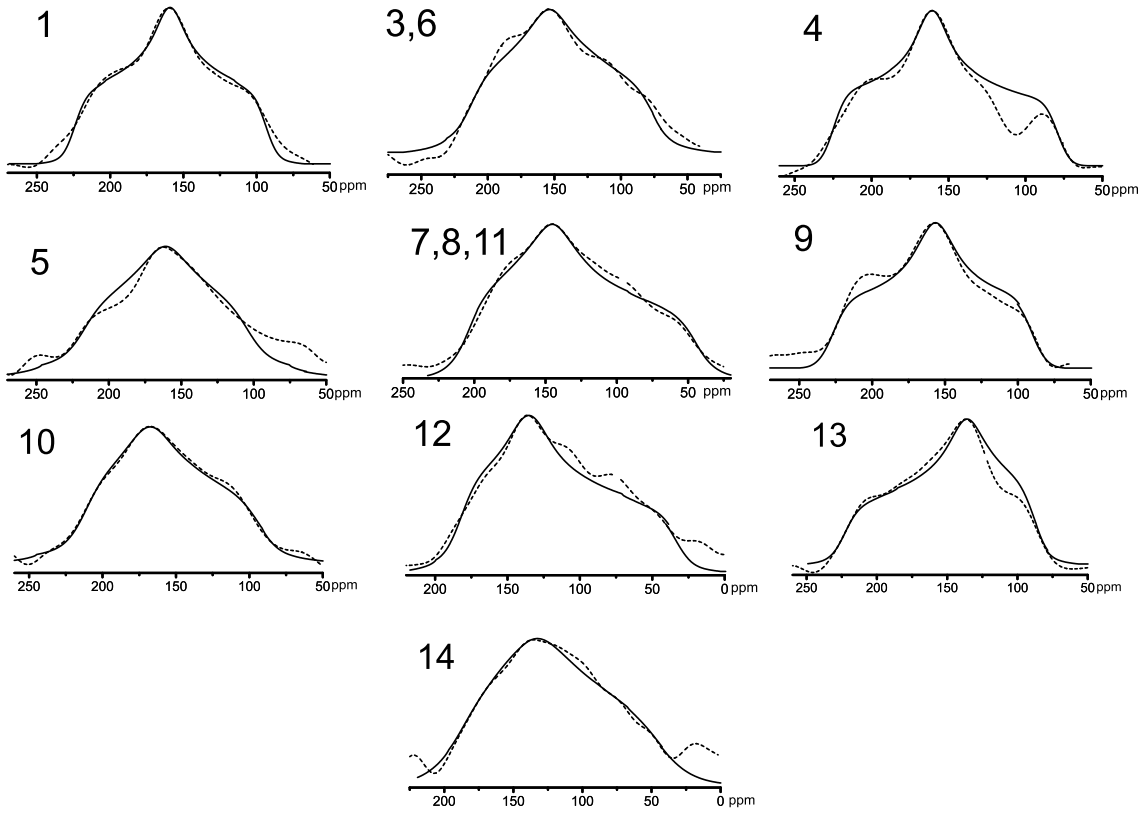

Figure 8.12: Cross sections from the 2D SUPER spectrum of 10BrPBBC. Solid curves denote theoretical simulations of CSA powder patterns.

powder patterns. Information on the CSA tensors from the central phenyl ring is crucial in defining the bending angle between the lateral wings in the molecular core.

8.4.3 Study of A131

Liquid crystals with biaxial nematic phases have been predicted theoretically by Freiser in 1970 [66]. Despite the interest in obtaining experimental evidence for this phase over the years, this topic has remained difficult. In recent years, the discovery of novel mesophases formed by the bent-core molecules have attracted much scientific interest including the possibility of biaxial nematic phases [67–85]. The determination of second rank tensorial physical properties in a bulk sample is an unambiguous method for the verification of the nematic phase biaxiality. The deuterium NMR method has been adopted in many investigations to identify the biaxial nematic phase [67, 68]. To assist the ordering study of biaxial nematic phase of bent-core molecules, the 2D SUPER experiment was performed on A131 to get the chemical shift tensors. The spectrum was obtained on a solid sample at room temperature using a 4 mm double resonance CP/MAS probe by rotating the sample at a spinning speed (f_{rot}) of 4.8

kHz.

Figure 8.13 shows the 2D SUPER spectrum in the solid phase of A131, together with the 1D isotropic spectrum (ω_2 projection) and ^{13}C peak assignments at the top. Some peaks are not labeled due to the uncertainty of peak assignments. The CSA powder patterns of different carbon sites can be retrieved from the ω_1 slices of Figure 8.13. The assignment of the aromatic carbon signals in these compounds is based on the isotropic chemical-shift prediction using a commercial software, the observed CSA powder patterns and a high resolution NMR study (given in next chapter) of A131 as a solute in $CDCl_3$. In Figure 8.14, the CSA powder patterns obtained for A131 from Figure 8.13 are shown. Each powder line shape (dotted lines) was simulated using WSOLIDS simulation package [34] to determine the principal components of the CSA tensor, and they are shown as solid curves in this figure for direct comparison. The CSA tensors for A131 derived from the SUPER are summarized in Table 8.5. Since some peaks are overlapping, the derived chemical shift tensors do not necessarily represent the principal values of the original peaks. These results may still be useful to study the ordering of biaxial nematic phase in A131.

Table 8.5: CSA Tensors for various carbon sites of A131 determined by SUPER.

sites	Z	Z'	5	17	20	21	14,15
σ_{xx}	125.7	121.9	95.5	98.3	88.9	78.3	65.1
σ_{yy}	132.7	128.9	151.5	150.3	155.9	159.3	152.1
σ_{zz}	233.2	233.9	213.5	210.3	207.9	209.3	188.1
σ_{iso}	163.9	161.6	153.5	152.9	150.9	148.9	135.1
sites	3,7	23	2,13	4	19	22	6,18
σ_{xx}	56.1	75.9	62.4	62.8	39.9	58.2	48.7
σ_{yy}	158.6	150.9	135.4	132.8	153.9	138.2	138.2
σ_{zz}	187.1	171.9	193.4	187.8	181.9	177.2	181.7
σ_{iso}	133.9	132.9	130.4	127.8	125.2	124.6	122.8

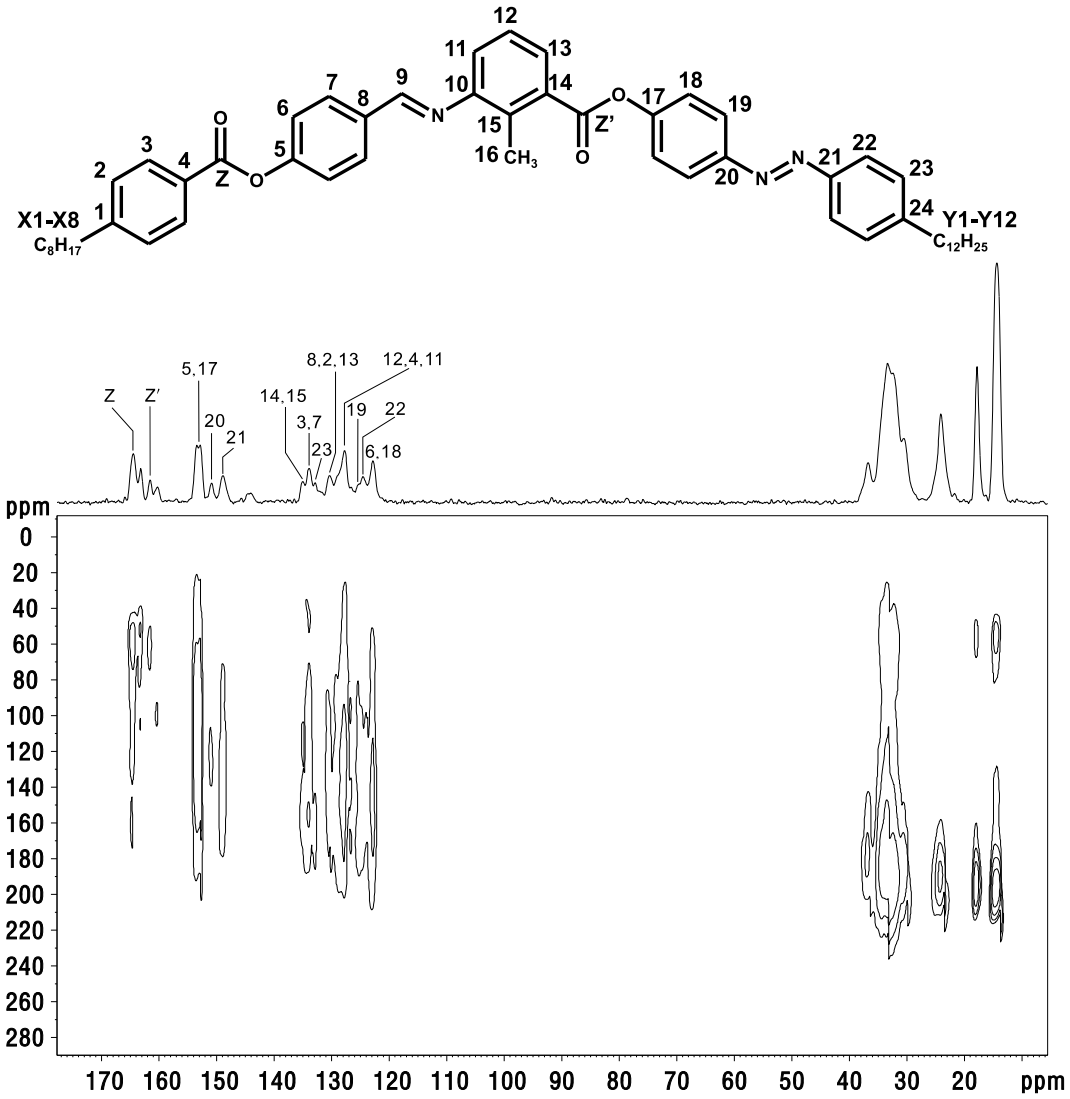

Figure 8.13: 2D SUPER spectrum in solid phase of A131. Some carbon sites are labeled.

.

8.5 SLF Study of Chiral Molecules

8.5.1 Study of 10B1M7

The 1D ^{13}C NMR study of 10B1M7 has been discussed in chapter 7. In the 1D data analysis the order parameters of the molecule are obtained based on the observed ^{13}C chemical shifts. To assist the assignment of ^{13}C peaks and demonstrate the SLF technique introduced in this chapter, 2D SLF experiment was performed on 10B1M7 at 105°C using the pulse sequence shown in Fig. 8.6. Generally, the Hartmann-Hahn matching condition during LG-CP was found to be very sensitive. Here the proton r.f. irradiation was switched between the two

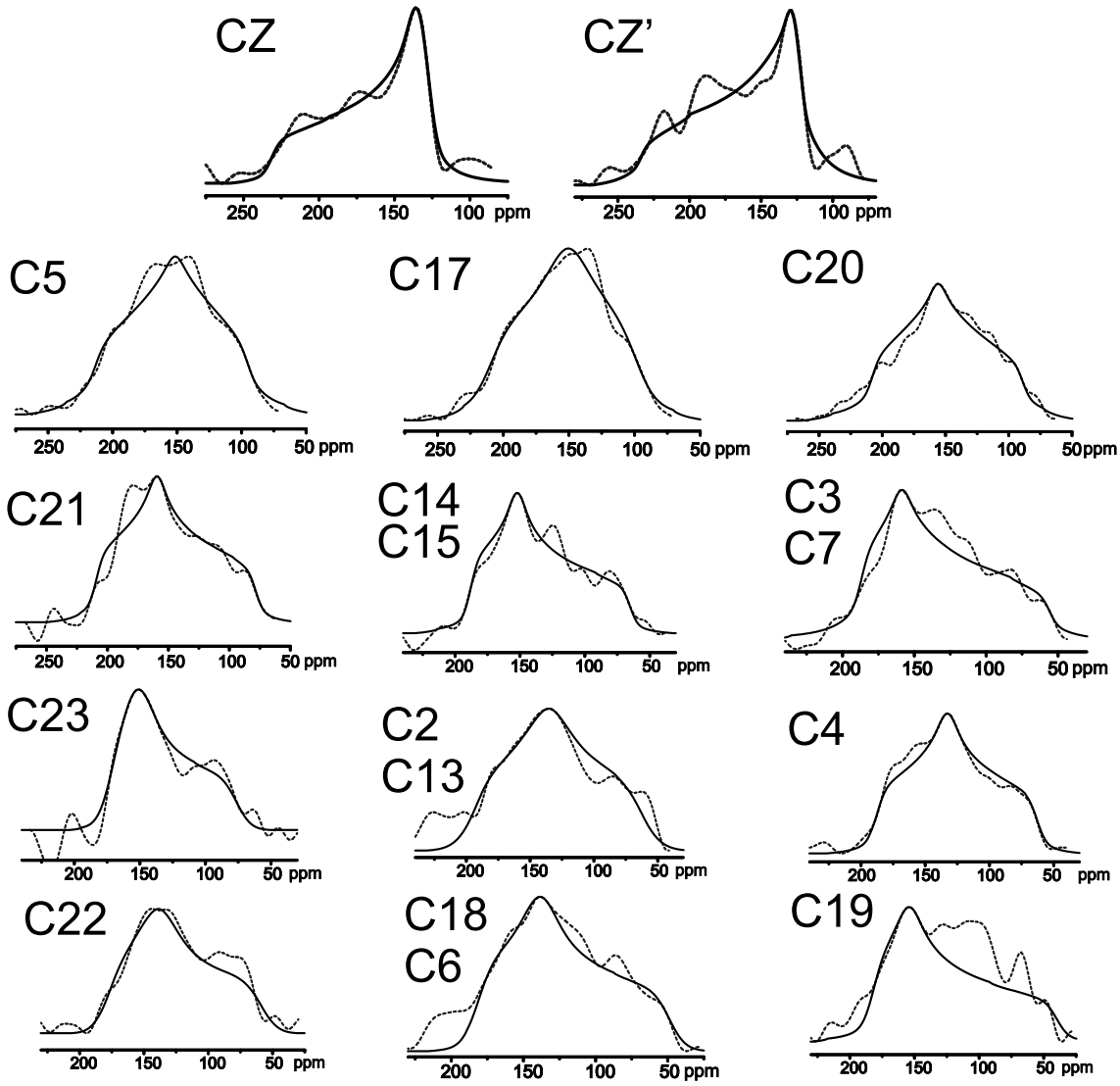

Figure 8.14: Cross sections from the 2D SUPER spectrum of A131. Solid curves denote theoretical simulations of CSA powder patterns.

LG conditions $\pm\Delta\omega_I$ for each 2π rotation of the proton magnetization about the effective field. The dipolar oscillations were observed on the CP buildup curves while homonuclear decoupling of protons using the FSLG sequence at a strength of 50.9 Hz was applied. During the t_2 period, heteronuclear decoupling was achieved by SPINAL-64 at a decoupling field of ca. 80 kHz. The number of t_1 increments was 32 with 32 scans per t_1 increment. Typical proton and carbon 90° pulse widths in SLF experiments were $3.1\mu s$ and $4.9\mu s$, respectively. The spectrum of the SLF experiment in the ω_2 dimension shows the normal proton-decoupled ^{13}C peaks, while the slices in the ω_1 dimension show the individual ^{13}C nuclei with the C-H dipolar couplings. The temperature gradient across the sample was estimated to be within 0.3 degrees.

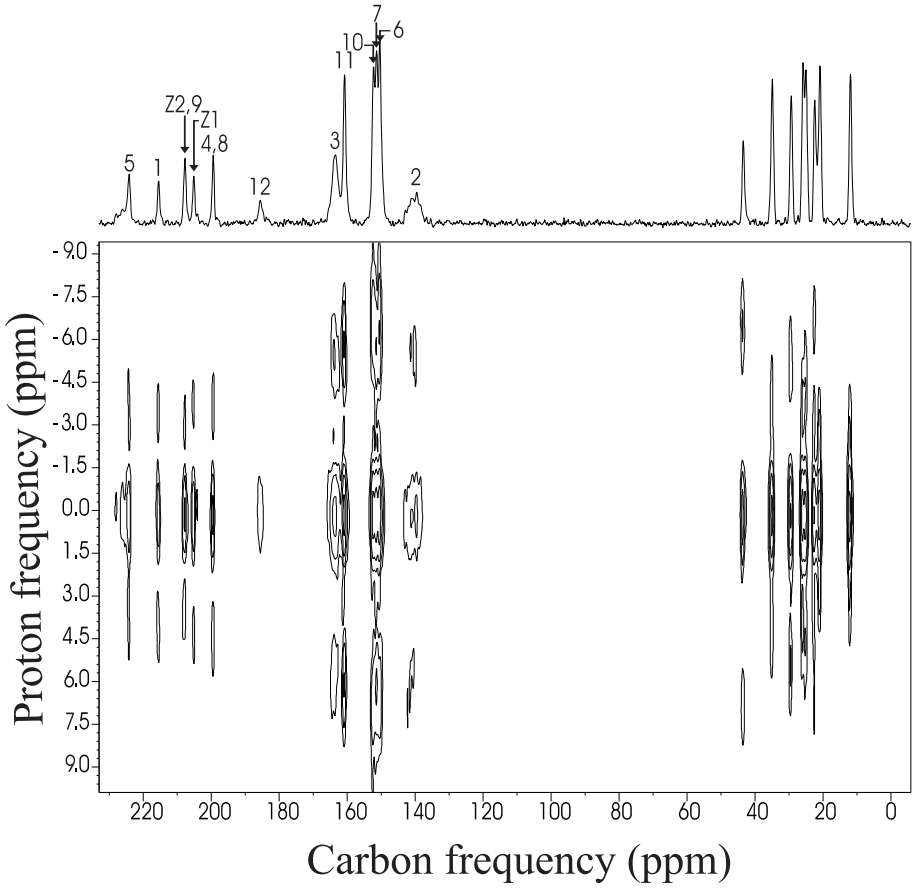

Figure 8.15: 2D SLF spectrum of 10B1M7 at 105°C using the pulse sequence of Figure 8.6.

.

Figure 8.15 shows a typical SLF spectrum of 10B1M7. In this figure, the carbon peaks are labeled the same as in the 1D ^{13}C peak assignment in chapter 7. Figure 8.16 shows some selected ω_1 slices from the aromatic region. The dipolar oscillation frequencies for carbons 6, 7, 10 and 11 are seen to be similar, and are larger than those of the quaternary carbons 5, 8, 9 and 12. We notice that there are central peaks due to the non-oscillatory components in the spectral slices. Using the dipolar splittings the local order parameters of phenyl rings in the biphenyl fragment can be studied. Here we define the local fragment frame z' is along the biphenyl part and x' is on the biphenyl plane. We kept the same $S_{z'z'}$ value and different $S_{x'x'} - S_{y'y'}$ values for the two phenyl rings in the biphenyl part, and varied the angle θ_{CH} to optimize the fit to the experimental splittings based on Eqs (8.47) and (8.50). Both the experimental and calculated results are given in Table 8.6. The calculated and experimental splittings are consistent. From the fitting the value $S_{z'z'} = 0.66$ for the biphenyl part was obtained. This value appears to be consistent with the corresponding S value found before. Also the segment biaxial order parameters $S_{x'x'} - S_{y'y'} = -0.02$ for phenyl ring '5,6,7,8' and $S_{x'x'} - S_{y'y'} = -0.01$ for phenyl ring '9,10,11,12' were determined. These values are similar

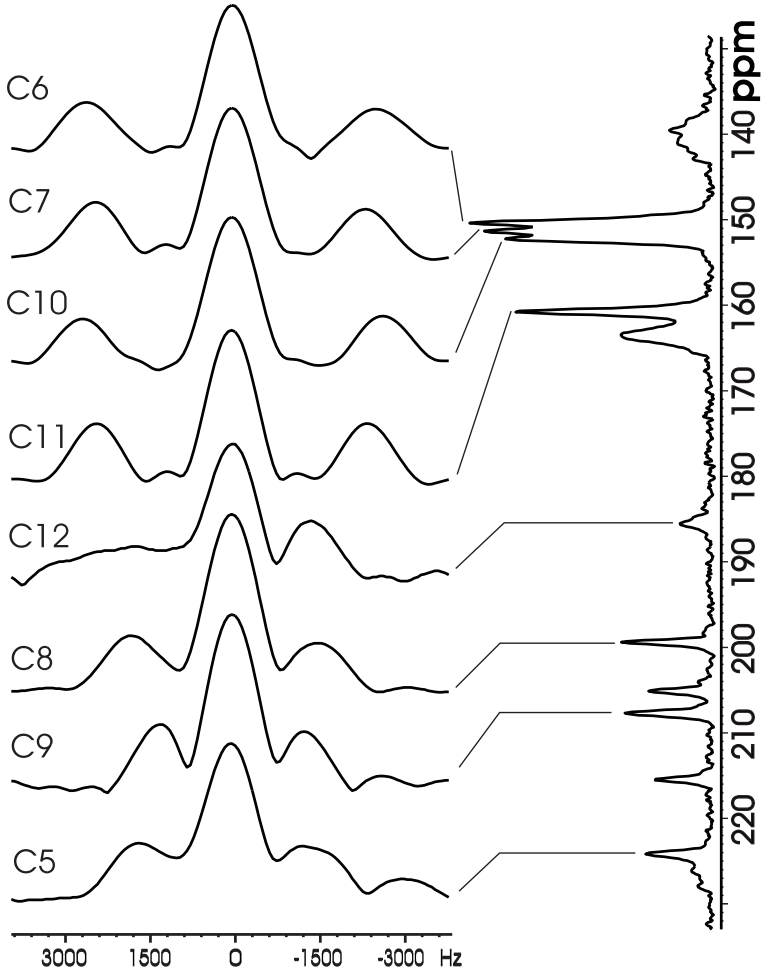

Figure 8.16: Plots of 1D slices in the ω_1 dimension of Figure 8.15 for some carbon sites of 10B1M7.

.

to the results we got before. The optimized angles between the C-H bond and the local z axis are $\theta_{CH} \approx 59.3°$ for site 11, $\theta_{CH} \approx 60.2°$ for site 10 and $\theta_{CH} \approx 60.1°$ for site 6.

8.5.2 Study of ZLL7/*

2D SLF NMR spectrum was carried out on a stationary ZLL7/* sample using the pulse sequence shown in Fig. 8.7. The dipolar oscillations were observed on the CP buildup curves when homonuclear FSLG decoupling at 34.4 kHz was applied during CP. During t_2, heteronuclear decoupling was achieved by SPINAL-64 at 45.4 kHz. To decrease the central peaks in the 2D SLF spectrum, polarization inversion [48, 49] for a fixed duration ($2ms$) was also included in the pulse sequence. The number of t_1 increments was 80 with 96 scans per t_1 increment, and the STATES method was used. A typical proton 90° pulse width in the 2D experiments was ca. 3.1 μs.

Table 8.6: Dipolar splittings of biphenyl fragment in 10B1M7 from SLF experiment, compared to the calculated results.

carbon sites	Expt. Splittings/$\sin\theta_m$ (kHz)	Calc. Splittings $2b$ (kHz)
5	2.92±0.03	2.80
6	5.11±0.01	5.10
7	4.81±0.01	4.95
8	3.10±0.04	2.81
9	2.56±0.04	2.85
10	5.29±0.01	5.20
11	4.75±0.01	4.74
12	2.80±0.03	2.89

The SLF spectrum, collected at 115°C, is shown in Fig. 8.17, in which the ω_2 dimension shows the normal proton-decoupled ^{13}C peaks (top trace), while the slices in the ω_1 dimension show the individual ^{13}C nuclei with the C-H dipolar couplings. Figure 8.18 shows some selected ω_1 slices from the aromatic region. The dipolar oscillation frequencies for carbons 9, 10, 13 and 14 seem to be similar, and are larger than those of the quaternary carbons 8, 11, 12 and 15. These observations are consistent with the ^{13}C peak assignments given previously [35].

Table 8.7: Dipolar splittings of biphenyl fragment in ZLL7/* from SLF experiment, compared to the calculated results.

carbon sites	Expt. Splittings/$\sin\theta_m$ (kHz)	Calc. Splittings $2b$ (kHz)
9	6.3±0.1	6.3
10	6.8±0.1	6.7
11	3.5±0.2	3.4
13	6.8±0.1	6.8
14	5.2±0.1	5.2
15	3.6±0.1	3.6

The local order parameter tensors of the phenyl rings in the biphenyl fragment can now be studied at 115°C using the C-H dipolar couplings observed in the SLF experiment. For each phenyl ring, one has four observed dipolar splittings (tabulated in Table 8.7) from which two unknowns $S_{z'z'}$ and $(S_{x'x'} - S_{y'y'})$ can be determined using Eq. (8.50). To determine the local order tensors for the two phenyl rings keeping $S_{z'z'}$ the same, we have chosen to optimize the ring geometry. For the outer phenyl ring, we found that θ_{CH}=59.5° and 57.8° for sites 9 and 10, respectively, and $S_{z'z'} = 0.71$, $(S_{x'x'} - S_{y'y'}) = -0.10$, whereas for the other ring in the

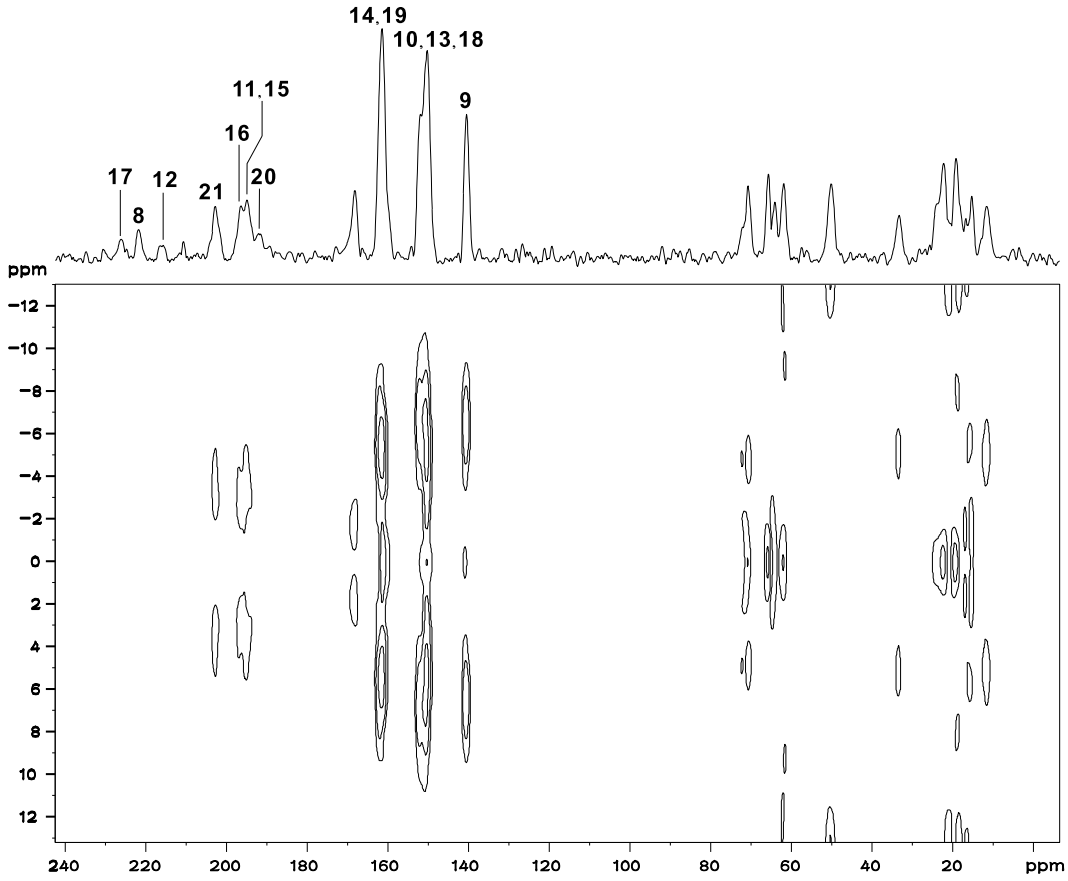

Figure 8.17: 2D SLF spectrum in SmA phase of ZLL7/* at 115°C using the pulse sequence of Figure 8.7.

.

biphenyl fragment θ_{CH}=60° (not varied) for site 13 and 60.2° for site 14, and $S_{z'z'} = 0.71$, $(S_{x'x'} - S_{y'y'}) = -0.11$. In this calculation, six target parameters were varied to give the best fit to the experimental splittings in Table 8.7. The calculated splittings are also listed in this table. The local $S_{z'z'}$ value appears to be consistent with the corresponding S value found from the deuteron work [86].

8.5.3 Study of 11EB1M7

The 1D ^{13}C NMR study of 11EB1M7 has appeared in chapter 7. In the 1D data analysis the order parameters of the molecule are dependent not only on the peak assignment but also on the assumed chemical shift tensors. Since the order parameters obtained from the dipolar splittings are completely independent of the selection of the chemical shift tensors, several SLF experiments were performed in SmA phase of this sample. The local order parameters for the biphenyl part are determined, which are found to be very consistent with

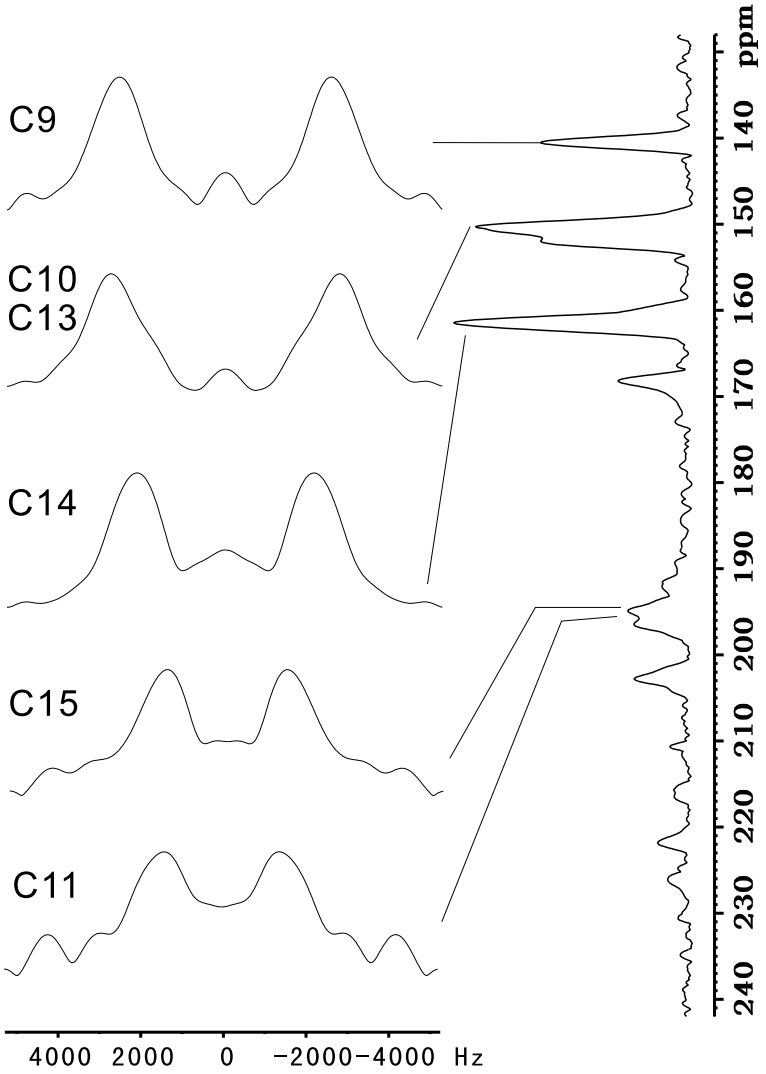

Figure 8.18: Plots of 1D slices in the ω_1 dimension of Figure 8.17 for some carbon sites.

.

the results obtained from the 1D ^{13}C experiment. In the SLF experiment the sample was first aligned in the magnetic field and then cooled to the SmA phase at four temperatures corresponding to the 1D experiments: 103.4°, 100.5°, 97.6°, 93.8°. The 90° proton pulse width was 3.3μs in the SLF pulse sequence. The FSLG homonuclear decoupling level was 26.3 kHz. The heteronuclear decoupling during signal acquisition used SPINAL-64 at 30.2 kHz. The number of t_1 increments was 80 with 512 scans per t_1 increment, and the STATES method was used for quadrature detection.

The SLF spectra at different temperatures are shown in Fig. 8.19-8.22, in which the ω_2 dimension shows the normal proton-decoupled ^{13}C peaks (top trace), while the slices in the ω_1 dimension show the individual ^{13}C nuclei with the C-H dipolar couplings. In Figure 8.20 the carbon peaks are labeled the same as in the 1D ^{13}C peak assignment in chapter 7. As

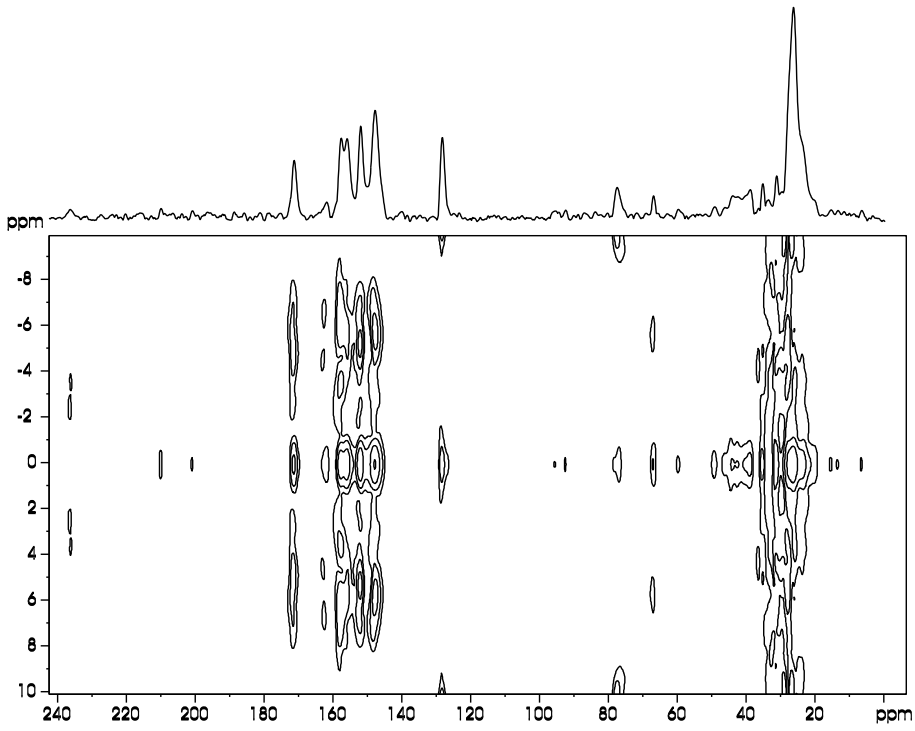

Figure 8.19: 2D SLF spectrum of 11EB1M7 at 93.8°C using the pulse sequence of Figure 8.7.

.

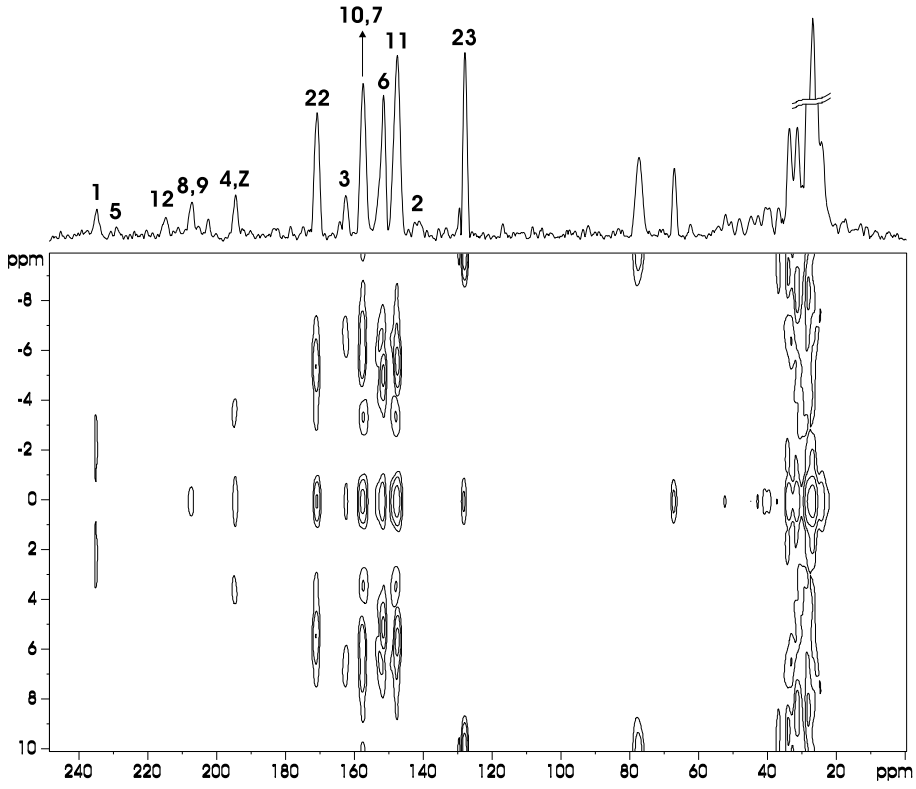

Figure 8.20: 2D SLF spectrum of 11EB1M7 with the carbon peaks assignment at 97.6°C using the pulse sequence of Figure 8.7.

.

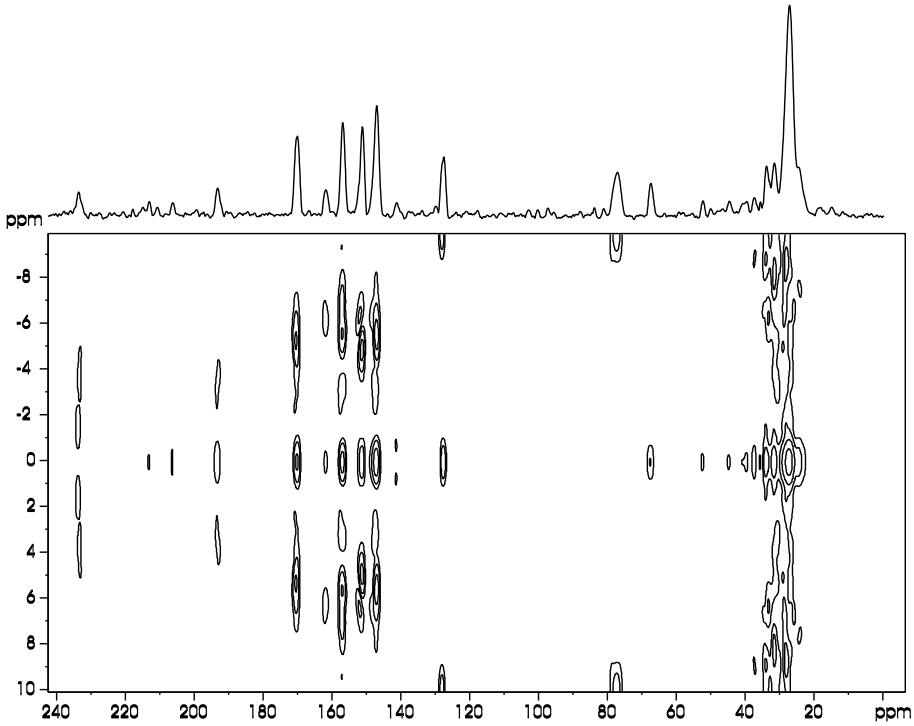

Figure 8.21: 2D SLF spectrum of 11EB1M7 at 100.5°C using the pulse sequence of Figure 8.7.

.

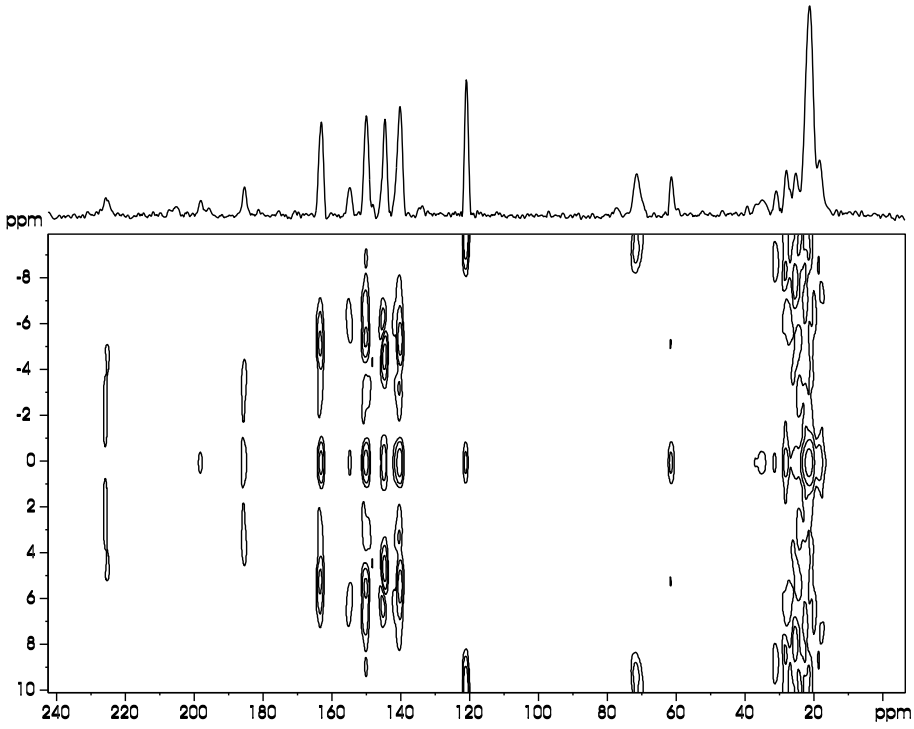

Figure 8.22: 2D SLF spectrum of 11EB1M7 at 103.4°C using the pulse sequence of Figure 8.7.

.

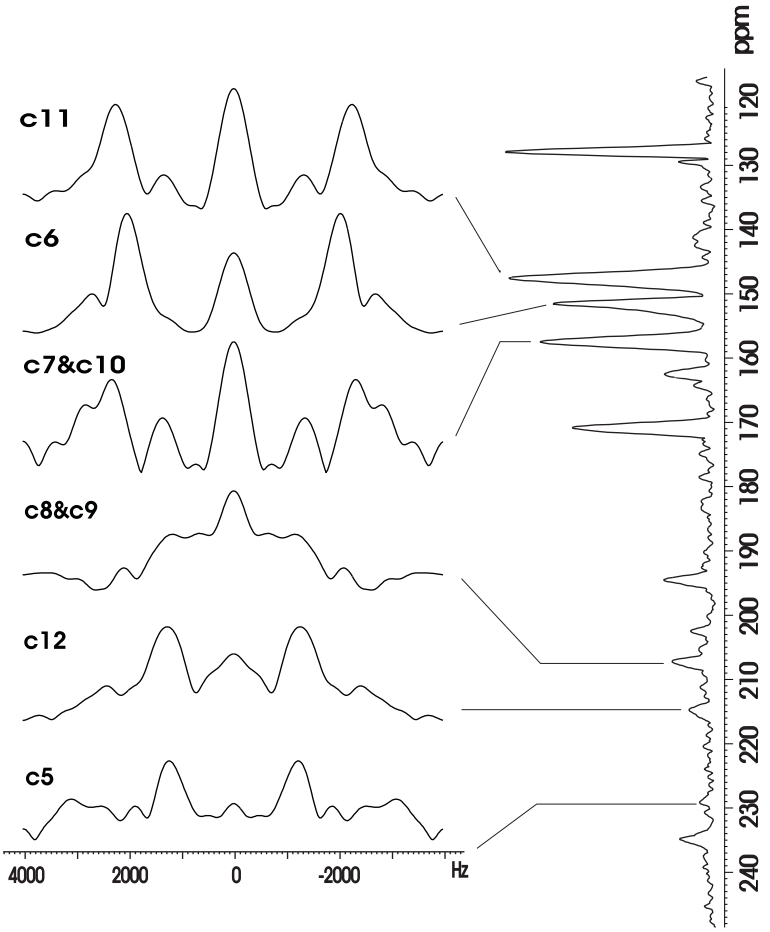

Figure 8.23: Plots of 1D slices in the ω_1 dimension of Figure 8.20 for some carbon sites.

.

an example, figure 8.23 shows some selected ω_1 slices from the aromatic region. The dipolar oscillation frequencies for carbons 6, 7, 10 and 11 seem to be similar, and are larger than those of the quaternary carbons 5, 8, 9 and 12. Using the dipolar splittings, the local order parameter tensors of the phenyl rings in the biphenyl fragment can be studied for all the temperatures. Here we still keep the same $S_{z'z'}$ value for the two phenyl rings in the biphenyl part and $S_{x'x'} - S_{y'y'}$ are allowed to be different. Also the angle θ_{CH} was varied to optimize the fit to the experiment splittings. Both the experimental and calculated results are given in Table 8.8. The angles β between the C-H bond and the local z' axis were fixed at 60° for site 7, 10, and 11, while β for site 6 appeared to require small deviation from the nominal value in order to better fit the experimental dipolar splittings. We found $\beta \approx 58.9°$ for site 6. From the fitting the local $S_{z'z'}$ value for the biphenyl part was obtained, which is plotted in Fig. 8.24. The local $S_{z'z'}$ values appear to be consistent with the corresponding S value found in the last chapter. Also the order parameters $S_{x'x'} - S_{y'y'}$ were determined to be around -0.065 ± 0.005.

Table 8.8: Dipolar splittings of biphenyl fragment in 11EB1M7 from SLF experiment, compared to the calculated results.

	Temp.=103.4°		Temp.=100.5°	
carbon sites	$\Delta\nu/\sin\theta_m$ (kHz)	$2b$ (kHz)	$\Delta\nu/\sin\theta_m$ (kHz)	$2b$ (kHz)
5	2.9±0.2	2.9	3.0±0.2	3.0
6	4.5±0.2	4.5	4.8±0.2	4.8
7	5.3±0.2	5.3	5.5±0.2	5.5
8	2.8±0.2	2.8	2.9±0.2	2.9
9	2.8±0.2	2.8	2.9±0.3	2.9
10	5.3±0.2	5.3	5.5±0.2	5.5
11	5.2±0.2	5.2	5.5±0.2	5.5
12	2.8±0.2	2.8	3.0±0.3	3.0
	Temp.=97.6°		Temp.=93.8°	
carbon sites	$\Delta\nu/\sin\theta_m$ (kHz)	$2b$ (kHz)	$\Delta\nu/\sin\theta_m$ (kHz)	$2b$ (kHz)
5	3.1±0.3	3.0	3.2±0.3	3.2
6	5.0±0.2	5.0	5.1±0.2	5.1
7	5.6±0.2	5.6	5.9±0.2	5.9
8	2.9±0.3	3.0	3.0±0.3	3.1
9	2.9±0.2	3.0	3.0±0.3	3.1
10	5.6±0.2	5.6	5.9±0.2	5.9
11	5.5±0.2	5.5	5.7±0.2	5.6
12	3.0±0.2	3.0	3.2±0.3	3.2

In this chapter, the SUPER experiment, a robust 2D ^{13}C NMR technique for obtaining quasi-static CSA powder patterns under MAS, was introduced. After the description of the theory for this experiment using quantum mechanical ideas, it was used to get the chemical shift tensors of different liquid crystal molecules. The SUPER experiment can give CSA measurements under standard MAS conditions routinely, and promises to provide many opportunities for improved structural identification and measurements of segmental orientation, conformation, and dynamics in solids. The 2D SLF experiments were also adopted by implementing the LG-CP sequence for accurate measurements of the heteronuclear dipolar couplings. The LG-CP sequence was demonstrated to efficiently suppress the chemical shift and frequency offset effects irrespective of the heteronuclear dipolar coupling value and therefore provided uniform dipolar resolution in the broad dipolar coupling range. In particular, high dipolar resolved spectra have been obtained with the PISLF sequence employing the coherent po-

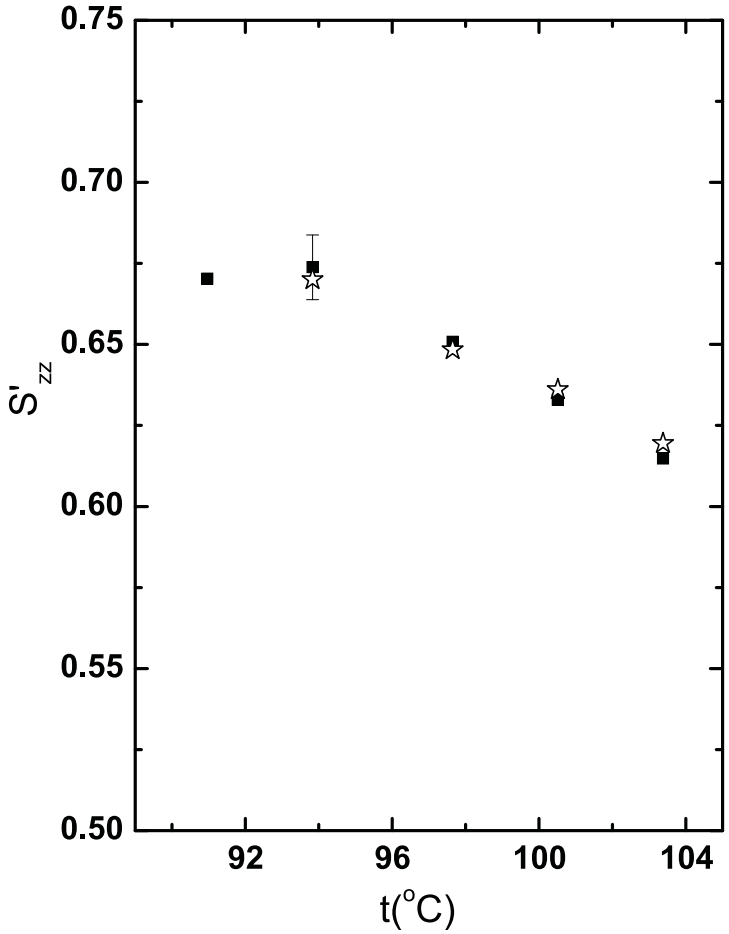

Figure 8.24: Comparison of local order parameters S'_{zz} for the biphenyl part obtained by 1D experiment (■) and SLF method (★).

.

larization transfer. The performance of the new approach is comparable to other existing techniques in terms of dipolar resolution of large dipolar couplings, but is superior for measuring the motionally reduced dipolar couplings in complex systems with a wide range of chemical shifts. The method can be further extended and used in advance multi-dimensional NMR experiments for the structural studies of liquid crystalline and biological samples.

References

[1] Andrew, E. R.; Bradbury, A.; Eades, R. G. *Nature* **1958**, *182*, 1659.

[2] Lowe, I. J. *Phys. Rev. Lett.* **1959**, *2*, 285.

[3] Schmidt-Rohr, K.; Spiess, H. W. *Multidimensional Solid-state NMR and Polymers*; Academic Press Inc., 1994.

[4] Duer, M. J. *Introduction to solid-state NMR spectroscopy*; Blackwell: Oxford ; Malden, MA, 2004.

[5] Herzfeld, J.; Berger, A. E. *J. Chem. Phys.* **1980**, *73*, 6021.

[6] Maricq, M. M.; Waugh, J. S. *J. Chem. Phys.* **1979**, *70*, 3300.

[7] Laws, D. D.; Bitter, H. M. L.; Jerschow, A. *Angew. Chem. Int. Ed.* **2002**, *41*, 3096.

[8] Dixon, W. T.; Schaefer, J.; Sefcik, M. D.; Stejskal, E. O.; Mckay, R. A. *J. Magn. Reson.* **1982**, *49*, 341.

[9] Dixon, W. T. *J. Chem. Phys.* **1982**, *77*, 1800.

[10] Antzutkin, O. N.; Song, Z. Y.; Feng, X. L.; Levitt, M. H. *J. Chem. Phys.* **1994**, *100*, 130.

[11] Raleigh, D. P.; Olejniczak, E. T.; Vega, S.; Griffin, R. G. *J. Am. Chem. Soc.* **1984**, *106*, 8302.

[12] Nielsen, N. C.; Bildsoe, H.; Jakobsen, H. J. *J. Magn. Reson.* **1988**, *80*, 149.

[13] Raleigh, D. P.; Olejniczak, E. T.; Griffin, R. G. *J. Chem. Phys.* **1988**, *89*, 1333.

[14] Raleigh, D. P.; Olejniczak, E. T.; Vega, S.; Griffin, R. G. *J. Magn. Reson.* **1987**, *72*, 238.

[15] Hemminga, M. A.; Dejager, P. A. *J. Magn. Reson.* **1983**, *51*, 339.

[16] Wu, X. L.; Zilm, K. W. *J. Magn. Reson. A* **1993**, *104*, 154.

[17] Wind, R. A.; Dec, S. F.; Lock, H.; Maciel, G. E. *J. Magn. Reson.* **1988**, *79*, 136.

[18] Stejskal, E. O.; Schaefer, J.; Waugh, J. S. *J. Magn. Reson.* **1977**, *28*, 105.

[19] Zeigler, R. C.; Wind, R. A.; Maciel, G. E. *J. Magn. Reson.* **1988**, *79*, 299.

[20] Hediger, S.; Meier, B. H.; Ernst, R. R. *Chem. Phys. Lett.* **1993**, *213*, 627.

[21] Sardashti, M.; Maciel, G. E. *J. Magn. Reson.* **1987**, *72*, 467.

[22] Barbara, T. M.; Williams, E. H. *J. Magn. Reson.* **1992**, *99*, 439.

[23] Peersen, O. B.; Wu, X. L.; Kustanovich, I.; Smith, S. O. *J. Magn. Reson. A* **1993**, *104*, 334.

[24] Peersen, O. B.; Wu, X. L.; Smith, S. O. *J. Magn. Reson. A* **1994**, *106*, 127.

[25] Metz, G.; Wu, X. L.; Smith, S. O. *J. Magn. Reson. A* **1994**, *110*, 219.

[26] Wu, Z. R.; Tjandra, N.; Bax, A. *J. Am. Chem. Soc.* **2001**, *123*, 3617.

[27] Crozet, M.; Chaussade, M.; Bardet, M.; Emsley, L.; Lamotte, B.; Mouesca, J. M. *J. Phys. Chem. A* **2000**, *104*, 9990.

[28] Hong, M. *J. Am. Chem. Soc.* **2000**, *122*, 3762.

[29] Delacroix, S. F.; Titman, J. J.; Hagemeyer, A.; Spiess, H. W. *J. Magn. Reson.* **1992**, *97*, 435.

[30] Alla, M. A.; Kundla, E. I.; Lippmaa, E. T. *Jetp Lett.* **1978**, *27*, 194.

[31] Tycko, R.; Dabbagh, G.; Mirau, P. A. *J. Magn. Reson.* **1989**, *85*, 265.

[32] Liu, S. F.; Mao, J. D.; Schmidt-Rohr, K. *J. Magn. Reson.* **2002**, *155*, 15.

[33] deAzevedo, E. R.; Hu, W. G.; Bonagamba, T. J.; Schmidt-Rohr, K. *J. Chem. Phys.* **2000**, *112*, 8988.

[34] Eichele, K.; Wasylishen, R. *WSOLIDS1 v. 1. 17.34,*; Dalhousie University, 2001.

[35] Xu, J.; Fodor-Csorba, K.; Dong, R. Y. *J. Phys. Chem. A* **2005**, *109*, 1998.

[36] Lee, M.; Goldburg, W. I. *Phys. Rev.* **1965**, *140*, A1261.

[37] Bielecki, A.; Kolbert, A. C.; Levitt, M. H. *Chem. Phys. Lett.* **1989**, *155*, 341.

[38] Waugh, J. S.; Huber, L.; Haeberlen, U. *Phys. Rev. Lett.* **1968**, *20*, 180.

[39] Haeberlen, U.; Waugh, J. S. *Phys. Rev. A* **1968**, *175*, 453.

[40] Mansfield, P. *J. Phys. C* **1971**, *4*, 1444.

[41] Rhim, W. K.; Elleman, D. D.; Vaughn, R. W. *J. Chem. Phys.* **1968**, *59*, 3740.

[42] Burum, D. P.; Rhim, W. K. *J. Chem. Phys.* **1979**, *71*, 944.

[43] Burum, D. P.; Linder, M.; Ernst, R. R. *J. Magn. Reson.* **1981**, *44*, 173.

[44] Takegoshi, K.; Mcdowell, C. A. *Chem. Phys. Lett.* **1985**, *116*, 100.

[45] Liu, H.; Glaser, S. J.; Drobny, G. P. *J. Chem. Phys.* **1990**, *93*, 7543.

[46] Iwamiya, J. H.; Sinton, S. W.; Liu, H.; Glaser, S. J.; Drobny, G. P. *J. Magn. Reson.* **1992**, *100*, 367.

[47] Levitt, M. H.; Suter, D.; Ernst, R. R. *J. Chem. Phys.* **1986**, *84*, 4243.

[48] Sinha, N.; Ramanathan, K. V. *Chem. Phys. Lett.* **2000**, *332*, 125.

[49] Wu, C. H.; Ramamoorthy, A.; Opella, S. J. *J. Magn. Reson. A* **1994**, *109*, 270.

[50] Nagaraja, C. S.; Ramanathan, K. V. *Liq. Cryst.* **1999**, *26*, 17.

[51] Hester, R. K.; Ackerman, J. L.; Neff, B. L.; Waugh, J. S. *Phys. Rev. Lett.* **1976**, *36*, 1081.

[52] Caldarelli, S.; Hong, M.; Emsley, L.; Pines, A. *J. Phys. Chem.* **1996**, *100*, 18696.

[53] Dvinskikh, S. V.; Zimmermann, H.; Maliniak, A.; Sandstrom, D. *J. Magn. Reson.* **2003**, *163*, 46.

[54] Fung, B. M.; Ermolaev, K.; Yu, Y. L. *J. Magn. Reson.* **1999**, *138*, 28.

[55] Hong, M.; Pines, A.; Caldarelli, S. *J. Phys. Chem.* **1996**, *100*, 14815.

[56] Opella, S. J.; Waugh, J. S. *J. Chem. Phys.* **1977**, *66*, 4919.

[57] States, D. J.; Haberkorn, R. A.; Ruben, D. J. *J. Magn. Reson.* **1982**, *48*, 286.

[58] Marini, A.; Veracini, C. A. *et al.*; private communication.

[59] Weissflog, W.; Lischka, C.; Diele, S.; Pelzl, G.; Wirth, I.; Grande, S.; Kresse, H.; Schmalfuss, H.; Hartung, H.; Stettler, A. *Mol. Cryst. Liq. Cryst.* **1999**, *333*, 203.

[60] Diele, S.; Grande, S.; Kruth, H.; Lischka, C. H.; Pelzi, G.; Weissflog, W.; Wirth, I. *Ferroelectrics* **1998**, *212*, 169.

[61] Pelzl, G.; Diele, S.; Grande, S.; Jakli, A.; Lischka, C.; Kresse, H.; Schmalfuss, H.; Wirth, I.; Weissflog, W. *Liq. Cryst.* **1999**, *26*, 401.

[62] Dong, R. Y.; Xu, J.; Benyei, G.; Fodor-Csorba, K. *Phys. Rev. E.* **2004**, *70*, 011708.

[63] Dong, R. Y.; Fodor-Csorba, K.; Xu, J.; Domenici, V.; Prampolini, G.; Veracini, C. A. *J. Phys. Chem. B* **2004**, *108*, 7694.

[64] Dehne, H.; Potter, M.; Sokolowski, S.; Weissflog, W.; Diele, S.; Wirth, I.; Kresse, H.; Schmalfuss, H. *Liq. Cryst.* **2001**, *28*, 1269.

[65] Fodor-Csorba, K.; Vajda, A.; Jákli, A.; Slugovc, C.; Trimmel, G.; Demus, D.; Gács-Baitz, E.; Holly, S.; Galli, G. *J. Mater. Chem.* **2004**, *14*, 2499.

[66] Freiser, M. J. *Phys. Rev. Lett.* **1970**, *24*, 1041.

[67] Severing, K.; Stibal-Fischer, E.; Hasenhindl, A.; Finkelmann, H.; Saalwachter, K. *J. Phys. Chem. B* **2006**, *110*, 15680.

[68] Figueirinhas, J. L.; Cruz, C.; Filip, D.; Feio, G.; Ribeiro, A. C.; Frere, Y.; Meyer, T.; Mehl, G. H. *Phys. Rev. Lett.* **2005**, *94*, 107802.

[69] Madsen, L. A.; Dingemans, T. J.; Nakata, M.; Samulski, E. T. *Phys. Rev. Lett.* **2004**, *92*, 145505.

[70] Acharya, B. R.; Primak, A.; Kumar, S. *Phys. Rev. Lett.* **2004**, *92*, 145506.

[71] Severing, K.; Saalwachter, K. *Phys. Rev. Lett.* **2004**, *92*, 125501.

[72] Coleman, D. A.; Fernsler, J.; Chattham, N.; Nakata, M.; Takanishi, Y.; Korblova, E.; Link, D. R.; Shao, R. F.; Jang, W. G.; Maclennan, J. E.; Mondainn-Monval, O.; Boyer, C.; Weissflog, W.; Pelzl, G.; Chien, L. C.; Zasadzinski, J.; Watanabe, J.; Walba, D. M.; Takezoe, H.; Clark, N. A. *Science* **2003**, *301*, 1204.

[73] Lubensky, T. C.; Radzihovsky, L. *Phys. Rev. E* **2002**, *66*, 031704.

[74] Weissflog, W.; Wirth, I.; Diele, S.; Pelzl, G.; Schmalfuss, H.; Schoss, T.; Wurflinger, A. *Liq. Cryst.* **2001**, *28*, 1603.

[75] Nakata, M.; Link, D. R.; Araoka, F.; Thisayukta, J.; Takanishi, Y.; Ishikawa, K.; Watanabe, J.; Takezoe, H. *Liq. Cryst.* **2001**, *28*, 1301.

[76] Luckhurst, G. R. *Thin Solid Films* **2001**, *393*, 40.

[77] Toledano, P.; Martins, O. G.; Neto, A. M. F. *Phys. Rev. E* **2000**, *62*, 5143.

[78] Walba, D. M.; Korblova, E.; Shao, R.; Maclennan, J. E.; Link, D. R.; Glaser, M. A.; Clark, N. A. *Science* **2000**, *288*, 2181.

[79] Heppke, G.; Jakli, A.; Rauch, S.; Sawade, H. *Phys. Rev. E* **1999**, *60*, 5575.

[80] Pelzl, G.; Diele, S.; Weissflog, W. *Adv. Mater.* **1999**, *11*, 707.

[81] Roy, A.; Madhusudana, N. V.; Toledano, P.; Neto, A. M. F. *Phys. Rev. Lett.* **1999**, *82*, 1466.

[82] Lorman, V. L.; Mettout, B. *Phys. Rev. Lett.* **1999**, *82*, 940.

[83] Macdonald, R.; Kentischer, F.; Warnick, P.; Heppke, G. *Phys. Rev. Lett.* **1998**, *81*, 4408.

[84] Link, D. R.; Natale, G.; Shao, R.; Maclennan, J. E.; Clark, N. A.; Korblova, E.; Walba, D. M. *Science* **1997**, *278*, 1924.

[85] Niori, T.; Sekine, T.; Watanabe, J.; Furukawa, T.; Takezoe, H. *J. Mater. Chem.* **1996**, *6*, 1231.

[86] Catalano, D.; Domenici, V.; Marini, A.; Veracini, C. A.; Bubnov, A.; Glogarova, M. *J. Phys. Chem. B* **2006**, *110*, 16459.

Chapter 9

Bent-core Mesogens: High-resolution NMR Study

9.1 Introduction to Bent-core Mesogens

Ferroelectricity [1, 2], discovered in 1975, and antiferroelectricity [3], discovered a decade later, play an important role in the area of liquid crystal (LC) research. These LC materials involve organic polar molecules with asymmetric (chiral) carbon site(s), and form tilted smectic phases showing helicoidal superstructures. Another new class of ferroelectric mesophases that have attracted much attention in recent years is given by achiral, but polar molecules with a rigid bent-core structure (e.g. a five-ring system) in addition to pendant lateral chains. The theoretical prediction of ferroelectricity formed by achiral molecules was first proposed in 1983 [4] and 1987 [5]. The first experimental discovery of a new class of LC phases with polar order formed by bent-core molecules was reported in 1996 by Niori et al. [6]. Many bent-core LC have since been synthesized to give one or more banana B phases (B_1, B_2, ..., B_7), or a nematic phase. The B phases are found not to mix with classical smectic phases of rod-like molecules. In the mean time, there are theoretical models proposed to explain the phase structure of these new B phases [7, 8]. This kind of material is interesting because of the optical switching between antiferroelectric and ferroelectric states shown by the B_2 phase. At present, the understanding of the formation or the lack of various B phases in bent-core LC at a molecular level is still lacking, and nuclear magnetic resonance spectroscopy [9, 10] has a successful record in tackling structure, molecular conformation and ordering in partially ordered fluids. In the last chapter, we have obtained the CSA tensors in 10BrPBBC and 10ClPBBC using the SUPER experiment. An example to extract ordering information from the observed chemical shifts of various carbon sites in the aromatic region of the ^{13}C spectrum

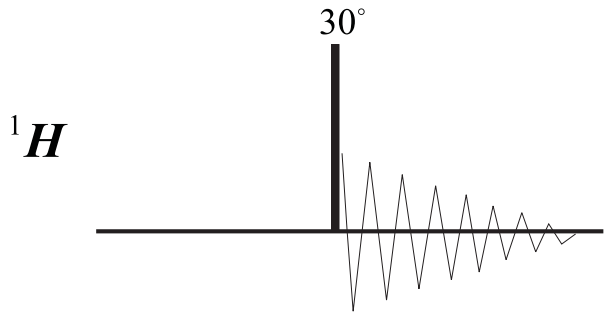

Figure 9.1: Pulse sequence of the standard high resolution ^{1}H NMR experiment.

obtained in the nematic phase of 10BrPBBC is given.

On the other hand, due to the high viscosity, slow dynamics of bent-core molecules' phases, and the small magnetic susceptibility anisotropy, different behaviors have been observed in the magnetic field. The alignment behavior of the directors with respect to the magnetic field is very important to obtain a high resolution spectrum of bent-core molecules. NMR experiments on solution samples of bent-core molecules are adopted here to assist the peak assignments of this type of molecule.

9.2 High Resolution NMR

9.2.1 The Standard ^{1}H and ^{13}C NMR Experiments

The NMR spectrum not only distinguishes how many different types of protons a molecule has, but also reveals how many of each type are contained within the molecule. The aim of the standard ^{1}H NMR experiment is to record a routine proton NMR spectrum in order to get structure-related information for the protons in the sample, i.e. chemical shifts, spin-spin couplings, and intensities [11, 12]. The ^{1}H transmitter pulse, creates an observable x, y-magnetization by tipping the magnetization vector towards the $-y$ axis through an angle α. The pulse sequence is shown in Fig. 9.1. Although a 90° pulse gives maximum signal intensity, a shorter pulse length of about $\alpha = 30°$ is used for data accumulation in order to avoid a long delay time of $5T_1$, which is necessary after a 90° pulse [13]. Using the product operators introduced in Chapter 2 to describe this process, one can get:

$$\hat{I}_z \xrightarrow{30° I_x} \cos 30° \hat{I}_z - \sin 30° \hat{I}_y \tag{9.1}$$

During the acquisition time chemical shifts and spin-spin couplings develop in the x, y plane to give:

$$\begin{aligned}
&\cos 30^\circ \hat{I}_z - \sin 30^\circ \hat{I}_y \xrightarrow{\Omega t I_z} \cos 30^\circ \hat{I}_z - \sin 30^\circ[-\hat{I}_y \cos \Omega t + \hat{I}_x \sin \Omega t] \\
&\cos 30^\circ \hat{I}_z - \sin 30^\circ \hat{I}_y \xrightarrow{\pi J t 2 \hat{I}_{1z} \hat{I}_{2z}} \cos 30^\circ \hat{I}_z - \sin 30^\circ[-\hat{I}_y \cos(\pi J t) + 2\hat{I}_x \hat{I}_z \sin(\pi J t)]
\end{aligned} \tag{9.2}$$

where Ω and J denote the frequency of chemical shift and spin-spin coupling. The signal is detected by the receiver in the x, y plane. From the above derivation one can see that the 30° pulse does not affect the information content of the signal. In the ^{1}H NMR spectrum, integral values associated with different NMR signals determine the number of protons in different hydrogen types in a molecule and can be useful in assigning signals to specific hydrogen types. So the information of a specific proton can be the number of equivalent hydrogens (integral), the chemical environment of each hydrogen type (proton chemical shift) and the number of neighboring hydrogens (multiplicity due to J coupling).

The standard ^{13}C NMR experiment is to record a ^{13}C NMR spectrum with proton broadband decoupling so as to get chemical shift information for structure determination. Figure 9.2 illustrates the standard pulse sequence. A 30° transmitter pulse is also used to avoid the the long delay time of $5T_1$. Proton broadband decoupling is performed by CPD such as Waltz16. During the acquisition time the chemical shift develops in the x, y plane and the resulting magnetization is detected by the receiver as follows:

$$\begin{aligned}
&\hat{S}_z \xrightarrow{30^\circ \hat{S}_x} \cos 30^\circ \hat{S}_z - \sin 30^\circ \hat{S}_y \\
&\cos 30^\circ \hat{S}_z - \sin 30^\circ \hat{S}_y \xrightarrow{\Omega t S_z} \cos 30^\circ \hat{S}_z - \sin 30^\circ[-\hat{S}_y \cos \Omega t + \hat{S}_x \sin \Omega t]
\end{aligned} \tag{9.3}$$

Here the spin-spin coupling interaction between ^{13}C nuclei is ignored due to their low abundance. Note that under routine conditions the ^{13}C signal areas are not necessarily proportional to the number of ^{13}C nuclei giving rise to that signal.

9.2.2 Proton Spin-spin Coupling

The chemical shift is not the only indicator used to assign NMR signals of a molecule. Because nuclei themselves influence each other, changing their energy and hence frequency of nearby nuclei as they resonate, this is known as spin-spin coupling (here only considering protons). Spin-spin coupling can be described as the indirect spin coupling of proton spins through the intervening bonding electrons. It occurs because there is some tendency for a bonding

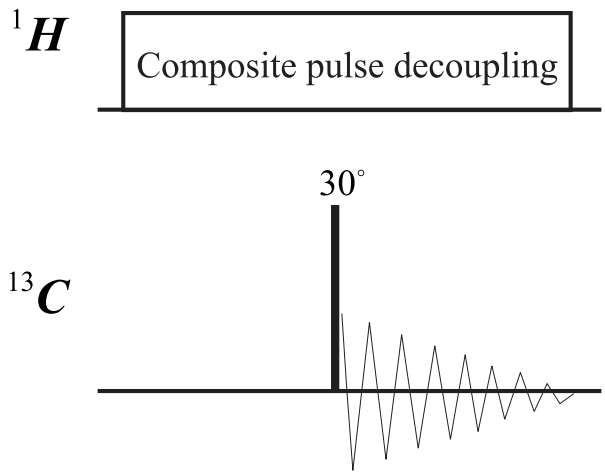

Figure 9.2: Pulse sequence of the standard high resolution ^{13}C NMR experiment.

electron to pair its spin with the spin of the nearest proton. The most important type in basic NMR is scalar coupling, J. The value of the coupling constant J depends on the distance between the two coupling nuclei, as well as their relative orientation towards each other and the character of the bonds between the two coupling nuclei. In the case of σ bonds, spin-spin couplings typically can only be observed across three bonds or fewer (e.g., H−C−C−H). If there are four bonds between the two coupling nuclei, the J-coupling constant typically already drops to zero. So-called long range couplings across a larger number of bonds typically only occurs if more polarizable π-bond systems are involved, e.g., H−C=C−C−H [14]. The J-coupling constant is independent of magnetic field strength because it is caused by the local magnetic field of another nucleus, not the spectrometer magnet. Therefore it is quoted in hertz (frequency) and not ppm (chemical shift). A typical ^{1}H coupling constant value would be 7 Hz.

The spin-spin coupling will split the proton NMR signals. For instance consider two neighboring protons. Due to the coupling to the two possible spin alignments of a proton, there are a total of four possible energy levels, and the number of possible transitions doubles. Since two transitions in a doublet have identical energy differences, they occur with the same probabilities, and the ratio of their intensities is 1 : 1. In this case, the spin-spin splitting rules can be explained empirically by the so-called $n + 1$ rule. A proton bonded to a carbon 'senses' the number of equivalent protons (n) on the carbon atom(s) next to it, and its resonance peak is split into $n + 1$ components. The relative intensities of the lines in various multiplets follow the Pascal's triangle [14, 15]. In NMR spectroscopy, equivalent protons generally mean chemically equivalent protons. Protons that are in the same chemical environment within a molecule are chemically equivalent. Equivalent protons produce signals that overlap with

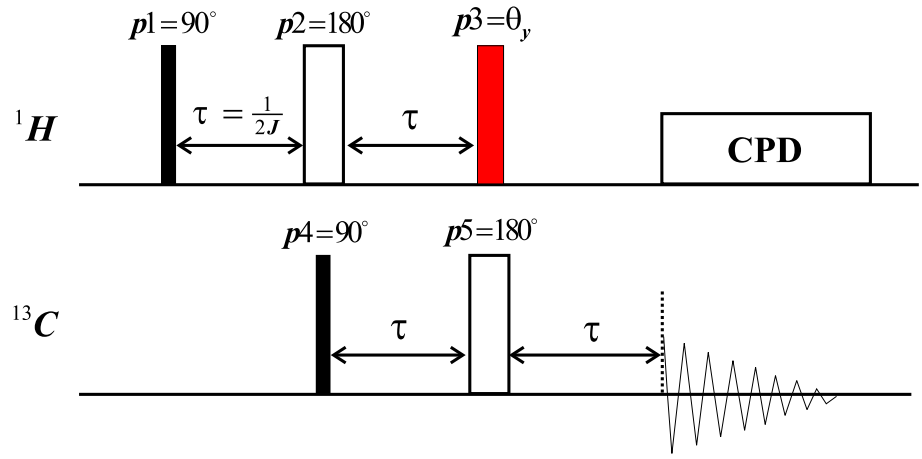

Figure 9.3: Pulse sequence of DEPT experiment.

each other, creating one larger signal. Chemical equivalence arises through bond rotation or molecular symmetry. If the J-coupling occurred among several sets of non-equivalent protons M, X... (i.e. $CH_n^M - CH_A = CH_n^X$) with n_M, n_X, etc. protons, then the protons of these groups couple independently with proton A. Additional splittings occur giving multiplets with $M_A = (n_M + 1) * (n_X + 1) \cdots$ components. This method will be adopted to assist the peak assignment of two bent-core molecules in this chapter.

9.2.3 DEPT-135 Experiment

The Distortionless Enhancement by Polarization Transfer (DEPT) sequence uses polarization transfer from protons to other nuclei via one covalent bond to increase signal strength [16–18]. The result of the DEPT pulse sequence is that the ^{13}C signals for carbon atoms in the molecule will exhibit different phases, depending on the number of hydrogens attached to each carbon. The experiment is typically used for CH_n multiplicity determination. Before using the sequence (shown in Fig. 9.3), first calibrate the 90° pulse widths of ^{1}H and ^{13}C. In the product operator formalism, we consider a C-H spin pair and neglect the effects of chemical shifts, since these are refocused by the 180° pulses. The first 90° proton pulse creates transverse magnetization of the protons which evolves with C, H spin coupling during the delay τ. If the delay is set as $\tau = 1/2J$ the cosine term becomes zero and the sine term unity, leaving pure anti-phase magnetization of the proton with respect to carbon in the Eq. (9.4). This anti-phase magnetization is converted into double quantum magnetization of carbon and proton by the first ^{13}C pulse [13]:

$$\gamma_H \hat{I}_z \xrightarrow{\frac{\pi}{2}\hat{I}_x} -\gamma_H \hat{I}_y \xrightarrow{\pi J \tau 2\hat{I}_z\hat{S}_z} \gamma_H 2\hat{I}_x\hat{S}_z \xrightarrow{\frac{\pi}{2}\hat{S}_x} -\gamma_H 2\hat{I}_x\hat{S}_y \tag{9.4}$$

This double quantum term does not further involve spin coupling during the second τ period. The transfer pulse $p3$ (θ_y) creates anti-phase magnetization of carbon with respect to proton, which during the third τ delay develops into in-phase carbon magnetization $\hat{S}_x$. C-H scalar coupling during acquisition is removed by decoupling the protons.

$$-\gamma_H 2\hat{I}_x\hat{S}_y \xrightarrow{\theta_y\hat{I}_y} \sin\theta_y\gamma_H 2\hat{I}_z\hat{S}_y \xrightarrow{2\pi J\tau\hat{I}_z\hat{S}_z} -\sin\theta_y\gamma_H\hat{S}_x \tag{9.5}$$

Note that only the observable terms are written out. Another signal contribution from carbon magnetization $\hat{S}_z$, which is converted into transverse carbon magnetization by the first 90° carbon pulse, is removed by the phase cycle. Since the proton magnetization is being transferred to the carbon polarization, the relaxation time of carbon is irrelevant. The repetition rate of the experiment is determined by the proton T_1 only. The proton pulse θ_y transforms the multiple quantum coherence into observable single quantum coherence. The intensity of the ^{13}C signal depends on the width of the θ_y pulse and on the number of protons coupled to to the ^{13}C nuclei. An enhancement of the intensity of the ^{13}C nuclei by a factor of γ_H/γ_C is also achieved [16–18]. Figure 9.4 illustrates the intensities of the signals arising from different groups for different pulse angles θ_y (45°, 90° and 135° ^{1}H pulses are used). For $\theta_y = 135°$ (DEPT-135), all carbons that have an attached proton provide a signal, but the phase of the signal will be different, depending on whether the number of attached hydrogens is an odd or an even number. Signals arising from CH or CH_3 groups will give positive peaks, while signals arising from CH_2 groups will form negative peaks [15]. Quaternary carbons, which bear no hydrogens and appear in the ^{13}C NMR spectra, are missing in the DEPT-135 spectrum.

9.2.4 C,H Correlation by Polarization Transfer (HETCOR)

The HETeronuclear CORrelation (HETCOR) experiment is a two dimensional C, H correlation experiment and it yields cross peaks for all protons and ^{13}C nuclei which are connected by a ^{13}C, ^{1}H coupling over one bond [19, 20]. The experiment encodes the proton chemical shift information on the ^{13}C signals. The assignment of one member of a spin coupled pair leads immediately to the assignment of the other. The pulse sequence that was proposed for such 2D experiment involves simply two 90° pulses, the last one being applied simultaneously to both nuclei. In order to refocus the heteronuclear coupling during the evolution time (t_1), a 180° ^{13}C pulse is also needed so that the protons will retain only the homonuclear coupling (shown in Figure 9.5) [13]. The first proton pulse creates $-I_y$ magnetization, which subsequently evolves under ^{1}H chemical shift during the evolution period t_1. The 180° ^{13}C pulse

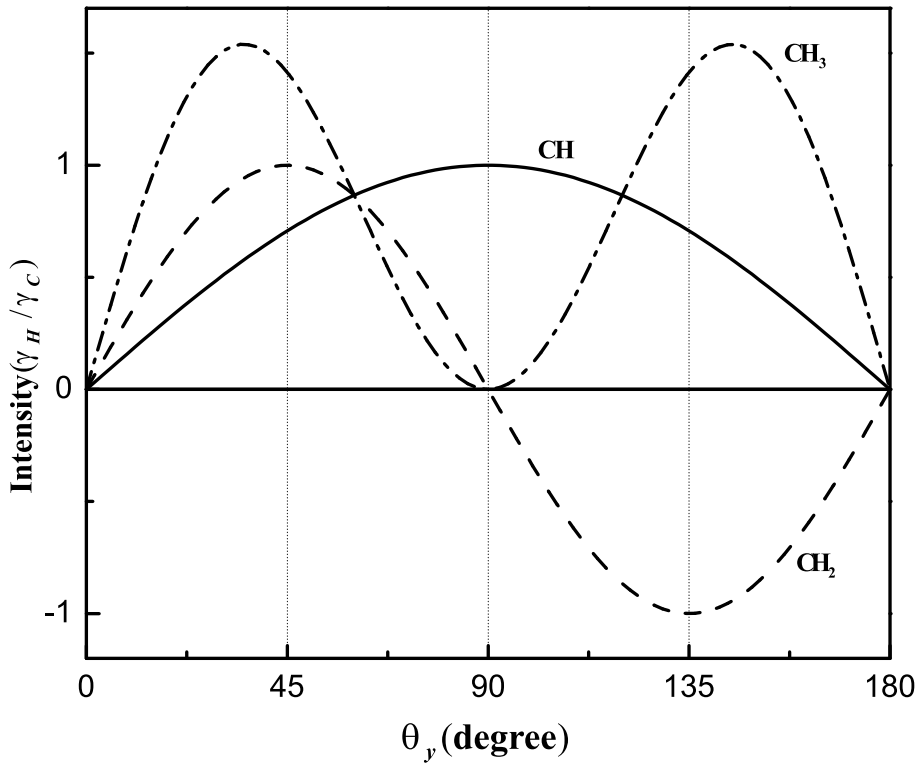

Figure 9.4: The intensities of CH, CH_2 and CH_3 signals as functions of the pulse angle θ_y in DEPT-135. CH:$(\sin\theta_y)-$, CH_2: $(2\sin\theta_y\cos\theta_y)--$, CH_3: $(4\sin\theta_y\cos^2\theta_y)-\cdot-$.

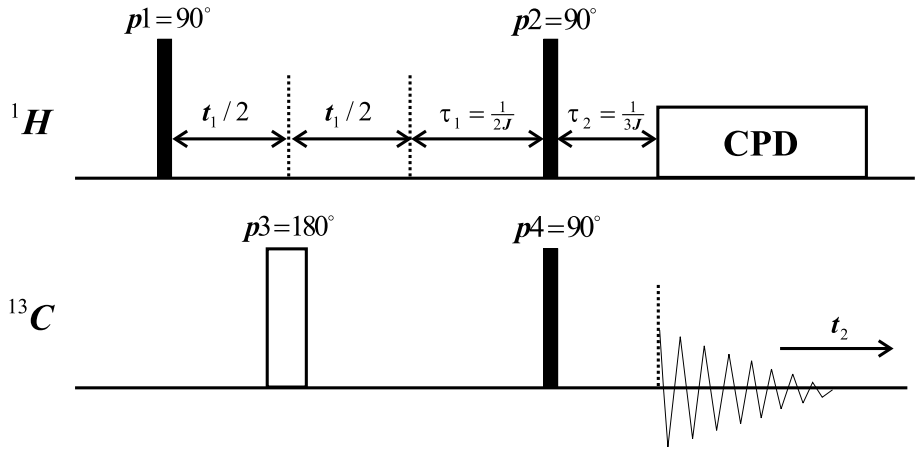

Figure 9.5: Pulse sequence of the HETCOR experiment.

in the middle of t_1 removes heteronuclear spin couplings during t_1.

$$\hat{I}_z \xrightarrow{\frac{\pi}{2}\hat{I}_x} -\hat{I}_y \xrightarrow{\Omega_H t_1 \hat{I}_z} -\hat{I}_y \cos\Omega_H t_1 + \hat{I}_x \sin\Omega_H t_1 \tag{9.6}$$

Note that Ω_H is the proton evolution frequency in the magnetic field. C, H spin couplings evolve during the delay τ_1, leading to an antiphase magnetization of proton with respect to carbon. If the delay τ_1 is set equal to $1/2J$, the corresponding cosine terms become zero, which insures an efficient polarization transfer to the ^{13}C nuclei by the anti-phase character of the heteronuclear coupling. Since $\pi J\tau_1 = \pi/2$ here, one can get

$$-\hat{I}_y \cos\Omega_H t_1 + \hat{I}_x \sin\Omega_H t_1 \xrightarrow{\pi J\tau_1 2\hat{I}_z\hat{S}_z} 2\hat{I}_x\hat{S}_z \cos\Omega_H t_1 + 2\hat{I}_y\hat{S}_z \sin\Omega_H t_1 \tag{9.7}$$

The simultaneous 90° pulses on proton and on ^{13}C nuclei transfers the proton magnetization to the ^{13}C nuclei whose intensity is modulated by the proton chemical shift. The process can be described as follows,

$$2\hat{I}_x\hat{S}_z \cos\Omega_H t_1 + 2\hat{I}_y\hat{S}_z \sin\Omega_H t_1 \xrightarrow{\frac{\pi}{2}\hat{I}_x, \frac{\pi}{2}\hat{S}_x} -2\hat{I}_z\hat{S}_y \sin\Omega_H t_1 \tag{9.8}$$

which only shows the observed term. The anti-phase magnetization is refocused during the delay τ_2 to give an observable in-phase magnetization.

$$-2\hat{I}_z\hat{S}_y \sin\Omega_H t_1 \xrightarrow{\pi J\tau_2 2\hat{I}_z\hat{S}_z} \sin\Omega_H t_1[-\cos(\pi J\tau_2)2\hat{I}_z\hat{S}_y + \sin(\pi J\tau_2)\hat{S}_x] \tag{9.9}$$

As the ^{13}C nuclei can be coupled to 1, 2 or 3 protons, an 'optimum' refocusing delay that takes into account the various multiplicities for the ^{13}C nuclei must be setup. The refocusing delay used in the standard sequence is about $1/3J$ (good intensity on CH, CH_2 and CH_3 type of carbons) [19, 20]. During the acquisition, the ^{13}C chemical shift evolves, while proton decoupling ensures that no dipolar coupling appears in ω_2 dimension.

9.3 High Resolution NMR Study of 10BrPBBC

In high resolution NMR of liquids, the quality of the sample has a profound effect on the quality of the resulting spectrum. Choice of the solvent depends on the solubility of the sample, chemical shift of the residual protons in ^{1}H NMR and position of signals in ^{13}C NMR (position of the solvent peaks can overlap with signals from the compound), chemical and physical properties of the solvent. In our experiment, the sample was prepared in a 5 mm NMR tube using Chloroform-d (99.8 atom % D) as the solvent, which contains 1% v/v TMS.

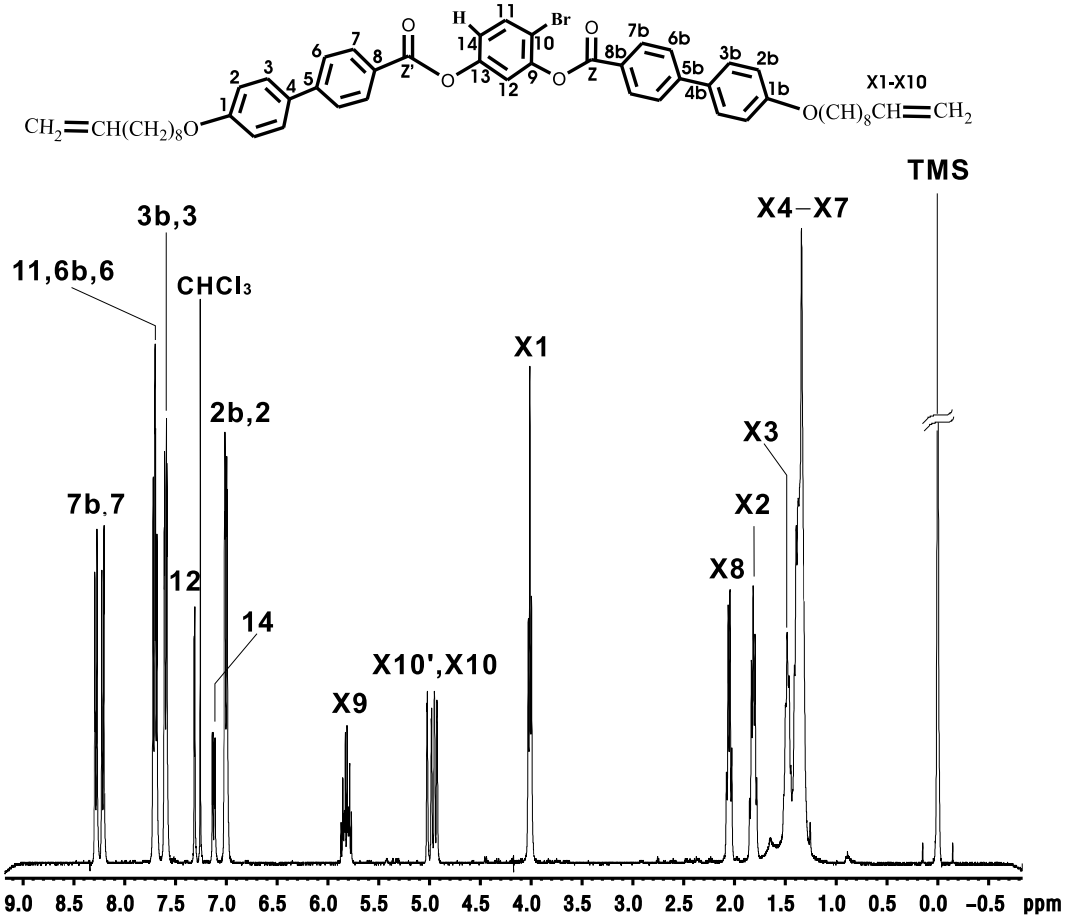

Figure 9.6: The ^{1}H NMR spectrum of 10BrPBBC with peak assignments.

9.3.1 ^{1}H NMR study of 10BrPBBC

The ^{1}H experiment was done using the pulse sequence shown in Figure 9.1 and the 90° pulse length for proton is 10.5μsec. Figure 9.6 shows the ^{1}H NMR spectrum of 10BrPBBC. The proton peak assignments are based on the integral area, chemical shift of common protons and the spin-spin couplings. The process of labeling the peaks will be addressed in more detail in the following.

Firstly, the chemical shift on the ^{1}H NMR spectrum is important because it tells about the chemical environment of the hydrogens. Knowing what affects chemical shift can be key to the determination of the chemical structure. Based on the chemical shift ranges for common types of protons, the chemical shifts of the methyl, methylene and methylidyne groups range from 0 to 6.5 ppm, while the chemical shifts of benzene protons range from 6.5 to 8.5 ppm due to the deshielding effect of the π electrons in the aromatic ring system [14, 15]. So the spectrum in Fig. 9.6 can be divided into two parts. In the upfield region, it gives the spectrum of the chain part of the molecule where protons are labeled as X1-X10 down to

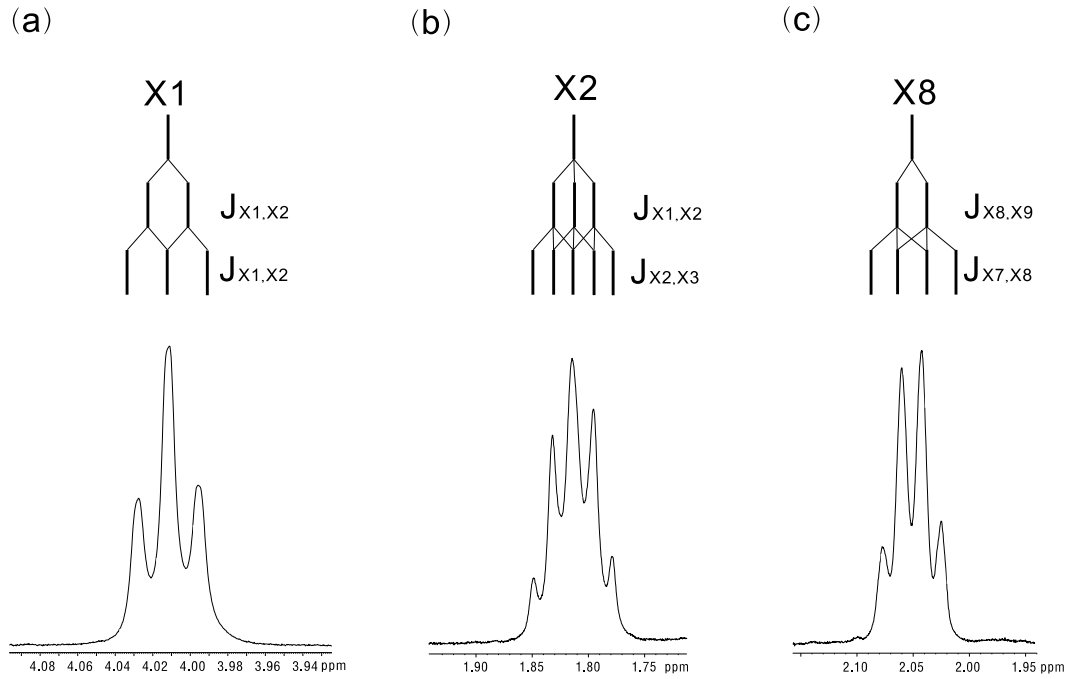

Figure 9.7: The expansion of ^{1}H NMR spectrum for peak X1, X2 and X8 in 10BrPBBC with the labeled J coupling interactions. The tree diagrams show the origin of the splitting patterns.

the chain end (see Fig. 1.14(a)). Figure 9.7 contains expansion regions of some signals so that the effect of J-couplings and the coupling constants can be determined. The best way to start the analysis of a complicated system is to start with the simplest splitting patterns. In this case, we will start with X1 first. For X1 hydrogens, they are different from the other methylene groups since there is an oxygen atom connected to the same carbon atom, thus the chemical shift will move downfield around 4.0 ppm. Since there are only two equivalent hydrogens on site X2 as neighbors, the splitting of X1 follows the Pascal's triangle and has a triplet with the J coupling constant, which is shown in Figure 9.7(a). Similarly, for X2-X7 protons all each have four equivalent protons, and according to the Pascal's triangle each peak will split into five peaks. To demonstrate this effect, the splitting diagram for X2 is shown as an example in Figure 9.7(b). Proton X8 interacts with three equivalent protons and splits into four peaks which are shown in Figure 9.7(c). The J couplings above originate from the same kind of chemical environment and the splittings are about 7Hz. Although there is also small interactions between X8 and X10 (or X10') which will result in smaller doublets, they broaden the line shape and are hard to observe here. The splittings of X9, X10 and X10' are more complex due to the π-bond. Figure 9.8 shows expansion regions of these peaks and the splitting diagrams. Here we need to note that the hydrogens of the terminal alkene will have their own chemical shifts and will couple with each other in the absence of molecular symmetry. This is a case of two-bond geminal coupling [15]. They

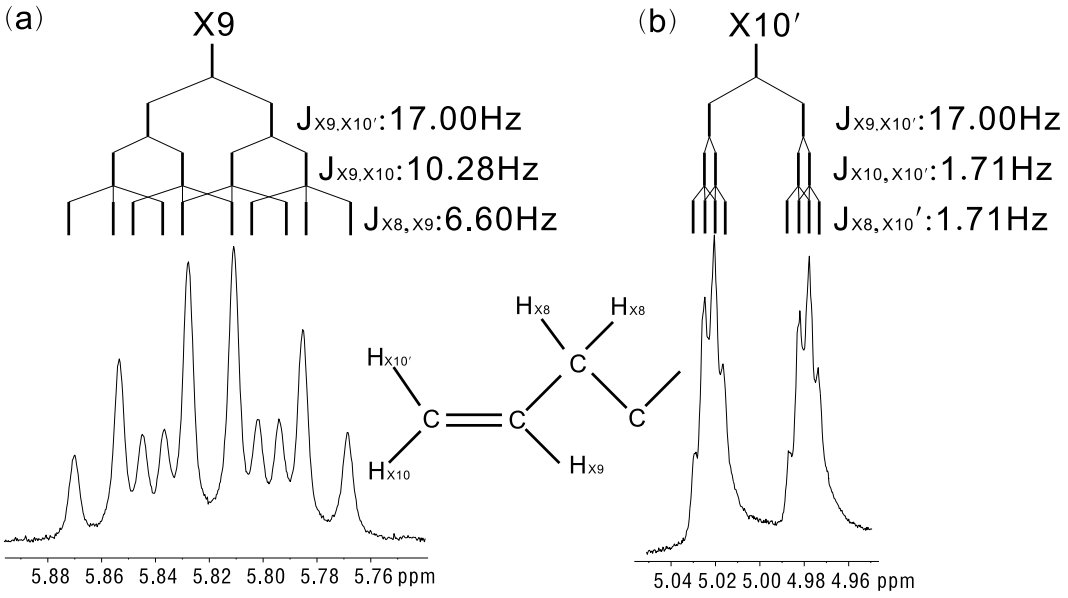

Figure 9.8: The expansion of ^{1}H NMR spectrum for peak X9 and X10 in 10BrPBBC with the labeled J coupling interactions. The tree diagrams show the origin of the splitting patterns and the molecular structure is also shown to clarify the interactions.

often show small doublets or multiplets of equal areas. So proton X9 will have three different kinds of coupling interactions . The '*trans*' interaction between X9 and X10' is the strongest interaction and splits the peak into a doublet with $J_{X9,X10'} = 17.0$Hz. This doublet then splits into a quartet under the '*cis*' interaction between X9 and X10. The final pattern is produced after the coupling interaction between X8 and X9 is applied on the quartet. This would lead to the tree diagram shown in Figure 9.8(a). Notice that overlap of peaks happens in the final pattern. In the case of X10 and X10', they have similar interactions and X10' will be discussed as an example. The peak of proton X10' was firstly split by the '*trans*'J-coupling interaction between X9 and X10'. Experiencing the interactions of $J_{X10,X10'}$, the doublet will split and further split by $J_{X8,X10'}$ again. Notice that when the two smaller couplings are equivalent (or nearly equivalent) the central lines in the final doublet coincide, and effectively give quartets instead of pairs of doublets. Since the signal is so weak here, the intensity is not necessarily proportional to the equivalent protons.

The peaks in the aromatic part can also be assigned based on the proton chemical shift prediction. The expansions of these peaks are shown in Figure 9.9-9.11. For the biphenyl part, the protons of 7(7b), 6(6b), 3(3b) and 2(b) undergo the J-coupling interactions from their neighbors such as $J_{6,7}$ ($J_{6b,7b}$) or $J_{2,3}$ ($J_{2b,3b}$) and for each peak there is a doublet produced. The molecule 10BrPBBC is not symmetric because the hydrogen atom on site 10 is substituted by a bromine atom. As a consequence, the chemical environment of its neighbor

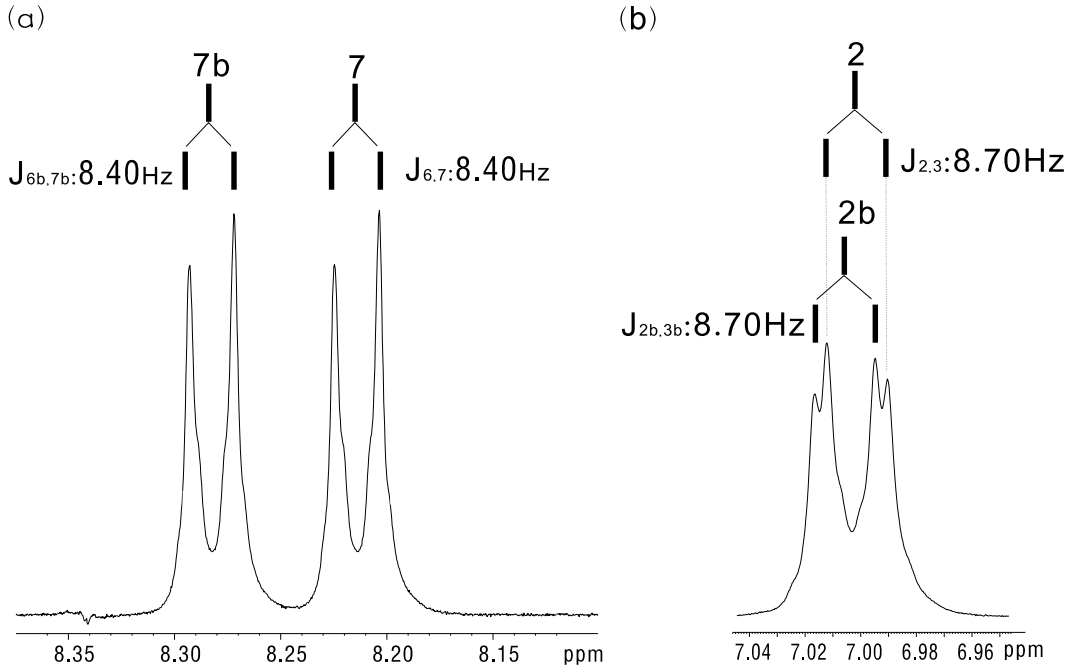

Figure 9.9: The expansion of ^{1}H NMR spectrum for peak 7(7b) and 2(2b) in 10BrPBBC with the labeled J coupling interactions. The tree diagrams show the origin of the splitting patterns.

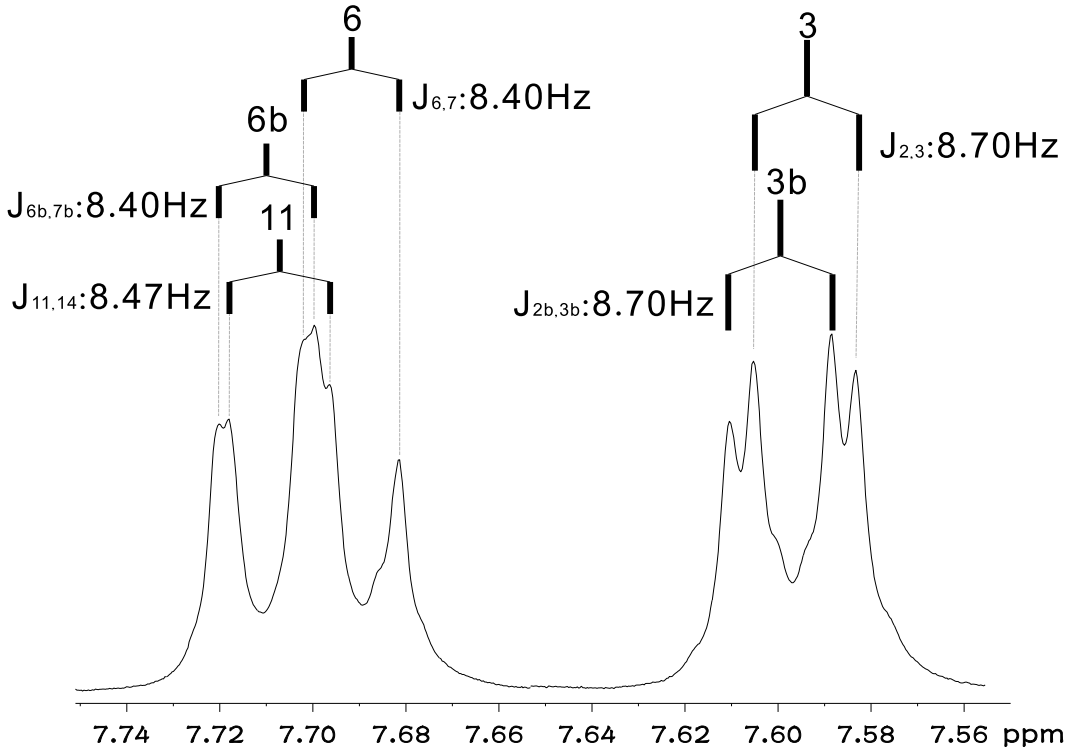

Figure 9.10: The expansion of ^{1}H NMR spectrum for peak 3(3b), 6(6b) and 11 in 10BrPBBC with the labeled J coupling interactions. The tree diagrams show the origin of the splitting patterns.

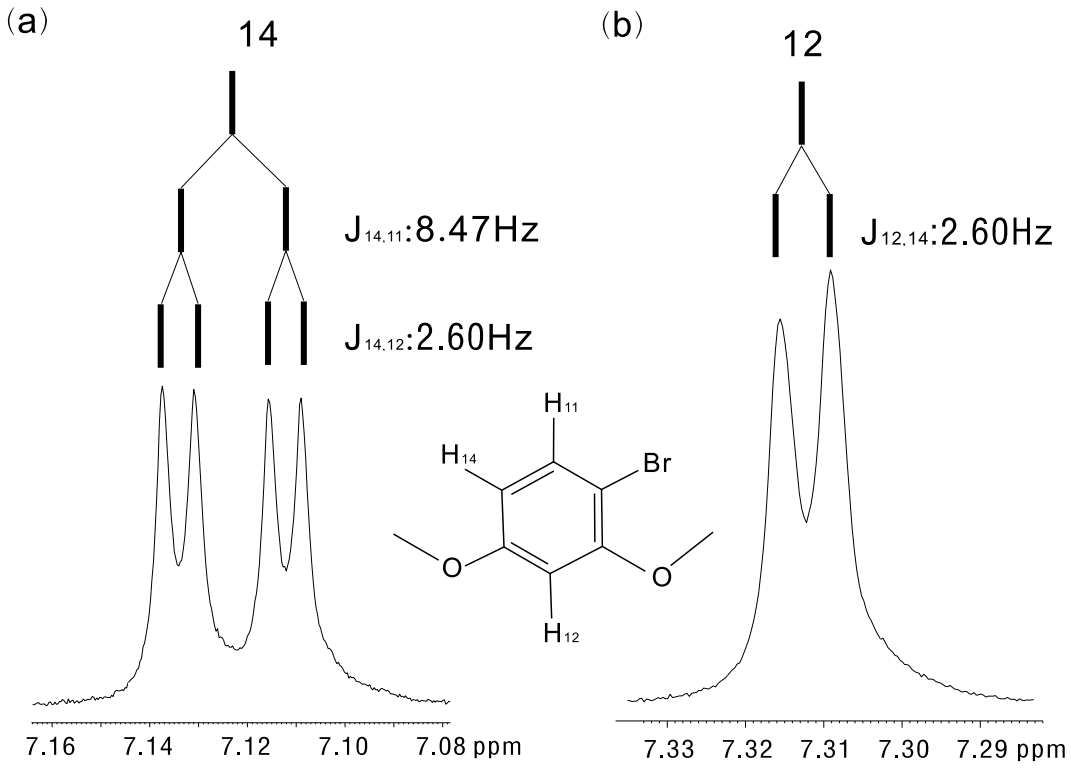

Figure 9.11: The expansion of ^{1}H NMR spectrum for peak 14 and 12 in 10BrPBBC with the labeled J coupling interactions. The tree diagrams show the origin of the splitting patterns and the molecular structure is also shown to clarify the interactions.

elements has changed and we find that the relative shifts $\Delta_{k,kb}$ ($= \delta_k - \delta_{kb}$, with k =2, 3, 6, 7) between the peaks of k and kb have the following relations:

$$\Delta_{7,7b} = 28.12Hz > \Delta_{6,6b} = 8.68Hz > \Delta_{3,3b} = 2.20Hz > \Delta_{2,2b} = 1.71Hz \qquad (9.10)$$

Note that proton 7b is shifted the most. Proton 11 experiences the J-coupling interaction from proton 14 to give a doublet, which is overlapped by the peaks of proton 6 and 6b (See figure 9.10). Although there is a five-bond interaction between 11 and 12, it is too weak to be observed. However, the four-bond interaction between 12 and 14 can be seen in figure 9.11. The signal of proton 14 is split into a doublet by the interaction of $J_{14,11}$ and then to a quartet pattern due to the $J_{14,12}$ interaction. For proton 12, it produces a doublet only by the interaction $J_{12,14}$. These peak assignments will be confirmed by the HETCOR experiment in the next subsection.

9.3.2 ^{13}C NMR study of 10BrPBBC

The ^{1}H broad-band decoupled ^{13}C NMR experiment of 10BrPBBC was performed using the pulse sequence shown in Fig. 9.2. The ^{13}C 90° pulse length in the experiment was 19μsec. To assist the peak assignments, the DEPT-135 ^{13}C NMR experiment was also carried out. Both spectra are shown in figure 9.12. By comparing spectra (a) and (b) in figure 9.12, one can differentiate the quaternary carbons (no peak), CH_2 groups (negative peak) and the other CH, CH_3 groups (positive peaks) in DEPT-135 spectrum. According to the ^{13}C chemical shift prediction, the peaks of quaternary carbons such as Z, Z', 1, 9, 13, 5, 8, 4, 10 can be assigned, where Z and Z' stay in the downfield due to the C=O bonds and 10 is in the upfield because of the bond with bromine. Carbons 1, 9, 13 locate in a more downfield direction due to the C-O bonds comparing to the carbons 5, 8, 4 which have C-C bonds. For this molecule, all the the CH_2 groups are in the chain part. Since carbon X10 has the C=C bond which shifts the peak to the downfield, one can assign this peak. For carbon X1, the C-O bond also can shift the peak downfield to around 68 ppm. There is no CH_3 group in this molecule, so all the positive peaks are CH groups. Note that X9 is the only CH group on the chain and due to the C=C_{X9}-C bond, its signal will be the most downfield among all the CH groups. The other CH groups can also be assigned based on the chemical environment and carbon chemical shift prediction as shown in figure 9.12. Since the ^{13}C NMR spectrum ranges between 0-170 ppm, which is much wider than that of ^{1}H NMR spectrum, the ^{13}C peaks from the biphenyl rings on the two sides overlapped and are hard to see. However, 7 and 7b show two separate peaks due to the proximity with the bromine atom.

To verify the ^{1}H and ^{13}C peak assignments, the 2D ^{1}H-^{13}C correlation experiment HETCOR was done on this molecule. The final 2D spectrum is shown in Figure 9.13 with the one dimensional spectra. The horizontal projection is the ^{13}C chemical shift spectrum and the vertical projection corresponds to that of ^{1}H. All the cross peaks are labeled in the contour plane. One can see that the peak assignments of both ^{1}H and ^{13}C spectra are consistent by producing cross peaks at the right positions. This confirms the peak assignments of all the high resolution spectra and further demonstrates the use of these techniques. Additionally, this assignment is consistent with the peak assignment of the 2D solid SUPER experiments in last chapter and it will help to study the ordering of 10BrPBBC in the next subsection.

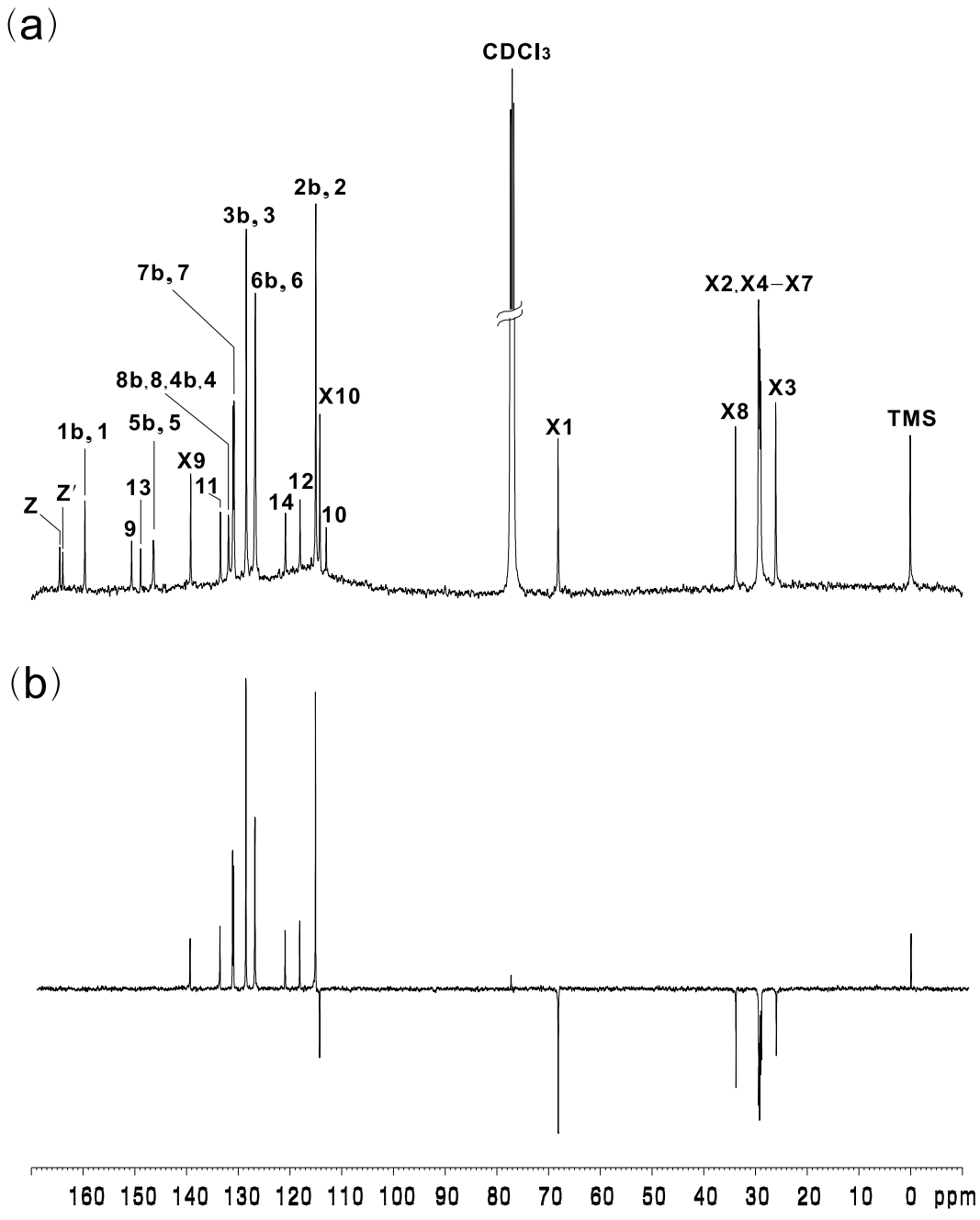

Figure 9.12: (a) The standard ^{13}C NMR spectrum of 10BrPBBC with peak assignments. (b) The DEPT-135 ^{13}C NMR spectrum of 10BrPBBC for comparison with (a).

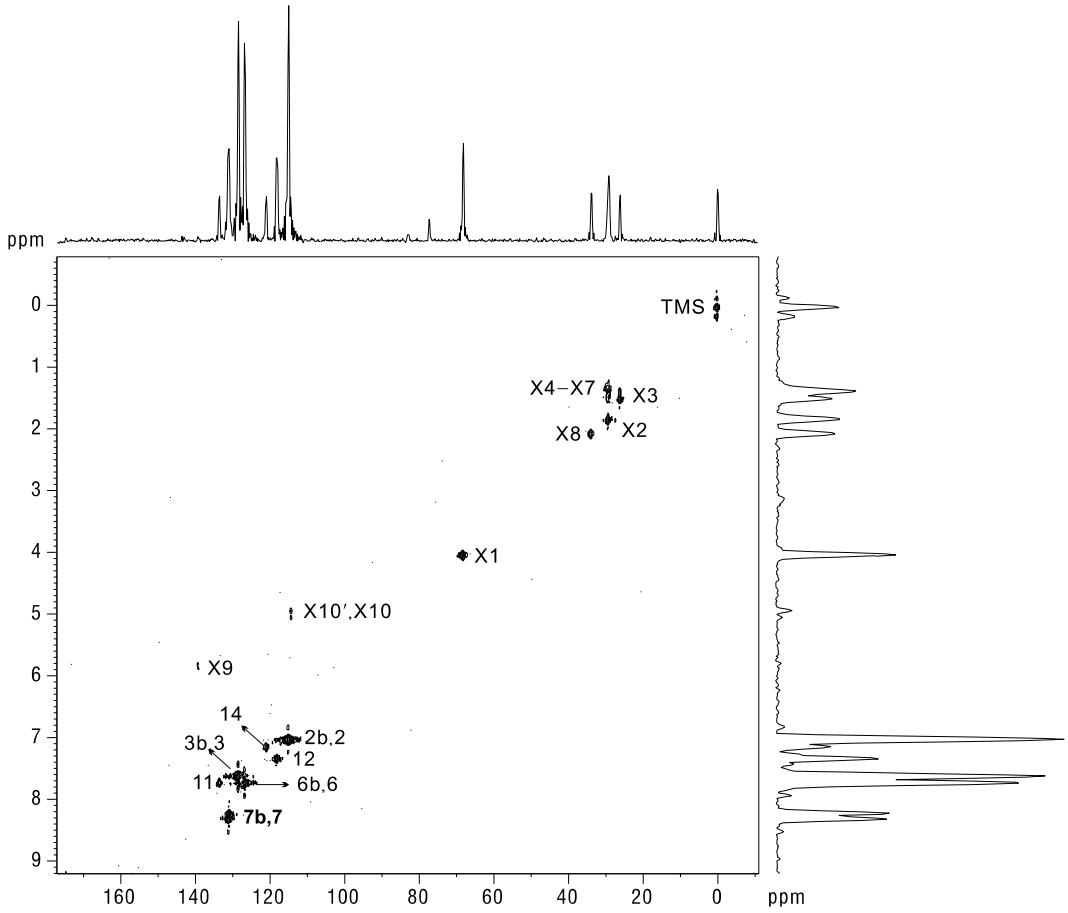

Figure 9.13: Two dimensional HETCOR spectrum of 10BrPBBC with their one dimensional projections. The contours are the cross peaks which are labeled correspondingly.

9.4 ^{13}C NMR Study of the Ordering of 10BrPBBC

The experiments on a static aligned nematic sample were carried out with a 2-channel Bruker HX probe, using standard CP for 2ms after a 90° (3.4 μs) proton irradiation. Proton decoupling during the ^{13}C signal acquisition was achieved by a SPINAL-64 pulse sequence [21] at a decoupling power of 39.4 kHz. The repetition rate was set at 3.5 s, and the number of scans for signal averaging was 856. The choice of the repetition rate is limited by the fact that nematic alignment of 10BrPBBC is only stable for an hour at the studied temperatures. We note that 10BrPBBC cannot be aligned below 69°C, while attempting to record a ^{13}C spectrum. Also radio frequency heating close to the clearing temperature T_c at a repetition rate of 3.5 s was undetectable. The two studied bent-core nematogens 10BrPBBC and 10ClPBBC appear to behave strangely under the field alignment process and the reason for this difficulty in field alignment has been postulated by Domenici [22]. More studies are needed to clarify this. Figure 9.14 shows typical ^{13}C spectra observed in the 10BrPBBC sample, one in

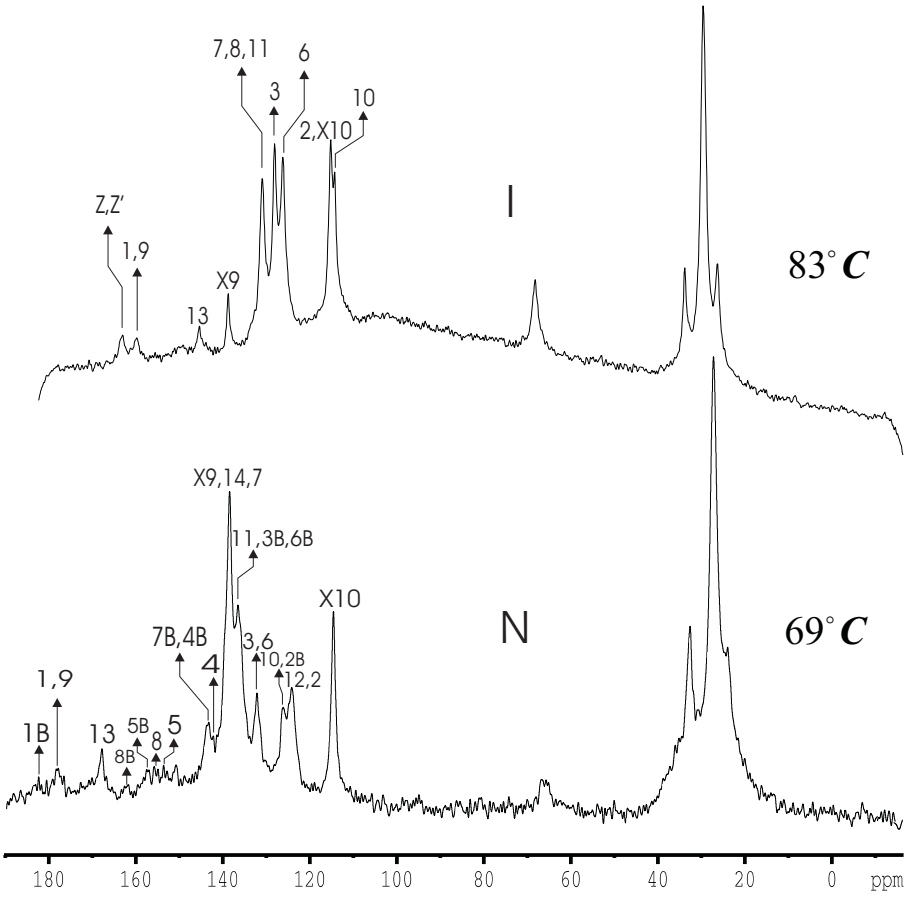

Figure 9.14: ^{13}C NMR spectra of the field aligned 10BrPBBC sample at 100.6MHz.

the isotropic phase and the other when the sample is aligned in the nematic phase close to T_C. The chemical shift σ of a carbon in a liquid crystalline phase is related to its isotropic chemical shift σ_{iso}, the components of the chemical shift tensor σ_{ij}, and local order parameter tensor S_{ij}. By selecting the z axis frame of the phenyl part as in Figure 1.14(b), from Eq. (7.36) the order parameter of the long local z axis for the phenyl part at 69 °C was obtained by fitting carbon sites 9-14 to give $S'_{zz} = 0.35$. Similarly, for the biphenyl fragment close to the bromine side ($S'_{z'z'} = 0.33$) and for the other biphenyl part ($S_{z''z''} = 0.26$) were found by fitting carbon sites 1(b)-8(b), respectively. The three ($S'_{xx} - S'_{yy}$) were found to be negligibly small. The calculated chemical shifts for the fitted carbon sites at this temperature are summarized in Table 9.1. The results imply that the local axis located on the central ring represents a more ordered axis, which is therefore assumed as the long molecular axis. The S'_{zz} value (0.35) is close to those reported previously [24]. The degree of ordering of these local z axes can be related by an approximate Eq. (7.37), $(S_{zz})_{biphenyl} \approx (S_{zz})_{phenyl} P_2(\cos\theta)$, where θ is the angle between the para axes of a biphenyl group and the long z axis. From this equation, the average angles $\theta_a \approx 12.6°$ and $\theta_b \approx 24.3°$ (Fig. 1.14(b)) are estimated. These two angles are consistent with the results from ^{2}H NMR measurements of a similar

Table 9.1: Calculated Chemical shifts for various carbon sites in ppm of 10BrPBBC at 69 °C.

sites	σ_{iso}	σ_{exp}	σ_{cal}	sites	σ_{iso}	σ_{exp}	σ_{cal}
1b	159.0	182.4	180.4	1	159.0	177.9	176.2
2b	114.7	126.1	127.0	2	114.7	124.1	124.6
3b	127.5	136.5	134.2	3	127.5	132.1	132.9
4b	122.6	143.2	145.5	4	122.6	142.1	141.0
5b	140.5	157.5	158.9	5	140.5	153.6	155.3
6b	127.5	136.5	134.2	6	127.5	132.1	132.9
7b	131.0	143.2	140.4	7	131.0	138.4	138.5
8b	130.7	162.1	162.5	8	130.7	155.8	156.2
9	158.3	177.9	176.5	12	117.5	124.1	123.9
10	111.2	126.1	126.4	13	149.4	167.8	167.8
11	131.0	136.5	135.9	14	121.3	138.4	139.9

* The results are based on Table 8.4 and Eq. (7.36) (for C_2, σ_{xx}= 8.7, σ_{yy}= 135.5, σ_{zz}= 192.6, from ref. [23]. The σ_{iso} values are those from the 1D projection in Fig. 8.10(2b), because of the better spectral resolution.)

mono-chlorine substituted bent-core mesogen($\theta_a \approx 11.8°$ and $\theta_b \approx 23.9°$) [25]. Thus, different halogen substitutents in the central ring do not seem to affect the value of θ_a and θ_b that much. The bending angle between the two lateral wings is estimated as 143.1° for 10BrPBBC.

In summary, we believe that the CSA tensors obtained from the SUPER experiments described in Chapter 8 could be useful for ^{13}C NMR studies of other banana-shaped molecules. Information on the CSA tensors from the central phenyl ring is crucial in defining the bending angle between the lateral wings in the molecular core.

9.5 High Resolution NMR Study of A131

9.5.1 ^{1}H NMR study of A131

The molecular structure of A131 is shown in Figure 9.15 with the labeled sites. Using the standard ^{1}H NMR pulse sequence shown in Figure 9.1, the 1D ^{1}H spectrum was obtained as shown in Figure 9.15. The 90° ^{1}H pulse width was 10.5μsec. Similar to the spectrum of 10BrPBBC, the assignment of the peaks is also based on the proton chemical shifts and their

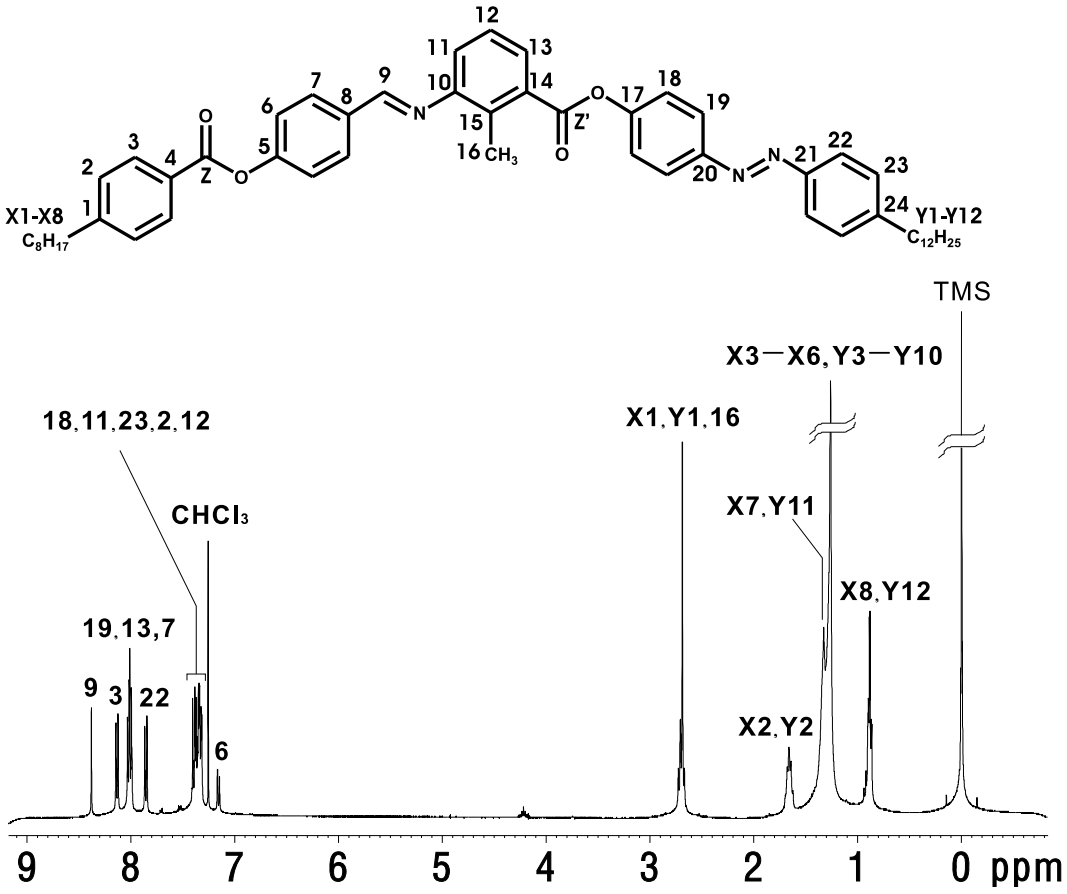

Figure 9.15: The ^{1}H NMR spectrum of A131 with peak assignments.

spin-spin couplings. For the two chain parts of A131, there are methyl (CH_3-) or methylene (-CH_2-) groups and their splitting patterns are produced strictly according to the Pascal's triangle. Peaks of protons X1, Y1 and X8, Y12 will split into pairs of triplet due to their two equivalent neighboring protons. Conversely signals of X7 and Y11 will split into six peaks (not resolved) affected by the five equivalent neighboring protons. For proton 16, there is no other protons next to it, so it will produce only one peak which overlaps with peaks from X1 and Y1. And the other protons X2-X6 and Y2-Y12, each splits into five peaks. The origin of these splitting patterns is similar to Figure 9.7. From the chemical environment analysis, the proton 9 can be assigned as it will stay in the most downfield position due to the connection with the -CH=N- bond.

To make the peak assignments of the aromatic protons, expansions of these peaks are plotted in Figure 9.16 and 9.17. Protons 2, 3, 6, 7, 18, 19, 22 and 23 all have one proton as neighbor, and each peak will split into a doublet. According to their chemical shift predictions and their coupling constants, these peaks can be assigned in Figure 9.16 and 9.17. The splitting pattern of the protons on the central ring part is a little complicated. Proton 12 has two

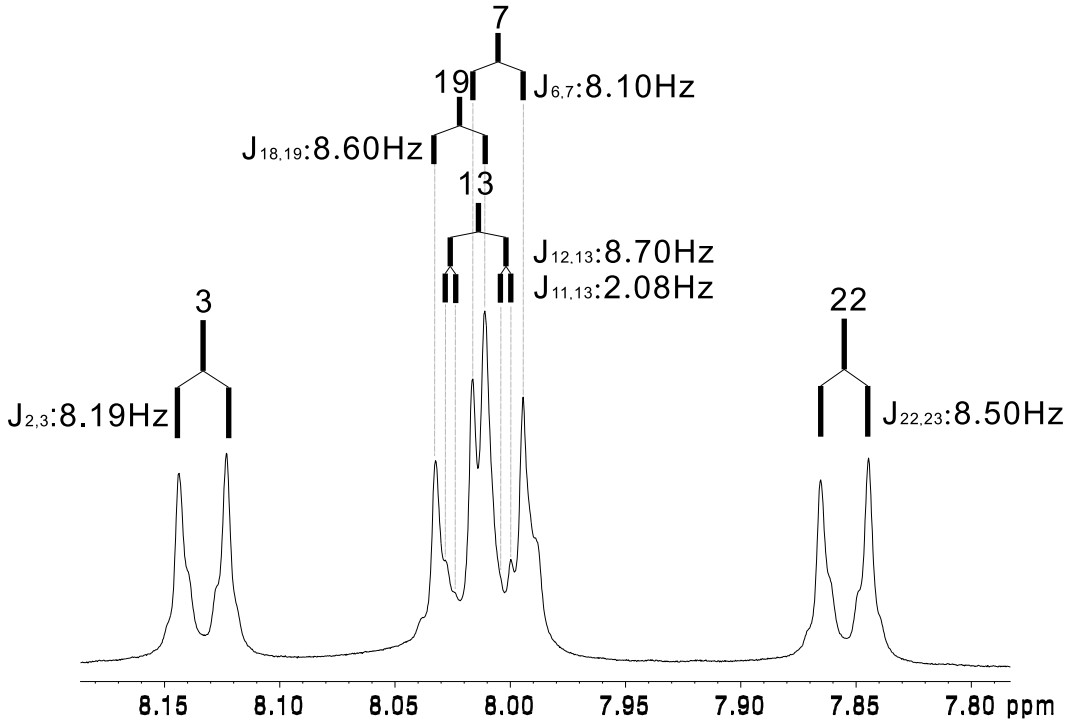

Figure 9.16: The expansion of ^{1}H NMR spectrum for peak 3, 7, 13, 19 and 22 in A131 with the labeled J coupling interactions. The tree diagrams show the origin of the splitting patterns.

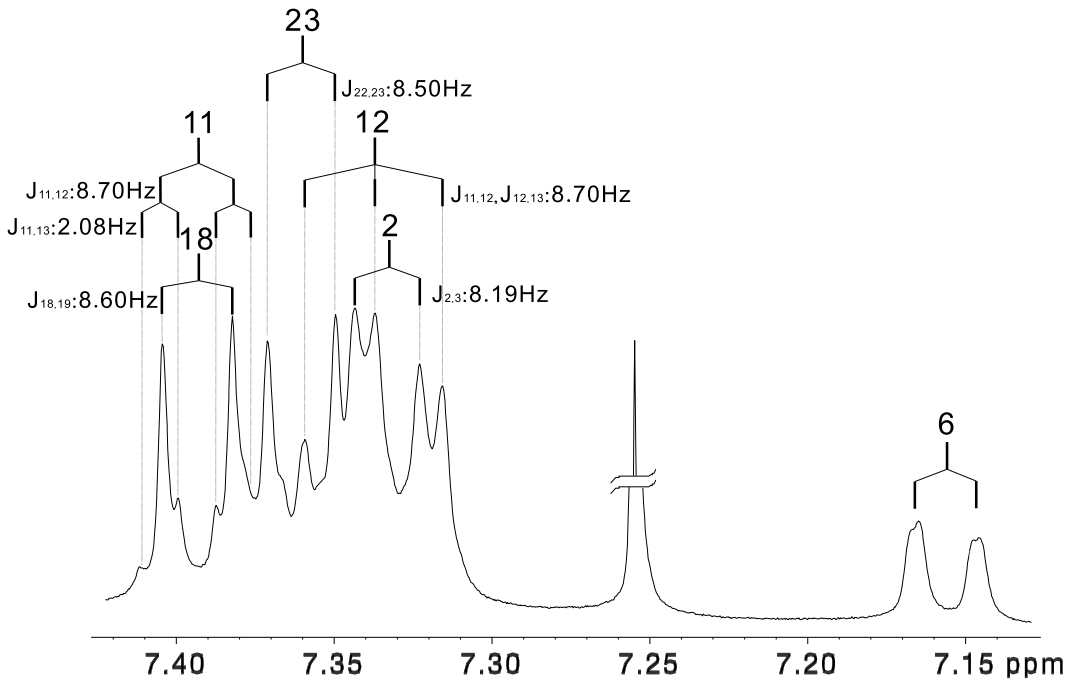

Figure 9.17: The expansion of ^{1}H NMR spectrum for peak 2, 6, 11, 12, 18 and 23 in A131 with the labeled J coupling interactions. The tree diagrams show the origin of the splitting patterns.

equivalent neighboring protons on site 11 and 13, so it will produce a triplet. And protons 11 and 13 can 'feel' each other after they are influenced by proton 12. So each of them will split into two pairs of doublets (shown in Figure 9.16 and 9.17). Since there is large overlap among peaks here, some of the splittings are hard to be observed or just become small shoulders. These peak assignments will be proved by 2D ^{1}H-^{13}C experiment of HETCOR in the next subsection.

9.5.2 ^{13}C NMR study of A131

The 1D ^{13}C NMR experiment was performed on A131 using the pulse sequence shown in Figure 9.2 and the 90° ^{13}C pulse width was 19μsec. Due to the low natural abundance of ^{13}C, to get a clear spectrum this experiment took about 7.5 hours. To help the ^{13}C peak assignment a DEPT-135 experiment was also done. Fig. 9.18 shows both of these 1D ^{13}C spectra. By comparing the spectra of (a) and (b) in Fig. 9.18, peaks from the quaternary carbons (no signal in DEPT-135) can be justified such as 1, 4, Z, 5, 8, 10, 14, 15, Z', 17, 20, 21, 24. Since Z and Z' have C=O bonds connected, they have the highest chemical shifts. On the other hand, the carbons on C-C bonds such as sites 4, 8, 14, 15, 24 and 1 will have lower chemical shifts compared to the carbons on C-O or C-N bonds such as sites 5, 17, 10, 21, 20. So these quaternary carbons can be assigned according to their chemical environments. On the other hand, the CH_2 groups can be decided from the negative peaks in the DEPT-135 experiment. All the CH_2 peaks come from the chain parts of A131 and they can be assigned based on the chemical shift positions. The two carbons X1 and Y1 at the beginning of the chain will produce the highest chemical shifts among all the CH_2 groups, while the two carbons X7 and Y11 at the end of the chain will produce the lowest chemical shifts. Now one can go to the positive peaks (CH or CH_3 group). There are three CH_3 groups in this molecule, i.e., 16, X8 and Y12. The signals that they produced are all located in the upfield region, which can be easily assigned to the last two peaks in this chemical shift region. It is noted that CH groups include carbon 9 (-CH=N-) and all the aromatic protonated carbons. Due to the -CH=N- bond interaction, carbon 9 will locate further downfield, which is assigned to the only positive peak in the downfield around 159 ppm (see the expansion graph in Fig. 9.18(a)). For all the aromatic carbons such as 2, 3, 6, 7, 11, 12, 13, 18, 19, 22 and 23, they range from 120 ppm to 132 ppm. Their peak assignments, based on the chemical shift prediction, are shown in the expansion graph in Fig. 9.18(a).

To double check the peak assignments of both the ^{1}H NMR spectrum and the ^{13}C NMR spectrum for A131, the 2D ^{1}H-^{13}C correlation experiment was also performed on this sample.

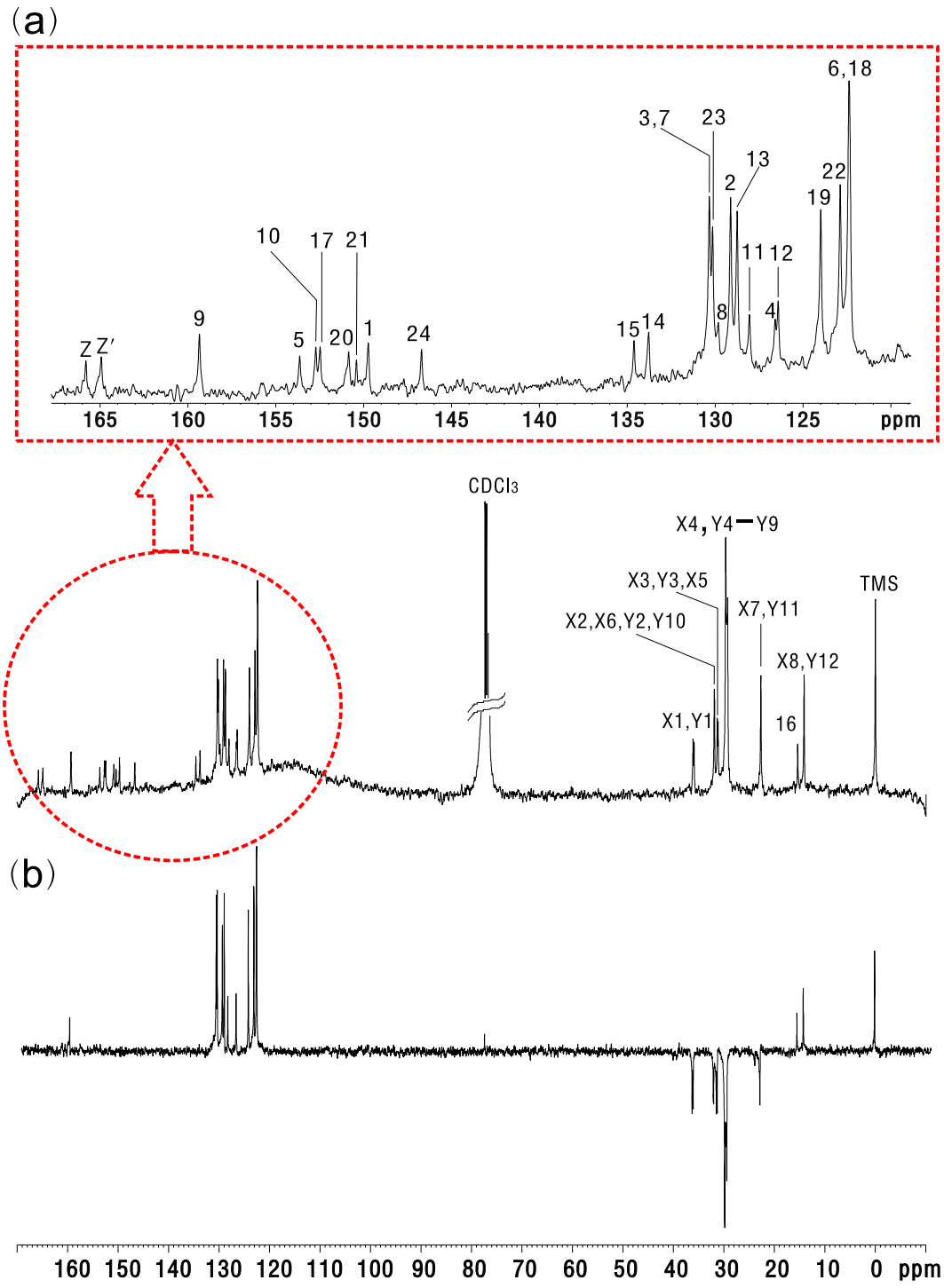

Figure 9.18: (a) The standard ^{13}C NMR spectrum of A131 with peak assignments. The expansion of part of the spectrum is also shown on the top. (b) The DEPT-135 ^{13}C NMR spectrum of A131 for comparison with (a).

Fig. 9.19(a) gives the contour plot of the spectrum with both the horizontal (1D ^{13}C spectrum) and vertical (1D ^{1}H spectrum) projections. The correlated peaks, which are labeled in the graph, are produced from a ^{13}C signal and the corresponding connected ^{1}H signal. To clarify part of this spectrum in Fig. 9.19(a), an enlarged graph is shown in Fig. 9.19(b) with the corresponding labeled signals. These peak assignments are consistent with those of both 1D ^{1}H spectrum and 1D ^{13}C spectrum we got before.

9.6 Conclusion

In this chapter, both solid and liquid state NMR techniques are used to study the bent-core liquid crystals. Using the solid state NMR techniques, the ordering of 10BrPBBC was studied using the chemical shift tensors we have obtained in the preceding chapter. The bending angle for the two wings has been determined which is very important for deciding the phase structure. In the liquid state NMR study, both ^{1}H and ^{13}C NMR experiments are introduced. DEPT and HETCOR experiments are adopted to assist the ^{13}C peak assignment. To demonstrate these techniques, two bent-core molecules 10BrPBBC and A131 are studied to show self-consistent peak assignments of the ^{1}H and ^{13}C spectra. These peak assignments are valuable for studying the ordering in bent-core liquid crystals and even their dynamics in the mesophases.

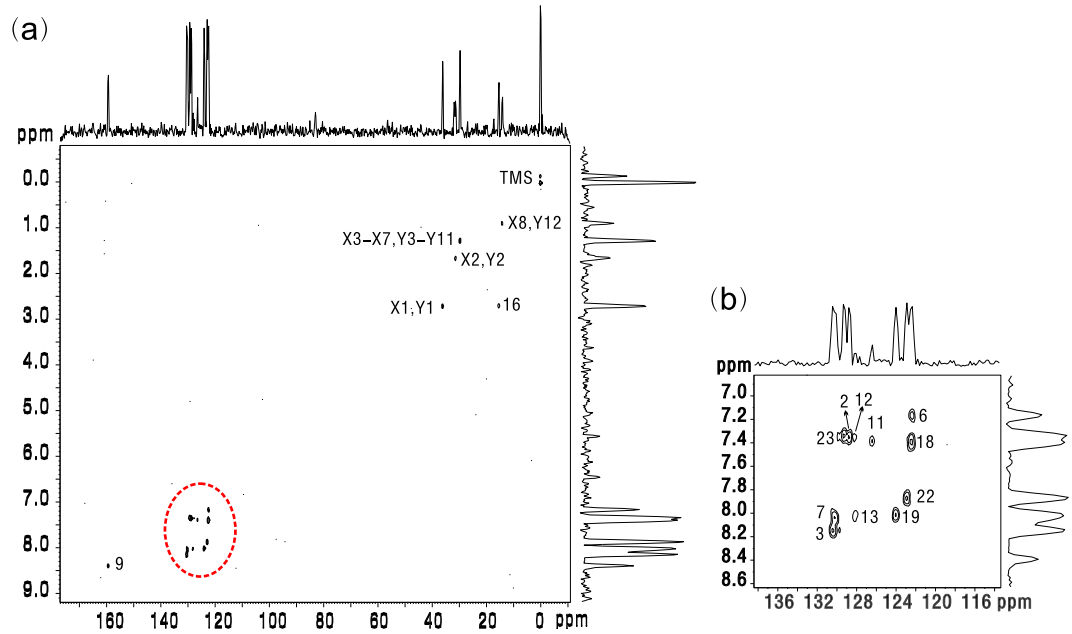

Figure 9.19: (a) Two dimensional HETCOR spectrum of A131 with their one dimensional projections. (b) The expansion plot of the circle part in (a). The contours are the cross peaks which are labeled correspondingly.

References

[1] Meyer, R. B.; Liebert, L.; Strzelecki, L.; Keller, P. *J. Physique Lett.* **1975**, *36*, L69.

[2] Blinc, R. *Physica Status Solidi B* **1975**, *70*, K29.

[3] Chandani, A. D. L.; Ouchi, Y.; Takezoe, H.; Fukuda, A.; Terashima, K.; Furukawa, K.; Kishi, A. *Jpn. J. Appl. Phys.* **1989**, *28*, L1261.

[4] Prost, J.; Barois, P. *J. Chimie Physique.* **1983**, *80*, 65.

[5] Petschek, R. G.; Wiefling, K. M. *Phys. Rev. Lett.* **1987**, *59*, 343.

[6] Niori, T.; Sekine, T.; Watanabe, J.; Furukawa, T.; Takezoe, H. *J. Mater. Chem.* **1996**, *6*, 1231.

[7] Selinger, J. V. *Phys. Rev. Lett.* **2003**, *90*, 165501.

[8] Jakli, A.; Toledano, P. *Phys. Rev. Lett.* **2002**, *89*, 275504.

[9] Dong, R. Y. *Nuclear Magnetic Resonance of Liquid Crystals*; Springer-Verlag, 1997.

[10] Burnell, E. E.; de Lange, C. A. *NMR of Ordered Liquids*; Kluwer Academic Publishers: Netherlands, 2003.

[11] Derome, A. E. *Modern NMR Techniques for Chemistry Research*; Pergamon, Oxford, 1987.

[12] Sanders, J. K. M.; Hunter, B. K. *Modern NMR Spectroscopy*, 2nd ed.; Oxford University Press, Oxford, 1993.

[13] Braun, S.; Kalinowski, H.-O.; Berger, S. *150 and More Basic NMR Experiments: A Practical Course*; Wiley-VCH, 1998.

[14] Silverstein, R. M.; Webster, F. X. *Spectrometric Identification of Organic Compounds*; John Wiley and Sons, Inc., 1998.

[15] Pavia, D. L.; Lampman, G. M.; Kriz, G. S. *Introduction to Spectroscopy*; Harcourt College Publishers, 2001.

[16] Schenker, K. V.; Vonphilipsborn, W. *J. Magn. Reson.* **1986**, *66*, 219.

[17] Doddrell, D. M.; Pegg, D. T.; Bendall, M. R. *J. Magn. Reson.* **1982**, *48*, 323.

[18] Bendall, M. R.; Doddrell, D. M.; Pegg, D. T. *J. Am. Chem. Soc.* **1981**, *103*, 4603.

[19] Bax, A.; Morris, G. A. *J. Magn. Reson.* **1981**, *42*, 501.

[20] Freeman, R.; Morris, G. A. *J. Chem. Soc. Chem. Commun.* **1978**, *16*, 684.

[21] Fung, B. M.; Khitrin, A. K.; Ermolaev, K. *J. Magn. Reson.* **2000**, *142*, 97.

[22] Domenici, V.; Veracini, C. A.; Zalar, B. *Soft Matter* **2005**, *1*, 408.

[23] Zheng, G.; Hu, J.; Zhang, X.; Shen, L.; Ye, C.; Webb, G. A. *J. Mol. Struct.* **1998**, *428*, 283.

[24] Dong, R. Y.; Xu, J.; Benyei, G.; Fodor-Csorba, K. *Phys. Rev. E.* **2004**, *70*, 011708.

[25] Dong, R. Y.; Fodor-Csorba, K.; Xu, J.; Domenici, V.; Prampolini, G.; Veracini, C. A. *J. Phys. Chem. B* **2004**, *108*, 7694.

Chapter 10

Conclusions

NMR is one of the most powerful and versatile techniques for determining the structures and properties of liquid crystals [1–3]. In this dissertation we have described several applications of ^{2}H and ^{13}C NMR methods to study the phase structures and dynamics of liquid crystals.

The dynamic range of NMR spectroscopy can be divided into three categories: extremely fast regime, intermediate regime and ultraslow regime. The ^{2}H NMR study carried out in this dissertation covers all the dynamic regimes. In the fast regime, the characteristic rates, $1/\tau$, are of the order of Larmor frequencies which fall in the range of 10^7 s^{-1} and faster. Relaxation time measurements are the most useful means for studying fast molecular reorientation and conformational equilibrium. The dynamics of both chiral rod-like and discotic liquid crystals were studied based on the spin relaxation theory. Since the spectral densities in the SmC* phase are not very sensitive to the biaxial character of this phase, it was studied by treating the phase as uniaxial but considering the tilt angle explicitly. This approach has served as a convenient way to study the biaxial phase using the relaxation study. Moreover, the dynamics of discotic molecules for an aligned sample in the magnetic field, HAT5a-d$_6$, were investigated using the anisotropic viscosity model. These results provided the dynamic information in the discotic phase at high temperatures, which can not be obtained using lineshape simulation studies.

At the other extreme of ultraslow motions, the dynamic rate is too slow to affect the line shape, but still faster than the longitudinal relaxation rate, $1/T_1 < 1/\tau < 1/T_2$. In this regime, 2D ^{2}H NMR exchange experiments were used to study the TGBA* and SmC* phase, resulting in a clear understanding of the novel behaviors of these phases at a molecular level. TGBA* phase is a relatively new liquid crystal phase and the molecular dynamics in this phase have never been investigated by the ^{2}H NMR method. Using the 2D ^{2}H NMR

exchange experiment, we have obtained the exchange spectrum of this sample. Based on the multisite jump model, the spectrum was successfully simulated using computer codes developed in this thesis. The twist angle ϕ_0 was obtained as about 26° for the first time in 11EB1M7, which is consistent with the x-ray results for the other samples in the literature. In addition, the simulation yielded the diffusion constant along the helices in the superstructure and the pitch length of the helix. Such diffusive information may not be easily obtained by pulsed field gradient NMR. To the best of our knowledge, this represents the first dynamic study of TGBA* phase using the NMR method. In the slow dynamic regime, the diffusion process along the smectic layers in the SmC* phase in BP8Cl was also investigated. To perform this study, the sample needed to be rotated 15° so that jumps across the soliton-like boundaries could result in observable changes in the Euler angles between the local director and the magnetic field.

In the intermediate dynamic range the exchange rates are of the order of the spin interactions and are responsible for the observed spectral patterns. The spectral line shape can provide information on the 'exchange'rates. By simulating line shapes of the experimental spectra, the exchange rates can be accurately determined. In this regime, a ^{2}H NMR angular dependent study was performed both on discotic and SmC* phases. The dynamics of disc-like monomeric and dimeric molecules were investigated. We studied both aligned and powder sample for the monomeric discotic molecules HAT5a-d_6. To simulate the rotational process of these molecules, three-site jump model and planar diffusion model were both adopted. The jump rate K_J or diffusion constant D_R was obtained and the simulation results from both methods were verified to be just as good. For the dimeric discotic liquid crystals, there is a spacer group connecting two disc molecules. To simulate the discotic liberation under the effect of the spacer group, a potential distribution was introduced. Since the dimer molecules DHAT5-C_{14} could not be aligned in the magnetic field, we studied the powder sample by varying the τ values in the solid echo pulse sequence. This approach has been applied to discotic powders for the first time. Using the Bloch-McConnell equation, the spectrum has been simulated using computer codes developed in this thesis and the diffusion constant obtained. By comparing the diffusion constants for the two discotic samples, we know that the planar motion in the dimer is at least 30 times smaller than that of the monomer, which means in dimer the spacer has stabilized the columnar structure, and given a larger temperature range for the mesophase, thereby providing enhanced charge and energy transport. Moreover, the structure and magnetic field response of SmC* phase were investigated in BP8Cl as an example. When the magnetic field is high enough, the helix can show soliton-like distortions. Landau theory was used to describe the distortions due to the magnetic field. The critical field (H_0^c) for unwinding the helical structure in this particular SmC* phase was derived as

about 30 Tesla.

In the ^{13}C NMR studies in this dissertation, both solid state and liquid state NMR techniques were used. The structure and ordering of liquid crystals can be obtained by fitting the chemical shifts of aromatic carbons and the C-H dipolar splittings. To fit the chemical shifts of these carbons, one needs the following information: the peak assignments in the isotropic phase, the chemical shift tensors and the peak assignments in the liquid crystal phases. This thesis has provided the methodology to make ^{13}C nuclei as a reliable means to get structural and ordering information in liquid crystals. To get the peak assignments in the isotropic phase, we need to study a solution sample using the liquid state NMR techniques. The liquid sample was prepared by dissolving a small amount of solid sample in some $CDCl_3$ solvent. Bent-core molecules were used to do high resolution liquid state NMR experiments. Both DEPT and HETCOR experiments were performed to study these molecules. These results could also assist the ^{13}C peak assignments of the studied chiral and achiral molecules. To fit the carbon chemical shifts, we also need to know the carbon chemical shift tensors. To get this information, the SUPER pulse sequence was used to carry out the experiment in the MAS probe. To this aim, MAS experiments with TOSS and SUPER were employed to get high resolution ^{13}C spectra of solids. Chemical shift tensors for some molecules were determined. These are important to study the structure and ordering of liquid crystals. To assign the peaks in the liquid crystal phase, we did the normal CP experiment. Using this pulse sequence, we have obtained the carbon chemical shifts at different temperatures. By fitting the carbon chemical shifts, we have determined the local order parameters of the phenyl and biphenyl parts for some molecules. One of the salient features in this portion of the thesis is the use of paritially deuterated mesogens to do ^{13}C NMR studies. The order parameter results could be verified with those from ^{2}H NMR. This thesis has shown that the ^{13}C NMR techniques can provide a good method to get the ordering of liquid crystals without the necessity of tedious chemical deuteration. Another method to get the ordering of liquid crystals is to measure the C-H dipolar splittings. To get this information, we adopted the LGCP/PISLF experiment. By measuring the dipolar splittings at different temperatures, the local order parameters for the biphenyl part were obtained. The results from both of these methods are consistent. So these techniques can further be used for structural studies of other non-deuterated liquid crystal samples.

Liquid crystal NMR spectroscopy can also be used for determining other physical properties of molecules. For example, the rotational viscosity coefficient was investigated based on a rotational diffusion model using the deuteron spin relaxation study [4]. Nowadays, NMR methods are widely used to investigate different liquid crystal phases and structures, e.g.

the biaxial nematic phase [5]. The experimental evidence for this phase still needs to be clarified. The bent-core A131 sample is known to show both a uniaxial nematic and a biaxial nematic phase. Solution state NMR and SUPER to give ^{13}C CSA tensors were carried out to pave the way to study the biaxial nematic phase. Preliminary ^{13}C NMR study of A131, however, has failed to clearly distinguish between its biaxial and uniaxial nematic phase. More sophisticated techniques are therefore required; this task remains a big challenge to NMR spectroscopists. On the other hand, modern NMR incorporates many complicated multi-pulse sequences such as RHODIUM and PDLF [6, 7]. In doing so, it can simplify the very complicated spectra that are often encountered in partially ordered liquid crystals. Most of the solid state NMR techniques used in this work can be easily adopted to study any molecular systems that show orientational and positional order.

References

[1] Dong, R. Y. *Annual Reports on NMR Spectroscopy* **2004**, *53*, 67.

[2] Laws, D. D.; Bitter, H. M. L.; Jerschow, A. *Angewandte Chemie-International Edition* **2002**, *41*, 3096.

[3] Burnell, E. E.; de Lange, C. A. *NMR of Ordered Liquids*; Kluwer Academic Publishers: Netherlands, 2003.

[4] Zakharov, A. V.; Komolkin, A. V.; Maliniak, A. *Phys. Rev. E* **1999**, *59*, 6802.

[5] Luckhurst, G. R. *Thin Solid Films* **2001**, *393*, 40.

[6] Caldarelli, S.; Hong, M.; Emsley, L.; Pines, A. *J. Phys. Chem.* **1996**, *100*, 18696.

[7] Fung, B. M.; Afzal, J.; Foss, T. L.; Chau, M. H. *J. Chem. Phys.* **1986**, *85*, 4808.

Appendices

Appendix A

Simulation and Fitting Programs for Discotic Liquid Crystals

Fortran 90 programs were used for the ^{2}H line shape simulations. The programs are listed below, where the IMSL numerical library and Qwins drawing library are used.

A.1 Simulation of ^{2}H Monomer Line Shapes

In the simulation of monomer line shapes, both threefold jump model and planar diffusion model (PDM) are used. Here the simulation program of the PDM for aligned sample is shown as follows:

```
MODULE publicdat
PARAMETER  PI=3.141592653589793238D0
PARAMETER NFID=256, NK=6
!theta0: the rotation angle.
!alpha, beita: the polar and azimuthul angle from the sample frame
! to the director frame.
!phi: the azimuthul angle from the C-D bond principle frame
!to the director frame.
!eta:biaxial parameter
!Tincr:time increment.
!Vfreq is (3/4) * NU_Q*Szz in khz
!*******************************************************
REAL*8 TAU,Tincr,eta,RT,GB,range
REAL*8 theta0
REAL*8 FID(NFID),Vfreq,Szz, FFTR(NFID),DR,width
INTEGER Ndata,Dwidth
REAL*8 DataDis(1:2,1:4096),offset, Specd
!Define spectrum region
REAL*8 Bspect, Espect
CHARACTER(255) datapath, inipath
PUBLIC::Bspect, Espect,Specd
PUBLIC:: Ndata, DataDis ,offset
PUBLIC:: TAU,FID,Tincr,Vfreq,Szz,Dwidth
END MODULE


PROGRAM Smain
```

```
USE publicdat
PARAMETER nsum=128
REAL*8 alpha,beita
Real*8 GaussD
REAL*8 FIDTEMP(NFID)
integer tt, tttemp
eta=0
TAU=0
FID=0
Tincr=0.008
DR=100.0D0
width=2
Dwidth=2
Szz=1
Vfreq=40.0D0
RT=1
GB=1
Bspect=20
Espect=46
theta0=0
range=2*PI
datapath='data.txt'
inipath='ini.txt'
CALL paths
CALL ini


beita=PI/2-3*width    ! integrate over beita
    DO  JSum=1,Dwidth*2

                alpha=2*PI/Nsum   ! integrate over alpha

DO Isum=1,Nsum


                CALL FREQ(alpha,beita,FIDTEMP)

                DO tt=1,NFID
                tttemp=tt
                GaussD=exp(-(0.5*(beita-PI/2)**2)/(width**2))/(sqrt(2*PI)*width)
                FID(tttemp)=FID(tttemp)+FIDTEMP(tttemp)*sin(beita)*GaussD
                ENDDO

alpha=alpha+2*PI/Nsum
ENDDO

    beita=beita+3*width/Dwidth
    ENDDO
CALL writefid
CALL FFT
CALL readdata
CALL Drawfft
END


SUBROUTINE writefid
USE publicdat
REAL*8 ttemp
OPEN(2,FILE="FID.txt")

ttemp=0D0
DO I=1, NFID
  WRITE(2,"(F16.9,F20.12)") ttemp,FID(I)
  ttemp=ttemp+Tincr
ENDDO
CLOSE(2)
RETURN
END



SUBROUTINE ini
```

```
USE publicdat
REAL*8 temp_ini(20)
INTEGER test,L
CHARACTER(150) temp
WRITE(*,"(A40)") "-----------Initial Values------------"
OPEN (3, FILE = inipath,STATUS='OLD')
i1=0
DO WHILE (.NOT. EOF(3) )
   test=0
   READ (3,"(A150)") temp
   L=LEN(temp)
   IF (temp .NE." ") THEN
      WRITE(*,"(A30)") temp
      test=0
      DO I=1,L
        IF (temp(I:I).EQ."=") THEN
            test=I+1
     EXIT
        END IF
      END DO
      IF (test.NE.0)THEN
        i1=i1+1
  READ(temp(test:L),*) temp_ini(i1)
      ENDIF
   END IF
END DO
IF (i1.NE.15) THEN
 WRITE(*,*) "ERROR_INITIAL VALUE NUMBERS,CHECK INI.TXT"
 STOP
ENDIF
WRITE(*,"(A40)") "-------------------------------------"
offset=temp_ini(1)
Bspect=temp_ini(2)
Espect=temp_ini(3)
Specd=temp_ini(4)
range=temp_ini(5)
Tincr=temp_ini(6)
TAU=temp_ini(7)
Vfreq=temp_ini(8)
Szz=temp_ini(9)
theta0=temp_ini(10)
eta=temp_ini(11)
DR=temp_ini(12)
width=temp_ini(13)
RT=temp_ini(14)
GB=temp_ini(15)
range=range*PI/180
Dwidth=width
width=width*PI/180
theta0=theta0*PI/180
TAU=TAU*(1D-3)
CLOSE(3)
RETURN
END


SUBROUTINE Readdata
USE publicdat
integer Nspace, L
CHARACTER(100) temp
REAL*8 psum, pave,pn
OPEN (3, FILE = datapath,STATUS='OLD')

READ (3,"(A100)") temp
READ (3,"(A100)") temp
Ndata=0
L=LEN(temp)

DO WHILE (.NOT. EOF(3) )
   READ (3,"(A100)") temp

      DO I=1,L
```

```
        IF ((temp(I:I).EQ." ").OR.(temp(I:I).EQ." ")) THEN
            Nspace=I
            EXIT
        END IF
       ENDDO

   Ndata=Ndata+1
   READ(temp(1:Nspace),*)  DataDis(1,Ndata)
   READ(temp(Nspace:L),*)  DataDis(2,Ndata)
END DO
CLOSE(3)
! normalize the data, correct the base line
psum=0
 pn=0
DO II=1,Ndata
   DataDis(1,II)=DataDis(1,II)/1000D0
   DataDis(2,II)=DataDis(2,II)/100000D0
   IF (DABS(DataDis(1,II)).GT.SpecD) THEN
     Psum= Psum+DataDis(2,II)
     pn=pn+1
   END IF
ENDDO

Pave=Psum/pn

OPEN (2, FILE = 'dataout.txt')
DO II2=1,Ndata
DataDis(2,II2)=DataDis(2,II2)-Pave
DataDis(1,II2)=DataDis(1,II2)+offset
WRITE(2,"(F20.12,A5,F20.10)")DataDis(1,II2),"    ",DataDis(2,II2)
ENDDO
CLOSE(2)

RETURN
END

!**************FFT and PLOT ROUTINES**********************

SUBROUTINE FFT
USE publicdat
REAL*8 temps
INTEGER ISWITCH, NIS
COMPLEX(8)  COMPLEXFID(NFID), COMPLEXFFTR(NFID)

DO NIS=1, NFID
COMPLEXFID(NIS)=DCMPLX(FID(NIS),0)
ENDDO

CALL DFFTCF (NFID, COMPLEXFID, COMPLEXFFTR)
DO NIS=1, NFID
FFTR(NIS)=(DREAL(COMPLEXFFTR(NIS)))
ENDDO

!Switch Positive and negtive freq part
DO ISWITCH=1, NFID/2
temps=FFTR(ISWITCH)
FFTR(ISWITCH)=FFTR(NFID/2+ISWITCH)
FFTR(NFID/2+ISWITCH)=temps
ENDDO
RETURN
END



SUBROUTINE Drawfft
    USE publicdat
    USE DFLIB

    INTEGER(2)    dummy,  i
    Real*8 maxdata,maxdata1,maxdata2, maxfid, locx, locy, increF, freq
    Real*8  Peak1, Peak2, Peakave
```

```
    INTEGER(4)    color
    TYPE (wxycoord)  wxy
! find maximum value of FFTR
   maxfid=0
   DO j=1, NFID
   IF (FFTR(j).GT.maxfid)THEN
   maxfid=FFTR(j)
   ENDIF
   ENDDO
maxfid=maxfid-FFTR(NFID)
! find maximum value in data, the region we are interested in
   maxdata1=0
   maxdata2=0
   DO j1=1, Ndata
       IF ((DataDis(1,j1).LT.(Espect+offset))
         .AND. (DataDis(1,j1).GT.(Bspect+offset))
         .AND. (DataDis(2,j1).GT.maxdata1))   THEN
           maxdata1= DataDis(2,j1)
           Peak1=DataDis(1,j1)
       ENDIF
       IF ((DataDis(1,j1).GT.(-Espect+offset))
         .AND. (DataDis(1,j1).LT.(-Bspect+offset))
         .AND.(DataDis(2,j1).GT.maxdata2))    THEN
           maxdata2= DataDis(2,j1)
           Peak2=DataDis(1,j1)
       ENDIF

   ENDDO
   maxdata=(maxdata1+maxdata2)*.5D0
   Peakave=0.5D0*(Peak1-Peak2)
   offset=-0.5D0*(Peak1+Peak2)
WRITE(*,"(A13,F8.4)") "Peak position:",Peakave

       status = SETWINDOW(.TRUE.,-Espect, -.1*maxdata , Espect, maxdata*1.45)
    freq=-1/(2*Tincr)

! RESIZE the FFTR
DO jr=1, NFID
  FFTR(jr)=(FFTR(jr)-FFTR(NFID))*maxdata/maxfid

END DO

!draw the data
status = SETCOLORRGB(#00FF00)
  locx  = DataDis(1,1)
  locy  = DataDis(2,1)
  CALL MOVETO_W( locx, locy,wxy )
  DO i2 = 1, Ndata
        locx  = DataDis(1,i2)
        locy  = DataDis(2,i2)
        dummy = LINETO_W ( locx, locy )
  END DO

!draw the fitting curve
status = SETCOLORRGB(#FF0000)
 locx  = freq
  locy  = FFTR(1)
  CALL MOVETO_W( locx, locy,wxy )
  freq=freq+1/(NFID*Tincr)
  DO i = 2, NFID
        locx  = freq
        locy  = FFTR(i)
        dummy = LINETO_W ( locx, locy )
     freq=freq+1/(NFID*Tincr)
   END DO



!Label Bspect and Esepct
status = SETCOLORRGB(#0000FF)
locx = Bspect+offset
length=.1*maxdata
```

```
CALL MOVETO_W( locx, 0D0,wxy  )
dummy = LINETO_W ( locx,length )
locx = Espect+offset
CALL MOVETO_W( locx, 0D0,wxy  )
dummy = LINETO_W ( locx, length)
locx = -Espect+offset
CALL MOVETO_W( locx, 0D0,wxy  )
dummy = LINETO_W ( locx, length)
locx = -Bspect+offset
CALL MOVETO_W( locx, 0D0,wxy  )
dummy = LINETO_W ( locx, length)

locx = SpecD+offset
CALL MOVETO_W( locx, 0D0,wxy  )
dummy = LINETO_W ( locx, length)
locx = -SpecD+offset
CALL MOVETO_W( locx, 0D0,wxy  )
dummy = LINETO_W ( locx, length)

!WRITE FFTR
increF=1/(NFID*Tincr)
OPEN(3,FILE="FFTR.txt")
freq=-1/(2*Tincr)
DO i3=1, NFID

WRITE(3,"(F16.9,F20.15)") freq,FFTR(i3)
freq=freq+increF
ENDDO
CLOSE(3)
RETURN
END


SUBROUTINE paths
USE publicdat
CHARACTER(255) temp

OPEN (3, FILE = 'file.txt',STATUS='OLD',IOSTAT=ios)
IF (ios .NE. 0) THEN

WRITE(*,*) "use the data.txt and ini.txt in loal directory. "
WRITE(*,*) "you can creat a file.txt including the file you want to display"
WRITE(*,*) "or it refer to the data.txt and ini.txt files in this folder."
RETURN
ENDIF
READ (3,*) temp

L=LEN_TRIM(temp)
WRITE(temp(L+1:150),"(A4)")'.txt'
datapath=temp
WRITE(temp(L+1:150),"(A7)")'ini.txt'
inipath=temp
close(3)
OPEN (2, FILE = datapath,STATUS='OLD',IOSTAT=ios)
IF (ios .NE. 0) THEN
WRITE(*,*) "data path is not correct. check file.txt"
STOP
ENDIF
close(2)

OPEN (2, FILE = inipath,STATUS='OLD',IOSTAT=ios)
IF (ios .NE. 0) THEN
WRITE(*,*) "ini file doest exist in the directory specified in file.txt. copy local directory ini.txt"
OPEN (3, FILE = inipath,STATUS='NEW')
OPEN (4, FILE = 'ini.txt',STATUS='OLD')
DO WHILE (.NOT. EOF(4) )
READ(4,"(A100)")temp
WRITE(3,"(A100)")temp
END DO
CLOSE(4)
CLOSE(3)
ENDIF
```

```
close(2)
WRITE(*,"(A10,A40,A15,A40)")"Data file:",datapath,"Initial file:",inipath
RETURN
END

!********************FREQENCY*******************************

SUBROUTINE FREQ(alpha,beita,FIDTEMP)
USE numerical_libraries
USE publicdat
COMPLEX(8) JUMPM(NK,NK),EVAL(NK),DIAGL(NK,NK),INVL(NK,NK)
COMPLEX(8) MATRIXB(NK,NK),EVALONE(NK), EVALTWO(NK)
REAL*8 alpha,beita
REAL*8 ak(NK),t,AA,BB,CC
REAL*8 FIDt,FIDTEMP(NFID)
REAL*8 aveVfreq,eta2
COMPLEX(8) EVALMATRIX(NK,NK),ENDM(NK,NK),CONENDM(NK,NK)


!Calculate A,B,C.

aveVfreq=-0.5*Vfreq*(1+eta)
eta2=Vfreq*0.25*(3-eta)/Szz

AA=(1.5*cos(theta0)*cos(theta0)-0.5)*(1.5*cos(beita)*cos(beita)-0.5)
   +0.75*sin(theta0)*sin(theta0)*sin(beita)*sin(beita)*cos(2*alpha)
   +0.75*sin(2*theta0)*sin(2*beita)*cos(alpha)
AA=2D0*PI*aveVfreq*AA
BB=0D0
CC=0.5*(1.5*cos(theta0)*cos(theta0)-0.5)*sin(beita)*sin(beita)
   +0.25*sin(theta0)*sin(theta0)*(1+cos(beita)*cos(beita))*cos(2*alpha)
   -0.25*sin(2*theta0)*sin(2*beita)*cos(alpha)
CC=2D0*PI*eta2*CC

!Define jump matrix
JUMPM=0D0
!the diagonal elements
JUMPM(1,1)=DCMPLX(0D0,AA)
JUMPM(2,2)=DCMPLX(DR,AA+CC)
DO IFREQ=3,NK
 JUMPM(IFREQ,IFREQ)=DCMPLX(((IFREQ-1)**2)*DR,AA)
END DO
!The tridiagonal elements
JUMPM(1,2)=DCMPLX(0D0,dsqrt(2D0)*BB)
JUMPM(2,1)=JUMPM(1,2)
DO IFREQ=2,NK-1
 JUMPM(IFREQ,IFREQ+1)=DCMPLX(0D0,BB)
END DO
DO IFREQ=3,NK
 JUMPM(IFREQ,IFREQ-1)=JUMPM(IFREQ-1,IFREQ)
END DO


JUMPM(1,3)=DCMPLX(0D0,dsqrt(2D0)*CC)
JUMPM(3,1)=JUMPM(1,3)
DO IFREQ=2,NK-2
 JUMPM(IFREQ,IFREQ+2)=DCMPLX(0D0,CC)
END DO
DO IFREQ=4,NK
 JUMPM(IFREQ,IFREQ-2)=JUMPM(IFREQ-2,IFREQ)
END DO
  DO IN=1, NK
     DO JN=1, NK
      JUMPM(IN,JN)=-JUMPM(IN,JN)
     END DO
  END DO

!write(*,*) AA,BB,CC,jumpm
!**********************set MATRIXB as utinity matrix, Initialize EVAL***********************
MATRIXB=0D0
EVAL=0D0
do uu=1,NK
```

```
MATRIXB(uu,uu)=1D0
enddo
!*****************************************************************************
!calculate the eignvalues and eigenvectors

CALL DGVCCG(NK,JUMPM,NK,MATRIXB,NK,EVALONE,EVALTWO,DIAGL,NK)   !!!EVAL are eigenvalues, DIAGL are eigenvectors.
do ttemp=1,NK
EVAL(ttemp)=EVALONE(ttemp)/EVALTWO(ttemp)
Enddo

!inverse DIAGL to INVL
CALL DLINCG (NK, DIAGL, NK, INVL, NK)

  DO IN=1, NK
   EVALMATRIX(IN,IN)=CDEXP(EVAL(IN)*DCMPLX(TAU))
  END DO
   ENDM=MATMUL(DIAGL,MATMUL(EVALMATRIX,INVL))
!Calculate the conjuate matrix of ENDM
  DO IN=1, NK
     DO JN=1, NK
      CONENDM(IN,JN)=CONJG(ENDM(IN,JN))
     END DO
  END DO
!Define the a0(0)=1, ak(0)=0 for k /= 0
ak=0D0
ak(1)=1D0


t=0
DO NIS=1, NFID

 FIDt=0
  DO IN=1, NK
   EVALMATRIX(IN,IN)=CDEXP(EVAL(IN)*DCMPLX(t+TAU))
  END DO

  ENDM=MATMUL(DIAGL,MATMUL(EVALMATRIX,INVL))
  ENDM=MATMUL(ENDM,CONENDM)

  DO IN=1, NK
     DO JN=1, NK
      FIDt=FIDt+DREAL(ENDM(IN,JN))*ak(JN)
     END DO
  END DO
FIDTEMP(NIS)=FIDt*Dexp(-0.5*(t*GB)**2-(t+2*tau)*RT)
t=t+Tincr
END DO
RETURN
END
```

In this program, the initial conditions and the experimental data form the input files, which are called by subroutines `ini` and `readdata`. Subroutine `FREQ(alpha,beita,FIDTEMP)` is the central part of the program and is used to calculate the value of $F(\theta_0, \alpha, \beta, t)$ in Eq. (4.38). In `FREQ(alpha,beita,FIDTEMP)`, the jump matrix `JUMPM` needs to be defined first. The eigenvalues and eigenvectors of this matrix are calculated using Fortran mathematical subroutines `DGVCCG` and `DLINCG`. Then $F(\theta_0, \alpha, \beta, t)$ can be constructed by matrix multiplication. In the main program we integrate $F(\theta_0, \alpha, \beta, t)$ over α and β, and the time domain signal `FID(tttemp)` is obtained, which represents $F(\theta_0, t)$ in Eq. (4.22). Finally the FID signal is Fourier transformed by `FFT` and the spectrum is plotted by `Drawfft` for comparing with the experimental data. The input file `ini.txt` is shown as an example

```
shift of data(KHz)=0.5
Defin peak region(begin)=20
Defin peak region(END)=150
Baseline Region= 100
```

```
range(deg.) = 360

T1 increment(ms) =0.0033
Tau(usec) =30
Vq freq(KHz)=133
order parameter=0.945
rotation angle(deg.)=0
eta=0.064
DR(RAD2*KHz) =7340
width(deg.)=11
relax term 1/T2(KHz)=3
Gauss B=9
```

and the input experimental data file `data.txt` is

```
Hz, Intensity, Freqency=61.421791, Temp.=360.0K 0deg
148867.015625    119575.656250
148719.062500    101001.593750
148571.093750    72605.062500
148423.140625    47778.718750
148275.156250    43021.125000

... ...

-148096.765625    62934.093750
-148244.734375    58810.312500
-148392.687500    117256.000000
-148540.656250    156963.375000
-148688.625000    115078.281250
```

A.2 Simulation of ^{2}H Dimer Line Shapes

The ^{2}H dimer powder line shapes are simulated using the following program:

```
MODULE publicdat
PARAMETER  PI=3.14159265358979238D0
PARAMETER NFID=256, NK=8  ! Nsite=2*NK+1
!phi0,theta0: the polar and azimuthul angle from the magnetic frame
! to the director frame.
!phi: the azimuthul angle from the C-D bond principle frame
!to the director frame.

!eta:biaxial parameter
!Tincr:time increment.
!Vfreq is (3/4) * NU_Q in khz
!************************************************
REAL*8 TAU,Tincr,phi,eta,RT,GB,range
REAL*8 betaV0
REAL*8 FID(NFID),Vfreq, FFTR(NFID),DR
INTEGER Ndata
INTEGER Nsite
REAL*8 DataDis(1:2,1:4096),offset, Specd
!Define spectrum region
REAL*8 Bspect, Espect
CHARACTER(255) datapath, inipath
PUBLIC::Bspect, Espect,Specd
PUBLIC:: Ndata, DataDis ,offset
PUBLIC:: TAU,FID,Tincr,Vfreq
END MODULE
```

```
PROGRAM Smain
USE publicdat
PARAMETER nsum=128
REAL*8 G0,phi0,theta0
REAL*8 avebetav0,varbetaV0
REAL*8 FIDTEMP(NFID)
integer tt, tttemp
eta=0
TAU=0
FID=0
Tincr=0.008
DR=10000.0D0
G0=1D0
Vfreq=40.0D0
RT=1
GB=1
Bspect=20
Espect=46
range=2*PI
Nsite=2*NK+1
!!
datapath='data.txt'
inipath='ini.txt'
CALL paths
CALL ini

do iphi=1,Nsum/2
temppeq=sqrt(betav0/PI)*exp(-betav0*(PI*iphi*2/Nsum)*(PI*iphi*2/Nsum))
if (temppeq .le. 0.01) then
range=(PI*iphi*2/Nsum)*2
exit
endif
enddo

write (*,*) "the range is", range*180/PI
Write (*,*) 'In the simulation we use Nsite=',Nsite,'   ', '
The corresponding jump angle is',(range/Nsite)*180/Pi,'degree'
OPEN(10,FILE="siminfo.txt")
write(10,*) "betaV0 is", betaV0
write(10,*) "the range is", range*180/PI
Write(10,*) 'In the simulation we use Nsite=',Nsite, '   ','
The corresponding jump angle is',(range/Nsite)*180/Pi,'degree'
close(10)

theta0=0

DO  JSum=1,Nsum/2+1
write(*,*) Jsum    !!!to check the running speed

phi0=0

DO Isum=1,Nsum/2+1
           CALL FREQ(phi0,theta0,FIDTEMP)

           DO tt=1,NFID
           tttemp=tt
               FID(tttemp)=FID(tttemp)+FIDTEMP(tttemp)*sin(theta0)
           ENDDO
phi0=phi0+2*PI/Nsum
ENDDO

theta0=theta0+2*PI/Nsum
ENDDO

CALL writefid
CALL FFT
CALL readdata
CALL Drawfft
END
```

```
SUBROUTINE writefid
USE publicdat
REAL*8 ttemp
OPEN(2,FILE="FID.txt")

ttemp=0D0
DO I=1, NFID

  WRITE(2,"(F16.9,F20.12)") ttemp,FID(I)
ttemp=ttemp+Tincr
ENDDO
CLOSE(2)
RETURN
END



SUBROUTINE ini
USE publicdat
REAL*8 temp_ini(20)
INTEGER test,L
CHARACTER(150) temp
WRITE(*,"(A40)") "-----------Initial Values------------"
OPEN (3, FILE = inipath,STATUS='OLD')
i1=0
DO WHILE (.NOT. EOF(3) )
   test=0
   READ (3,"(A150)") temp
   L=LEN(temp)
   IF (temp .NE." ") THEN
!  Search = number
      WRITE(*,"(A30)") temp
      test=0
      DO I=1,L
        IF (temp(I:I).EQ."=") THEN
            test=I+1

     EXIT
        END IF
      END DO
      IF (test.NE.0)THEN
        i1=i1+1
  READ(temp(test:L),*) temp_ini(i1)
      ENDIF
   END IF
END DO
IF (i1.NE.13) THEN
 WRITE(*,*) "ERROR_INITIAL VALUE NUMBERS,CHECK INI.TXT"
 STOP
ENDIF
WRITE(*,"(A40)") "-------------------------------------"
offset=temp_ini(1)
Bspect=temp_ini(2)
Espect=temp_ini(3)
Specd=temp_ini(4)

range=temp_ini(5)
TAU=temp_ini(6)
Tincr=temp_ini(7)
Vfreq=temp_ini(8)
betaV0=temp_ini(9)
eta=temp_ini(10)
DR=temp_ini(11)
RT=temp_ini(12)
GB=temp_ini(13)
range=range*PI/180
TAU=TAU*(1D-3)
CLOSE(3)
RETURN
END
```

```
SUBROUTINE Readdata
USE publicdat
integer Nspace, L
CHARACTER(100) temp
REAL*8 psum, pave,pn
OPEN (3, FILE = datapath,STATUS='OLD')

READ (3,"(A100)") temp
READ (3,"(A100)") temp
Ndata=0
L=LEN(temp)

DO WHILE (.NOT. EOF(3) )
   READ (3,"(A100)") temp

      DO I=1,L
        IF ((temp(I:I).EQ." ").OR.(temp(I:I).EQ." ")) THEN
            Nspace=I
            EXIT
        END IF
       ENDDO

   Ndata=Ndata+1
   READ(temp(1:Nspace),*)  DataDis(1,Ndata)
   READ(temp(Nspace:L),*)  DataDis(2,Ndata)
END DO
CLOSE(3)
! normalize the data, correct the base line
psum=0
 pn=0
DO II=1,Ndata
   DataDis(1,II)=DataDis(1,II)/1000D0
   DataDis(2,II)=DataDis(2,II)/100000D0
   IF (DABS(DataDis(1,II)).GT.SpecD) THEN
     Psum= Psum+DataDis(2,II)
     pn=pn+1
   END IF

ENDDO

Pave=Psum/pn

OPEN (2, FILE = 'dataout.txt')
DO II2=1,Ndata
DataDis(2,II2)=DataDis(2,II2)-Pave
DataDis(1,II2)=DataDis(1,II2)+offset
WRITE(2,"(F20.12,A5,F20.10)")DataDis(1,II2),"    ",DataDis(2,II2)
ENDDO
CLOSE(2)

RETURN
END

!************FFT and PLOT ROUTINES***************
SUBROUTINE FFT
USE publicdat
REAL*8 temps
INTEGER ISWITCH, NIS
COMPLEX(8)  COMPLEXFID(NFID), COMPLEXFFTR(NFID)

DO NIS=1, NFID
COMPLEXFID(NIS)=DCMPLX(FID(NIS),0)
ENDDO

!CALL DFFTCI (NFID, WFFTC)
!!CALL DF2TCF (NFID, COMPLEXFID, COMPLEXFFTR, WFFTC, CPY)
CALL DFFTCF (NFID, COMPLEXFID, COMPLEXFFTR)
DO NIS=1, NFID
FFTR(NIS)=(DREAL(COMPLEXFFTR(NIS)))
ENDDO
```

```
!Switch Positive and negtive freq part
DO ISWITCH=1, NFID/2
temps=FFTR(ISWITCH)
FFTR(ISWITCH)=FFTR(NFID/2+ISWITCH)
FFTR(NFID/2+ISWITCH)=temps
ENDDO
RETURN
END

SUBROUTINE Drawfft
    USE publicdat
    USE DFLIB

    INTEGER(2)    dummy,  i
    Real*8 maxdata,maxdata1,maxdata2, maxfid, locx, locy, increF, freq
    Real*8  Peak1, Peak2, Peakave

    INTEGER(4)    color
    TYPE (wxycoord)  wxy
! find maximum value of FFTR
   maxfid=0
   DO j=1, NFID
   IF (FFTR(j).GT.maxfid)THEN
   maxfid=FFTR(j)
   ENDIF
   ENDDO
maxfid=maxfid-FFTR(NFID)
! find maximum value in data, the region we are interested in
   maxdata1=0
   maxdata2=0
   DO j1=1, Ndata
       IF ((DataDis(1,j1).LT.(Espect+offset))
      .AND. (DataDis(1,j1).GT.(Bspect+offset))
      .AND.(DataDis(2,j1).GT.maxdata1))   THEN
           maxdata1= DataDis(2,j1)
           Peak1=DataDis(1,j1)
       ENDIF
       IF ((DataDis(1,j1).GT.(-Espect+offset))
      .AND. (DataDis(1,j1).LT.(-Bspect+offset))
      .AND.(DataDis(2,j1).GT.maxdata2))   THEN
           maxdata2= DataDis(2,j1)
           Peak2=DataDis(1,j1)
       ENDIF

   ENDDO
   maxdata=(maxdata1+maxdata2)*.5D0
   Peakave=0.5D0*(Peak1-Peak2)
   offset=-0.5D0*(Peak1+Peak2)
WRITE(*,"(A13,F8.4)") "Peak position:",Peakave

       status = SETWINDOW(.TRUE.,-Espect, -.1*maxdata , Espect, maxdata*1.45)
    freq=-1/(2*Tincr)

! RESIZe the FFTR
DO jr=1, NFID
  FFTR(jr)=(FFTR(jr)-FFTR(NFID))*maxdata/maxfid

END DO

!draw the data
status = SETCOLORRGB(#00FF00)
  locx  = DataDis(1,1)
  locy  = DataDis(2,1)
  CALL MOVETO_W( locx, locy,wxy )
  DO i2 = 1, Ndata
        locx  = DataDis(1,i2)
        locy  = DataDis(2,i2)
        dummy = LINETO_W ( locx, locy )
  END DO

!draw the fitting curve
status = SETCOLORRGB(#FF0000)
```

```
 locx  = freq
  locy  = FFTR(1)
  CALL MOVETO_W( locx, locy,wxy )
  freq=freq+1/(NFID*Tincr)
  DO i = 2, NFID
        locx  = freq
        locy  = FFTR(i)
        dummy = LINETO_W ( locx, locy )
     freq=freq+1/(NFID*Tincr)
   END DO



!Label Bspect and Esepct
status = SETCOLORRGB(#0000FF)
locx = Bspect+offset
length=.1*maxdata
CALL MOVETO_W( locx, 0D0,wxy  )
dummy = LINETO_W ( locx,length )
locx = Espect+offset
CALL MOVETO_W( locx, 0D0,wxy  )
dummy = LINETO_W ( locx, length)
locx = -Espect+offset
CALL MOVETO_W( locx, 0D0,wxy  )
dummy = LINETO_W ( locx, length)
locx = -Bspect+offset
CALL MOVETO_W( locx, 0D0,wxy  )
dummy = LINETO_W ( locx, length)

locx = SpecD+offset
CALL MOVETO_W( locx, 0D0,wxy  )
dummy = LINETO_W ( locx, length)
locx = -SpecD+offset
CALL MOVETO_W( locx, 0D0,wxy  )
dummy = LINETO_W ( locx, length)

!WRITE FFTR
increF=1/(NFID*Tincr)
OPEN(3,FILE="FFTR.txt")
freq=-1/(2*Tincr)
DO i3=1, NFID

WRITE(3,"(F17.9,F24.15)") freq,FFTR(i3)
freq=freq+increF
ENDDO
CLOSE(3)
RETURN
END


SUBROUTINE paths
USE publicdat
CHARACTER(255) temp

OPEN (3, FILE = 'file.txt',STATUS='OLD',IOSTAT=ios)
IF (ios .NE. 0) THEN

WRITE(*,*) "use the data.txt and ini.txt in loal directory. "
WRITE(*,*) "you can creat a file.txt including the file you want to display"
WRITE(*,*) "or it refer to the data.txt and ini.txt files in this folder."
RETURN
ENDIF
READ (3,*) temp

L=LEN_TRIM(temp)
WRITE(temp(L+1:150),"(A4)")'.txt'
datapath=temp
WRITE(temp(L+1:150),"(A7)")'ini.txt'
inipath=temp
close(3)
OPEN (2, FILE = datapath,STATUS='OLD',IOSTAT=ios)
IF (ios .NE. 0) THEN
```

```
WRITE(*,*) "data path is not correct. check file.txt"
STOP
ENDIF
close(2)
OPEN (2, FILE = inipath,STATUS='OLD',IOSTAT=ios)
IF (ios .NE. 0) THEN
WRITE(*,*) "ini file doest exist in the directory specified in file.txt. copy local directory ini.txt"
OPEN (3, FILE = inipath,STATUS='NEW')
OPEN (4, FILE = 'ini.txt',STATUS='OLD')
DO WHILE (.NOT. EOF(4) )
READ(4,"(A100)")temp
WRITE(3,"(A100)")temp
END DO
CLOSE(4)
CLOSE(3)
ENDIF
close(2)
WRITE(*,"(A10,A40,A15,A40)")"Data file:",datapath,"Initial file:",inipath
RETURN
END

!*********************FREQENCY*******************************

SUBROUTINE FREQ(phi0,theta0,FIDTEMP)
USE numerical_libraries
USE publicdat
COMPLEX(8) JUMPM(NSITE,NSITE),EVAL(NSITE),DIAGL(NSITE,NSITE),INVL(NSITE,NSITE)
COMPLEX(8) MATRIXB(Nsite,Nsite),EVALONE(NSITE), EVALTWO(NSITE)
REAL*8 Krate(0:Nsite+1,0:Nsite+1)
REAL*8 Dphi,phi0,theta0
REAL*8 Fre(NSITE),Pequ(NSITE),t,AA,BB
REAL*8 FIDt,FIDTEMP(NFID)
COMPLEX(8) EVALMATRIX(NSITE,NSITE),ENDM(NSITE,NSITE),CONENDM(NSITE,NSITE)

!Calculate all feqencies and possibility of equilibium distribution.
Dphi=range/Nsite
phi=-Dphi*NK
DO ii=1,NSITE
!write (*,*) phi*180/Pi
AA=1.5*((sin(theta0))**2)*((cos(phi0-phi))**2)-0.5
BB=0.5*eta*(((cos(theta0))**2)-((sin(theta0))**2)*((sin(phi0-phi))**2))
Fre(ii)=Vfreq*(AA+BB)
Pequ(ii)=dsqrt(betaV0/PI)*dexp(-betaV0*phi**2)   !!!equilibium distribution
phi=phi+Dphi

ENDDO

!*************Define the Rate constants for the jump diffusion**************
Num=(Nsite+1)/2
Krate=0D0
Krate(num,num+1)=DR/(Dphi)**2
Krate(num+1,num)=Krate(num,num+1)*Dexp(-betaV0*Dphi**2)
Do jj=num+1,Nsite-1
Krate(jj,jj+1)=2*DR/(Dphi)**2-Krate(jj,jj-1)
Krate(jj+1,jj)=krate(jj,jj+1)*Dexp(-2*betaV0*Dphi*(Dphi*(jj-num)+0.5*Dphi))
Enddo
Do jj=1,num-1
Krate(jj,jj+1)=Krate(Nsite+1-jj,Nsite-jj)
Krate(jj+1,jj)=Krate(Nsite-jj,Nsite-jj+1)
Enddo


!*****************Define jump matrix*****************************************
JUMPM=0D0
DO IFREQ=1,NSITE
JUMPM(IFREQ,IFREQ)=DCMPLX(-(Krate(IFREQ+1,IFREQ)+Krate(IFREQ-1,IFREQ)),-2*PI*Fre(IFREQ))
END DO
DO IFREQ=2,NSITE
JUMPM(IFREQ,IFREQ-1)=DCMPLX(Krate(IFREQ,IFREQ-1),0D0)
ENDDO
DO IFREQ=1,NSITE-1
JUMPM(IFREQ,IFREQ+1)=DCMPLX(Krate(IFREQ,IFREQ+1),0D0)
```

```
ENDDO


!**********************set MATRIXB as utinity matrix, Initialize EVAL***********************
MATRIXB=0D0
EVAL=0D0
do uu=1,nsite
MATRIXB(uu,uu)=1D0
enddo
!*******************************************************************************
!calculate the eignvalues and eigenvectors

CALL DGVCCG(NSITE,JUMPM,NSITE,MATRIXB,Nsite,EVALONE,EVALTWO,DIAGL,NSITE)
!EVAL are eigenvalues,DIAGL are eigenvectors.
do ttemp=1,nsite
EVAL(ttemp)=EVALONE(ttemp)/EVALTWO(ttemp)
Enddo

!inverse DIAGL to INVL
!write(*,*) "go"
CALL DLINCG (NSITE, DIAGL, NSITE, INVL, NSITE)                !!INVL=invers(X)

  DO IN=1, NSITE
   EVALMATRIX(IN,IN)=CDEXP(EVAL(IN)*DCMPLX(TAU))
  END DO
   ENDM=MATMUL(DIAGL,MATMUL(EVALMATRIX,INVL))
!Calculate the conjuate matrix of ENDM
  DO IN=1, NSITE
     DO JN=1, NSITE
      CONENDM(IN,JN)=CONJG(ENDM(IN,JN))
     END DO
  END DO

t=0
DO NIS=1, NFID

 FIDt=0
  DO IN=1, NSITE
   EVALMATRIX(IN,IN)=CDEXP(EVAL(IN)*DCMPLX(t+TAU))
  END DO

  ENDM=MATMUL(DIAGL,MATMUL(EVALMATRIX,INVL))
  ENDM=MATMUL(ENDM,CONENDM)

  DO IN=1, NSITE
     DO JN=1, NSITE
      FIDt=FIDt+DREAL(ENDM(IN,JN))*Pequ(JN)
     END DO
  END DO
FIDTEMP(NIS)=FIDt*Dexp(-0.5*(t*GB)**2-(t+2*tau)*RT)
t=t+Tincr
END DO
RETURN
END
```

Again there are input files `ini.txt` and `data.txt` for this program,which are similar to those of monomer line shape simulation. The simulated signal is also Fourier transformed and plotted using subroutines `FFT` and `Drawfft`, respectively. The subroutine `FREQ(phi0,theta0, FIDTEMP)` is used to calculate $F(\alpha, \beta, t)$ in Eq. (4.26), which is corresponding to `FIDTEMP` in the program. In the subroutine `FREQ(phi0,theta0,FIDTEMP)`, the jump rates `Krate` are firstly defined, then the jump matrix `JUMPM` is constructed based on Eq. (4.46). After the eigenvalues and eigenvectors of the matrix are calculated using subroutines `DGVCCG` and `DLINCG`, the signal `FIDTEMP` of certain orientation (α, β) is obtained. In the main program, `FIDTEMP` is integrated for different orientations and the simulated FID signal `FID(tttemp)` is obtained.

Appendix B

Simulation and Fitting Programs for 2D TGBA* Phase

To simulate the 2D spectrum in the TGBA* Phase, the Fortran program is shown as follows:

```
MODULE publicdat
PARAMETER  PI=3.141592653589793238D0
PARAMETER NFID=128, NSITE=14
!phi0 is the jump angle
!eta:biaxial parameter
!Tincr:time increment.
!Vfreq is (3/4) * NU_Q in khz
REAL*8 TAU,Tincr,range
REAL*8 FID2D(NFID,NFID), Vfreq, FFTR2D(NFID,NFID),GB,KJ,RT
INTEGER Ndata

!Define spectrum region
REAL*8 Bspect, Espect, eta
CHARACTER(255) inipath
PUBLIC::Bspect, Espect
PUBLIC:: Ndata
PUBLIC:: TAU,FID,Tincr,Vfreq,GB,RT
END MODULE

!*********************************************

PROGRAM Smain
USE publicdat
REAL*8 G0,alpha,beita,phi,T1
REAL*8 FIDTEMP(NFID)
INTEGER NSUM
NSUM=32
G0=1D0
Vfreq=40.0D0
!!
Bspect=20
Espect=46
range=2*PI
!!
inipath='tgbaini.txt'
CALL ini
T1=0D0
DO Jt=1,NFID
!************for 1 T1**********
write (*,*) Jt

beita=Pi/2
```

```
alpha=0
DO ksum=1,Nsum/2+1
phi=0
DO Isum=1, NSUM+1
CALL FREQ_PHI(alpha,beita,phi,T1,FIDTEMP)
DO It=1,NFID
 FID2D(Jt,It)=FID2D(Jt,It)+FIDTEMP(It)
ENDDO
phi=phi+2*PI/NSUM
END DO
alpha=alpha+2*PI/Nsum
ENDDO
!*****************************

T1=T1+Tincr
END DO
CALL FFT
CALL writesep
CALL Drawfft
WRITE(*,*)"frequency range:",1/(2*Tincr)
END


SUBROUTINE writesep
USE publicdat
REAL*8 ttemp
OPEN(2,FILE="FIDCOS.txt")
  DO IN = 1, NFID
      WRITE(2,"(256F28.8)") (FFTR2D(IN,JN), JN=1,NFID)
  ENDDO
CLOSE(2)
RETURN
END



SUBROUTINE ini
USE publicdat
REAL*8 temp_ini(20)
INTEGER test,L
CHARACTER(150) temp
WRITE(*,"(A40)") "-----------Initial Values------------"
OPEN (3, FILE = inipath,STATUS='OLD')
i1=0
DO WHILE (.NOT. EOF(3) )
   test=0
   READ (3,"(A150)") temp
   L=LEN(temp)
   IF (temp .NE." ") THEN
      WRITE(*,"(A30)") temp
      test=0
      DO I=1,L
        IF (temp(I:I).EQ."=") THEN
            test=I+1
     EXIT
        END IF
       END DO
       IF (test.NE.0)THEN
         i1=i1+1
  READ(temp(test:L),*) temp_ini(i1)
      ENDIF
   END IF
END DO
IF (i1.NE.10) THEN
 WRITE(*,*) "ERROR_INITIAL VALUE NUMBERS,CHECK INI.TXT"
 STOP
ENDIF
WRITE(*,"(A40)") "-------------------------------------"
TAU=temp_ini(1)
Tincr=temp_ini(2)
GB=temp_ini(3)
Vfreq=temp_ini(4)
```

```
Bspect=temp_ini(5)
Espect=temp_ini(6)
KJ=temp_ini(7)
range=temp_ini(8)
eta=temp_ini(9)
RT=temp_ini(10)
range=range*pi/180.0

CLOSE(3)
RETURN
END

!**************FFT and PLOT ROUTINES***************
SUBROUTINE FFT
USE publicdat
REAL*8 temps,BASL,FFTR(NFID)
INTEGER ISWITCH, NIS
COMPLEX(8)  COMPLEXFID(NFID), COMPLEXFFTR(NFID)
!**************FFT at T2 domain*****************

DO  IN=1, NFID

DO NIS=1, NFID
COMPLEXFID(NIS)=DCMPLX(FID2D(IN,NIS),0)
ENDDO


CALL DFFTCF (NFID, COMPLEXFID, COMPLEXFFTR)
DO NIS=1, NFID
FFTR(NIS)=(DREAL(COMPLEXFFTR(NIS)))
ENDDO

!Switch Positive and negtive freq part
DO ISWITCH=1, NFID/2
temps=FFTR(ISWITCH)
FFTR(ISWITCH)=FFTR(NFID/2+ISWITCH)
FFTR(NFID/2+ISWITCH)=temps
ENDDO

DO JN=1, NFID
!BASLine correction
FFTR2D(IN,JN)=FFTR(JN)-(FFTR(1)+FFTR(NFID))/2D0
END DO

END DO

!*************FFT at T1 domain***************

DO  IN=1, NFID

DO NIS=1, NFID
COMPLEXFID(NIS)=DCMPLX(FFTR2D(NIS,IN),0)
ENDDO

CALL DFFTCF (NFID, COMPLEXFID, COMPLEXFFTR)
DO NIS=1, NFID
FFTR(NIS)=(DREAL(COMPLEXFFTR(NIS)))
ENDDO

!Switch Positive and negtive freq part
DO ISWITCH=1, NFID/2
temps=FFTR(ISWITCH)
FFTR(ISWITCH)=FFTR(NFID/2+ISWITCH)
FFTR(NFID/2+ISWITCH)=temps
ENDDO

DO JN=1, NFID
FFTR2D(JN,IN)=FFTR(JN)-(FFTR(1)+FFTR(NFID))/2D0
END DO

END DO
!times 10 for very value
```

```
DO  IN=1, NFID
   DO NIS=1, NFID
   FFTR2D(NIS,IN)=FFTR2D(NIS,IN)*10D0
   ENDDO
ENDDO
RETURN
END

SUBROUTINE Drawfft
    USE publicdat
    USE DFLIB

    INTEGER(2)    dummy,  i
    Real*8  maxfid, minfid,locx, locy, increF, freq1,freq2
    Real*8  width

    INTEGER(4)    color
    TYPE (wxycoord)  wxy
  maxfid=0
  minfid=0
  DO IN = 1, NFID
     DO JN = 1, NFID
     IF (FFTR2D(IN,JN).GT.maxfid) THEN
     maxfid=FFTR2D(IN,JN)
     ENDIF
     IF (FFTR2D(IN,JN).LT.minfid) THEN
     minfid=FFTR2D(IN,JN)
     ENDIF


  ENDDO
  ENDDO
  WRITE(*,*)maxfid,minfid
  width=Espect/NFID

    status = SETWINDOW(.TRUE.,-Espect, -Espect, Espect, Espect)
    freq1=-1/(2*Tincr)

  DO IN = 1, NFID
    freq2=-1/(2*Tincr)
    DO JN = 1, NFID
        color=INT(1000000*FFTR2D(IN,JN)/maxfid)
        locx  = freq1
        locy  = freq2
         status = SETCOLORRGB(color)
       dummy = RECTANGLE_W( $GFILLINTERIOR, locx-width, locy-width, locx+width, locy+width )

     freq2=freq2+1/(NFID*Tincr)
   END DO
    freq1=freq1+1/(NFID*Tincr)
  END DO
RETURN
END


!***************FREQENCY******************


SUBROUTINE FREQ_PHI(alpha,beita,Phi,T1,FIDTEMP)
USE numerical_libraries
USE publicdat
COMPLEX(8) JUMPM(NSITE,NSITE),EVAL(NSITE),DIAGL(NSITE,NSITE),INVL(NSITE,NSITE)
REAL*8 Phi,Fre(NSITE),t,distr,cosbeta,T1
REAL*8 conv,FIDt,FIDTEMP(NFID)
real*8 alpha, beita, aveVfreq, AA, BB1, BB2
COMPLEX(8) EVALMATRIX(NSITE,NSITE),ENDM(NSITE,NSITE),ENDMT2(NSITE,NSITE),
           ENDMMIX(NSITE,NSITE),ENDMT1(NSITE,NSITE)

Fre=0
!Calculate all feqencies.
DO ii=1,NSITE
aveVfreq=0.5*Vfreq
```

```
AA=-(1+eta)*(1.5*cos(beita)*cos(beita)-0.5)
BB=0.5*(3-eta)*sin(beita)*sin(beita)*cos(2*(alpha-phi))
Fre(ii)=aveVfreq*(AA+BB)
phi=phi+range/Nsite
ENDDO

!Define jump matrix for the mixing time
JUMPM=0
DO IFREQ=1,NSITE
 JUMPM(IFREQ,IFREQ)=DCMPLX(-2D0*KJ)
ENDDO
JUMPM(1,Nsite)=DCMPLX(KJ)
JUMPM(Nsite,1)=DCMPLX(KJ)
DO IFREQ=2,NSITE
 JUMPM(IFREQ,IFREQ-1)=DCMPLX(KJ)
ENDDO
DO IFREQ=1,NSITE-1
 JUMPM(IFREQ,IFREQ+1)=DCMPLX(KJ)
ENDDO
!calculate the eignvalues and eigenvectors
CALL DEVCCG(NSITE,JUMPM,NSITE,EVAL,DIAGL,NSITE)
!inverse DIAGL to INVL
CALL DLINCG (NSITE, DIAGL, NSITE, INVL, NSITE)

  DO IN=1, NSITE
   EVALMATRIX(IN,IN)=CDEXP(EVAL(IN)*DCMPLX(TAU))
  END DO
   ENDMMIX=MATMUL(DIAGL,MATMUL(EVALMATRIX,INVL))


!Define jump matrix
JUMPM=0
DO IFREQ=1,NSITE
 JUMPM(IFREQ,IFREQ)=DCMPLX(-2D0*KJ,-2*PI*Fre(IFREQ))
ENDDO
JUMPM(1,Nsite)=DCMPLX(KJ)
JUMPM(Nsite,1)=DCMPLX(KJ)
DO IFREQ=2,NSITE
 JUMPM(IFREQ,IFREQ-1)=DCMPLX(KJ)
ENDDO
DO IFREQ=1,NSITE-1
 JUMPM(IFREQ,IFREQ+1)=DCMPLX(KJ)
ENDDO
!calculate the eignvalues and eigenvectors
CALL DEVCCG(NSITE,JUMPM,NSITE,EVAL,DIAGL,NSITE)
!inverse DIAGL to INVL
CALL DLINCG (NSITE, DIAGL, NSITE, INVL, NSITE)
  DO IN=1, NSITE
   EVALMATRIX(IN,IN)=CDEXP(EVAL(IN)*DCMPLX(T1))
  END DO
   ENDMT1=MATMUL(DIAGL,MATMUL(EVALMATRIX,INVL))
!take real part
 DO IN=1, NSITE
  DO JN=1, NSITE
   ENDMT1(IN,JN)=DCMPLX(DREAL(ENDMT1(IN,JN)))
  ENDDO
ENDDO

t=0
DO NIS=1, NFID
  DO IN=1, NSITE
   EVALMATRIX(IN,IN)=CDEXP(EVAL(IN)*DCMPLX(t))
  END DO
   ENDMT2=MATMUL(DIAGL,MATMUL(EVALMATRIX,INVL))

  ENDM=MATMUL(ENDMT2,MATMUL(ENDMMIX,ENDMT1))

 FIDt=0
  DO IN=1, NSITE
     DO JN=1, NSITE
      FIDt=FIDt+DREAL(ENDM(IN,JN))
```

```
     END DO
  END DO
!line broading function
conv=DEXP(-0.5*(t*GB)**2-0.5*(T1*GB)**2-t*RT-T1*RT)
FIDTEMP(NIS)=FIDt*conv
t=t+Tincr
END DO
END
```

In this program the time domain signal is firstly calculated in t_2 dimension by subroutine `FREQ_PHI(alpha,beita,Phi,T1,FIDTEMP)`, then the 2D signal `FID2D(Jt,It)` is obtained in the main program. After Fourier transformation for both dimensions, the simulated spectrum is obtained. The the typical input file for this program is

```
mixtime(ms) = 3
T1 increment(ms) =0.02
Gaussion Broading= 0.1
Vq frequency=6.5
Defin peak region(begin)=0
Defin peak region(END)=25
Jump rate(KHz)=7.5
range (deg)=360
eta=0
RT=2
```

Appendix C

Simulation and Fitting Programs for Dipolar Splittings to Obtain the Order Parameters

To simulate dipolar splittings in the 2D SLF spectrum and get the order parameters, the Fortran program is shown as follows:

```
MODULE publicdat
PARAMETER NA=6,MA=7
PARAMETER Pi=3.141592654
PUBLIC:: NA, MA,Pi
REAL Rch ,Rcc,Dch,ANGL1,ANGL2
INTEGER num_c
CHARACTER(20) name(50),type(50)
REAL split(50,2),temp_p(NA,2)
PUBLIC ::Rch,Rcc,Dch, ANGL1,ANGL2,name, orient,num_c,split,temp_p,type
END MODULE

!*****************************************
PROGRAM globals
USE publicdat
REAL*8 Y(MA),P(MA,NA)
REAL*8 X(NA)
REAL*8 FTOL

Rch=1.09
Rcc=1.4
Dch=30.19
ANGL1=60
ANGL2=60

OPEN (5, FILE = 'result.txt')
CALL ini
CALL Readpeak

DO ini_i=1,MA
   DO ini_j=1,NA
      P(ini_i,ini_j)=temp_p(ini_j,1)
   END DO
END DO
   DO ini_j2=1,NA
      P(ini_j2+1,ini_j2)=temp_p(ini_j2,2)
   END DO
  FTOL=0.001
   DO M1=1,4
      FTOL=FTOL/10
```

```
        DO J=1,MA
             DO I=1, NA
                X(I)=P(J,I)
             END DO
             Y(J)= FUNC(X)
        ENDDO
   CALL AMOEBA(P,Y,NA,FTOL)
   ENDDO

   CALL WRITEDATA(P,Y)
close(5)
END

!*****************************************
SUBROUTINE WRITEDATA(P,Y)
   USE publicdat
   REAL*8 P(MA,NA),Y(MA),OUT(NA)
   CHARACTER*256 temp
   INTEGER begins
   DO I=1, NA
      OUT(I)=0
DO J=1,MA
  OUT(I)=OUT(I)+P(J,I)
      ENDDO
  OUT(I)=OUT(I)/MA
   END DO
begins=1
 DO I=1,num_c
begins=I*8-7
   WRITE(temp(begins:255),*)name(I)
 ENDDO
WRITE(5,"(A150)")temp
WRITE(5,*) "Experimental splitting"
 DO I=1,num_c
begins=I*8-7
   WRITE(temp(begins:255),*)(split(I,1)-split(I,2))/1000
 ENDDO
WRITE(5,"(A150)")temp
WRITE(5,*) "Theoretical splitting"
DO I=1,num_c
   begins=I*8-7
   WRITE(temp(begins:255),*)GETSPLIT(OUT,I,type(I))
 ENDDO
WRITE(5,"(A150)")temp
WRITE(5,*) "S  (Sxx-Syy)1, (Sxx-Syy)2  Phi1   Phi2  Phi3"
WRITE(5,*)OUT
WRITE(5,*) "The error square is "
WRITE(5,*)FUNC(OUT)
END

!*****************************************
  FUNCTION FUNC(X)
    USE publicdat
    REAL*8 X(NA)
    REAL*8 sumsg,temp2
      sumsg=0
  DO I=1,num_c
       temp2=GETSPLIT(X,I,type(I))-(split(I,1)-split(I,2))/1000
       sumsg=sumsg+temp2**2
  END DO
    FUNC=sumsg
    RETURN
 END

  FUNCTION GETSPLIT(X,I,ctype)
   USE publicdat
    INTEGER I
    CHARACTER(20) ctype
    REAL*8 X(NA)
    REAL*8 p2,pxx
    REAL Rtemp,ang1,ang2,Rcht,split1,split2
```

```
      ang1=ANGL1+X(4)
      ang2=ANGL2+X(6)
      ang3=ANGL1
      ang4=ANGL2+X(5)
      Rcht=Rch

 SELECT CASE (ctype)
  CASE ("A1")
       p2=3*cos(ang1*Pi/180)**2-1
       pxx=sin(ang1*Pi/180)**2
       split1=(Dch/(Rcht**3))*(p2*X(1)+pxx*X(2))
       Rtemp=sqrt(Rcht**2+Rcc**2-2*cos((180-ang2)*Pi/180)*Rcht*Rcc)
       pxx=(Rcht*sin(ang2*Pi/180)/Rtemp)**2
       p2=2-3*pxx
       split2= (Dch/(Rtemp**3))*(p2*X(1)+pxx*X(2))

       GETSPLIT=SQRT(split1**2+split2**2)

  CASE ("B1")
       Rtemp=sqrt(Rcht**2+Rcc**2-2*cos((ang1+60)*Pi/180)*Rcht*Rcc)
       pxx=((1.732*Rcc/2+Rcht*sin(ang1*Pi/180))/Rtemp)**2
       p2=2-3*pxx
       GETSPLIT=ABS((Dch/(Rtemp**3))*(p2*X(1)+pxx*X(2)))*sqrt(2.0)
  CASE ("A2")
       p2=3*cos(ang2*Pi/180)**2-1
       pxx=sin(ang2*Pi/180)**2
       split1=(Dch/(Rcht**3))*(p2*X(1)+pxx*X(2))
       Rtemp=sqrt(Rcht**2+Rcc**2-2*cos((180-ang1)*Pi/180)*Rcht*Rcc)
       pxx=(Rcht*sin(ang1*Pi/180)/Rtemp)**2
       p2=2-3*pxx
       split2= (Dch/(Rtemp**3))*(p2*X(1)+pxx*X(2))

       GETSPLIT=SQRT(split1**2+split2**2)

  CASE ("B2")
       Rtemp=sqrt(Rcht**2+Rcc**2-2*cos((ang2+60)*Pi/180)*Rcht*Rcc)
       pxx=((1.732*Rcc/2+Rcht*sin(ang2*Pi/180))/Rtemp)**2
       p2=2-3*pxx
       GETSPLIT=ABS((Dch/(Rtemp**3))*(p2*X(1)+pxx*X(2)))*sqrt(2.0)
  CASE ("A3")
       p2=3*cos(ang3*Pi/180)**2-1
       pxx=sin(ang3*Pi/180)**2
       split1=(Dch/(Rcht**3))*(p2*X(1)+pxx*X(3))
       Rtemp=sqrt(Rcht**2+Rcc**2-2*cos((180-ang4)*Pi/180)*Rcht*Rcc)
       pxx=(Rcht*sin(ang4*Pi/180)/Rtemp)**2
       p2=2-3*pxx
       split2= (Dch/(Rtemp**3))*(p2*X(1)+pxx*X(3))

       GETSPLIT=SQRT(split1**2+split2**2)

  CASE ("B3")
       Rtemp=sqrt(Rcht**2+Rcc**2-2*cos((ang3+60)*Pi/180)*Rcht*Rcc)
       pxx=((1.732*Rcc/2+Rcht*sin(ang3*Pi/180))/Rtemp)**2
       p2=2-3*pxx
       GETSPLIT=ABS((Dch/(Rtemp**3))*(p2*X(1)+pxx*X(3)))*sqrt(2.0)
  CASE ("A4")
       p2=3*cos(ang4*Pi/180)**2-1
       pxx=sin(ang4*Pi/180)**2
       split1=(Dch/(Rcht**3))*(p2*X(1)+pxx*X(3))
       Rtemp=sqrt(Rcht**2+Rcc**2-2*cos((180-ang3)*Pi/180)*Rcht*Rcc)
       pxx=(Rcht*sin(ang3*Pi/180)/Rtemp)**2
       p2=2-3*pxx
       split2= (Dch/(Rtemp**3))*(p2*X(1)+pxx*X(3))

       GETSPLIT=SQRT(split1**2+split2**2)

  CASE ("B4")
       Rtemp=sqrt(Rcht**2+Rcc**2-2*cos((ang4+60)*Pi/180)*Rcht*Rcc)
       pxx=((1.732*Rcc/2+Rcht*sin(ang4*Pi/180))/Rtemp)**2
       p2=2-3*pxx
       GETSPLIT=ABS((Dch/(Rtemp**3))*(p2*X(1)+pxx*X(3)))*sqrt(2.0)
```

```
   CASE DEFAULT
       WRITE(*,*)"THE CARBORN TYPE IS ERROR CHECK IT:",type(I)
       STOP
  END SELECT
 RETURN
END


!************* Read the initial values**************************

SUBROUTINE ini
USE publicdat
INTEGER test,L
CHARACTER(100) temp
OPEN (3, FILE = 'ini.txt',STATUS='OLD')
i1=0
DO WHILE (.NOT. EOF(3) )
  READ (3,"(A100)") temp
IF (temp .NE." ") THEN
i1=i1+1
READ(temp,*)temp_p(i1,1),temp_p(i1,2)
ENDIF
END DO
  IF (i1 .NE. NA ) THEN
    WRITE(*,*) "ERROR_INITIAL VALUE NOT EQAL" ,NA,"CHECK INI.TXT", i1
    STOP
   ENDIF
CLOSE(3)


WRITE(5,*)"++++++++++++++++++++++FITING SPLIT PEAKS(SLF) ++++++++++++++++++++++++"
WRITE(5,*)"Initial value: S  (Sxx-Syy)1, (Sxx-Syy)2  Phi1   Phi2  Phi3 (Chang from top line to bottom line)"
DO tempi=1,2
 DO disp_i=1,NA
   WRITE(temp(disp_i*8-7:100),"(F7.2)") temp_p(disp_i,tempi)
 END DO
 WRITE(5,"(A50)")temp
END DO
WRITE(5,*)"++++++++++++++++++++++++++++++++++++++++++++++++++++++++++++++++++++++"
RETURN
END


!************Read all the peak value from peaks.txt ******************
!*********read name, split and orient of every peak to three arrays*******
SUBROUTINE Readpeak
USE publicdat
CHARACTER(256) temp

OPEN (1, FILE = 'peaks.txt')
num_c=1
READ (1,"(A100)") temp
WRITE(5,"(A100)") temp
DO WHILE (.NOT. EOF(1) )
     READ (1,"(A255)") temp
 IF (temp .EQ. " ") THEN
 EXIT
 ENDIF
      READ(temp,*) name(num_c),type(num_c), split(num_c,1),split(num_c,2)
10     FORMAT(A6,A6,F11.3,F11.3,F9.3)
      WRITE(5,10) name(num_c),type(num_c),split(num_c,1),split(num_c,2)
    split(num_c,1)=split(num_c,1)/0.816
    split(num_c,2)=split(num_c,2)/0.816
      num_c=num_c+1
END DO
  num_c=num_c-1
CLOSE(1)
RETURN
END

!*****************************************
    SUBROUTINE AMOEBA(P,Y,NDIM,FTOL)
```

```
IMPLICIT INTEGER (I-N)
IMPLICIT REAL*8 (A-H,O-Z)
PARAMETER (NMAX=13,ALPHA=1.0D00,BETA=0.5D00)
PARAMETER (GAMMA=2.0D00,ITMAX=500)
DIMENSION P(NDIM+1,NDIM),Y(NDIM+1)
REAL*8 PR(NMAX),PRR(NMAX),PBAR(NMAX)
MPTS=NDIM+1
ITER=0
1 ILO=1
IF(Y(1).GT.Y(2))THEN
  IHI=1
  INHI=2
ELSE
  IHI=2
  INHI=1
ENDIF
DO I=1,MPTS
  IF(Y(I).LT.Y(ILO)) ILO=I
  IF(Y(I).GT.Y(IHI))THEN
    INHI=IHI
    IHI=I
  ELSE IF(Y(I).GT.Y(INHI))THEN
    IF(I.NE.IHI) INHI=I
  ENDIF
        ENDDO
RTOL=2.0D00*DABS(Y(IHI)-Y(ILO))/(DABS(Y(IHI))+DABS(Y(ILO)))
IF(RTOL.LT.FTOL)RETURN
IF(ITER.EQ.ITMAX) THEN
  write(6,*) 'Amoeba exceeding maximum iterations.'
  write(6,*) 'EXITING AMOEBA'
  go to 44
ENDIF
ITER=ITER+1
DO J=1,NDIM
  PBAR(J)=0.0D00
ENDDO
DO I=1,MPTS
  IF(I.NE.IHI)THEN
    DO J=1,NDIM
      PBAR(J)=PBAR(J)+P(I,J)
    ENDDO
  ENDIF
ENDDO
DO J=1,NDIM
  PBAR(J)=PBAR(J)/NDIM
  PR(J)=(1.0D00+ALPHA)*PBAR(J)-ALPHA*P(IHI,J)
ENDDO
YPR=FUNC(PR)

IF(YPR.LE.Y(ILO))THEN
  DO J=1,NDIM
    PRR(J)=GAMMA*PR(J)+(1.0D00-GAMMA)*PBAR(J)
  ENDDO
  YPRR=FUNC(PRR)
  IF(YPRR.LT.Y(ILO))THEN
    DO J=1,NDIM
      P(IHI,J)=PRR(J)
    ENDDO
    Y(IHI)=YPRR
  ELSE
    DO J=1,NDIM
      P(IHI,J)=PR(J)
    ENDDO
    Y(IHI)=YPR
  ENDIF
ELSE IF(YPR.GE.Y(INHI))THEN
  IF(YPR.LT.Y(IHI))THEN
    DO J=1,NDIM
      P(IHI,J)=PR(J)
    ENDDO
    Y(IHI)=YPR
  ENDIF
```

```
  DO J=1,NDIM
    PRR(J)=BETA*P(IHI,J)+(1.0D00-BETA)*PBAR(J)
  ENDDO
  YPRR=FUNC(PRR)
  IF(YPRR.LT.Y(IHI))THEN
    DO J=1,NDIM
      P(IHI,J)=PRR(J)
    ENDDO
    Y(IHI)=YPRR
  ELSE
    DO I=1,MPTS
      IF(I.NE.ILO)THEN
DO J=1,NDIM
  PR(J)=0.5D00*(P(I,J)+P(ILO,J))
  P(I,J)=PR(J)
        ENDDO
        Y(I)=FUNC(PR)
      ENDIF
    ENDDO
  ENDIF
ELSE
  DO J=1,NDIM
    P(IHI,J)=PR(J)
  ENDDO
  Y(IHI)=YPR
ENDIF

GO TO 1
44    CONTINUE
    END
```

The typical input files for this program are `ini.txt`

```
0.62    0.67
-0.03   0
-0.03   0
0       1
0       1
0       1
```

and `peaks.txt`

```
name type peak1     peak2
C5    B4  1281.22   -1225.19
C6    A4  2066.47   -2016.85
C7    A3  2317.76   -2268.13
C8    B3  1218.40   -1168.78
C9    B2  1218.40   -1168.78
C10   A2  2317.76   -2268.13
C11   A1  2286.35   -2236.72
C12   B1  1249.81   -1200.19
```